University of Glasgow

Mahmoud, Mohamed Hosny Elsayed (2026) *Exploring the potential of red mud and naturally occurring materials for water treatment: sustainable strategies for the effective removal of antibiotics.* PhD thesis.

https://theses.gla.ac.uk/85706/

Copyright and moral rights for this work are retained by the author

A copy can be downloaded for personal non-commercial research or study, without prior permission or charge

This work cannot be reproduced or quoted extensively from without first obtaining permission from the author

The content must not be changed in any way or sold commercially in any format or medium without the formal permission of the author

When referring to this work, full bibliographic details including the author, title, awarding institution and date of the thesis must be given

Enlighten: Theses
https://theses.gla.ac.uk/
research-enlighten@glasgow.ac.uk

University of Glasgow

Exploring the potential of red mud and naturally occurring materials for water treatment: sustainable strategies for the effective removal of antibiotics

Mohamed Hosny Elsayed Mostafa Mahmoud

Submitted in fulfillment of the requirements for the Degree of Doctor of Philosophy

School of Chemistry

College of Science and Engineering

University of Glasgow

September 2025

Abstract

Amidst growing concerns over water pollution and the continuous discharge of pharmaceuticals (e.g., antibiotics) into water bodies worldwide, addressing sustainable wastewater treatment techniques has become a pressing priority. In addition, today's world faces numerous issues such as resource depletion, water shortage, soil pollution, increased demand for energy, and other critical problems. Therefore, it is essential to use waste materials that could be of potential benefit in such applications. These waste materials are generally classified into natural and industrial (man-made) wastes. One of these industrial waste materials is red mud, which is the main byproduct of the aluminium production industry whether using the Bayer or sintering processes. Red mud causes many environmental issues including water and soil pollution because of its high alkalinity. In addition, dry and wet storage of red mud is not effective because of red mud leaching into soil and groundwater. Therefore, as outlined in this study, three different samples of red mud from India and China were used to extract valuable metal oxides such as titania (TiO_2) and haematite (α-Fe_2O_3) to be used in the adsorption of ceftriaxone and doxycycline, which are common antibiotics discharged into water systems. Red mud samples were investigated and the extracted metal oxides were proved to be more efficient.

α-Fe_2O_3 is also easily and ecofriendly synthesized using *Typha latifolia* (*T. latifolia*), which is a cosmopolitan plant species that causes serious environmental issues when dominating ecosystems, and therefore there is great value in making use of the excessive biomass of this plant. Additionally, TiO_2 was prepared in a more conventional way using titanium tetraisopropoxide and water. A comparative study between the efficacy of the two metal oxides and their commercial counterparts, which were used as a benchmark, in removing the two antibiotics from model and the River Clyde water samples was undertaken in this work. The impregnation and doping effects using different dopants were also investigated.

Biogenic iron oxide (BIOX) constitutes another waste material that is produced naturally by *Leptothrix* bacteria, and it holds significant potential in environmental management. These naturally derived materials offer a sustainable and eco-friendly substitute for synthetic iron oxides, with promising applications in water purification, pollution control, and resource recovery. Pristine, calcined, and BIOX materials reduced under different gas mixtures were investigated in this study. The effect of seasonal variation on the efficiency of BIOX materials

was also covered. Additionally, the catalytic effect of BIOX and red mud-based iron oxides was tested for ammonia synthesis.

Table of Contents

Abstract ……1

List of figures……...9

List of schemes…….23

List of tables……...24

List of equations……..25

List of abbreviations…….....27

Acknowledgements……..28

Author's declaration…….29

1. Introduction…….....30

1.1. Treatment and removal techniques of antibiotics …….....34

1.2. Materials used in the removal of antibiotics…….…….37

1.3. The environmental issues of *T. latifolia* and its potential in water treatment …….……..40

1.4. The Bayer Process, the release of red mud, and its challenges and opportunities ……41

1.5. Properties, applications, and preparation methods of TiO_2 and its extraction from red mud……46

1.5.1. TiO_2 preparation methods……48

1.5.2. Extraction techniques of TiO_2 from red mud ……..50

1.6. Extraction of iron and iron-containing minerals from red mud……..51

1.6.1. Iron oxides and oxy(hydroxides)…….51

1.6.2. Extraction techniques of iron and iron oxides from red mud……..54

1.6.3. Haematite and its use as a catalyst……...56

1.7. Biogenic iron oxide and its potential applications……..58

1.8. The Haber-Bosch process of ammonia synthesis using iron-based catalysts and its challenges ……59

1.9. Project aims…….61

2. Materials and methods……...62

2.1. Chemicals and reagents……...62

2.2. Preparation of *T. latifolia* extract……62

2.3. Preparation of titania and its composites……63

2.4. Green synthesis of haematite……..64

2.5. Extraction of TiO_2 from red mud……66

2.6. Extraction of α-Fe_2O_3 from red mud……...69

2.7. Biogenic iron oxide samples collection and preparation of 2-line ferrihydrite……..71

2.8. Reduction and calcination of BIOX and 2-line ferrihydrite samples…….73

2.9. Testing the catalytic activity of iron oxide-based waste materials and their composites in the ammonia synthesis process……..75

2.10. Collection of a water sample from the River Clyde…..……....76

2.11. Characterization techniques…….77

2.12. The photocatalytic degradation of CEF and DOXY……..……..78

2.13. Adsorption of CEF and DOXY using different adsorbents…….79

2.14. Determination of the ionic strength and the interfering ion effect……..…….....84

2.15. Regeneration of the representative adsorbent materials……...84

2.16. The catalytic degradation of CEF through Fenton degradation and photocatalysis by 5 % Fe 5% Cu-TiO_2 ……85

2.17. Determination of the point of zero charge (PZC) of all adsorbents by salt addition method……86

2.18. Synthesis of calcium alginate beads and reduced BIOX 1-bead composite…….87

2.19. Potentiometric titration to quantify the concentration of basic and acidic surface sites of different samples……88

2.20. Determination of nitrate leaching in water samples…….88

2.21. Determination of sulfate release in water samples from the photodegradation of CEF……89

2.22. Determination of nitrite release in water samples from the photodegradation of CEF and DOXY……90

3. The investigation of lab-prepared TiO_2, red mud-derived TiO_2, and different α-Fe_2O_3 samples in the removal of CEF……..……..………….92

3.1. Introduction……....92

3.2. Powder XRD analysis of different α-Fe_2O_3, TiO_2, and red mud samples……..93

3.3. FTIR analysis of *T. latifolia* and its green synthesized α-Fe_2O_3……...100

3.4. BET analysis of different α-Fe_2O_3, TiO_2 samples, and composites of TiO_2 extracted from the Chinese red mud by the acid baking method……..……...101

3.5. SEM and EDX analysis of TiO_2 extracted from the Chinese red mud by the acid baking and the alkali roasting methods…….……. .105

3.6. The photolysis of CEF……..109

3.7. Identification of the degradation products of CEF powder using TGA-MS……....113

3.8. Identification of CEF and DOXY degradation products in water using the turbidimetric and the Griess reagent methods……...116

3.9. Removal of CEF by α-Fe_2O_3, TiO_2, and TiO_2 composites……....119

3.9.1. Self-degradation and Speciation of CEF over different pH levels…..……...119

3.9.2. A comparison between the efficiency of different α-Fe_2O_3 and TiO_2 samples in CEF adsorption……135

3.9.3. A comparison between the red mud-derived TiO_2 and α-Fe_2O_3 samples, and the effect of using different metals on the adsorption efficiency…….137

3.10. Catalytic and photocatalytic degradation of CEF……..…….148

3.11. Role of nitrate in the adsorption of CEF using 5% Fe 5% Cu-TiO_2……...153

3.12. Effect of initial concentration of CEF, adsorbent dose, stirring rate, and time on CEF adsorption using 5% Fe 5% Cu-TiO_2……...156

3.13. Recycling and Application of 5% Fe 5% Cu-TiO_2 in the adsorption of CEF from tap, Clyde River, and real wastewater samples……..159

3.14. ICP-OES analysis of CEF aqueous solutions…….……160

3.15. Determination of nitrate leaching from 5% Fe 5% Cu-TiO_2……. 162

3.16. Adsorption mechanism of CEF by TiO_2 composites……. 163

3.17. The effect of ionic strength and interfering ions……169

3.18. The effect of temperature on the adsorption efficiency and the adsorption isotherms...172

3.19. The scalability and selectivity of 5% Fe 5% Cu-TiO_2……176

3.20. The economic analysis of producing TiO_2 and 5% Fe 5% Cu-TiO_2……..……182

3.21. Conclusions……184

4. Exploring the applicability of red mud-derived TiO_2 and α-Fe_2O_3 in the removal of doxycycline…….186

4.1. Introduction……...186

4.2. Powder XRD analysis of red mud-derived α-Fe_2O_3……..……..……186

4.3. Investigating the efficiency of red mud, red mud-extracted TiO_2 and α-Fe_2O_3, and commercial TiO_2 and α-Fe_2O_3 in adsorbing DOXY species……...188

4.4. EDX and SEM analysis of red mud-derived α-Fe_2O_3 …….……199

4.5. Investigation of DOXY self-degradation and photolysis, and identification of potential degradation products……201

4.5.1. The photolysis of DOXY under UV light, the photocatalytic activity of α-Fe_2O_3 and TiO_2, and the effect of temperature on DOXY stability……..203

4.5.2. Identification of potential degradation products of DOXY powder…….....209

4.6. Economic cost analysis of α-Fe_2O_3 production…….212

4.7. The environmental considerations of extracting α-Fe_2O_3 and TiO_2 from red mud……..213

4.8. Conclusions……..214

5. Transforming biogenic iron oxide into zero-valent iron for sustainable removal of antibiotics from water.…….……215

5.1. Introduction……...215

5.2. Powder XRD analysis of BIOX and 2-line ferrihydrite samples……...……...215

5.3. BET analysis of BIOX and 2-line ferrihydrite…….....225

5.4. SEM and EDX analysis of BIOX and 2-line ferrihydrite…….227

5.5. The investigation of BIOX and 2-line ferrihydrite materials in the removal of DOXY..……237

5.5.1. Investigating the effect of initial concentration of DOXY, adsorbent dose, stirring rate, adsorption time on the removal of DOXY, and recycling of reduced BIOX 1……..…….242

5.5.2. The adsorption isotherms of DOXY adsorption using reduced BIOX 1…….…..250

5.5.3. The effect of ionic strength and interfering ions on the adsorption efficiency of reduced BIOX 1……251

5.5.4. Investigation of DOXY removal mechanism…….……...255

5.5.5. The economic and the environmental analyses of using reduced BIOX materials in the removal of DOXY……262

5.5.6. The scalability and selectivity of reduced BIOX 1……265

5.6. The investigation of BIOX and 2-line ferrihydrite materials in CEF removal…….266

5.7. Conclusions……...269

6. Testing BIOX and red mud-based iron oxides in ammonia synthesis using the Haber-Bosch process……270

6.1. Introduction……...270

6.2. Testing the catalytic activity of iron oxide-based waste materials and their composites in the ammonia synthesis process……270

6.3. Conclusions……...276

7. Conclusions and future recommendations…….....……...277

References……..…….…….....280

Appendices…..…….……300

Appendix 1……...300

Appendix 2……....302

Appendix 3……....313

Appendix 4……....349

Appendix 5……....360

List of figures

Fig 1.1. The number of publications related to the antibiotics' removal from wastewater in different countries (**a**) over the last 36 years (**b**). Data obtained from Scopus [34]……..34

Fig 1.2. The most common techniques used for the removal of antibiotics from wastewater…….36

Fig 1.3. The most common materials are used for the removal of antibiotics from wastewater including biochar, activated carbon, graphene, etc……..40

Fig 1.4. The global alumina production in 2023 showing the biggest contributing countries of red mud waste into the environment [94]…….……42

Fig 1.5. The mechanism of photocatalytic degradation of organic pollutants using TiO_2 [126] in which the electrons travel from the valance band to the conduction band leaving behind holes in the valance band upon the absorption of UV light by TiO_2. These photogenerated holes and electrons result in forming hydroxyl and superoxide radicals, respectively, that degrade organic pollutants…….47

Fig 1.6. The three natural crystalline phases of TiO_2 are anatase (tetragonal), rutile (tetragonal), and brookite (orthorhombic) [131] with copyright permission from Elsevier…..48

Fig 1.7. TEM images of the synthesized (**a**) spherical, (**b**) rod-like, and (**c**) wire-like TiO_2 nanoparticles at pH 8.5, pH 10.5, and pH 10.5 after adding ethylenediamine (shape controller), respectively, [134] with permission from the American Chemical Society…….……..49

Fig 1.8. The various iron-containing minerals in red mud……..……..52

Fig 1.9. Crystal structure and crystallographic data of haematite (**a**), magnetite (**b**), and maghemite (**c**). Fe^{2+} (black), Fe^{3+} (green), and O^{2-} (red) [146]. The crystal structure shows the orthorhombic unit cell and the 3D structure of goethite **(d)** [147] with permission from Springer Nature. The crystal structure of siderite, where the orange polyhedral is trigonally distorted (elongated along c-axis) $Fe^{2+}O_6$-octahedra and the violet triangles are CO_3 groups **(e)** [148] with a copyright permission from Springer Nature…….....53

Fig 2.1. A photo of the Possil Marsh site where the samples of *T. Latifolia* were collected on the 22nd April 2022……..……..63

Fig 2.2. TGA profile of the dehydration of $Fe(OH)_3$ to α-Fe_2O_3 under 2% oxygen in argon mixture using a ramp rate of 10 °C per minute from room temperature to 550 °C followed by an isothermal hold at 550 °C for three hours to show the mass loss in mg as a function of temperature °C (**a**) and time in minutes (**b**). Powder XRD pattern of α-Fe_2O_3 produced from the dehydration of $Fe(OH)_3$ during the TGA analysis (**c**)……..66

Fig 2.3. Three sites in the River Allander; first site **(a)**, pond **(b)**, and crag **(c, d, e, f,** and **g)**, where the biogenic iron oxide samples were collected. The samples collected during the summertime (**a**-**c**) and those collected during the winter (**d**-**g**)……...……..73

Fig 2.4. A schematic representation of the reactor used in the reduction of BIOX samples either under pure H_2 or H_2/N_2 mixture for different times and temperatures……....74

Fig 2.5. A simplified diagram of the reduction programmes used to reduce BIOX to reduced BIOX materials at different times and temperatures either under pure H_2 or H_2/N_2…….75

Fig 2.6. The area where a water sample was collected from the River Clyde, particularly near Kelvingrove Park, in the West End, Glasgow, the United Kingdom on the 29th July 2024 (**a**), and on the 10th February 2025 (**b**)……...……..77

Fig 2.7. The reactors used in the photocatalytic degradation of CEF and DOXY under UV (**a**) and visible light (**b**).……...79

Fig 2.8. The calibration curve of CEF **(a)** and DOXY **(b)** using different concentrations starting from 15 and 25 ppm, respectively, up to 100 ppm…….....80

Fig 2.9. The adsorption efficiency of CEF using 5% Fe 5% Cu-TiO_2. [C_o = 25 ppm, pH 3, stirring rate = 800 rpm, T = 20 ± 2 °C, volume = 20 mL, and dose = 0.01 g]……...81

Fig 2.10. The removal efficiency of DOXY after 90 minutes using Chinese RM-derived TiO_2. [C_o = 25 ppm, pH 9, stirring rate = 750 rpm, T = 20 ± 2 °C, volume = 20 mL, and dose = 0.01 g]…….82

Fig 2.11. The UV-Vis spectrum after using BIOX (pond) material at pH 5 in DOXY adsorption in the wavelength range of 200-450 nm **(a)** and 200-800 nm **(b)**……..……..83

Fig 2.12. The determination of the PZC of reduced BIOX material (1h 700 °C H_2/N_2) using the salt addition method by measuring the change in the pH after 24 hours of stirring……86

Fig 2.13. The UV-Vis spectrum of the calibration curve of the yellow-coloured 5-nitro salicylic acid chromophore **(a)**, and the images of the standard solutions of NO_3^--N in the range of 0.1 to 5 ppm after the formation of the chromophore **(b)**……89

Fig 2.14. The calibration curve of different sulfate concentrations ranging from 10 to 1000 ppm **(a)** and the corresponding images of these concentrations **(b)**……..90

Fig 2.15. The UV-Vis spectrum of the calibration curve of different nitrite concentrations (in the form of potassium nitrite) ranging from 0.1 to 4 ppm **(a)** and the corresponding images of these concentrations **(b)**…….91

Fig 3.1. Powder XRD pattern of commercial **(a)**, green synthesized **(b)**, and lab-prepared α-Fe_2O_3 (**c**), commercial P25 **(d)** [202], lab-prepared TiO_2 **(e)**. The patterns show high crystallinity of commercial α-Fe_2O_3 and TiO_2 due to their bigger domain size compared to their prepared counterpart samples……...95

Fig 3.2. Powder XRD patterns of Chinese red mud **(a)**, TiO_2 extracted from Chinese red mud by the alkali roasting method **(b)**, and by the acid baking method **(c)**, (**a**, **b**, and **c** from [202]) This figure indicates the presence of multiple mineral phases in the raw red mud, whereas the TiO_2 extracted via the acid baking method exhibits a potentially purer crystalline phase composition, as evidenced by its fewer unidentified reflections……...97

Fig 3.3. Powder XRD patterns Indian red mud RM 7 **(a)**, TiO_2 extracted from Indian RM 7 by the alkali roasting method **(b)**, and by the acid baking method **(c)**, where the anatase phase was clearer as more well defined TiO_2 reflections were observed along with fewer reflections of other minerals in the acid baking-extracted sample……...98

Fig 3.4. Powder XRD pattern of Indian red mud RM 8 **(a)**, and TiO_2 extracted from Indian RM8 by the alkali roasting method **(b)**, and by the acid baking method **(c)**. showing similar results to TiO_2 extracted from the other red mud samples…….……99

Fig 3.5. Powder XRD patterns of 5% Fe 5% Cu-TiO_2 **(a)** extracted from Chinese red mud by the acid baking method [202], and copper nitrate trihydrate salt **(b)**…….. ……....100

Fig 3.6. FTIR spectra of *T. latifolia* powder dried at 60° C **(a)**, 150° C **(b)**, 300° C **(c)**, and green synthesized α-Fe_2O_3 **(d)** showing the decreasing intensity of OH band by increasing the temperature and evaporating more water content from *T. latifolia* powder……101

Fig 3.7. Nitrogen physisorption isotherms of commercial **(a)**, red mud-derived (**b**), and green synthesized α-Fe_2O_3 **(c)**, and P25 (**d**), lab-prepared TiO_2 **(e)**, and TiO_2 extracted from Chinese RM by the acid baking method **(f)**. (**d** and **f** from [202])……...104

Fig 3.8. SEM images and EDX spectra of by the alkali roasting method-derived TiO_2 **(a-h)** showing their flake-like morphology with tapered needles…….107

Fig 3.9. SEM images and EDX spectra of TiO_2 extracted by the acid baking method **(a-h)** showing their irregular morphology and indicating a potentially higher purity than TiO_2 extracted by the alkali roasting method……...109

Fig 3.10. The degradation of CEF under UV light (photolysis) at pH 3 at 10 cm **(a)**, 5 cm **(b)**, and at pH 7 at 5 cm **(c)**. [C_o = 25 ppm, stirring rate = 800 rpm, T = 20 ± 2 °C, and volume = 20 mL]……...111

Fig 3.11. LC-MS results of CEF solution before (**a**) and after UV degradation (**b**)…….....112

Fig 3.12. TGA and derivative weight profile of CEF powder (**a**) and the mass spectrum ion curve for 2 m/z (**b**), 16 (**c**), 17 (**d**), 18 (**e**), 30 (**f**), 34 (**g**), 43 (**h**), 44 (**i**), 45 (**j**), 32 (**k**), and 64 (**l**)……..116

Fig 3.13. The images of the released sulfate in the form of a turbid solution of barium sulfate after the photodegradation of 25 **(a)**, 200 **(b)**, and 500 ppm **(c)** CEF under UV light, and the control experiments of DW **(d)**, and 5% Fe 5% Cu-TiO_2 **(e)**……..117

Fig 3.14. The UV-Vis spectra of the nitrite released after the photodegradation of 25 and 200 ppm CEF along with the control experiments of DW and 5% Fe 5% Cu-TiO_2 **(a)**, 25, 100, and 500 ppm DOXY along with the control experiments of DW and reduced BIOX 1 **(b)**, the images of different concentrations of DOXY solutions **(c)**, and 25 ppm CEF before and after the photodegradation **(d)**……..119

Fig 3.15. FTIR spectra of CEF powder from the batch that showed self-degradation in acidic conditions at pH 2, 3, and 4 (**a**), and the powder from the batch that did not show self-degradation (**b**)…….121

Fig 3.16. The UV-Vis spectra of control experiments of CEF solutions at pH 2 **(a-b)**, pH 3 **(c-d)**, pH 4 **(e-f)**, pH 5 **(g)**, pH 7 **(h)**, pH 9 **(i)**, and pH 11 **(j)**. [C_o = 25 ppm, stirring rate = 800 rpm, T = 20 ± 2 °C, and volume = 20 mL]……..124

Fig 3.17. Chromatographic parts of LC-MS results of CEF solutions before and after the self-degradation at pH 2 (**a-b**), pH 3 (**c-d**), and pH 4 (**e-f**) to investigate the self-degradation of CEF……..127

Fig 3.18. LC-MS results of CEF solution before and after self-degradation at pH 3 (**a-b**) indicating that the release of gaseous products occurs during the degradation process, which get converted to undesired products such as sulfates and nitrites……128

Fig 3.19. The structure of CEF ($C_{18}H_{18}N_8O_7S_3$) highlighting the major functional groups (large circles) and the specific atoms within those groups that undergo protonation or deprotonation as a function of pH (small circles) [202]……..……130

Fig 3.20. The proposed structures of CEF at pH 2 where the nitrogen atom attached to the methyl group in hydroxytriazinone and the amine group in the aminothiazole ring are protonated and the overall surface charge is positive (cationic form) (**a**), 2.37 < pH ≤ 3 where the carboxylic group is deprotonated and the overall charge is less positive (cationic form) (**b**), 3 < pH < 3.5 where the amine deprotonates and goes back to the neutral form and the overall charge becomes almost zero (Zwitterionic form) (**c**), 4.21 < pH < 10.74 where the protonated nitrogen atom gets deprotonated and becomes neutral and the charge becomes negative (anionic form) (**d**), and pH > 10.74 where the amide group might deprotonate and the overall charge becomes more negative (anionic form) (**e**). These CEF ($C_{18}H_{18}N_8O_7S_3$) forms were derived from [202]...……133

Fig 3.21. Zeta potential measurements of aqueous CEF solutions at pH 2 where the nitrogen atom attached to the methyl group in hydroxytriazinone and the amine group in the aminothiazole ring are protonated and the overall charge becomes 4.6 mV (**a**), pH 3 where the OH of the carboxylic group is deprotonated and the charge is 2.5 mV (**b**), pH 3.5 (**c**) and pH 4 (**d**) where the amine group deprotonates and the surface charge becomes -0.3 mV and -1.4

mV, respectively, pH 5 (**e**) where the protonated nitrogen atom gets deprotonated, and the charge becomes -16.3 mV and decreases to -17.2 mV at pH 7 (**f**) and -19.5 mV at pH 9 (**g**), and at pH 11 where the NH of the amide group can deprotonate and the charge drops to -22.2 mV (**h**)…….135

Fig 3.22. A comparison between the CEF adsorption efficiency of commercial **(a)**, and green synthesized α-Fe_2O_3 **(b)**, and lab-prepared TiO_2 **(c)**. [C_o = 25 ppm, stirring rate = 800 rpm, T = 20 ± 2 °C, volume = 20 mL, and dose = 0.01 g]……136

Fig 3.23. A comparison between the adsorption efficiency of TiO_2 extracted by the acid baking method from RM 7 **(a)**, RM 8 **(b)**, and Chinese red mud **(c)**, and TiO_2 extracted by the alkali roasting method from RM 7 **(d)**, RM 8 **(e)**, and Chinese red mud **(f)**, and the removal efficiency of Chinese red mud-derived α-Fe_2O_3 **(g)** and lab-prepared α-Fe_2O_3 **(h)**. [C_o = 25 ppm, stirring rate = 800 rpm, T = 20 ± 2 °C, volume = 20 mL, and dose = 0.01 g]. (**c** and **f** from [202])……...139

Fig 3.24. The UV-Vis spectrum of CEF after using TiO_2 extracted from the three red mud samples by the alkali roasting method. [C_o = 25 ppm, pH = 3, stirring rate = 800 rpm, T = 20 ± 2 °C, volume = 20 mL, and dose = 0.01 g]……..140

Fig 3.25. CEF adsorption efficiency by 10% Co-TiO_2 **(a)**, 10% Ni-TiO_2 **(b)**, and 10% Zn-TiO_2 **(c)** using TiO_2 extracted from Chinese RM by the acid baking method. [C_o = 25 ppm, stirring rate = 800 rpm, T = 20 ± 2 °C, volume = 20 mL, and dose = 0.01 g] [202]……....141

Fig 3.26. CEF adsorption efficiency by 2% Cu-TiO_2 **(a)**, 5% Cu-TiO_2 **(b)**, 10% Cu-TiO_2 **(c)**, 2% Fe-TiO_2 **(d)**, 5% Fe-TiO_2 **(e)**, 10% Fe-TiO_2 **(f)**, 5% Fe 5% Cu-TiO_2 **(g)**, and CEF adsorption capacity by 5% Fe 5% Cu-TiO_2 **(h)** using TiO_2 extracted from Chinese RM by the acid baking method. [C_o = 25 ppm, stirring rate = 800 rpm, T = 20 ± 2 °C, volume = 20 mL, and dose = 0.01 g] [202]……..144

Fig 3.27. Control (blank) experiments of CEF removal efficiency by $Fe(NO_3)_3$ **(a)**, $Co(NO_3)_2$ **(b)**, $Ni(NO_3)_2$ **(c)**, $Cu(NO_3)_2$ **(d)**, and $Zn(NO_3)_2$ **(e)** in aqueous solutions of CEF [C_o = 25 ppm, stirring rate = 800 rpm, T = 20 ± 2 °C, volume = 20 mL, and dose = 0.01 g]. (**a** and **d** from [202])..…….146

Fig 3.28. The UV-Vis spectrum of the aqueous solution of 0.002 M $Fe(NO_3)_3$…….146

Fig 3.29. The catalytic degradation efficiency of CEF species by 5% Fe 5% Cu-TiO_2 using H_2O_2 across the pH scale 3-11 **(a)**, control experiments of CEF degradation efficiency by H_2O_2 across the same pH range **(b)**, and the photocatalytic effect of 5% Fe 5% Cu-TiO_2 under UV light at pH 7 **(c)**. [C_o = 25 ppm, stirring rate = 800 rpm, T = 20 ± 2 °C, volume = 20 mL, and dose = 0.01 g]. (**a** and **b** from [202])……149

Fig 3.30. The photocatalytic activity of P25 **(a-c)**, and lab-prepared TiO_2 **(d)** in CEF degradation under UV light. [C_o = 25 ppm, pH = 7, stirring rate = 800 rpm, T = 20 ± 2 °C, volume = 20 mL, and dose = 0.01 g]……...151

Fig 3.31. CEF solutions with pH levels fom 3 to 11 before **(a)**, and after adding TiO_2 on two different colored backgrounds **(b-c)**……152

Fig 3.32. The photocatalytic activity of commercial **(a)** and Chinese red mud-derived α-Fe_2O_3 **(b)** in CEF degradation under visible light. [C_o = 25 ppm, pH = 7, stirring rate = 800 rpm, T = 20 ± 2 °C, volume = 20 mL, and dose = 0.01 g]……153

Fig 3.33. The adsorption efficiency of calcined 5% Fe 5% Cu-TiO_2 **(a)**, 5% Fe 5% Cu-TiO_2 prepared using commercial α-Fe_2O_3 and CuO **(b)**, the control (blank) experiment of commercial α-Fe_2O_3 **(c),** commercial CuO **(d),** and commercial α-Fe_2O_3 and CuO **(e)**. [C_o = 25 ppm, stirring rate = 800 rpm, T = 20 ± 2 °C, volume = 20 mL, and dose = 0.01 g]……155

Fig 3.34. Powder XRD patterns of 5% Fe 5% Cu-TiO_2 after calcination **(a)** and after CEF adsorption at pH 3 **(b)**. [C_o = 25 ppm, stirring rate = 800 rpm, T = 20 ± 2 °C, volume = 20 mL, and dose = 0.01 g]. The difference in the intensity between **Fig 3.34.a** and **b** is simply due to variations in how the samples were packed on the sample holder, which is a very common occurrence in XRD measurements……...156

Fig 3.35. Effect of variation in initial concentration of CEF **(a)** [pH = 7, stirring rate = 800 rpm, T = 20 ± 2 °C, and dose = 0.01 g]**,** dose **(b)** [C_o = 25 ppm, pH = 7, stirring rate = 800 rpm, and T = 20 ± 2 °C], stirring rate **(c)** [C_o = 25 ppm, pH = 7, T = 20 ± 2 °C, and dose = 0.01 g], and time effect [C_o = 25 ppm, pH = 7, stirring rate = 800 rpm, T = 20 ± 2 °C, and dose = 0.01 g] **(d)** on the efficacy of 5% 5% Cu-TiO_2. CEF adsorption in tap water **(e)** [202], the River Clyde water collected on 29th July 2024 **(f)** [C_o = 25 ppm, stirring rate = 800 rpm, T = 20 ± 2 °C, volume = 20 mL, and dose = 0.01 g], and recycling of 5% Fe 5% Cu-TiO_2 after

75 minutes (**g**) [C_o = 25 ppm, stirring rate = 800 rpm, T = 20 ± 2 °C, volume = 20 mL, pH = 7, and dose = 0.01 g]……..…...159

Fig 3.36. The concentration of leached iron **(a)** and copper **(b)** from 5% Fe 5% Cu-TiO_2 as determined by ICP-OES analysis. [C_o = 25 ppm, stirring rate = 800 rpm, T = 20 ± 2 °C, volume = 20 mL, and dose = 0.01 g] [202]……..161

Fig 3.37. The initial screening of DW **(a)** and the River Clyde water samples collected on the 29th July 2024 **(b)** and the 10th February 2025 **(c)** using ICP-OES…….162

Fig 3.38. The UV-Vis spectra of the 5-nitro salicylic acid chromophore in fresh **(a)** and one year-old 5% Fe 5% Cu-TiO_2 samples **(b)** indicating very low levels of nitrate leaching from both sample sets and confirming their safe applicability in water treatment……...163

Fig 3.39. FTIR spectra of CEF powder **(a)**, 5% Fe 5% Cu-TiO_2 before **(b)**, and after CEF adsorption **(c)**……...164

Fig 3.40. XPS spectra of 5% Fe 5% Cu-TiO_2 including Cu 2p before **(a)**, and after CEF adsorption **(b)**, Fe 2p before **(c)**, and after CEF adsorption **(d)**, Ti 2p before **(e)**, and after CEF adsorption **(f)**, N 1s before **(g)**, and after CEF adsorption **(h)**…….……167

Fig 3.41. TGA and derivative weight profile of 5% Fe 5% Cu-TiO_2 prior to (**a**) and after 50 ppm CEF adsorption at pH 7 (**b**) indicating higher mass loss after CEF adsorption……...168

Fig 3.42. The effect of different concentrations of NaCl **(a)**, Ca^{2+} ($CaCl_2$) **(b)**, Ca^{2+} (CaO) **(c)**, Mg^{2+} (MgO) **(d)**, Si(IV) (amorphous SiO_2) **(e)**, and SO_4^{2-} **(f)** on the adsorption efficiency of 5% Fe 5% Cu-TiO_2. [C_o = 25 ppm, pH = 7, volume = 20 mL, dose = 0.01 g, stirring rate = 800 rpm, and T = 20 ± 2 °C]……...171

Fig 3.43. The temperature effect on the adsorption efficiency of 5% Fe 5% Cu-TiO_2 at 20 °C (**a**), 25 °C (**b**), 30 °C (**c**), 35 °C (**d**), and the control experiments at the same temperatures (**e-h**). [C_o = 25 ppm, pH = 7, volume = 20 mL, dose = 0.01 g, and stirring rate = 800 rpm]…...174

Fig 3.44. Effect of variation in initial concentration of CEF **(a),** Linear adsorption isotherm plots of Langmuir (**b**) and Freundlich (**c**) of CEF adsorption by 5% Fe 5% Cu-TiO_2. [pH = 7, stirring rate = 800 rpm, and dose = 0.01 g]. The two plots look very linear, but Langmuir

isotherm model better fits the experimental results because of its slightly higher adjusted R^2 value (0.99)……..176

Fig 3.45. The scalability test of 5% Fe 5% Cu-TiO_2 in adsorbing CEF in 100 mL using 0.05 g (**a**) and 1000 mL using 0.5 g (**b**) using the same solid-to-liquid ratio (0.5 g/L) and the same initial concentration of CEF. [C_o = 25 ppm, pH 7, stirring rate = 800 rpm, T = 20 ± 2 °C]…177

Fig 3.46. The removal efficiency of 5% Fe 5% Cu-TiO_2 toward DOXY in single-batch mode and in presence of CEF (**a**), the self-degradation of DOXY and in presence of CEF (**b**), the UV-Vis spectrum of the control experiment of DOXY & CEF at pH 9 (**c**), the spectrum of the actual experiment at pH 9 (**d**), and the control experiment of copper nitrate with DOXY (**e**) after 90 minutes. [C_o = 25 ppm, volume = 20 mL, dose = 0.01 g, stirring rate = 800 rpm, and T = 20 ± 2 °C]……..180

Fig 3.47. The chromatographic parts of the LC-MS spectra of blank CEF and DOXY solutions at pH 3 (**a**), pH 5 (**c**), and the same solutions but after the adsorption using 5% Fe 5% Cu-TiO_2 at the same pH levels with the same order (**b**, and **d**) after 90 minutes. [C_o = 25 ppm, volume = 20 mL, dose = 0.01 g, stirring rate = 800 rpm, and T = 20 ± 2 °C]…….182

Fig 4.1. Powder XRD pattern of red mud-derived α-Fe_2O_3 with a domain size of 20 nm showing the main reflections similar to those observed in commercial α-Fe_2O_3……187

Fig 4.2. The structure of DOXY species showing its three dissociation constants (pKa) at pKa1 = 3.02, pKa2 = 7.97, and pKa3 = 9.15……..189

Fig 4.3. Proposed speciation of DOXY structures at different pH levels to show the net positive charge (cationic form) at pH ≤ 3, the Zwitterionic structure at 3.02 < pH < 7, the net negative charge (anionic form) at 7 ≤ pH ≤ 9.15, and the more negative charge (anionic form) at pH ≥ 9.15…….191

Fig 4.4. Zeta potential measurements of aqueous solutions of DOXY with a net positive charge (7.6 mV) at pH 3 due to the protonation of the nitrogen atom of the dimethyl amine group (**a**), an almost zero charge (Zwitterionic from -0.2 mV) at pH 5 because of the deprotonation of the hydroxyl group (**b**), a net negative charge of -15.0 mV at pH 7 due to the deprotonation of the phenolic OH group (**c**), a more negative charge (-18.5 mV) at pH 9 resulting from the deprotonation of the nitrogen atom (**d**), and -26.4 mV pH 11 (**e**)……..192

Fig 4.5. The speciation of DOXY as a function of pH [276] showing the change of the overall surface charge of DOXY species from the cationic to the Zwitterionic and then to the anionic form by increasing the pH of the solution……...193

Fig 4.6. Control experiments of the pH effect on the self-degradation of DOXY at pH 9 **(a)** and pH 11 **(b)** for 14.5 months. [C_o = 25 ppm, volume = 20 mL, stirring rate = 750 rpm, T = 20 ± 2 °C]……..195

Fig 4.7. A comparison between the efficiency of pristine red mud **(a)**, P25 **(b)**, commercial α-Fe_2O_3 **(c)**, red mud-derived TiO_2 **(d)**, and red mud-derived α-Fe_2O_3 **(e)** in removing DOXY after 90 minutes. [C_o = 25 ppm, stirring rate = 750 rpm, T = 20 ± 2 °C, volume = 20 mL, and dose = 0.01 g]……...196

Fig 4.8. The UV-Vis spectra of pristine red mud **(a)**, commercial α-Fe_2O_3 **(b)**, red mud-derived TiO_2 **(c)**, and red mud-derived α-Fe_2O_3 **(d)** in adsorbing DOXY. [C_o = 25 ppm, pH = 7, stirring rate = 750 rpm, T = 20 ± 2 °C, volume = 20 mL, and dose = 0.01 g]…….197

Fig 4.9. The efficiency of red mud-derived α-Fe_2O_3 under visible light that contained both α-Fe_2O_3 and Fe_3O_4 in removing DOXY (**a**) its powder XRD pattern (**b**), and the removal efficiency of commercial Fe_3O_4 after 90 minutes (**c**), which was used as a control test. [C_o = 25 ppm, stirring rate = 750 rpm, T = 20 ± 2 °C, volume = 20 mL, and dose = 0.01 g]……199

Fig 4.10. SEM images **(a, c, e, g,** and **h)** and EDX spectra of α-Fe_2O_3 **(b, d,** and **f)** show high iron content compared to the other components. The images revealed clusters of rod-shaped materials that varied in size. Irregularly shaped particles were observed to partially cover some of these clusters……201

Fig 4.11. The proposed transformation pathways of DOXY hydrolysis showing different mechanisms such as decarbonylation and deamidation [212] …….……...203

Fig 4.12. The degradation of DOXY under UVA light (photolysis) at pH 4.5 and pH 11 at 5 cm (**a**) and their UV-Vis (**b-c**) and the chromatographic part of LC-MS spectra prior to (**d-e**) and after (**f-g**) the degradation. [C_o = 25 ppm, stirring rate = 750 rpm, T = 20 ± 2 °C, and volume = 20 mL]…….206

Fig 4.13. The photocatalytic degradation of DOXY under UV light using P25 (**a-d**) and visible light using commercial α-Fe_2O_3 (**e**). [C_o = 25 ppm, pH = 7, dose = 0.01 g, stirring rate = 750 rpm, T = 20 ± 2 °C, and volume = 20 mL]……..208

Fig 4.14. The UV-Vis spectra of DOXY after 90 minutes of stirring at 20 °C (**a**) and three times at 35 °C (**b-d**). [C_o = 25 ppm, pH 7, stirring rate = 750 rpm, and volume = 20 mL]….209

Fig 4.15. TGA and derivative weight profile of DOXY powder (**a**) and the mass spectrum ion curve for 2 m/z (**b**), 16 (**c**), 18 (**d**), 30 (**e**), 32 (**f**), 43 (**g**), 44 (**h**), and 45 (**i**)……212

Fig 5.1. Powder XRD patterns of pristine and calcined BIOX (first site) **(a)** second site (crag) and 2-line ferrihydrite **(b)**, and third site (pond) **(c)**…… ……...217

Fig 5.2. The magnetic property of calcined BIOX samples: BIOX first site **(a)**, BIOX crag **(b)**, Pond **(c)**, and reduced BIOX 1 **(d-g)**……...218

Fig 5.3. Powder XRD patterns of reduced BIOX at 300 °C for 1 hour under pure H_2 **(a)** and H_2/N_2 **(b)**……..……221

Fig 5.4. Powder XRD patterns of P25 **(a)**, reduced BIOX material under pure H_2 **(b)**, H_2/N_2 for 1 hour at different temperatures **(c)**, at different temperatures for 6, 8, and 10 hours (H_2/N_2) **(d)**, at 500 °C and 700 °C for different times (H_2/N_2) **(e)**, at different temperatures for 8 and 10 hours (H_2/N_2) **(f)**, reduced 2-line ferrihydrite at various temperatures for different times (H_2/N_2) and reduced Chinese RM and reduced Chinese RM-derived α-Fe_2O_3 (H_2/N_2) **(g)**. P25 was used as an internal standard in panels **b-g**……223

Fig 5.5. Powder XRD patterns of reduced BIOX material under pure H_2 **(a)**, H_2/N_2 for 1 hour at different temperatures **(b)**, at 500 °C and 700 °C for different times (H_2/N_2) **(c)**, at different temperatures for 6 and 8 hours (H_2/N_2) **(d)**, at different temperatures for 8 and 10 hours (H_2/N_2) **(e)**, reduced 2-line ferrihydrite at various temperatures for different times (H_2/N_2) **(f)**, and reduced Chinese RM and reduced Chinese RM-derived α-Fe_2O_3 (H_2/N_2) **(g)**. Reduced BIOX 1 at 700 °C for 2 hours followed by 400 °C for 4 hours and then 500 °C for 4 hours was used as a standard in all panels……225

Fig 5.6. Nitrogen physisorption isotherms of the pristine BIOX first site **(a)**, second site (crag) **(b)**, reduced BIOX 1 **(c)**, reduced BIOX 500 °C 10h H_2/N_2 **(d)**, reduced BIOX 700 °C 8h H_2/N_2 **(e)**, and 2-line ferrihydrite **(f)**……227

Fig 5.7. SEM images **(a** and **b)** and EDX spectrum of BIOX first site **(c)**, SEM images **(d-f)** and EDX spectrum of BIOX second site (crag) **(g)**, SEM images **(h** and **i)** and EDX spectrum of BIOX third site (Pond) **(j)**, SEM images **(k** and **l)** and EDX spectrum of 2-line ferrihydrite **(m)**……230

Fig 5.8. SEM images **(a-c)** and EDX spectrum of calcined BIOX first site **(d)**, SEM images **(e-h)** and EDX spectrum of calcined BIOX second site (crag) **(i)**, SEM images **(j-l)** and EDX spectrum of calcined BIOX third site (Pond) **(m)**……...233

Fig 5.9. SEM images of pristine BIOX (crag) collected in January 2025 **(a-b)**, SEM **(c-d)** and EDX spectrum of reduced BIOX 1 **(e)**, SEM **(f-g)** and EDX after DOXY adsorption in DW **(h)**, and in the River Clyde water sample **(i-l)**…….236

Fig 5.10. SEM image of reduced BIOX 1 **(a)** and its elemental mapping; C (**b**), Fe **(c)**, O **(d)**, Si **(e)**, Ca **(f)**, and Al **(g)**……..237

Fig 5.11. The efficiency of three BIOX samples collected during the summertime and the calcined crag **(a)**, and pristine and calcined crag (wintertime), SiO_2, and 2-line ferrihydrite (**b**) in removing DOXY after 90 minutes. [C_o = 25 ppm, stirring rate = 750 rpm, T = 20 ± 2 °C, volume = 10 mL, and dose = 0.005 g]…….238

Fig 5.12. The efficiency of 37% HCl-leached summertime **(a)** and wintertime **(b)** crag samples in adsorbing DOXY after 90 minutes. [C_o = 25 ppm, pH = 7, stirring rate = 750 rpm, T = 20 ± 2 °C, volume = 10 mL, and dose = 0.005 g]…….239

Fig 5.13. The efficiency of reduced BIOX materials under pure H_2 for 1 hour at different temperatures (**a**), under H_2/N_2 for 1 hour at different temperatures (**b**), under H_2/N_2 for different times at different temperatures (**c** and **d**), reduced BIOX 1, reduced 2-line ferrihydrite materials, reduced Chinese RM, and reduced Chinese RM-derived α-Fe_2O_3 (**e**), and reduced BIOX 1 (summertime) (**f**) under H_2/N_2 in removing DOXY from DW after 90 minutes. [C_o = 25 ppm, stirring rate = 750 rpm, T = 20 ± 2 °C, volume = 10 mL, and dose = 0.005 g]. The solid-to-liquid ratio in all these experiments is equivalent to 0.5 g/L……..242

Fig 5.14. The effect of variation in initial concentration of DOXY using 0.0025 g **(a)**, 0.005 g **(b)**, and 0.01 g **(c)** [pH = 7 and stirring rate = 750 rpm], stirring rate **(d)** [C_o = 25 ppm, pH = 7, and dose = 0.005 g]**,** time effect **(e)** [C_o = 25 ppm, pH = 7, stirring rate = 750 rpm, and

dose = 0.005 g], recycling **(f)** [C_o = 25 ppm, pH = 7, stirring rate = 750 rpm, and dose = 0.005 g] on the adsorption efficiency and capacity of 10 mL of DOXY by reduced BIOX 1 after 90 minutes. The pH variation of the River Clyde water sample **(g)** [C_o = 25 ppm, stirring rate = 750 rpm, and dose = 0.005 g]……248

Fig 5.15. The removal of DOXY by reduced BIOX 1-bead composite and pristine calcium alginate beads after 90 minutes (**a**), and the composite beads prior to (**b**), and after DOXY removal (**c**). [C_o = 25 ppm, stirring rate = 750 rpm, and dose = 0.1 g]……....249

Fig 5.16. The removal of DOXY by reduced BIOX (500 °C for 10 hours) bead composite and pristine calcium alginate beads after 90 minutes using 1wt/v% (**a**), 2wt/v% (**b**), and 4wt/v% (**c**) concentration of calcium chloride and sodium alginate solutions. [C_o = 25 ppm, stirring rate = 750 rpm, and dose = 0.1 g]……250

Fig 5.17. Linear adsorption isotherm plots of Langmuir (**a**) and Freundlich (**b**) models. [pH = 7, stirring rate = 750 rpm, and dose = 0.005 g]……251

Fig 5.18. The efficiency of reduced BIOX 1 in adsorbing DOXY in the presence of different concentrations of NaCl (**a**), Ca^{2+} ($CaCl_2$) **(b)**, control experiment of Ca^{2+} ($CaCl_2$) **(c)**, Ca^{2+} (CaO) **(d)**, control experiment of Ca^{2+} (CaO) **(e)**, Mg^{2+} (MgO) **(f)**, control experiment of Mg^{2+} (MgO) **(g)**, SO_4^{2-} **(h)**, control experiment of SO_4^{2-} **(i)**, and Si(IV) (SiO_2) **(j)** after 90 minutes. [C_o = 25 ppm, pH = 7, volume = 10 mL, dose = 0.005 g, stirring rate = 750 rpm, and T = 20 ± 2 °C]…….254

Fig 5.19. XPS spectra of reduced BIOX 1 including a wide scan before **(a)**, and after **(b)**, Fe 2p before DW stirring **(c)**, Fe 2p before **(d)**, and after **(e)**, O 1s before **(f)**, and after **(g)**, C 1s before **(h)**, and after **(i)**, and N 1s after DOXY adsorption (**j**)…….259

Fig 5.20. TGA and derivative weight profile of reduced BIOX 1 before (**a**) and after adsorption of 200 ppm (**b**), and 500 ppm (**c**) of DOXY, and the mass spectrum ion curve for 32 m/z before (**d**), and after 200 ppm DOXY adsorption (**e**)…….……..261

Fig 5.21. Powder XRD patterns of reduced BIOX 1 after being soaked in water and dried, and after adsorption of different concentrations (50, 100, 200, and 500 ppm) of DOXY to show the stability of zero-valent iron after being used in water and aqueous DOXY solutions……262

Fig 5.22. The concentration of leached iron from reduced BIOX 1 after 90 minutes of 25 ppm DOXY removal in DW **(a)**, the River Clyde water samples **(b)**, different concentrations of DOXY in DW at pH 7 **(c)**, and upon recycling for 5 times in DW at pH 7 (**d**) as measured by ICP-OES analysis. [Stirring rate = 750 rpm, T = 20 ± 2 °C, volume = 10 mL, and dose = 0.005 g]…….264

Fig 5.23. The upscaling of reduced BIOX 1 in adsorbing 25 ppm (**a**) and 50 ppm (**b**) of DOXY in 100 mL. [Dose = 0.05 g, pH 7, stirring rate = 750 rpm, and T = 20 ± 2 °C]……...265

Fig 5.24. The efficiency of reduced BIOX 1 in removing DOXY and DOXY in presence of CEF (**a**) and the self-degradation of DOXY and in presence of CEF (**b**) after 90 minutes. [C_o = 25 ppm, volume = 10 mL, dose = 0.005 g, stirring rate = 750 rpm, and T = 20 ± 2 °C]……266

Fig 5.25. CEF removal efficiency by BIOX materials from different sites **(a)**, 2-line ferrihydrite, reduced BIOX 1, and reduced 2-line ferrihydrite (NH_3 synthesis conditions) **(b)**. [C_o = 25 ppm, stirring rate = 750 rpm, T = 20 ± 2 °C, volume = 10 mL, dose = 0.005 g, time = 90 minutes]……...267

Fig 6.1. Conductivity profiles for BIOX crag **(a)**, synthetic 2-line ferrihydrite **(b)**, Chinese red mud **(c)**, and Chinese red mud-derived α-Fe_2O_3 door **(d)** and window side **(e)** after reaction with 3:1 H_2/N_2 at 400 °C and 500 °C for 4 hours each……272

Fig 6.2. Conductivity profiles for 2% K-α-Fe_2O_3 **(f)**, 5% K-α-Fe_2O_3 door **(b)** and window side **(c)**, 10% K-α-Fe_2O_3 door **(d)** and window side **(e)** after reaction with 3:1 H_2/N_2 at 400 °C and 500 °C for 4 hours each……...274

Fig 6.3. Conductivity profiles for 5% Co-α-Fe_2O_3 door side **(a)**, window side **(b)**, and commercial α-Fe_2O_3 door side **(c)**, and window side **(d)**, after reaction with 3:1 H_2/N_2 at 400 °C and 500 °C for 4 hours each……...……275

List of schemes

Scheme 2.1. Schematic illustration of TiO_2 synthesis by the alkali roasting method [202]. The process starts by mixing and heating red mud with burnt lime and soda ash to form sodium titanate. The acid leaching of the metal-free solid residue to form water-soluble $TiOSO_4$ followed by thermal hydrolysis to precipitate $Ti(OH)_4$, which is then calcined into TiO_2…...68

Scheme 2.2. Schematic illustration of TiO_2 synthesis by the acid baking method [202]. The method begins with mixing and baking red mud with H_2SO_4 followed by water leaching to remove the metal components and purifying the remaining titanium in the sample. Subsequently, the sample is neutralized, dried in the oven, and calcined to produce TiO_2…..69

Scheme 2.3. A simple demonstration of the extraction of α-Fe_2O_3 from Chinese red mud that began with mixing red mud with oxalic acid to form ferric oxalates, which were then photocatalytically reduced into ferrous oxalates. Subsequently, the oxalates were washed with ethanol to remove impurities and lastly calcined to produce α-Fe_2O_3……..71

List of tables

Table 1.1. Chemical structures of some common antibiotics including ceftriaxone and doxycycline that are investigated in the current study……...32

Table 3.1. Surface areas of Fe and Cu-TiO_2 composites using TiO_2 extracted from Chinese red mud by the acid baking method……...104

Table 3.2. The PZC of the adsorbents reported in Chapter 3……..147

Table 3.3. The (CHN) elemental analysis of 5% Fe 5% Cu-TiO_2 prior to and after CEF adsorption at pH 7..……..168

Table 4.1. The PZC of the adsorbents reported in Chapter 4..… ……..…….198

Table 5.1. A comparison of the adsorption capacity of reduced BIOX 1 with other materials reported in the literature for the removal of DOXY……244

Table 5.2. Concentration of basic and acidic sites of some of the adsorbents used in this chapter…….....256

Table 5.3. CHN analysis of reduced BIOX 1 before and after DOXY adsorption at pH 7…260

Table 5.4. The PZC of the BIOX and 2-line ferrihydrite materials used in this study……...268

List of equations

$Al(OH)_3 + NaOH \rightarrow Na[Al(OH)_4]$ eq. (1.1)

$Na[Al(OH)_4] \rightarrow Al(OH)_3 \downarrow + NaOH$ eq. (1.2)

$2Al(OH)_3 \rightarrow Al_2O_3 + 3H_2O$ eq. (1.3)

$Al^{3+} + 3e^- \rightarrow Al$ eq. (1.4)

$2O^{2-} + C \rightarrow CO_2 \uparrow + 4e^-$ eq. (1.5)

So, the overall reaction is $2Al_2O_3 + 3C \rightarrow 4Al + 3CO_2$ eq. (1.6)

$Fe^{3+}(aq) + e^- \rightarrow Fe^{2+}(aq)$ eq. (1.7)

$2\ Fe^{3+}(aq) + 3\ H_2O \rightarrow Fe_2O_3\ (s) + 6\ H^+(aq)$ eq. (1.8)

$2\ Fe^{2+}(aq) + 3\ H_2O \rightarrow Fe_2O_3\ (s) + 6\ H^+(aq) + 2\ e^-$ eq. (1.9)

$N_2(g) + 3H_2(g) \rightleftharpoons 2NH_3(g) \quad \Delta H = -92.4\ kJ/mol$ eq. (1.10)

$Ti[OCH(CH_3)_2]_4\ (aq) + 4\ H_2O\ (l) \rightarrow Ti(OH)_4\ (s) + 4\ CH_3CH(OH)CH_3$ eq. (2.1)

$2\ Ti(OH)_4\ (s) \rightarrow 2\ TiO_2\ (s) + 4\ H_2O\ (g)$ eq. (2.2)

$Fe(NO_3)_3.9H_2O\ (aq) + 3\ NaOH\ (aq) \rightarrow Fe(OH)_3\ (s) + 3\ NaNO_3\ (aq) + 9\ H_2O\ (l)$ eq. (2.3)

$2\ Fe(OH)_3\ (s) \rightarrow Fe_2O_3\ (s) + 3\ H_2O\ (g)$ eq. (2.4)

$\%\ Adsorption = 100 \times (A_0 - A)/A_0$ eq. (2.5)

$Adsorption\ capacity\ (mg/g) = [(Co - Ce)/m] \times V$ eq. (2.6)

$Fe^{2+} + H_2O_2 \rightarrow Fe^{3+} + OH^- + \bullet OH$ eq. (2.7)

$Fe^{3+} + H_2O_2 \rightarrow Fe^{2+} + H^+ + \bullet OOH$ eq. (2.8)

$2H_2O_2 \rightarrow \bullet OH + \bullet OOH + H_2O$ eq. (2.9)

$Basic\ site\ concentration\ (mmol/g) = [[C_{acid} \times \Delta V] / m_{adsorbent}] \times 1000$ eq. (2.10)

$CaO + H_2O \rightarrow Ca(OH)_2$ eq. (3.1)

$$\ln K = -\frac{\Delta H\ ads}{RT} + \frac{\Delta S}{R} \quad \text{eq. (3.2)}$$

$$\mathrm{qe} = \frac{\mathrm{qmax} * \mathrm{KL} * \mathrm{Ce}}{1 + \mathrm{KL} * \mathrm{Ce}} \quad \text{eq. (3.3)}$$

$$\frac{1}{\mathrm{qe}} = \frac{1}{\mathrm{qmax} * \mathrm{KL}} * \frac{1}{\mathrm{Ce}} + \frac{1}{\mathrm{qmax}} \quad \text{eq. (3.4)}$$

$$\ln \mathrm{qe} = \ln \mathrm{KF} + \frac{1}{\mathrm{n}} \ln \mathrm{Ce} \quad \text{eq. (3.5)}$$

$$\mathrm{qe} = \mathrm{KF} * \mathrm{Ce}^{1/n} \quad \text{eq. (3.6)}$$

List of abbreviations

Abbreviation	Definition
T. latifolia	*Typha latifolia*
DW	Deionized water
CEF	Ceftriaxone
DOXY	Doxycycline
TCs	Tetracyclines
BIOX	Biogenic iron oxide
RM	Red mud
P25	Commercial TiO_2
SEM	SEM Scanning Electron Microscopy
EDX	Energy Dispersive X-ray Spectroscopy
BET	Brunauer-Emmett-Teller Surface Area
CHN	Carbon-Hydrogen-Nitrogen analysis
XPS	X-ray photoelectron spectroscopy
TGA	Thermal Gravimetric Analysis
FTIR	Fourier transform infrared spectroscopy
LC-MS	Liquid chromatography-mass spectrometry
ICP-OES	Inductively coupled plasma-optical emission spectroscopy
UV-Vis	Ultraviolet-Visible spectroscopy
XRD	X-ray diffraction
NIST	National Institute of Standards and Technology
PZC	Point of zero charge
WHO	World health organization
PFO	Pseudo-First-Order
PSO	Pseudo-Second-Order
GO	Graphene oxide

Acknowledgements

First and foremost, I must thank God (Almighty) for all his blessings and the experiences that I had throughout my whole life, and I wish that God (Almighty) is satisfied with what I am doing in my life. I would like to thank my supervisor Prof. Justin Hargreaves for teaching me how to be a critical thinker and not just following the literature of chemistry and materials science, which is essential for anyone who wants to be a good scientist. Also, many thanks for his assistance and support throughout the PhD project, useful discussions, and for giving me the opportunity to participate in many conferences. Many thanks to my parents and my brother Mahmoud for their continuous support over the years. I would also like to thank my friends and colleagues at the school; Angela the forever problem solver in the Hargreaves group, Zhang and Erin, my demonstration teammates, Katy and Lucy, for all the good times and chats that we had. A special mention must also go to Rachel for her friendship, support and help over the last three years. Special thanks to Rana for her friendship, support and help throughout the scholarship. Many thanks to the technical staff at University of Glasgow, with special mention to Jim Gallagher for his help with the SEM and EDX, Andy Monaghan for his help with so many things, along with all the chats about football and Liverpool Football Club, Gangi Reddy Ubbara, Giovanni Rossi, Christopher Kelly, Craig Bradley, Euan Stobbs, Marcox Pun, Claire Wilson, and Connor Fleming for their very kind help with all analytical services. Many thanks to the professors of the heterogeneous catalysis section Prof. David Lennon, Prof. David Jackson, and Dr Emma Gibson. Furthermore, I would like to thank my Egyptian supervisor; Prof. Manal Fawzy for guiding, helping, funding, and supporting me during my MSc. project and throughout my time in Egypt, and for her continuous support and collaboration even after coming to the UK. Special thanks to Dr. Abdelazeem for his support, guidance, discussions, and collaboration over the years. Many thanks to the Department of Environmental Sciences and my professors at Alexandria University; Prof. Nadia Badr, Prof. Assem Barakat, and Prof. Ashraf Amer for their very kind help and support over the years and particularly during the scholarship application. Special thanks to all my Egyptian friends; Mohamed Ibrahim, Ahmed Hegazy, Mohamed Ashry, Mohamed Eshra, Mahmoud Magdy, Mahmoud Fethaa, Moemen Adel, Moataz Elsayed, Ahmed Abdelfatah, Amr Ibrahem, Ahmed Abdelhamed, Hazem Mamdouh, Mohamed Ashraf, Kareem Abdelgawad, Mahmoud Hafez, Omar Taha, and Moustafa Mahmoud.

This PhD project is funded by a full scholarship (MM32/21) from the Egyptian Ministry of Higher Education & Scientific Research represented by the Egyptian Bureau for Cultural & Educational Affairs in London.

Author's Declaration

I declare that this thesis is the result of my own work, except where reference is made to the contribution of others. This work has not been submitted for any other degree at the University of Glasgow or any other institution.

Chapter 1

1. Introduction

Water is one of the most essential resources for sustaining life on earth. Even though living species, ecosystems, and humans require access to safe and clean water, large amounts of untreated as well as inappropriately treated wastewater from domestic, industrial, and agricultural sources are still dumped into water bodies [1]. Wastewater is released into different watercourses including fresh, marine, and brackish water bodies, and causes water pollution [2]. Subsequently, this pollution results in direct and indirect effects on the health and well-being of humans and natural ecosystems. Various pollutants pose deleterious impacts on water quality, which are mainly categorized into inorganic, such as heavy metals [3], and organic pollutants including dyes, pesticides, detergents, and pharmaceutical wastes [4].

Numerous compounds constitute the pharmaceuticals category including antibiotics, antivirals, antifungals, analgesics, antiepileptics, anticancer drugs, antidiabetic compounds, and hormone regulators [5]. Moreover, the cosmetics industry and personal care products are contributing to and exacerbating the water pollution issue [6]. Pharmaceutical wastes are commonly detected in surface and groundwater [7]. Using pharmaceuticals is primarily for protecting human health and enhancing the quality of life [8]. However, the significant increase in the human population around the world, which is attributed to medical and scientific advancements (e.g., the Haber-Bosch Process), along with the excessive and irrational use of these products has led to the release of non-biodegradable waste into water that needs highly efficient treatment techniques to restore the original water quality.

Pharmaceutical compounds are widely found in watercourses and each of these has its structure and mechanism of action, making it difficult to identify and analyze them, and also to remove them from wastewater [9]. The absence of guidelines and concentration limits for pharmaceutical discharge adds to the problem. Additionally, the wide range of antibiotics in pharmaceutical effluents from a few μg/L to a few mg/L, which differs from one country to another, as reported by Bielen *et al.* [10] exacerbates the issue. Therefore, further measures and monitoring steps should be employed to ensure that the concentration of these wastes does not increase [11]. Although pharmaceuticals potential effect on aquatic organisms and human health is still controversial and ambiguous [12], many investigations have indicated that these chemicals can imitate the function of endogenous steroid hormones, resulting in comparable

responses to these hormones [13]. Therefore, pharmaceuticals that get discharged into the environment are considered one of the major types of disruptors of the endocrine system that could result in different health issues such as thyroid gland disruption [14-17]. Furthermore, the high degree of stability and non-biodegradability of pharmaceuticals has further complicated their removal from wastewater [18] and resulted in their circulation through different ecosystems and organisms.

For example, antibiotics can persist in soil and sediment for weeks and months, which is based on their physical and chemical properties (e.g., polarity, stability, etc) [19]. In a recent study, Walters *et al.* [20] investigated the degradation of antibiotics in biosolid-amended soils over three years and found that different antibiotics such as azithromycin, which belongs to the macrolide class of antibiotics, shows high persistency with a half-life time of more than a year. Antibiotics show direct and indirect effects on bacterial species [19]. The direct effect is that antibiotics can negatively affect non-pathogenic (useful) bacteria, which are responsible for essential ecosystem functions, whereas the indirect effects include the emergence of antibiotic-resistant bacterial strains that can destabilize natural ecosystems, cause genetic mutations, and eventually threaten human life. In the context of the direct effect, antibiotics such as tetracycline can affect the activities of denitrifying microorganisms and inhibit their growth [21]. Consequently, the concentration of nitrates and nitrites increases and then they get transported to water courses via runoff, which leads to eutrophication [22]. Eutrophication can result in algal blooms, depletion of dissolved oxygen, and death of aquatic organisms, particularly those sensitive to dissolved oxygen levels.

The most common classification of antibiotics is based on their chemical structures as shown in **Table 1.1**, and it includes beta-lactams such as penicillin and cephalosporin, aminoglucosides such as gentamicin, macrolides such as erythromycin, tetracyclines such as doxycycline, quinolones such as levofloxacin and ciprofloxacin, and sulfonamides such as sulfamethoxazole. In addition, the mechanism of action is another way of classifying antibiotics into protein synthesis inhibitors (e.g., tetracyclines and macrolides), nucleic acid synthesis inhibitors (e.g., fluoroquinolones and metronidazole), and cell membrane function inhibitors (e.g., daptomycin). The source of antibiotics constitutes another variable for categorizing antibiotics into naturally occurring antibiotics (e.g., penicillin), semisynthetic (e.g., ceftriaxone), and synthetic antibiotics (e.g., sulfonamides). Also, the spectrum of activity is another factor to differentiate between various antibiotics as some of them are broad-

spectrum such as tetracyclines, which could be used with Gram-positive and Gram-negative bacteria, while other antibiotics are narrow spectrum showing efficiency against certain strains of bacteria e.g., penicillin (Gram-positive), and aztreonam (Gram-negative).

Table 1.1. Chemical structures of some common antibiotics including ceftriaxone and doxycycline that are investigated in the current study.

The antibiotic's name and chemical formula	Antibiotic's chemical structure
Gentamicin ($C_{21}H_{43}N_5O_7$)	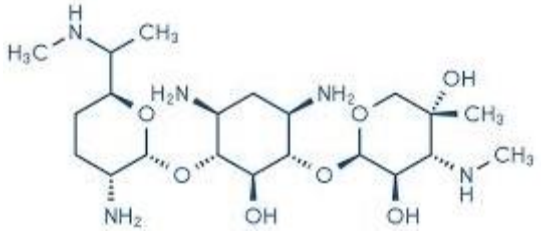
Erythromycin ($C_{37}H_{67}NO_{13}$)	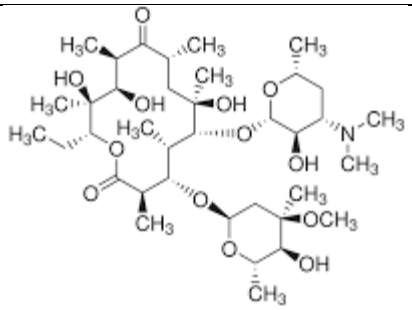
Doxycycline ($C_{22}H_{24}N_2O_8$)	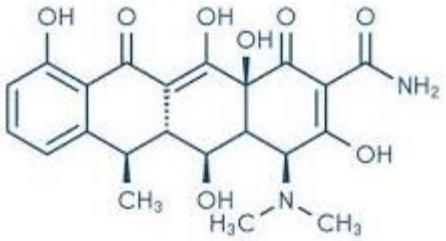
Levofloxacin ($C_{18}H_{20}FN_3O_4$)	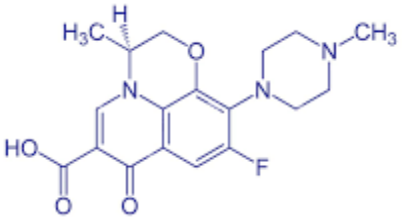
Sulfamethoxazole ($C_{10}H_{11}N_3O_3S$)	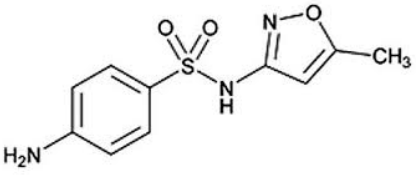

Metronidazole ($C_6H_9N_3O_3$)	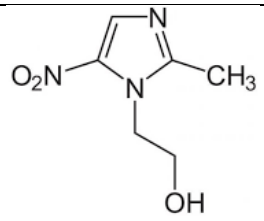
Ceftriaxone ($C_{18}H_{18}N_8O_7S_3$)	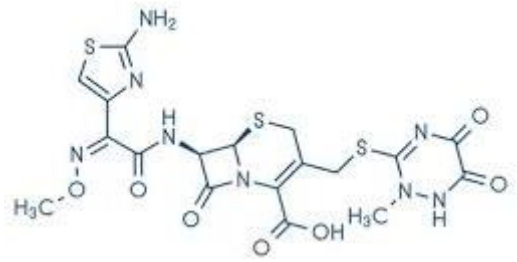

According to a report by the European Environment Agency in 2018, only 38% of EU surface water was assessed to be in an acceptable chemical state while 46% was not, the rest, about 16%, could not be determined [23]. Large numbers of pharmaceutical compounds are used within the EU countries to treat both human and animal diseases. Out of these pharmaceuticals, about 477 pharmaceutical compounds were recently detected in the European countries' and the United Kingdom's surface water [24]. Most of these compounds were found in Spain, Germany, France, Sweden, and the United Kingdom, where monitoring of these pharmaceuticals is frequently undertaken. However, this does not prove that the water of other countries does not contain such contaminants, as they need further investigation, which is limited because of the unavailable measurements in these countries [25]. The concentration of various pharmaceuticals including antibiotics such as ciprofloxacin and sulfamethoxazole was found to be up to 3.5 μg/L in a study that was carried out in Greece in 2015 [26].

Based on the information provided by the EU, antibiotic-resistant bacteria were responsible for approximately 671,689 infections and about 33,000 fatalities in 2015 [27]. The excessive and medically unjustified use of antibiotics is the main reason for increased antibiotic-resistance bacteria [28]. The annual global production of antibiotics is about 100,000 tons and about 5,500 tons out of this amount are for tetracyclines [29]. Approximately, 60 - 85% of the antibiotics are not assimilated inside human bodies, so they are excreted into sewage systems [30]. Furthermore, the production and utilization of antibiotics are escalating at a substantial rate, and with no effective actions, production could be doubling by 2030 [31]. Therefore, the

EU initiated “the European One Health Action Plan” as a response to the antibiotics' negative impacts by raising public awareness of the irrational use of these compounds along with their hard biodegradable nature [25]. According to the United States Environmental Protection Agency (USEPA), emerging pollutants such as antibiotics are compounds for which there are no regulations and their impact is unknown or not well understood [32]. As stated by Zhang *et al.* [33] China is the world's biggest producer and user of antibiotics.

According to the aforementioned facts, the problem of antibiotic discharge into various water courses is of interest, and similarly the search for treatment techniques and different materials with low production costs that could be efficiently employed in water treatment. As shown in **Fig 1.1.b** the research interest of the scientific community toward the removal of antibiotics waste from wastewater started in 1989 with most of the publications coming from China (**Fig 1.1.a**). Subsequently, the number of publications commenced to substantially increase particularly at the beginning of the new millennium and reached 7199 at the beginning of 2025.

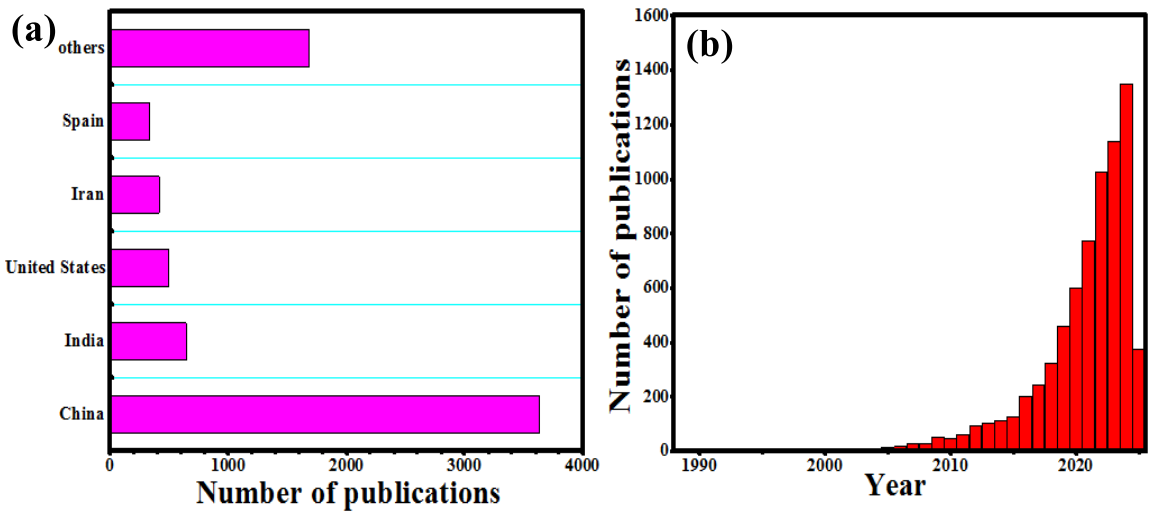

Fig 1.1. The number of publications related to the antibiotics' removal from wastewater in different countries (**a**) over the last 36 years (**b**). Data obtained from Scopus [34].

1.1. Treatment and removal techniques of antibiotics

Diverse water treatment techniques, as represented in **Fig 1.2**, including adsorption, membrane technology, and advanced oxidation processes such as electrochemical oxidation, non-thermal

plasma, ozonolysis, and photocatalysis have been developed to remove antibiotics from wastewater.

Many studies have shown that adsorption is an appropriate technology due to its simplicity, low energy requirement, and reduced costs [35]. Additionally, the utilization of magnetic adsorbents has been recently applied as an efficient technique for environmental decontamination, owing to the ease with which magnetic separation may extract adsorbents by application of an external magnetic field [36]. Adsorption is one of the common removal techniques for antibiotics and it involves various processes such as electrostatic interactions, ion exchange, surface complexation, and hydrogen bonding [37]. However, the inefficient regeneration of adsorbents and the difficulty of their upscaling are common issues that are encountered. Also, the disposal of adsorbents at the end of their lifetime is another issue, which could be solved by desorbing and storing the pollutant, followed by trying to retrieve the remaining of the raw materials that could be useful either in the same or a different application. Additionally, shifting the issue of antibiotics from being dissolved in dynamic aquatic systems to being stored in the solid phase on the adsorbent surface makes the problem much easier to manage.

The utilization of membrane technology is safe and environmentally friendly particularly when it is combined with other treatment techniques (e.g., adsorption and catalytic degradation) [38]. Pore size, surface charge, and hydrophilicty/hydrophobicity of the membranes are the main controlling factors in membrane technology [39]. However, there are certain limitations when applying this technology such as membrane fouling along with the cost required for replacing these membranes.

Electrochemical advanced oxidation has recently gained researchers' interest for removing different organic contaminants including antibiotics waste owing to its reduced cost and acceptable degradation efficacy [40]. Also, the applicability of coupling this technique with membranes to filter off the remaining antibiotics which were not completely degraded helps improving the overall removal efficacy [41]. Yet, certain issues diminish the efficiency of this technique and devaluate its applicability in water remediation including the presence of colloids, particulate matter, and other inorganic wastes that get deposited on the surface of the electrodes and compete with the pharmaceuticals intended to be degraded [42]. The possible

release of toxic ions from the heavy metal-containing electrodes into water represents another issue of the wide-scale application of this technique [43].

Non-thermal (cold) plasma is another type of advanced oxidation processes that was investigated over the last few years in the degradation of antibiotics at atmospheric pressure and room temperature. This technique depends on the ionization of gases such as oxygen and nitrogen or even just air using dielectric barrier discharge to produce radicals (e.g., hydroxyl (•OH), ozone (O_3), superoxide ($O_2^{\bullet -}$), and nitrogen dioxide (NO_2•) radicals), which can degrade antibiotics at low temperatures [44]. The efficiency of non-thermal plasmas can be improved by combining a catalyst or a UV light source, but the high cost of the equipment used represents a significant challenge in upscaling this technique.

Other advanced oxidation processes such as photolysis, ozonation, Fenton degradation, and photocatalysis are among the efficient wastewater treatment techniques [45]. Light-driven photocatalytic degradation has received considerable attention because of its cost-effectiveness, eco-friendliness, and high efficacy [46]. In this treatment, visible or ultraviolet light is absorbed by a semiconductor material or a metallic material exhibiting the surface plasmon resonance (SPR) phenomenon, resulting in the generation of free radicals such as reactive oxygen species that include singlet oxygen and superoxide radicals, which can degrade the antibiotic waste [47]. When light energy is absorbed with an amount higher than the semiconductor photocatalytic material's bandgap energy, an electron transfer from the valence band to the conduction band occurs, resulting in the formation of positive holes in the valence band. As a result, the free electrons in the conduction band and the holes in the valence band will produce superoxide ($O_2^{\bullet -}$) and hydroxyl (•OH) radicals, respectively, which can degrade antibiotics. It is therefore of interest to modify or synthesize novel photocatalytic materials for this purpose in the field of advanced oxidation treatment of wastewater. On the contrary, the incomplete mineralization and the formation of toxic byproducts whose toxicity is unknown or could be even more toxic than the parent pollutant is considered one of the major constraints of the degradation/oxidation processes.

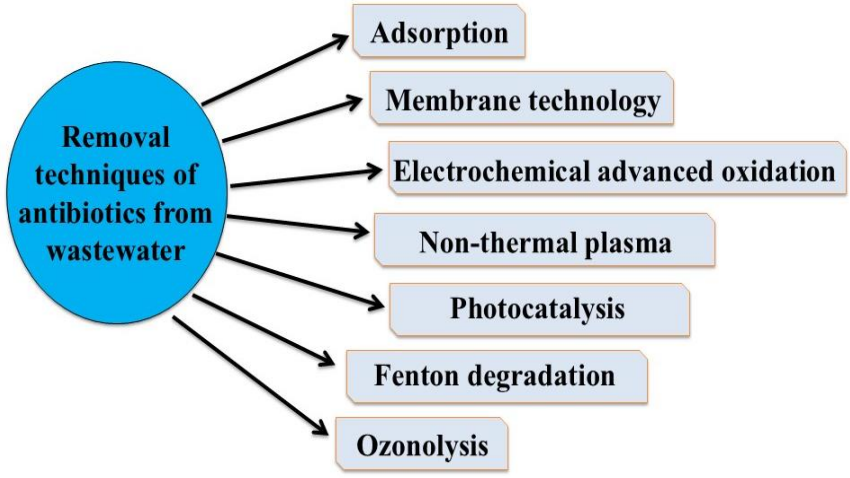

Fig 1.2. The most common techniques used for the removal of antibiotics from wastewater.

1.2. Materials used in the removal of antibiotics

Numerous materials can be utilized in the removal of antibiotics from wastewater as shown in **Fig 1.3.** such as nanomaterials that range in size from a few nanometers to less than 100 nm, which hold the potential to provide promising solutions to a wide range of environmental issues around the world such as water treatment because of their low-cost and highly efficient performance [48]. Nanowires, nanotubes, films, particles, and quantum dots constitute the most common sorts of nanomaterials [49, 50]. Among these nanomaterials, metal and metal oxide nanoparticles such as silver, zinc oxide, silicon oxide, iron oxide, and titanium oxide have been widely used in water treatment due to their large surface area, facile synthesis, and shape-dependent optical and electronic properties as previously explained in numerous studies [51-53]. Wastewater treatment, drug delivery, diagnostics, sensors, medical imaging, and cancer treatment are just some of the many applications of these nanomaterials [54, 55]. Therefore, these materials represent a suitable option in the field of antibiotic removal.

Metal-organic frameworks (MOFs) are crystalline materials having a periodic network, and hybrid and porous structures generated by the self-assembly of metal ions with organic ligands [56]. MOFs are heavily investigated and were proven to be of high surface area, stability, and surface tunability [57, 58]. Subsequently, they started to be widely used in different applications such as membrane fabrication, gas and water storage, biomedical imaging, catalysis, and adsorption. Furthermore, it has to be mentioned that scientists have recently begun to use these materials in the removal of antibiotics [59].

Graphene, which was reported in 2004 by Geim and Novoselov [60] 42 years after its early reporting in Boehm's article in 1962 [61], has been considered one of the strongest materials ever known. Graphene has an extremely large surface area (up to 2600 m^2/g), high thermal conductivity (3000 W/m.K), and transparency (a single layer of graphene absorbs only 2.3% of visible light) [62-64]. Consequently, it is employed in many different applications such as energy storage, coatings and anti-corrosion materials, sensors, electronics, drug delivery vehicles, as well as wastewater treatment [65-67]. Different types of mechanical exfoliation, which is a top-down method, such as tape and metal-assisted exfoliation are used to produce graphene, but it is hard to produce a single layer of graphene free of contamination with a low cost using this technique [68]. Also, the low stability of graphene sheets is another issue [68], and therefore the quality may not be that high. Chemical vapor deposition is a common bottom-up technique to produce graphene, but the high cost of this technique is a major limitation [69]. Therefore, these production methods are not cost-effective as they are not suitable for large-scale production. On the other hand, flash Joule heating, another top-down technique, has been used recently to up-cycle different carbon-based waste materials such as plastics and food waste by turning them into graphene [70]. This method received the attention of many industrial sectors because it can help recover metals (e.g., cobalt, nickel, and cadmium) from different materials such as coal fly ash instead of leaving these metals to leach into soil and water courses [71].

Carbon nanotubes (CNTs) are a material that constitutes one of the available options for removing antibiotic wastes from wastewater due to their high tensile strength, high surface area, elasticity, flexibility, and chemical and thermal stability [72]. CNTs are categorized into single-walled, double-walled, and multi-walled nanotubes [73]. Three methods could be utilized in producing CNTs including chemical vapor deposition, electric arc discharge, and laser ablation [74]. Despite all the above-mentioned privileges of CNTs, they are poorly dissolved in many solvents including water [75]. Therefore, various studies are currently concerned with the modification of CNTs such as functionalizing them with polymers (e.g., a bound phase) to improve their applicability in water treatment.

Activated carbon is a carbonaceous material that is black, porous, and of high surface area [76]. On a large scale, activated carbon has been deemed one of the most extensively employed materials in wastewater and air treatment processes [77, 78] owing to its applicability in removing different sorts of inorganic and organic waste materials including

antibiotic wastes. The main mechanism of removing contaminants by activated carbon is adsorption through the diffusion of contaminants' molecules into the activated carbon pores. The smaller the molecules, the deeper the diffusion into the activated carbon porous structure [76]. Activated carbon is generally prepared in a three-step process consisting of raw materials pretreatment, carbonization at low temperatures, and eventually activation [76]. The majority of carbon-based materials such as coal, wood, agricultural waste, and plants could be utilized as a raw material for preparing activated carbon [79]. The selection of the carbon source is the main factor in determining the production cost and physical and chemical properties of the resultant activated carbon.

Fly ash is a solid grey powder made up primarily of dust-like particles that are released as a byproduct of coal-fired power plants [80]. Ash might contain high silica content and several metal oxides including CaO, MgO, and Al_2O_3 [81, 82]. The ash byproducts are generally sent to landfills, resulting in increasing the waste load in these sites along with environmental pressures associated with the release of these wastes into terrestrial and aquatic ecosystems [83]. Therefore, many researchers commenced to focus on making use of ash wastes and employ them in different applications such as enhancing the production of biogas [84], the production of cement, and as a structural filler [85]. Moreover, ash waste such as oil palm ash was previously utilized in wastewater treatment, particularly in the adsorption of tetracycline, a common antibiotic, as reported by Khanday and Hameed [86].

One of the materials that has grabbed the attention of researchers in removing harmful wastes from wastewater systems is biochar owing to its special properties including adsorption of different types of organic and inorganic pollutants, high water retention capacity, enhancement of soil fertility, and better crop productivity along with the availability of surface modification using lots of different functional groups and compounds to obtain high removal efficiencies [87]. Agricultural wastes constitute the most common precursors used for the preparation of biochar, so the majority of biochar contains high levels of carbon and other elements [88]. What adds more value to biochar is the possibility of using it in various applications including adsorption and as a support for various materials to be employed in catalysis and photocatalysis based on the preparation strategy [89]. Biochar has recently been investigated in the removal of pharmaceutical wastes including antibiotics from aqueous solutions and the results were promising [90]. Not only is biochar employed in wastewater treatment, but it also represents a very promising solution for climate change by storing carbon. However, biochar

has some limitations such as the relatively low removal efficiency of certain pollutants. Such a limitation could be overcome by modifying the biochar surface with different materials such as metallic nanoparticles that have many unique characteristics, which can enhance the performance of biochar. Antibiotics can also be removed by TiO_2 and different iron oxides, which are discussed below in detail.

Within the context of making use of waste materials in the removal of antibiotics, *T. Latifolia*, which is an invasive plant species found all over the world, and red mud, which is the main byproduct of the alumina production industry using Bayer process, could be used for this task.

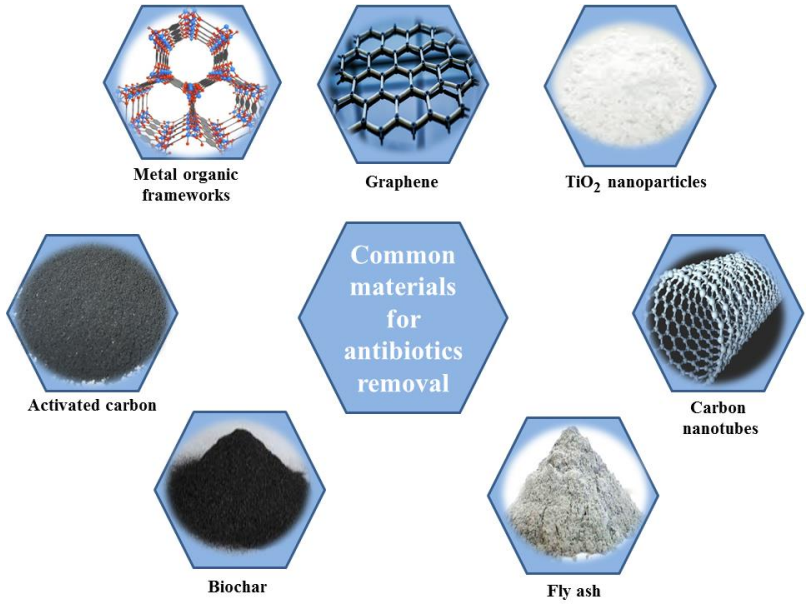

Fig 1.3. The most common materials are used for the removal of antibiotics from wastewater including biochar, activated carbon, graphene, etc.

1.3. The environmental issues of *T. latifolia* and its potential in water treatment

T. Latifolia, which is commonly known as cattail, is a common emergent aquatic plant species considered an essential part of the flora in many shallow water environments. *T. Latifolia* is a macrophyte that efficiently accumulates heavy metals and can thus be employed in the removal of heavy metals. However, this species usually creates large, monospecific stands in different habitats [91] owing to its capability of spreading quickly because of its fibrous root structure and rhizomes. Therefore, the overgrowth of this species results in turning water bodies into dry land [92] and disrupting the ecological balance of these ecosystems by

depleting the available nutrients and dissolved oxygen as well as outcompeting with other species. Thus, the excessive biomass of *T. Latifolia* was used in the current study to control its overgrowth and to investigate its potential in synthesizing α-Fe_2O_3, which can be used in antibiotics removal.

1.4. The Bayer Process, the release of red mud, and its challenges and opportunities

The industrial revolution, which started in the second half of the 18th Century and constitutes a quintessential part of recent human history, is considered a mixed blessing. On the one hand, the industrial revolution was one of the main pillars on which human civilization, progress, prosperity, and dramatic increase in population numbers were based. On the other hand, several global environmental issues such as climate change, air, soil, and water pollution, as well as the most critical issue of biodiversity loss were all reckoned as the inevitable result of such technological and industrial development.

One of the main industrial processes upon which the fabrication of various products is heavily reliant is the Bayer Process, which was developed by the Austrian scientist Carl Josef Bayer in 1888 for producing alumina from its ore bauxite, which is then electrochemically reduced into aluminium metal. Such a process enabled humans to produce aluminium and use it in the manufacture of utensils, refrigerators, packaging materials, computers, airplanes, transportation means, and drugs. However, based on the aforementioned fact, everything has its own positive and negative aspects, and concerning the negative aspects of the Bayer Process, it is the release of significant amounts of red mud that could be up to 80% higher than the aluminium being produced [93].

The Bayer process starts with crushing the bauxite ore followed by digestion using hot caustic soda to produce sodium aluminate according to the following equation.

$$Al(OH)_3 + NaOH \rightarrow Na[Al(OH)_4] \qquad \text{eq. (1.1)}$$

Consequently, the slurry is allowed to settle and the solid residue that constitutes the red mud is filtered. Then the sodium aluminate solution is cooled and seeded with fine $Al(OH)_3$ crystals to initiate the precipitation of aluminium in the form of $Al(OH)_3$. Therefore, it is possible to recycle NaOH solution.

$$Na[Al(OH)_4] \rightarrow Al(OH)_3 \downarrow + NaOH \quad \text{eq. (1.2)}$$

Subsequently, $Al(OH)_3$ is washed, filtered, and calcined (dehydrated) at 1000 - 1200 °C to produce alumina according to the following equation;

$$2Al(OH)_3 \rightarrow Al_2O_3 + 3H_2O \quad \text{eq. (1.3)}$$

Lastly, the alumina is electrochemically reduced into aluminium via Hall-Héroult process. In this process, the alumina solution is mixed with molten cryolite (Na_3AlF_6) to lower the melting point from 2000 °C to around 950-1000 °C. Subsequently, the alumina is reduced to aluminium metal at the cathode according to this equation

$$Al^{3+} + 3e^- \rightarrow Al \quad \text{eq. (1.4)}$$

Simultaneously, a carbon electrode is oxidized to carbon dioxide at the anode;

$$2O^{2-} + C \rightarrow CO_2 \uparrow + 4e^- \quad \text{eq. (1.5)}$$

So, the overall reaction is $2Al_2O_3 + 3C \rightarrow 4Al + 3CO_2$ eq. (1.6)

Many countries throughout the world are producing alumina and China is at the top of this list by producing about 82 million metric tons in 2023 as displayed in **Fig 1.4** [94] resulting in releasing red mud, which is the main byproduct of the aluminium production process, into the environment.

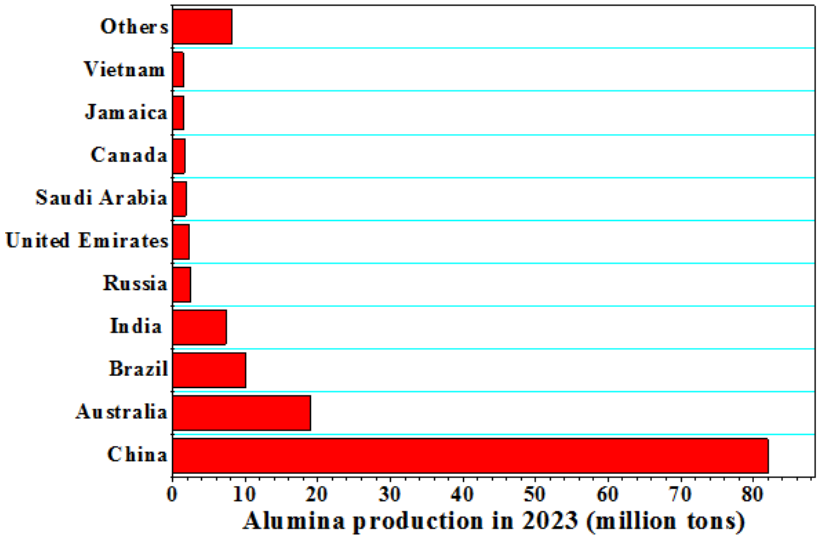

Fig 1.4. The global alumina production in 2023 showing the biggest contributing countries of red mud waste into the environment [94].

In the Bayer Process, a solution of caustic soda (sodium hydroxide) is used to digest the bauxite and dissolve aluminium silicate, so a highly alkaline waste material of red mud is produced as a byproduct [95]. Red mud poses several environmental challenges, including its highly alkaline pH, typically ranging from 10 to 13, the large quantities generated that require extensive storage, and its potential to contaminate surrounding ecosystems [96]. Red mud can be either stored via wet or dry storage and each option has its drawbacks such as air-transport and leaching, which causes groundwater and soil contamination, disruption of crop growth and production that has a direct negative influence on the international economy, and definitely affect human health [93, 97]. In response to some of these issues, vegetative cover can be planted in red mud disposal regions to lessen the hazardous dust formed by dry red mud [98]. Thus, it is imperative to explore alternative methods to leverage this material, a task meriting the focused attention of the scientific community, especially given the red mud's rich content of valuable rare earth metals and various metal oxides content including aluminium oxide (Al_2O_3), calcium oxide (CaO), titanium oxide (TiO_2), and different forms of iron oxide [99]. In general, iron oxides constitute 30 to 60% of red mud, different phases of aluminium oxides represent 10 - 20%, silica is about 3 to 10%, sodium and calcium oxides range between 10 and 20%, titania could be about 5% or less, and the remaining could be other metal oxides and rare earth elements [100].

In today's world, several countries are encountered by scarcity of natural resources owing to the excessive and unsustainable use of these resources in the last few decades, particularly after the Second World War. Such a scarcity constitutes a major barrier to the industrial development of these countries, so it became essential to use the available resources sustainably and to make use of waste materials by recovering and extracting valuable resources from them. In this regard, the concept of sustainable development has evolved recently and is based on the utilization of natural resources to meet the needs of the current generation without endangering the future of the next generations [101]. This concept integrates three main aspects: environmental, economic, and social aspects. In this context, scandium, lanthanum, neodymium, praseodymium, and yttrium are just some examples of rare earth metals found in red mud, so it is considered polymetallic source material [102]. Endeavoring to recover all these metals and metal oxides and make good use of them as raw materials in different industries is reckoned to be the best strategy of how to deal with such a massive load of red mud waste material.

It is worth mentioning that there are many useful applications for red mud and one common example for these applications is the infrastructure and building materials including cement production [103], glass and ceramics manufacturing [104], and pigment manufacturing [105]. Red mud was recently applied in road construction in many countries such as India [106]. Also, it is used as a construction filler in dams and embankments [107], as well as in the synthesis of corrosion-resistant materials [108]. A sustainable act of using a mixture of agricultural waste (hazelnut shells) and red mud in brick production resulted in the production of eco-friendly bricks with light weight, higher thermal insulation, and enhanced water absorption, along with reducing the pressure on natural clay utilization [109]. Red mud could be employed in agricultural applications including treatment of acidified lands and enriching the soil with many essential elements [110]. However, this has to be further investigated as red mud contains heavy metals. Moreover, red mud could be utilized for fabricating fertilizers as was recently achieved through a hydrothermal leaching process using potassium hydroxide to remove sodium and concentrate potassium and silicon in the final product [111]. Other environmental applications of red mud, which are related to air pollution are continuously investigated such as the removal of toxic vapors (e.g., carbon monoxide and elemental mercury) from flue gas [112, 113]. Red mud could be processed in fabricating catalytic materials to eliminate nitrogen oxides via catalytic reduction, and carbon monoxide and volatile organic compounds by catalytic oxidation [112].

Red mud is considered one of the materials that proved high efficacy in the field of wastewater treatment because it can be used in multiple composite formations and due to its applicability in various treatment techniques such as coagulation, catalytic and photocatalytic degradation, and adsorption of toxic organic and inorganic water pollutants. Acid treatment and heat treatment are the two major treatment techniques that enable red mud to be utilized in wastewater decontamination, yet the produced red mud via the former exhibited better performance [93]. Copper, which is a common cationic pollutant in water, was successfully removed by acid-treated red mud [114] and in the same regard, ciprofloxacin, which is a highly used antibiotic for treating bacterial infections was removed by 97% through the adsorption on an acid-activated red mud [115]. Also, red mud after being treated in acidic and saline conditions showed applicability as a coagulant in the removal of phosphorus [116].

Not only is red mud used as an adsorbing material, but it could also be employed as a catalyst in different types of advanced oxidation processes, particularly due to the porous nature of red

mud that allows the pollutants to accumulate on its surface and initiate the catalytic degradation process [93]. Additionally, the high content of iron in red mud plays an important role in the degradation of lots of different toxic water pollutants through the Fenton reaction [117]. Furthermore, the iron content of red mud has proved to be responsible for activating the persulfate and releasing sulfate free radicals that degrade numerous organic pollutants such as propylparaben [118]. The photocatalytic activity of red mud was also confirmed in a recent study that was carried out by Shi *et al.* [119] in which a comparison between unmodified (pristine) and modified (calcined at 350 °C) red mud in degrading tetracycline under visible light indicated the higher efficiency of the calcined sample, which was 88% compared to 66% for the pristine sample. Therefore, it was concluded that treatment or modification of red mud has a positive impact on its performance.

In agreement with the above-mentioned catalytic applications, red mud found its way into industrial catalytic applications such as the catalytic conversion of benzene into phenol with conversion efficiency and selectivity of 87% and 85%, respectively [120]. Therefore, producing catalytic materials from red mud offers many advantages including low production cost, good catalytic efficacies that could be further improved through more investigation and research work, and making use of a waste material (red mud) in the removal of other waste materials [93].

The circular economy refers to an economic model that aims to minimize waste generation and maximize the reuse, recycling, and regeneration of materials in a closed-loop system by improving the efficiency of production processes and using waste materials from certain industries as inputs or feedstock for other industries. It is an alternative to the traditional linear economy model, where products are manufactured, used, and discarded as waste [121]. In the circular economy, the focus is on creating sustainable and regenerative systems that reduce environmental impact and relieve pressure on natural resources to make them available for future generations by promoting long-term resource efficiency, which is definitely in accordance with the concept of sustainable development as first defined in 1987 and further clarified in the United Nations Conference on Environment and Development (Earth Summit) in 1992. Additionally, the circular economy is in line with the United Nations' Sustainable Development Goals that were set in 2015. Of particular relevance; goals number 6 (clean water and sanitation) by reducing the amount of wastes released into water bodies, number 12 (responsible consumption and production) by extending the lifetime of products and designing

them to be used in other applications by the end of their lifetime, and number 17 (partnerships for the goals) through the integration between different corporations and industries to use each other's waste materials.

1.5. Properties, applications, and preparation methods of TiO_2 and its extraction from red mud

Titanium dioxide (TiO_2) offers several advantages, including high chemical and thermal stability and corrosion resistance, making it durable across diverse applications. It is of a low production cost, non-toxic, and biocompatible nature that ensures safety for use in different applications such as food industry (e.g., candy, chocolate, ice cream, etc) and cosmetics (e.g., sunscreen products). Additionally, its high refractive index provides excellent brightness as it reflects visible light, which is ideal for pigments [122]. Other applications include photocatalytic reduction of CO_2 [123]. However, the potential effects of TiO_2 on human health still need to be further investigated.

TiO_2 can have a high surface area that results in achieving a high adsorption capacity. In this context, TiO_2 samples synthesized by Kim *et al.* [124] using sol-gel method ranged between 186 and 210 m^2/g by varying the starting materials. Therefore, it is a common adsorbent used in wastewater treatment to remove different pollutants. TiO_2 is a widely used n-type semiconductor material with strong light absorbance properties since its early use in the oxygen evolution reaction from water by Fujishima and Honda in 1972 [125]. TiO_2 nanoparticles are more photocatalytically efficient than bulk TiO_2 because of their fine particle size, high surface-to-volume ratio, and better charge transport [123]. Thus, TiO_2 nanoparticles are of interest due to their high efficacy in working as a photocatalyst in water treatment. However, titania's efficiency is limited to ultraviolet (UV) light, which constitutes less than 5% of sunlight, due to its large bandgap energy (3-3.2 eV) as shown in **Fig 1.5**. The mechanism of photocatalytic degradation starts with the absorbance of UV light by TiO_2, and then the electrons will be excited and transferred from the valence band to the conduction band. This results in forming radicals that can then degrade the organic pollutants as clarified by Sujatha *et al.* [126] in **Fig 1.5**. TiO_2 can be easily modified or functionalized with various nanomaterials and transition metals or by coupling with other semiconductors to enhance its photocatalytic degradation efficiency under visible light as reported by Pelaez *et al.* [127] and adsorption of antibiotics as recently investigated by Gan *et al.* [128] who recorded an

adsorption capacity of 889 mg/g of ciprofloxacin using TiO_2 modified with 10 wt% of copper ions. Another study was carried out by Sanguanpak *et al.* [129] to remove six different antibiotics including amoxicillin and others from hospital wastewater by applying a composite of TiO_2 and a geopolymer of metakaolin, where the removal efficiency ranged between 38% and 75% by adsorption and up to 74 - 86% through the combination of adsorption and photodegradation. Metakaolin is the thermally activated, dehydroxylated product of kaolinite, formed by calcining kaolin at about 600-900 °C. It is an amorphous and highly reactive pozzolan that finds extensive use in cementitious systems, geopolymers, various advanced ceramic applications, and it could also be applied in the formulation of different adsorbents. It is worth mentioning that environmental concerns arise from the release of TiO_2 and other types of nanoparticles into the environment which may pose ecological risks in the long run because of their extremely small particle size.

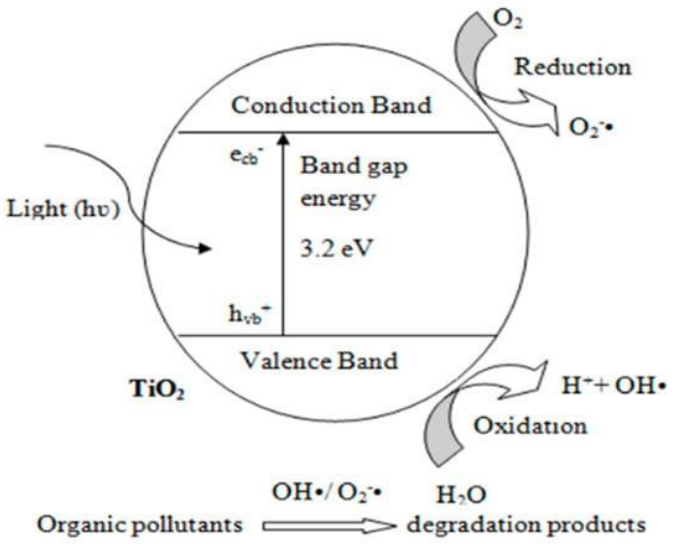

Fig 1.5. The mechanism of photocatalytic degradation of organic pollutants using TiO_2 [126] in which the electrons travel from the valance band to the conduction band leaving behind holes in the valance band upon the absorption of UV light by TiO_2. These photogenerated holes and electrons result in forming hydroxyl and superoxide radicals, respectively, that degrade organic pollutants.

TiO_2 has three natural crystalline phases including anatase (tetragonal), rutile (tetragonal), and brookite (orthorhombic) as shown in **Fig 1.6**. Anatase and brookite polymorphs are thermally stable up to 500-600 °C, but their phase changes into rutile at higher temperatures [122]. Anatase has more open structure and higher surface energy, whereas rutile is denser and more

compact. This results in higher reactivity of anatase. Also, the refractive index of rutile is higher, so it is used in pigments. The bandgap energy of anatase is 3.2 eV, whereas the bandgap of rutile is 3 eV. Rutile is more thermodynamically stable. While anatase and rutile are the common polymorphs of TiO_2, brookite is less common due to the difficulty of its preparation, but it can be highly photoactive and even more efficient than the commercial Degussa P25 if the right facets are exposed to light [130]. Commercial TiO_2 (P25) is a well-characterized and mixed phase photocatalyst with approximately 80% anatase and 20% rutile, known for excellent performance in photocatalytic degradation. Therefore, it is used in various applications and widely applied as a benchmark for photocatalysis. P25 has a surface area of around 55 m^2/g, and an average particle size of 25 nm.

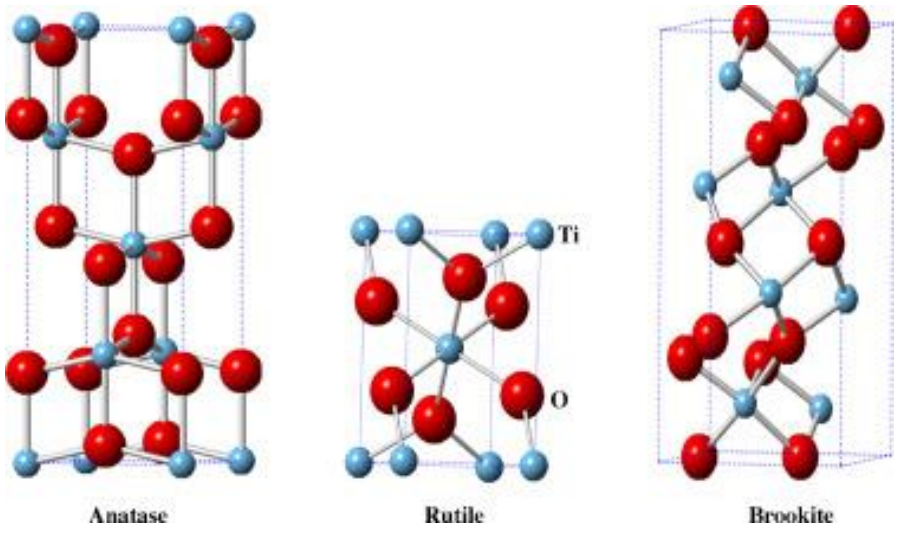

Fig 1.6. The three natural crystalline phases of TiO_2 are anatase (tetragonal), rutile (tetragonal), and brookite (orthorhombic) [131] with copyright permission from Elsevier.

1.5.1. TiO_2 preparation methods

Various methods are used to produce TiO_2 such as the sol-gel method, which is the most common method because of its cost-effectiveness and simplicity [123]. Sol-gel can result in nanoparticles formation, but it mainly produces TiO_2 layers or coatings. The sol-gel method starts with the hydrolysis of a titanium precursor such as titanium tetraisopropoxide in an aqueous solvent followed by polycondensation during which cross-linked gel structures are formed [132]. Lastly, the gel is dried and calcined to produce TiO_2. Factors such as pH, the reaction time and temperature, and the molar ratios of the reactants could be varied to control the nanoparticles' morphology and other properties [123, 133]. Lee *et al.* [134] indicated how

the variation in the preparation conditions of TiO_2 nanoparticles can affect their particle size and shape as the particles were spherical with an average size of 20 nm when using a pH of 8.5 during the preparation. Upon using a higher pH (10.5) the particles turned into a rod shape with a width of 20 nm and a length of 100 nm, and by adding ethylenediamine, which was used as a shape controller, to the reaction, the morphology changed to a wire shape with a width of 20 nm and a doubled length of 200 nm (**Fig 1.7.a-c**). Different factors could be controlled to move from TiO_2 layers/coatings to nanoparticles such as lowering the concentration of the titanium precursor to prevent the formation of a highly viscous gel. Also, lowering the temperature along with increasing the water content can lead to faster hydrolysis and subsequently forming smaller/fine particles [135].

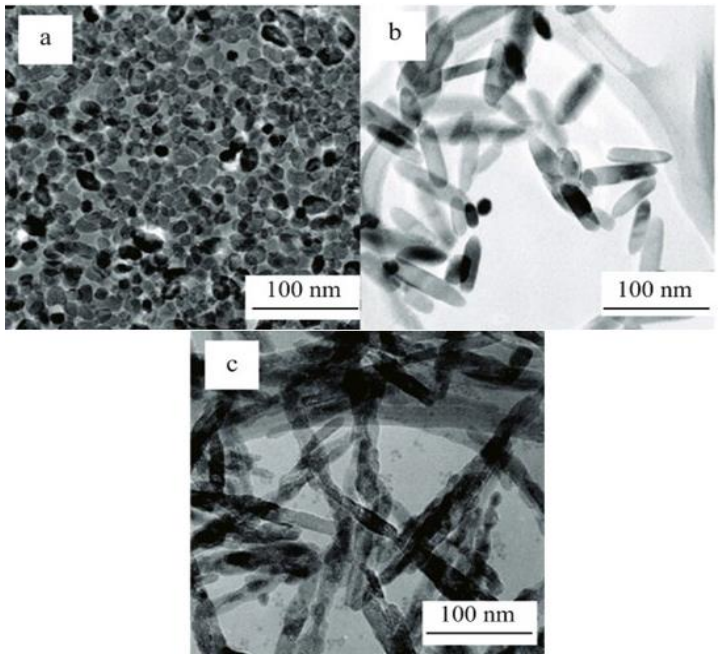

Fig 1.7. TEM images of the synthesized (**a**) spherical, (**b**) rod-like, and (**c**) wire-like TiO_2 nanoparticles at pH 8.5, pH 10.5, and pH 10.5 after adding ethylenediamine (shape controller), respectively, [134]. This figure is used with permission from the American Chemical Society.

Hydrothermal synthesis is another technique to prepare TiO_2 nanoparticles using aqueous solvents under elevated temperatures above room temperature (≈ 200 °C) and pressures exceeding one atmosphere in a sealed system such as an autoclave. This technique facilitates crystal growth, phase transformation, and phase equilibrium, ultimately resulting in the formation of fine to ultra-fine crystals [136]. Additionally, the hydrothermal synthesis can

produce microporous TiO_2 nanoparticles with a particle size range of 1-7 nm [137]. In this method, a titanium precursor is mixed with a highly concentrated NaOH (10-15 M), heated in an autoclave for 16 up to 72 hours in a temperature range of 110 - 180 °C. Subsequently, the formed precipitate is washed with water and HCl followed by calcination to form TiO_2 nanoparticles [123]. The reagents' concentration, molar ratios, temperatures, and reaction times can control the characteristics of the synthesized nanoparticles. The solvothermal method is very similar to hydrothermal synthesis except for using organic instead of the aqueous solvents.

The anodic oxidation method uses titanium foils as the anode for oxidation within a fluoride-containing electrolyte, such as HF, NaF, or KF, in a two-electrode electrochemical setup. A platinum foil functions as the cathode, with an applied potential ranging between 20 and 100V to produce TiO_2 nanoparticles [138]. The microwave-assisted method is a technique by which the conventional energy-intensive thermal heating used in the above-mentioned preparation methods is replaced by very quick microwave heating, which can result in better crystallinity and smaller particle size [123, 139]. Other techniques that could be used to synthesize TiO_2 nanoparticles include the direct oxidation method of titanium metal using different oxidants such as H_2O_2 [140], sonochemical, and chemical vapor deposition [123].

1.5.2. Extraction techniques of TiO_2 from red mud

TiO_2 can be sourced from red mud using several methods including pyrometallurgy that involves extracting iron from red mud either through reducing red mud volume by magnetic separation to isolate iron or by melting the material in a blast, low, or electric furnace, resulting in the production of pig iron [95]. Consequently, the remaining residue after removing the iron would have concentrated TiO_2 that could be separated by acid leaching [141]. High energy requirements accompanied by the high cost make the scale-up of this technique harder. In general, there is not much information available on the cost of red mud treatment due to variations in red mud composition, energy prices, and furnace efficiencies. However, the average cost of red mud treatment is estimated to be 9$ per ton [142], which is about 3% of the price of one ton of alumina. On the other hand, the hydrometallurgical extraction of TiO_2 using different acids offers more cost-effective extraction with milder temperatures [141].

1.6. Extraction of iron and iron-containing minerals from red mud

1.6.1. Iron oxides and oxyhydroxides

Red mud comprises different types of iron-containing minerals that vary according to the type of aluminium production process and the location of the bauxite ore. Haematite (α-Fe_2O_3) and magnetite (Fe_3O_4) constitute the major iron-containing minerals of red mud along with other components such as maghemite (γ-Fe_2O_3), goethite (α-FeOOH), and siderite ($FeCO_3$) as shown in **Fig 1.8** [143]. The crystal structure of α-Fe_2O_3 (**Fig 1.9.a**), which is anti-ferromagnetic below the Morin temperature (260 K) and weakly ferromagnetic at ambient temperature, is the same as that of rhombohedral corundum (α-Al_2O_3). The oxygen atoms in α-Fe_2O_3 are arranged in a hexagonal close-packed arrangement, with two-thirds of the octahedral sites occupied by Fe^{3+} and the remaining one-third vacant [144]. Fe_3O_4 is a ferrimagnetic iron oxide and the most naturally occurring magnetic substance on Earth [145]. Unlike other iron oxides, Fe_3O_4 contains Fe^{2+} and Fe^{3+} ions, contributing to its inverse spinel structure. Its ferrimagnetic behaviour arises from the arrangement of iron ions in the unit cell: the eight Fe^{3+} ions in octahedral sites align antiparallel to the eight Fe^{3+} ions in tetrahedral sites, effectively canceling out their magnetic moments (**Fig 1.9.b**). However, the presence of eight Fe^{2+} ions in octahedral sites, whose spins are not canceled, generates a net magnetic moment. γ-Fe_2O_3 typically forms in a cubic spinel structure, where all or most Fe exists in the trivalent state [144]. Fe^{3+} ions are randomly distributed across both tetrahedral and octahedral sites (**Fig 1.9.c**). However, it can also undergo tetragonal distortion due to the ordered arrangement of cation vacancies [145].

α-FeOOH forms in the orthorhombic crystal system, where Fe^{3+} ions are octahedrally coordinated by oxide and hydroxide ions (**Fig 1.9.d**). The FeO_6 octahedra are linked by shared edges and corners, creating chains along the crystallographic c-axis and resulting in a slightly distorted, layered structure. A distinguishing feature of α-FeOOH is the presence of hydroxyl groups, with the structure elongated along the c-axis due to the specific connectivity of the octahedra. $FeCO_3$, part of the calcite carbonate group, crystallizes in a trigonal system with rhombohedral symmetry. Its structure features Fe^{2+} ions coordinated by six oxygen atoms, forming an octahedral arrangement (**Fig 1.9.e**). These octahedra are interconnected through planar carbonate groups (CO_3^{2-}), resulting in a repeating layered framework. The planar triangular arrangement of the carbonate groups (CO_3^{2-}) and the positioning of Fe^{2+} ions in octahedral sites contribute to the structure's high symmetry and stability.

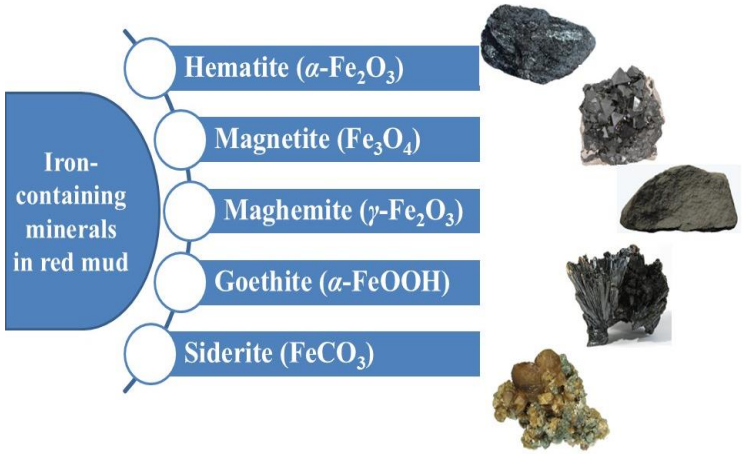

Fig 1.8. The various iron-containing minerals in red mud including hematite, magnetite, maghemite, goethite, and siderite.

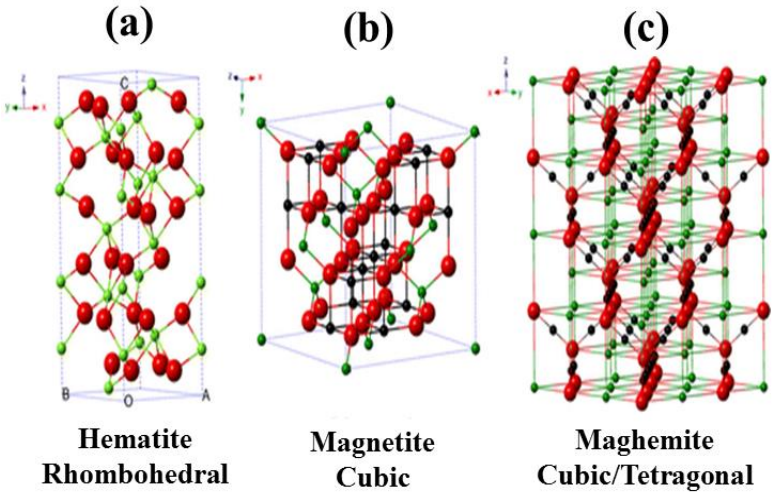

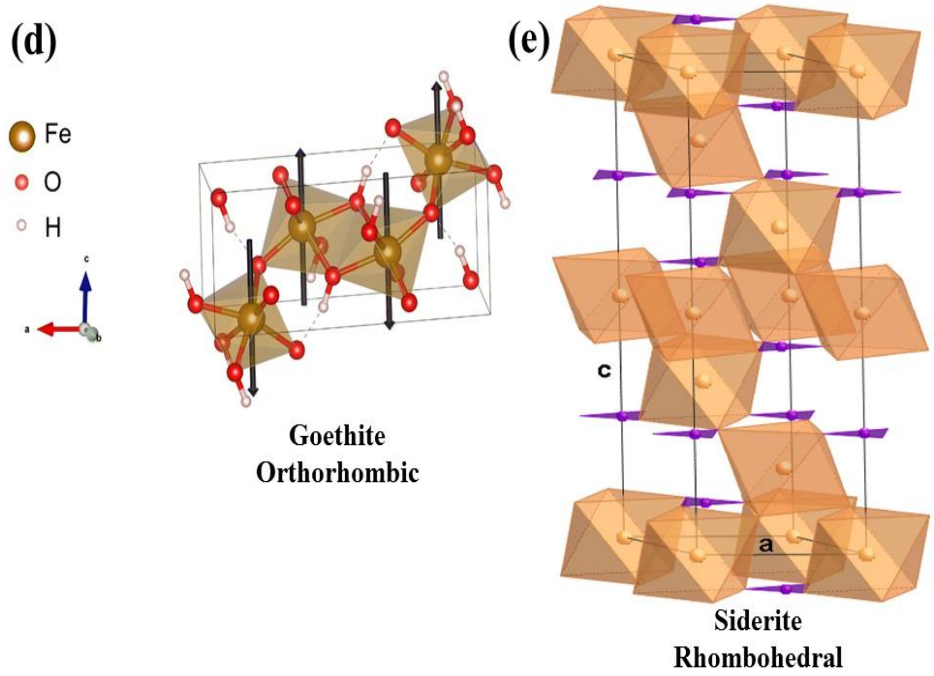

Fig 1.9. Crystal structure and crystallographic data of haematite (**a**), magnetite (**b**), and maghemite (**c**). Fe^{2+} (black), Fe^{3+} (green), and O^{2-} (red) [146]. The crystal structure shows the orthorhombic unit cell and the 3D structure of goethite **(d)** [147] with permission from Springer Nature. The crystal structure of siderite, where the orange polyhedral unit is trigonally distorted (elongated along c-axis) $Fe^{2+}O_6$-octahedra and the violet triangles are CO_3 groups **(e)** [148] with a copyright permission from Springer Nature.

The Pourbaix diagram of iron serves as a thermodynamic roadmap that illustrates how iron responds to different pH levels and redox potentials, allowing to anticipate corrosion, passivation, and mineral transformations in aqueous environments. The diagram shows the speciation of iron across different pH and redox potential conditions [149]. The boundaries in a Pourbaix diagram correspond to acid-base (pH) or redox equilibria and indicate the conditions under which two species can coexist. Horizontal lines show the redox reactions, whereas the vertical lines represent the pH-dependent reactions, and the sloped lines display pH and redox-based transitions [150]. In this diagram such as the one presented in **Fig 1.10** at 25 °C, metallic iron is stable only in a limited zone of moderately reducing conditions. This region is known as the immunity region [151].

When the environment becomes more oxidizing, iron tends to form ferric oxides such as α-Fe_2O_3, which create protective layers on the metal surface. Under slightly reducing and alkaline conditions, Fe_3O_4 becomes the dominant stable phase, reflecting the interplay

between Fe^{2+} and Fe^{3+} species and its importance in environmental redox cycles. However, in acidic or strongly reducing environments, these protective solids dissolve, yielding aqueous Fe^{2+} or Fe^{3+} and making corrosion more likely. Eq. (1.7) represents a redox reaction that is separated by a horizontal line, whereas equation eq. (1.8) shows a pH-dependent reaction, and eq. (1.9) refers to a reaction that depends on both factors and represented by sloped line [152].

$$Fe^{3+}(aq) + e^{-} \rightarrow Fe^{2+}(aq) \qquad \text{eq. (1.7)}$$

$$2\,Fe^{3+}(aq) + 3\,H_2O \rightarrow Fe_2O_3\,(s) + 6\,H^{+}(aq) \qquad \text{eq. (1.8)}$$

$$2\,Fe^{2+}(aq) + 3\,H_2O \rightarrow Fe_2O_3\,(s) + 6\,H^{+}(aq) + 2\,e^{-} \qquad \text{eq. (1.9)}$$

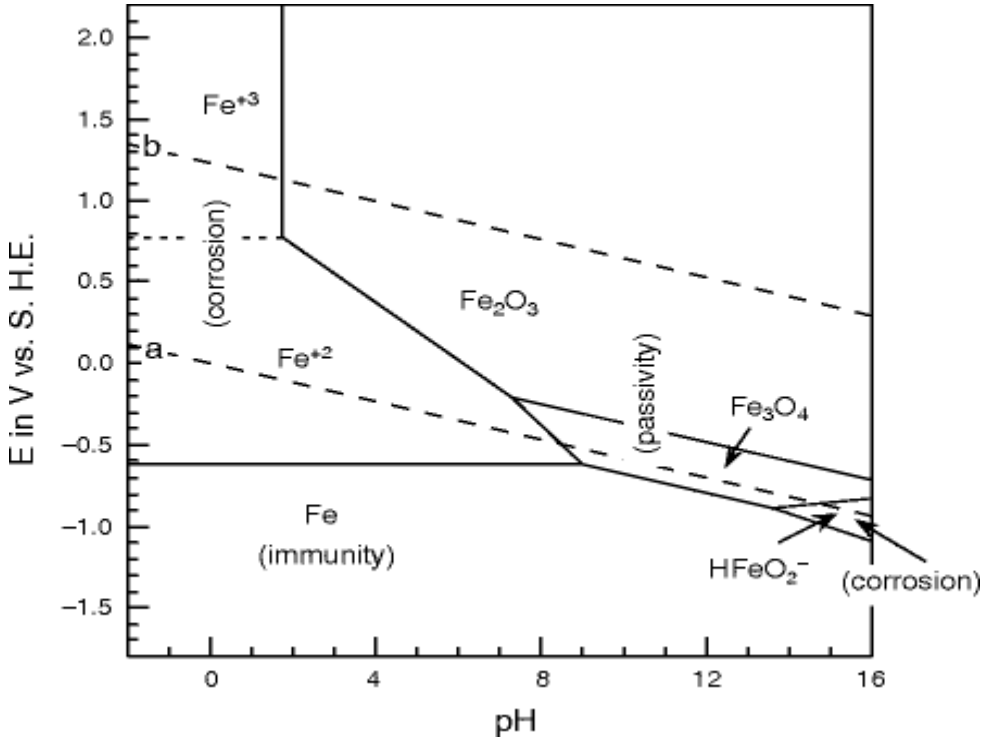

Fig 1.10. Iron Pourbaix diagram at 25 °C with permission from Springer Nature [151] showing how the phase and the oxidation state of iron differ by changing pH levels and redox potentials, allowing to anticipate corrosion, passivation, and mineral transformations in aqueous environments.

1.6.2. Extraction techniques of iron and iron oxides from red mud

Various techniques are utilized for the separation and recovery of these iron oxides, and they are generally categorized into physical, chemical, electrochemical, and biological methods. Firstly, the physical methods consist of gravity separation, magnetic separation, and flotation.

Gravity separation of mineral components of red mud mainly depends on the difference in their density, particle size, and shape [153]. Magnetic separation, one of the conventional physical extraction methods of iron oxides from red mud, was used for a long time due to its low cost and facile operation. However, the extraction was not efficient (about 43%) since haematite is not a strong magnetic material, so it needs a high magnetic field [153]. Therefore, this technique was upgraded into a high gradient superconducting magnetic separation system by applying a stronger magnetic field resulting in almost 65% recovery. However, the stronger magnetic field attracted other non-target materials such as weak and non-magnetic materials, diminishing the iron grade [154]. Flotation is another physiochemical technique that was employed by many workers in which they used some functional groups such as the acidic functional groups (e.g., carboxyl groups) in humic materials (flocculants) to selectively extract about 85% of the iron oxide from red mud as these groups work efficiently at pH ≥ 10 [155]. However, harsh chemicals such as hydrochloric, sulfuric, and hydrofluoric acids as well as sodium hydroxide are used in preparing these flocculants [155-157], which are also used in hydrometallurgical extraction. Therefore, physical techniques offer some advantages including low cost compared to other extraction techniques and simple operation. However, some negative aspects need to be considered such as the low extraction efficiency and using harsh chemicals in the case of physiochemical techniques.

Secondly, chemical methods including pyrometallurgy and hydrometallurgy are commonly applied in extracting iron oxides and other materials from red mud. Hydrometallurgy refers to the extraction of iron oxides and other target materials by acid leaching, solvent extraction, and precipitation. Several factors including temperature, acid concentration, leaching time, and liquid-solid ratio affect the extraction efficacy [158]. The acid leaching step could be done using hydrochloric, nitric, glacial acetic, or oxalic acids with different concentrations, but using high acid concentrations was confirmed to be more efficient [158]. Hydrometallurgy does not necessarily need high temperature, but the high alkalinity of red mud requires large volumes of acids which add to the cost and result in the formation of acidic waste that must be neutralized. Therefore, various techniques including red mud treatment with acidic waste could be applied to solve these issues [153].

Pyrometallurgy is a high-temperature process in which chemical-reducing agents such as coal char, graphite, and coke are used to extract iron and iron oxides [159]. Roasting and smelting processes constitute the most common pyrometallurgical methods for iron extraction, but their

high energy requirement represents a limiting factor [159]. Consequently, numerous amendment techniques are continuously investigated to cut down their operation cost such as fluidization using fixed bed reactors that require a temperature of 500 °C [160] instead of 1000 - 1300 °C that is usually used in pyrometallurgy. Other techniques that could also be used for extracting iron from red mud are thermal plasma technology [161] and microwave heating [162].

Thirdly, it is worth mentioning that the electrochemical technique is another technique that could be used to extract iron metal from red mud. However, it does not lead to high extraction efficacies due to the low conductivity induced by the formation of bubbles on the electrodes in the red mud suspension [163]. Lastly, bioleaching represents an interesting ecofriendly and inexpensive technique for iron recovery using microorganisms such as bacteria and fungi, but the extraction efficiency is still a limiting factor since the majority of microorganisms cannot thrive in the highly alkaline conditions of red mud [153]. Thus, it is essential to search for microorganisms capable of tolerating extremely high pH levels [153]. Also, this process is slow and can take up a month as reported by Vakilchap *et al.* [164] who achieved an extraction efficiency of 25% of iron from red mud using *Aspergillus niger*. Consequently, it could be concluded that numerous techniques could be applied for the extraction of iron and iron oxides from red mud. However, each one has its limitations that need to be considered and carefully addressed in future research to enhance the extraction efficiency.

1.6.3. Haematite and its use as a catalyst

Haematite is one of the most important phases of iron oxide owing to its abundance in the earth's crust, low production cost, facile regeneration under certain conditions (e.g., high temperature and oxidizing conditions), high stability, and corrosion resistance, so it is used as a catalyst in several applications [165]. Generally, α-Fe_2O_3 is the ultimate iron oxide at the end of the transformation/oxidation series of other iron oxides [166] and it was historically used in paintings due to its reddish brown colour, stability, and high refractive index. The energy band gap of haematite, an n-type semiconductor, is about 1.9 - 2.2 eV [167]. It is worth mentioning that almost 40% of sunlight is in the visible region. Therefore, haematite could be used as a photocatalyst due to its capability of absorbing this visible light. According to these unique properties of haematite, it is employed in numerous industries such as pigment manufacture

and gas sensor production [168] and as a photoelectrode in solar water splitting to produce hydrogen [169].

One of the most accessible and affordable methods for removing hazardous metals from wastewater is to use iron. The high efficacy of iron oxides in the adsorption of heavy metals was confirmed in previous studies due to their ease of usage, accessibility, and eco-friendliness. Additionally, when employed in wastewater treatment processes, it does not result in the formation of serious secondary pollutants [170]. Several modifications could be applied to enhance the efficiency of iron oxides including ligand attachment and the addition of polymers that increase the surface functional groups, improve the dispersion, and inhibit their aggregation [171]. In this regard, haematite nanostructures showed high efficacy in the adsorption of various heavy metals such as the hexavalent chromium that was removed with an efficiency of 95% [172] and it was also efficiently used in adsorbing nickel and cadmium ions with almost 80.5% and 96%, respectively [173]. Many haematite composites were investigated in the adsorption of antibiotics. For instance, a composite of haematite-biochar was tested as an adsorbent of norfloxacin and it showed a high removal efficiency of 81.6% [174].

Although haematite can work as a photocatalyst in the visible region due to its low bandgap energy, it has some drawbacks that limit its efficiency such as the fast rate of electron-hole recombination, low absorption coefficient, and low charge transfer. Therefore, several techniques such as the impregnation of other photocatalytic materials into haematite, morphological control, and synthesis of heterostructures are utilized to increase the lifetime of electron-hole separation since the mixture of two photocatalysts with narrow and wide bandgap energies enhances the photocatalytic performance [175]. Graphene, graphene oxide (GO), graphitic carbon nitrides, biochar, MOFs, ZrO_2, TiO_2, as well as numerous metal nanoparticles including Au and AgNPs, represent some of the materials that are utilized in enhancing the photocatalytic efficacy of haematite.

In a recent study, Kaur *et al.* [176] investigated the positive effect of adding AgNPs to a heterostructure of α-Fe_2O_3/ZnO and the result was 76.4% degradation of ciprofloxacin compared to 43% and 63% using α-Fe_2O_3 and ZnO, respectively, under natural sunlight. Such a result confirmed the role of AgNPs in enhancing the charge transfer leading to high photodegradation efficiency. In another study, a composite of α-Fe_2O_3/GO was very

efficiently applied in the photoreduction of hexavalent to trivalent chromium since the reduction efficiency was about 95% compared to 25% using pristine α-Fe_2O_3 under visible light [177]. In contrast to pristine graphene, graphene oxide exhibits superior dispersibility, higher chemical reactivity, greater ease of functionalization, enhanced adsorption and catalytic capabilities, improved compatibility in composite materials, and lower production cost. These benefits stem from the plentiful oxygen-bearing functional groups on its surfaces and edges, which significantly broaden its processing flexibility and potential applications [178]. Additionally, the possibility of using α-Fe_2O_3, which was hydrometallurgically extracted from red mud, as a photo-Fenton catalyst after being mixed with cupric oxide (CuO) in degrading malachite green was proved in a very recent study carried out by Nanda *et al.* [179] in which the degradation efficiency was 98%.

1.7. Biogenic iron oxide and its potential applications

Biogenic iron oxides (BIOX) are iron-containing compounds naturally produced by bacteria. *Gallionella* and *Leptothrix* species of bacteria are filamentous, sheathed microorganisms that flourish in iron-rich environments like freshwater streams, wetlands, and soils where they contribute significantly to the biogeochemical cycling of iron [180]. The presence of these bacteria is often associated with the appearance of an oily film on the water surface. They are recognized for their unique ability to oxidize ferrous iron (Fe^{2+}) into ferric iron (Fe^{3+}), resulting in the formation of iron oxide precipitates. *Gallionella* usually forms twisted stalks, whereas *Leptothrix* creates long, thread-like filaments surrounded by a sheath that becomes coated with iron oxides as they metabolize iron from their surroundings [181]. This iron oxide has a tubular or filamentous morphology with a high surface area and a poor crystalline structure like that of synthetic 2-line ferrihydrite. These tubes have an inner diameter of approximately 1 μm and varying lengths up to 200 μm, and the sheaths are averaging 0.15 μm in thickness [182]. Synthetic ferrihydrite has two crystal structures; 2-line and 6-line where the powder XRD pattern of the first one has two very broad reflections, and the pattern of the other one has six very broad reflections.

When BIOX accumulates in water courses, pipes, wells, and other systems, it results in the clogging of these systems [183]. However, there is potential to make use of these oxides in various applications. BIOX produced by *Leptothrix* bacteria can be applied in wastewater treatment as they possess good properties, such as a high surface area, reactivity, and the

ability to adsorb different pollutants. Additionally, BIOX can function as a catalyst or catalyst support in various chemical reactions, particularly those involved in industrial processes. In this regard, BIOX was used by Alharthi *et al.* [184] as a catalyst in the cracking of methane to produce hydrogen. Additionally, the catalytic efficiency of different sorts of biogenic iron oxides and oxyhydroxides was applied by Shopska *et al.* [185] in CO oxidation. Using BIOX as a support in preparing Pd catalysts was undertaken by Mandai *et al.* [186] who used these catalysts in the solvent-free Suzuki-Miyaura coupling.

BIOX was previously used in water treatment such as the removal of phosphorus [187] and heavy metals such as lead and uranium [188]. Other researchers used BIOX in removing dissolved organic matter from collected stream water [189]. In a recent study, Rico and Hargreaves [190] investigated the reduction and nitridation of BIOX samples under H_2/N_2 and NH_3, respectively. The authors confirmed the preserved tubular morphology of BIOX after both processes at 500 °C leaving the door open for a further investigation of these reduced and nitrided structures in different applications. Therefore, the current study builds on their research in using BIOX structures before and after the reduction in the removal of antibiotics particularly ceftriaxone and doxycycline from different water samples.

1.8. The Haber-Bosch Process of ammonia synthesis using iron-based catalysts and its challenges

The Haber-Bosch Process stands as one of the most transformative technological breakthroughs in modern human history, playing a foundational role in the expansion of agricultural productivity and industrial chemistry. Developed in the early 20th Century, it enabled the synthesis of ammonia (NH_3) on an industrial scale using an iron-based catalyst from atmospheric nitrogen and hydrogen gas from steam reforming process, providing a cornerstone for the production of synthetic nitrogen-based fertilizers [191]. The far-reaching impacts of this process extend to global food security and geopolitical stability. It has been a driving force behind the sharp increase in agricultural output and global population growth, helping to reduce hunger and malnutrition in various parts of the world. However, its intensive energy demand, and environmental footprint also pose critical challenges in the context of climate change and sustainability.

The Haber-Bosch Process began with the pioneering work of German chemist Fritz Haber, who, in 1909, achieved the catalytic production of ammonia in a laboratory environment.

Seeing the significance of this discovery, Carl Bosch, a chemist and engineer at BASF, took on the challenging task of adapting the method for large-scale industrial use. By 1913, Bosch had successfully established the first high-pressure industrial ammonia production facility in Germany [192]. This achievement marked the birth of large-scale nitrogen fixation. The Haber-Bosch Process liberated agriculture from reliance on limited natural fixed nitrogen sources, allowing for widespread availability of nitrogen fertilizers. Today, it is estimated that more than half of the world's population relies on food grown using fertilizers produced through this method.

The underlying chemical reaction of the Haber-Bosch process is:

$$N_2(g) + 3H_2(g) \rightleftharpoons 2NH_3(g) \qquad \Delta H = -92.4 \text{ kJ/mol} \qquad \text{eq. (1.10)}$$

The synthesis of ammonia is exothermic, meaning it releases energy, and is favored thermodynamically at lower temperatures. However, the strong triple bond in molecular nitrogen (N≡N), with a bond dissociation energy of approximately 941 kJ/mol, makes the reaction kinetically sluggish. Overcoming this requires a high-pressure (150 - 300 atm) and high-temperature (400 - 500 °C) environment to drive the reaction at industrially viable rates and to produce acceptable yields [193]. The reaction is typically facilitated using an iron-based catalyst promoted with oxides such as K_2O, Al_2O_3, and CaO to enhance its activity and longevity.

Hydrogen is most commonly derived from steam methane reforming of natural gas, a process that consumes significant energy and emits substantial quantities of CO_2. The overall energy requirement for ammonia synthesis is immense as it accounts for nearly 1-2% of the world's total energy consumption and is responsible for approximately 1.6% of global CO_2 emissions [194]. Also, the high cost of the new developed catalysts that could operate the synthesis process at lower pressures and temperatures is another challenge on the list of limitations and challenges. In this context, the iron oxides derived from the natural and industrial waste materials used in the current study were tested in NH_3 synthesis as a step towards finding new catalysts to reduce the production cost and making the process greener and more sustainable.

1.9. Project aims

With increasing concerns about water contamination and the release of persistent pharmaceuticals, including antibiotics, into aquatic ecosystems worldwide, developing sustainable wastewater treatment methods has become an urgent necessity along with avoiding the generation and release of secondary pollutants, which in some cases can be more toxic than the main target pollutant. In this regard, Ceftriaxone (CEF), which is a third-generation cephalosporin antibiotic used effectively in the treatment of respiratory and urinary tract system infections caused by various gram-positive and gram-negative bacteria for both animals and humans, results in water pollution [195]. Doxycycline (DOXY) is the second antibiotic selected and investigated in this study since it is very commonly used to treat various infections such as skin, chest, and dental infections as well as sexually transmitted infections (e.g., Chlamydia). Therefore, the eco-friendly removal of both antibiotics from wastewater is the first main goal of this study.

The second main goal of this work is to make use of waste materials either found in nature or released into the environment from anthropogenic activities in the adsorption of the above-mentioned antibiotics. Therefore, *T. latifolia* was used to synthesize α-Fe_2O_3 which was characterized and used in the first chapter of results along with the lab-prepared TiO_2. Additionally, different synthesis conditions were investigated in this chapter. Then TiO_2 was extracted from red mud by two methods and a comparison between the efficacies of TiO_2 produced by each one is thoroughly discussed. In the second chapter of results, red mud-extracted α-Fe_2O_3 and TiO_2 were used in the removal of DOXY. The last chapter of results provides an insight into the applicability of using pristine BIOX, collected from three different sites (Milngavie, Scotland), calcined, and reduced BIOX materials in the adsorption of the two antibiotics. This study thoroughly investigated the effects of various transition and post-transition metals, interfering ions, and other experimental parameters. It proposes the mechanism of antibiotic removal and compares the efficiencies of adsorption and degradation for each antibiotic, including the identification of potential degradation products. Furthermore, the applicability of the biogenic and red mud-based iron oxides in ammonia synthesis was evaluated. Overall, the work aligns with the principles of sustainable synthesis and the circular economy.

Chapter 2

2. Materials and methods

2.1. Chemicals and reagents

Copper (II) nitrate trihydrate ($Cu(NO_3)_2.3H_2O$ 98%) was supplied by Riedel-de Haen (Honeywell). Zinc nitrate hexahydrate ($Zn(NO_3)_2.6H_2O$ 98%) was supplied by Alfa Aesar. Iron nitrate nonahydrate ($Fe(NO_3)_3.9H_2O$ 99%) and N-(1-Napthyl)-ethylenediamine dichloride (NED) were procured from Thermo Fisher Scientific. Calcium oxide (CaO), sodium carbonate (Na_2CO_3), sulfuric acid (H_2SO_4), cobalt nitrate hexahydrate ($Co(NO_3)_2.6H_2O$ >98%), nitric acid (HNO_3) (70%), and sodium hydroxide (NaOH) (98-100%) were supplied by Fisher Scientific. Calcium chloride hexahydrate ($CaCl_2.6H_2O$) was obtained from Aldrich, sodium chloride (NaCl) was supplied by Fisher, sodium sulfate anhydrous (Na_2SO_4), copper (II) oxide (CuO), titanium tetraisopropoxide ($Ti[OCH(CH_3)_2]_4$), magnesium oxide (MgO), amorphous silica (SiO_2), glycerol ($C_3H_8O_3$), phosphoric acid (H_3PO_4), and salicylic acid ($C_7H_6O_3$) were procured from Sigma Aldrich. Hydrogen peroxide (H_2O_2) was purchased from Merck. Nickel nitrate hexahydrate ($Ni(NO_3)_2.6H_2O$ 99%) was obtained from Janssen Chimica. Sodium nitrate ($NaNO_3$) (99.5%) was supplied by Hopkin & Williams. Oxalic acid ($(COOH)_2$) was obtained from Hopkin & Williams. Absolute ethanol (C_2H_5OH) was obtained from Winchester. Hydrochloric acid (HCl) (36.5-38%) was supplied by Honeywell Fluka. Commercial titania (Aeroxide P25) was supplied by Thermo Fisher Scientific. Commercial haematite (α-Fe_2O_3 99.8%) was procured by Strem chemicals. Potassium nitrite (KNO_2 97%) was from Acros. Sulfanilamide was from VWR. Commercial magnetite (Fe_3O_4) was supplied by Aldrich. Doxycycline Hyclate ($C_{22}H_{24}N_2O_8$) was supplied by El-Nile Pharmaceutical Company. Ceftriaxone sodium antibiotic powder ($C_{18}H_{18}N_8O_7S_3Na_2$) was purchased from Sandoz Pharmaceutical Company, Egypt. A red mud sample from Shandong province in China was provided by Dr. Hannian Gu. Also, two red mud samples from India (RM 7 and RM 8) were very kindly provided by Dr Vidya Batra from TERI University, New Dehli. All the purities are presented in mass%.

2.2. Preparation of *T. latifolia* extract

In the current study, *T. Latifolia* was collected from Possil Marsh, Glasgow, the United Kingdom (**Fig 2.1**) on the 22nd April 2022, and the coordinates are 55.9047573,-4.2644770. *T. Latifolia* (shoot) was rinsed with deionized water (DW) several times to remove impurities or

dirt, and then shredded and allowed to dry in the open air followed by oven drying overnight at 60° C. Subsequently, the dried *T. Latifolia* was ground in a stainless-steel mixer to obtain the fine powder. Subsequently, five grams of the powder were dissolved in 100 mL of DW, then the solution was heated and stirred at 80 °C for 60 min, and finally, it was filtered, and the filtrate was preserved at 4 °C for further use.

Fig 2.1. A photo of the Possil Marsh site where the samples of *T. Latifolia* were collected on the 22nd April 2022.

2.3. Preparation of titania and its composites

The sol-gel method was used in the current study in which 10 mL of DW was drop-wise added to 10 mL of titanium tetraisopropoxide, as prepared by mixing titanium tetrachloride with isopropanol at low temperature and continuous stirring and mixed for one hour at 80 °C. The mixture was stirred for an hour at 80 °C. Subsequently, a white slurry was formed, dried, and then calcined at 400 °C for two hours to produce TiO_2 as indicated by equations 2 and 3.

$$Ti[OCH(CH_3)_2]_4\,(aq) + 4\,H_2O\,(l) \rightarrow Ti(OH)_4\,(s) + 4\,CH_3CH(OH)CH_3 \qquad \text{eq. (2.1)}$$

$$2\,Ti(OH)_4\,(s) \rightarrow 2\,TiO_2\,(s) + 4\,H_2O\,(g) \qquad \text{eq. (2.2)}$$

Different metal ions including iron (Fe^{3+}), cobalt (Co^{2+}), nickel (Ni^{2+}), copper (Cu^{2+}), and zinc (Zn^{2+}) were used to produce 10 wt% composites of TiO_2 through a wet impregnation method by mixing 72.3 mg, 49.3 mg, 49.9 mg, 38.0 mg, and 45.5 mg of the nitrate salts of the above-mentioned metals, respectively, with 100 mg of TiO_2 in DW. The composite solutions were

stirred and heated at 90 °C for 90 minutes followed by overnight drying at 110 °C. 14.4 mg and 36.1 mg of iron nitrate were mixed with 100 mg of TiO_2 to prepare 2% and 5 wt% loadings, respectively. 7.6 mg and 19.0 mg of copper nitrate were mixed with 100 mg of TiO_2 to prepare 2 and 5 wt%, respectively. 9.1 mg and 22.7 mg of zinc nitrate were mixed with the same amount of TiO_2 to prepare 2 and 5 wt%, respectively. Cu, Zn, and Fe-TiO_2 samples were further subjected to calcination at 400 °C for two hours to compare their adsorption efficiency before and after the calcination step. It must be noted that using equal mass loadings of the impregnated metals does not imply equal amounts in moles nor equal numbers of adsorption sites, since the atomic masses of Fe, Co, Ni, Cu, and Zn are different. This factor may account for part of the observed differences in antibiotic adsorption efficiency. Therefore, this factor is strongly recommended to be further investigated in future studies.

2.4. Green synthesis of haematite

The green synthesis of haematite was simply undertaken by stirring ferric nitrate nonahydrate solution (0.1 M) with the aqueous extract of *T. latifolia* with a ratio of 1:1 for one hour at 65 ± 5 °C. This process produces a brown/black precipitate of $Fe(OH)_3$. Subsequently, the mixture was centrifuged to separate the precipitate, and then it was washed with DW followed by oven drying at 60 °C. This precipitate was believed to be $Fe(OH)_3$ due to its amorphous powder XRD pattern. The role of the plant extract was to precipitate the Fe^{3+} ions by increasing the pH from 1.7 to 2.36 through its OH-containing phytoconstituents including saponins, triterpenes, and phenols [196], and polyphenols (flavonols) such as quercetin [197]. It is suggested that these phytoconstituents can chelate Fe^{3+} ions and reduce their effect in acidifying the solution, which can result in the above-mentioned slight pH increase accompanied by the precipitation of Fe^{3+} ions as $Fe(OH)_3$. A control experiment was undertaken using $Fe(NO_3)_3$ and NaOH to confirm the role of the OH in precipitating $Fe(OH)_3$. Lastly, the dried precipitate was calcined (dehydrated) in a tube furnace at 550 °C for three hours to convert $Fe(OH)_3$ into α-Fe_2O_3. This procedure is similar to that reported by Naz *et al.* [198], but using ferric nitrate instead of ferric chloride.

$$Fe(NO_3)_3.9H_2O\ (aq) + 3\ NaOH\ (aq) \rightarrow Fe(OH)_3\ (s) + 3\ NaNO_3\ (aq) + 9\ H_2O\ (l) \qquad \text{eq. (2.3)}$$

$$2\ Fe(OH)_3\ (s) \rightarrow Fe_2O_3\ (s) + 3\ H_2O\ (g) \qquad \text{eq. (2.4)}$$

The molar masses of 2 $Fe(OH)_3$, α-Fe_2O_3, and 3 H_2O are 213.7, 159.7, and 54.0 g/mol, respectively. So, the percentage of water loss during the dehydration of $Fe(OH)_3$ to α-Fe_2O_3 in theory is (54 / 213.7) × 100 = 25.2%. To confirm this calculation, TGA-MS analysis was carried out under 2% oxygen in argon mixture using a ramp rate of 10 °C per minute from room temperature to 550 °C followed by an isothermal hold at 550 °C for three hours to show the mass loss in mg as a function of temperature °C (**Fig 2.2.a**) and time in minutes (**Fig 2.2.b**). The dehydration time was 233 minutes including 53 minutes to increase the temperature from around 20 °C to 550 °C followed by 180 minutes of hold at 550 °C. As shown in **Fig 2.2.a** and **b**, the mass decreased from 21.5 g to 15.2 g with a mass loss percentage of 29.3%, which is close to the theoretical percentage confirming the dehydration process shown in eq. (2.4). It should be noted that **Fig 2.2.a** and **b** are not combined into a single figure because doing so would distort the display, as the temperature is held constant for three hours during the isothermal stage. To further confirm the dehydration of $Fe(OH)_3$ and its conversion into α-Fe_2O_3 during the TGA analysis, the powder XRD of the remaining powder at the end of the TGA analysis was checked, and it clearly showed the reflections of α-Fe_2O_3 as shown in **Fig 2.2.c**. The domain size of the resultant α-Fe_2O_3 was 30 nm, which is very close to the size of green synthesized α-Fe_2O_3 and lab-prepared α-Fe_2O_3 that were 33 and 34 nm, respectively.

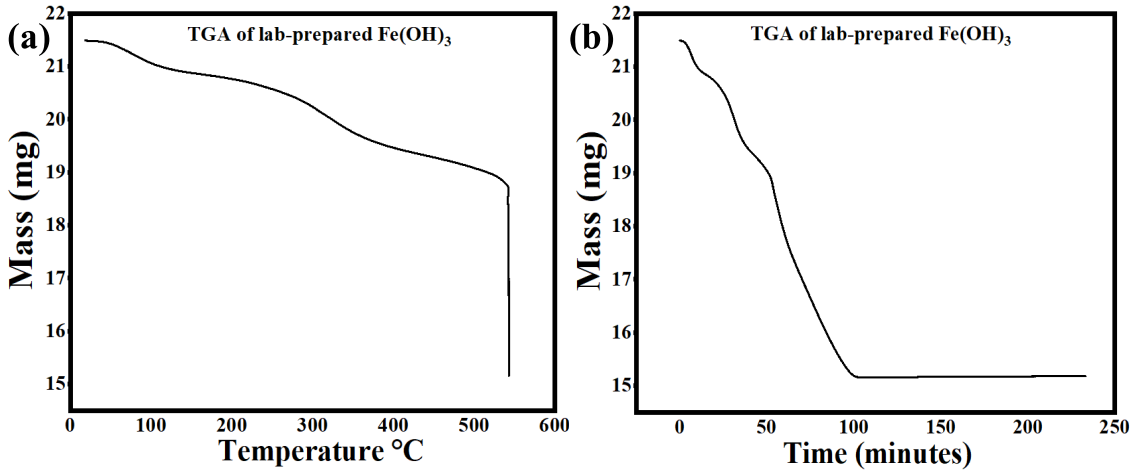

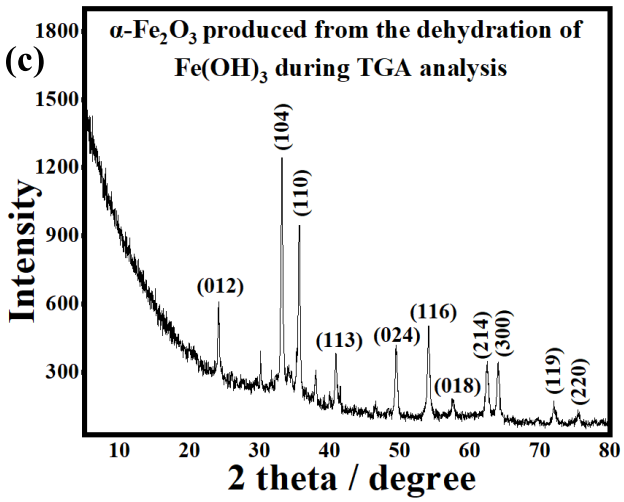

Fig 2.2. TGA profile of the dehydration of $Fe(OH)_3$ to α-Fe_2O_3 under 2% oxygen in argon mixture using a ramp rate of 10 °C per minute from room temperature to 550 °C followed by an isothermal hold at 550 °C for three hours to show the mass loss in mg as a function of temperature °C (**a**) and time in minutes (**b**). Powder XRD pattern of α-Fe_2O_3 produced from the dehydration of $Fe(OH)_3$ during the TGA analysis (**c**).

2.5. Extraction of TiO_2 from red mud

Two methods were used to extract TiO_2 from red mud; the first one is called the alkali roasting [199], which is similar to the procedure employed by Li *et al.* [200], as it starts with alkali addition, followed by acid leaching, water leaching, thermal hydrolysis, and calcination as shown in **Scheme 2.1**. Firstly, 5 g of red mud powder was mixed with 5 g of burnt lime (calcium oxide) and 5 g of soda ash (sodium carbonate) and then heated at 900 °C to form sodium titanate in the sample. Subsequently, the produced powder was crushed, extracted with hot water, and filtered to remove the metal components. The residue was acid-leached using concentrated H_2SO_4 (18 M) in a ratio of 1 mL of acid to each gram of the produced residue to form water-soluble titanium species such as titanyl sulfate ($TiOSO_4$). The product was then water-leached and stirred for one hour at room temperature with a solid-to-liquid ratio of 1:10 (w/v) followed by filtration. The filtrate was then subjected to thermal hydrolysis at 100-110 ℃ for 2 hours to precipitate titanium hydroxide. Finally, the precipitate was filtered and calcined at 900 °C for 2 hours to produce titanium oxide (TiO_2).

The second method was the direct acid baking [201] in which 10 g of the red mud sample was mixed with 10 mL of concentrated H_2SO_4 (18 M) in a ratio of 1 mL of acid to each gram of

red mud and stirred for 30 minutes as shown in **Scheme 2.2**. Subsequently, the sample was transferred to a 50 mL crucible, and the crucible was placed inside a muffle furnace for 120 minutes at 350 °C. After that, the baked product was left to leach in DW for 2 hours with a liquid-to-solid ratio of 10 mL to 1 g to remove Fe, Al, and Si components. This step causes titanium leaching as well, but it helps purifying the remaining titanium in the sample. Afterward, water was decanted, and the precipitated solid was washed several times with DW to neutralize its pH. Lastly, the washed precipitate was overnight-dried in the oven at 90 °C followed by calcination at 400 °C for 3 hours to produce titanium oxide (TiO_2). TiO_2 produced by the direct acid baking method was modified with the same metals, impregnation percentages, and the preparation procedures used with the composites of the lab-prepared TiO_2.

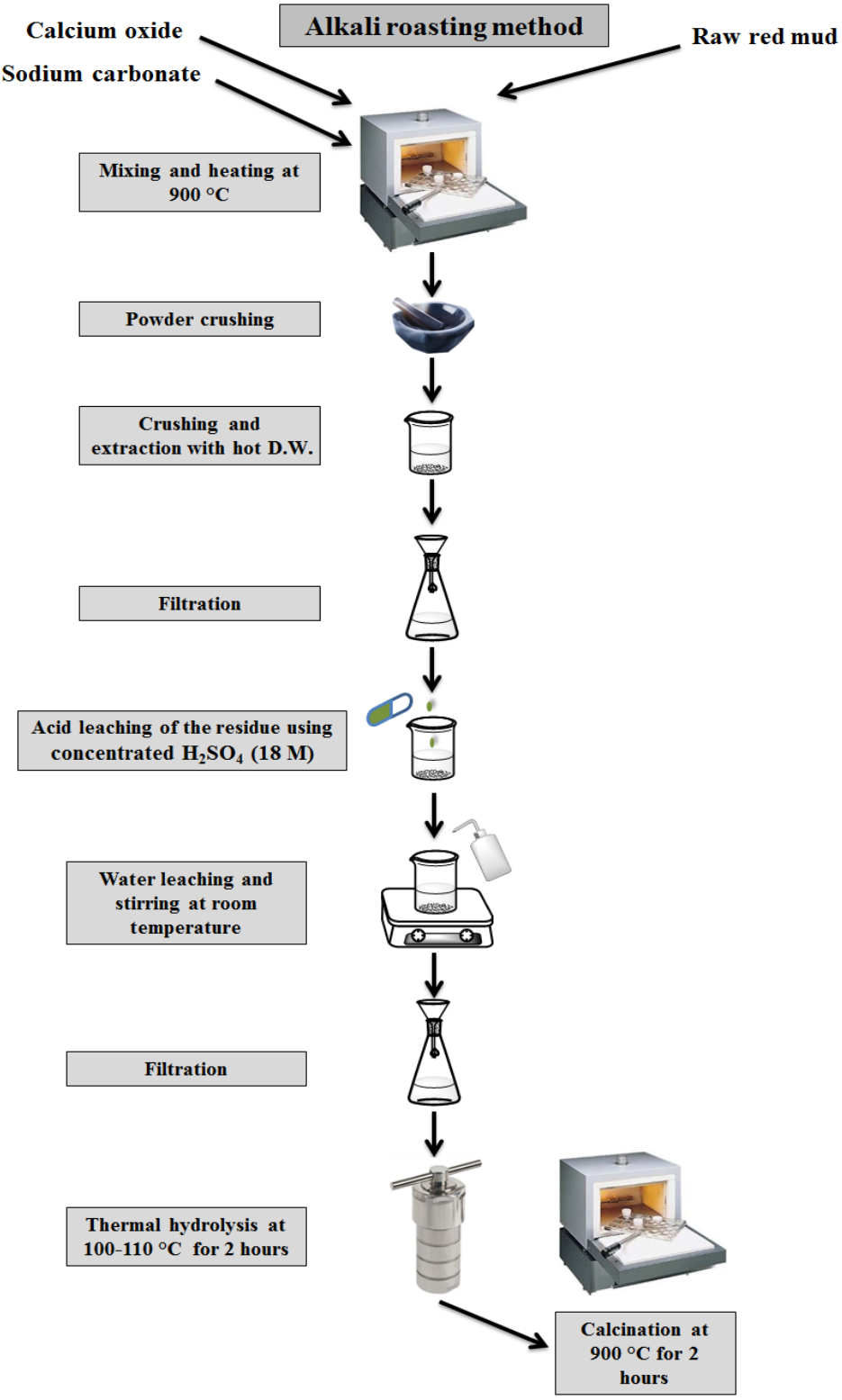

Scheme 2.1. Schematic illustration of TiO_2 synthesis by the alkali roasting method [202]. The process starts by mixing and heating red mud with burnt lime and soda ash to form sodium titanate. The acid leaching of the metal-free solid residue to form water-soluble $TiOSO_4$ followed by thermal hydrolysis to precipitate $Ti(OH)_4$, which is then calcined into TiO_2.

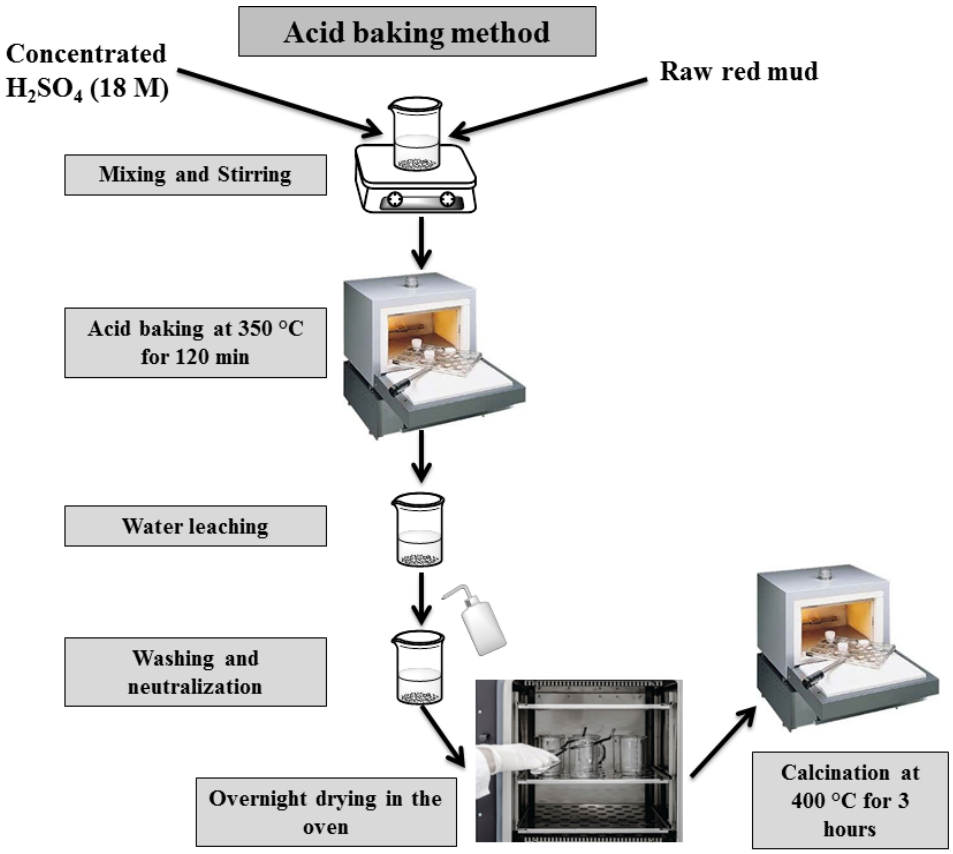

Scheme 2.2. Schematic illustration of TiO_2 synthesis by the direct acid baking method [202]. The method begins with mixing and baking red mud with H_2SO_4 followed by water leaching to remove the metal components and purifying the remaining titanium in the sample. Subsequently, the sample is neutralized with DW, dried in the oven, and calcined to produce TiO_2.

2.6. Extraction of α-Fe_2O_3 from red mud

Oxalic acid leaching followed by photocatalytic reduction is considered the appropriate extraction method with low iron-content red mud to produce ferrous oxalate, while the microwave reduction followed by magnetic separation is more suitable when using high iron-content red mud [203]. The Chinese red mud used in this study has a low iron content as indicated by its light red or orange colour and also by the previously reported XRF results of the same sample [204], so the first method was used. Oxalic acid solution (2 mol/L) was used to extract ferric oxalate ($Fe_2(C_2O_4)_3$) from red mud, which was converted into ferrous oxalate (FeC_2O_4) upon exposure to ultraviolet (UVA) light using a mercury lamp (λ = 365 nm, 125 Watts) [158]. For the sake of comparison and employing more sustainable extraction

procedures, the artificial laboratory light was used as a visible light source. The solid-to-liquid ratio of red mud to oxalic acid was 1 gram:20 mL. Red mud was first mixed with oxalic acid, stirred, and heated at 80 °C for two hours followed by exposure to UVA light for five hours. Subsequently, the solution was left to allow the precipitation of the yellow-coloured FeC_2O_4, the liquid was decanted, and the precipitate was washed with ethanol to remove the impurities. FeC_2O_4 was then centrifuged and overnight dried at 80 °C. Finally, FeC_2O_4 was calcined at 550 °C for three hours in static air using a 25 °C per minute ramp rate to produce α-Fe_2O_3. Similar extraction procedures were previously employed by Gu *et al.* [205]. The extraction procedures used in the current study are presented in **Scheme 2.3**.

Upon conducting the XRF analysis to determine the percentages of α-Fe_2O_3 and TiO_2 in the Chinese red mud sample, α-Fe_2O_3 constituted 25.4% and TiO_2 represented 3.8%. The amount of the produced α-Fe_2O_3 and TiO_2 from 10 g of red mud were 3 g and 1 g, respectively, and therefore their apparent yields were 118% and 265% in the same respective manner. This can be attributed to impurities in both extracted metal oxide samples.

The XRF method directly detected the percentages of the metal oxides in the sample and all the non-detected elements, which were 33% of the sample, were represented by carbon. This method is different from the one used by Gu *et al.* [204], which was employed to characterize the same Chinese red mud sample, as their method detected the percentages of the elements not the oxides. Therefore, the metal oxides method better suited the quantification of α-Fe_2O_3 and TiO_2 in the current study.

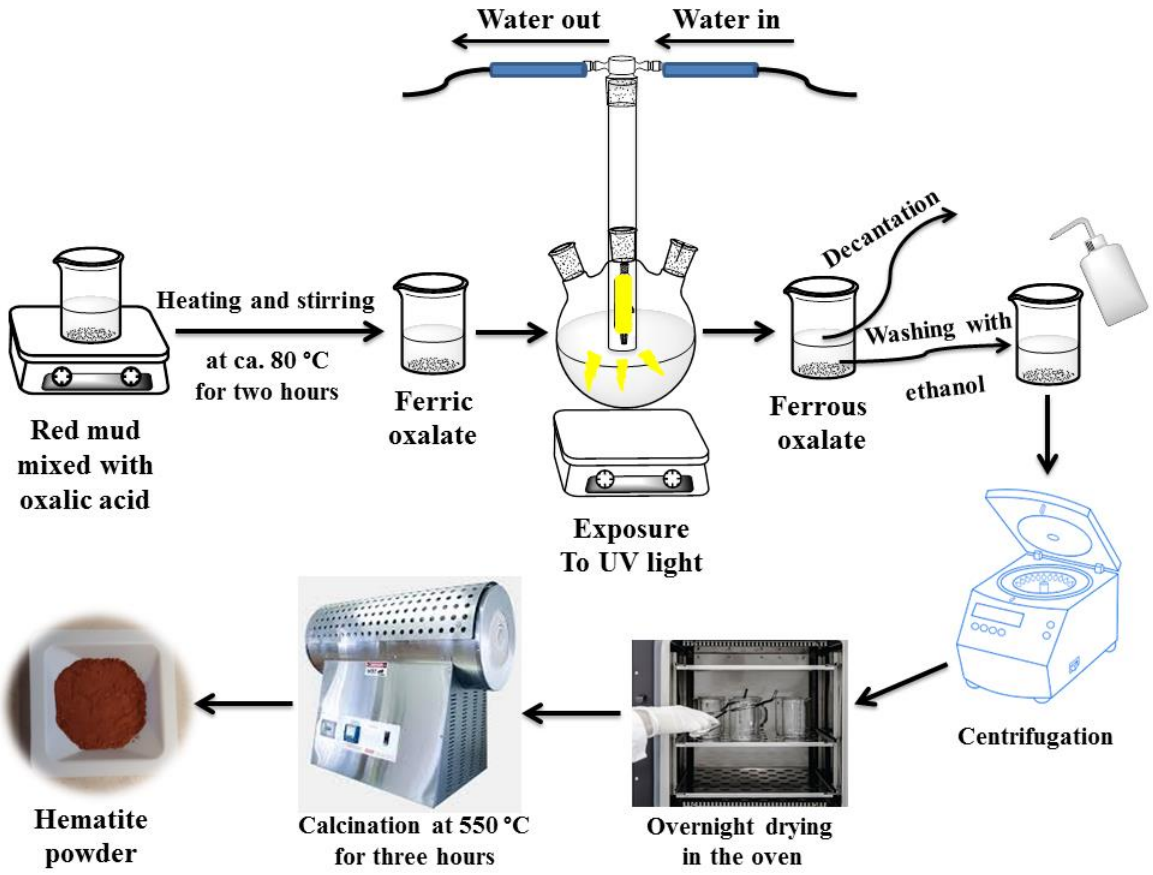

Scheme 2.3. A simple demonstration of the extraction of α-Fe_2O_3 from Chinese red mud that began with mixing red mud with oxalic acid to form ferric oxalates, which were then photocatalytically reduced into ferrous oxalates. Subsequently, the oxalates were washed with ethanol to remove impurities and lastly calcined to produce α-Fe_2O_3.

Software tools that were used to draw the figures in this thesis include ChemDraw, Origin, Microsoft Excel, and Microsoft PowerPoint.

2.7. Biogenic iron oxide samples collection and preparation of 2-line ferrihydrite

Biogenic iron oxide samples were collected from three sites in the River Allander in Milngavie as shown in **Fig 2.3.a-c**, a town very close to Glasgow in Scotland, the United Kingdom. These samples were collected during the summertime on the 4th July 2024. The crag sample was collected one more time on the 18th January 2025 (**Fig 2.3.d-g**), and the effect of seasonal variation on the performance of this sample will be shown in Chapter 5. The location of two out of the three sites (pond and crag) is very near to Allander Coaches bus company depot and the coordinates are 55.952306, -4.327822. An oily film on the water surface is

observed in these images, which is an indication of the bacterial presence (*Leptothrix*) in this environment. The samples were transferred to the lab at the School of Chemistry, University of Glasgow, within an hour and washed with DW many times (around 1 L of DW for each gram of biogenic iron oxide) followed by vacuum filtration to remove any impurities such as insects and twigs. Subsequently, the samples were dried for two days in the oven at 55 °C, and after that, the samples were ready for characterization and adsorption experiments.

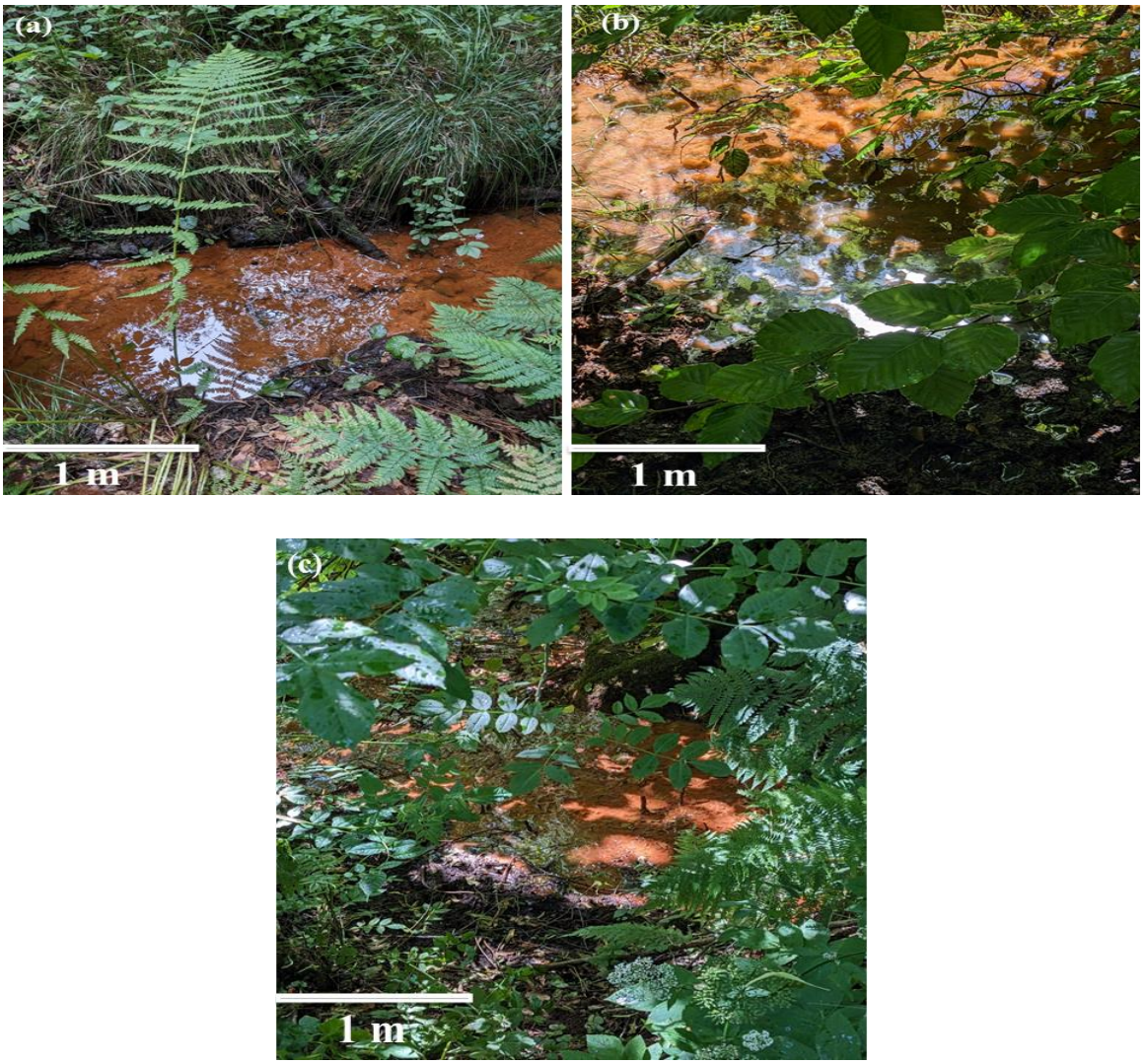

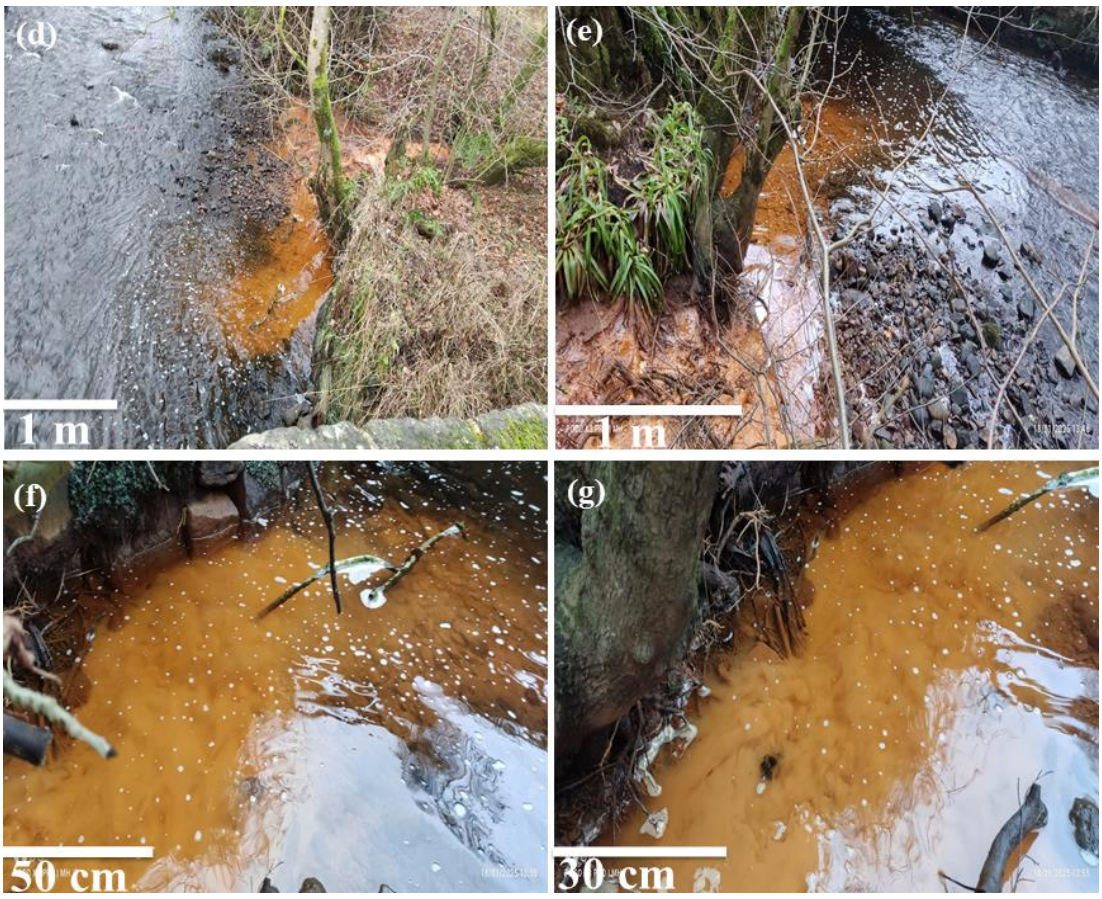

Fig 2.3. Three sites in the River Allander; first site **(a)**, pond **(b)**, and crag **(c, d, e, f,** and **g)**, where the biogenic iron oxide samples were collected. The samples collected during the summertime (**a**-**c**) and those collected during the winter (**d**-**g**).

2-line ferrihydrite ($Fe_5HO_8{\cdot}4H_2O$) was prepared in the lab according to a published procedure [206] by mixing 50 mL of 2 M $Fe(NO_3)_3$ solution with 25 mL of 6 M NaOH followed by the dropwise addition of 1 M NaOH until the pH of the solution got close to 7 with a total volume of about 100 mL. The solution was continuously stirred during the addition of NaOH and for two hours after adjusting the pH. Subsequently, the brown precipitate of 2-line ferrihydrite was filtered via centrifugation and washed several times with DW Eventually, the material was oven-dried at 55 °C for two days.

2.8. Reduction and calcination of BIOX and 2-line ferrihydrite samples

As shown in **Fig 2.4** either pure H_2 or a H_2/N_2 (75% / 25%) mixture (BOC, 99.99%) was applied to reduce the BIOX, 2-line ferrihydrite, Chinese RM, and Chinese RM-derived α-Fe_2O_3 samples, which were placed between two pieces of quartz wool inside a quartz tube that

was placed inside a tube furnace to control the temperature. Subsequently, the reactor effluent gas was bubbled in a low-concentration H_2SO_4 (0.00108 M) in a glass flask from which the gas was eventually vented into an extraction cabinet. The reduction programmes under pure H_2 were at 300 °C, 400 °C, 500 °C, 600 °C, and 700 °C for one hour employing a ramp rate of 20 °C per minute. Similar reduction programmes were used under H_2/N_2. Other programmes were also investigated including 700 °C for two, four, eight, and ten hours, 500 °C for four and ten hours, 700 °C for two hours followed by four hours at 400 °C, 700 °C for two hours followed by four hours at 500 °C, four hours at 400 °C followed by four hours at 500 °C, and 700 °C for two hours followed by four hours at 400 °C followed by four hours at 500 °C. The three BIOX samples were calcined in the air in a tube furnace at 550 °C for three hours employing a ramp rate of 25 °C per minute. These different reduction programmes are shown in **Fig 2.5**.

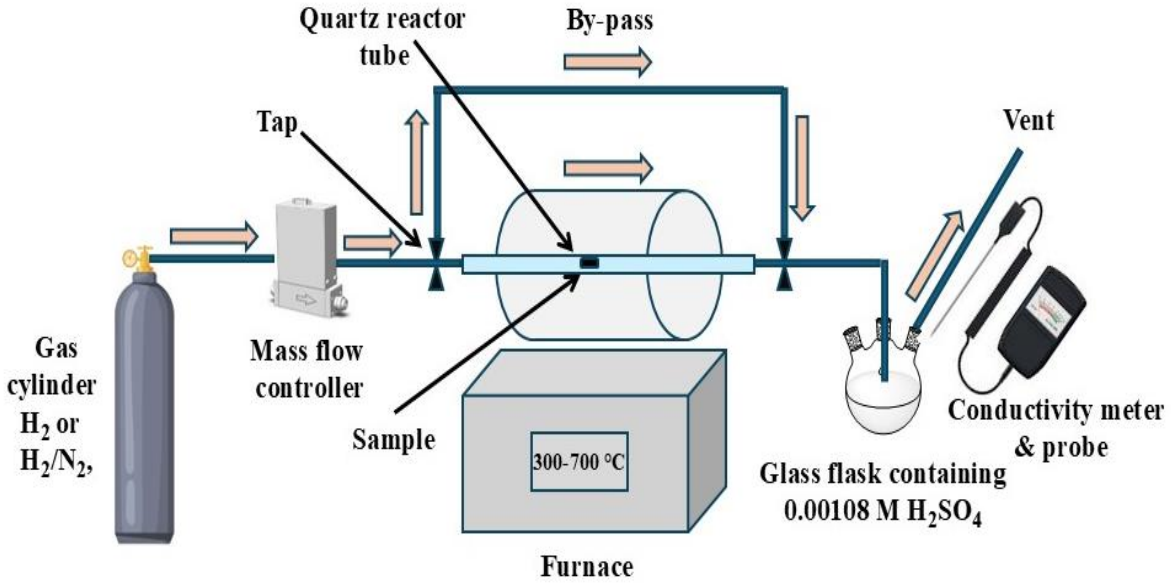

Fig 2.4. A schematic representation of the reactor used in the reduction of BIOX samples either under pure H_2 or H_2/N_2 mixture for different times and temperatures.

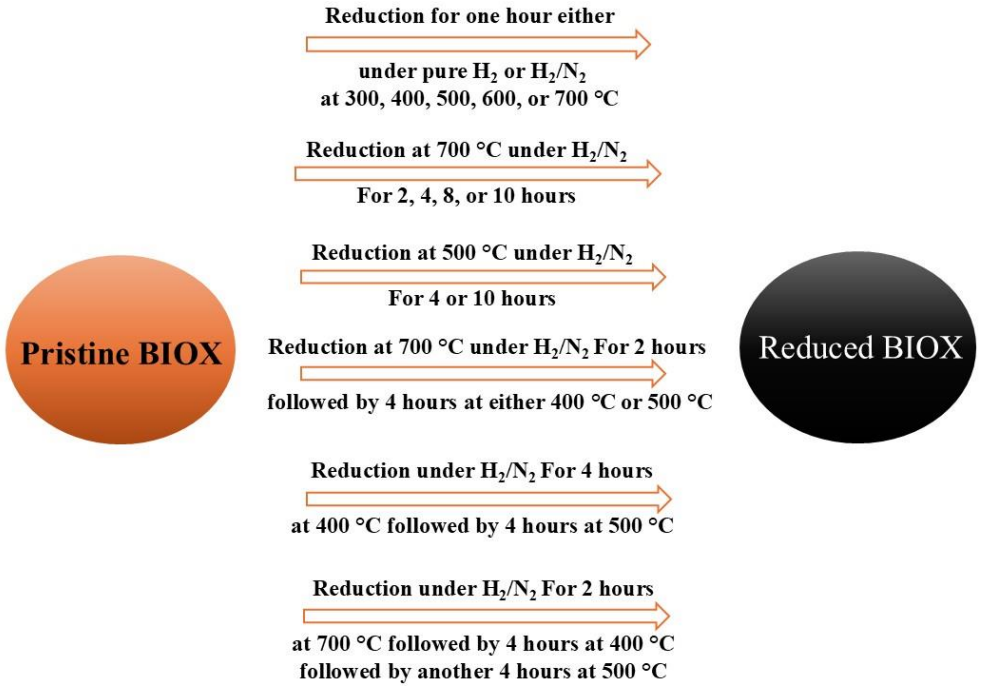

Fig 2.5. A simplified diagram of the reduction programmes used to reduce BIOX to reduced BIOX materials at different times and temperatures either under pure H_2 or H_2/N_2.

2.9. Testing the catalytic activity of iron oxide-based waste materials and their composites in the ammonia synthesis process

The same setup (**Fig 2.4**) was used to test the catalytic activity of BIOX (crag), 2-line ferrihydrite, Chinese RM, Chinese RM-derived α-Fe_2O_3, and its composites in ammonia synthesis at atmospheric pressure under H_2/N_2 (75% / 25%). 2, 5, and 10 wt% K-α-Fe_2O_3 were prepared by mixing 0.05, 0.13, and 0.26 g of KNO_3 with 1 g of α-Fe_2O_3 in DW followed by stirring and heating at 90 °C for 90 minutes followed by overnight drying at 100 °C. Subsequently, the samples were calcined at 550 °C for three hours with a ramp rate of 10 °C/min. 5%wt Co-α-Fe_2O_3 was prepared by mixing 0.25 g of $Co(NO_3)_2.6H_2O$ with 1 g of α-Fe_2O_3, using the same procedures.

The materials were first pretreated under H_2/N_2 at 700 °C for two hours to remove the oxides on the materials' surface. Subsequently, the reactors were cooled down to 400 °C, where the catalytic activity was tested for four hours, followed by an additional four hours at 500 °C. The effectiveness of each material in producing ammonia was evaluated by monitoring the change in conductivity of a 200 mL sulfuric acid solution (0.00108 mol/L) at five-minute intervals using a conductivity meter. The reactor outlet gas was bubbled through this solution,

and the resulting decrease in conductivity was recorded. This decline indicates the formation of ammonium ions, produced when ammonia reacts with protons in the acid as reported by Daisley [207]. This is because the conductivity of NH_4^+ species is less than that of H^+. The experimental approach and calculation method were adapted from the procedure originally developed by Mckay [208].

2.10. Collection of a water sample from the River Clyde

A water sample was collected during the summertime on the 29th July 2024 from the River Clyde, near Kelvingrove Park, in the West End, Glasgow, the United Kingdom (**Fig 2.6.a**). This water sample is used in Chapters 3 and 4 and another sample was collected from the same area on the 10th February 2025 (**Fig 2.6.b**) and is used in Chapter 5. The pH of both samples was approximately 7 and the conductivity was about 300 µs/cm compared to 2.8 µs/cm of DW The ICP-OES analysis of the River Clyde and DW samples is discussed in Chapter 3 to investigate their elemental composition.

Fig 2.6. The area where a water sample was collected from the River Clyde, particularly near Kelvingrove Park, in the West End, Glasgow, the United Kingdom on the 29th July 2024 (**a**), and on the 10th February 2025 (**b**).

2.11. Characterization techniques

The Miniflex powder diffractometer (Rigaku) benchtop X-ray diffractometer (XRD) equipped with a Cu Kα source (1.5418 Å) was used to study the materials, operating within a 2θ range of 5-85°, utilizing a step size of 0.015 and a counting rate of 20°/min. Surface area measurements were performed using the BET method on a Quadrasorb Automated Surface Area & Pore Size Analyzer (Evo) with nitrogen gas as the adsorbate at -196 °C. The degassing conditions included holding samples at a temperature of 130 °C for 16 hours and employing a 1 °C per minute ramp rate. The pore size distribution was identified using the Barrett-Joyner-Halenda (BJH) model using the nitrogen desorption branches of the isotherms. The morphology and the elemental composition were determined via a Scanning Electron Microscope (SEM) equipped with a Tescan Clara EDX (Energy Dispersive X-ray spectrometer) operating at an accelerating voltage of 0.2-30 kV.

For the determination of leached metal ions, including copper at 327 nm, iron at 261 nm, and zinc at 213 nm inductively coupled plasma-optical emission spectroscopy (ICP-OES) analysis was conducted using a MY2131CP01 Agilent Technologies instrument. These wavelengths were specifically selected to avoid interference with other metals. The ICP-OES measurements were repeated three times, and the average concentrations were recorded. An

Exeter Analytical Inc CE-440 elemental analyzer was used to combust the samples for CHN analysis.

An Agilent High-Resolution Liquid Chromatography-Mass spectrometer (LC-MS G6125B). The National Institute of Standards and Technology (NIST) database was used to investigate the degradation of DOXY and CEF under UV light. Mobile phase A was 30% acetonitrile solution and mobile phase B was 70% formic acid solution (0.1% acid solution in ultrapure water). The two phases were used in a gradient mode by changing the percentage of mobile phase A to 50%, then to 70%, and then back to 30%. The flow rate was adjusted at 0.3 $mL.min^{-1}$ while the injection volume was 20 µL. The capillary voltage is 3500 V and is used in the positive ion mode.

A TA Instruments TGA Q500 instrument was used to run TGA analysis where the samples were placed in an alumina crucible and heated from room temperature to 950 °C with a ramp rate of 10 °C per minute under 100 mL/minute argon to prevent the oxidation of samples as much as possible. The TA instrument was connected to a mass spectrometer to detect the released gases. Fourier Transform Infrared Spectroscopy (FTIR-8400S Shimadzu) was employed to examine the main functional groups of CEF, DOXY, and different composites. XPS (X-ray photoelectron spectroscopy) analysis was conducted using a 375 W and 25 mA Kratos photoelectron spectrometer (Shimadzu) equipped with an Al Kα source (8.35 Å), and the charge correction was undertaken using C 1s (adventitious carbon) at 284.8 eV. Zeta potential measurements were undertaken using Anton Paar Litesizer DLS 500. The measurements were triplicated, and the average results were reported. X-ray Fluorescence (XRF) analysis was carried out using Shimadzu 7200, and the percentages of the metal oxides in the Chinese red mud sample were determined using carbon to account for the elements that can not be detected by the XRF.

2.12. The photocatalytic degradation of CEF and DOXY

The photocatalytic reactor consisted of a mercury lamp as an ultraviolet (UVA) light source (λ = 365 nm, 125 Watts) inserted in either a three-bottle neck glassware or a regular beaker that contains the antibiotic solution (**Fig 2.7.a**). There is a water inlet, and a water outlet used to cool the mercury lamp that gets hot with time. The temperature of the solution increased from 20 ± 2 °C to 25 ± 1 °C with time, but this did not cause thermal degradation of CEF. The temperature effect on DOXY was inconsistent as the absorbance sometimes remained

unchanged and at other times increased or decreased. However, the elevated temperature over long-time experiments can sometimes cause partial evaporation of the antibiotic solutions, leading to an insignificant increase in the absorbance of their UV peaks. Another reactor was used for photocatalysis under visible light, equipped with an LED lamp and a small side fan for cooling. The solution temperature remained stable within 20 ± 2 °C.

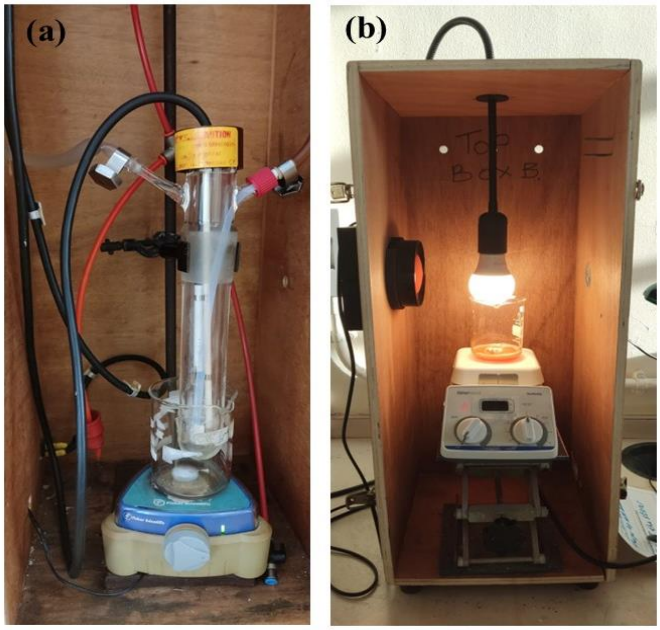

Fig 2.7. The reactors used in the photocatalytic degradation of CEF and DOXY under UV (**a**) and visible light (**b**).

2.13. Adsorption of CEF and DOXY using different adsorbents

The initial variable explored in the adsorption experiments of CEF and DOXY involved modifying the pH levels using 0.1 M HCl and 0.1 M NaOH as measured using a pH meter (Thermo Fisher Scientific). The uncontrolled pH of the aqueous CEF and DOXY solutions (25 ppm) was 5.8 and 4.5, respectively. Different pH values, including 3, 5, 7, 9, and 11, were employed to assess the adsorption efficiency using 20 mL of either antibiotic with a concentration of 25 ppm under dark conditions. This variable was used in most of the experiments in the current study because of the unavailability of getting a real wastewater sample and determining its pH. Therefore, producing an adsorbent that can be used over a wide pH scale was considered one of the main goals of this study.

Other variables were tested to optimize the adsorption efficiency, including the initial concentration of the antibiotic (15, 25, 50, 75, 100, 200, and 500 ppm), the adsorbent dose (0.005, 0.0075, and 0.01 g), and the stirring rate ranging from 0 rpm up to 1200 rpm. The range of these variables was slightly changed based on the results obtained in each chapter. A calibration curve was prepared for each antibiotic, as shown in **Fig.2.8.a-b**. It was observed that the UV-Vis spectra became noisy at higher concentrations, particularly at 100 ppm and up to 500 ppm. This occurred because the corresponding absorbance values approached the upper sensitivity limit of the spectrometer and the transmitted light becomes very small, outside of detection limit. So, the detector cannot reliably differentiate signal from noise. This issue could be resolved using a cuvette that has a path length of 0.5 cm instead of the cuvette that is usually 1 cm length. Alternatively, these high concentrations could be diluted to bring the absorbance peaks within the reliable range corresponding to 25 - 50 ppm. Subsequently, the dilution factor could then be applied to calculate removal efficiency.

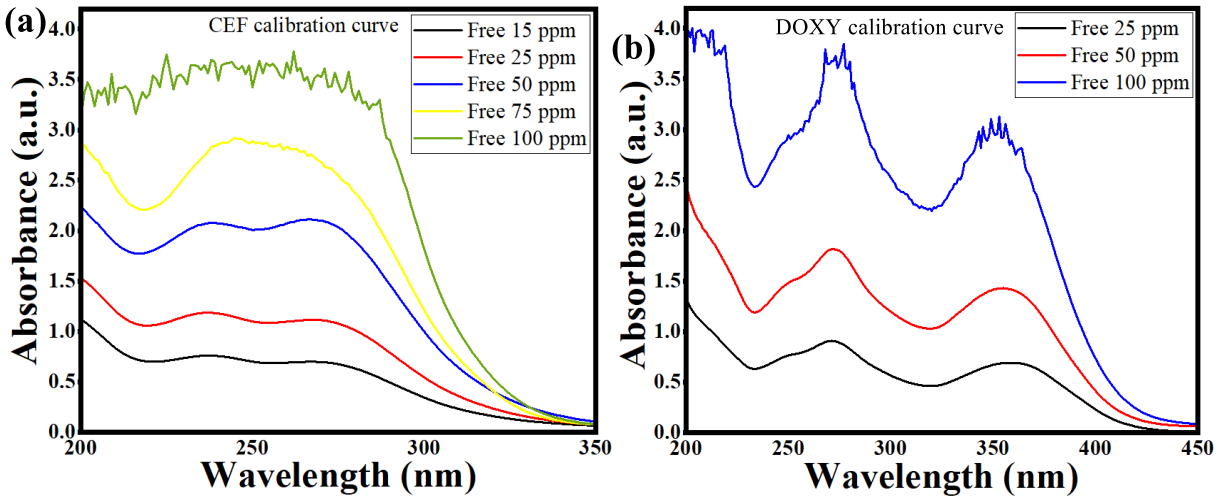

Fig 2.8. The calibration curve of CEF **(a)** and DOXY **(b)** using different concentrations starting from 15 and 25 ppm, respectively, up to 100 ppm.

The adsorption efficiency of the antibiotic was determined using the following equation:

$$\% \text{ Adsorption} = 100 \times (A_0 - A)/A_0 \qquad \text{eq. (2.5)}$$

where A_0 represents the initial antibiotic concentration measured by UV-Vis spectroscopy (UV-1800 Shimadzu) and a quartz cuvette with a path length of 1 cm, while A corresponds to the antibiotic concentration after a given time measured by the method following the separation of the adsorbent using centrifugation (TD4A-WS Desk centrifuge). As an example

of calculating the adsorption efficiency using the raw data obtained by UV-Vis spectroscopy, the absorbance of a 25 ppm CEF solution (pH 3) at 265 nm was 1.21 a.u. before the adsorption, and then 0.01 g of 5% Fe 5% Cu-TiO_2 was added to the solution followed by stirring for 75 minutes. Subsequently, the absorbance decreased to 0.53 a.u. as shown in **Fig 2.9**. So, by applying the above-mentioned equation, the adsorption efficiency would be = 100 × (1.21 - 0.53) / 1.21 = 56%.

It should be noted that C_0 refers to the initial concentration of the antibiotic in aqueous solution (in ppm or mg/L), whereas the dose (in grams) represents the mass of adsorbent used to remove the antibiotic from that solution. These two parameters are reported in the captions of all removal-efficiency bar graphs and UV-Vis spectra.

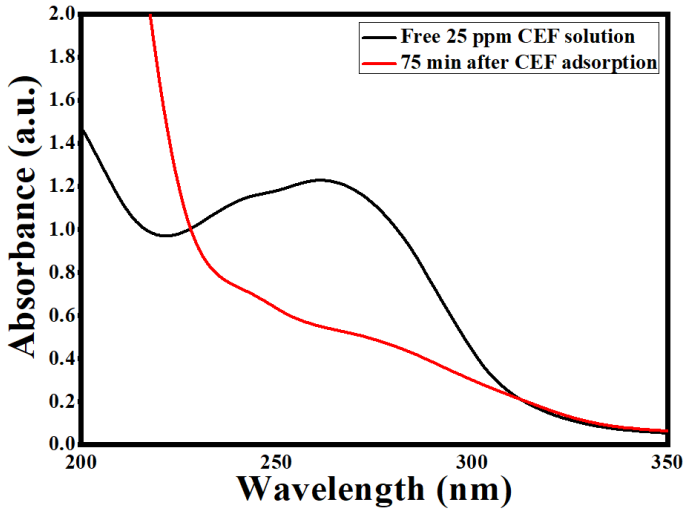

Fig 2.9. The adsorption efficiency of CEF using 5% Fe 5% Cu-TiO_2. [C_o = 25 ppm, pH 3, stirring rate = 800 rpm, T = 20 ± 2 °C, volume = 20 mL, and dose = 0.01 g].

An example of calculating the adsorption efficiency of DOXY using the raw data obtained by UV-Vis spectroscopy, the absorbance of a 25 ppm DOXY solution (pH 9) at 370 nm was 0.76 a.u. before the adsorption, and then 0.01 g of Chinese RM-derived TiO_2 was added to the solution followed by stirring for 90 minutes. Subsequently, the absorbance decreased to 0.24 a.u. as shown in **Fig 2.10**. So, by applying the above-mentioned equation, the removal efficiency would be = 100 × (0.76 - 0.24) / 0.76 = 68%.

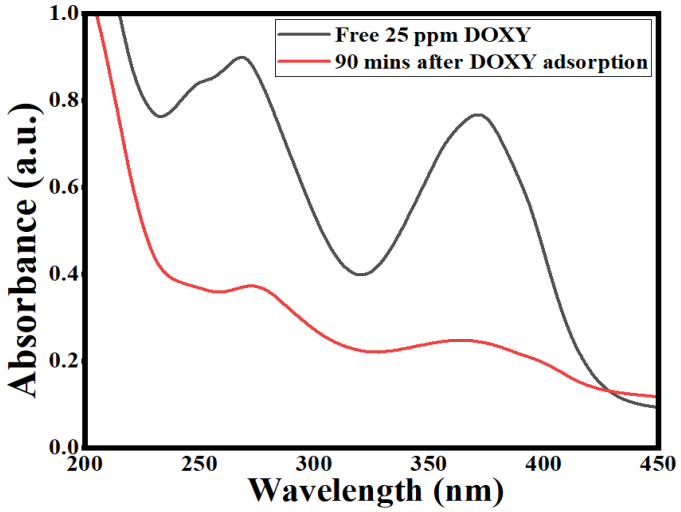

Fig 2.10. The removal efficiency of DOXY after 90 minutes using Chinese RM-derived TiO_2. [C_o = 25 ppm, pH 9, stirring rate = 750 rpm, T = 20 ± 2 °C, volume = 20 mL, and dose = 0.01 g].

The adsorption capacity is calculated by the following formula:

Adsorption capacity (mg/g) = [(Co - Ce) /m] x V eq. (2.6)

In this equation, Co denotes the initial concentration of the antibiotic in ppm wt/vol (mg/L), Ce is the concentration at equilibrium in ppm (mg/L), m refers to the mass of the adsorbent in grams (g), and V represents the volume of solution in liters (L).

All UV-Vis spectra were baseline-corrected so that each experiment started from the same onset of the free solution spectrum at 800 nm before the removal process. Some spectra in this study may appear to start from different onsets, but this is only because they are displayed from 350 nm (CEF) or 450 nm (DOXY) to highlight the regions where the chromophore peaks appear. In all cases, the spectra were aligned to the same onset, as clarified by extending the wavelength to 800 nm as shown in **Fig. 2.11.a-b**. The UV-Vis spectra for all samples and their corresponding control experiments are provided in the Appendices.

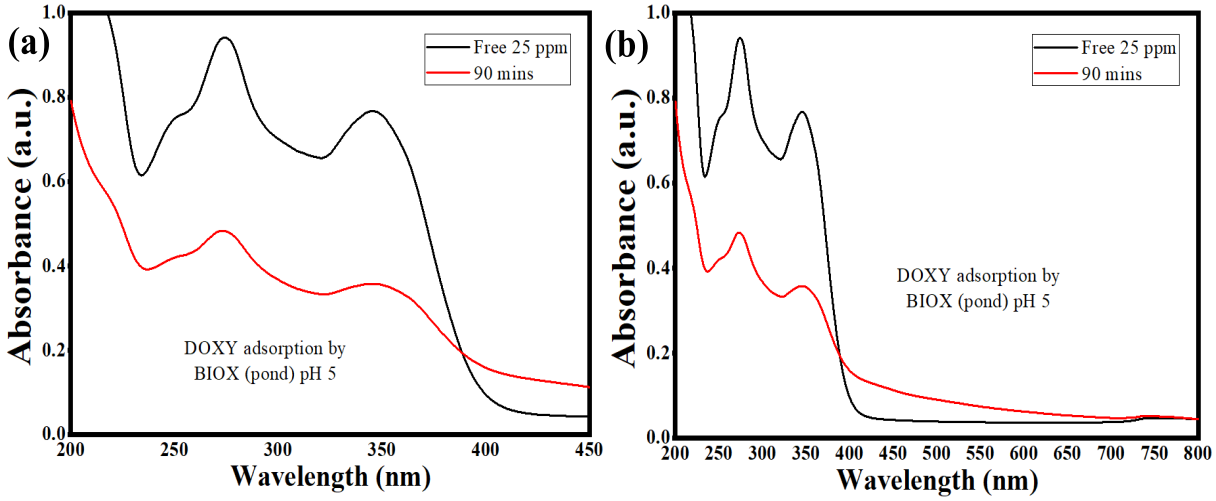

Fig 2.11. The UV-Vis spectrum after using BIOX (pond) material at pH 5 in DOXY adsorption in the wavelength range of 200-450 nm **(a)** and 200-800 nm **(b)**.

All experiments were conducted twice except for the key materials, where they were tested multiple times upon investigating different factors (e.g., the adsorbent dose), and the average values were reported with an error percentage of ± 5%. In some cases, experiments were repeated three or four times due to factors that initially affected reproducibility. For example, replacing hot plates influenced the results because some plates warmed up over time, and the position of the stirrer bar also played a role. This issue was resolved by consistently using the same hot plates that maintained stable temperatures. Additionally, changing the laboratory location impacted results, as some labs became cold in winter, either due to non-functioning radiators or because the large room area exceeded the heating capacity of the available radiators. To address this, experiments were performed in smaller laboratories where the temperature could be more easily maintained at 20 ± 2 °C. On the few sunny days of summer, experiments were carried out in other laboratories, which were equipped with an air conditioner (e.g., the XRD lab) to keep the temperature stable. A thermocouple was used throughout to monitor and record the experimental temperature.

To work out the theoretical %C expected after the adsorption of 25 ppm CEF, the percentage of carbon in CEF was calculated based on its atomic composition. The mass of 18 carbon atoms in a mole of CEF is 216 g. Dividing this by the molecular weight of CEF (554.6 g) and multiplying by 100 gives a carbon content of 39%. If 25 ppm of CEF is present in 20 mL of solution, this corresponds to 0.5 mg of CEF. The total mass of carbon is therefore 0.5 mg ×

0.39 = 0.19 mg. The adsorption efficiency was 54%, as reported in the following chapter for 5% Fe 5% Cu-TiO_2 at pH 7 (**Fig. 3.36.a**), the mass of adsorbed carbon would be 0.54 × 0.19 mg = 0.11 mg. The adsorbent mass used in 20 mL of 25 ppm CEF is 10 mg. Thus, the percentage of adsorbed carbon is (0.11 mg / 10 mg) × 100 = 1.1%.

Knowing the %C in 5% Fe 5% Cu-TiO_2 before adsorption is 0.54%, which was measured by CHN and the result is reported in Chapter 3, the theoretical %C after adsorption should be 1.1% + 0.5% = 1.6%. The actual %C determined by CHN analysis was 1.7%, which is close to the theoretical value. A similar approach was applied to calculate the %C after DOXY adsorption. All CHN analysis results have an uncertainty of ±0.3%.

2.14. Determination of the ionic strength and the interfering ion effect

Different concentrations of NaCl ranging from 0.01 M to 0.4 M or mol/L were mixed with the antibiotic solution at different pH levels prior to the addition of adsorbents. The NaCl concentration was chosen to simulate natural salinity levels, which can average around 0.59 mol/L in seawater, corresponding to 35 parts per thousand, to on average in seawater [209]. The ionic strength effect of divalent ions such as Ca^{2+} was also covered in this study using 50, 100, 200, and 500 mg/L of Ca^{2+} equivalent to 0.0012, 0.0024, 0.0049, and 0.0124 mol/L $CaCl_2.6H_2O$, respectively. Also, the same Ca^{2+} concentrations were tested using CaO. Similarly, the effect of Mg^{2+} was tested within the range of 50-500 mg/L using MgO. The effect of 5, 25, and 100 ppm of Si(IV) was studied using amorphous silica. Additionally, the effect of SO_4^{2-} ions was investigated with a concentration range of 50 - 1000 mg/L equivalent to 0.0005 - 0.01 mol/L of Na_2SO_4. For instance, one mL from the stock SO_4^{2-} solution (10 g/L) is added to 9 mL of the antibiotic aqueous solution to prepare a final volume of 10 mL with 1000 mg/L of SO_4^{2-}.

Blank experiments were undertaken without using any adsorbents. The concentrations of Ca^{2+}, Mg^{2+}, and SO_4^{2-} were selected based on the reported values of WHO in the guidelines of drinking water quality [210], whereas the concentration of Si(IV) was based on the values reported in the surface and groundwater of the UK by Neal *et al.* [211] in 2005.

2.15. Regeneration of the representative adsorbent materials

In the recycling or regeneration process, the used adsorbents were first centrifuged, followed by mixing with NaOH (0.1 M) to desorb either CEF or DOXY from the adsorbent surface

through the electrostatic repulsion along with the self-degradation of DOXY in alkaline conditions. Subsequently, the adsorbents were washed by DW several times until the pH of the washing got close to 7, followed by oven-drying (110-120 °C) to get them in a solid form. Self-degradation of DOXY is attributed to the hydrolysis in alkaline conditions [212].

2.16. The catalytic degradation of CEF through Fenton degradation and photocatalysis by 5% Fe 5% Cu-TiO_2

The Fenton reaction is a common advanced oxidation process that is used to degrade different pollutants by generating highly reactive radicals such as the hydroxyl radicals (•OH) from hydrogen peroxide in the presence of iron ions according to the following equation

$$Fe^{2+} + H_2O_2 \rightarrow Fe^{3+} + OH^- + \bullet OH \qquad \text{eq. (2.7)}$$

Subsequently, the regeneration of Fe^{2+} is achieved through the reaction of Fe^{3+} with H_2O_2.

$$Fe^{3+} + H_2O_2 \rightarrow Fe^{2+} + H^+ + \bullet OOH \qquad \text{eq. (2.8)}$$

So, the overall reaction using both iron species (Fe^{3+} and Fe^{2+}) is

$$2H_2O_2 \rightarrow \bullet OH + \bullet OOH + H_2O \qquad \text{eq. (2.9)}$$

The degradation efficiency of the Fenton reaction could be improved by using catalyst composites, which could be further enhanced by employing a source of light (visible or UV) to achieve photo-Fenton degradation.

In the Fenton degradation experiments of the current study, the pH of five CEF solutions with a volume of 20 mL and a concentration of 25 ppm was varied over a range of 3 - 11. Subsequently, 0.01 g of 5% Fe 5% Cu-TiO_2 was added to each solution and then the solutions were subjected to stirring at 800 rpm under dark conditions for the attainment of the adsorption-desorption equilibrium. The used experimental conditions are the optimum conditions are discussed in **Section 3.12** in Chapter 3. Then 1 mL of H_2O_2 (0.1 M) was added to each solution and stirred for 120 minutes. The adsorption efficiency and the catalytic degradation efficiency after each 30 minutes of H_2O_2 addition for 120 minutes were measured using the above-mentioned UV-Vis spectroscopy and equation 1. Also, blank/control experiments were conducted using H_2O_2 without adding 5% Fe 5% Cu-TiO_2 over the same pH range to test its catalytic degradation efficiency.

Regarding the photocatalytic degradation of CEF, 5% Fe 5% Cu-TiO_2 was used as an adsorbent for 75 minutes under dark conditions at pH 7. Subsequently, it was removed by centrifugation and the CEF solution was exposed to UV light with 5 cm between the lamp and the solution surface until the degradation stopped, which took about 240 minutes. This step was carried out due to the degradation of CEF under UV light without a catalyst through photolysis. Then, 5% Fe 5% Cu-TiO_2 was added back to the solution to test its photocatalytic efficiency in degrading the remaining of CEF over 120 minutes.

2.17. Determination of the point of zero charge (PZC) of all adsorbents by the salt addition method

A simple procedure, the salt addition method [213], was undertaken to determine the PZC of the adsorbents (the pH at which the net surface charge is zero), and hence the surface charge is positive at pH levels below the PZC and negative at pH levels higher than the PZC. The PZC was determined by mixing the materials with 0.1 M $NaNO_3$ solutions across a pH range of 3 to 10 and stirring the suspensions for 24 hours using a magnetic stirrer. Initially, the pH of the $NaNO_3$ solutions was adjusted using 0.01 M HNO_3 and 0.01 M NaOH. The adsorbents were then added to the pH-adjusted solutions and stirred for 24 hours. Afterward, the suspensions were centrifuged to separate the adsorbents, and the final pH of each supernatant was measured. The difference between the initial and final pH values (ΔpH) was plotted on the ordinate (y-axis), while the initial pH values were plotted on the abscissa (x-axis) to determine the PZC. As an example, the PZC of reduced BIOX material (1h 700 °C H_2/N_2), which is 7.5, is measured by drawing a horizontal line from the zero point on the ordinate axis followed by drawing a vertical line from the intersection point of the horizontal line with the main line to the abscissa axis as shown in **Fig 2.12**. Control experiments were undertaken using the same procedure but without adding any adsorbents, and the results showed no pH change.

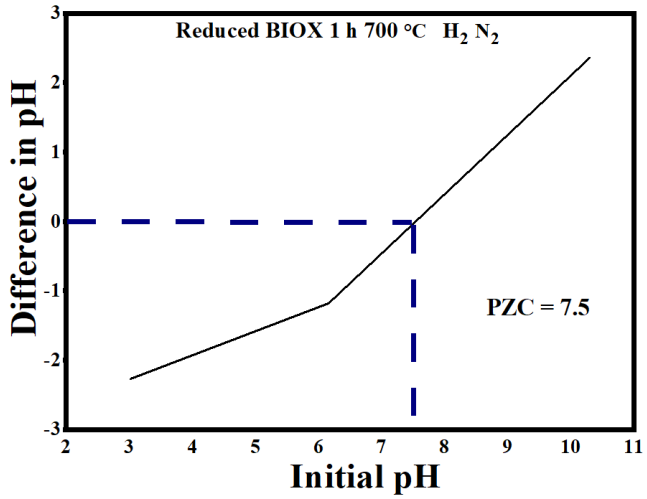

Fig 2.12. The determination of the PZC of reduced BIOX material (1h 700 °C H_2/N_2) using the salt addition method by measuring the change in the pH after 24 hours of stirring.

2.18. Synthesis of calcium alginate beads and reduced BIOX 1-bead composite

The focus in synthesizing the composite beads using reduced BIOX 1 was based on its magnetic property, which makes separation easier. Firstly, a hardening solution was prepared by dissolving 0.5 g of $CaCl_2.6H_2O$ in 50 mL DW to get a 1%wt/v solution. 0.5 g of sodium alginate powder was dissolved in 50 mL DW via slight heating and stirring to get the same wt/v ratio, and then 0.05 g of reduced BIOX 1 was added to 10 mL of the alginate solution. Subsequently, the mixture was sonicated for an hour, and then it was very slowly dropped into the hardening solution via a glass pipette followed by stirring for an hour. Lastly, the beads were rinsed with DW and left to dry in the air. Pristine beads were prepared in the same way without using reduced BIOX 1. The preparation procedures are similar to those previously reported [214]. It was not feasible to try other ratios and concentrations due to the unavailability of enough amount of reduced BIOX 1 sourced from the same site (crag) at the same time of the year. However, there was enough amount of the BIOX material that was reduced at 500 °C for 10 hours. Therefore, the same above-mentioned preparation procedures were used with this material along with other higher ratios by duplicating and quadrupling the above-mentioned wt/v ratio (2%wt/v and 4%wt/v) of both $CaCl_2$ and sodium alginate solutions.

2.19. Potentiometric titration to quantify the concentration of basic and acidic surface sites of different samples

A conventional titration method, which is commonly used to determine acidic and basic sites of different materials [215], was used in this study. To quantify the basic sites of multiple samples, a control experiment was run first by titrating 50 mL of 0.01 M NaCl against 0.02 M HCl until the pH of the solution reached 2.05. The titre volume of HCl was 14.5 mL. Consequently, each adsorbent was added to the NaCl solution, stirred for some time, and then titrated in the same way. The titre of the control experiment was subtracted from that of each adsorbent-containing sample to work out ΔV and then to work out the basic sites' concentration using the following equation:

$$\text{Basic site concentration (mmol/g)} = [[C_{acid} \times \Delta V] / m_{adsorbent}] \times 1000 \quad \text{eq. (2.10)}$$

where C is the concentration of HCl (mol/L), ΔV is the subtraction result of the control titre from the adsorbent titre (L), and m is the adsorbents mass (g).

A similar procedure was applied to quantify the acidic surface sites, using 0.02 M NaOH as the titrant instead. The titration was carried out until the solution pH reached 11.28, and the titre volume for the control experiment in this case was 9 mL. The pH values of 2.05 and 11.28 were set as the pH change beyond these values becomes very slow. This is related to using diluted HCl and NaOH (0.02 M) to avoid the big jumps caused by the higher concentration of these solutions (0.1 M).

2.20. Determination of nitrate leaching in water samples

The nitrate leaching from some of the adsorbents used in the current study was tested by the nitration of salicylic acid method [216]. The theory behind this method is that the nitrate reacts with salicylic acid in highly acidic medium to form 5-nitro salicylic acid, which turns yellow and absorbs visible light at 410 nm in strongly alkaline conditions (pH higher than 12). To start with the blank, 0.2 mL of water was first mixed with 0.8 mL of 5% wt/v of salicylic acid in concentrated H_2SO_4. This solution was prepared by dissolving 5 g of salicylic acid powder in 100 mL of H_2SO_4, and the solution was then stored in a brown bottle in the fridge. Subsequently, 19 mL of 2M NaOH was added to make a final volume of 20 mL, and then the mixture was left for a few minutes to cool down before checking the absorbance on a UV-Vis spectrometer.

In the same way, 0.2 mL of standard solutions of NO_3^--N with concentration ranging from 0.1 to 5 ppm in the final volume (20 mL) were used to do the calibration curve. The stock solution of NO_3^--N (5000 ppm) was prepared by dissolving 0.722 g of KNO_3 in 20 mL DW and then it was serial diluted to obtain the concentration range that could be detected by the UV-Vis spectroscopy. The concentration is based on the atomic mass of nitrogen in nitrates and is therefore expressed as NO_3^--N. For instance, 0.2 mL of the stock solution was diluted with DW to a total volume of 10 mL to obtain a concentration of 100 ppm. Then, 0.2 mL of this intermediate solution was mixed with the aforementioned reagents and further diluted to a final volume of 20 mL to achieve a concentration of 1 ppm. The use of 0.2 mL each time is intended to avoid reducing or even losing the sensitivity of the method. The calibration curve is shown in **Fig 2.13.a** and it indicated the increased absorbance by raising the NO_3^--N concentration to 5 ppm. **Fig 2.13.b** shows the images of the standard solutions.

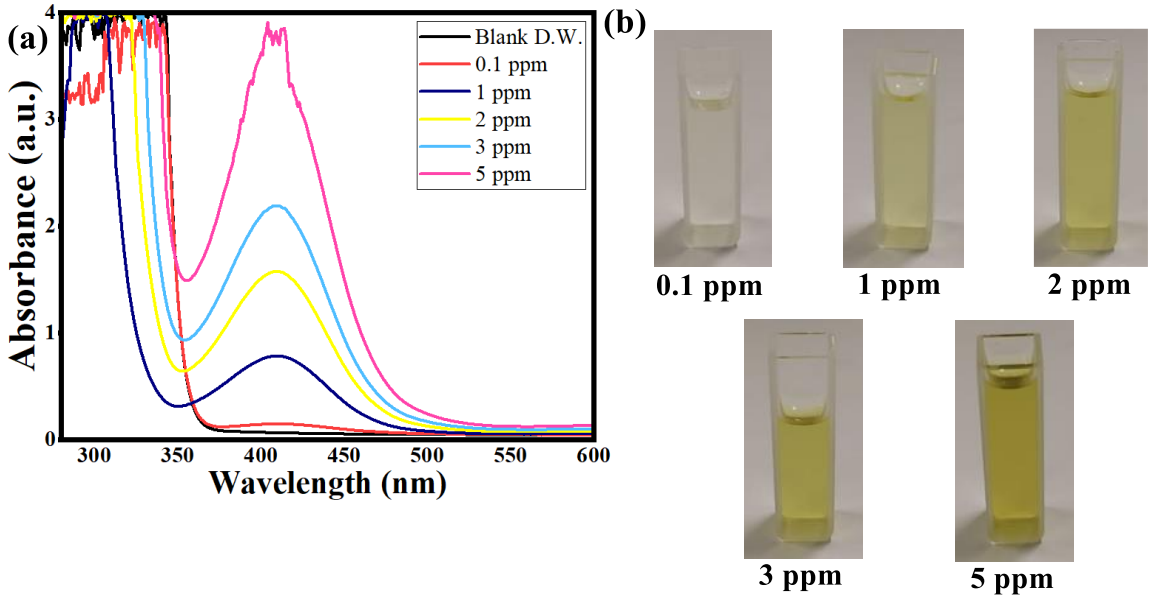

Fig 2.13. The UV-Vis spectrum of the calibration curve of the yellow-coloured 5-nitro salicylic acid chromophore **(a)**, and the images of the standard solutions of NO_3^--N in the range of 0.1 to 5 ppm after the formation of the chromophore **(b)**.

2.21. Determination of sulfate release in water samples from the photodegradation of CEF

The turbidimetric method was used to determine the concentration of released sulfate [217] from the photodegradation of CEF under UV light. Firstly, a stock solution of 1000 ppm of

SO_4^{2-} was prepared by dissolving 0.14 g of anhydrous sodium sulfate in 100 mL of DW. The conditioning reagent was prepared by dissolving 15 g of NaCl in a mixture of 10 mL glycerol, 6 mL of concentrated HCl, and 20 mL of ethanol. Lastly, the solution was topped up to 100 mL using DW and vigorously stirred to dissolve the NaCl. To test the sulfate concentration, 10 mL of a sample was mixed with 10 mL of the conditioning reagent followed by the addition of 0.6 g of barium chloride to form the turbid solution of barium sulfate, which settled down as a precipitate after some time. Consequently, the absorbance of the turbid solution was checked by the spectrometer at 420 nm. The calibration curve was prepared using 10, 100, and 1000 ppm of sulfate as shown in **Fig 2.14.a** and the images corresponding to these concentrations are displayed in **Fig 2.14.b**.

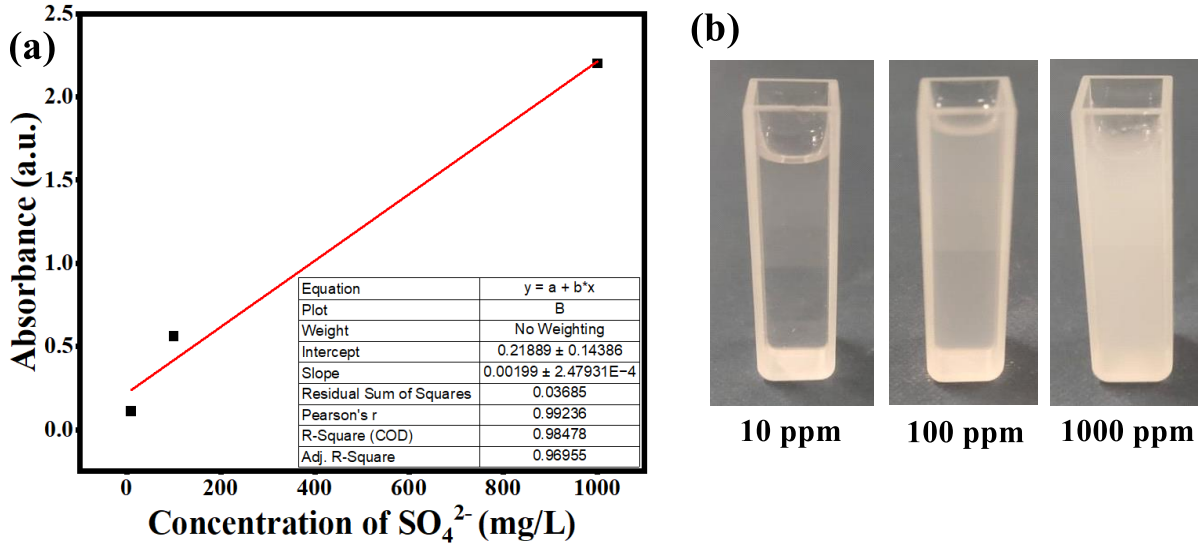

Fig 2.14. The calibration curve of different sulfate concentrations ranging from 10 to 1000 ppm **(a)** and the corresponding images of these concentrations **(b)**.

2.22. Determination of nitrite release in water samples from the photodegradation of CEF and DOXY

The Griess reagent method was used to determine the nitrite released from the degradation of CEF and DOXY [218]. 0.5 g of sulfanilamide and 0.05 g of N-(1-Napthyl)-ethylenediamine dichloride (NED) were dissolved in 40 mL of DW mixed with 5 mL of concentrated phosphoric acid, and lastly the solution was topped up to 50 mL with DW to prepare the Griess reagent, which had to be stored in the fridge and used within one week. A calibration curve was plotted using NO_2^- concentrations ranging from 0.1 to 4 ppm in the form of

potassium nitrite as shown on the UV-Vis spectrum in **Fig 2.15.a** and the corresponding images of these concentrations are shown in **Fig 2.15.b**. The stock solution of potassium nitrite was prepared by dissolving 1 mg of potassium nitrite salt in 50 mL of DW to have a final concentration of 10 ppm. To develop the red or pink-coloured azo dye, 1 mL of Griess reagent was added to 10 mL of the nitrite sample and the mixture was left for 30 minutes and then the absorbance was checked at 540 nm by the UV-Vis spectrometer.

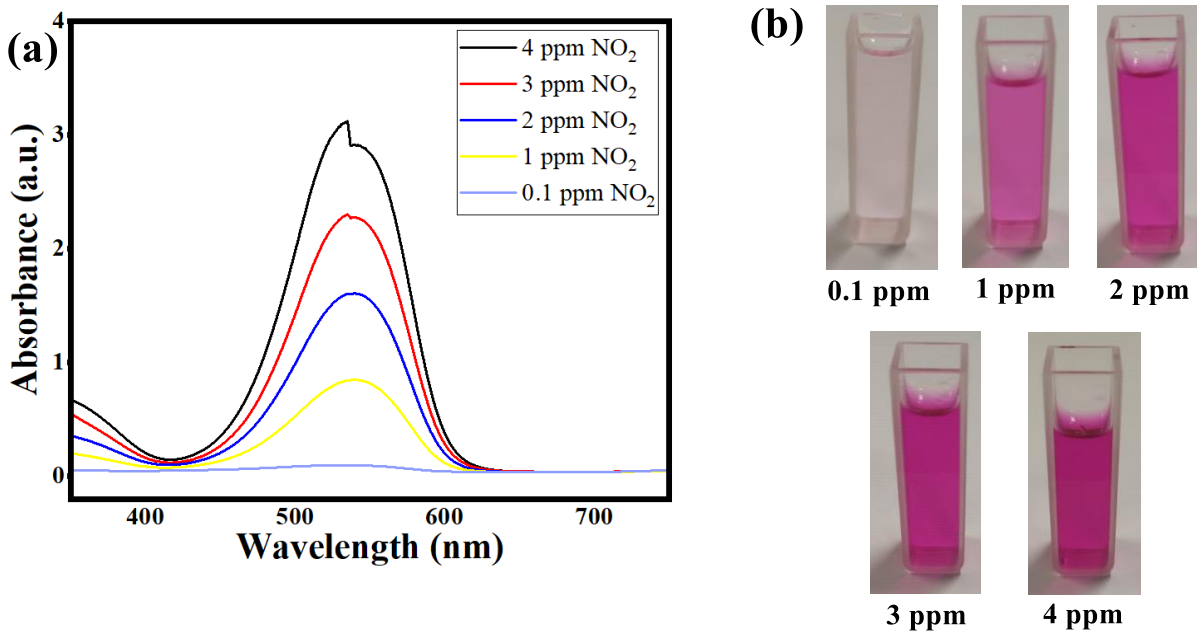

Fig 2.15. The UV-Vis spectrum of the calibration curve of different nitrite concentrations (in the form of potassium nitrite) ranging from 0.1 to 4 ppm **(a)** and the corresponding images of these concentrations **(b)**.

Chapter 3

3. The investigation of lab-prepared TiO_2, red mud-derived TiO_2, and different α-Fe_2O_3 samples in the removal of CEF

3.1. Introduction

CEF is part of the cephalosporin class of antibiotics, which are structurally and functionally related to penicillin [219]. The origins of cephalosporins trace back to an accidental discovery in 1940s by Professor Giuseppe Brotzu in Sardinia where he successfully isolated *Cephalosporium acremonium*, a fungus that produced three distinct antibiotic compounds effective against both Gram-positive and Gram-negative bacteria [219, 220]. In the 1950s, Guy Newton and Sir Edward Abraham successfully isolated cephalosporin C from *Cephalosporium acremonium* and elucidated its chemical structure [221]. The first synthetic derivative of cephalosporin C, cephalothin, was introduced in the 1960s, marking the beginning of a series of advancements across multiple generations of cephalosporins. CEF, a third-generation broad-spectrum cephalosporine, was developed for medical use in 1980 [220] and was modified to resist β-lactamase degradation, an enzyme produced by many resistant bacterial strains [222]. Today, it is one of the most widely prescribed antibiotics valued for its broad applicability, cost-effectiveness, and convenience [220]. Consequently, it is one of the main pharmaceutical pollutants released into the water.

Therefore, the degradation of CEF and its environmental concerns are discussed in this chapter. The speciation of CEF, its functional groups, and how this affects the adsorption efficiency is clarified. Three red mud samples from China and India were used to produce TiO_2 through two different methods: the alkali roasting and the acid baking methods. SEM/EDX and XRD analyses were used to assess the structure and the purity of the extracted TiO_2. A comparison between differently sourced TiO_2 and α-Fe_2O_3 samples along with their commercial counterparts as benchmarks was covered. Different techniques were investigated to improve the performance of the lab-prepared TiO_2, among which the impregnation with metals was found to be the effective technique. The calcination effect on the adsorption efficacy of TiO_2 composites was investigated. The selectivity and scalability of one of these composites were explored. Furthermore, environmental and economic cost-analysis were covered.

3.2. Powder XRD analysis of different α-Fe_2O_3, TiO_2, and red mud samples

XRD is a fundamental technique used to determine the crystalline structure and phase composition of materials. In the current study, it was used to investigate the differences between the various α-Fe_2O_3 and TiO_2 samples, and how these differences would affect their performance. The powder XRD pattern of the commercial haematite (α-Fe_2O_3) (**Fig 3.1.a**) was similar to that of the green synthesized (**Fig 3.1.b**), and the lab-prepared haematite (**Fig 3.1.c**) where the reflections were very well defined and detected at 2θ degrees of 24.11°, 33.15°, 35.58°, 40.83°, 49.41°, 53.99°, 57.63°, 62.34°, 63.96°, 72.08°, and 75.50° that are attributed to the reflections of (012), (104), (110), (113), (024), (116), (018), (214), (300), (119), and (220), respectively, according to JCPDS No. 33-0664.

The powder XRD pattern of commercial TiO_2 (P25) exhibited both anatase and rutile phases as shown in **Fig 3.1.d**. Most of the reflections were for the anatase phase, whereas some at 27.30°, 36.00°, and 41.10° representing the reflections of (110), (101), and (111) were attributed to the rutile phase [JCPDS file number 21-1276] as in agreement with [223]. Lab-prepared TiO_2 only showed the anatase phase (**Fig 3.1.e**), with reflections at (101), (004), (200), (105), (211), (204), (116), (220), and (215), matching JCPDS file number 21-1272. These reflections appeared at 2θ values of 25.40°, 38.00°, 48.10°, 54.10°, 55.20°, 62.80°, 69.10°, 70.40°, and 75.30°, respectively [224].

By comparing the crystallinity of the commercial α-Fe_2O_3 and TiO_2 samples to their prepared counterpart samples, it was clear that the reflections of the commercial samples were sharper, indicating their higher crystallinity, which could be attributed to their larger coherent diffraction domain size. So, to account for this difference in crystallinity, the Scherrer equation ($D = K\lambda/(\beta\ Cos\theta)$) was used to determine the domain size where D is the domain size in Å, λ is the wavelength in Å, β is the full width at half maximum in radians, θ is the Bragg angle in radians or degrees, K is the dimensionless Scherrer constant (usually around 0.9). The apparent domain sizes of commercial α-Fe_2O_3 and TiO_2 were 74 nm and 21 nm, respectively, whereas the sizes of green synthesized α-Fe_2O_3, lab-prepared α-Fe_2O_3, and lab-prepared TiO_2 were 33 nm, 34 nm, and 7 nm, respectively. Although the coherent diffraction domain size is not necessarily equivalent to the particle size, the significantly smaller domain size of the lab-prepared TiO_2 compared to the other four samples may be associated with its higher surface

area (**Fig. 3.7.e**). This higher surface area could, in turn, contribute to the improved adsorption efficiency observed for this sample, as discussed and shown in **Fig. 3.22.c**.

However, it should be noted that the Scherrer equation must be applied with caution, as it has several major limitations. These include instrumental broadening, anisotropy of the powder samples, and microstrain effects, as highlighted by Hargreaves [225]. Such factors are not accounted for in the Scherrer calculation and can lead to inaccuracies in the estimated domain size.

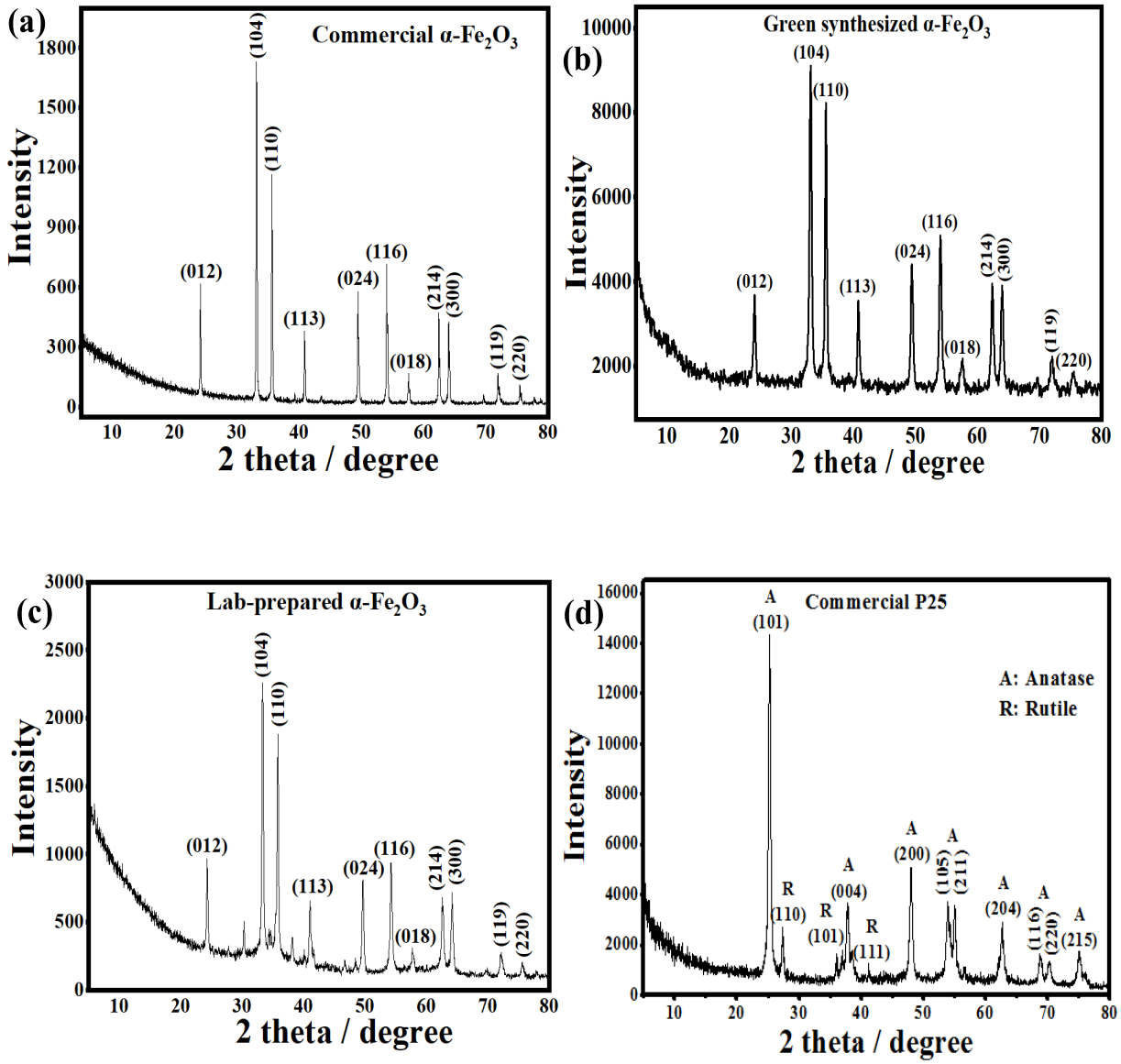

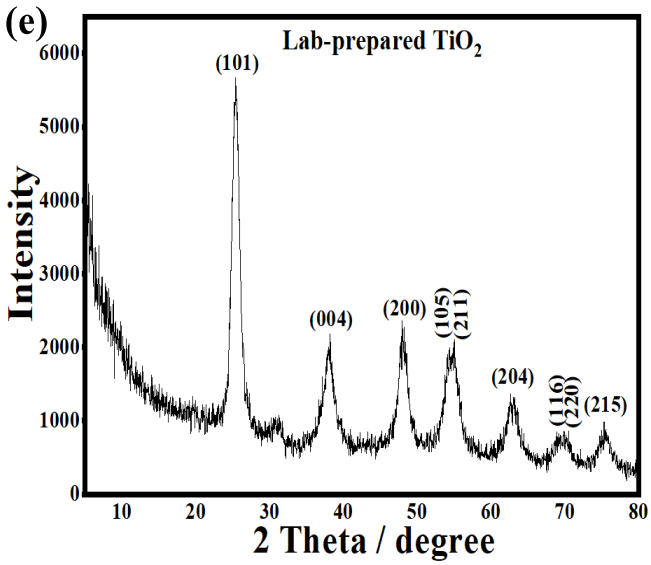

Fig 3.1. Powder XRD pattern of commercial **(a)**, green synthesized **(b)**, and lab-prepared α-Fe_2O_3 (**c**), commercial P25 **(d)** [202], and lab-prepared TiO_2 **(e)**. The patterns show high crystallinity of commercial α-Fe_2O_3 and TiO_2 due to their bigger domain size compared to their prepared counterpart samples.

The powder XRD pattern of the raw Chinese red mud indicated the presence of some mineral phases including sodalite at 13.91°, calcite at 41.00° and 59.70°, goethite at 21.45°, gibbsite at 37.26° and 64.16°, haematite at 24.23°, 33.20°, 35.72°, 41.00°, 54.12°, 62.54, 64.16, and 72.11°, quartz at 42.63°, and titania at 25.32°, 37.26°, 49.52°, 54.12°, 56.01°, 62.54° and 69.29° (**Fig 3.2.a**). Some of the reflections are assigned to two possible minerals, reflecting uncertainty in phase identification. Such a composition was in agreement with Gu *et al.* [226] who characterized the same red mud sample from the same area (Shandong) in China. Upon conducting the same analysis for the extracted titania from Chinese red mud using the alkali roasting method, it was clear that titania was impure as there were some mineral phases still present as shown in **Fig 3.2.b**, and the titania phase was mostly anatase along with other unknown reflections.

In contrast to the powder XRD pattern of TiO_2 extracted using the alkali roasting method, the TiO_2 obtained via the acid baking method exhibited a potentially purer crystalline phase composition, confirmed by EDX analysis, with well-defined anatase reflections and fewer unidentified reflections (**Fig 3.2.c**). A reflection that might correspond to aluminium sulfate at around 26.50° was observed in both TiO_2 samples, possibly due to the interaction of alumina

with the sulfuric acid used in the two extraction methods. These results were in agreement with those reported by Agrawal and Dhawan [201], whose acid baking method was used in the current study. However, this reflection might correspond to silicate or the rutile phase in the alkali roasting extracted-TiO_2 because it was calcined at 900 °C. Generally, the transition from anatase to rutile occurs at around 600 °C, but this temperature can vary depending on the TiO_2 precursor, heating duration, ramping rate, and the presence of impurities [227].

The Indian red mud sample (RM 7) exhibited similar mineral phases to those detected in the Chinese red mud as seen in **Fig 3.3.a** and in agreement with previous published articles that made use of RM 7 [204]. The TiO_2 extracted from RM 7 using the alkali roasting method was in the anatase phase; however, like the TiO_2 extracted from the Chinese red mud, it displayed poorly defined reflections and the presence of other mineral phases (**Fig 3.3.b**). When the acid baking method was used to extract TiO_2 from RM 7, the anatase phase was clearer as more well defined TiO_2 reflections were observed along with fewer reflections of other minerals (**Fig 3.3.c**). Another red mud sample from India (RM 8) showed some mineralogical components similar to the other red mud samples (**Fig 3.4.a**). The TiO_2 extracted from RM 8 using the alkali roasting method revealed the existence of anatase phase, along with several unidentified reflections and additional minerals (**Fig 3.4.b**). In agreement with the other TiO_2 samples, the acid baking method produced TiO_2 with more well-defined reflections from RM 8 (**Fig 3.4.c**).

The domain size of the acid baking derived-TiO_2 from the Chinese red mud was 20 nm, whereas that of the TiO_2 extracted by the alkali roasting method was 24 nm. Similarly, the domain sizes of the alkali roasting derived-TiO_2 from RM 7 (34 nm) and RM 8 (35 nm) were higher than those extracted by the acid baking method, which were 17 nm and 32 nm in the same respective manner. Such a result could be attributed to the better performance of the acid baking derived-TiO_2 samples as shown in **Fig 3.23**. However, these domain sizes might be inaccurate as all the extracted TiO_2 samples have impurities from the red mud.

The potentially purer crystalline phase composition with well-defined reflections of TiO_2 produced by the acid baking method could be related to its simpler and fewer steps compared to the alkali roasting method. These fewer steps minimized the likelihood of introducing additional contaminants or impurities during the extraction process. It must be noted that the identification of reflections in all the samples shown in **Fig 3.2**, **Fig 3.3**, **Fig 3.4**, and **Fig 3.5.a**

carries a degree of uncertainty, as they were derived from red mud samples, which contain numerous impurities. It must be mentioned that the identification of the reflections of all samples was conducted by matching the results obtained in the current study with previously published results in the literature.

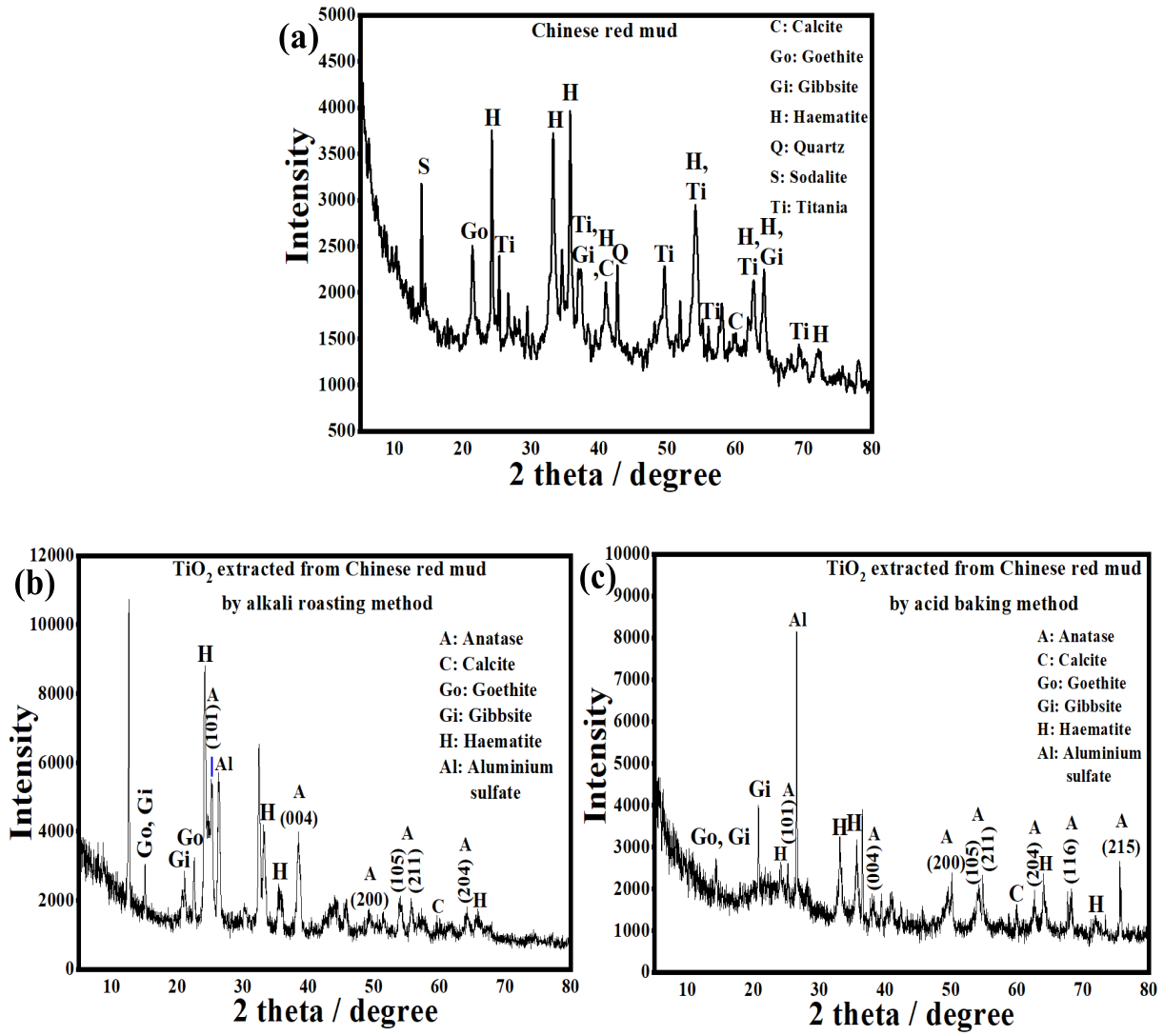

Fig 3.2. Powder XRD patterns of Chinese red mud **(a)**, TiO_2 extracted from Chinese red mud by the alkali roasting method **(b)**, and by the acid baking method **(c)**. (**a**, **b**, and **c** from [202]). This figure indicates the presence of multiple mineral phases in the raw red mud, whereas the TiO_2 extracted via the acid baking method exhibits a potentially purer crystalline phase composition, as evidenced by its fewer unidentified reflections.

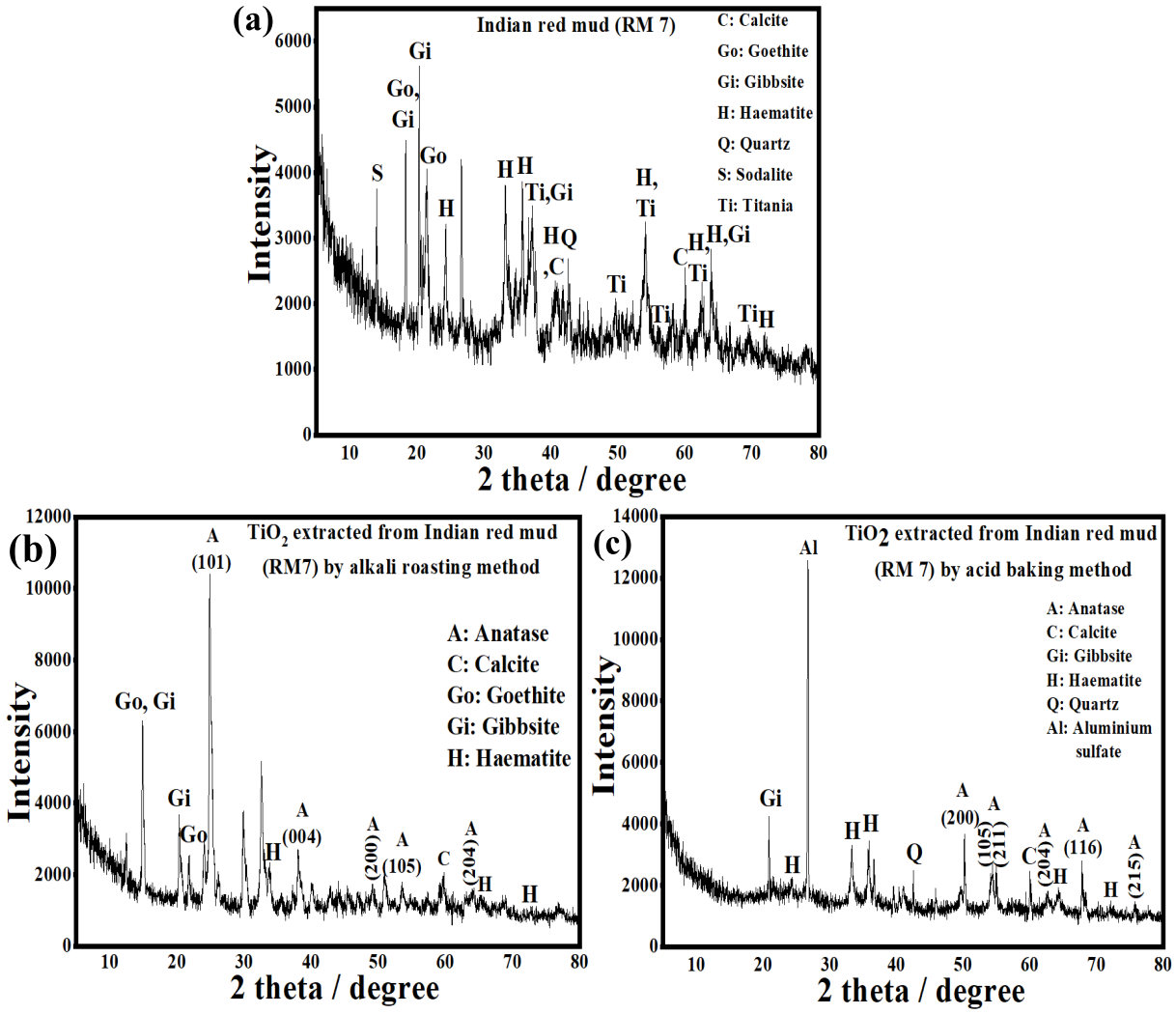

Fig 3.3. Powder XRD patterns Indian red mud RM 7 **(a)**, TiO_2 extracted from Indian RM 7 by the alkali roasting method **(b)**, and by the acid baking method **(c)**, where the anatase phase was clearer as more well defined TiO_2 reflections were observed along with fewer reflections of other minerals in the acid baking-extracted sample.

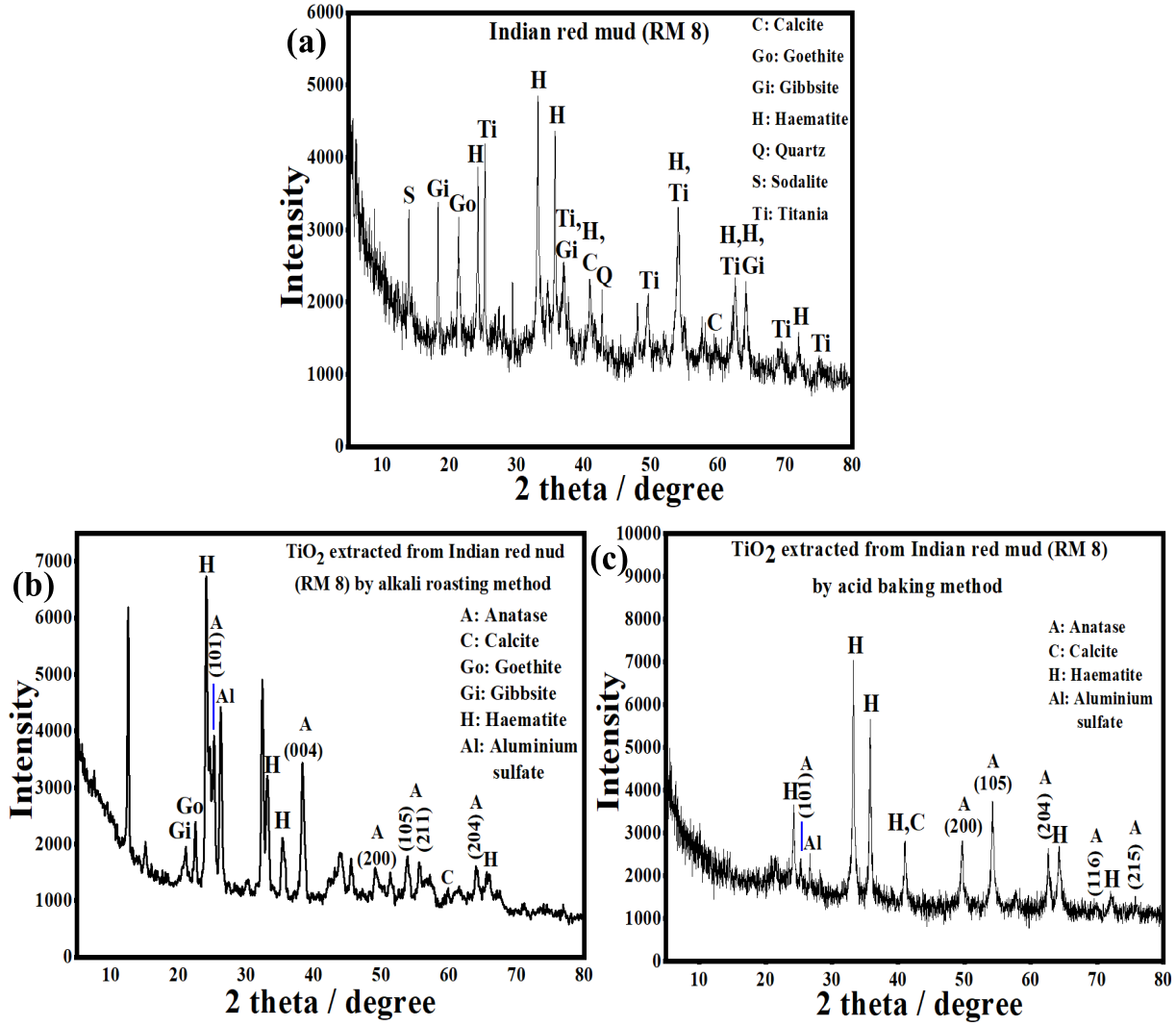

Fig 3.4. Powder XRD pattern of Indian red mud RM 8 **(a)**, and TiO_2 extracted from Indian RM8 by the alkali roasting method **(b)**, and by the acid baking method **(c)**. showing similar results to TiO_2 extracted from the other red mud samples.

Powder XRD pattern of 5% Fe 5% Cu-TiO_2 using TiO_2 extracted from Chinese red mud by the acid baking method showed a distinguishing reflection at 12.7° (**Fig 3.5.a**), that might be corresponding to the (001) reflection of hydrated copper nitrate salts [228]. However, the main reflection of the copper nitrate salt used in the current study was observed at a slightly higher 2θ (15.1°) as shown in **Fig 3.5.b**. To verify this discrepancy, the preparation of 5% Fe 5% Cu-TiO_2 was repeated and its powder XRD along with that of the copper nitrate salt were retested, yet similar patterns were obtained. Thus, the reason for the difference in the 2θ values might be related to the coordination between copper and TiO_2. This may lead to increased interplanar

spacing and a lower 2θ value. The domain size of titania in 5% Fe 5% Cu-TiO_2 (**Fig 3.5.a**) was 113 nm, but it increased to 121 nm as the reflections became narrower after CEF adsorption (**Fig 3.34.b**). This might be an indication of 5% Fe 5% Cu-TiO_2 sintering during the adsorption of CEF.

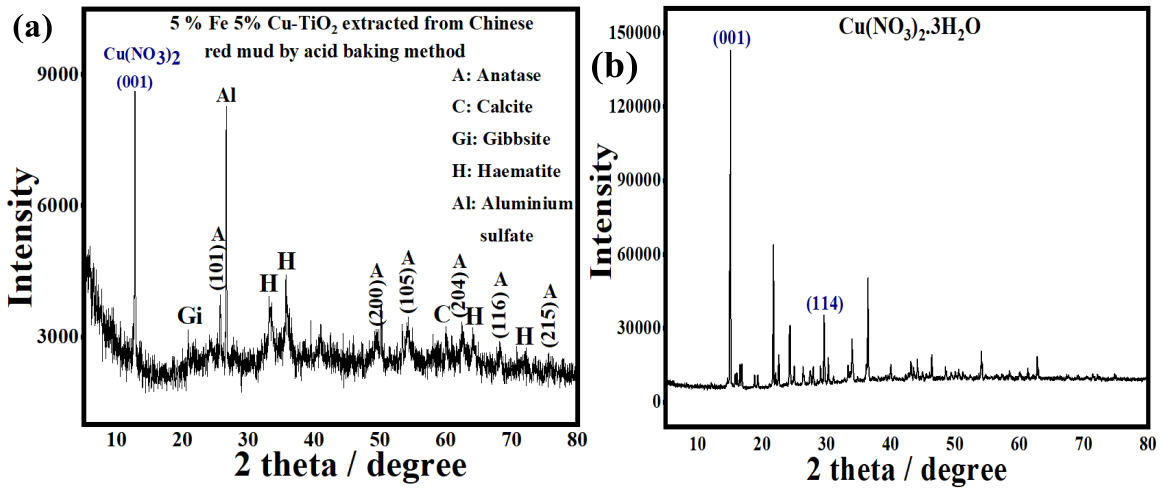

Fig 3.5. Powder XRD patterns of 5% Fe 5% Cu-TiO_2 **(a)** extracted from Chinese red mud by the acid baking method [202] and copper nitrate trihydrate salt **(b)**.

FTIR is an analytical technique used to identify the chemical bonds, and functional groups present in a material by measuring how it absorbs infrared radiation. Therefore, it was used in investigating the composition of *T. latifolia* and the role of its functional groups in synthesizing α-Fe_2O_3 in the next section.

3.3. FTIR analysis of *T. latifolia* and its green synthesized α-Fe_2O_3

To clarify the role of OH-containing phytoconstituents in *T. latifolia*, FTIR analysis was conducted. The plant powder was analyzed after drying at 60 °C, 150 °C, and 300 °C to evaporate the residual moisture and see if the OH band is still detected at high temperatures such as 300 °C. The intensity of the OH decreased by increasing the temperature as more water evaporated from *T. latifolia* powder (**Fig. 3.6.a-c**). However, a broad absorption band appeared at 3345 cm^{-1} after drying the sample at 300 °C to evaporate the water as much as possible. This peak might be associated with hydrogen-bonded OH groups of phenols [229], and this observation could support the involvement of OH groups in the precipitation of Fe^{3+} ions as $Fe(OH)_3$, which was subsequently calcined/dehydrated to form α-Fe_2O_3. The dried samples were cooled in a desiccator under vacuum for a few minutes before checking them by

the FTIR to prevent the absorption of air moisture, which can increase the intensity of the OH band. Notably, the same OH band was still detected in the FTIR spectrum of the green-synthesized α-Fe_2O_3, but with a very low intensity (**Fig. 3.6.d**), potentially indicating the presence of surface-bound OH functional groups.

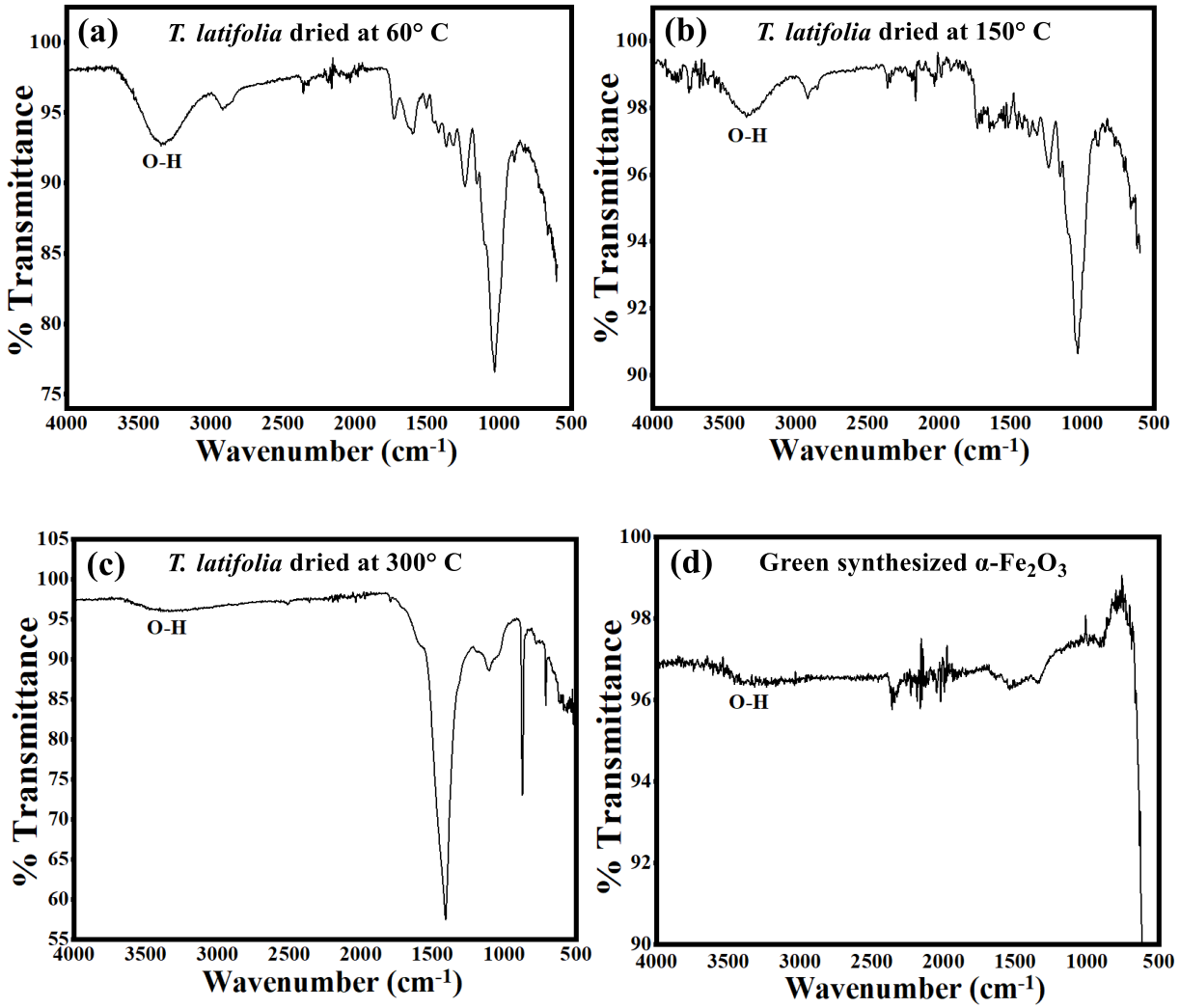

Fig 3.6. FTIR spectra of *T. latifolia* powder dried at 60° C **(a)**, 150° C **(b)**, 300° C **(c)**, and green synthesized α-Fe_2O_3 **(d)** showing the decreasing intensity of OH band by increasing the temperature and evaporating more water content from *T. latifolia* powder.

3.4. BET analysis of different α-Fe_2O_3, TiO_2 samples, and composites of TiO_2 extracted from the Chinese red mud by the acid baking method

One of the essential parameters that can affect the performance of adsorbents is the surface area as high surface area and porosity usually results in a more efficient adsorption. Therefore,

the BET gas adsorption method was used to determine the surface areas in the current study. The surface area of the commercial α-Fe_2O_3 was only 20 m^2/g (**Fig 3.7**.**a**) whereas the surface area of red mud-derived and green synthesized α-Fe_2O_3 samples were 85 and 42 m^2/g, respectively (**Fig 3.7**.**b** and **c**). The surface area measurement of commercial α-Fe_2O_3 might be inaccurate because the adsorption-desorption lines do not close at a relative pressure of 0.42 as would be expected from the tensile strength effect [230], and the BET machine was subsequently unavailable to repeat the measurement. The hysteresis type of red mud-derived α-Fe_2O_3 seems to be H1 with cylindrical pores, whereas that of green synthesized α-Fe_2O_3 could be H3 with wedge-shaped pores. Similarly, the surface area of the commercial P25, which was 56 m^2/g as shown in **Fig 3.7**.**d**, was significantly less than that of lab-prepared and Chinese red mud-derived TiO_2, which measured 223 m^2/g (**Fig 3.7**.**e**), and 139 m^2/g (**Fig 3.7**.**f**), respectively. Consequently, the adsorption efficiency of the commercial samples was expected to be generally lower than their counterparts. The hysteresis type of the three TiO_2 samples could be H1 with cylindrical pores, especially the lab-prepared TiO_2. The BET type of all materials reported in this chapter seems to be IV.

Impregnating TiO_2 with metals might increase or decrease its surface area based on several factors including the concentration of the impregnating metal, synthesis or impregnation procedures, and specific characteristics of both the impregnating metal and TiO_2. In this regard, Mogal *et al.* [231] reported an increase in the surface area of TiO_2 from 37 m^2/g to a range of 51 - 82 m^2/g by doping TiO_2 with different ratios of silver (0.75 - 3.5 wt%). Similarly, Tiwari *et al.* [232] observed an increased surface area of TiO_2 from 41 m^2/g to 88 m^2/g using 1 wt% of platinum.

10% Cu-TiO_2 and 10% Fe-TiO_2 exhibited surface areas of 92 m^2/g and 93 m^2/g (**Table 3.1**), respectively, which are lower than that of TiO_2 extracted from Chinese red mud (139 m^2/g) by the acid baking method. Similarly, the surface areas of 2% Cu-TiO_2, 2% Fe-TiO_2, 5% Cu-TiO_2, 5% Fe-TiO_2, and 5% Fe 5% Cu-TiO_2 were also lower than the pristine TiO_2, measuring 53 m^2/g, 114 m^2/g, 58 m^2/g, 65 m^2/g, and 55 m^2/g, respectively. All Fe and Cu-TiO_2 composites of this chapter are prepared in 2, 5, or 10 wt% and their nitrogen physisorption isotherms are provided in **Appendix 1.1** (**Fig S1**). The hysteresis type of all these composites is probably H3 with wedge shape pores except for 5% Cu-TiO_2 and 10% Cu-TiO_2 as they are believed to be H1 with cylindrical pores.

The major trend of the diminished surface areas of all materials observed in the current study could be attributed to the occupation of TiO_2 surface sites by the impregnating metals along with the filling of TiO_2 pores with these metals resulting in the formation of less accessible surfaces, which is consistent with the observation of Di Paola *et al.* [233]. The obtained results are also in agreement with Abdelouahab Reddam *et al.* [234] who observed decreased surface area of a commercial titania sample (P25) after impregnation with copper, iron, and manganese. Within the same context, Grover *et al.* [235] observed the decline in the surface area of different types of TiO_2 including P25 and synthesized TiO_2 nanotubes from 56 m^2/g and 176 m^2/g to 48 m^2/g and 152 m^2/g, respectively, upon depositing 1 wt% Cu on the two materials. All of the adsorbents shown in **Fig 3.7** were microporous as their pore size was less than 2 nm except for lab-prepared TiO_2, red mud-derived TiO_2, and 2% Fe-TiO_2 as their pore sizes were almost 3 nm, 11 nm, and 8 nm, respectively. So, the three materials might be mesoporous.

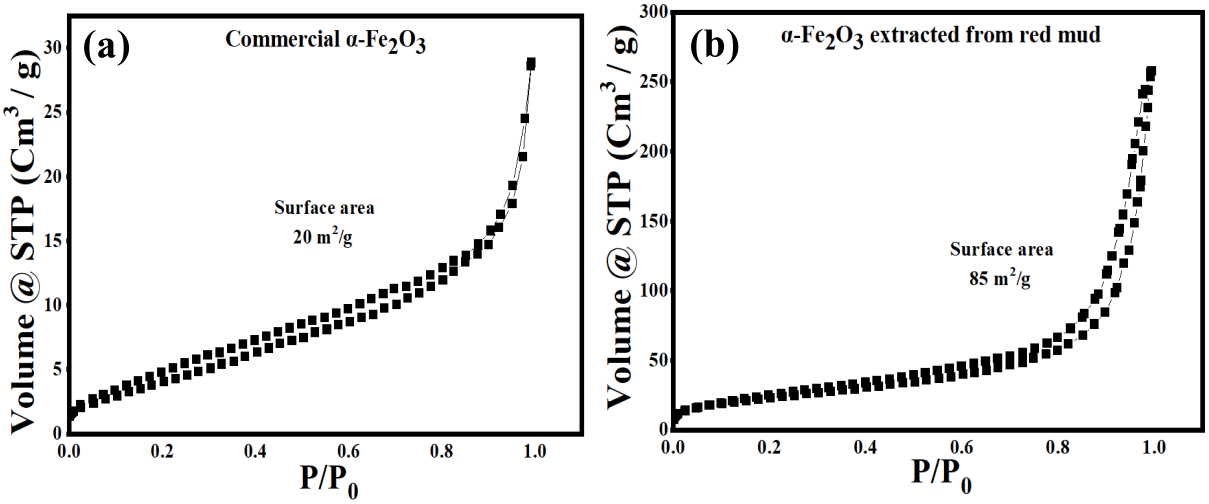

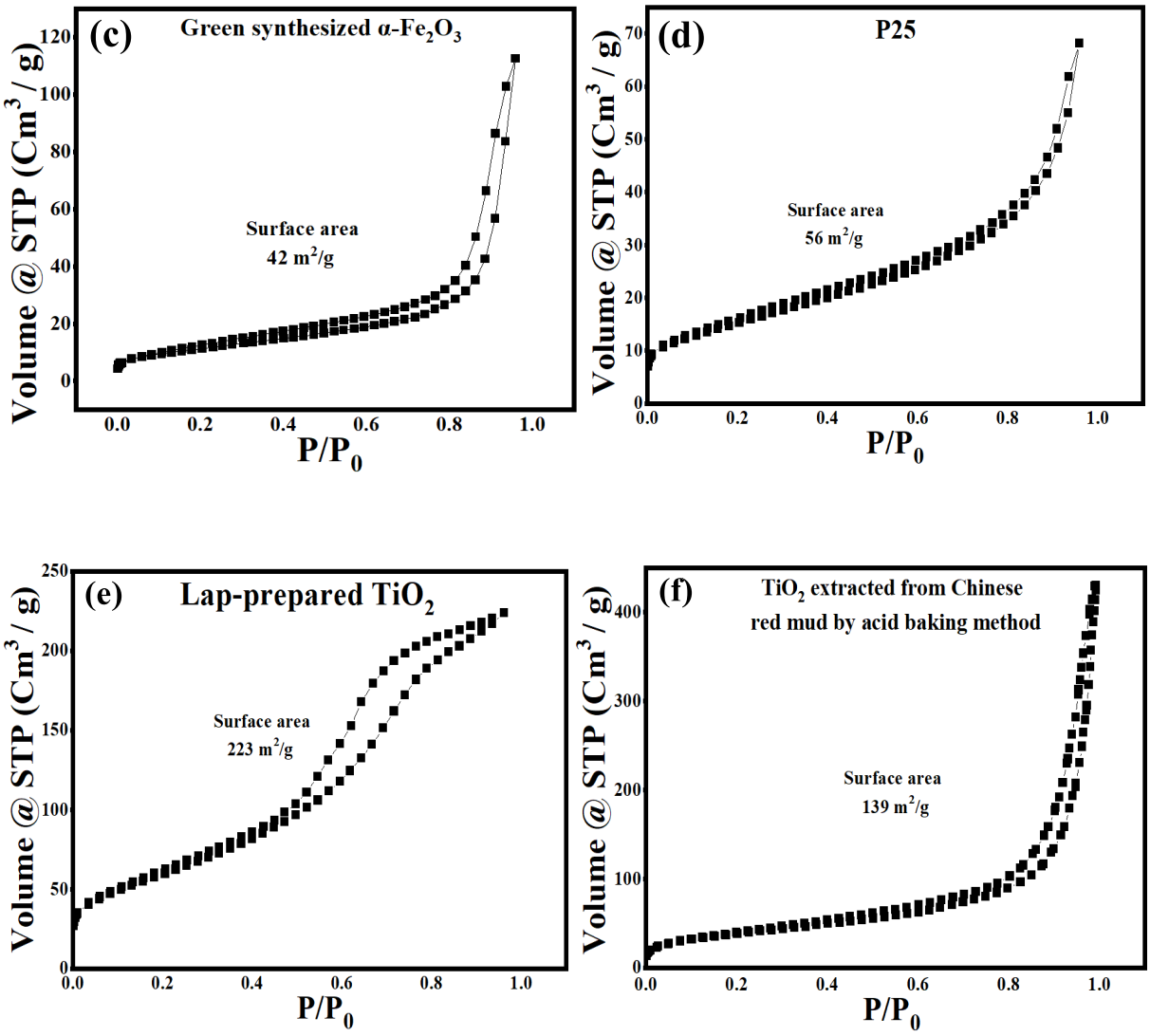

Fig 3.7. Nitrogen physisorption isotherms of commercial **(a)**, red mud-derived (**b**), and green synthesized α-Fe_2O_3 **(c)**, and P25 (**d**), lab-prepared TiO_2 **(e)**, and TiO_2 extracted from Chinese RM by the acid baking method **(f)**. (**d** and **f** from [202]).

Table 3.1. Surface areas of Fe and Cu-TiO_2 composites using TiO_2 extracted from Chinese red mud by the acid baking method.

Adsorbent	Surface area (m^2/g)
2% Cu-TiO_2	53
5% Cu-TiO_2	58
10% Cu-TiO_2	92
2% Fe-TiO_2	114
5% Fe-TiO_2	65

10% Fe-TiO_2	93
5% Fe 5% Cu-TiO_2	55

3.5. SEM and EDX analysis of TiO_2 extracted from the Chinese red mud by the acid baking and the alkali roasting methods

SEM accompanied by EDX, is an indispensable technique in characterizing catalytic and adsorbent materials. It was employed in the current study to investigate the morphology of TiO_2 samples extracted from the Chinese red mud and to check which sample is purer, which was then correlated with the higher adsorption efficiency. SEM analysis revealed a flake-like morphology with tapered needles for TiO_2 extracted employing the alkali roasting method (**Fig 3.8.a, c, e, g,** and **h**) compared to the irregular morphology of TiO_2 extracted by the acid baking method from Chinese red mud (**Fig 3.9.a, c, e, g,** and **h**). As shown in **Fig 3.8.b, d,** and **f**, the elemental composition of TiO_2 extracted by the alkali roasting method included sodium, calcium, nitrogen, and vanadium with different percentages, which were not detected in the EDX spectrum of TiO_2 extracted by the acid baking method (**Fig 3.9.b, d,** and **f**). The detection of these elements could be attributed to the use of a large number of chemicals in the alkali roasting method. Therefore, this result may reflect the higher purity of TiO_2 extracted by the acid baking method by detecting fewer elements in the EDX spectrum.

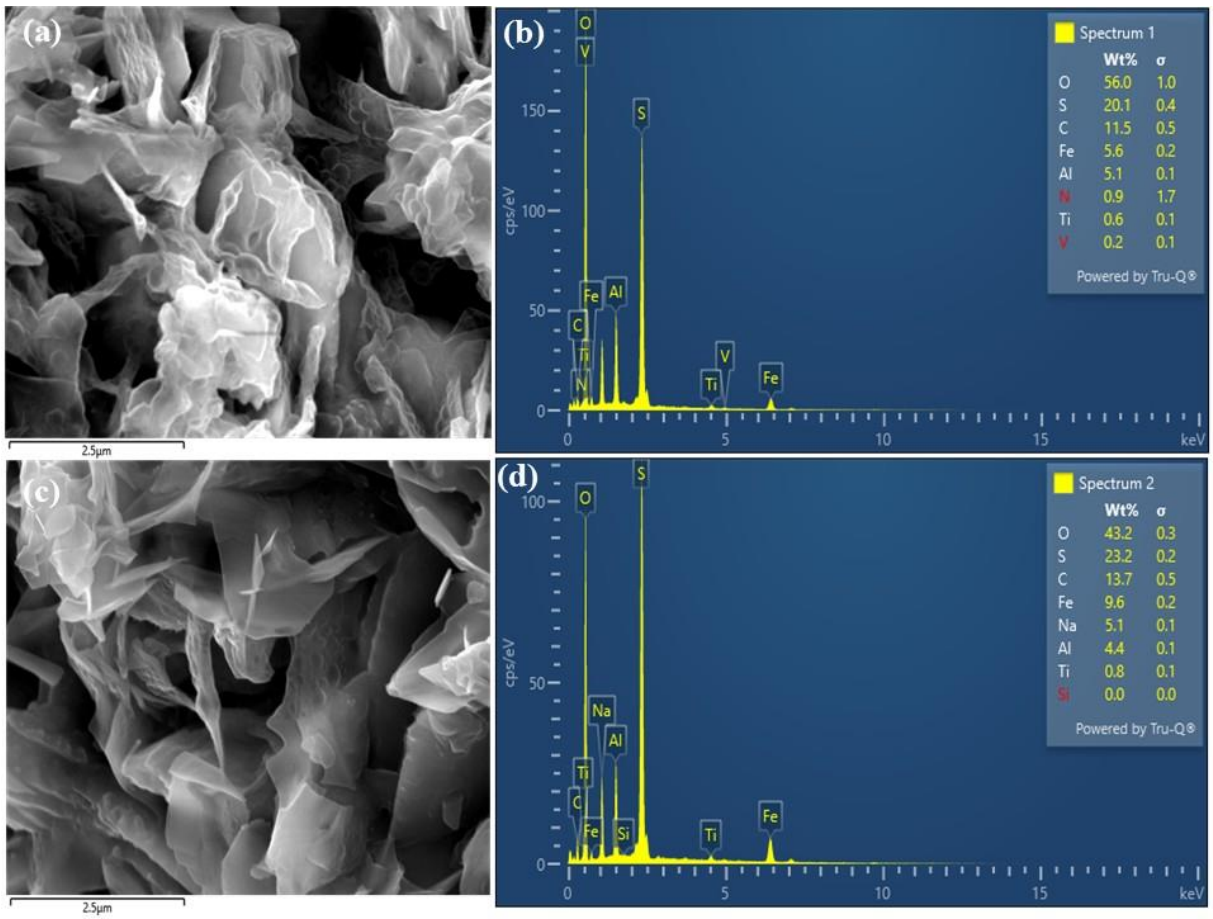
(a)
2.5µm
(b)
O
V
S
Fe
Al
C
Ti
N
V
Ti
Fe
cps/eV
keV
Spectrum 1
Wt% σ
O 56.0 1.0
S 20.1 0.4
C 11.5 0.5
Fe 5.6 0.2
Al 5.1 0.1
N 0.9 1.7
Ti 0.6 0.1
V 0.2 0.1
Powered by Tru-Q®
(c)
2.5µm
(d)
S
O
Na
Al
Ti
C
Fe
Si
Ti
Fe
cps/eV
keV
Spectrum 2
Wt% σ
O 43.2 0.3
S 23.2 0.2
C 13.7 0.5
Fe 9.6 0.2
Na 5.1 0.1
Al 4.4 0.1
Ti 0.8 0.1
Si 0.0 0.0
Powered by Tru-Q®

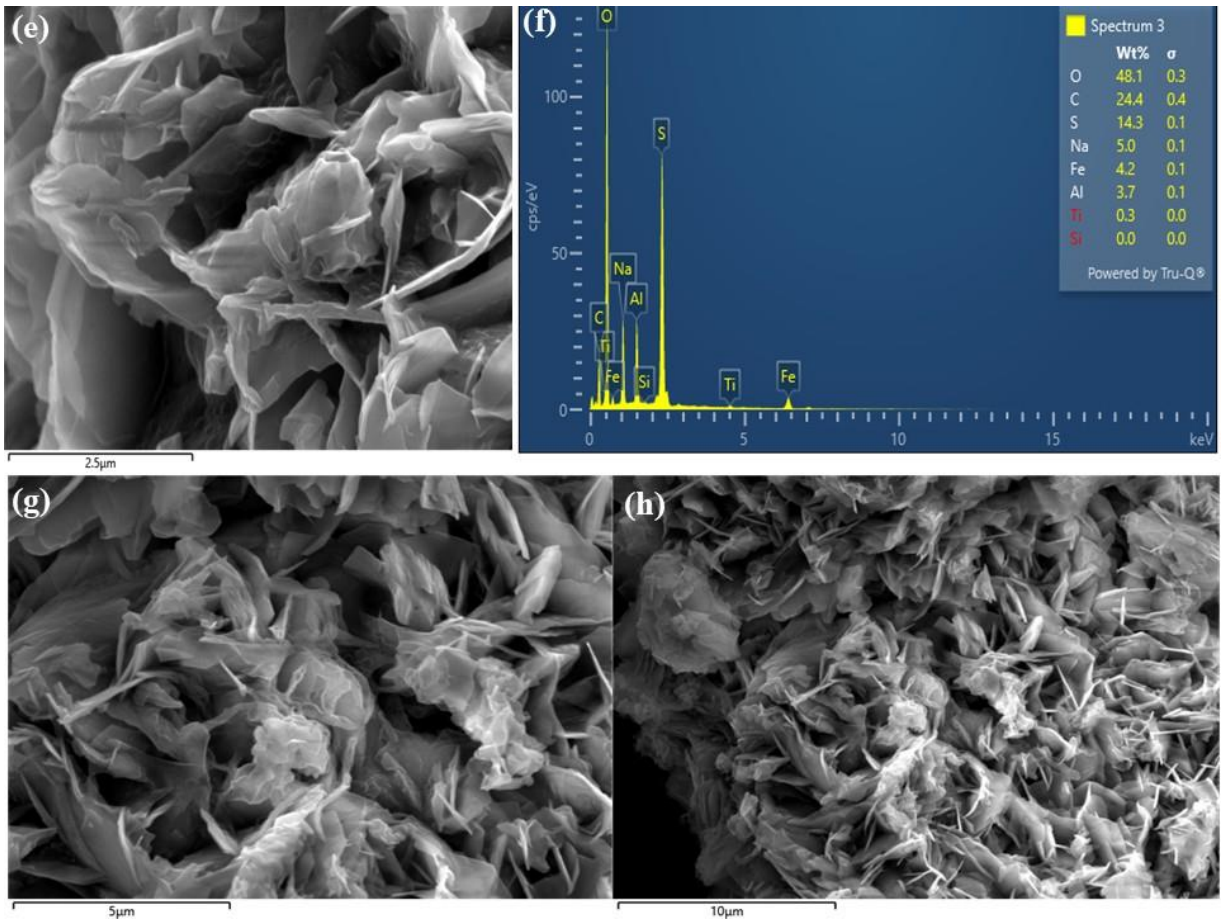

Fig 3.8. SEM images and EDX spectra of by the alkali roasting method-derived TiO_2 **(a-h)** showing their flake-like morphology with tapered needles.

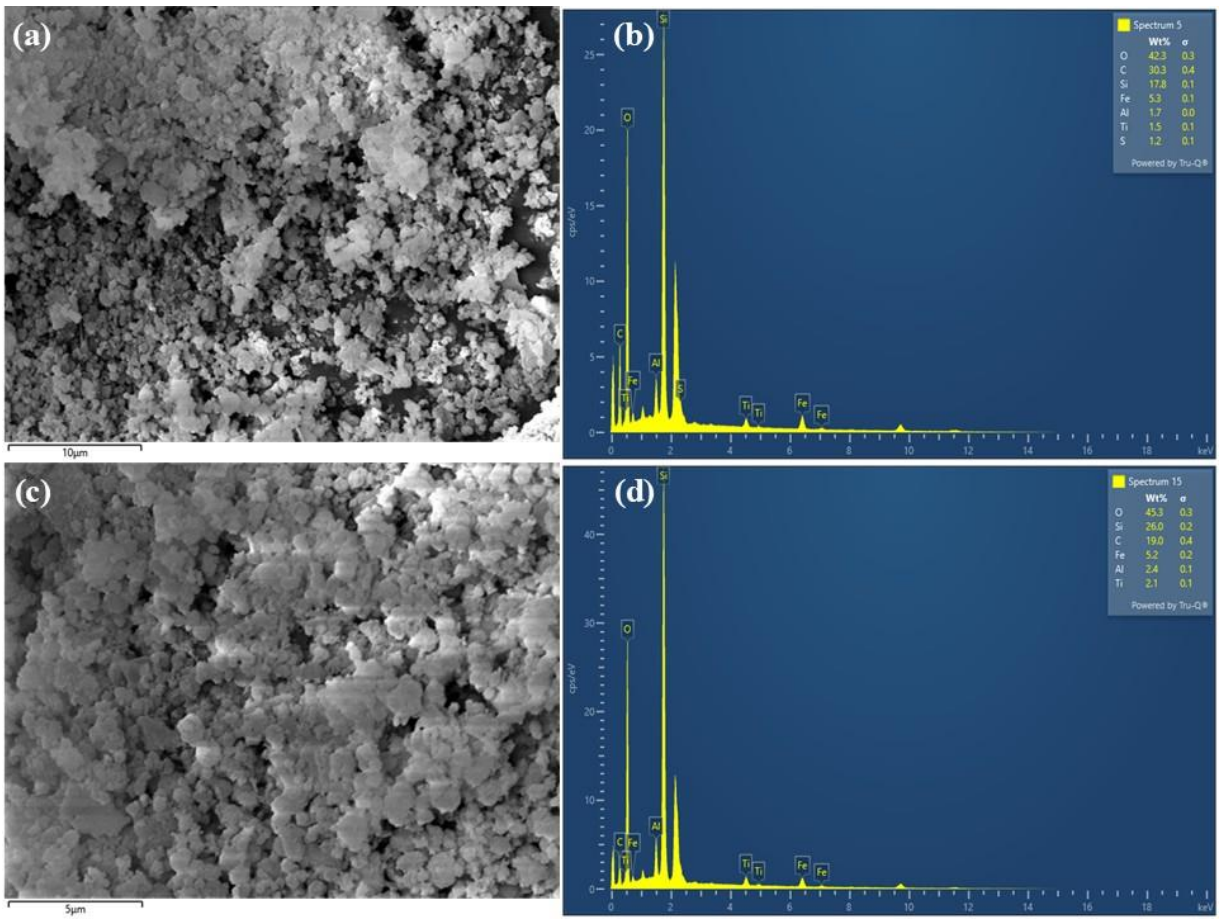
(a)
10µm
(b)
Spectrum 5
Wt% σ
O 42.3 0.3
C 30.3 0.4
Si 17.8 0.1
Fe 5.3 0.1
Al 1.7 0.0
Ti 1.5 0.1
S 1.2 0.1
Powered by Tru-Q®
cps/eV
keV
(c)
5µm
(d)
Spectrum 15
Wt% σ
O 45.3 0.3
Si 26.0 0.2
C 19.0 0.4
Fe 5.2 0.2
Al 2.4 0.1
Ti 2.1 0.1
Powered by Tru-Q®
cps/eV
keV

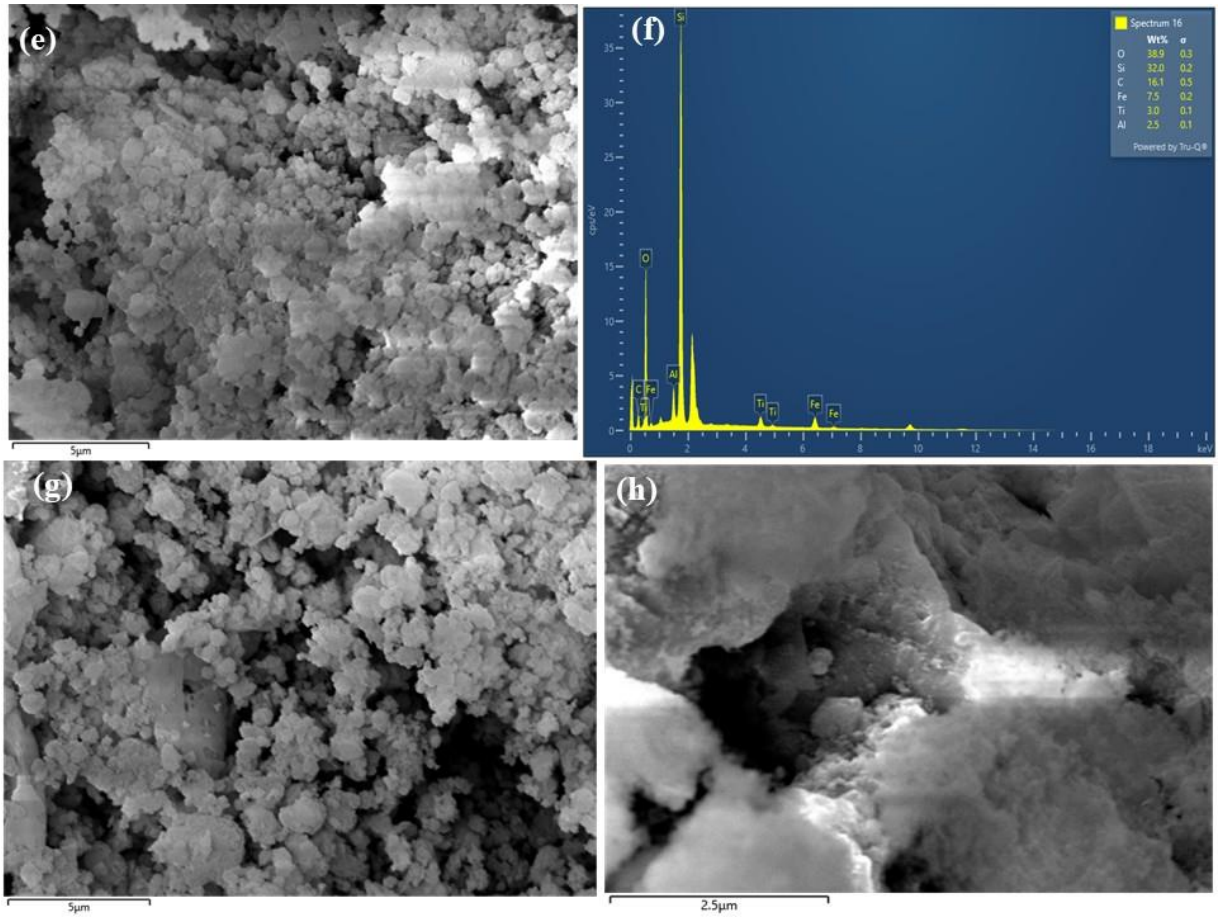

Fig 3.9. SEM images and EDX spectra of TiO_2 extracted by the acid baking method **(a-h)** showing their irregular morphology and indicating a potentially higher purity than TiO_2 extracted by the alkali roasting method.

3.6. The photolysis of CEF

The degradation of CEF under UV light (photolysis) without using any materials was first investigated to get an insight into the efficiency of this process and its environmental considerations. As mentioned in **Section 2.12**, a 125-Watt UV lamp was used to degrade CEF at two different distances (5 and 10 cm) from the CEF solution and two pH levels (3 and 7). The degradation efficiency after two hours at pH 3 was 29% and 49% at 10 cm and 5 cm, respectively (**Fig 3.10.a** and **b**). Increasing the time to five hours improved the degradation efficacy to 71% and after leaving the CEF solution for a week away from the UV light, the efficacy went up to 77%. The absorbance of the UV peak increased after using the UV light for an hour after that week, possibly due to evaporation of the solution, which concentrated the

CEF (**Fig 3.10.b**). No CEF degradation was observed under visible light either artificial laboratory or natural sunlight.

Additionally, the photolysis was undertaken at pH 7 for two hours and the efficiency was 47% (**Fig 3.10.c**), which was very similar to that of pH 3. The arrow in **Fig 3.10.c** shows the absorbance going down over the two hours of degradation with a measurement taken every ten minutes because it was not feasible to put all these measurements in the figure's ligand such as **Fig 3.10.a** and **b**. Thus, controlling the two factors (distance and time) can effectively enhance the degradation efficacy. However, the potential toxicity of the intermediate and final degradation products must be considered. In this context, LC-MS analysis was carried out to identify these products. As shown in **Fig 3.11.a**, the main peak of CEF molecular ion was detected at m/z 555 and it almost disappeared after the degradation at pH 3 (5 cm) (**Fig 3.11.b**). The other detected peaks either prior to or after the degradation are attributed to the presence of impurities in the LC-MS column itself, which were confirmed at different retention times by running DW as a control (**Fig S2.a-g**). It was therefore concluded that the degradation products are primarily gases released during the degradation process, which would result in the formation of sulfates and nitrites in aqueous solutions. These gases were detected and analyzed using TGA-MS, as discussed in **Section 3.7**, and the sulfates and nitrites were detected by the turbidimetric method and the Griess reagent method, respectively.

According to the literature, one of the potentially toxic and stable intermediates is thiotriazinone (m/z = 145), which is generally used in producing beta-lactam antibiotics such as CEF [236], and it can last in water for a long time [237]. The possibility of this intermediate being released during the degradation in the current study cannot be confirmed as some of the column impurities show up at the same m/z ratio. Researchers usually try to test the toxicity of the antibiotic's degradation products on specific cell lines, bacterial strains, and even aquatic organisms (e.g., fish). However, determining the toxicity of these intermediate and degradation products is not that straightforward because they might be of different toxicity levels to different organisms, which requires a deep investigation of their toxicity profiles. Therefore, the degradation of CEF is not considered an environmentally safe option to use. However, the Fenton degradation and the photocatalytic efficacies of one of the Chinese RM-derived TiO_2 composites (5% Fe 5% Cu-TiO_2) along with the commercial and lab-prepared TiO_2 samples were investigated under UV light in this chapter just to have an insight into their photocatalytic efficacy. Within the same context, the photocatalytic efficiency of the

commercial and the Chinese red mud-derived α-Fe_2O_3 was investigated under visible light. On the other hand, adsorption offers a safer and more effective alternative for removing CEF from wastewater, especially when using non-toxic adsorbents such as titanium and iron oxides, even in the event of leaching. Therefore, this method was employed and thoroughly investigated in this study using titanium and iron oxides derived from various waste materials.

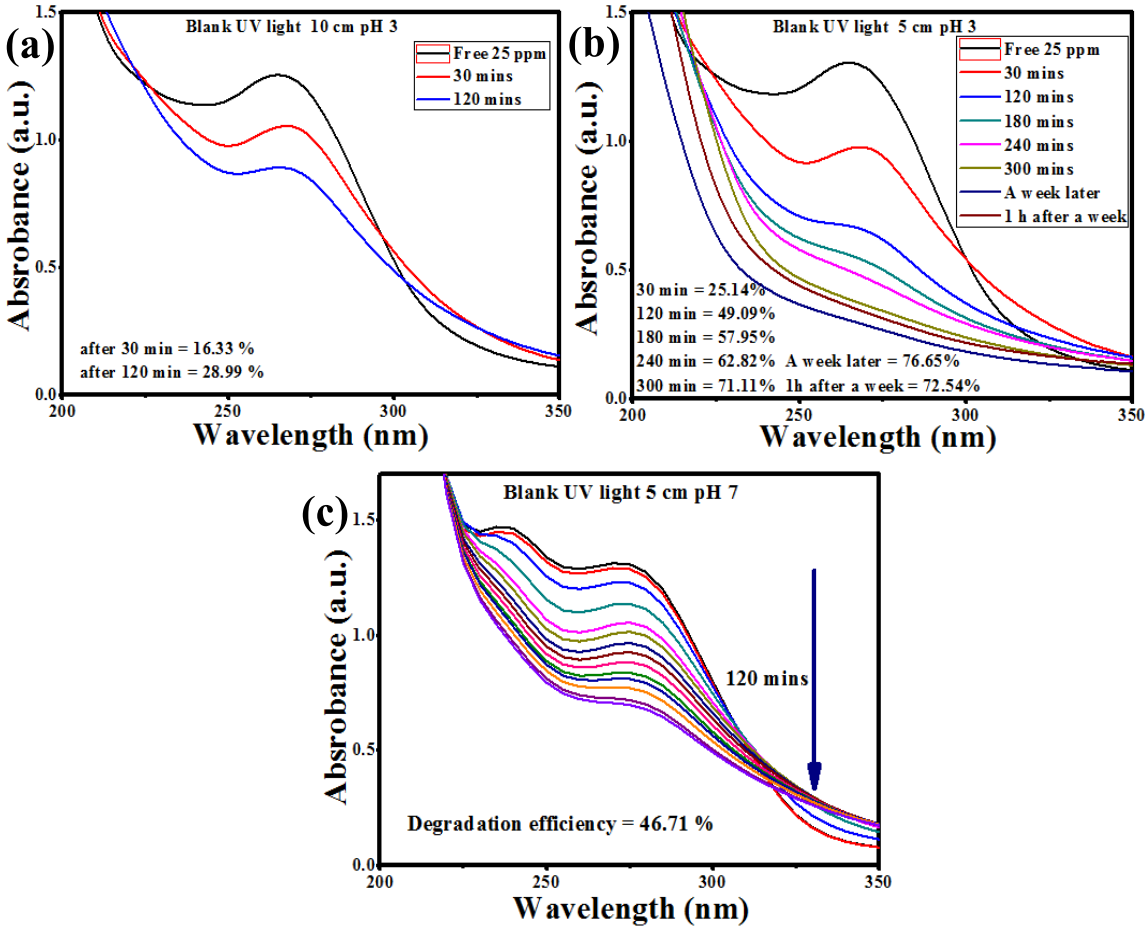

Fig 3.10. The degradation of CEF under UV light (photolysis) at pH 3 at 10 cm **(a)**, 5 cm **(b)**, and at pH 7 at 5 cm **(c)**. [C_o = 25 ppm, stirring rate = 800 rpm, T = 20 ± 2 °C, and volume = 20 mL].

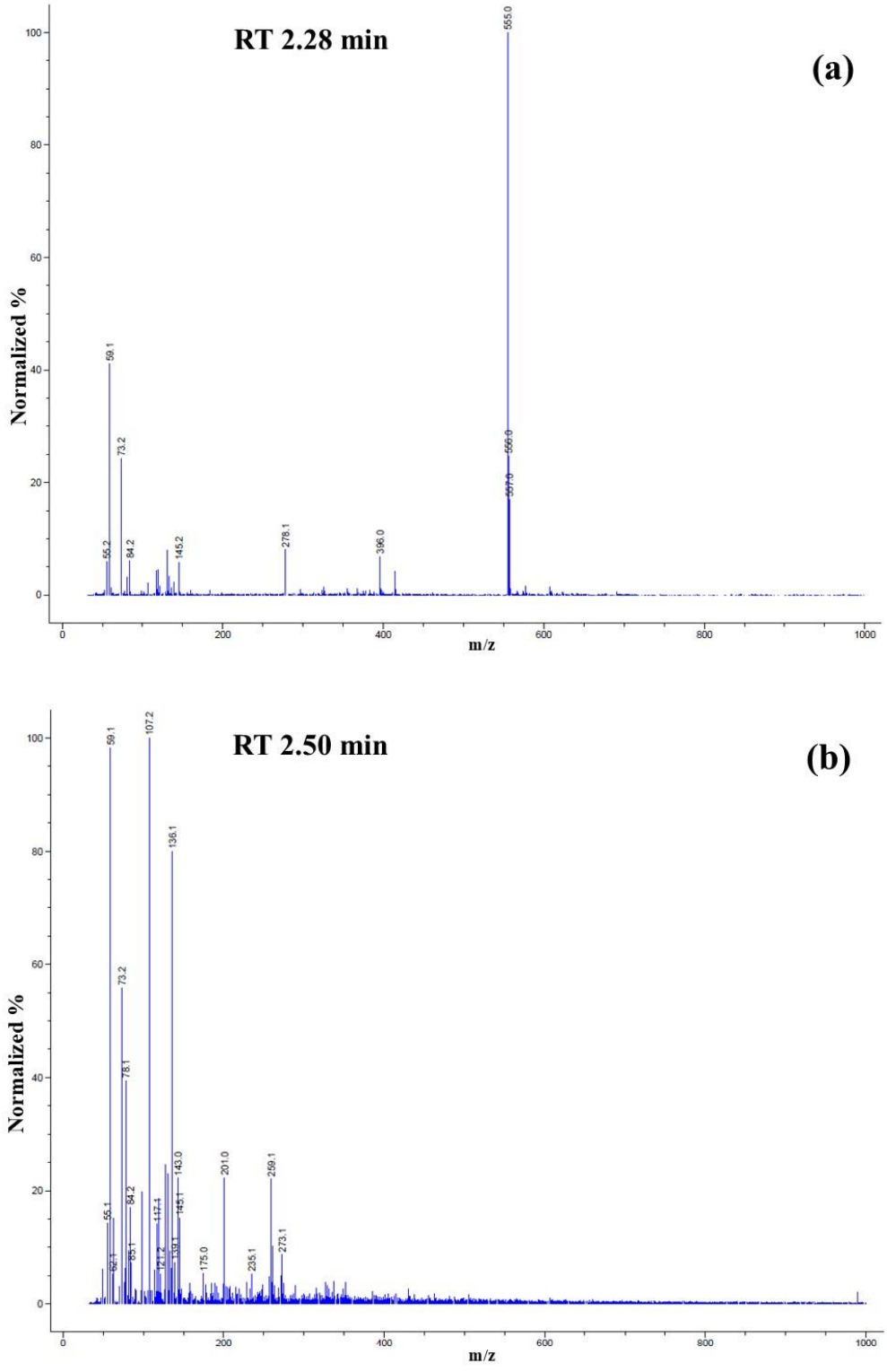

Fig 3.11. LC-MS results of CEF solution before (**a**) and after UV degradation (**b**).

3.7. Identification of the degradation products of CEF powder using TGA-MS

Based on the LC-MS results, TGA equipped with a mass spectrometry, was used to identify the possible gaseous products released from the degradation of CEF powder under argon. It has to be mentioned that using this technique was only to give an idea about the possible degradation products due to the unavailability of *in situ* FTIR analysis. Thus, it does not necessarily mean that all these gases are released at room temperature, which is different from the thermal degradation using TGA. The TGA curve (**Fig 3.12.a**) showed a continuous mass loss with five main stages approximately at 85 °C, 152 °C, 263 °C, 373 °C, and 717 °C as shown in the derivative weight profile corresponding to a total weight loss of 92%. By looking at the masses of the released gases, H_2 was detected at around 625 °C (**Fig 3.12.b**). This could be related to the cracking and dehydrogenation of the heterocyclic rings of CEF that need a high temperature.

Two peaks with a m/z of 16 were observed in **Fig 3.12.c**. The first peak nearly at 250 °C was sharp, whereas the second one was broad and centered around 600 °C, possibly indicating the release of CH_4. The first sharp peak was also observed in the spectra of 30, 34, 44, and 45 m/z (**Fig 3.12.f, g, i, and j**), which could be attributed to the β-lactam ring opening as it is the least stable ring, and the release of different gases such as NO, H_2S, CO_2 and $(CH_3)_2NH$ at the same time. The second peak could be related to the decomposition of one of the heterocyclic rings. The release of H_2O was confirmed by detecting two main peaks around 100 °C and 250 °C corresponding to a weight loss of 5% and another 5%, respectively (**Fig 3.12.e**). This result is in agreement with Qi *et al.* [238] who reported a weight loss of 9.2% due to the release of H_2O. The possibility of ammonia release from CEF degradation cannot be confirmed as the signal profiles of 17 and 18 m/z are similar as shown in **Fig 3.12.d-e**.

By comparing the signal profiles of 30 and 34 m/z (**Fig 3.12.f and g**) to that of the oxygen (32 m/z) (**Fig 3.12.k**), it was clear that the three profiles were different, indicating the possible release of NO and/or H_2S, respectively. The detection of three peaks in the mass spectrum ion curve at 30 m/z, compared to a single peak at 34 m/z, may be attributed to the higher number of nitrogen atoms relative to sulfur atoms in the CEF structure. Similarly, the mass spectra of 43 and 45 m/z (**Fig 3.12.h and j**) compared to that of CO_2 (44 m/z) (**Fig 3.12.i**), were different and the spectra indicated that isocyanic acid (HNCO) (43 m/z) and dimethyl amine ($(CH_3)_2NH$) (45 m/z) along with carbon dioxide could be released from the degradation of

CEF. The release of HNCO could be related to the use of isocyanate functional group (R-NCO) in the synthesis of β-lactam antibiotics [239]. In the same context, due to the sulfur atoms present in the CEF structure, a broad signal possibly corresponding to SO_2 (64 m/z), centered at approximately 425 °C, was also observed (**Fig. 3.12.l**).

Although the analysis was carried out under argon, very small amounts of oxygen were still detected at the beginning of the analysis (**Fig 3.12.k**) that could be getting into the system upon transferring the sample into the analysis chamber. The detection of CO_2 and H_2O is in agreement with Mamdouh *et al.* [240] who investigated the thermal degradation of CEF and its metal complexes. Most of the publications related to water treatment and the degradation of antibiotics including CEF such as [241-243] claim that the main degradation products are safe, typically CO_2 and H_2O, while neglecting potentially toxic gases such as NO and SO_2, which could very easily result in the formation of nitrites and sulfates in water, particularly when the complete mineralization is achieved in their studies. Therefore, selecting a water treatment technique must be considered very carefully as the degradation of antibiotics might result in products that are more toxic than the parent pollutant itself. Unfortunately, quantification of the released gases, which is essential to accurately assess the extent of their toxicity, is unavailable with the current TGA-mass spectrometry instrument. Thus, this aspect should be considered in future studies. It should be noted that combining the mass spectra into fewer graphs is not feasible, as this would reduce the clarity of the figures and make them difficult to distinguish.

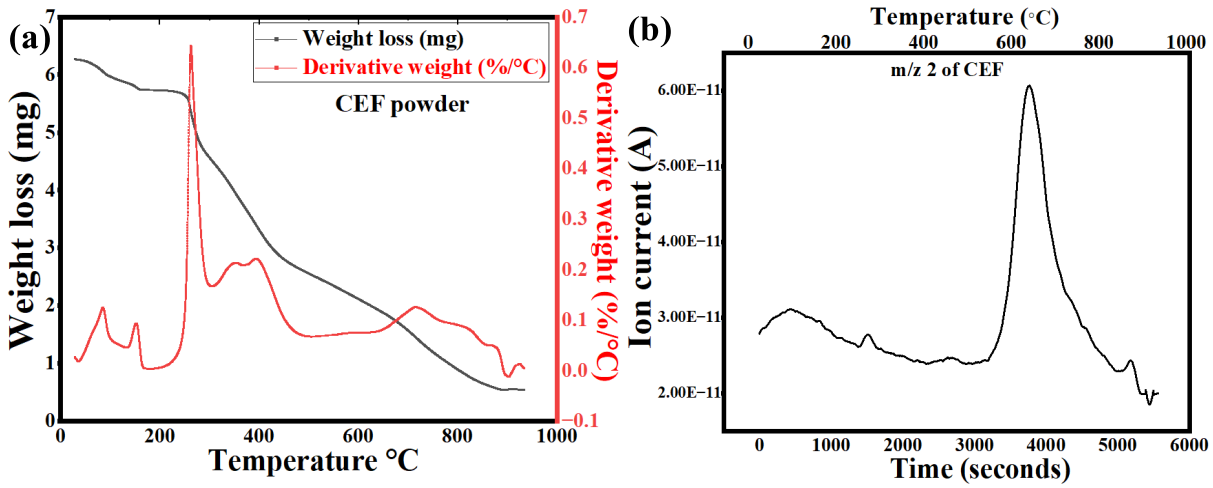

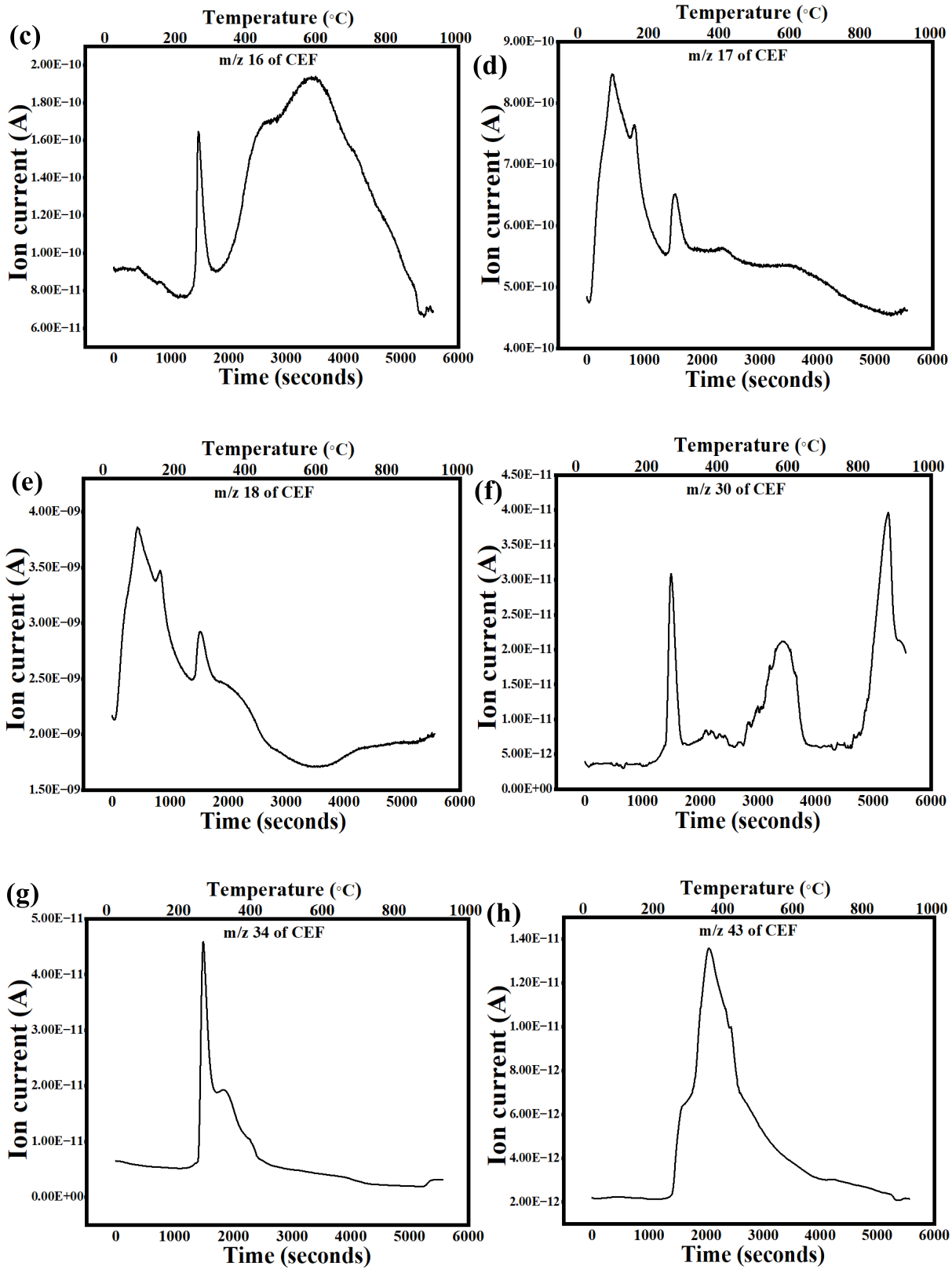
(c)
m/z 16 of CEF
Temperature (°C)
0 200 400 600 800 1000
Ion current (A)
2.00E−10
1.80E−10
1.60E−10
1.40E−10
1.20E−10
1.00E−10
8.00E−11
6.00E−11
0 1000 2000 3000 4000 5000 6000
Time (seconds)
(d)
m/z 17 of CEF
Temperature (°C)
0 200 400 600 800 1000
Ion current (A)
9.00E−10
8.00E−10
7.00E−10
6.00E−10
5.00E−10
4.00E−10
0 1000 2000 3000 4000 5000 6000
Time (seconds)
(e)
m/z 18 of CEF
Temperature (°C)
0 200 400 600 800 1000
Ion current (A)
4.00E−09
3.50E−09
3.00E−09
2.50E−09
2.00E−09
1.50E−09
0 1000 2000 3000 4000 5000 6000
Time (seconds)
(f)
m/z 30 of CEF
Temperature (°C)
0 200 400 600 800 1000
Ion current (A)
4.50E−11
4.00E−11
3.50E−11
3.00E−11
2.50E−11
2.00E−11
1.50E−11
1.00E−11
5.00E−12
0.00E+00
0 1000 2000 3000 4000 5000 6000
Time (seconds)
(g)
m/z 34 of CEF
Temperature (°C)
0 200 400 600 800 1000
Ion current (A)
5.00E−11
4.00E−11
3.00E−11
2.00E−11
1.00E−11
0.00E+00
0 1000 2000 3000 4000 5000 6000
Time (seconds)
(h)
m/z 43 of CEF
Temperature (°C)
0 200 400 600 800 1000
Ion current (A)
1.40E−11
1.20E−11
1.00E−11
8.00E−12
6.00E−12
4.00E−12
2.00E−12
0 1000 2000 3000 4000 5000 6000
Time (seconds)

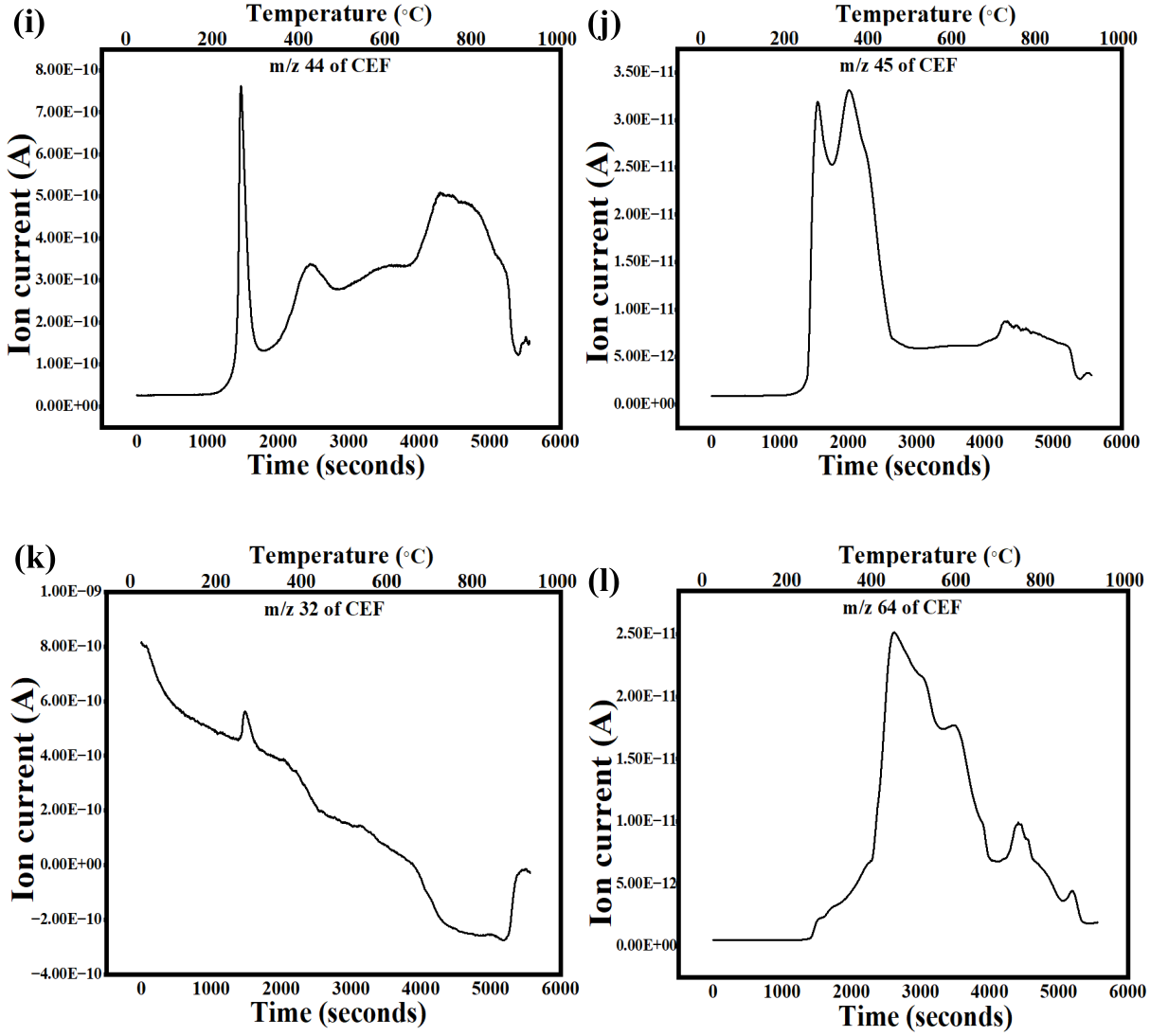

Fig 3.12. TGA and derivative weight profile of CEF powder (**a**) and the mass spectrum ion curve for 2 m/z (**b**), 16 (**c**), 17 (**d**), 18 (**e**), 30 (**f**), 34 (**g**), 43 (**h**), 44 (**i**), 45 (**j**), 32 (**k**), and 64 (**l**).

3.8. Identification of CEF and DOXY degradation products in water using the turbidimetric and the Griess reagent methods.

The degradation of CEF with a concentration of 25 ppm under UV light, which had an efficiency of 79% resulted in the release of 10.38 ppm of sulfate measured in the form of barium sulfate. Upon increasing the concentration of CEF to 200 and 500 ppm, the degradation efficiency was 64% and 49%, respectively, and the released sulfate was 31.63 and 44.44 ppm in the same respective manner. The images corresponding to the sulfate concentrations are displayed in **Fig 3.13.a-c**. Although all these sulfate concentrations are within the EPA of sulfate in drinking water (250 ppm) [244], they might cause adverse effects

on the aquatic organisms if the UV-treated water is released directly into water bodies. The control experiment, which was undertaken using DW (**Fig 3.13.d**), and the aqueous CEF solutions after using 5% Fe 5% Cu-TiO_2 as an adsorbent at different pH levels (**Fig 3.13.e**) did not show any sulfate formation. These results indicate the essential role of CEF degradation in releasing undesired products. Additionally, they confirmed that the removal of CEF using 5% Fe 5% Cu-TiO_2, which is discussed in **Section 3.16**, was only through adsorption not degradation.

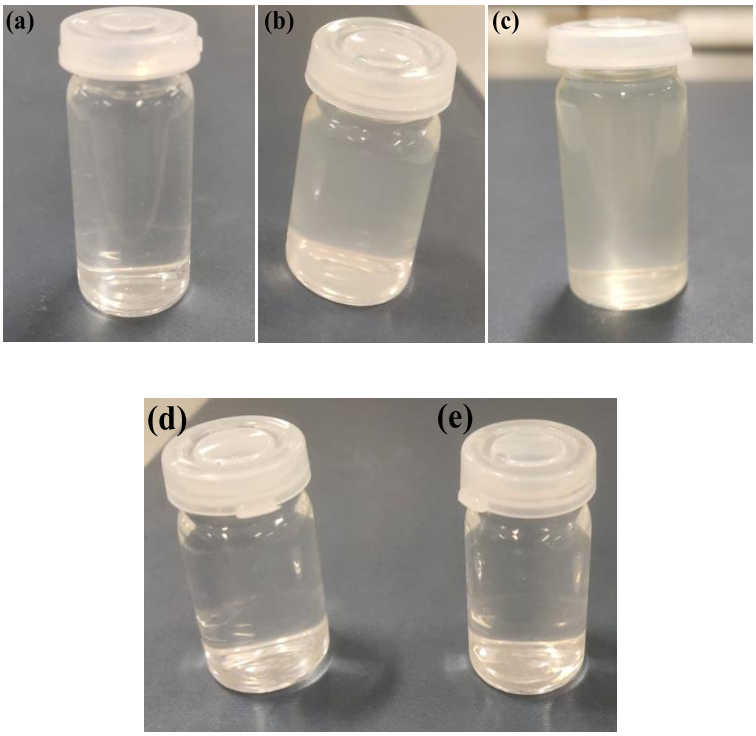

Fig 3.13. The images of the released sulfate in the form of a turbid solution of barium sulfate after the photodegradation of 25 **(a)**, 200 **(b)**, and 500 ppm **(c)** CEF under UV light, and the control experiments of DW **(d)**, and 5% Fe 5% Cu-TiO_2 **(e)**.

The photodegradation of 25 ppm (79%) and 200 ppm (64%) of CEF under UV light resulted in the release of 0.20 and 0.75 ppm of nitrite in water (**Fig 3.14.a**). The change in colour of CEF solution (25 ppm) before and after the degradation is shown in **Fig 3.14.d**. Unexpectedly, the photodegradation of 500 ppm of CEF did not result in any nitrite release. 0.27, 0.61, and 0.64 ppm of nitrite were detected in the aqueous samples of DOXY, after the degradation of 25 ppm (75%), 100 ppm, (41%), and 500 ppm (34%) (**Fig 3.14.b**), respectively. DOXY is the second antibiotic investigated in the current study and is discussed in detail in Chapter 4. However, the results of its degradation products are presented alongside the CEF results for

comparative purposes. The images of these DOXY solutions before and after the degradation are presented in **Fig 3.14.c**. The concentrations of the released nitrite from both antibiotics were within the permissible limit of the WHO [210], which is 1 ppm in drinking water. However, this does not mean that it is safe to release nitrite from the degradation of antibiotics as that could be considered an unnecessary risk by adding more nitrite to the already existing concentrations in water (bioaccumulation). Therefore, any further release of undesired pollutants such as sulfates and nitrites should be avoided.

Similar to the abovementioned results of the absence of any sulfate in DW and after CEF adsorption using 5% Fe 5% Cu-TiO_2, no nitrite was detected in DW and after the adsorption of either CEF or DOXY using 5% Fe 5% Cu-TiO_2 (**Fig 3.14.a**) and reduced BIOX 1 (**Fig 3.14.b**), respectively. Reduced BIOX 1 is the primary adsorbent used for DOXY removal in Chapter 5, but it is included in this section for the same comparative purposes mentioned above. Additionally, it is worth mentioning that no nitrate detection was observed after the photodegradation of either antibiotic.

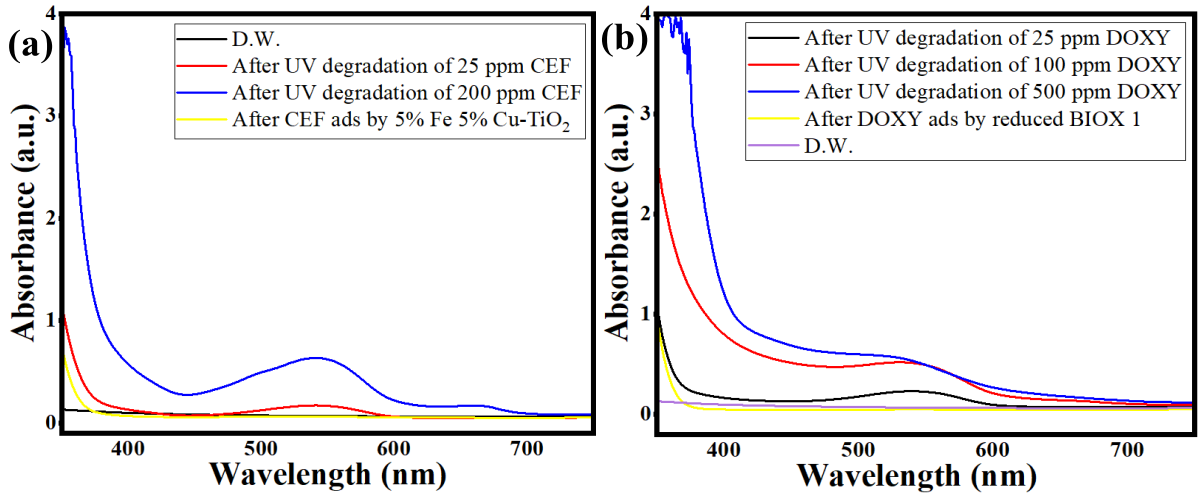

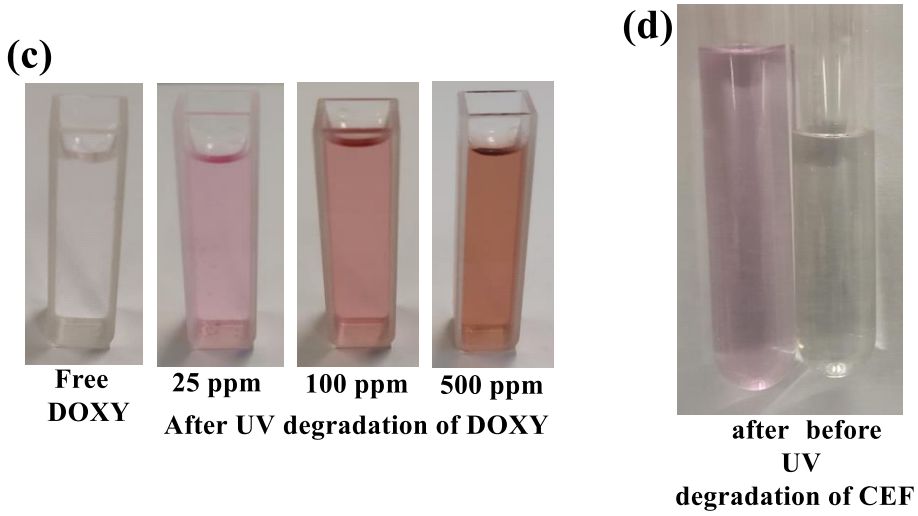

Fig 3.14. The UV-Vis spectra of the nitrite released after the photodegradation of 25 and 200 ppm CEF along with the control experiments of DW and 5% Fe 5% Cu-TiO_2 **(a)**, 25, 100, and 500 ppm DOXY along with the control experiments of DW and reduced BIOX 1 **(b)**, the images of different concentrations of DOXY solutions **(c)**, and 25 ppm CEF before and after the photodegradation **(d)**.

3.9. Removal of CEF by α-Fe_2O_3, TiO_2, and TiO_2 composites

3.9.1. Self-degradation and Speciation of CEF over different pH levels

A set of control experiments was conducted over a wide pH range (2 to 11) to investigate the stability of CEF. These experiments provide insight into the potential self-degradation of CEF and the degradation products that may be released solely by altering the solution pH, as well as the influence of pH on CEF speciation and surface charge. The second UV peak of CEF usually shows up at 260-265 nm in the pH range of 2 to 4, but the wavelength increases to 270-275 nm at higher pH levels. CEF deprotonation increases electron delocalization at high pHs, which lowers the energy gap for electronic transitions and shifts the absorbance to longer wavelengths (Bathochromic shift). Additionally, if the wavelength shift was accompanied by a change in absorbance, this means that molar extinction coefficient has also changed, since absorbance is directly proportional to the extinction coefficient when concentration and path length are constant, according to the Beer-Lambert law ($A = \varepsilon bc$, where A is the absorbance (unitless), ε is the molar extinction coefficient ($L.mol^{-1}.cm^{-1}$), b is the path length (cm), and c is the concentration ($mol.L^{-1}$)). However, this did not affect the removal efficiency

calculations as they were done based on the maximum absorbance of the peak at each pH level on its own before and after the treatment.

As shown in **Fig. 3.16.g-j**, CEF remained stable after 30 minutes of stirring at pH 5 and above. No degradation was observed across this range, even after 210 minutes of continuous stirring and after leaving the solutions unstirred for more than two months. Also, no degradation was observed at pH 3 using the CEF vial that was used for investigating almost all the materials reported in this chapter except for two α-Fe_2O_3 samples (Chinese RM-derived and lab-prepared α-Fe_2O_3) and the samples reported in Chapter 5. However, upon testing another vial, self-degradation (hydrolysis) was observed under dark conditions at pH 2, 3, and 4, likely due to β-lactam ring opening resulting from the compound's instability in strongly acidic environments [245].

To further check this issue, two more vials were tested and one of them showed self-degradation over the same pH range and the other one did not. This inconsistency did not affect the results reported in this chapter as they were obtained using the same vial that did not show self-degradation with the only exception of the two above-mentioned α-Fe_2O_3 samples, whereas the results of Chapter 5 were obtained using another vial that showed self-degradation consistently. This variation in CEF stability could be attributed to differences in sealing, packaging, storage, and shipping conditions as previously reported by Qi *et al.* [238] that the stability of commercial CEF products varies with storage temperature and sealing conditions. So, as a sort of quality control, the spectra of the CEF batches were checked with the FTIR spectrometer. However, the spectrum of the batch that showed self-degradation in acidic conditions at pH 2, 3, and 4 (**Fig. 3.15.a**) was similar to the one that did not show any self-degradation (**Fig. 3.15.b**). Therefore, the FTIR analysis was not so helpful in differentiating between the two batches, as the peaks of the functional groups such as C=O were almost the same. However, this point is suggested to be further investigated in future work using other techniques to look at salts, water content, and excipients, which could be one of the reasons behind the variation in stability of CEF.

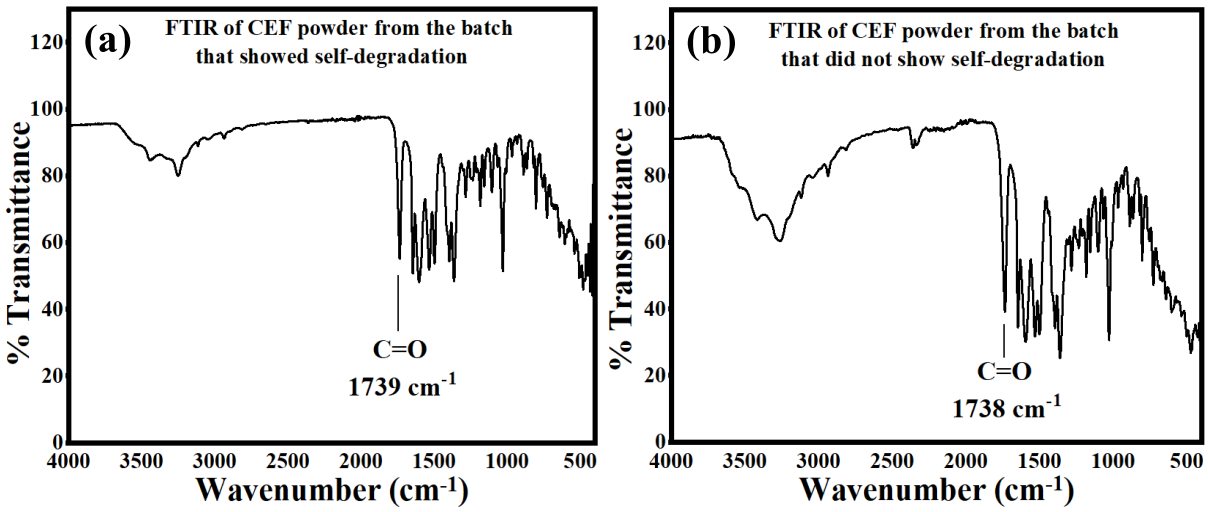

Fig 3.15. FTIR spectra of CEF powder from the batch that showed self-degradation in acidic conditions at pH 2, 3, and 4 (**a**), and the powder from the batch that did not show self-degradation (**b**).

The extent of self-degradation was 3% after 30 minutes, increasing slightly to 5% after 60 minutes at pH 2. The solution remained relatively stable with continued stirring up to 210 minutes. However, degradation continued during storage without stirring, reaching 18% after 50 days and it remained unchanged after that (**Fig. 3.16.a**).

Similar trends were observed at pH 3 and pH 4, where self-degradation reached 7% and 3%, respectively, after 60 minutes of stirring. These values increased to 27% and 15%, respectively, after 50 days of storage (**Fig. 3.16.c** and **e**). In this context, Shrestha *et al.* [246] reported a self-degradation efficiency of 7% for CEF after 30 minutes under acidic conditions using 0.1 M HCl, without specifying the exact pH or providing data on degradation efficiency over longer periods. The experiments were also conducted under continuous stirring to determine whether the degradation values could be achieved quicker. At pH 2, degradation reached 13% after one day of stirring and increased to 18% after three days (**Fig. 3.16.b**). However, on the fourth day, the UV-Vis peak absorbance increased due to evaporation. At pH 3, the highest degradation observed was 18% after one day, which remained unchanged up to three days, before the peak increased on the fourth day (**Fig. 3.16.d**). At pH 4, 12% degradation was observed after one day, but the peak gradually increased on subsequent days (**Fig. 3.16.f**).

LC-MS was also used to indicate the self-degradation of CEF and identify the possible degradation products. The chromatographic parts of CEF solution pre and post the self-degradation at pH 2 showed the same intensity at the retention time of 2.5 minutes (**Fig. 3.17.a-b**) when the molecular ion peak of CEF (m/z of 555) was observed at that pH. This decrease was more pronounced at pH 3 (**Fig. 3.17.c-d**) and pH 4 (**Fig. 3.17.e-f**) at the retention times of 3 minutes. However, these chromatographic results did not align with the actual degradation percentages measured by UV-Vis spectroscopy. Therefore, LC-MS was not used for any quantification in this study.

As for the peaks detected post-degradation, most were already present in the spectra of the undegraded solutions such as those of pH 3 (**Fig. 3.18.a-b**), but they became more prominent following self-degradation due to the reduced intensity of the CEF molecular ion. This finding is consistent with previous observations during CEF photolysis under UV light, further supporting the release of gaseous products during the degradation process, which get converted to sulfates and nitrites.

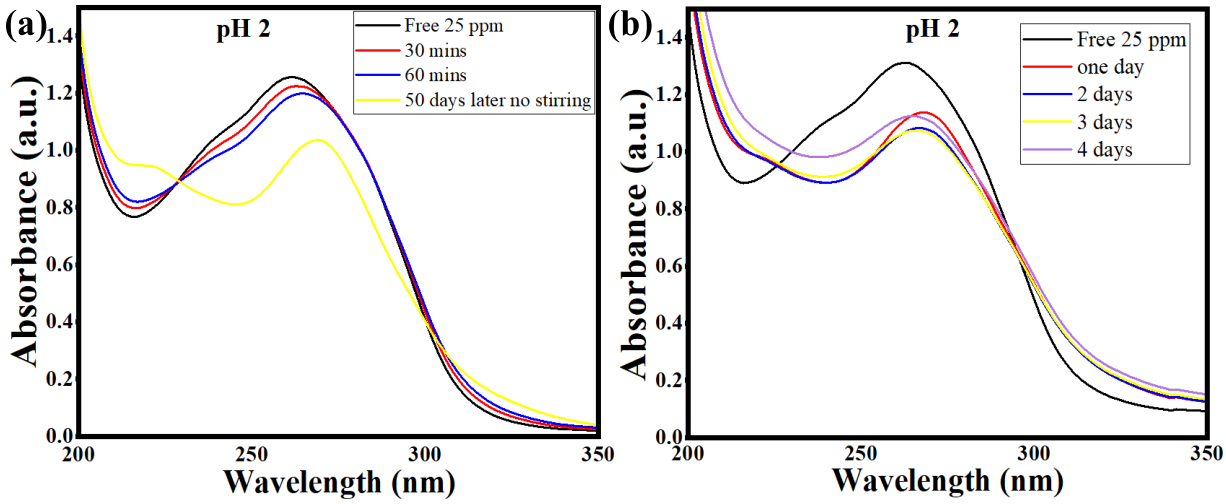

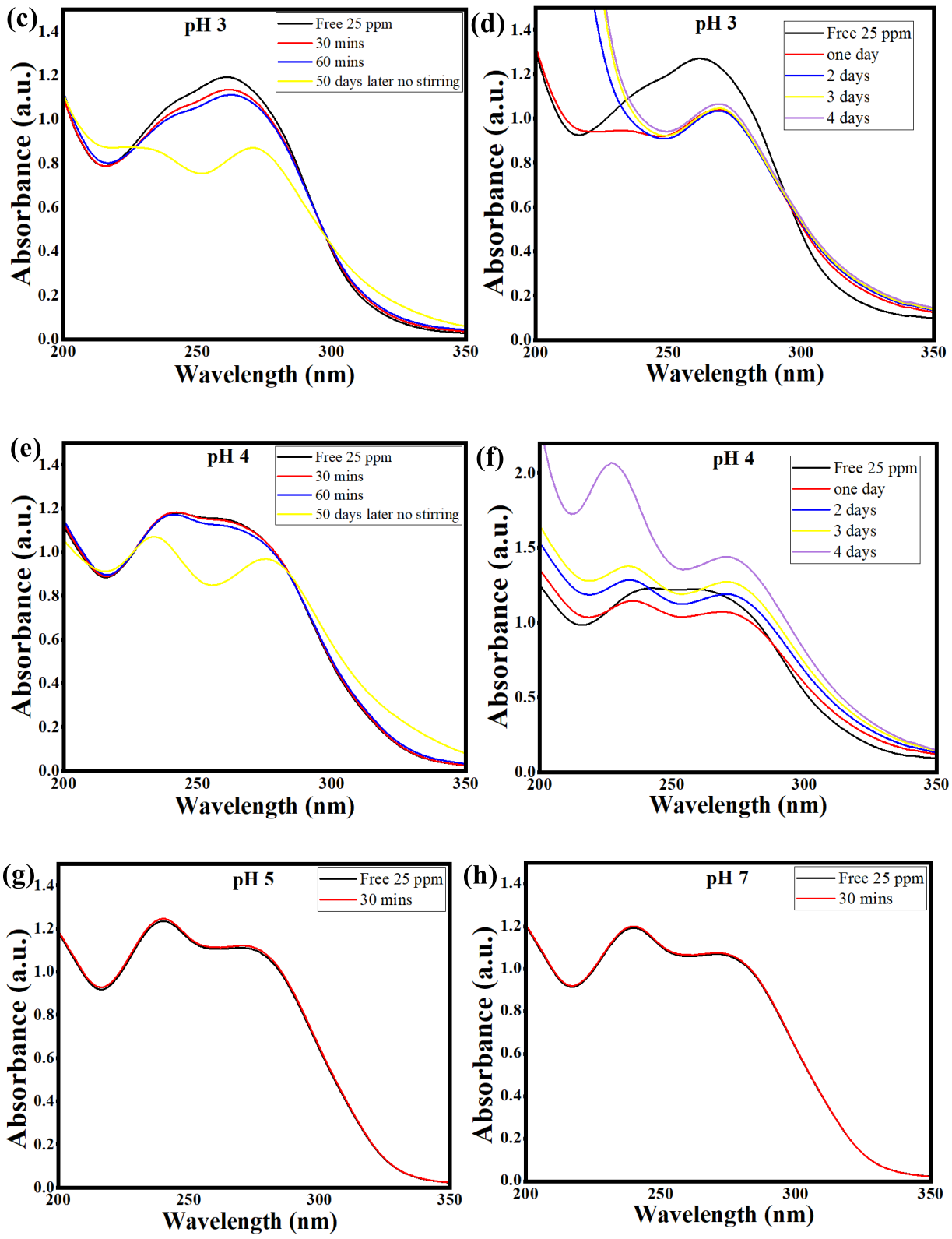
(c)
pH 3
Free 25 ppm
30 mins
60 mins
50 days later no stirring
Absorbance (a.u.)
Wavelength (nm)
(d)
pH 3
Free 25 ppm
one day
2 days
3 days
4 days
Absorbance (a.u.)
Wavelength (nm)
(e)
pH 4
Free 25 ppm
30 mins
60 mins
50 days later no stirring
Absorbance (a.u.)
Wavelength (nm)
(f)
pH 4
Free 25 ppm
one day
2 days
3 days
4 days
Absorbance (a.u.)
Wavelength (nm)
(g)
pH 5
Free 25 ppm
30 mins
Absorbance (a.u.)
Wavelength (nm)
(h)
pH 7
Free 25 ppm
30 mins
Absorbance (a.u.)
Wavelength (nm)

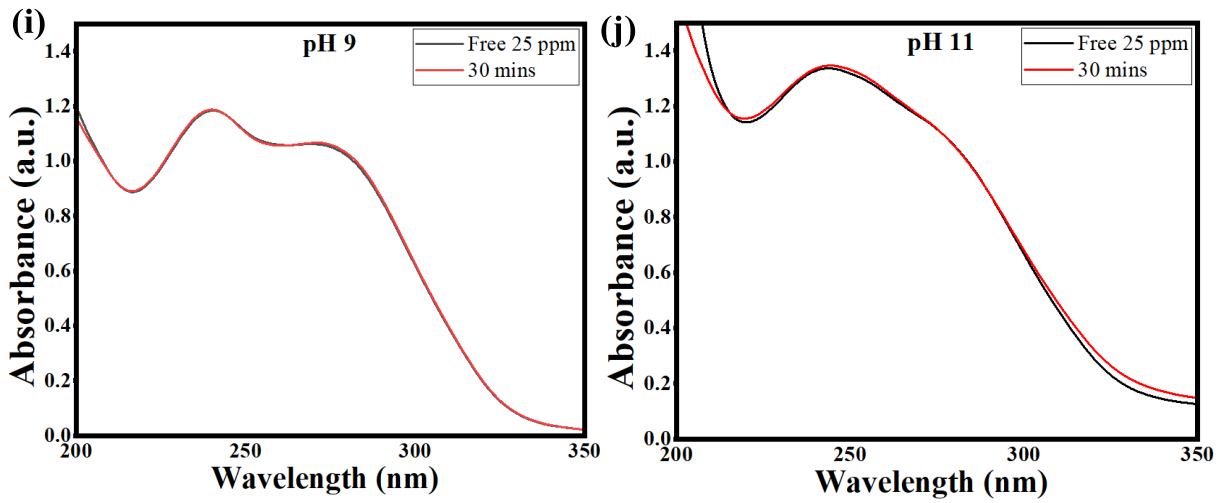

Fig 3.16. The UV-Vis spectra of control experiments of CEF solutions at pH 2 **(a-b)**, pH 3 **(c-d)**, pH 4 **(e-f)**, pH 5 **(g)**, pH 7 **(h)**, pH 9 **(i)**, and pH 11 **(j)**. [C_o = 25 ppm, stirring rate = 800 rpm, T = 20 ± 2 °C, and volume = 20 mL].

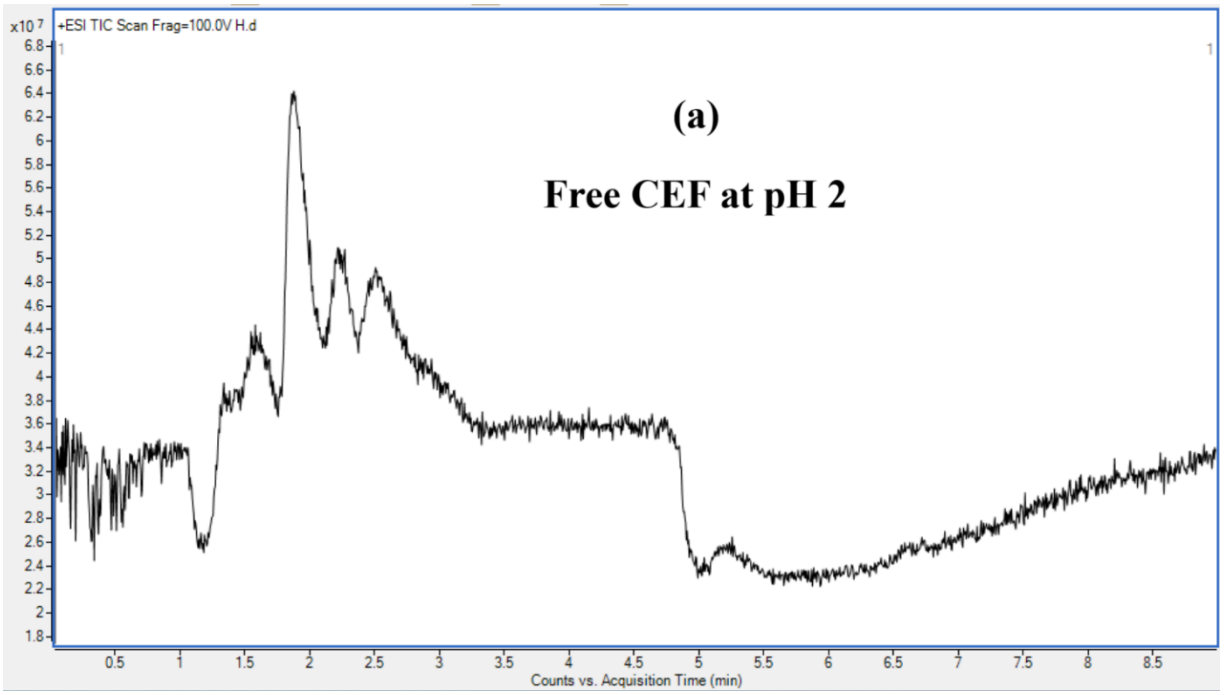

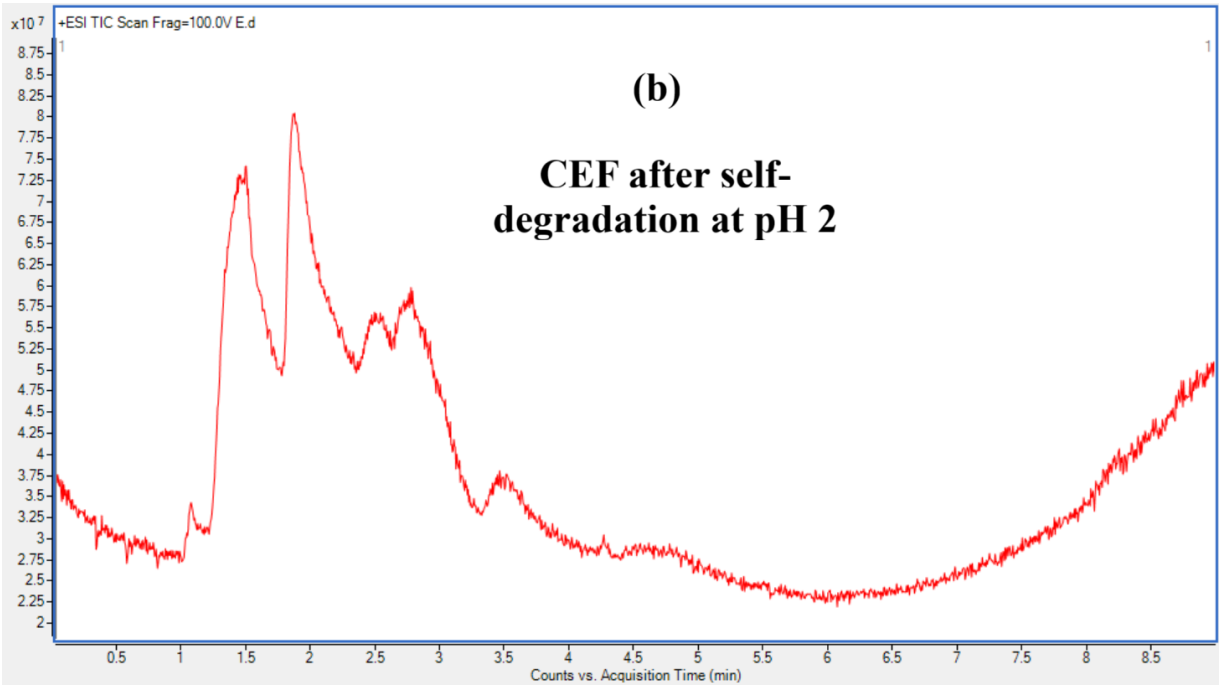
x10 7
+ESI TIC Scan Frag=100.0V E.d
(b)
CEF after self-degradation at pH 2
Counts vs. Acquisition Time (min)

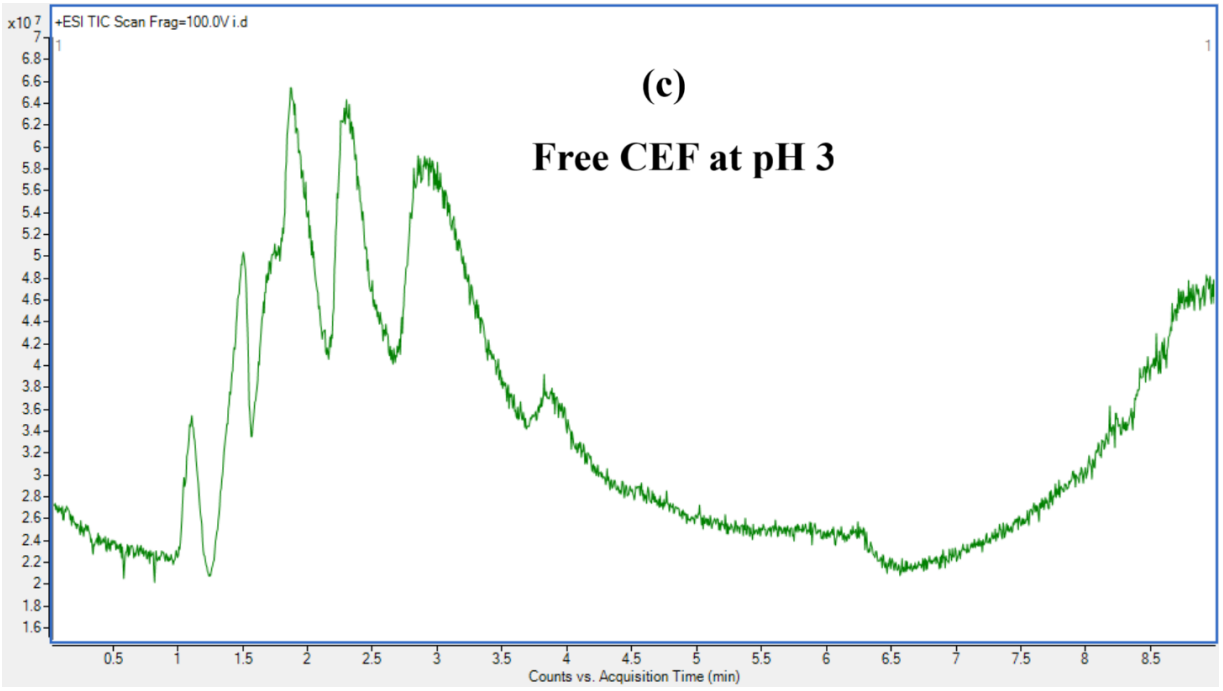
x10 7
+ESI TIC Scan Frag=100.0V i.d
(c)
Free CEF at pH 3
Counts vs. Acquisition Time (min)

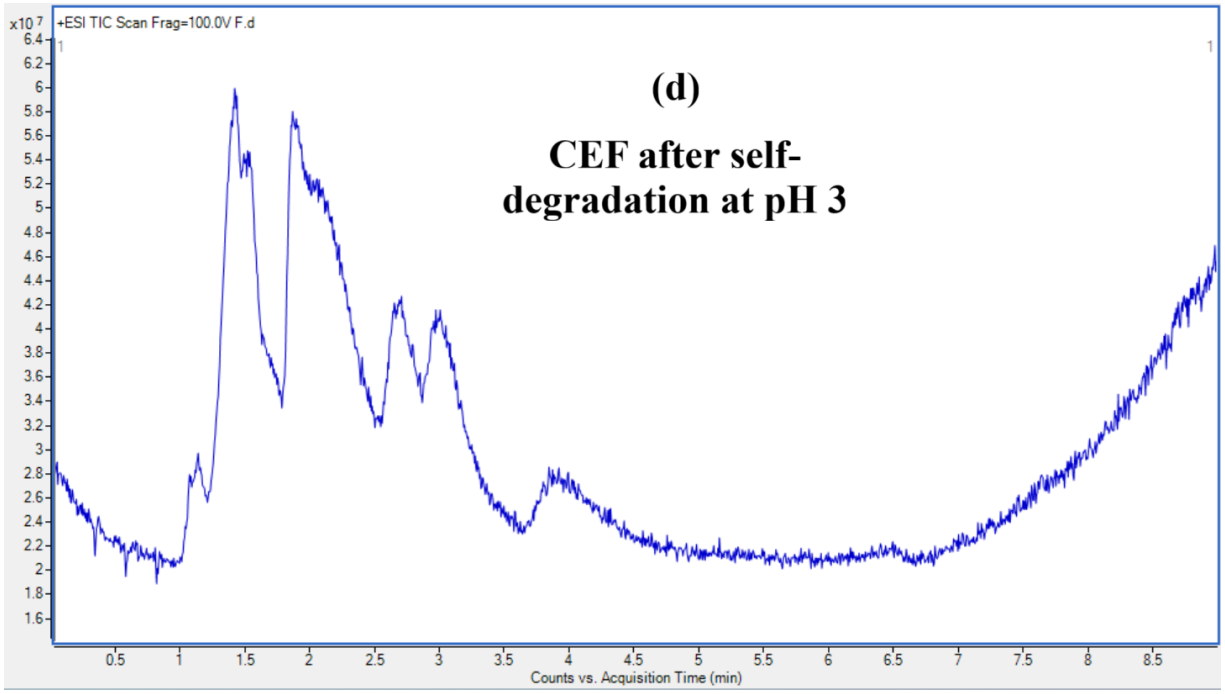
x10 7
+ESI TIC Scan Frag=100.0V F.d
(d)
CEF after self-degradation at pH 3
Counts vs. Acquisition Time (min)

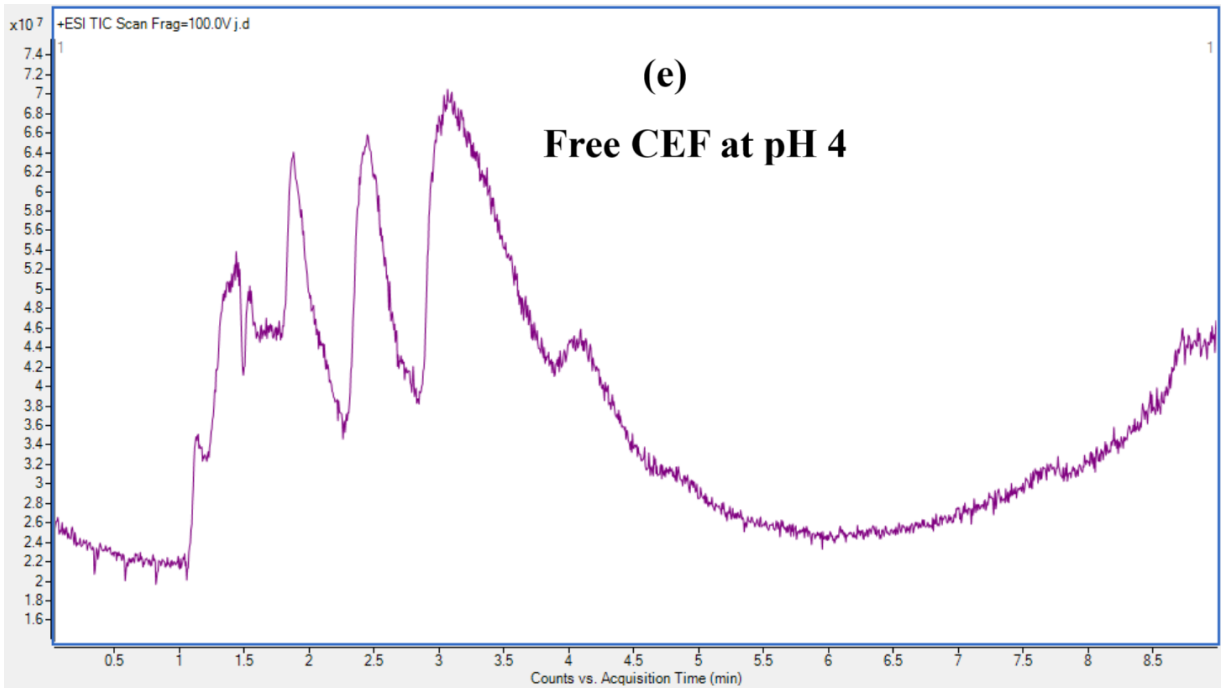
x10 7
+ESI TIC Scan Frag=100.0V j.d
(e)
Free CEF at pH 4
Counts vs. Acquisition Time (min)

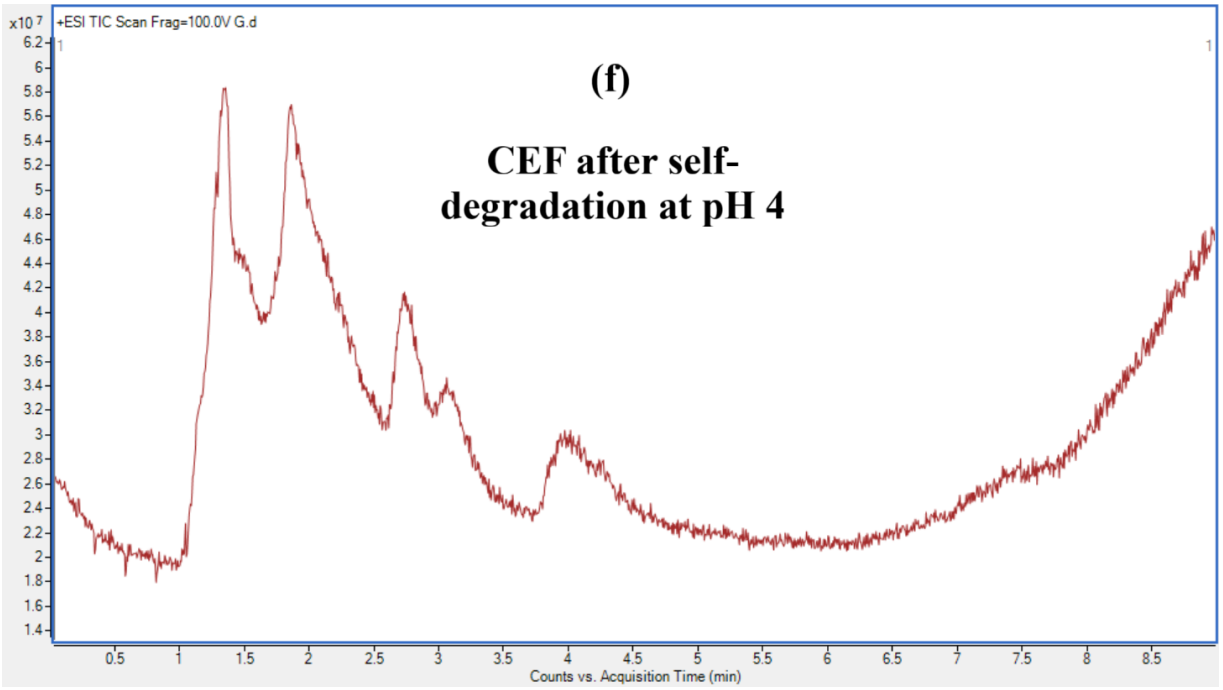

Fig 3.17. Chromatographic parts of LC-MS results of CEF solutions before and after the self-degradation at pH 2 (**a-b**), pH 3 (**c-d**), and pH 4 (**e-f**) to investigate the self-degradation of CEF.

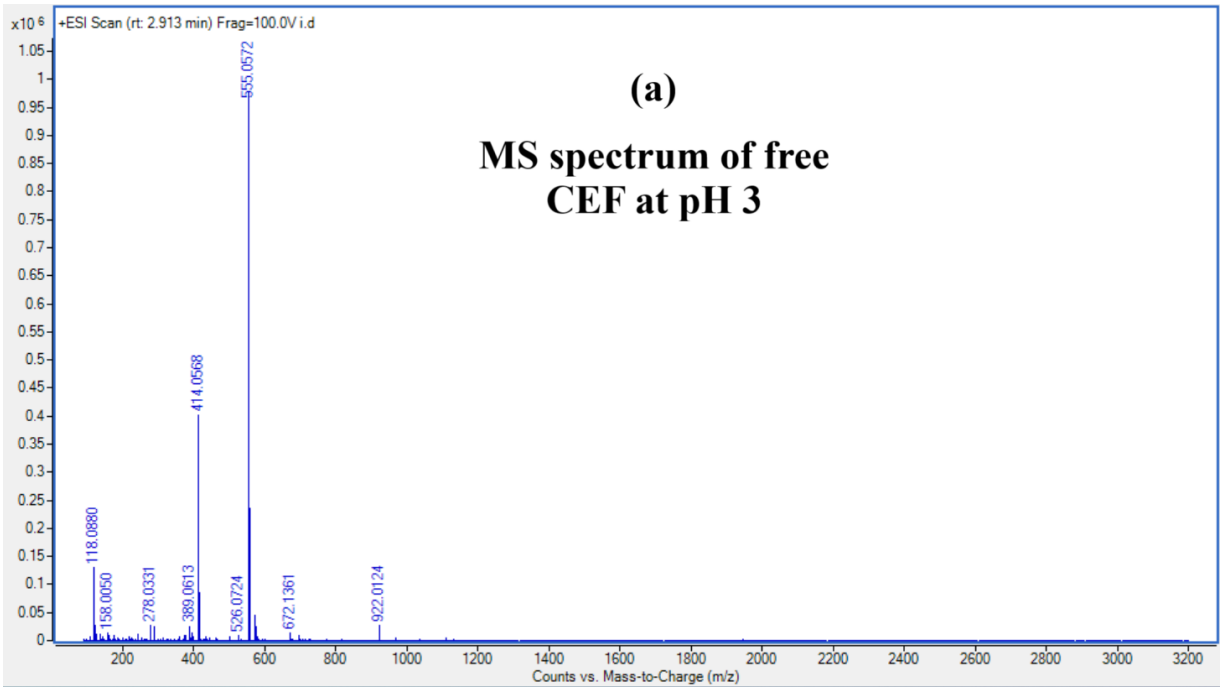

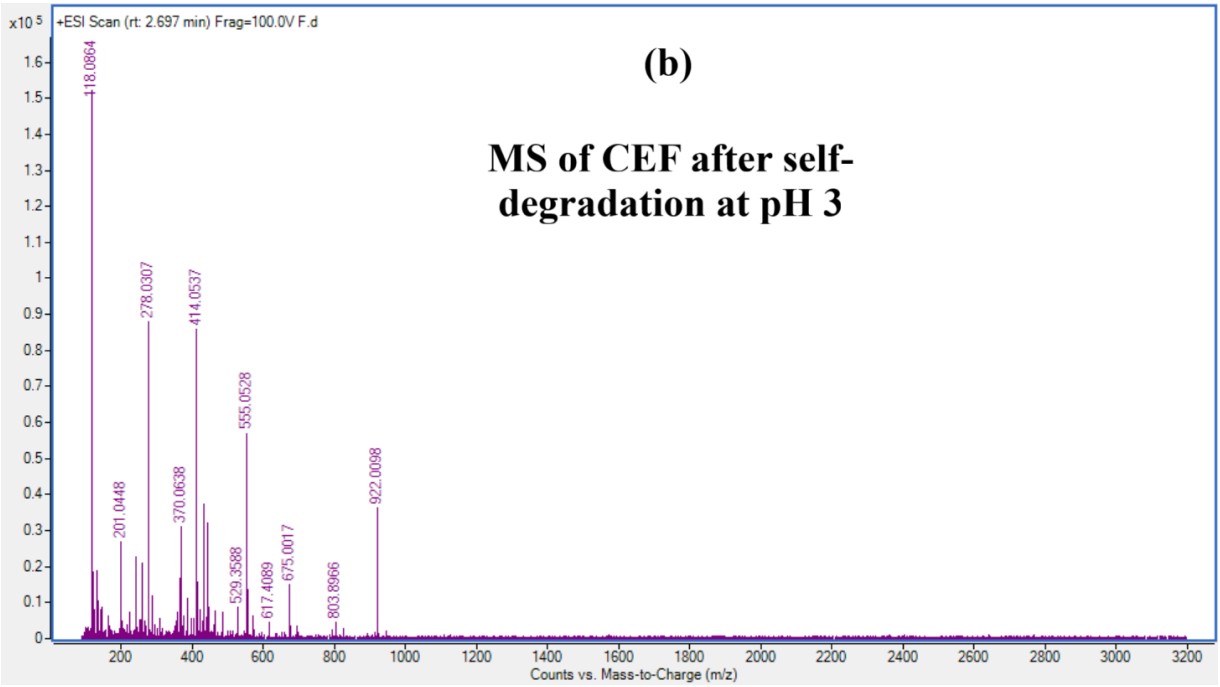

Fig 3.18. LC-MS results of CEF solution before and after self-degradation at pH 3 (**a-b**) indicating that the release of gaseous products occurs during the degradation process, which get converted to undesired products such as sulfates and nitrites.

According to Aleksić *et al.* [247] CEF has four acid dissociation constant (p*Ka*) values including pKa_1 2.37 of the carboxylic group, which is a low value for a carboxylic species, pKa_2 3.03 of the aminothiazole species, and pKa_3 4.21 of the hydroxytriazinone species, along with pKa_4 10.74 of the amide functional group (**Fig 3.19**). Therefore, CEF molecules are in a cationic form at very low pH levels. By increasing the pH these molecules will be in a Zwitterionic form, and by further increasing the pH they will be in an anionic form, which is in accord with Zaki and Hafez [248] who reported the negative charge of CEF molecules at pH 6.

When 5% Fe 5% Cu-TiO_2 was tested at pH 1 and pH 2 to clarify the speciation of CEF at different pH levels, the adsorption efficiency was found to be 5% and 30%, respectively. This result indicated the electrostatic repulsion between the adsorbent and the positively charged CEF at pH < 2.37 because the nitrogen atom (**Fig 3.20.a**), which is attached to the methyl group, in hydroxytriazinone and the amine group in the aminothiazole ring are protonated. Other N atoms in hydroxytriazinone are less susceptible to protonation because of the resonance caused by the alternating single and double bonds. Similarly, the nitrogen atom of

the amide group is less susceptible to protonation due to its resonance with the ketone group. To further support this assumption, zeta potential measurements indicated that the surface charge was 4.6 mV at pH 2 (**Fig 3.21.a**). Zeta potential measurements determine the electrical potential at the slipping plane of particles dispersed in a liquid, which provide an insight into the surface charge and stability of the colloidal system.

By increasing the pH beyond 2.37, the OH of the carboxylic group (pKa = 2.37) is suggested to deprotonate and become negatively charged (**Fig 3.20.b**). Thus, overall net positive charge decreases, and therefore zeta potential decreases to 2.5 mV at pH 3 (**Fig 3.21.b**). By increasing the pH beyond the pKa of the aminothiazole group, which is 3, the above-mentioned amine group loses a proton and becomes neutral. So, the overall surface charge decreases and becomes zero, which is known as Zwitterionic form (**Fig 3.20.c**). A Zwitterionic form (or Zwitterion) is a molecular structure in which the same molecule carries both a positive charge and a negative charge simultaneously, but the overall net charge is zero, which is also known as the isoelectric point. This was confirmed by recording a zeta potential of -0.3 mV which is almost zero at pH 3.5 (**Fig 3.21.c**) and the very slight increase of the negative charge to -1.4 mV at pH 4 (**Fig 3.21.d**). Therefore, the lowest electrostatic repulsion is suggested to be the main factor behind observing the highest adsorption efficiency in the Zwitterionic range between pH 3 and pH 4. This is why efficiency increased to 58% and 63% at pH 3 (**Fig 3.26.g**) and pH 4, respectively.

By further increasing the pH beyond 4.21 (pKa of hydroxytriazinone), the protonated nitrogen atom gets deprotonated and becomes neutral (**Fig 3.20.d**). Subsequently, the negative surface charge starts to dominate as indicated by the zeta potential of -16.3 mV at pH 5 (**Fig 3.21.e**), which then keeps increasing to -17.2 mV and -19.5 mV at pH 7 and pH 9, respectively (**Fig 3.21.f** and **Fig 3.21.g**). This results in electrostatic repulsion between CEF and 5% Fe 5% Cu-TiO_2 (PZC = 5.8) at higher pH levels leading to a reduction in adsorption efficiency. Lastly, by increasing the pH beyond 10.74 (pKa of the amide group), NH of the amide group might lose a proton, becomes negatively charged (**Fig 3.20.e**), and the negative surface charge increases to -22.2 mV (**Fig 3.21.h**) accompanied by a further reduction in adsorption efficiency. However, this represents only a proposed mechanism of CEF speciation based on the obtained adsorption and zeta potential results, and it may or may not fully reflect what actually occurs during the adsorption process. The structure and functional groups of CEF are shown in **Fig 3.19**.

Fig 3.21 shows the distribution of zeta potential values and their corresponding relative frequencies. A single sharp peak indicates a homogeneous surface charge, whereas a broad peak reflects variations in surface charge.

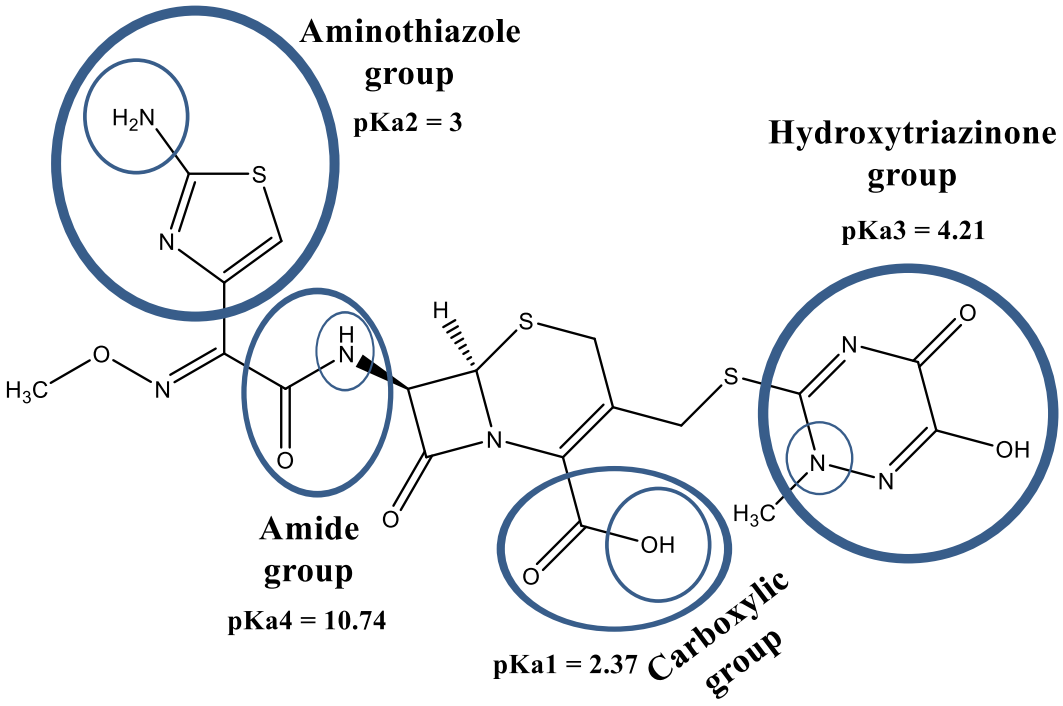

Fig 3.19. The structure of CEF ($C_{18}H_{18}N_8O_7S_3$) highlighting the major functional groups (large circles) and the specific atoms within those groups that undergo protonation or deprotonation as a function of pH (small circles) [202].

(a)

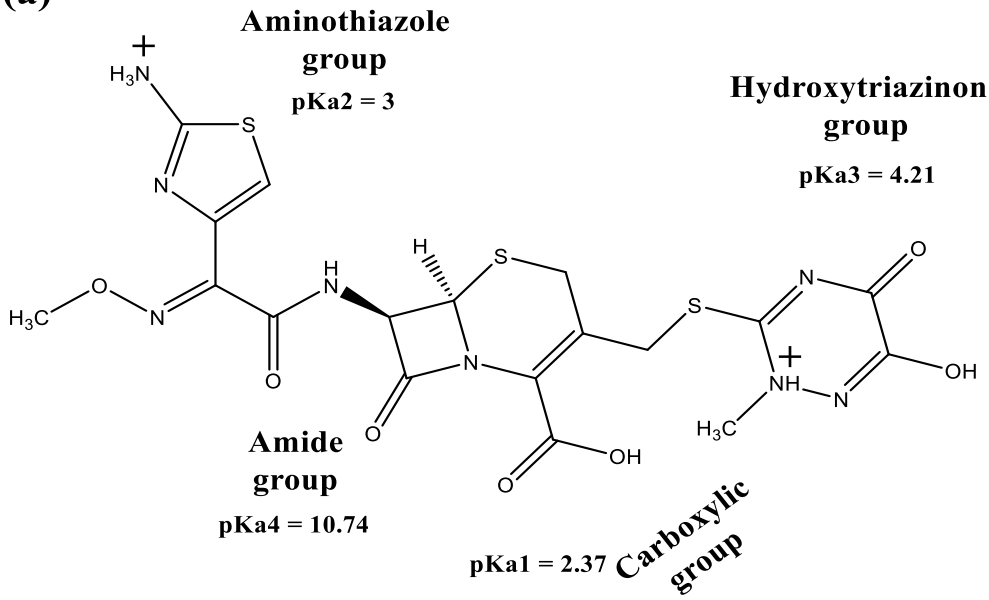

CEF species at pH 2 and the overall charge is positive (Cationic form)

(b)

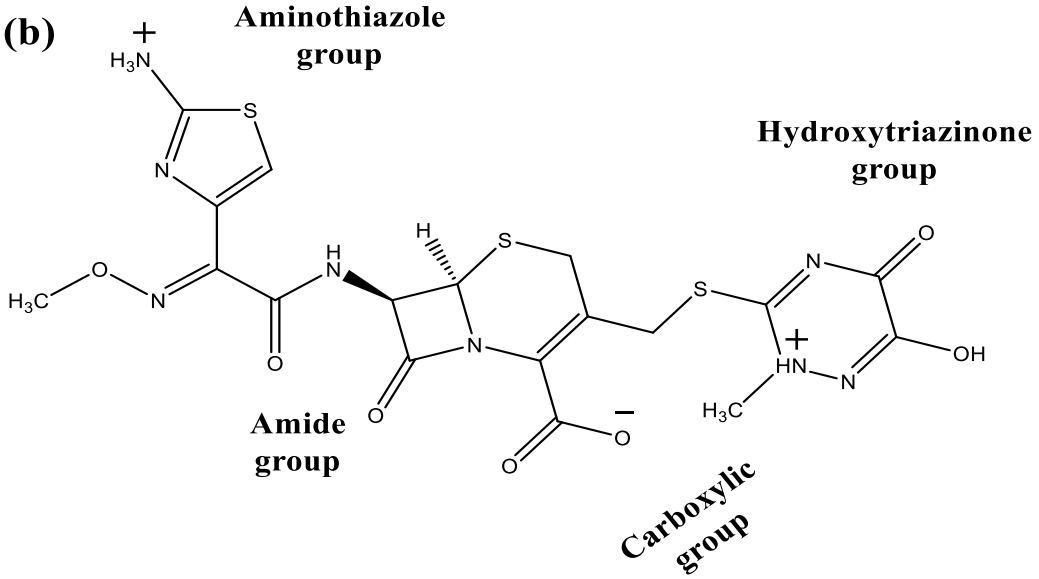

CEF species at 2.37 < pH ≤ 3 and the overall charge is less positive (Cationic form)

(c)

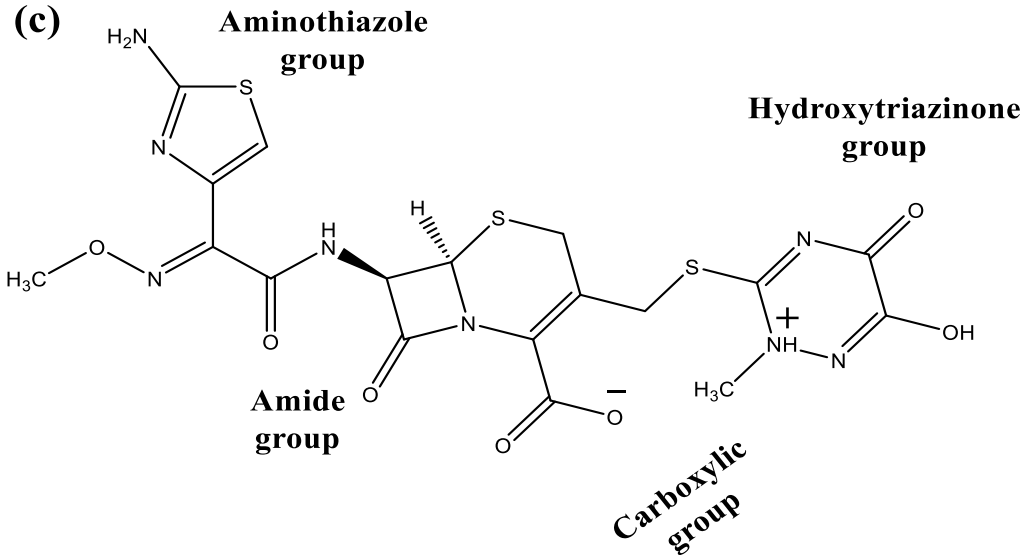

CEF species at 3 < pH < 3.5 and the overall charge is almost zero (Zwitterionic form)

(d)

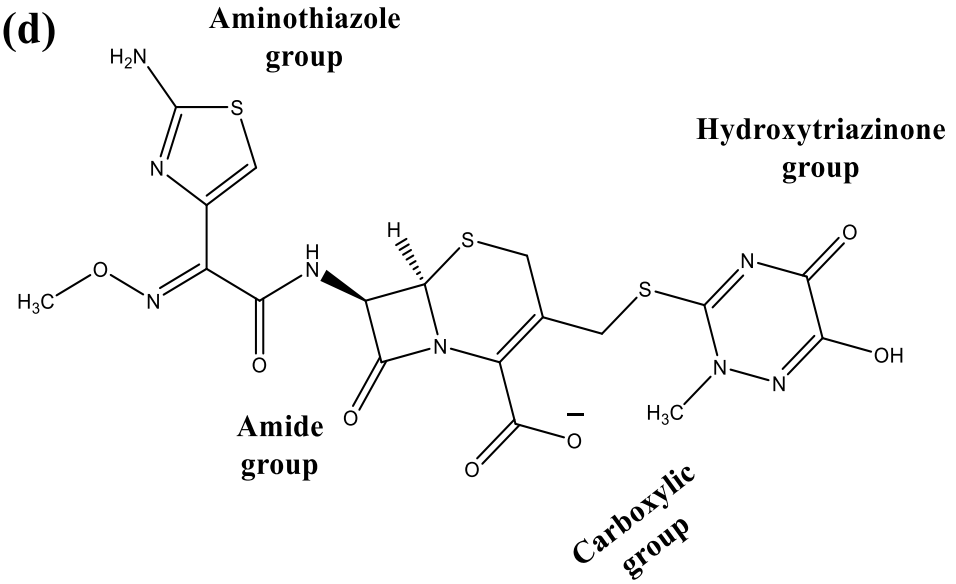

CEF species at 4.21 < pH < 10.74 and the overall charge is negative (Anionic form)

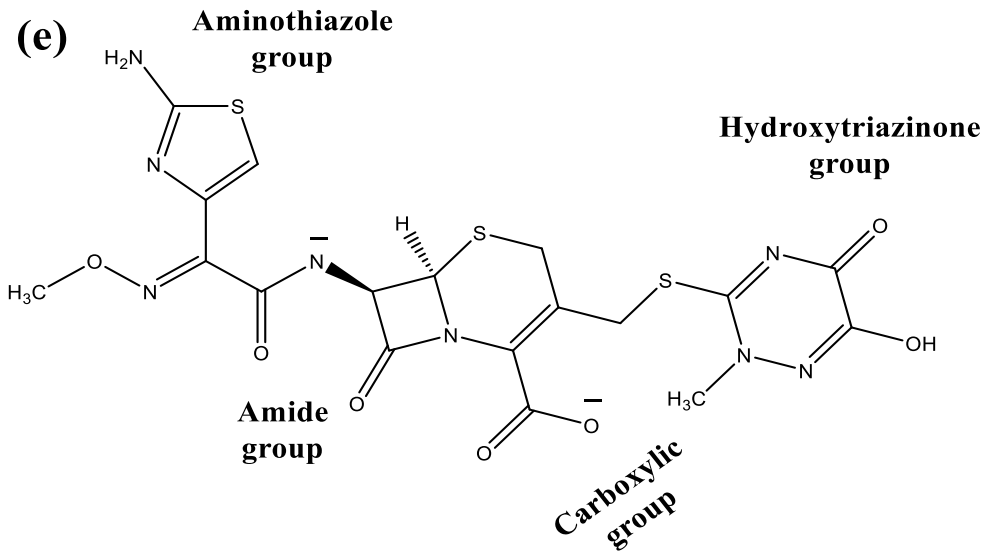

Fig 3.20. The proposed structures of CEF at pH 2 where the nitrogen atom attached to the methyl group in hydroxytriazinone and the amine group in the aminothiazole ring are protonated and the overall surface charge is positive (cationic form) (**a**), 2.37 < pH ≤ 3 where the carboxylic group is deprotonated and the overall charge is less positive (cationic form) (**b**), 3 < pH < 3.5 where the amine deprotonates and goes back to the neutral form and the overall charge becomes almost zero (Zwitterionic form) (**c**), 4.21 < pH < 10.74 where the protonated nitrogen atom gets deprotonated and becomes neutral and the charge becomes negative (anionic form) (**d**), and pH > 10.74 where the amide group might deprotonate and the overall charge becomes more negative (anionic form) (**e**). These CEF ($C_{18}H_{18}N_8O_7S_3$) forms were derived from [202].

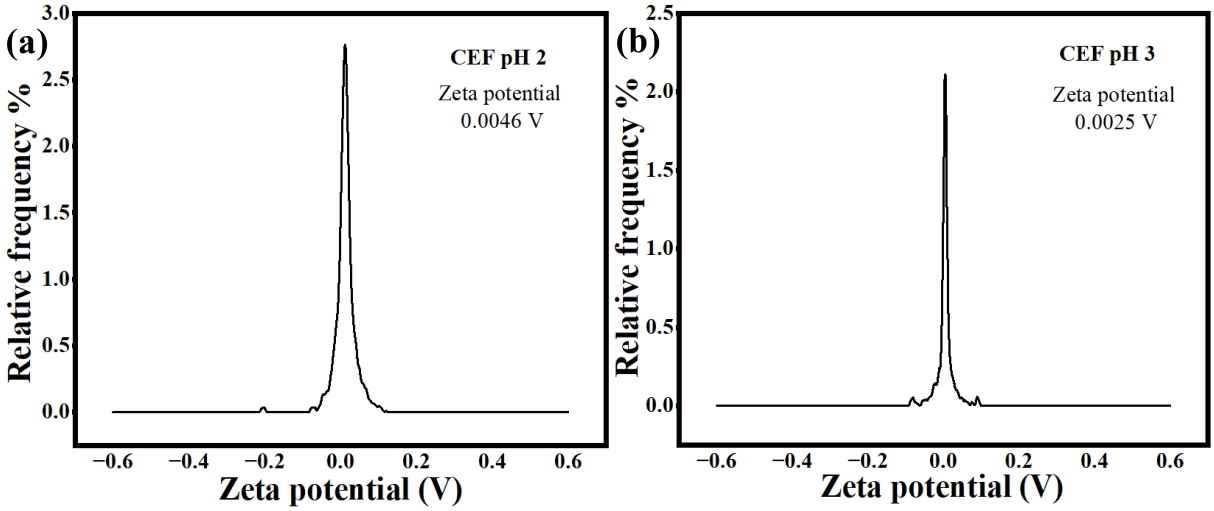

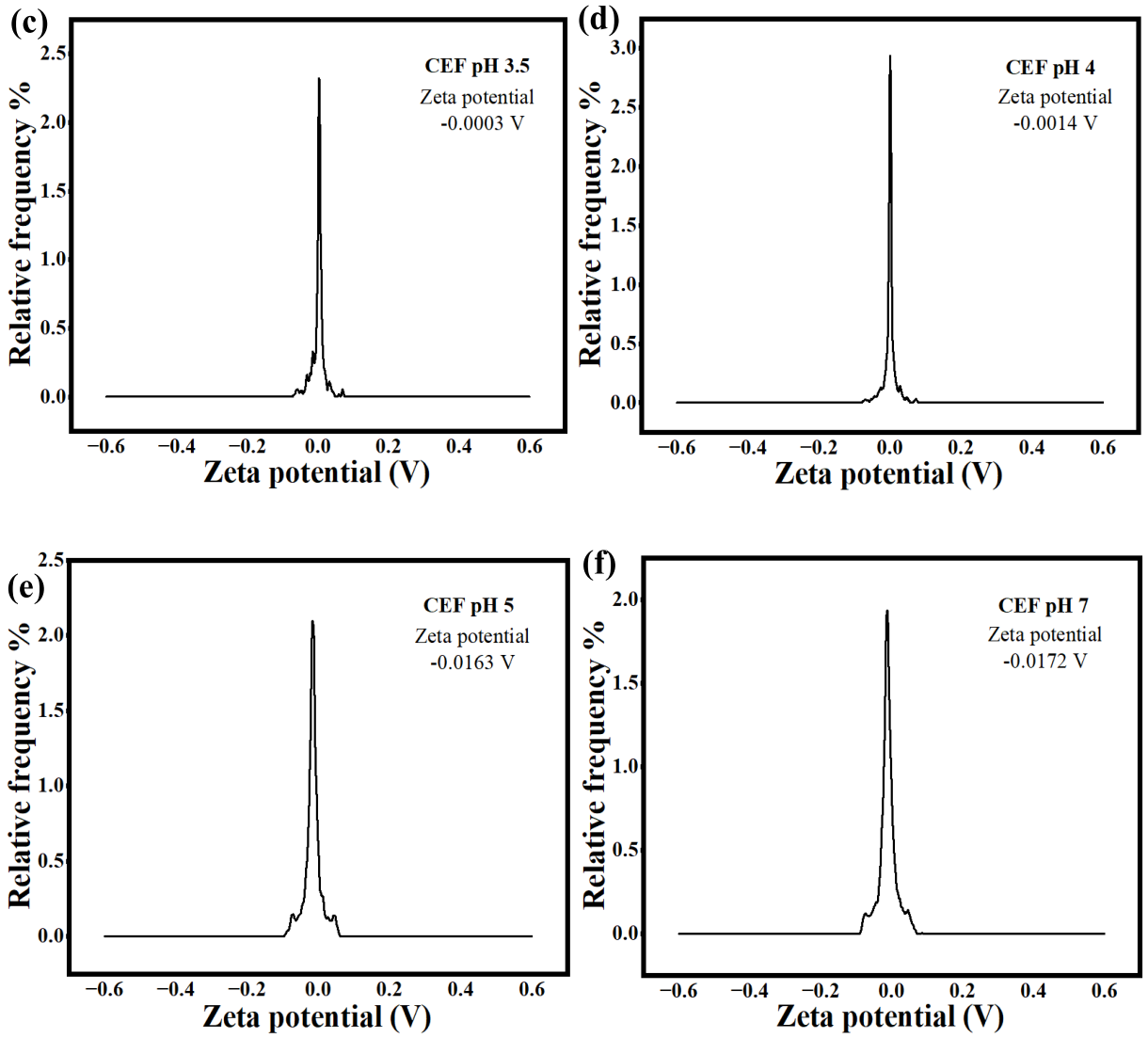
(c)
CEF pH 3.5
Zeta potential
-0.0003 V
Relative frequency %
Zeta potential (V)
(d)
CEF pH 4
Zeta potential
-0.0014 V
Relative frequency %
Zeta potential (V)
(e)
CEF pH 5
Zeta potential
-0.0163 V
Relative frequency %
Zeta potential (V)
(f)
CEF pH 7
Zeta potential
-0.0172 V
Relative frequency %
Zeta potential (V)

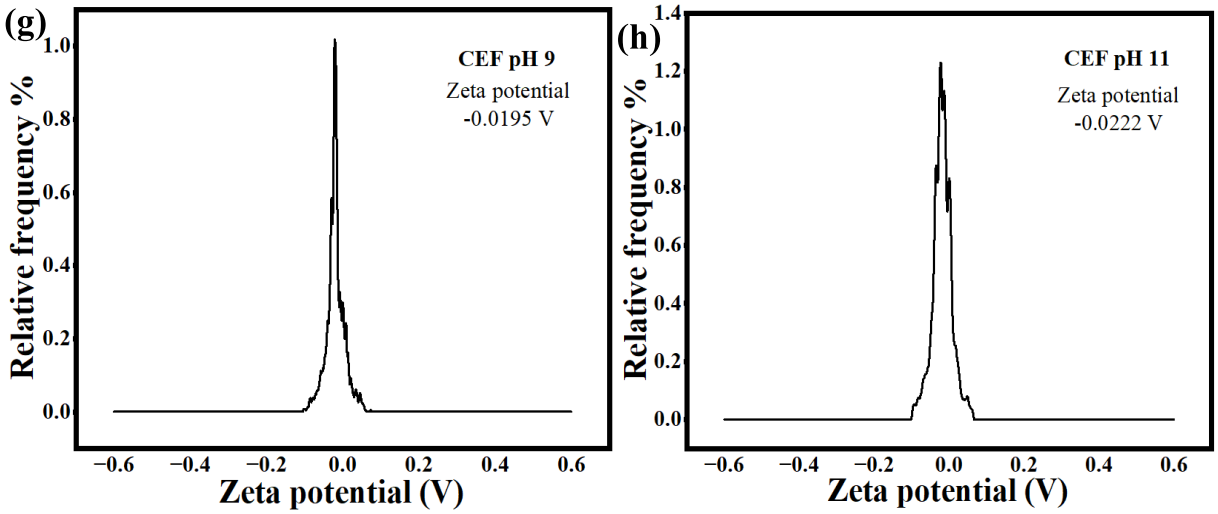

Fig 3.21. Zeta potential measurements of aqueous CEF solutions at pH 2 where the nitrogen atom attached to the methyl group in hydroxytriazinone and the amine group in the aminothiazole ring are protonated and the overall charge becomes 4.6 mV (**a**), pH 3 where the OH of the carboxylic group is deprotonated and the charge is 2.5 mV (**b**), pH 3.5 (**c**) and pH 4 (**d**) where the amine group deprotonates and the surface charge becomes -0.3 mV and -1.4 mV, respectively, pH 5 (**e**) where the protonated nitrogen atom gets deprotonated, and the charge becomes -16.3 mV and decreases to -17.2 mV at pH 7 (**f**) and -19.5 mV at pH 9 (**g**), and at pH 11 where the NH of the amide group can deprotonate and the charge drops to -22.2 mV (**h**).

3.9.2. A comparison between the efficiency of different α-Fe_2O_3 and TiO_2 samples in CEF adsorption.

A comparative study was conducted to determine the CEF adsorption efficiency by commercial, and green synthesized α-Fe_2O_3 and lab-prepared TiO_2. The performance of the three materials was similar as they all exhibited their adsorption capabilities over acidic conditions (**Fig 3.22.a-c**). This adsorption trend is mainly related to the PZC values of these adsorbents in the range of 4.9 - 6.5 as indicated in **Table 3.2**. The adsorbents, which are positively charged at pH levels below their PZC values, are electrostatically attracted to the Zwitterionic CEF species at pH 3 and the negatively charged species at pH 5. Consequently, the adsorption efficiency substantially declines by increasing the pH beyond their PZCs due to the electrostatic repulsion between their negative surface charge and the negatively charged CEF. Other factors contributing to the process are investigated in the adsorption mechanism in

Section 3.16. The performance of lab-prepared α-Fe_2O_3, which was prepared using iron nitrate and sodium hydroxide, is discussed below and that of P25 is discussed in **Section 3.10**.

The lab-prepared TiO_2 was slightly more efficient compared to the other ones. Such a result could be attributed to its high surface area (223 m^2/g) compared to the surface areas of commercial α-Fe_2O_3, green synthesized α-Fe_2O_3, and P25 which are 20 m^2/g, 42 m^2/g, and 56 m^2/g, respectively. Therefore, the lab-prepared TiO_2 was further investigated through impregnation with various metals. This strategy was meant to enhance the efficiency whether by increasing the PZC of TiO_2 which was 5.4 (**Table 3.1**) or by enabling complex formation of TiO_2 composites with CEF.

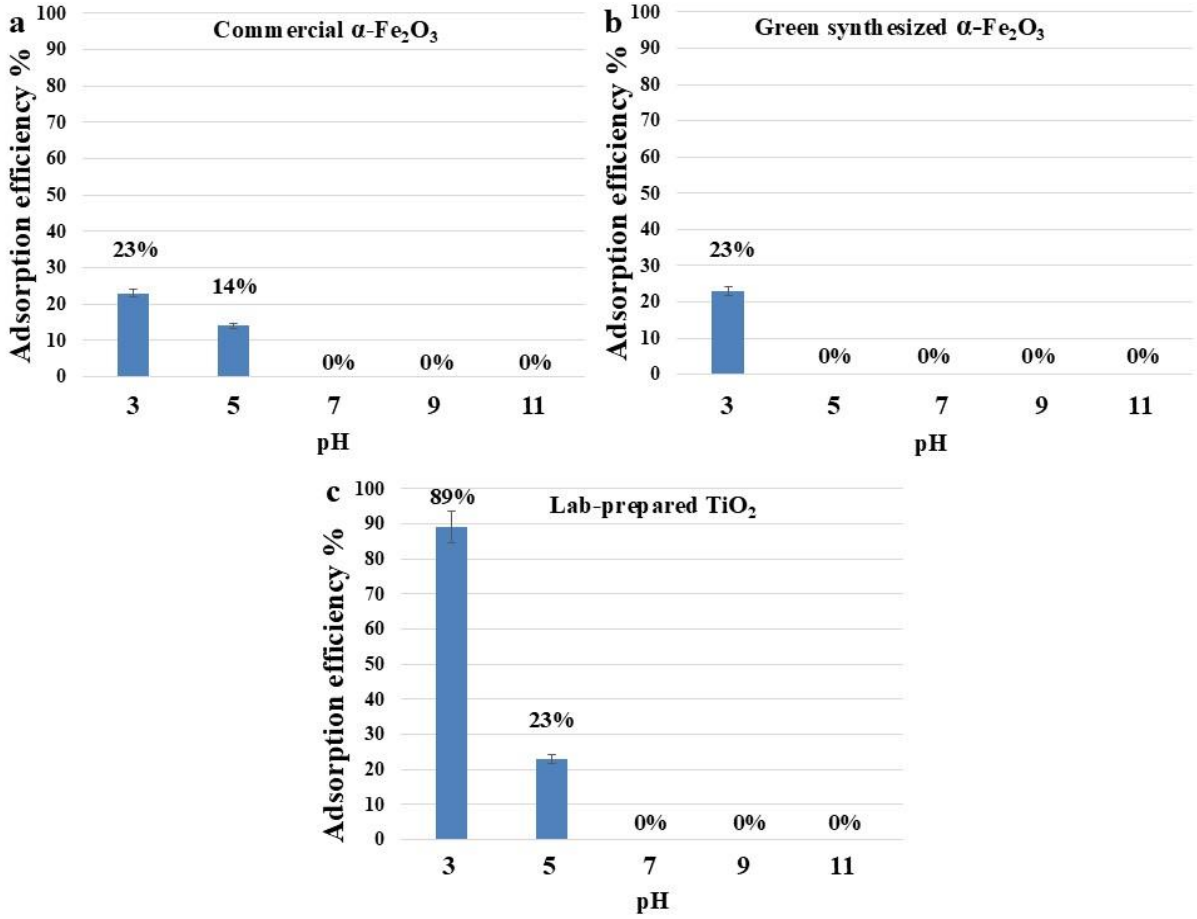

Fig 3.22. A comparison between the CEF adsorption efficiency of commercial **(a)**, and green synthesized α-Fe_2O_3 **(b)**, and lab-prepared TiO_2 **(c)**. [C_o = 25 ppm, stirring rate = 800 rpm, T = 20 ± 2 °C, volume = 20 mL, and dose = 0.01 g].

3.9.3. A comparison between the red mud-derived TiO_2 and α-Fe_2O_3 samples, and the effect of using different metals on the adsorption efficiency

The effect of five metals including Fe, Co, Ni, Cu, and Zn was investigated in enhancing the adsorption efficiency of the lab-prepared TiO_2. These metals were selected based on their availability and low cost. The effect of metal ion impregnation was evaluated at different loading percentages. The resulting composites exhibited good adsorption efficiency across the entire pH range; however, their performance declined after calcination (**Fig S6** and **S7** are provided in **Appendix 3.1**). Consequently, the same metals were further investigated with red mud-derived TiO_2, and the effect of calcination was examined using one of its composites. The focus on red mud-derived TiO_2 in the remainder of this chapter stems from the aim of utilizing the large quantities of this waste material, which otherwise poses a significant risk of water and soil pollution.

When a comparative study was conducted to determine the CEF adsorption efficiency by different samples of TiO_2, it was clear that TiO_2 extracted from Chinese RM by the acid baking method (**Fig 3.23.c**) had a relatively high efficiency over most of the pH levels. The adsorption trend of TiO_2 samples extracted by the acid baking method (**Fig 3.23.a-c**) was similar to that of the above-mentioned TiO_2 samples, as the adsorption efficiency dropped with increasing pH. This behaviour could be accredited to the higher degree of crystallinity of TiO_2 extracted by the acid baking method.

In contrast, TiO_2 samples extracted by the alkali roasting method exhibited a completely opposite trend as the adsorption efficiency was improving by increasing pH (**Fig 3.23.d-f**). Such a result could be attributed to the previously mentioned impurity of TiO_2 as indicated by the EDX spectrum along with the poorly crystalline structure shown in the powder XRD patterns accompanied by many undefined/unknown reflections. These impurities caused the absorbance to increase instead of decreasing as shown in **Fig 3.24**. In addition to these unexpected results, the PZCs of the three-alkali roasting-extracted TiO_2 samples were in the range of 2.1 to 2.6, and after 30 minutes of CEF adsorption, they started desorption.

Therefore, the Chinese RM based-TiO_2 was further investigated through impregnation with the same above-mentioned metals. By the time Chinese red mud-derived α-Fe_2O_3 and lab-prepared α-Fe_2O_3 were investigated, a new CEF vial was used and self-degradation under acidic conditions (pH 2, 3, and 4) was detected as previously mentioned in **Section 3.9.1**.

Upon testing the two samples, they exhibited low adsorption efficiency, and it was only limited to pH 3 (**Fig 3.23.g** and **h**), which could be related to self-degradation. Therefore, no further work was undertaken to investigate any of the α-Fe_2O_3 samples in removing CEF, except for two experiments under visible light to investigate their photocatalytic efficacy, and also because there were not enough Indian red mud samples either RM 7 or RM 8 to extract α-Fe_2O_3.

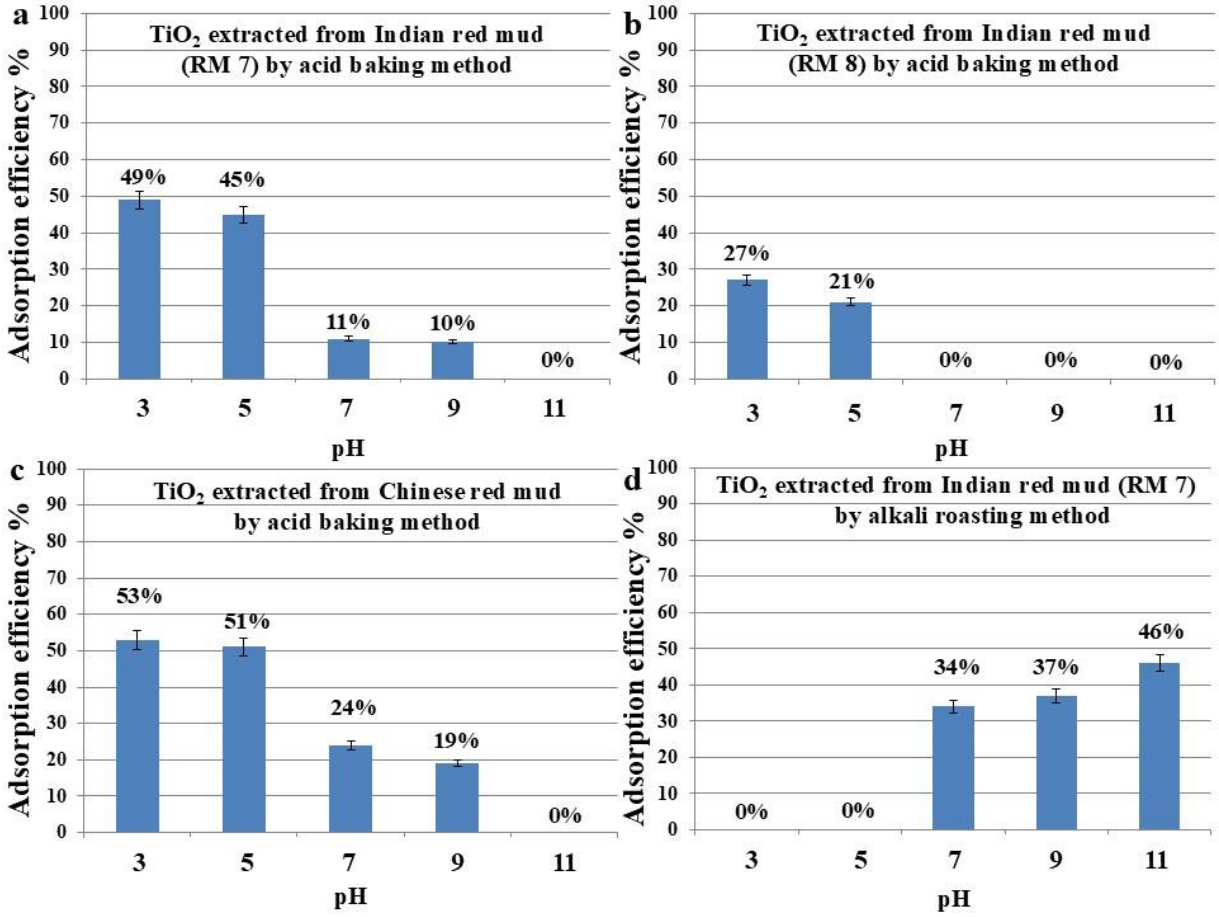

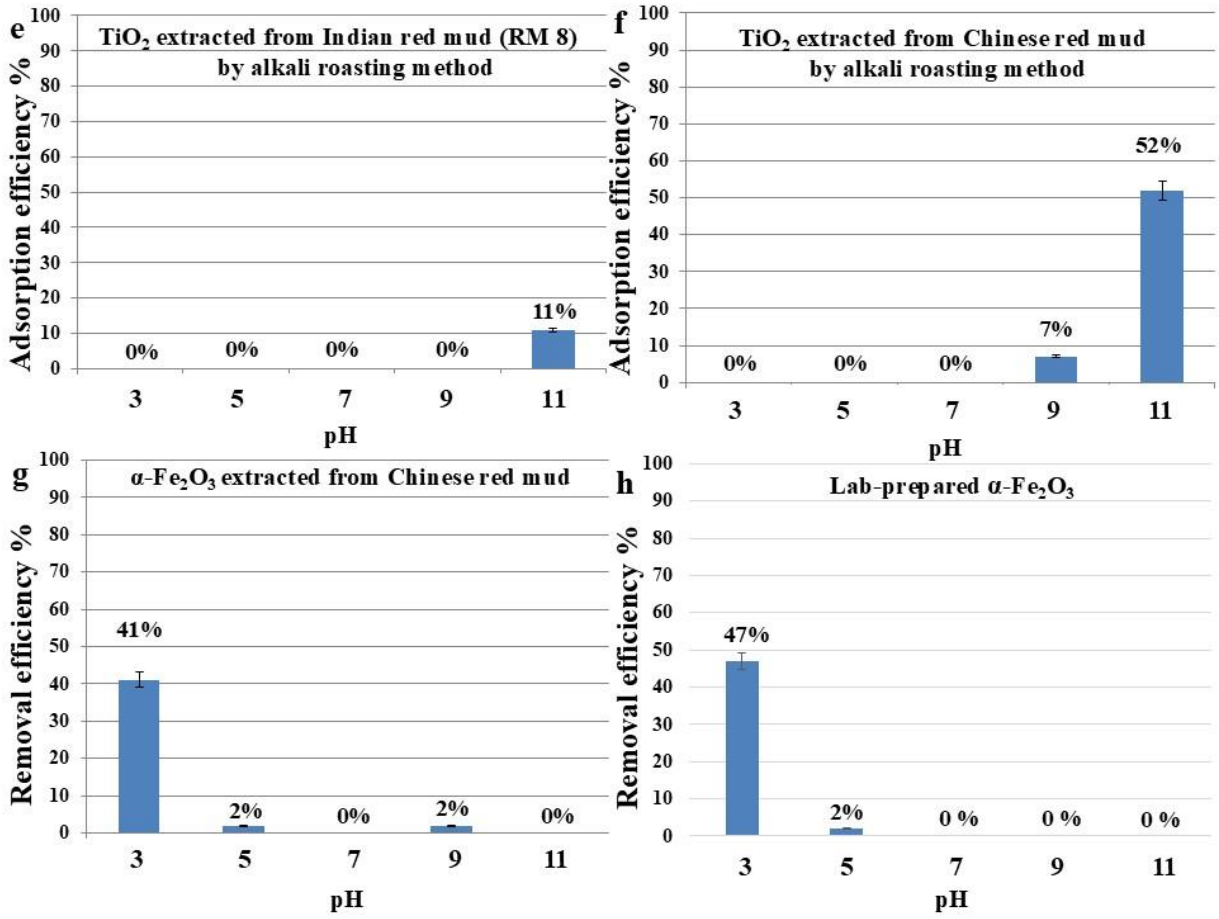

Fig 3.23. A comparison between the adsorption efficiency of TiO_2 extracted by the acid baking method from RM 7 **(a)**, RM 8 **(b)**, and Chinese red mud **(c)**, and TiO_2 extracted by the alkali roasting method from RM 7 **(d)**, RM 8 **(e)**, and Chinese red mud **(f)**, and the removal efficiency of Chinese red mud-derived α-Fe_2O_3 **(g)** and lab-prepared α-Fe_2O_3 **(h)**. [$C_o = 25$ ppm, stirring rate = 800 rpm, T = 20 ± 2 °C, volume = 20 mL, and dose = 0.01 g]. (**c** and **f** from [202]).

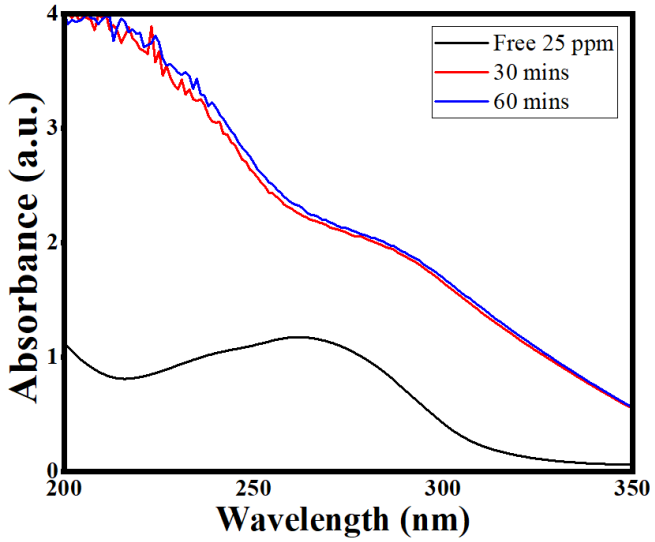

Fig 3.24. The UV-Vis spectrum of CEF after using TiO_2 extracted from the three red mud samples by the alkali roasting method. [C_o = 25 ppm, pH = 3, stirring rate = 800 rpm, T = 20 ± 2 °C, volume = 20 mL, and dose = 0.01 g].

A wide survey was undertaken using an impregnation percentage of 10 wt% of each one of the above-mentioned metals. Three out of the five metals including (Co^{2+}, Ni^{2+}, and Zn^{2+}) did not show promising adsorption results, and they had a negative impact on the efficiency of TiO_2 at acidic and neutral pH levels as shown in **Fig 3.25.a-c**. Therefore, the three metals were excluded from further studies, and the focus was only on the composites of (Fe^{3+} and Cu^{2+}) since the performance of 10% Fe-TiO_2 and 10% Cu-TiO_2 was better over most of the investigated pH levels as shown in **Fig 3.18.f** and **Fig 3.18.c**, respectively.

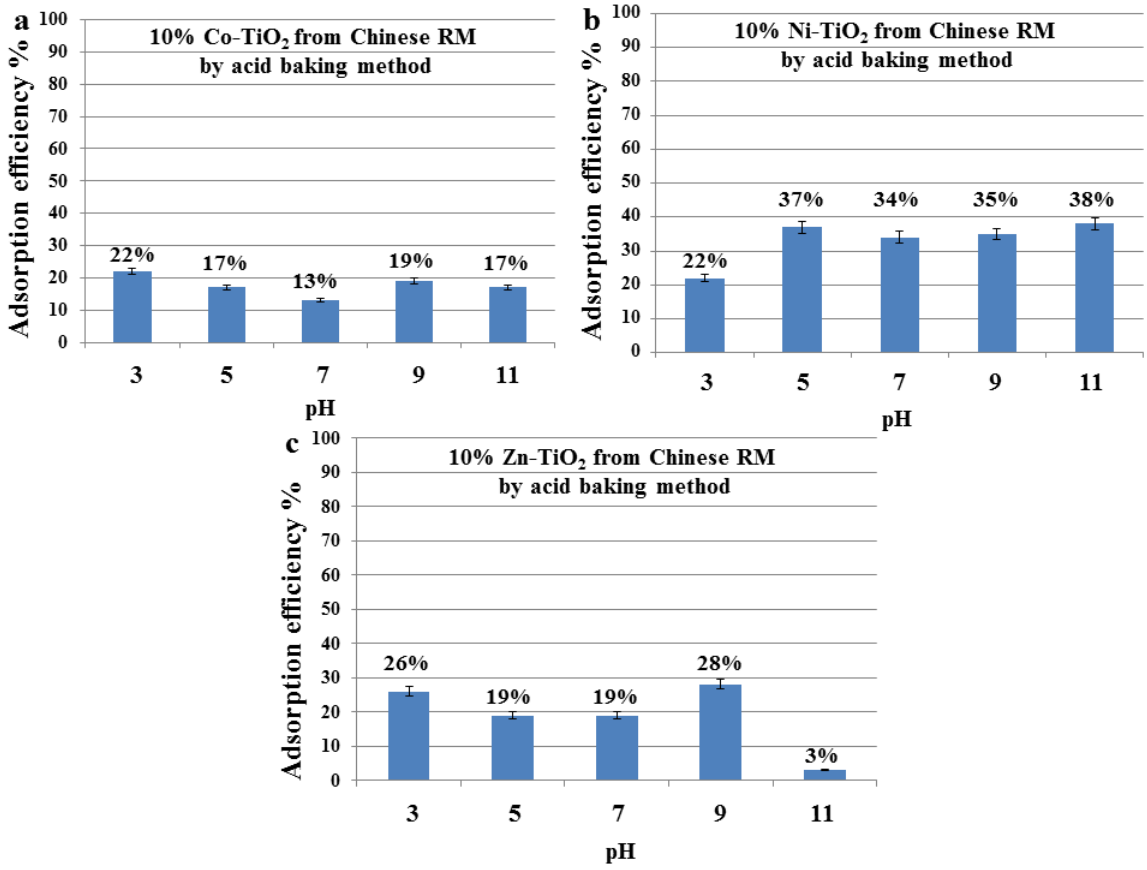

Fig 3.25. CEF adsorption efficiency by 10% Co-TiO_2 **(a)**, 10% Ni-TiO_2 **(b)**, and 10% Zn-TiO_2 **(c)** using TiO_2 extracted from Chinese RM by the acid baking method. [C_o = 25 ppm, stirring rate = 800 rpm, T = 20 ± 2 °C, volume = 20 mL, and dose = 0.01 g] [202].

The adsorption results showed that the impregnation using copper ions with a percentage of 2%, 5% and 10% only improved the performance of TiO_2 extracted from Chinese red mud in neutral and alkaline media (**Fig 3.26.a, b** and **c**). Among the three percentages, 10% Cu-TiO_2 showed the best performance, which can be attributed to the enhanced electrostatic attraction towards the negatively charged CEF species because of the high PZC value of 6.3 compared to 5.9 and 3.7 for 5% Cu-TiO_2 and 2% Cu-TiO_2, respectively. While using iron with 2% loading did not improve the adsorption efficiency at any pH level as shown in **Fig 3.26.d**. This could be related to the increased electrostatic repulsion indicated by its low PZC value that is 3.3 compared to that of the extracted TiO_2 (PZC = 4). Regarding 5% Fe-TiO_2, the performance was generally better than that of 2% Fe-TiO_2 possibly due to the improved complexation that was even extended to pH 11 by showing 10% of CEF adsorption (**Fig 3.26.e)** as a result of increasing the Fe loading. Similar to 10% Cu-TiO_2, the performance of 10% Fe-TiO_2 was better than the other loadings of iron as it increased the adsorption efficiency of TiO_2 over the

whole pH range except at pH 11 (**Fig 3.26.f**) because of its higher PZC value (4.2) resulting in a further improved electrostatic attraction.

According to the above-mentioned results, it was evident that the electrostatic attraction between the positively charged TiO_2 complexes and the negatively charged CEF species is improved by increasing the metal loading. In addition, it was clear that the adsorption efficiency of Cu-TiO_2 complexes was better under alkaline conditions as could be attributed to their higher PZC values. In contrast, Fe-TiO_2 complexes were better over the acidic pH range with lower PZC values. This could be ascribed to the stronger Lewis acidity and the higher charge density of Fe^{3+} compared Cu^{2+} in the TiO_2 complexes resulting in better complexation and electrostatic attraction at low pH levels. Therefore, a new composite made of both Cu and Fe was synthesized by using both metals with a metal loading of 5% to produce 5% Fe 5% Cu-TiO_2 to improve the adsorption efficiency across most of the pH scale.

As shown in **Fig 3.26.g**, 5% Fe 5% Cu-TiO_2 showed a better performance compared to all the previously discussed materials as the adsorption efficiency was above 50% over most of the pH range, which could be the result of the synergistic effect between copper and iron ions. Even though the surface area of this material was less than that of pristine TiO_2 (139 m^2/g) similar to 10 % Fe-TiO_2 and 10% Cu-TiO_2 as it was 55 m^2/g, the PZC was found to be 5.8 indicating the possible improved electrostatic attraction. High surface area is an important factor that can influence the adsorption efficacy as previously discussed, but other factors are suggested to be more important in the current study such as the synergistic effect of metal salt precursors, which is discussed below. So based on these results, 5% Fe 5% Cu-TiO_2 was selected to be further investigated using more factors. The adsorption capacity of 5% Fe 5% Cu-TiO_2 was 29, 27.5, 27, 26, and 25 mg/g at pH levels 3, 5, 7, 9, and 11, respectively, as shown in **Fig 3.26.h**. It should be noted that the adsorption efficiencies presented in the bar graphs throughout this thesis were calculated from the difference between the initial and final absorbance values measured by UV-Vis spectroscopy. To further validate the adsorption performance of key samples, such as 5% Fe 5% Cu-TiO_2, complementary techniques including TGA and CHN analyses were employed. Additionally, the turbidimetric and Griess reagent assays along with TGA and CHN confirmed that the removal of the antibiotics (CEF and DOXY) occurred exclusively through adsorption, ensuring that no undesired by-products such as sulfates or nitrites were generated.

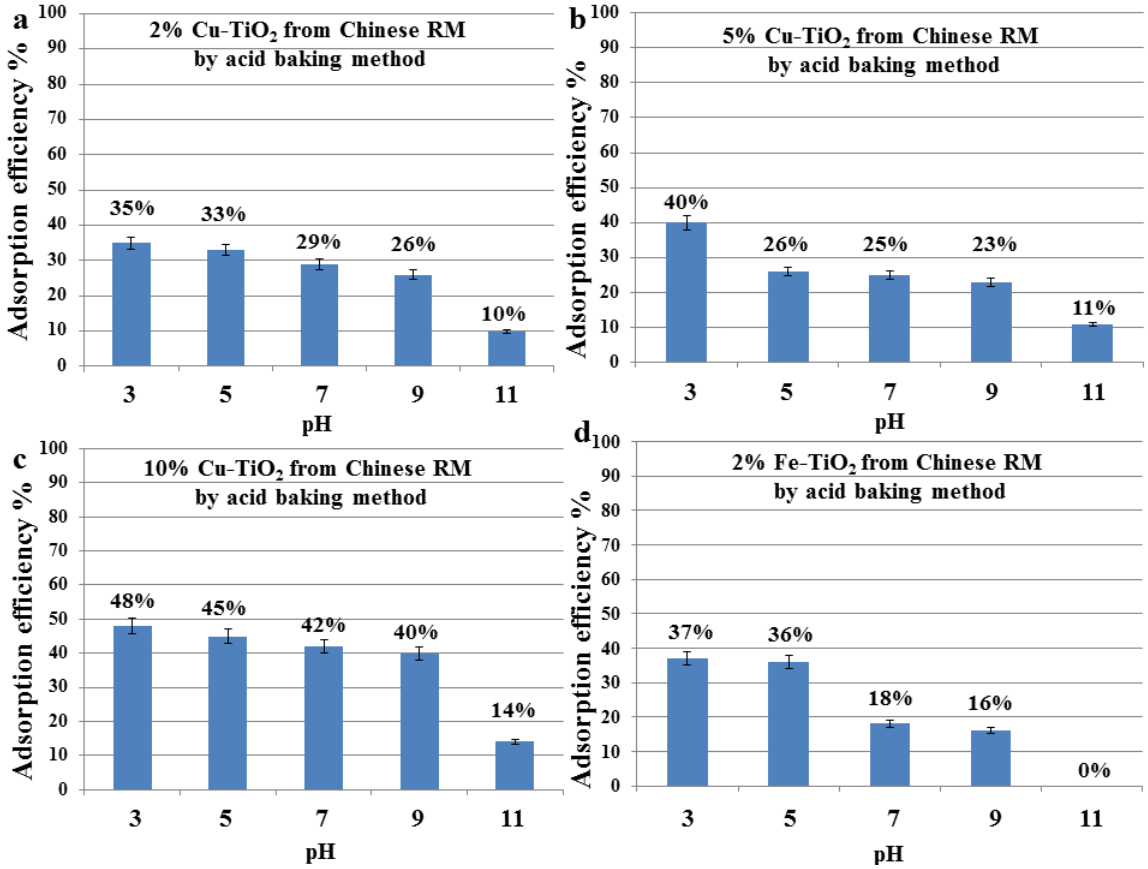
a
2% Cu-TiO2 from Chinese RM
by acid baking method
Adsorption efficiency %
35%
33%
29%
26%
10%
pH
b
5% Cu-TiO2 from Chinese RM
by acid baking method
Adsorption efficiency %
40%
26%
25%
23%
11%
pH
c
10% Cu-TiO2 from Chinese RM
by acid baking method
Adsorption efficiency %
48%
45%
42%
40%
14%
pH
d
2% Fe-TiO2 from Chinese RM
by acid baking method
Adsorption efficiency %
37%
36%
18%
16%
0%
pH

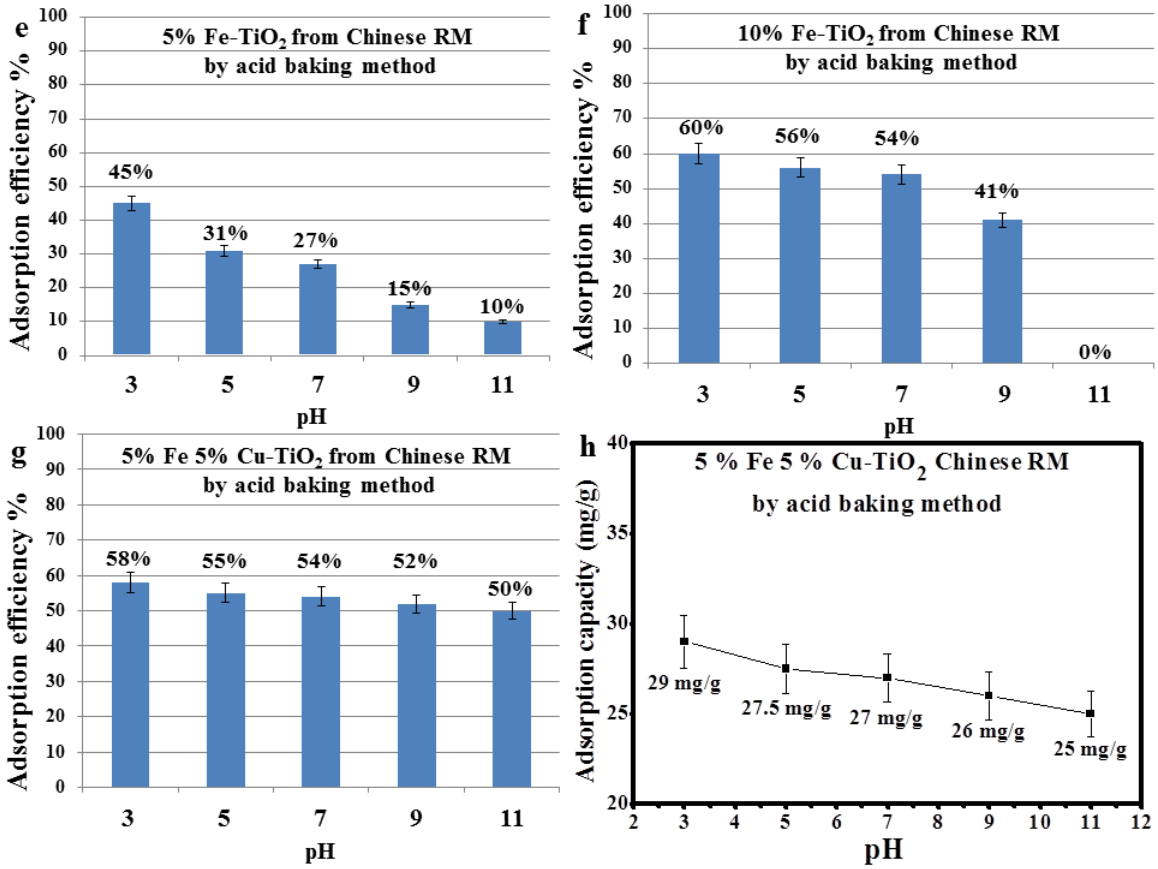

Fig 3.26. CEF adsorption efficiency by 2% Cu-TiO_2 **(a)**, 5% Cu-TiO_2 **(b)**, 10% Cu-TiO_2 **(c)**, 2% Fe-TiO_2 **(d)**, 5% Fe-TiO_2 **(e)**, 10% Fe-TiO_2 **(f)**, 5% Fe 5% Cu-TiO_2 **(g)**, and CEF adsorption capacity by 5% Fe 5% Cu-TiO_2 **(h)** using TiO_2 extracted from Chinese RM by the acid baking method. [C_o = 25 ppm, stirring rate = 800 rpm, T = 20 ± 2 °C, volume = 20 mL, and dose = 0.01 g] [202].

Control experiments were conducted using the salt precursors of $Fe(NO_3)_3$, $Co(NO_3)_2$, $Ni(NO_3)_2$, $Cu(NO_3)_2$, and $Zn(NO_3)_2$ in the aqueous solutions of CEF to investigate their efficacies, and also to determine if there is a synergistic effect between these precursors and TiO_2. The only precursor that exhibited a CEF removal over the whole pH scale was the copper salt as shown in **Fig 3.27.d**, while the zinc precursor was effective at pH 3, 5, and 11 (**Fig 3.27.e**). $Co(NO_3)_2$ (**Fig 3.27.b**) and $Ni(NO_3)_2$ (**Fig 3.27.c**) exhibited a very low removal efficiency in alkaline conditions. These metal salts appeared active particularly under neutral and alkaline conditions because they form solid precipitates of metal hydroxides, which themselves can adsorb CEF. These interactions contributed to the enhanced removal efficiencies observed for Co-, Ni-, Cu-, and Zn-TiO_2 composites compared to pristine TiO_2.

Furthermore, the improved CEF removal under alkaline conditions, particularly at pH 11, is primarily attributed to the increased metals' loading from 2% to 10%.

On the other hand, the iron precursor did not remove CEF across the entire pH range (**Fig. 3.27.a**), and the UV-Vis spectra resembled those of the alkali-roasting-extracted TiO_2, with absorbance increasing after 60 minutes of stirring. This result is attributed to the spectral overlap between the CEF peak and that of iron nitrate, as the metal salt absorbs UV light at approximately 295 nm (**Fig 3.28**). However, this result does not mean that there is no synergistic effect between the iron precursor and TiO_2, as all Fe-TiO_2 adsorbents demonstrated considerably higher efficacy compared to pristine TiO_2. A control experiment was undertaken using *T. latifolia* powder, which was used in synthesizing α-Fe_2O_3, and it did not adsorb CEF. Similarly, the Chinese red mud did not show any CEF adsorption.

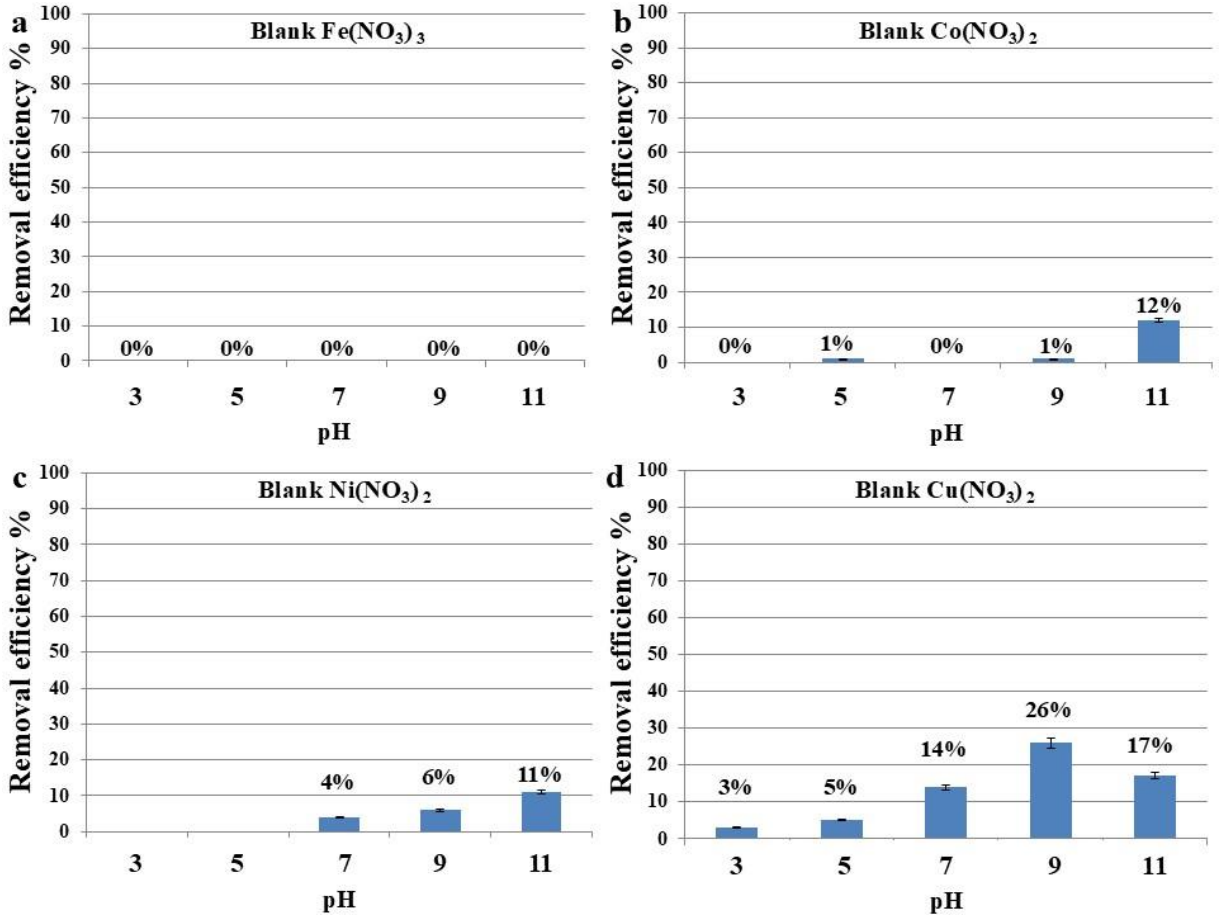

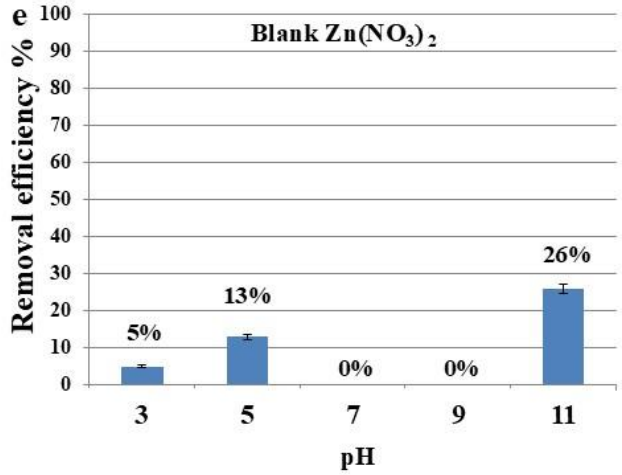

Fig 3.27. Control (blank) experiments of CEF removal efficiency by $Fe(NO_3)_3$ **(a)**, $Co(NO_3)_2$ **(b)**, $Ni(NO_3)_2$ **(c)**, $Cu(NO_3)_2$ **(d)**, and $Zn(NO_3)_2$ **(e)** in aqueous solutions of CEF [$C_o = 25$ ppm, stirring rate = 800 rpm, $T = 20 \pm 2$ °C, volume = 20 mL, and dose = 0.01 g]. (**a** and **d** from [202]).

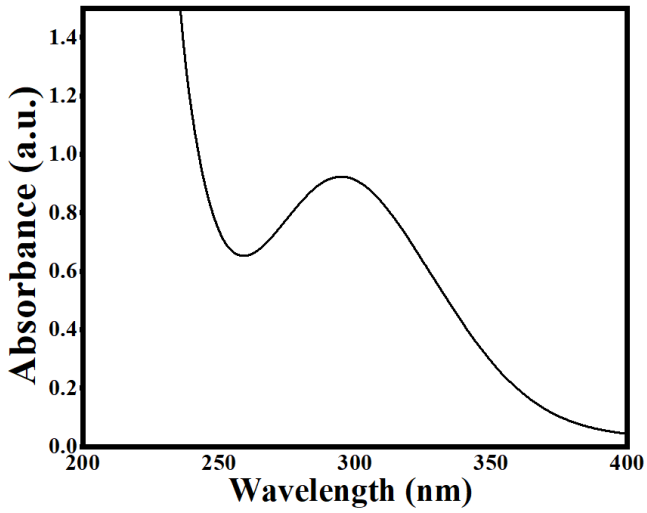

Fig 3.28. The UV-Vis spectrum of the aqueous solution of 0.002 M $Fe(NO_3)_3$.

Table 3.2. The PZC of the adsorbents reported in Chapter 3.

Adsorbent	PZC
TiO_2 extracted from Chinese RM by the alkali roasting method	2.1
TiO_2 extracted from Indian RM 8 by the alkali roasting method	2.5
TiO_2 extracted from Indian RM 7 by the alkali roasting method	2.6
2% Fe-TiO_2 extracted from Chinese RM by the acid baking method	3.3
5% Fe-TiO_2 extracted from Chinese RM by the acid baking method	3.3
2% Cu-TiO_2 extracted from Chinese RM by the acid baking method	3.7
TiO_2 extracted from Chinese RM by the acid baking method	4.0
10% Fe-TiO_2 extracted from Chinese RM by the acid baking method	4.2
TiO_2 extracted from Indian RM 7 by the acid baking method	4.4
Commercial TiO_2 (P25)	4.9
Lab-prepared TiO_2	5.4
5% Fe 5% Cu-TiO_2 extracted from Chinese RM by the acid baking method	5.8
T. latifolia	5.8
5% Cu-TiO_2 extracted from Chinese RM by the acid baking method	5.9
Green synthesized α-Fe_2O_3	6.3
10% Cu-TiO_2 extracted from Chinese RM by the acid baking method	6.3
Commercial α-Fe_2O_3	6.5
Chinese red mud-derived α-Fe_2O_3	6.7
Chinese red mud	7.4

3.10. Catalytic and photocatalytic degradation of CEF

The catalytic efficiency of 5% Fe 5% Cu-TiO_2 in the degradation of CEF using H_2O_2, which is used in Fenton degradation, was investigated over the same pH range of adsorption experiments (3-11). Although the degradation of CEF is not considered a safe removal option, 5% Fe 5% Cu-TiO_2 was used as a Fenton catalyst and a photocatalyst just to test its catalytic efficiency. The obtained results after 120 minutes of adding H_2O_2 indicated a slight increase in the removal efficiency of CEF over the whole pH range after running adsorption experiments to attain the adsorption/desorption equilibrium, which were undertaken before adding H_2O_2. As shown in **Fig 3.29.a**, the removal efficiency improved to 68-69% in acidic and neutral conditions and slightly increased by 6% in alkaline conditions. The better improvement in the removal efficiency under acidic conditions was expected, as the optimal pH range for Fenton degradation is approximately 3 [249]. The obtained result indicated the low catalytic efficiency of 5% Fe 5% Cu-TiO_2 in activating H_2O_2 and producing free radicals such as hydroxyl radicals (•OH) that could result in high degradation efficiencies if produced in large numbers. A set of control experiments was carried out over the same pH range using only H_2O_2 where the removal efficiencies were 10% or even less as displayed in **Fig 3.29.b** indicating the need for a catalyst to activate H_2O_2.

Regarding the photocatalytic efficiency of 5% Fe 5% Cu-TiO_2 under UV light, the material was first tested as an adsorbent under dark conditions and the efficiency, as previously mentioned, was 54% at pH 7. Subsequently, the adsorbent was removed via centrifugation to account for the photolysis of CEF under UV light, which was 16% as the efficiency increased to 70% (**Fig 3.29.c**). Upon adding 5% Fe 5% Cu-TiO_2, the efficiency marginally increased to 72%, indicating the very low photocatalytic activity of 5% Fe 5% Cu-TiO_2 in generating reactive oxygen species under UV light.

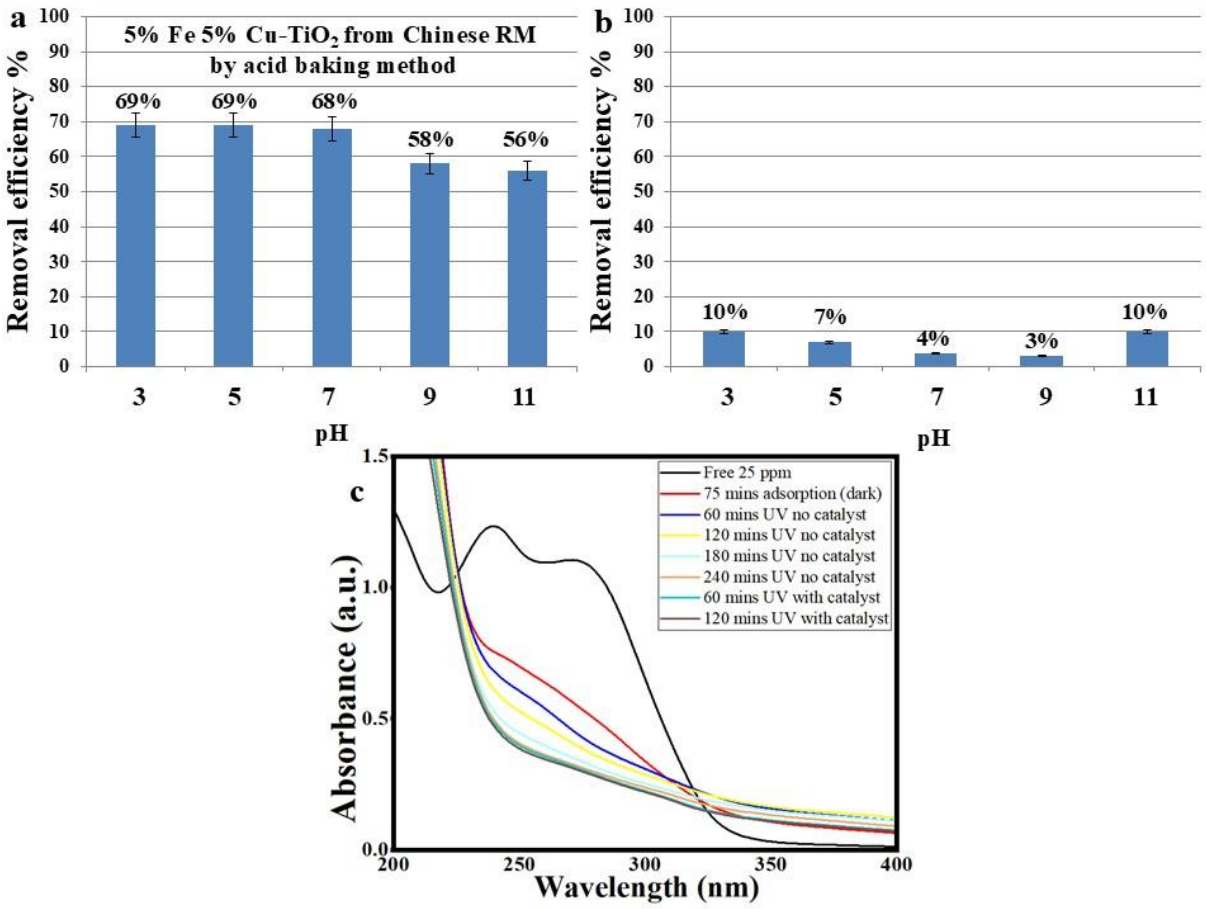

Fig 3.29. The catalytic degradation efficiency of CEF species by 5% Fe 5% Cu-TiO_2 using H_2O_2 across the pH scale 3-11 **(a)**, control experiments of CEF degradation efficiency by H_2O_2 across the same pH range **(b)**, and the photocatalytic effect of 5% Fe 5% Cu-TiO_2 under UV light at pH 7 **(c)**. [C_o = 25 ppm, stirring rate = 800 rpm, T = 20 ± 2 °C, volume = 20 mL, and dose = 0.01 g]. (**a** and **b** from [202]).

Within the same context, the photocatalytic degradation efficiency of P25 was evaluated, but the results were inconsistent. As shown in **Fig. 3.30.a**, the initial adsorption efficiency was 12%. After removing P25 and initiating UV photolysis of the CEF solution in the photocatalytic reactor, a degradation efficiency of 64% was achieved after 125 minutes, resulting in a total removal efficiency of 76%. However, upon extending the irradiation time to 180 and 210 minutes, the absorbance increased due to evaporation.

The experiment was repeated twice (**Fig. 3.30.b** and **c**), and in both cases, the absorbance increased from the beginning after the adsorption step, despite centrifugation and filtration of P25 before UV-Vis measurements, a step carried out before measuring the efficiency of all

materials. This anomaly may be attributed to interference from the white hue caused by P25, which is known to absorb UV light, potentially affecting the measurements by absorbing UV from the UV-Vis lamp. In the repeated experiments, UV photolysis in the absence of P25 led to 30% and 31% CEF degradation in **Fig. 3.30.b** and **c**, respectively, after 240 minutes. These values were calculated using the absorbance at free 25 ppm (black lines) as the reference initial absorbance. No further degradation was observed beyond 240 minutes.

To assess the actual photocatalytic contribution of P25, it was reintroduced into the solution. In **Fig. 3.30.b**, the degradation efficiency was 30% after 60 minutes and increased to 36% after 120 minutes, with no further improvement afterward. Similarly, in **Fig. 3.30.c**, efficiencies of 35% and 42% were observed at 60 and 120 minutes, respectively. However, the absorbance increased after 200 minutes, which could be attributed to either evaporation or the desorption of CEF from P25 surface. A similar trend was observed for the lab-prepared TiO_2 (**Fig. 3.30.d**), where the absorbance increased immediately after adsorption, then gradually decreased under UV light. Its photocatalytic activity was 19% after 60 minutes and it was almost the same after 120 minutes. These results indicated the higher photocatalytic activity of P25.

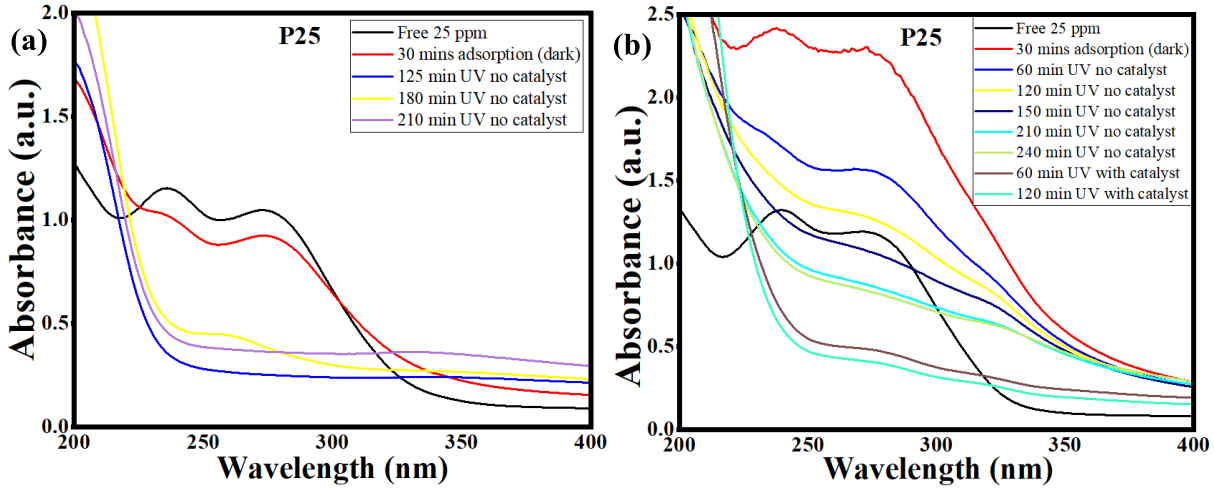

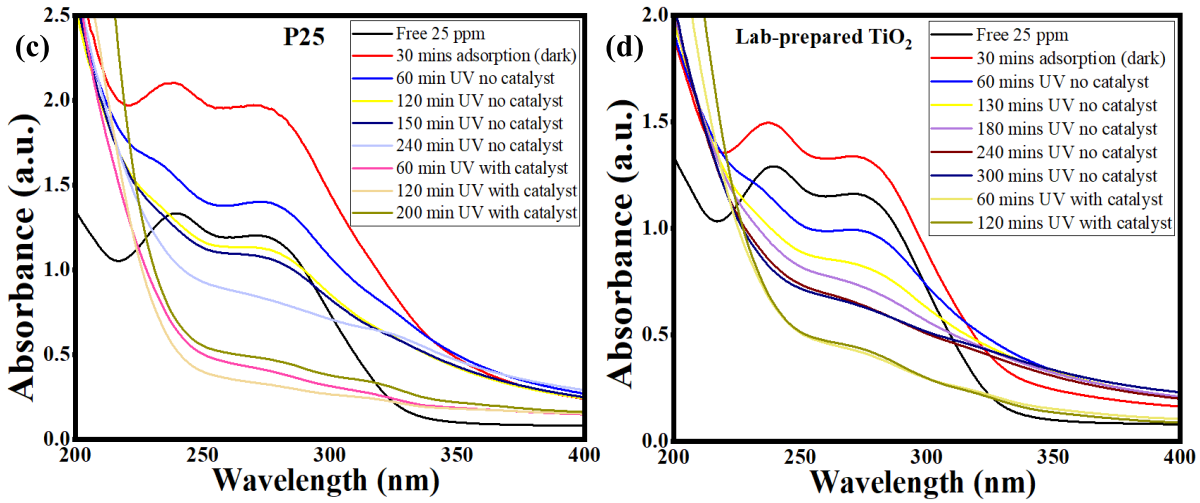

Fig 3.30. The photocatalytic activity of P25 **(a-c)**, and lab-prepared TiO_2 **(d)** in CEF degradation under UV light. [C_o = 25 ppm, pH = 7, stirring rate = 800 rpm, T = 20 ± 2 °C, volume = 20 mL, and dose = 0.01 g].

To further illustrate the white hue caused by P25 in CEF solutions, photographs were taken of the solutions across the investigated pH range (3 - 11) before (**Fig. 3.31.a**) and after treatment with P25 (**Fig. 3.31.b** and **c**). The images show that the intensity of white hue increased with raising pH.

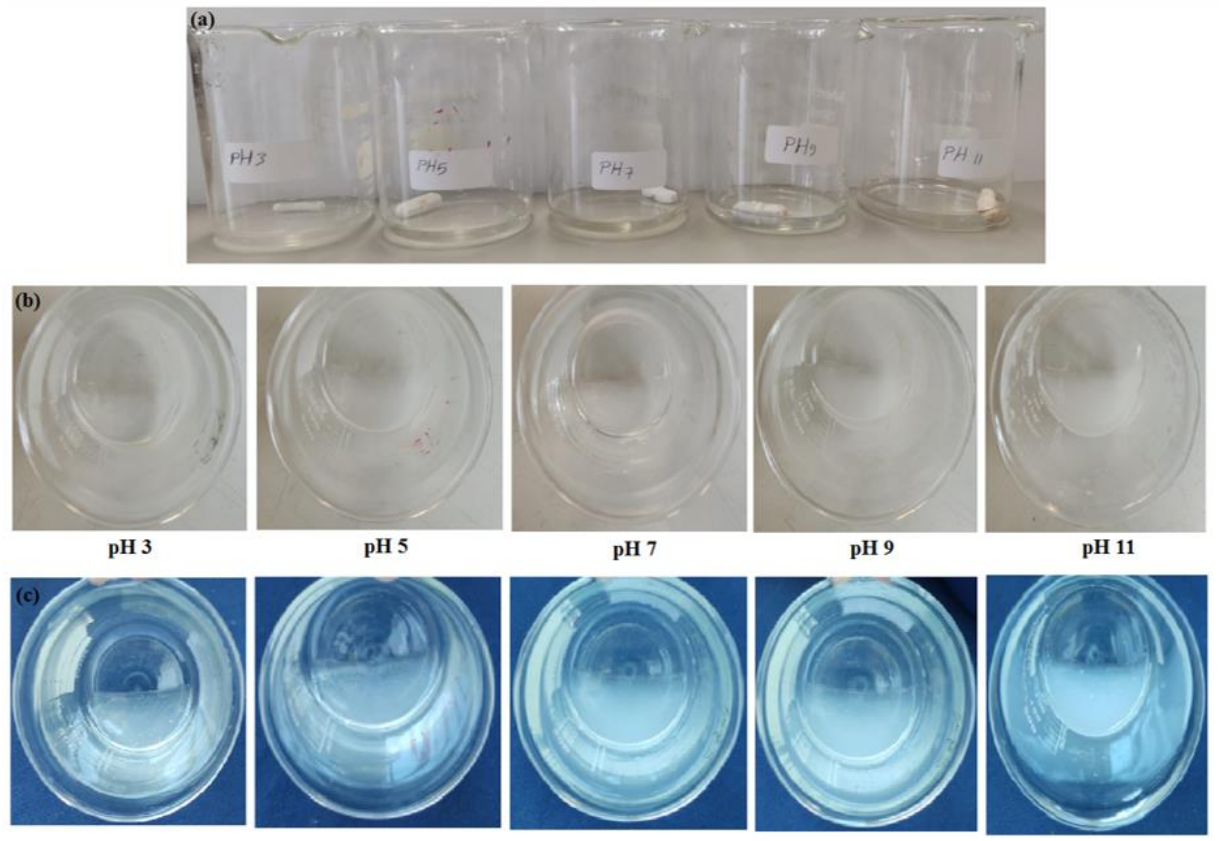

Fig 3.31. CEF solutions with pH levels fom 3 to 11 before **(a)**, and after adding TiO_2 on two different colored backgrounds **(b-c)**.

Building on the aforementioned results, the photocatalytic performance of both commercial and Chinese red mud-derived α-Fe_2O_3 was evaluated under visible light. Neither material exhibited any removal efficiency through adsorption or photodegradation at pH 7, as evidenced by an increase in absorbance upon illumination with the LED lamp (**Fig 3.32.a-b**). No CEF degradation was observed using only visible light as a control experiment.

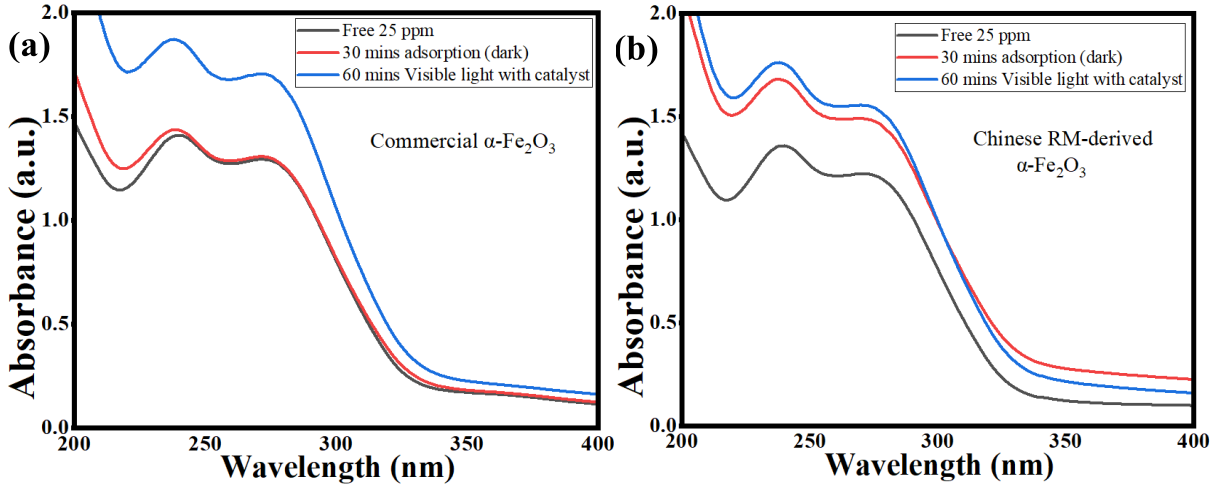

Fig 3.32. The photocatalytic activity of commercial **(a)** and Chinese red mud-derived α-Fe_2O_3 **(b)** in CEF degradation under visible light. [C_o = 25 ppm, pH = 7, stirring rate = 800 rpm, T = 20 ± 2 °C, volume = 20 mL, and dose = 0.01 g].

3.11. Role of nitrate in the adsorption of CEF using 5% Fe 5% Cu-TiO_2

Using calcined 5% Fe 5% Cu-TiO_2 led to a decrease in the adsorption efficiency across all pH levels, especially in the alkaline conditions as illustrated in **Fig 3.33.a**. This outcome could be attributed to the decomposition of nitrate, which plays a key role in removing CEF at all pH levels, particularly in the alkaline conditions as confirmed by the control experiment of $Cu(NO_3)_2.3H_2O$ (**Fig 3.27.d**). Additionally, the efficiency drop after calcination could be attributed to other factors such as the loss of active surface sites because of the metal agglomeration on the TiO_2 surface. This result was further confirmed by a control experiment using 5% Fe 5% Cu-TiO_2 prepared with commercial α-Fe_2O_3 and CuO as sources of the 5% Fe and 5% Cu, respectively, instead of $Fe(NO_3)_3.9H_2O$ and $Cu(NO_3)_2.3H_2O$. This composite clearly exhibited a lower adsorption efficiency across the investigated pH range (**Fig 3.33.b**) compared to the uncalcined 5% Fe 5% Cu-TiO_2, as the performance was similar to that of calcined 5% Fe 5% Cu-TiO_2, and confirming the effective role of nitrate in removing CEF.

The control experiment of commercial α-Fe_2O_3 exhibited very poor performance (**Fig 3.33.c**) as previously discussed. Commercial CuO performed better than α-Fe_2O_3 in acidic and neutral conditions (**Fig 3.33.d**). Consequently, using both α-Fe_2O_3 and CuO resulted in an adsorption efficacy that approximately reflects the average performance of the two materials combined (**Fig 3.33.e**). This outcome was similar to that of the control experiment in **Fig 3.33.b**, though

with higher efficacy at pH 3 and 5, and lower efficacy at pH 7 and 9 (**Fig 3.33.e**). Although the combined performance of α-Fe_2O_3 and CuO (control experiment) was superior to that of $Cu(NO_3)_2.3H_2O$ at pH 3 and 5 (**Fig 3.27.d**), and also better than $Fe(NO_3)_3.9H_2O$ across most of the pH range (**Fig 3.27.a**), it did not enhance the performance of red mud-derived TiO_2 as effectively as $Fe(NO_3)_3.9H_2O$ and $Cu(NO_3)_2.3H_2O$ did over the entire investigated pH range. This further highlights the crucial role of nitrates in improving the performance of red mud-derived TiO_2.

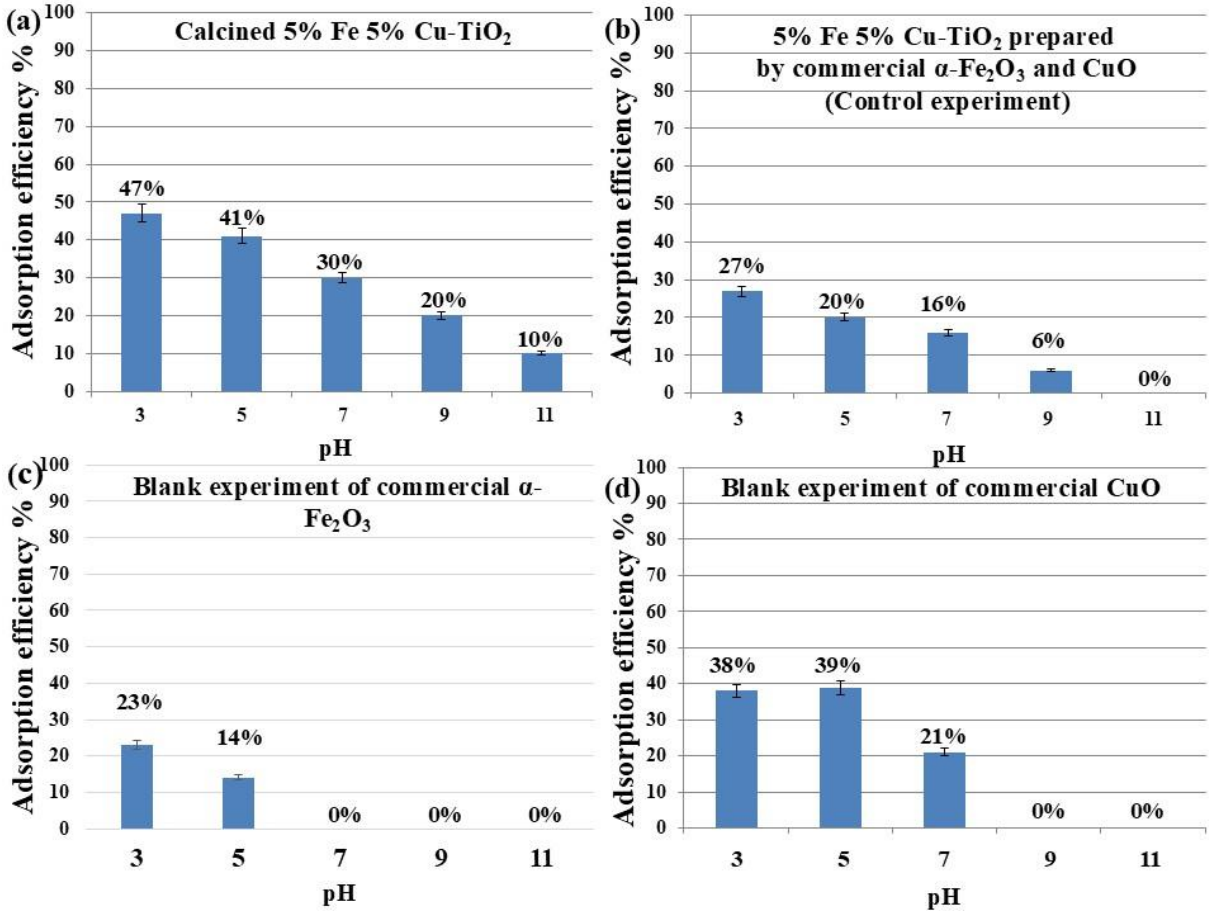

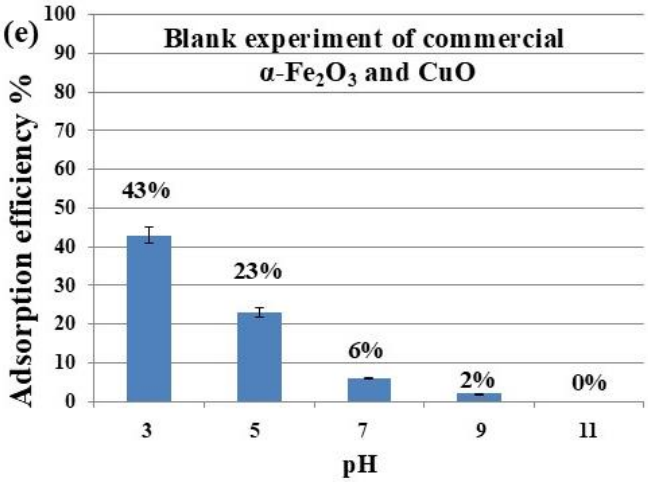

Fig 3.33. The adsorption efficiency of calcined 5% Fe 5% Cu-TiO_2 **(a)**, 5% Fe 5% Cu-TiO_2 prepared using commercial α-Fe_2O_3 and CuO **(b)**, the control (blank) experiment of commercial α-Fe_2O_3 **(c),** commercial CuO **(d),** and commercial α-Fe_2O_3 and CuO **(e)**. [C_o = 25 ppm, stirring rate = 800 rpm, T = 20 ± 2 °C, volume = 20 mL, and dose = 0.01 g].

The powder XRD pattern of 5% Fe 5% Cu-TiO_2 after calcination confirmed the disappearance of the copper nitrate reflection (**Fig 3.34.a**). Similarly, the pattern of the uncalcined 5% Fe 5% Cu-TiO_2 showed the disappearance of the same reflection after CEF adsorption indicating nitrate leaching (**Fig 3.34.b**). Therefore, 5% Fe 5% Cu-TiO_2 should be used under conditions that do not cause the leaching of either metals or nitrates, as discussed in the ICP and nitrate detection results sections below.

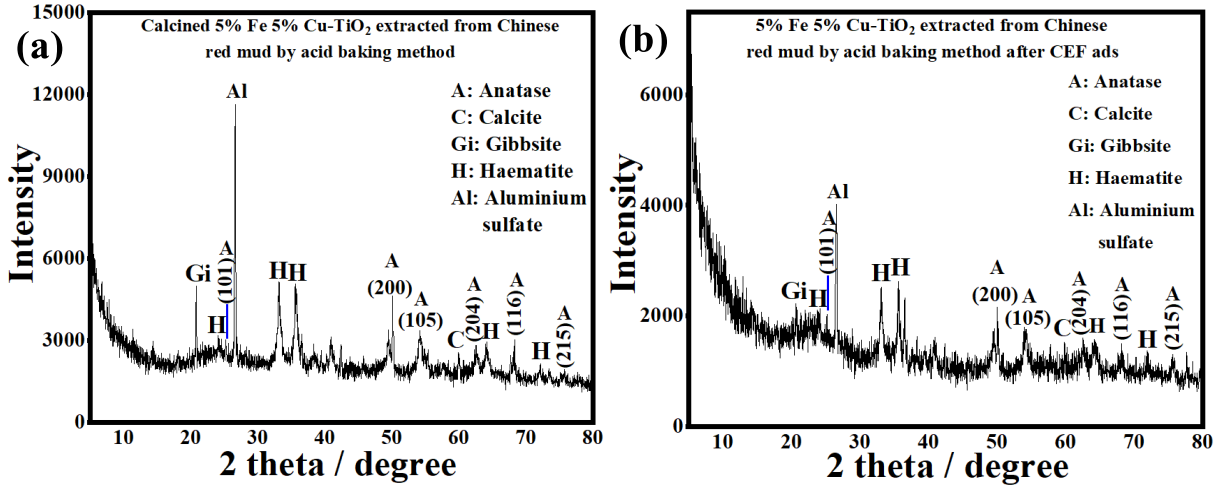

Fig 3.34. Powder XRD patterns of 5% Fe 5% Cu-TiO_2 after calcination **(a)** and after CEF adsorption at pH 3 **(b)**. [C_o = 25 ppm, stirring rate = 800 rpm, T = 20 ± 2 °C, volume = 20 mL, and dose = 0.01 g]. The difference in the intensity between **Fig 3.34.a** and **b** is simply due to variations in how the samples were packed on the sample holder, which is a very common occurrence in XRD measurements.

3.12. Effect of initial concentration of CEF, adsorbent dose, stirring rate, and time on CEF adsorption using 5% Fe 5% Cu-TiO_2

The effects of other factors including the initial concentration of CEF, the adsorbent dose, the stirring rate, adsorption time, and recycling were also investigated using 5% Fe 5% Cu-TiO_2 at pH 7. Apparently, the highest adsorption efficiency (54%) was achieved at 25 and 50 ppm upon testing the effect of the initial concentration of CEF as shown in **Fig 3.35.a**. However, the maximum adsorption capacity was obtained at the highest tested concentration of 100 ppm, where the values increased progressively from 16, 27, 54, and 75 mg/g at 15, 25, 50, and 75 ppm, respectively, to 92 mg/g at 100 ppm. At higher concentrations, the stronger interaction between CEF and the adsorbent surface promotes more efficient transport of CEF species, reduces the relative effect of competitive adsorption from other solutes or interfering species in wastewater, and thereby enhances the overall adsorption process.

When comparing the obtained adsorption capacity with previously published capacities, many factors should be considered including the solution volume, concentration of pollutants, and the adsorbent dose and its surface area. Thus, there is a significant variation in the published adsorption capacities of CEF ranging between 844 mg/g [250] to as low as 0.72 mg/g [251]

depending on the conditions applied. So by comparing the obtained capacity in the current study when using 100 ppm of CEF (92 mg/g) with Olusegun *et al.* [252] who used a similar adsorbent dose (0.01 g) and CEF concentration (100 ppm), but a different volume (15 mL), it was concluded that their adsorption capacity was higher as it was 109 mg/g using ferrihydrite with 10% silica rice husk. This difference can be attributed to the higher surface area (255 m^2/g) of their material compared to 55 m^2/g of 5% Fe 5% Cu-TiO_2. In contrast, at 25 ppm CEF, the adsorption capacity obtained in the current study (27 mg/g) was markedly higher than the 3.5 mg/g reported by Mahmoud *et al.* [253] using a titania-based adsorbent (nano-titanium oxide/chitosan/nano-bentonite) under nearly identical experimental conditions (CEF concentration: 25 ppm, adsorbent dose: 0.01 g, solution volume: 20 mL, room temperature). Although the surface area of their material (16 m^2/g) was less than that of 5% Fe 5% Cu-TiO_2, this alone does not justify the large difference in adsorption capacity. These comparisons indicate that it is inappropriate to claim the superiority of one adsorbent over another without accounting for the influence of experimental conditions.

Although the adsorption efficiency increased from 37% to 54% when the dose of 5% Fe 5% Cu-TiO_2 was raised from 5 mg to 10 mg (**Fig. 3.35.b**), the lower dose of 5 mg proved to be the most effective, yielding adsorption capacities of 37, 32, and 27 mg/g at 5 mg, 7.5 mg, and 10 mg, respectively. Regarding the stirring rate, increasing it from 0 to 800 rpm enhanced the adsorption efficiency from 24% to 54% and the capacity from 12 mg/g to 27 mg/g (**Fig. 3.35.c**). This improvement is likely due to the higher diffusion rate and mass transfer of CEF molecules toward the adsorbent surface.

The extent of CEF adsorption with time was investigated in the current study. As shown in **Fig. 3.35.d**, the adsorption was rapid, with 31% of CEF removed within the first minute and equilibrium reached by 30 minutes at 54% adsorption. The extent of adsorption remained constant up to 75 minutes and beyond, suggesting that the process is chemisorption and an equilibrium process. This behavior can be explained by the abundance of surface-active sites at the beginning of adsorption, which were progressively occupied by CEF until equilibrium was established, at which point no further sites were available. These results highlight the efficiency of 5% Fe 5% Cu-TiO_2, as equilibrium was achieved within a relatively short time. The adsorption capacity increased from 15.5 mg/g to 27 mg/g as the contact time was extended from 1 to 30 minutes.

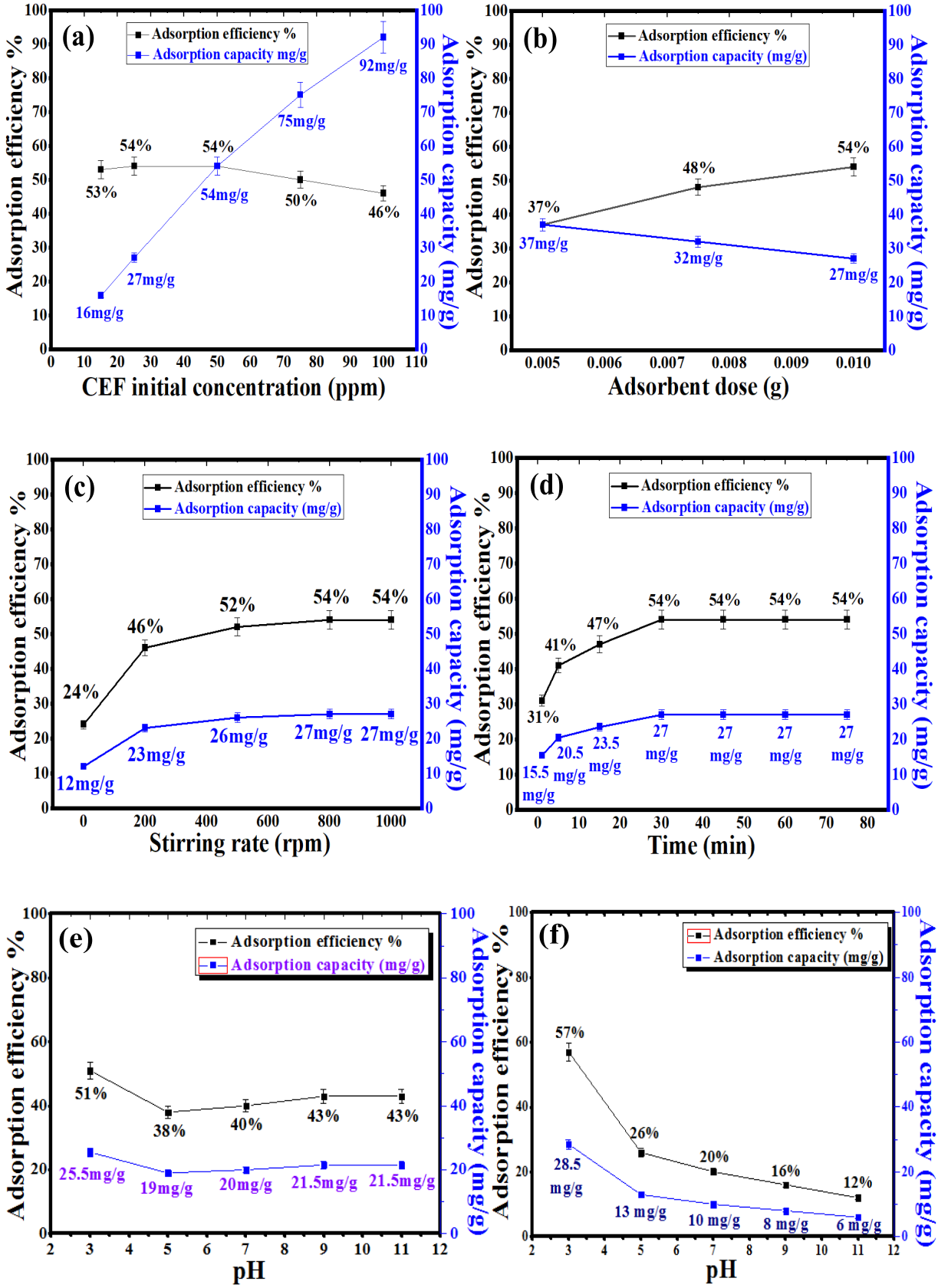
(a)
Adsorption efficiency %
Adsorption capacity mg/g
Adsorption efficiency %
Adsorption capacity (mg/g)
CEF initial concentration (ppm)
53%
54%
54%
50%
46%
16mg/g
27mg/g
54mg/g
75mg/g
92mg/g
(b)
Adsorption efficiency %
Adsorption capacity (mg/g)
Adsorbent dose (g)
37%
48%
54%
37mg/g
32mg/g
27mg/g
(c)
Adsorption efficiency %
Adsorption capacity (mg/g)
Stirring rate (rpm)
24%
46%
52%
54%
54%
12mg/g
23mg/g
26mg/g
27mg/g
27mg/g
(d)
Adsorption efficiency %
Adsorption capacity (mg/g)
Time (min)
31%
41%
47%
54%
54%
54%
54%
15.5 mg/g
20.5 mg/g
23.5 mg/g
27 mg/g
27 mg/g
27 mg/g
27 mg/g
(e)
Adsorption efficiency %
Adsorption capacity (mg/g)
pH
51%
38%
40%
43%
43%
25.5mg/g
19mg/g
20mg/g
21.5mg/g
21.5mg/g
(f)
Adsorption efficiency %
Adsorption capacity (mg/g)
pH
57%
26%
20%
16%
12%
28.5 mg/g
13 mg/g
10 mg/g
8 mg/g
6 mg/g

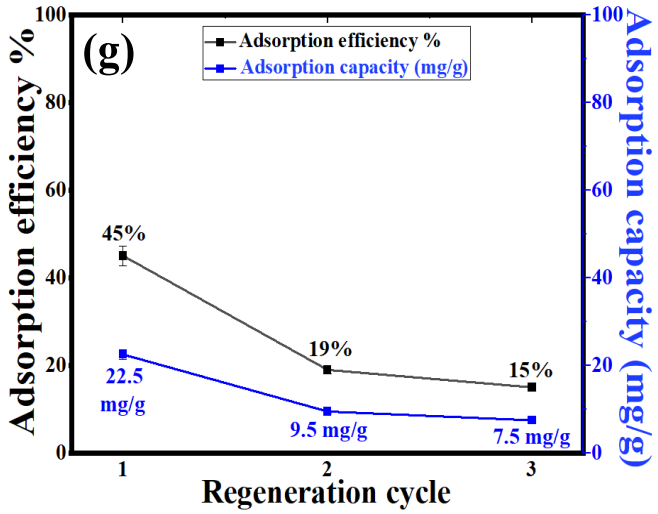

Fig 3.35. Effect of variation in initial concentration of CEF **(a)** [pH = 7, stirring rate = 800 rpm, T = 20 ± 2 °C, and dose = 0.01 g]**,** dose **(b)** [C_o = 25 ppm, pH = 7, stirring rate = 800 rpm, and T = 20 ± 2 °C], stirring rate **(c)** [C_o = 25 ppm, pH = 7, T = 20 ± 2 °C, and dose = 0.01 g], and time effect [C_o = 25 ppm, pH = 7, stirring rate = 800 rpm, T = 20 ± 2 °C, and dose = 0.01 g] **(d)** on the efficacy of 5% 5% Cu-TiO_2. CEF adsorption in tap water **(e)** [202], the River Clyde water collected on 29th July 2024 **(f)** [C_o = 25 ppm, stirring rate = 800 rpm, T = 20 ± 2 °C, volume = 20 mL, and dose = 0.01 g], and recycling of 5% Fe 5% Cu-TiO_2 after 75 minutes (**g**) [C_o = 25 ppm, stirring rate = 800 rpm, T = 20 ± 2 °C, volume = 20 mL, pH = 7, and dose = 0.01 g].

3.13. Recycling and Application of 5% Fe 5% Cu-TiO_2 in the adsorption of CEF from tap, Clyde River, and real wastewater samples

A step towards investigating the applicability of 5% Fe 5% Cu-TiO_2 in different water samples was undertaken by testing the adsorption efficiency of this composite in removing CEF from tap water samples. Although the adsorption efficiency of 5% Fe 5% Cu-TiO_2 in tap water at pH 3 was the highest with an efficiency of 51% and an adsorption capacity of 25.5 mg/g similar to that observed using DW, the adsorption trend was different as the efficiency decreased at pH 5, followed by a slight increase at pH 7 and 9, and then it remained constant at pH 11 as shown in **Fig 3.35.e**. Such an irregular adsorption trend could be attributed to the presence of interfering ions in the water sample. So, the applicability of 5% Fe 5% Cu-TiO_2 in adsorbing CEF from tap water samples, which were drawn during the summer in 2023 from

the Webb lab in the Joseph Black Building at Glasgow University, over the whole pH range was verified based on the observed results.

Within the same context, the performance of 5% Fe 5% Cu-TiO_2 was investigated using a water sample collected from the River Clyde in Glasgow, United Kingdom, particularly at Kelvingrove Park in the West End on the 29th July 2024. The results showed that the highest adsorption efficiency (57%) accompanied by the highest adsorption capacity (28.5 mg/g) were observed at pH 3, and then the efficacy dropped to just 12% with an adsorption capacity of 6 mg/g at pH 11 (**Fig 3.35.f**). This low performance, similar to what was observed with tap water, may be attributed to the presence of interfering ions such as calcium, magnesium, and silicon in the water sample. These ions were identified using ICP-OES, as discussed below, and their specific effects are further examined in **Section 3.17**.

However, the applicability of this adsorbent in treating real wastewater samples (e.g., from hospitals) has not yet been investigated, as obtaining such samples is currently challenging. Using these samples would be valuable, as it would allow us to determine the actual concentration of CEF in real wastewater, understand its interactions with various interfering ions and other contaminants in the matrix, and evaluate how these factors influence adsorption efficiency. Additionally, it would help validate the proposed adsorption mechanism under realistic conditions. Therefore, this aspect should be addressed in future studies. Unfortunately, 5% Fe 5% Cu-TiO_2 retained most of its efficacy only after the first regeneration cycle, with an efficiency of 45%, which then dropped to 15% by the fourth cycle (**Fig 3.35.g**). The regeneration of the sample was undertaken *via* centrifugation, followed by mixing with 0.1 mol/L NaOH to desorb CEF from the 5% Fe 5% Cu-TiO_2 surface through the electrostatic repulsion in alkaline conditions. Subsequently, 5% Fe 5% Cu-TiO_2 was washed by DW several times until the washing became neutral (pH 7), followed by oven-drying at 110-120 °C.

3.14. ICP-OES analysis of CEF aqueous solutions

The concentration of leached iron and copper metals from 5% Fe 5% Cu-TiO_2 was measured by ICP-OES analysis to determine the effect of using them in wastewater treatment. Although the water resulting from the currently used adsorption process was not intended to be directly used for drinking, it is important to make sure that the concentration of leached iron is within the limits of the World Health Organization (WHO) for iron ions in drinking water that is 0.3

ppm. As shown in **Fig 3.36.a**, there is no actual trend in the concentration of leached iron as it fluctuated by increasing the pH from 3 up to 11, but it was within the WHO limit over the acidic conditions. In **Fig 3.36.b**, the concentration of leached copper from the same composite was decreasing by increasing the pH from 3 to 9, but it slightly increased at pH 11. Also, it has to be mentioned that the concentration of leached copper was close to the WHO limit of copper ions in drinking water that is 2 ppm except for pH 3. Therefore, it was concluded that 5% Fe 5% Cu-TiO_2 could be safely used in adsorbing CEF from wastewater in the pH range of 5 to 9.

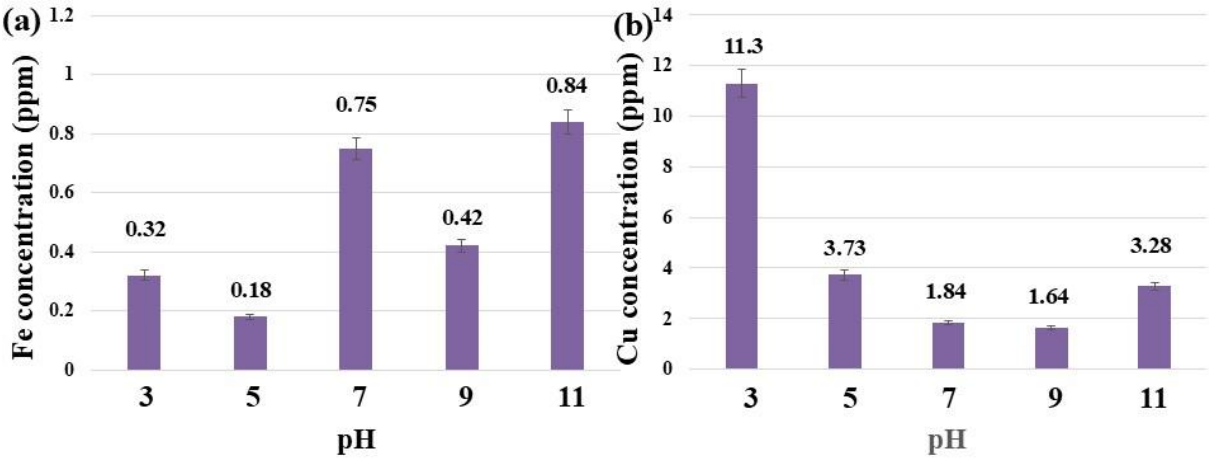

Fig 3.36. The concentration of leached iron **(a)** and copper **(b)** from 5% Fe 5% Cu-TiO_2 as determined by ICP-OES analysis. [C_o = 25 ppm, stirring rate = 800 rpm, T = 20 ± 2 °C, volume = 20 mL, and dose = 0.01 g] [202].

The DW sample and two samples from the River Clyde water, which were collected on the 29th July 2024 and the 10th February 2025, were initially screened by the ICP-OES to identify the existing elements in both samples as a background. The results indicated the high purity of DW as it only had very low concentrations of calcium and silicon (**Fig 3.37.a**), which will always be there, while low concentrations of magnesium, silicon, and other elements, and a relatively high concentration of calcium were detected in the River Clyde water samples (**Fig 3.37.b** and **c**). Therefore, the effects of calcium, magnesium, and silicon on the performance of the main adsorbents used for the removal of CEF and DOXY were investigated in the current study. The concentrations of elements found in DW remain relatively constant throughout the year.

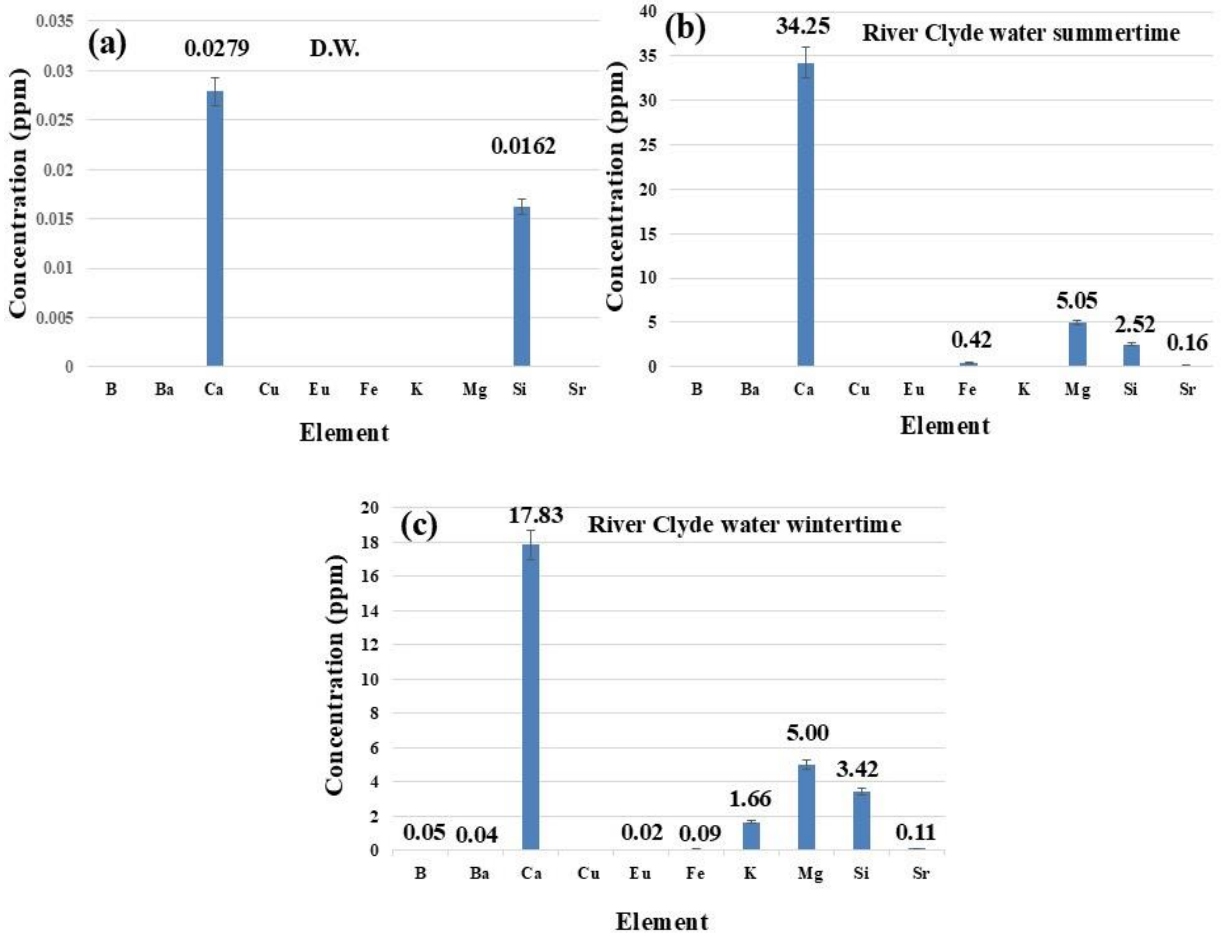

Fig 3.37. The initial screening of DW **(a)** and the River Clyde water samples collected on the 29th July 2024 **(b)** and the 10th February 2025 **(c)** using ICP-OES.

3.15. Determination of nitrate leaching from 5% Fe 5% Cu-TiO_2

High concentrations of nitrates in drinking water can cause methemoglobinemia in infants under six months of age, commonly known as blue baby syndrome. This condition occurs when nitrates are reduced to nitrites, which then react with haemoglobin in the blood to form methemoglobin, a form that cannot carry oxygen effectively. Therefore, it is essential to ensure that any nitrate leached into water remains within the WHO guideline limit of 50 ppm NO_3^-, which is equivalent to 11.3 ppm NO_3^--N [210]. Within this context, the safety of using 5% Fe 5% Cu-TiO_2 in CEF adsorption was assessed by measuring the amount of leached nitrate (NO_3^--N) in water using the salicylic acid nitration method. Upon testing nitrate leaching from freshly used 5% Fe 5% Cu-TiO_2 samples in CEF adsorption, the concentration was 0.15 ppm at pH 5 and ranged from 0 to 0.1 ppm at the remaining pH levels (**Fig 3.38.a**). Another batch of samples, which had been used and stored for a year, showed no leaching

except for 0.43 ppm and 0.27 ppm at pH 5 and pH 9, respectively (**Fig 3.38.b**). All concentrations are well below the guideline limit, indicating that 5% Fe 5% Cu-TiO_2 can be safely applied in water treatment across a wide pH range.

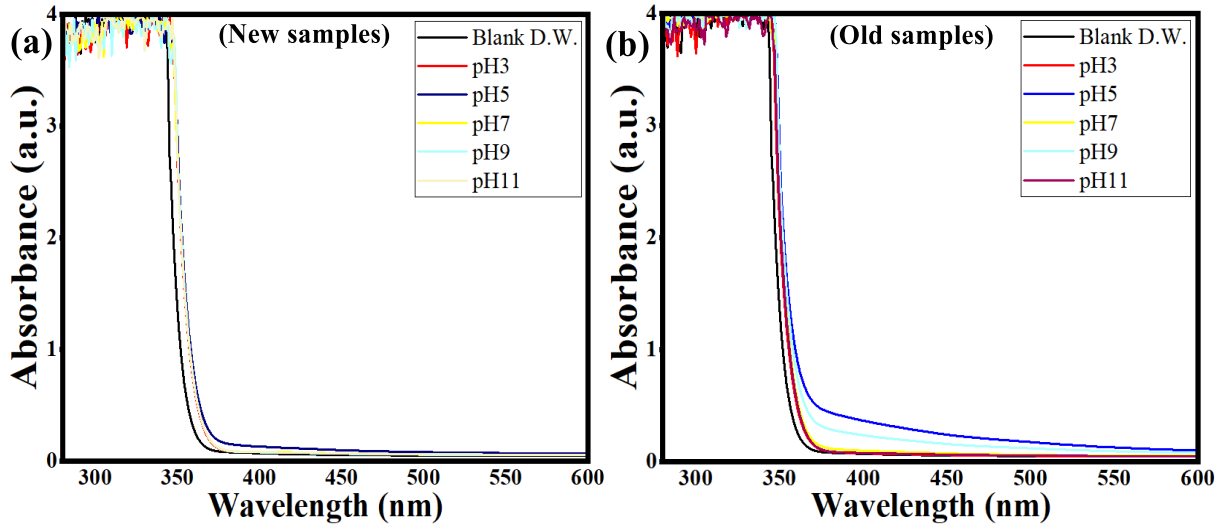

Fig 3.38. The UV-Vis spectra of the 5-nitro salicylic acid chromophore in fresh **(a)** and one year-old 5% Fe 5% Cu-TiO_2 samples **(b)** indicating very low levels of nitrate leaching from both sample sets and confirming their safe applicability in water treatment.

3.16. Adsorption mechanism of CEF by TiO_2 composites

Generally, various mechanisms contribute to pollutant removal during adsorption processes, including electrostatic attraction and coordination interactions. Additionally, hydrogen bonding between the surface hydroxyl groups of TiO_2 and functional groups in CEF such as COOH, C=O, and NH represents another possible adsorption pathway. FTIR analysis was used to further investigate the chemical adsorption of CEF on the surface of 5% Fe 5% Cu-TiO_2 experimentally. As shown in **Fig 3.39.a**, a band coressponding to C=O group stretching was detected at 1739 cm^{-1}. This group is for the β-lactam ring of CEF [254]. The spectrum of 5% Fe 5% Cu-TiO_2 showed a Ti-O peak at 1084 cm^{-1} as shown in **Fig 3.39.b**, which was almost the same after CEF adsorption as shown in **Fig 3.39.c**. However, the C=O group appeared at 1775 cm^{-1} after the adsorption indicating a possible coordination between CEF and copper ions similar to the result reported by AbouEllef *et al.* [255] who investigated the coordination of CEF and copper chloride.

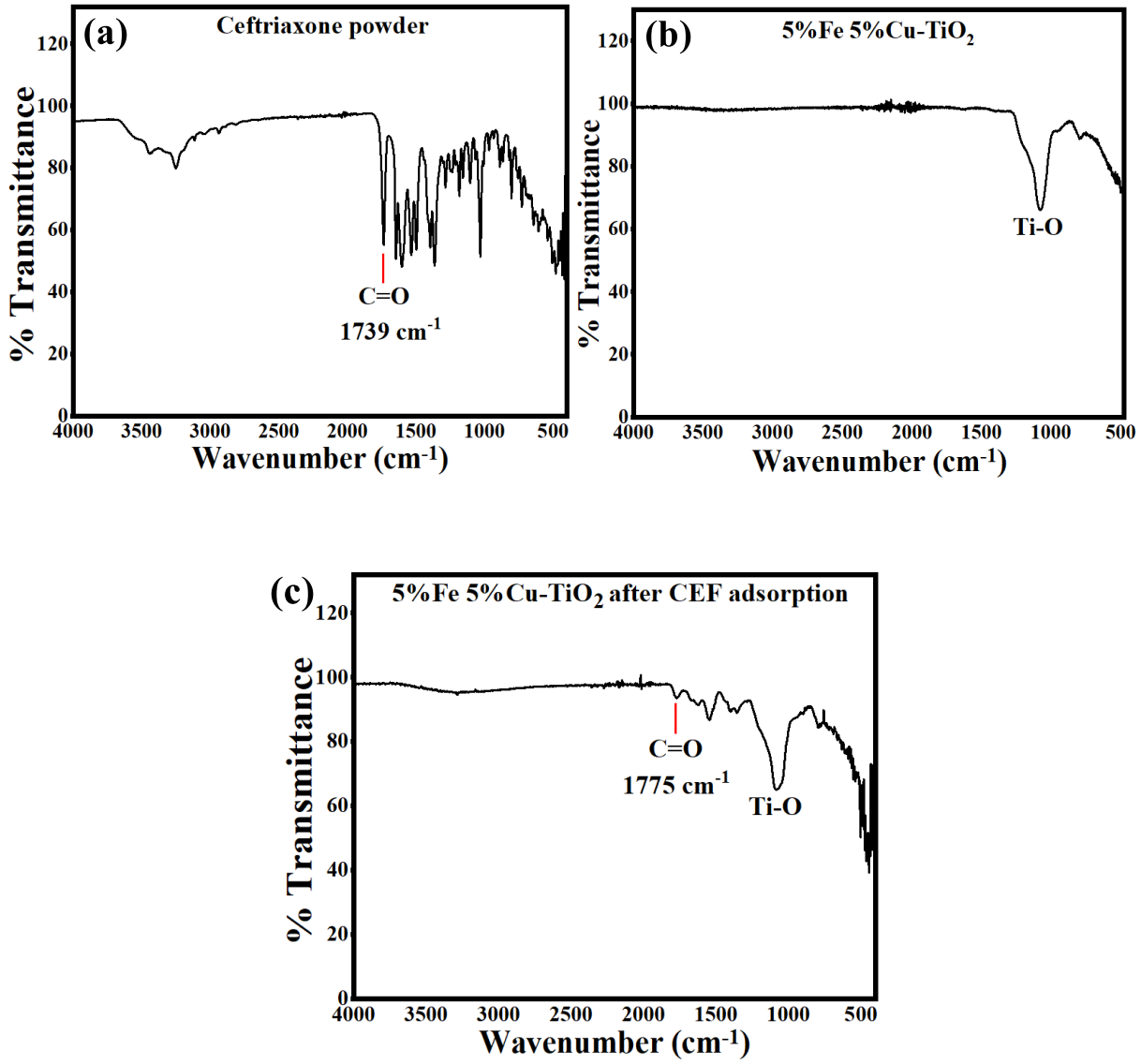

Fig 3.39. FTIR spectra of CEF powder **(a)**, 5% Fe 5% Cu-TiO_2 before **(b)**, and after CEF adsorption **(c)**.

Coordination could be contributing to the adsorption process, which is achieved by the donation of pairs of electrons from the functional groups of CEF such as the oxygen atom of the carboxylate group or the nitrogen atom of the amino group to the metals of the adsorbent acting as Lewis acidic centres. The strength of the coordinate bond can vary depending on the specific ligands and coordination environment. In general, Cu^{2+} and Fe^{3+} can have a coordination number of up to 6. So, they can coordinate with CEF as previously investigated by Refat *et al.* [256]. Furthermore, the higher charge density of Fe^{3+} compared to Cu^{2+} could result in more electrostatic attraction to the negatively charged CEF species.

In this regard, XPS was used to study the possibility of coordination or complex formation of 5% Fe 5% Cu-TiO_2 with CEF. Cu^{2+} $2p_{3/2}$ and $2p_{1/2}$ were observed at 935.0 and 954.9 eV, respectively, as shown in **Fig 3.40.a**. The two peaks shifted to 932.9 and 952.6 eV, respectively, after CEF adsorption (**Fig 3.40.b**). This result indicates the reduction of Cu^{2+} into Cu^{+} potentially because of an electron transfer from CEF to Cu^{2+}. Unexpectedly, the satellite peak, which was at 963.0 eV, disappeared after the adsorption process. This peak originates as when the Cu^{2+} stays excited, it loses some of its kinetic energy, and therefore it shows up at higher binding energy compared to the main peak. The peaks of Fe^{3+} including Fe $2p_{3/2}$ and Fe $2p_{1/2}$ were detected at 711.5 and 725.1 eV, respectively, as shown in **Fig 3.40.c**. Upon CEF adsorption, the two peaks shifted to 711.2 and 725.3 eV, respectively (**Fig 3.40.d**). Ti(IV) $2p_{3/2}$ and $2p_{1/2}$ peaks were observed at 458.5 and 464.3 eV, respectively (**Fig 3.40.e**). After CEF adsorption, both peaks very slightly shifted to 458.4 and 464.2 eV, respectively (**Fig 3.40.f**), which indicated their less likely interaction with CEF. A Ti^{0} $2p_{1/2}$ peak, possibly resulting from the reduction of Ti(IV) by X-ray irradiation during the analysis, was detected at 459.5 eV but disappeared after the adsorption process. This observation is questionable, as any reduction of Ti(IV) should be detectable either before or after the adsorption, not exclusively in one condition. No peaks were detected on **Fig 3.40.g**. However, a nitrogen (N 1s) peak was clearly observed at 399.9 eV (**Fig 3.40.h**), after CEF adsorption. This peak could be related to the protonated N of hydroxytriazinone or the protonated amine group of the aminothiazole ring. Such a result indicated the possible interaction of nitrogen with Cu^{2+} and Fe^{3+}.

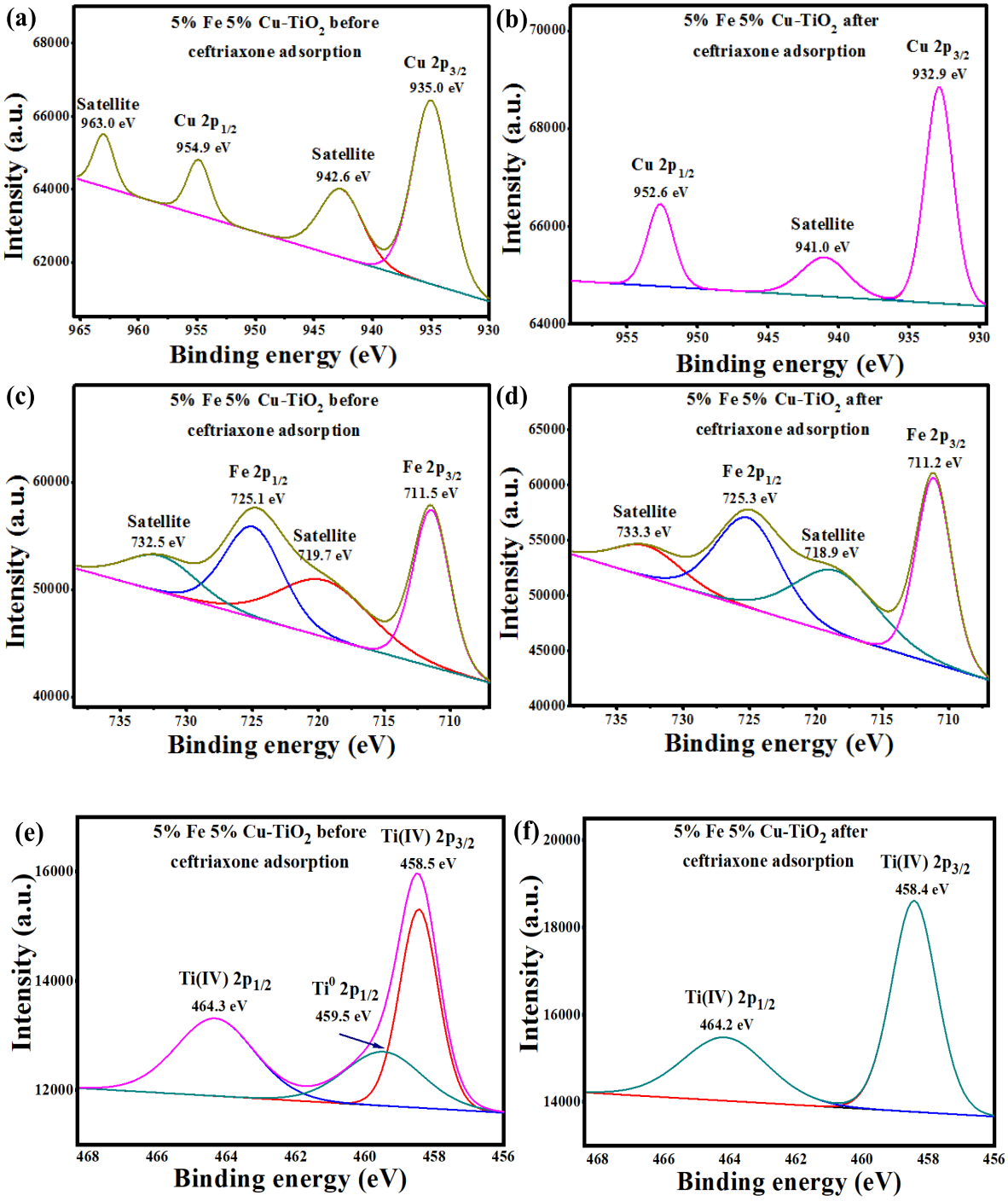
(a)
5% Fe 5% Cu-TiO2 before ceftriaxone adsorption
Satellite 963.0 eV
Cu 2p1/2 954.9 eV
Satellite 942.6 eV
Cu 2p3/2 935.0 eV
Intensity (a.u.)
Binding energy (eV)
(b)
5% Fe 5% Cu-TiO2 after ceftriaxone adsorption
Cu 2p1/2 952.6 eV
Satellite 941.0 eV
Cu 2p3/2 932.9 eV
Intensity (a.u.)
Binding energy (eV)
(c)
5% Fe 5% Cu-TiO2 before ceftriaxone adsorption
Satellite 732.5 eV
Fe 2p1/2 725.1 eV
Satellite 719.7 eV
Fe 2p3/2 711.5 eV
Intensity (a.u.)
Binding energy (eV)
(d)
5% Fe 5% Cu-TiO2 after ceftriaxone adsorption
Satellite 733.3 eV
Fe 2p1/2 725.3 eV
Satellite 718.9 eV
Fe 2p3/2 711.2 eV
Intensity (a.u.)
Binding energy (eV)
(e)
5% Fe 5% Cu-TiO2 before ceftriaxone adsorption
Ti(IV) 2p1/2 464.3 eV
Ti0 2p1/2 459.5 eV
Ti(IV) 2p3/2 458.5 eV
Intensity (a.u.)
Binding energy (eV)
(f)
5% Fe 5% Cu-TiO2 after ceftriaxone adsorption
Ti(IV) 2p1/2 464.2 eV
Ti(IV) 2p3/2 458.4 eV
Intensity (a.u.)
Binding energy (eV)

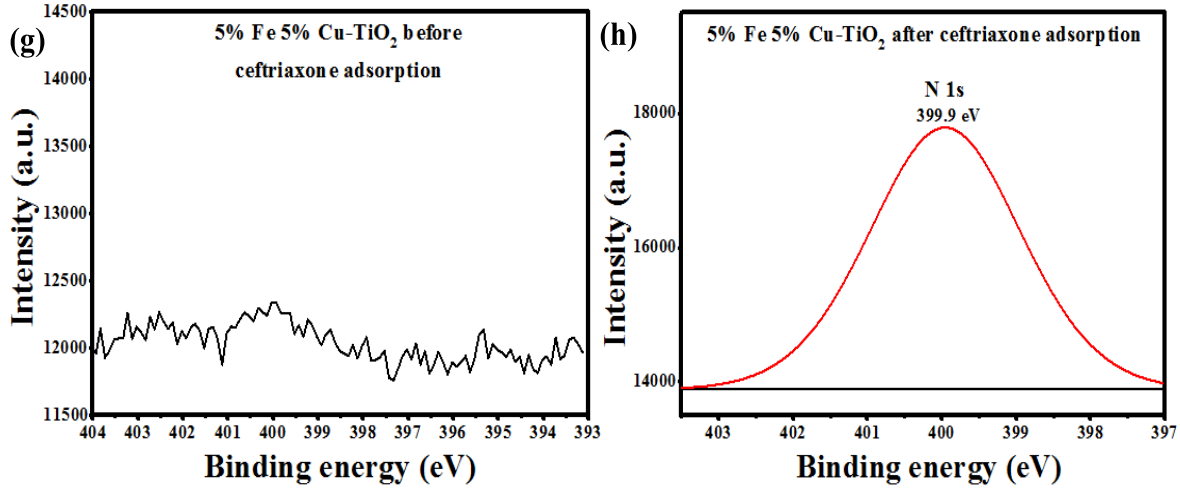

Fig 3.40. XPS spectra of 5% Fe 5% Cu-TiO_2 including Cu 2p before **(a)**, and after CEF adsorption **(b)**, Fe 2p before **(c)**, and after CEF adsorption **(d)**, Ti 2p before **(e)**, and after CEF adsorption **(f)**, N 1s before **(g)**, and after CEF adsorption **(h)**.

The CHN elemental analysis was conducted to confirm CEF adsorption by comparing the percentages of carbon, hydrogen, and nitrogen before and after the adsorption process at pH 7 using 5% Fe 5% Cu-TiO_2. As shown in **Table 3.3**, the percentages of C, H, and N before adsorption were 0.54%, 0.38%, and 0.0%, respectively. After adsorption of 25 ppm CEF, these values increased to 1.71%, 0.94%, and 0.90%, respectively, due to the presence of these elements in the CEF structure. The theoretical %C after adsorption was calculated to be 1.59% based on the adsorption efficiency of 54% (**Fig. 3.35.a**), which is close to the measured value.

For 50 ppm CEF adsorption, the theoretical %C was 2.64% according to the adsorption efficiency of 54% (**Fig. 3.35.a**), and the measured value was 2.62%. In the case of 100 ppm CEF adsorption, the theoretical %C was 4.12% based on the adsorption efficiency of 46%, (**Fig. 3.35.a**) while the measured value was 3.85%, which is also within the error range. Overall, these results confirmed the adsorption of different conecentrations of CEF onto 5% Fe 5% Cu-TiO_2.

Table 3.3. The (CHN) elemental analysis of 5% Fe 5% Cu-TiO_2 prior to and after CEF adsorption at pH 7.

Element	Atomic % of C	Atomic % of H	Atomic % of N
5% Fe 5% Cu-TiO_2	0.54%	0.38%	0.00%
5% Fe 5% Cu-TiO_2 after 25 ppm CEF adsorption	1.71%	0.94%	0.90%
5% Fe 5% Cu-TiO_2 after 50 ppm CEF adsorption	2.62%	0.89%	1.49%
5% Fe 5% Cu-TiO_2 after 100 ppm CEF adsorption	3.85%	0.94%	1.72%

Within the same context of comparing 5% Fe 5% Cu-TiO_2 before and after 50 ppm CEF adsorption, TGA analysis was performed under argon and showed a higher weight loss after adsorption (39.3%) compared to 16.5% for pristine 5% Fe 5% Cu-TiO_2. The increase factor in weight loss, calculated as 39.3% / 16.5% = 2.38, is close to the theoretical %C increase of 5% Fe 5% Cu-TiO_2 after adsorption, which is 2.64% - 0.54% = 2.10%. Therefore, this result further confirmed the adsorption of CEF.

The TGA-DSC curves (**Fig. 3.41.a** and **b**) revealed four main stages of mass loss for the sample before adsorption, occurring over approximately 16-173 °C, 173-385 °C, 385-531 °C, and 531-812 °C. Four stages were also observed after adsorption, but within slightly different temperature ranges: 20-165 °C, 165-365 °C, 365-532 °C, and 532-800 °C.

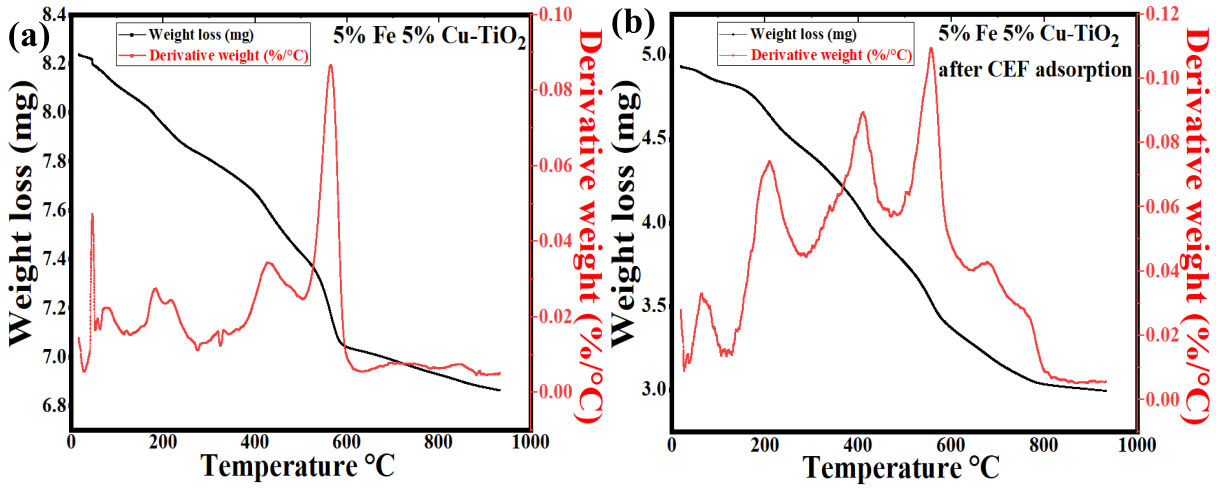

Fig 3.41. TGA and derivative weight profile of 5% Fe 5% Cu-TiO_2 prior to (**a**) and after 50 ppm CEF adsorption at pH 7 (**b**) indicating higher mass loss after CEF adsorption.

3.17. The effect of ionic strength and interfering ions

The current study explored the salting-out effect, a process where salts like NaCl are added to solutions to precipitate and separate molecules [257, 258], to assess its impact on the adsorption efficiency of 5% Fe 5% Cu-TiO_2. NaCl was specifically chosen due to the use of HCl and NaOH in adjusting the pH of CEF solutions, which results in the formation of NaCl when these solutions are combined and can increase ionic strength. The adsorption efficiency slightly fluctuated from 56% to 51% (**Fig 3.42.a**) by increasing the NaCl concentration from 0.01 M to 0.4 M at pH 7, which was selected to simulate natural conditions. This result is very close to the efficiency of 5% Fe 5% Cu-TiO_2 that was 54% without any NaCl as shown in **Fig 3.26.g**. Additionally, the control experiments using the same NaCl concentrations, conducted without the presence of an adsorbent, showed no CEF removal at pH 7 and therefore, further confirming that NaCl does not have an effect.

This study also examined the effect of ionic strength of different ions that were detected in DW and the River Clyde water samples including Ca^{2+}, Mg^{2+}, and Si(IV). **Fig 3.42.b** demonstrates that the adsorption efficiency of 5% Fe 5% Cu-TiO_2 varied in the range of 36% to 42% and generally decreased in the presence of different Ca^{2+} concentrations of 50, 100, 200, and 500 mg/L, corresponding to 1.2 mM, 2.4 mM, 4.9 mM, and 2.4 mM $CaCl_2.6H_2O$, respectively. CaO was also used as precursor of Ca^{2+}, and it resulted in a more evident drop in the adsorption efficacy as shown in **Fig 3.42.c**. This outcome may be explained by the formation of $Ca(OH)_2$ in the CEF solution according to eq. (3.1). $Ca(OH)_2$ has a low solubility (Ksp = 5.5×10^{-6} at 25 °C) and it increases the pH, which was adjusted to 7 using NaOH. Consequently, this might result in altering or disrupting the surface charges, leading to electrostatic repulsion.

$$CaO + H_2O \rightarrow Ca(OH)_2 \qquad \text{eq. (3.1)}$$

The results of both Ca^{2+} precursors are likely due to the electrostatic attraction between Ca^{2+} ions and the negatively charged 5% Fe 5% Cu-TiO_2 at pH 7 (PZC = 5.8), causing competition between Ca^{2+} and CEF for adsorption sites on the 5% Fe 5% Cu-TiO_2 surface. This result is in line with Mahmoud *et al.* [253] who reported a decline in the adsorption efficiency of CEF from about 80% to 31% in the presence of 4000 mg/L of $CaSO_4$ using a nanobentonite-nanotitania-chitosan composite.

The presence of Mg^{2+} ions in CEF solutions with concentrations ranging from 50 to 500 mg/L exhibited a slight negative effect on the adsorption efficiency as it decreased from 54% to around 50% (**Fig 3.42.d**). Similar to CaO, dissolving MgO in water led to the formation of $Mg(OH)_2$, which raised the pH and increased the electrostatic repulsion between CEF and the adsorbent, since both carried negative charges. Upon testing the effect of Si(IV) over the range of 5-100 mg/L using amorphous SiO_2, the efficiency improved to 62-65% (**Fig 3.42.e**). This improvement could be attributed to the hydrogen bonding between silanol (Si-OH) groups and CEF. This result might be related to that reported by Olusegun *et al.* [252] who used a composite of ferrihydrite and 10% silica rice husk to enhance the adsorption efficiency of ferrihydrite from 50 to 55%. The focus was on the oxide form of both Mg^{2+} and Si(IV) as it had a stronger effect on the adsorption efficiency of 5% Fe 5% Cu-TiO_2 with Ca^{2+}.

Similarly, the impact of SO_4^{2-} ions was assessed within a concentration range of 50 to 1000 mg/L, corresponding to 0.5 mM to 10 mM of Na_2SO_4. A notable decrease in adsorption efficiency was observed, with efficiency further declining to 34% as SO_4^{2-} concentration increased from 50 to 1000 mg/L (**Fig 3.42.f**). Such a result could be attributed to the effect of sodium ions in Na_2SO_4, which could be reacting with the negatively charged carboxylic group of CEF at pH 7 and resulting in the formation of sodium salts of CEF that favor being soluble more than getting adsorbed onto 5% Fe 5% Cu-TiO_2. Thus, the adsorption efficiency declined. This result is also similar to that obtained by Mahmoud *et al.* [253] who observed a reduction in the adsorption efficiency of CEF from approximately 80% to 40% in the presence of 4000 mg/L of Na_2SO_4. The control experiments of Ca^{2+}, Mg^{2+}, Si(IV), and SO_4^{2-} without using the adsorbent did not show any removal efficiency.

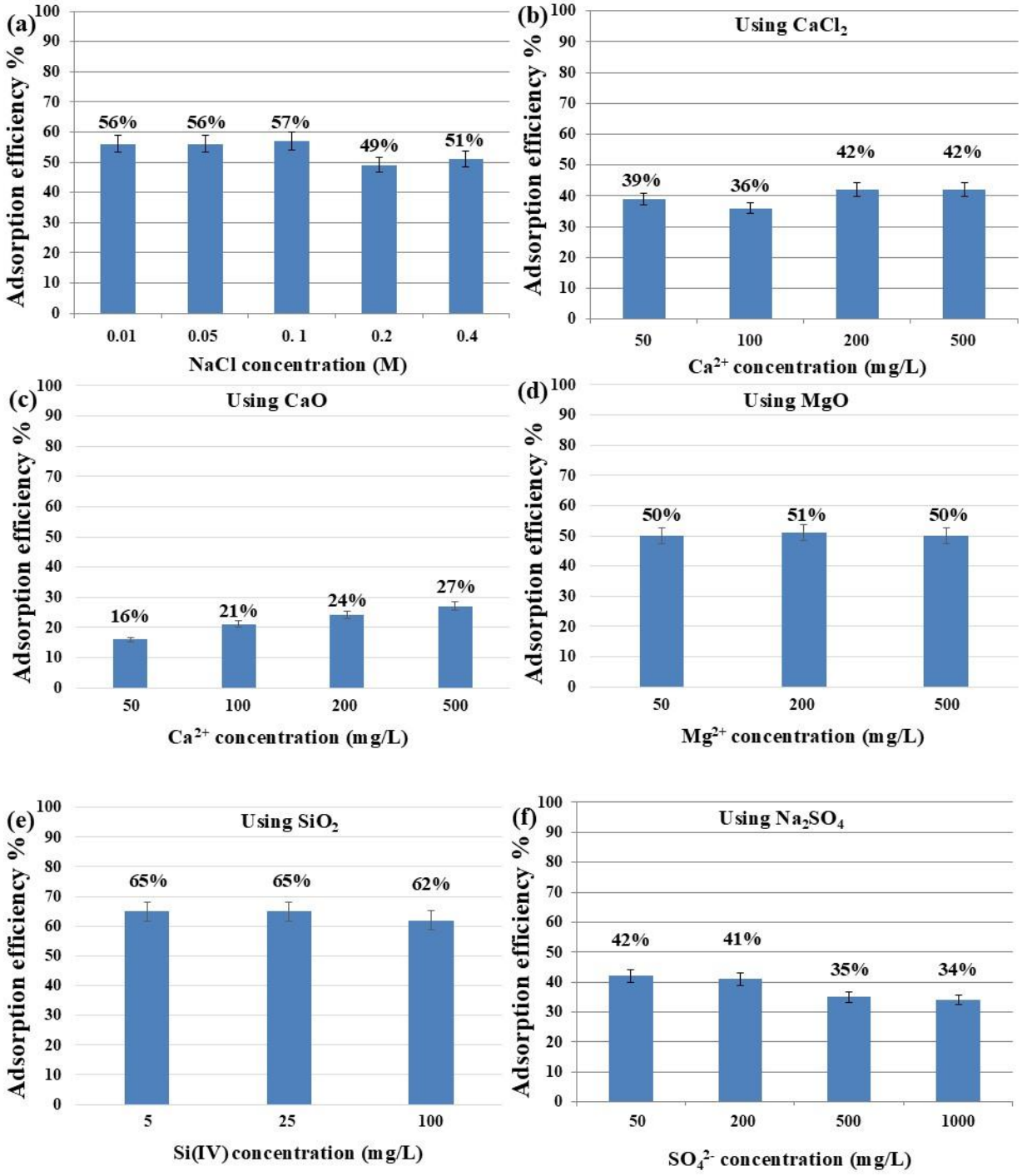

Fig 3.42. The effect of different concentrations of NaCl **(a)**, Ca^{2+} ($CaCl_2$) **(b)**, Ca^{2+} (CaO) **(c)**, Mg^{2+} (MgO) **(d)**, Si(IV) (amorphous SiO_2) **(e)**, and SO_4^{2-} **(f)** on the adsorption efficiency of 5% Fe 5% Cu-TiO_2. [C_o = 25 ppm, pH = 7, volume = 20 mL, dose = 0.01 g, stirring rate = 800 rpm, and T = 20 ± 2 °C].

3.18. The effect of temperature on the adsorption efficiency and the adsorption isotherms

No thermal degradation was observed in the control experiment of CEF at 20 °C at pH 7 (**Fig 3.43.e**) and the adsorption efficiency using 5% Fe 5% Cu-TiO_2 was 53% (**Fig. 3.43.a**). However, the CEF absorbance increased at temperatures higher than 20 °C due to evaporation (**Fig 3.43.f-h**). To account for this effect, the adsorption efficacies shown in **Fig. 3.43.b-d** were calculated relative to the absorbance of the corresponding control experiment at each temperature after 75 minutes (**Fig. 3.43.f-h**). The corrected efficacies were therefore 49%, 58%, and 62% at 25 °C, 30 °C, and 35 °C, respectively.

Despite the fluctuating adsorption trend, it could be considered an endothermic process as the efficiency generally increased by raising the temperature to 35 °C. The van't Hoff equation [259] is usually used to determine the heat of adsorption.

$$\ln K = -\frac{\Delta H\ ads}{RT} + \frac{\Delta S}{R} \qquad \text{eq. (3.2)}$$

However, plotting the points on the graph as a function of temperature was non-linear. Therefore, the value of the heat of adsorption was inaccurate and cannot be used.

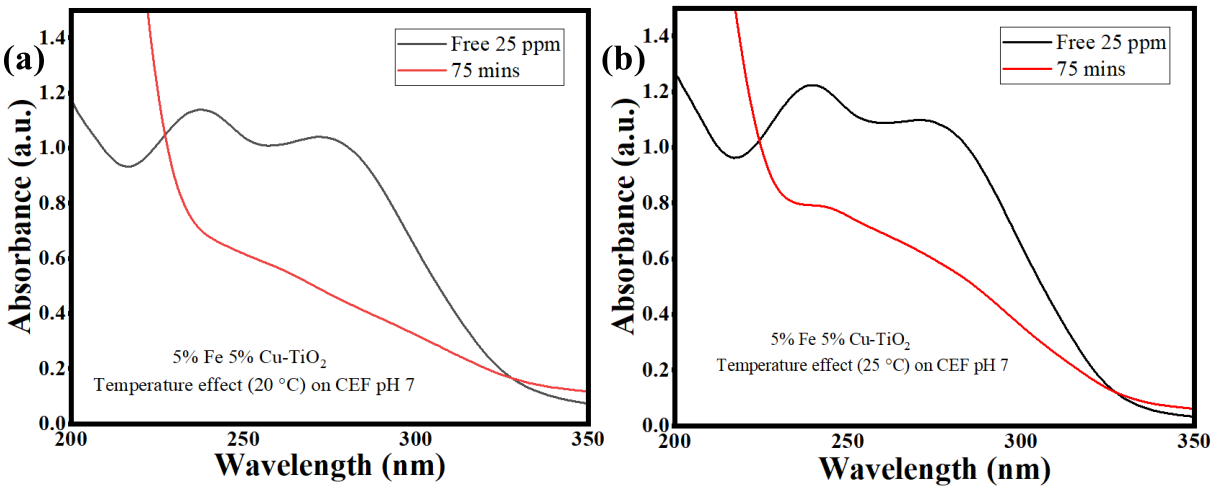

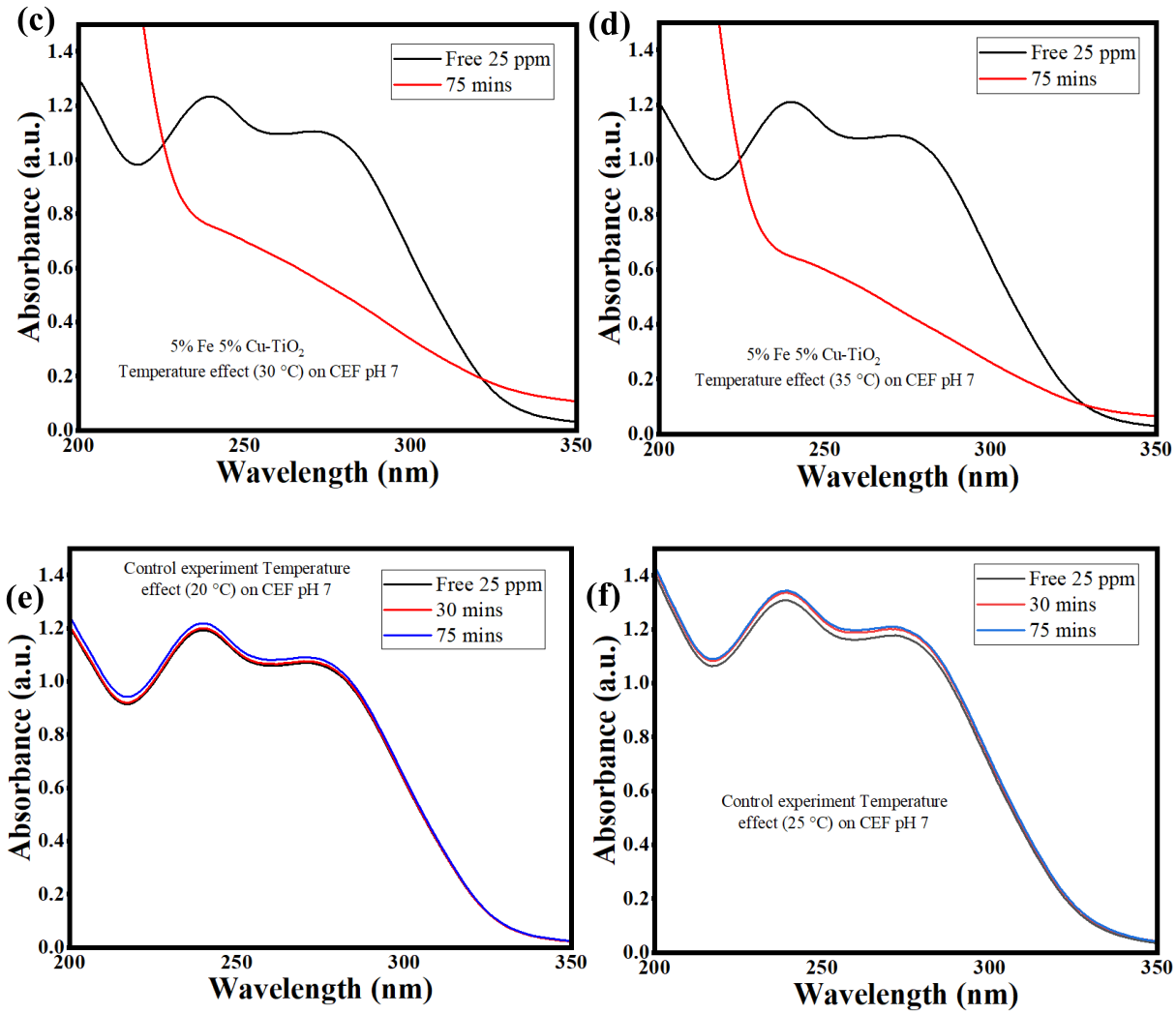
(c)
Free 25 ppm
75 mins
Absorbance (a.u.)
5% Fe 5% Cu-TiO2
Temperature effect (30 °C) on CEF pH 7
Wavelength (nm)
(d)
Free 25 ppm
75 mins
Absorbance (a.u.)
5% Fe 5% Cu-TiO2
Temperature effect (35 °C) on CEF pH 7
Wavelength (nm)
(e)
Control experiment Temperature effect (20 °C) on CEF pH 7
Free 25 ppm
30 mins
75 mins
Absorbance (a.u.)
Wavelength (nm)
(f)
Free 25 ppm
30 mins
75 mins
Absorbance (a.u.)
Control experiment Temperature effect (25 °C) on CEF pH 7
Wavelength (nm)

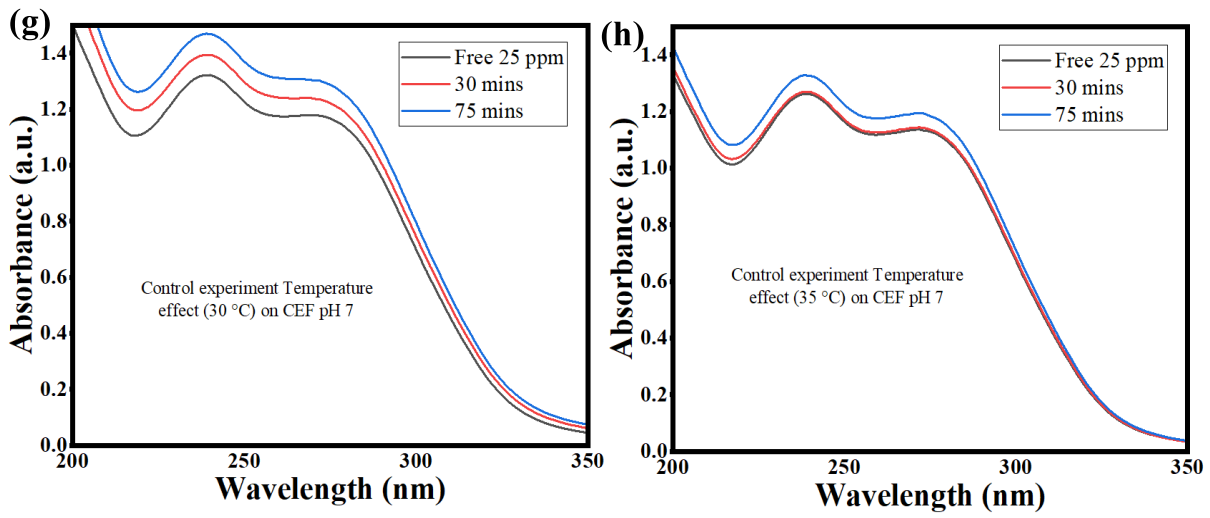

Fig 3.43. The temperature effect on the adsorption efficiency of 5% Fe 5% Cu-TiO_2 at 20 °C (**a**), 25 °C (**b**), 30 °C (**c**), 35 °C (**d**), and the control experiments at the same temperatures (**e-h**). [C_o = 25 ppm, pH = 7, volume = 20 mL, dose = 0.01 g, and stirring rate = 800 rpm].

To investigate how CEF interacts with the adsorbent, the most two common isotherm models, Langmuir and Freundlich [260], were used as they offer insights into different types of adsorption mechanisms and surface properties. The non-linear form of Langmuir equation is:

$$qe = \frac{qmax * KL * Ce}{1 + KL * Ce} \qquad \text{eq. (3.3)}$$

So, by taking the reciprocal of both sides $\frac{1}{qe} = \frac{1 + KL * Ce}{qmax * KL * Ce}$ then by splitting the numerator $\frac{1}{qe} = \frac{1}{qmax * KL * Ce} + \frac{KL * Ce}{qmax * KL * Ce}$ and then

$$\frac{1}{qe} = \frac{1}{qmax * KL * Ce} + \frac{1}{qmax}$$

so, the linear form is $\frac{1}{qe} = \frac{1}{qmax * KL} * \frac{1}{Ce} + \frac{1}{qmax}$ eq. (3.4)

which follows the straight-line equation: Y = M * X + C

where Ce is the equilibrium concentration of the adsorbate in mg/L, qe is the equilibrium monolayer adsorption capacity in mg/g, qmax is the maximum monolayer adsorption capacity in mg/g, KL is the Langmuir constant in L/mg.

By plotting 1/Ce on the abscissa and 1/qe on the ordinate, the slope and the intercept will be 1/qmax * KL and 1/qmax, respectively. To use the linear form, five CEF concentrations were used including 15, 25, 50, 75, and 100 ppm at pH 7. As shown in **Fig 3.44.a**, the adsorption capacity (qe) increased from 16 mg/g to 27, 54, 75, and 92 mg/g by increasing the concentration from 15 to 25, 50, 75, and 100 ppm, respectively. The corresponding equilibrium concentration (Ce) of these adsorption capacities was 7.05, 11.5, 23, 37.5, 54 mg/L, respectively.

These results were used in the above-mentioned Langmuir equation and also in the linear form of Freundlich equation as follows:

$$\ln qe = \ln KF + \frac{1}{n} \ln Ce \qquad \text{eq. (3.5)}$$

Which is derived by taking the ln of the non-linear form of the following equation:

$$qe = KF * Ce^{1/n} \qquad \text{eq. (3.6)}$$

where ln Ce is on the abscissa and ln qe on the ordinate, the slope and the intercept are 1/n and ln KF, respectively.

By comparing the R^2 values of both isotherm equations (**Fig 3.44.b** and **c**), it was not straightforward to determine which model better fits the experimental results as the R^2 values were very close. However, the partial better fitting of Langmuir model might indicate a homogeneous adsorption (i.e., equal distribution) [261] of CEF on the surface of 5% Fe 5% Cu-TiO_2.

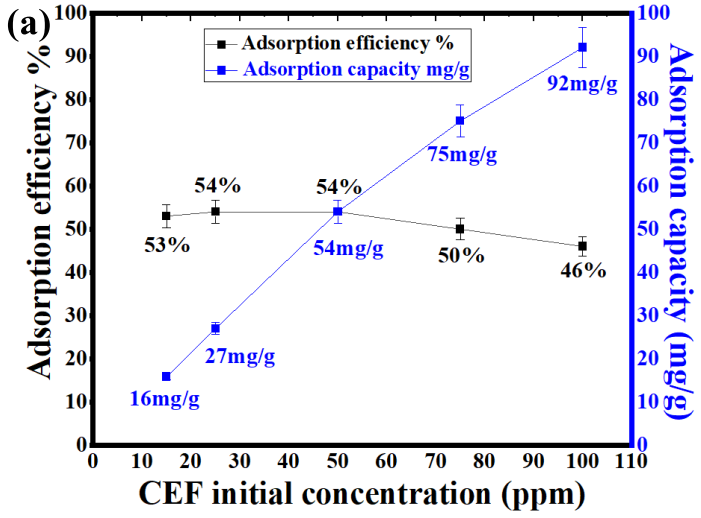

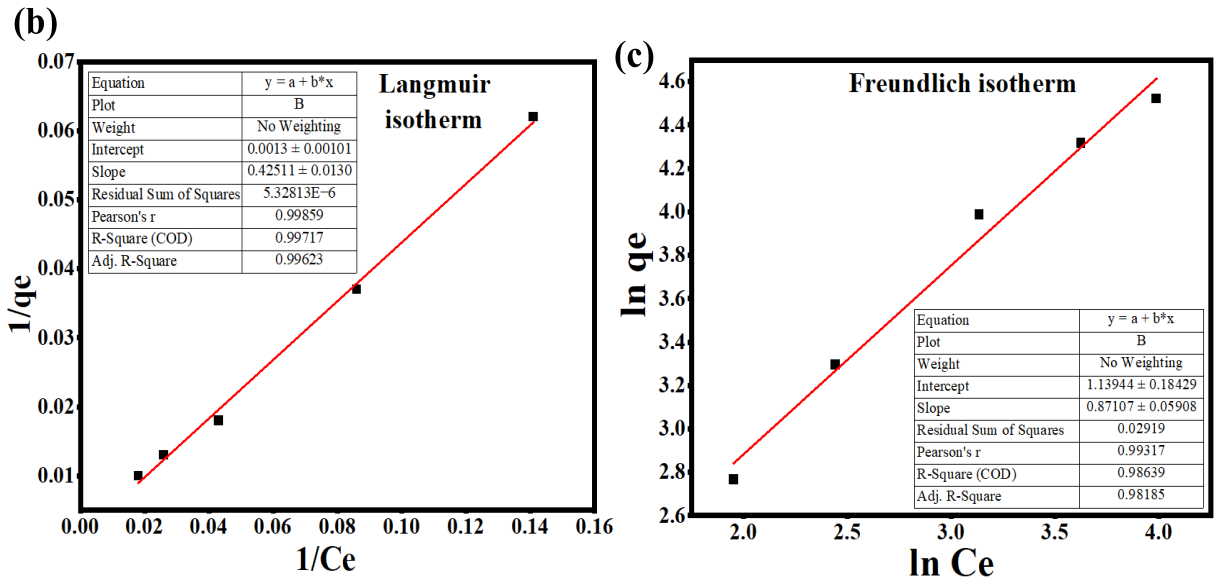

Fig 3.44. Effect of variation in initial concentration of CEF **(a),** Linear adsorption isotherm plots of Langmuir (**b**) and Freundlich (**c**) of CEF adsorption by 5% Fe 5% Cu-TiO_2. [pH = 7, stirring rate = 800 rpm, and dose = 0.01 g]. The two plots look very linear, but Langmuir isotherm model better fits the experimental results because of its slightly higher adjusted R^2 value (0.99).

3.19. The scalability and selectivity of 5% Fe 5% Cu-TiO_2

It should be noted that the mass of all adsorbents used throughout this thesis was fixed at a solid-to-liquid ratio of 0.5 g per 1 L. However, other ratios are recommended for investigation in future studies. Upon scaling the volume of CEF from 20 mL up to 100 and 1000 mL using the same concentration (25 ppm) accompanied by increasing the dose of 5% Fe 5% Cu-TiO_2 to 0.05 g and 0.5 g to keep using the same solid-to-liquid ratio, the adsorption efficacy was 29% and 25%, respectively, after 30 minutes (**Fig 3.45.a** and **b**). Such a result could be attributed to the mass transfer limitation that is induced by the excessive CEF volume. By extending the adsorption time to 60 minutes in the first case, the efficacy increased to 52%, followed by a gradual rise to 57% at 150 minutes, remaining nearly unchanged at 180 minutes and beyond. When the solution volume was 1000 mL, a longer duration, 250 minutes, was required to reach a comparable efficiency of 59%. No additional adsorption was observed beyond that time. It must also be mentioned that none of the adsorbents in the current study achieved 100% adsorption efficiency due to the establishment of an adsorption equilibrium in

all experiments. This was confirmed by the plateau observed in the kinetics experiments including the stirring rate and time effect.

To estimate the surface area required to achieve complete removal of CEF, the number of moles in solution was first calculated. The mass used in most experiments was 0.025 g (corresponding to a concentration of 25 mg/L), and with a molar mass of 554.58 g/mol, this yields 4.5×10^{-5} mol. The number of molecules was then obtained by multiplying the number of moles by Avogadro's number: 4.5×10^{-5} mol $\times$ 6.02×10^{23} = 2.7×10^{19} molecules. The area of one molecule of CEF is not available in literature. So, it has to be computed using computational chemistry models, which are not currently available within our toolbox. Thus, if we just assumed that the area of one molecule is 7.2×10^{3} Å^2. Therefore, the total molecular area of CEF in a 25 mg/L solution is 2.7×10^{19} molecules $\times$ 7.2×10^{3} Å^2 = 1.94×10^{23} Å^2 (≈ 1944 m^2). Accordingly, the surface areas of the adsorbents used in this study are inadequate and probably considered a contributing factor to the inability to achieve 100% adsorption efficiency. This is just an assumption as the actual area of a CEF molecule is currently unavailable.

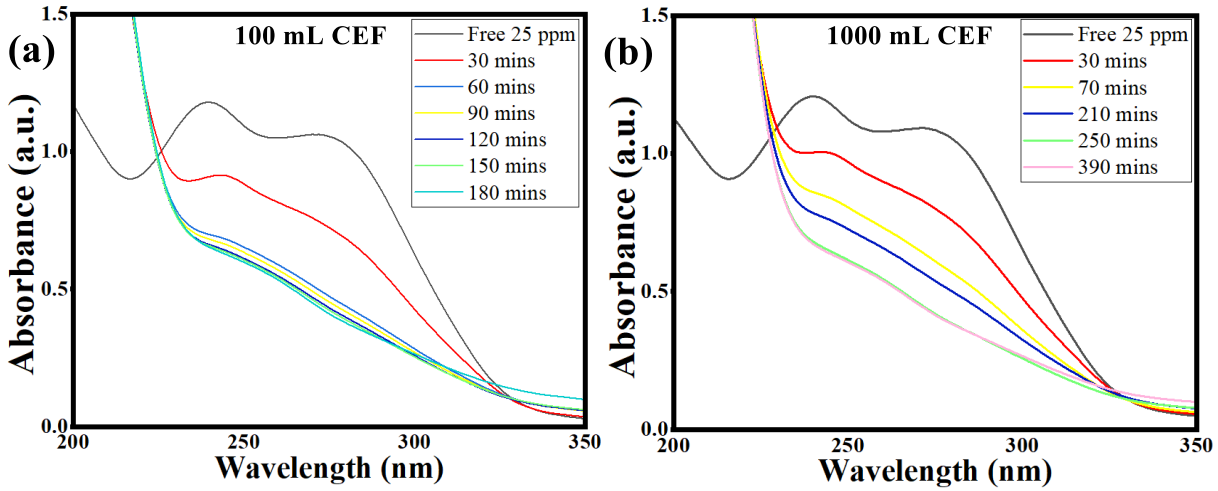

Fig 3.45. The scalability test of 5% Fe 5% Cu-TiO_2 in adsorbing CEF in 100 mL using 0.05 g (**a**) and 1000 mL using 0.5 g (**b**) using the same solid-to-liquid ratio (0.5 g/L) and the same initial concentration of CEF. [C_o = 25 ppm, pH 7, stirring rate = 800 rpm, and T = 20 ± 2 °C].

To further assess the applicability of 5% Fe 5% Cu-TiO_2 in wastewater treatment, it was tested in the removal of DOXY, and in the simultaneous removal of DOXY and CEF. As shown in **Fig 3.46.a**, the efficiency of 5% Fe 5% Cu-TiO_2 in removing DOXY was improving by

increasing the pH as it was 81% at pH 11. This result is related to the electrostatic repulsion between the adsorbent and the positively charged DOXY at pH 3, whereas the self-degradation of DOXY in alkaline conditions (**Fig 3.46.b**) along with the synergistic effect of the metals used with TiO_2 particularly at high pH levels enhanced the removal efficiency in these conditions. The control experiment with copper nitrate showed DOXY removals of 20% at pH 9 and 38% at pH 11 (**Fig 3.46.e**), whereas iron nitrate caused an increase in absorbance, similar to its effect on CEF.

The self-degradation of DOXY is discussed in detail in Chapter 4, and the results were consistent across multiple capsule packs. A similar trend was observed upon removing DOXY in the presence of CEF. It was expected to observe low removal efficiency when the two antibiotics coexist because they interfere with each other and compete over the adsorption sites of 5% Fe 5% Cu-TiO_2. However, the removal efficiency of DOXY was better at pH 7 and 9 in the presence of CEF. This result could be attributed to the higher percentage of DOXY self-degradation at pH 9, but there is no clear justification of what happened at pH 7.

It was not possible to determine the adsorption efficiency of CEF in this binary system because the UV peak of CEF overlapped with that of DOXY in the range of 241-271 nm, whereas the peak at 375 nm was used to work out the removal efficiency of DOXY (**Fig 3.46.c** and **d**). In addition, the chromatographic parts of the LC-MS spectra were not that useful in solving this issue as the calculated adsorption efficiencies did not match the efficiencies of the UV-Vis spectra. For example, the adsorption efficiency of DOXY in the presence of CEF was about 50% and 27% at pH 3 and pH 5, respectively, using the chromatographic results shown in **Fig 3.47.a-d**, whereas the UV-Vis spectra showed 7% and 17%, respectively. So, as previously mentioned, the LC-MS results cannot be accurately used for quantification. The results of the other pH levels, which did not also match those of the UV-Vis spectra, along with the mass spectra of these LC-MS results are shown in **Fig S3** and **Fig S4**, respectively, in **Appendix 2**.

Based on the demonstrated applicability of 5% Fe 5% Cu-TiO_2 in removing two antibiotics and its promising scalability results, it can be concluded that this adsorbent holds potential for use in wastewater treatment plants. However, further investigations involving other pollutants are necessary to gain deeper insight into its practical applicability.

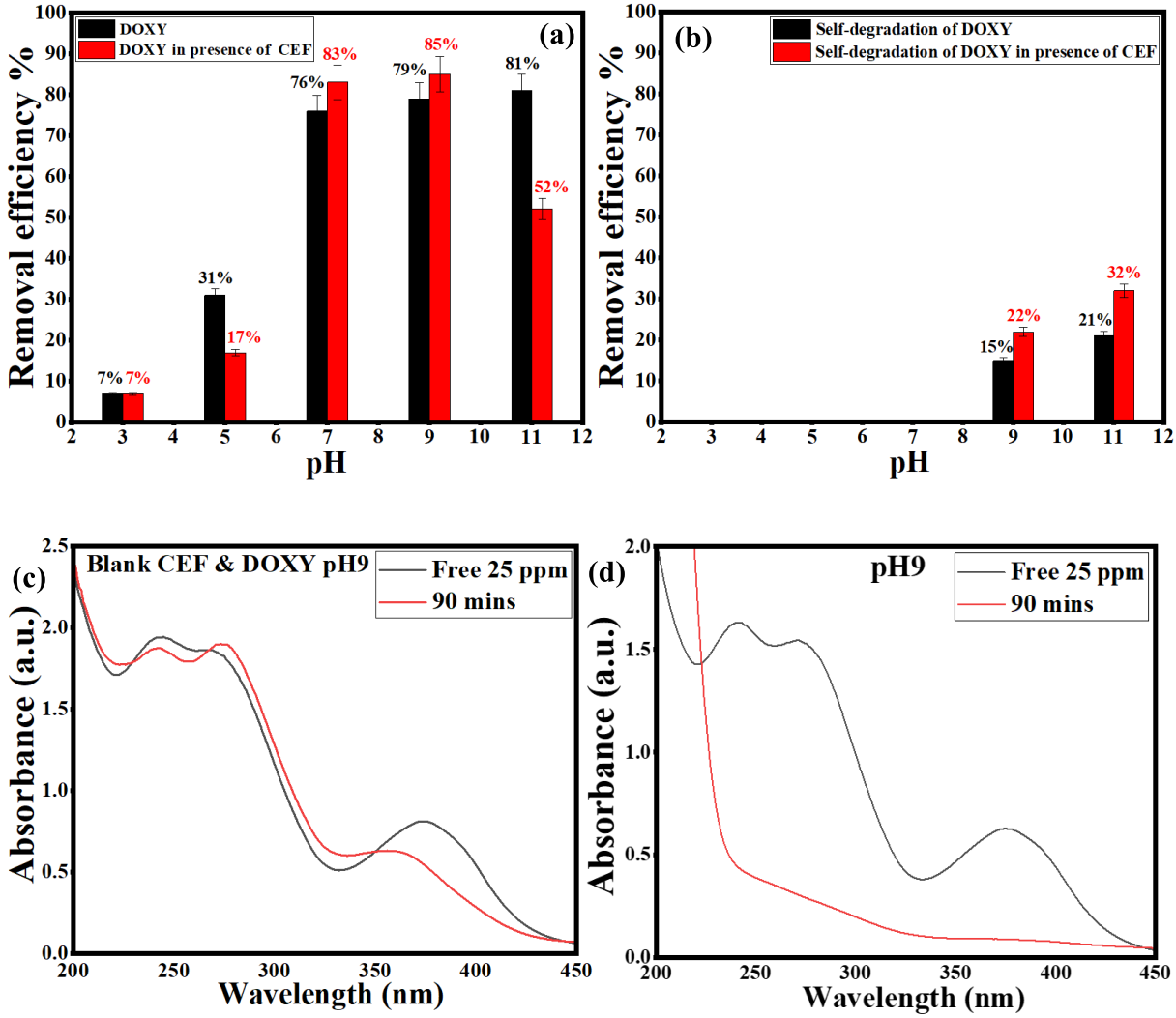
(a)
DOXY
DOXY in presence of CEF
Removal efficiency %
pH
7%
7%
31%
17%
76%
83%
79%
85%
81%
52%
(b)
Self-degradation of DOXY
Self-degradation of DOXY in presence of CEF
Removal efficiency %
pH
15%
22%
21%
32%
(c)
Blank CEF & DOXY pH9
Free 25 ppm
90 mins
Absorbance (a.u.)
Wavelength (nm)
(d)
pH9
Free 25 ppm
90 mins
Absorbance (a.u.)
Wavelength (nm)

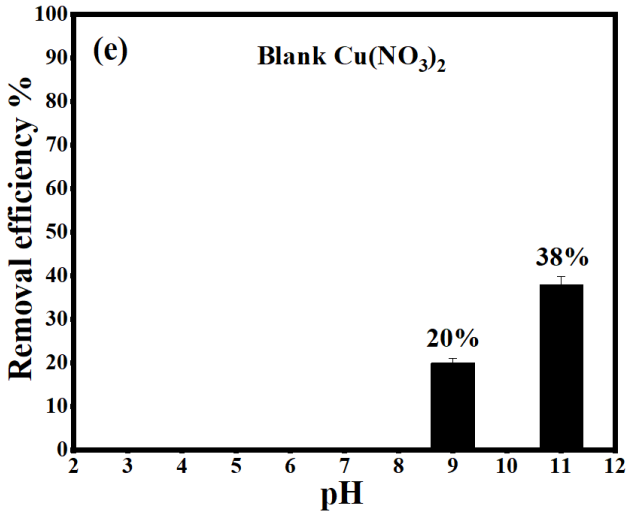

Fig 3.46. The removal efficiency of 5% Fe 5% Cu-TiO_2 toward DOXY in single-batch mode and in presence of CEF (**a**), the self-degradation of DOXY and in presence of CEF (**b**), the UV-Vis spectrum of the control experiment of DOXY & CEF at pH 9 (**c**), the spectrum of the actual experiment at pH 9 (**d**), and the control experiment of copper nitrate with DOXY (**e**) after 90 minutes. [C_o = 25 ppm, volume = 20 mL, dose = 0.01 g, stirring rate = 800 rpm, and T = 20 ± 2 °C].

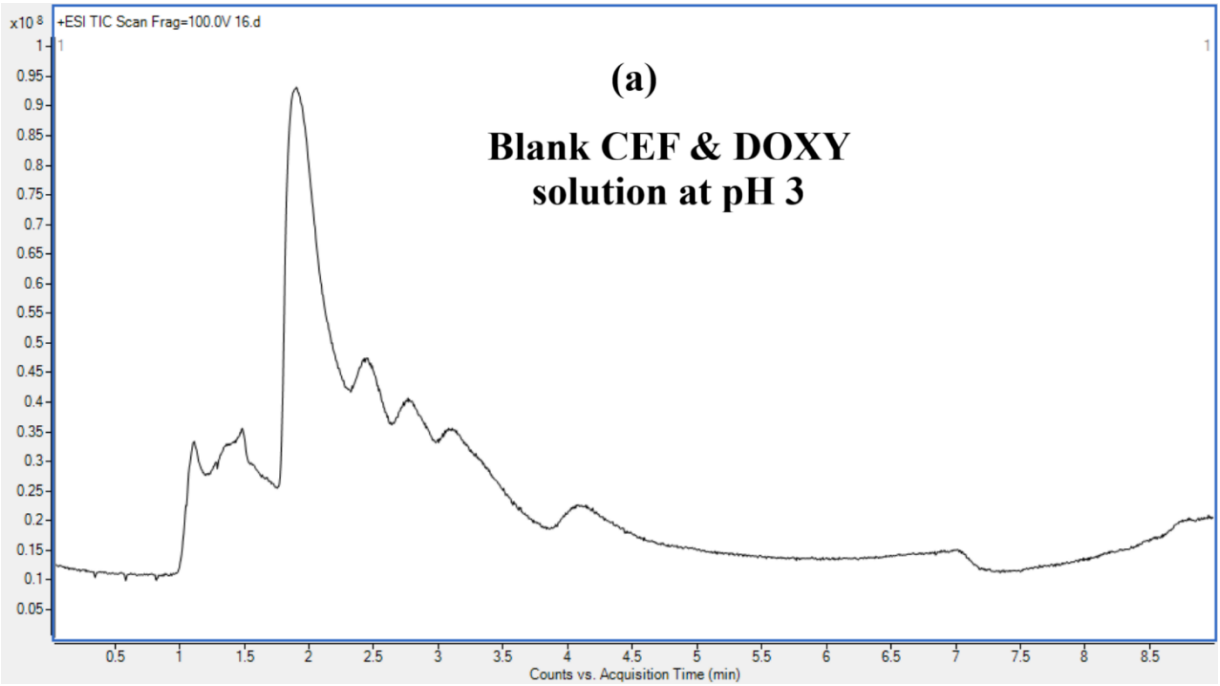

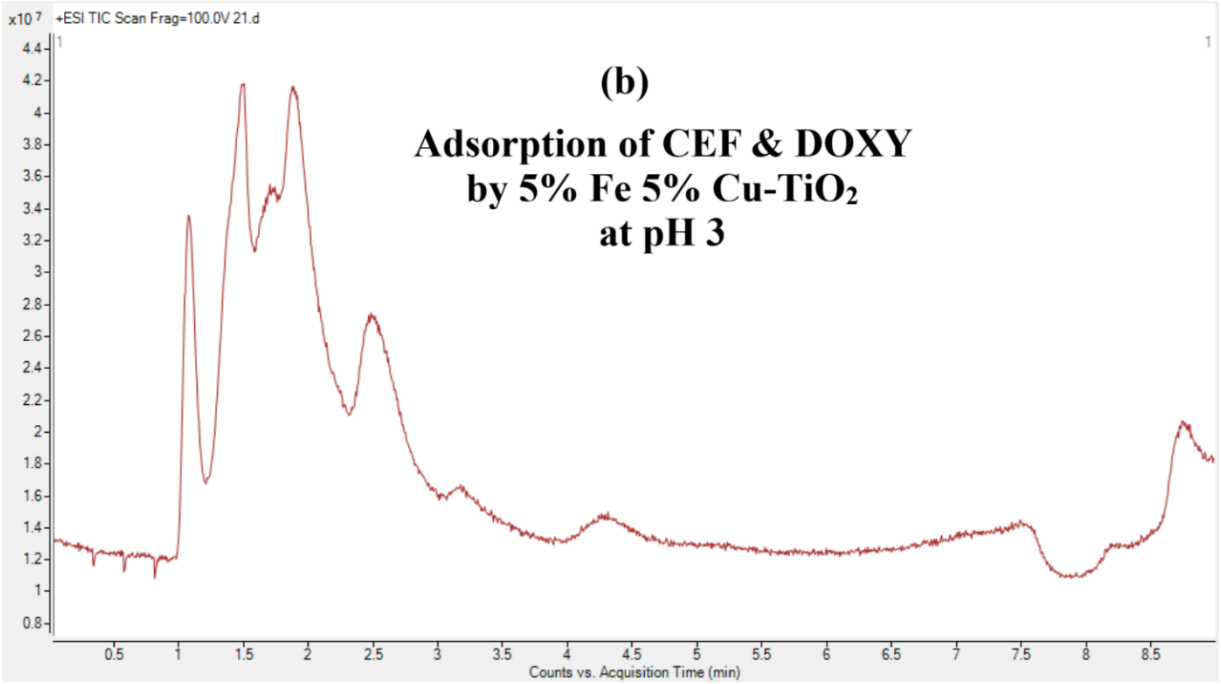
x10 7
+ESI TIC Scan Frag=100.0V 21.d
(b)
Adsorption of CEF & DOXY
by 5% Fe 5% Cu-TiO2
at pH 3
Counts vs. Acquisition Time (min)

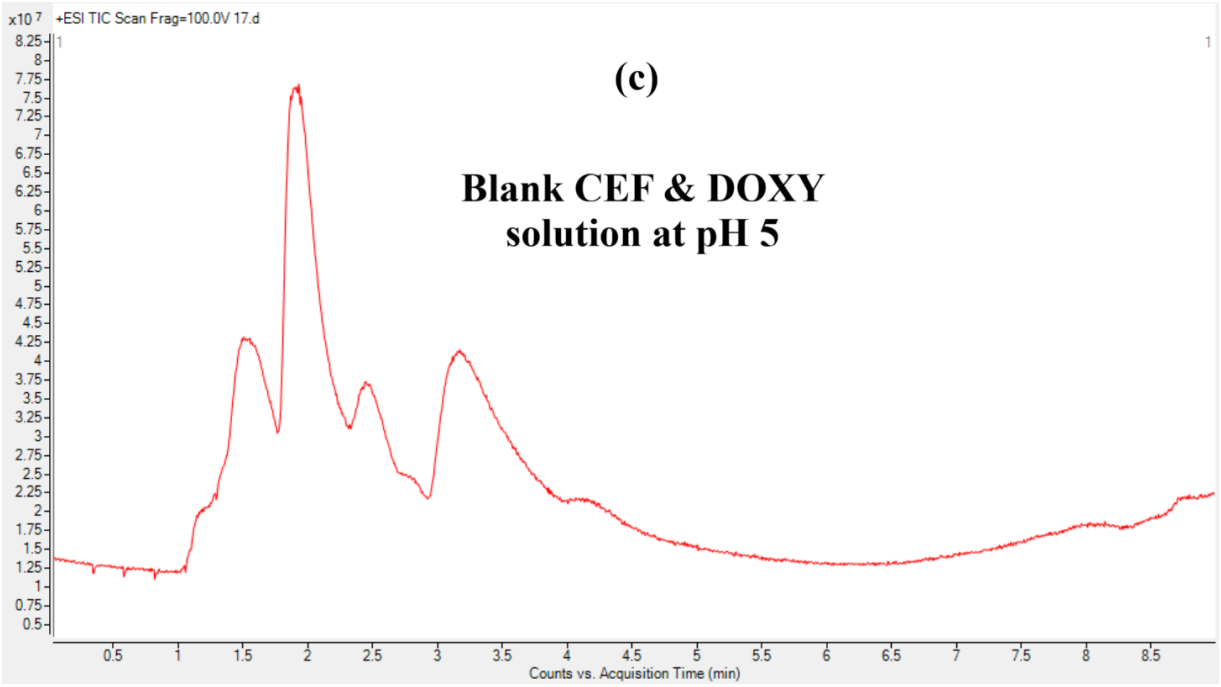
x10 7
+ESI TIC Scan Frag=100.0V 17.d
(c)
Blank CEF & DOXY
solution at pH 5
Counts vs. Acquisition Time (min)

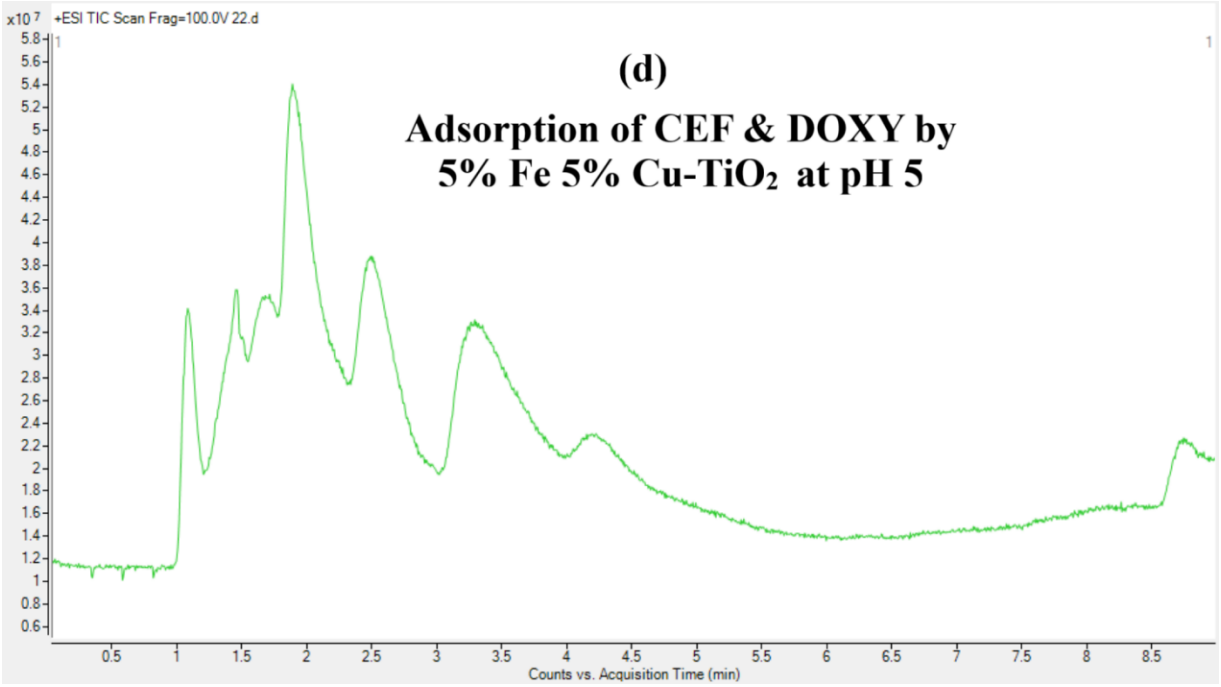

Fig 3.47. The chromatographic parts of the LC-MS spectra of blank CEF and DOXY solutions at pH 3 (**a**), pH 5 (**c**), and the same solutions but after the adsorption using 5% Fe 5% Cu-TiO_2 at the same pH levels with the same order (**b**, and **d**) after 90 minutes. [C_o = 25 ppm, volume = 20 mL, dose = 0.01 g, stirring rate = 800 rpm, and T = 20 ± 2 °C].

3.20. The economic analysis of producing TiO_2 and 5% Fe 5% Cu-TiO_2

Producing TiO_2 and 5% Fe 5% Cu-TiO_2 was a simple procedure developed on a laboratory scale, eliminating the need for high levels of technology or extensive labour. Thus, expenses associated with labour wages, taxes, maintenance, and management were not considered in this very rough calculation. The main factors in calculating the production cost of one gram of any material include the prices of the used chemicals, water, and electricity charges in January 2024.

Regarding the chemical cost required to produce one g of TiO_2 by the alkali roasting method would be approximately £ 1.01 and the calculation is as follow: 2.50 liters of H_2SO_4 cost £ 40.30 [262], so the used 10 mL in the current study are £ 0.16. 500 g of CaO currently cost £ 66.20 [263], so the 5 g used in this study were £ 0.66. 500 g of Na_2CO_3 cost £ 19.10 [264], so the used 5 g were for £ 0.19. The chemicals' prices were available on the suppliers official websites. In addition, an average of 10 L of water was estimated to be used for washing, neutralizing, and extracting TiO_2 would cost £ 0.06 based on the charges of the Scottish Water

company [265]. Furthermore, the average cost of the total number of hours of using the electric furnaces and ovens in this work was approximately £ 0.62 [266]. Therefore, the total cost of producing one g of TiO_2 by the alkali roasting method would be around £ 1.69.

For the production cost of one gram of TiO_2 by the acid baking method, it would be the same as the alkali roasting method, but without CaO and Na_2CO_3, so the total cost of this method was about £ 0.84. The cost of chemicals used in modifying one g of TiO_2 extracted using the acid baking method by 5%Fe 5%Cu would be just £ 0.06. In detail, 500 g of $Fe(NO_3)_3{\cdot}(H_2O)_9$ cost £ 46.60 [267], so 5% of iron contained in 0.36 g of this salt based on using 1 g of TiO_2 was £ 0.03. 500 g of $Cu(NO_3)_2{\cdot}(H_2O)_3$ cost £ 90.37 [268], so 5% Cu based on using 1 g of TiO_2 is equivalent to 0.19 g of this salt, which cost about £ 0.03. Thus, the total cost of producing 1 g of 5% Fe 5% Cu-TiO_2 would be around £ 0.90.

The cost of 50 g of commercial TiO_2 (P25) was £ 78.6 [269], so 1 g cost about £ 1.57. Therefore, by comparing the costs of commercial TiO_2 by that extracted using the acid baking method and its composite (5% Fe 5% Cu-TiO_2), it is apparent that these two materials were cheaper and with higher adsorption efficiency confirming their economic potential.

3.21. Conclusions

Based on the obtained results, adsorption presents an effective and environmentally safer alternative for the removal of CEF compared to UV-induced degradation, which may generate potentially toxic products such as NO and SO_2. These gases are converted into nitrites and sulfates in aqueous environments. Consequently, these nutrients can promote eutrophication, leading to algal blooms and a reduction in dissolved oxygen levels, which adversely affects aquatic species that are sensitive to such changes. The lab-prepared TiO_2 demonstrated promising performance and was more efficient than commercial TiO_2 (P25), likely due to its higher surface area. Impregnating the lab-prepared TiO_2 with different percentages of Fe, Zn, Co, Ni, and Cu ions led to a substantial improvement in adsorption performance. This enhancement was attributed to the formation of metal hydroxide precipitates, which promoted the co-precipitation of CEF onto these hydroxide phases, resulting in improved removal efficiency.

EDX along with XRD analyses revealed a potentially purer crystalline phase composition in TiO_2 extracted using the acid baking method compared to the alkali roasting method, which correlated with improved adsorption efficiency. The TiO_2 derived from Chinese red mud via the former method showed promising results, generally outperforming its commercial counterpart (P25) as well as the TiO_2 extracted from the Indian RM7 and RM8 samples. Therefore, it was selected to be thoroughly investigated in this chapter. Different percentages of iron and copper ions were used in impregnating TiO_2 to improve its adsorption efficiency and among them, 5% Fe 5% Cu-TiO_2 was shown to be the best adsorbent as it resulted in adsorbing more than 50% of CEF species across most of the pH scale. None of the adsorbents in the current study achieved 100% adsorption efficiency due to the establishment of an adsorption equilibrium in all experiments as confirmed by the plateau observed in the kinetics experiments including the stirring rate and time effect. In addition, the low surface area of these adsorbents could be considered another contributing factor to the inability to achieve 100% adsorption efficiency.

The proposed removal mechanism involved electrostatic interactions, hydrogen bonding, complexation, and a synergistic effect between TiO_2 and the metal salt precursors through the metal hydroxide precipitates, in addition to self-degradation observed with only two α-Fe_2O_3 samples specifically at pH 3. The negative effect of the calcination on the performance of 5%

Fe 5% Cu-TiO_2 was confirmed. The applicability of this material for the removal of DOXY, particularly under neutral and alkaline conditions, was also validated, either in the absence or presence of CEF. Moreover, 5% Fe 5% Cu-TiO_2 was successfully scaled up, achieving 59% adsorption of CEF from a 1000 mL solution after 250 minutes.

Regarding the safety parameter of applying metal nitrate precursors in adsorbing CEF species, ICP-OES analysis revealed that the leaching of iron and copper ions from 5% Fe 5% Cu-TiO_2 is in alignment with the WHO standards under various conditions; specifically at pH 5. Additionally, the salicylic acid nitration method confirmed that all leached nitrate concentrations were well below the guideline limit. Moreover, a simple very crude economic analysis confirmed the economic efficiency of TiO_2 and 5% Fe 5% Cu-TiO_2 produced by the acid baking method compared to the commercial TiO_2.

Chapter 4

4. Exploring the applicability of red mud-derived TiO_2 and α-Fe_2O_3 in the removal of doxycycline

4.1. Introduction

Tetracyclines (TCs) are among the most frequently used and commercially available antibiotics worldwide, valued for their broad antimicrobial activity against both human and animal diseases and affordability [270]. They are either extracted from *Streptomyces* species or produced through semi-synthetic modifications of natural compounds. First identified in the 1940s, tetracyclines are effective against a diverse range of pathogens, including both Gram-positive and Gram-negative bacteria, as well as organisms like *Chlamydia*, *Mycoplasma*, and certain protozoa [271]. TCs derive their name from their structure, which consists of four (*tetra*-) interconnected hydrocarbon rings (-*cycles*-) [270]. TCs have also been used at subtherapeutic doses in animal feed to enhance growth in livestock, poultry, and aquaculture [272]. This extensive use raises significant concerns, as it can contribute to the development of antibiotic resistance in gut microbiota and lead to the presence of drug residues in food products, and the surrounding environment [273]. Therefore, the removal of DOXY, a member of the TCs family, is investigated in this chapter.

Continuing with the investigation of red mud, particularly the Chinese sample, α-Fe_2O_3 was extracted from red mud, and it is used in the removal of DOXY in this chapter. TiO_2, which was extracted from the same red mud by the acid baking method, is explored and compared to α-Fe_2O_3. The formation of different species of DOXY by changing the pH of the solution is clarified. Additionally, the factors contributing to the removal of DOXY along with the possible degradation products of DOXY are detailed. Economic and environmental considerations of extracting α-Fe_2O_3 from red mud are also covered.

4.2. Powder XRD analysis of red mud-derived α-Fe_2O_3

The powder XRD pattern of pristine red mud (**Fig 3.2.a**) showed the presence of various mineral components, including calcite, goethite, gibbsite, haematite, quartz, sodalite, and titania. The absence of these mineral peaks in the pattern of red mud-extracted α-Fe_2O_3 (**Fig 4.1**) compared to that of red mud-extracted TiO_2 using the acid baking method, which is in the anatase phase (**Fig 3.2.c**), along with the very well-defined reflections of α-Fe_2O_3 indicated the

better crystallinity and extraction of α-Fe_2O_3 from red mud compared to that of TiO_2. This observation agreed with the EDX results (**Fig 4.6**), which indicated a high percentage of iron and a low percentage of titanium in red mud-extracted α-Fe_2O_3 and also in red mud-extracted TiO_2, which was reported in Chapter 3. In the same context, the similarity between the powder XRD patterns of red mud-extracted α-Fe_2O_3 (**Fig 4.1**) and commercial α-Fe_2O_3 (**Fig 3.1.a**) is higher than that of red mud-extracted TiO_2 (**Fig 3.2.c**) and commercial TiO_2 (P25) (**Fig 3.1.d**) patterns. The powder XRD pattern of red mud-derived α-Fe_2O_3 shows the main peaks at 2θ ranges of 24.14°, 33.18°, 35.63°, 40.94°, 49.52°, 54.02°, 57.68°, 62.45°, 64.08°, 72.21°, and 75.50° that correspond to the (012), (104), (110), (113), (024), (116), (018), (214), (300), (119), and (220) reflections, respectively, [JCPDS Card No. 33-0664]. The domain size of this sample is 20 nm, which is less than that of the other hematite samples reported in Chapter 3, indicating the lower crystallinity of this sample. Such a result could be attributed to the presence of impurities in the red mud derived-α-Fe_2O_3 that can disrupt the long-range order of α-Fe_2O_3 crystallite. This pattern is similar to the one reported in [274] that also extracted α-Fe_2O_3 from red mud. The other unknown reflections in **Fig 4.1** could be related to impurities from red mud.

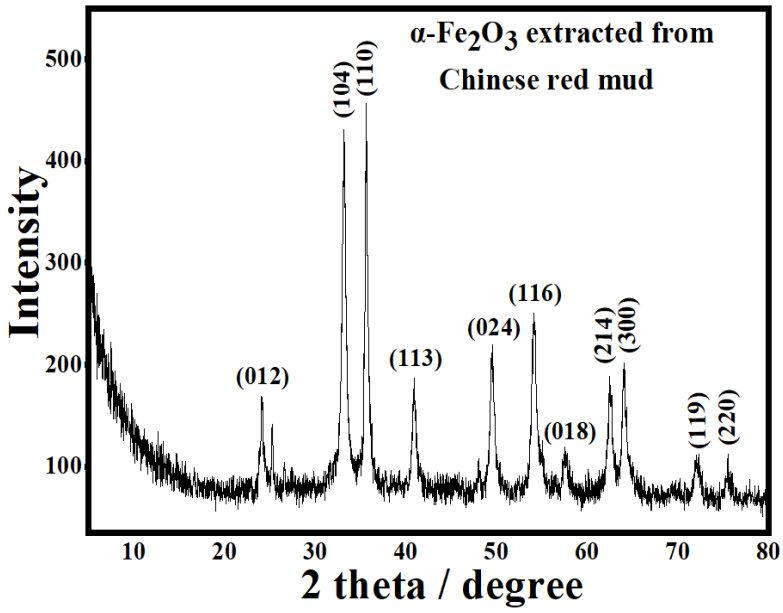

Fig 4.1. Powder XRD pattern of red mud-derived α-Fe_2O_3 with a domain size of 20 nm showing the main reflections similar to those observed in commercial α-Fe_2O_3.

4.3. Investigating the efficiency of red mud, red mud-extracted TiO_2 and α-Fe_2O_3, and commercial TiO_2 and α-Fe_2O_3 in adsorbing DOXY species

According to previously published studies including [275], it is well known that DOXY has three dissociation constants (pKa) as presented in **Fig 4.2** due to the presence of various functional groups such as hydroxyl, ketone, and amino groups. Therefore, DOXY mainly exists in a cationic form (positively charged) at pH ≤ 3 (pKa1 = 3.02) where the dimethyl amine group is protonated (**Fig 4.3**). This assumption was supported by the measured zeta potential as it was 7.6 mV at pH 3 (**Fig 4.4.a**).

The amine group is unlikely to protonate at pH ≤ 3 because of its resonance with the ketone group. Then the hydroxyl group, which is the closest one to the amine group, starts to deprotonate at pH 3.02 resulting in the appearance of a negative charge. The resonance of pKa1 moiety results in the delocalization of this charge. Therefore, positive and negative charges are coexisting on DOXY surface (Zwitterionic form) up to pH less than 7 as indicated by the very low surface charge of 0.2 mV, which is almost zero at pH 5 in **Fig 4.4.b**.

Adjusting the pH to 7, which is close to pKa2 (7.97), leads to the deprotonation of the phenolic OH group and the emergence of an additional delocalized negative charge on the moiety associated with pKa2, resulting in the anionic form of DOXY with a net negative charge. This was indicated by the measured zeta potential that was -15.0 mV at pH 7 (**Fig 4.4.c**).

Further increasing the pH to 9 and beyond, pKa3 (9.15), results in the deprotonation of dimethyl amine group and causing the net surface charge to become more negative as the zeta potential was -18.5 mV (**Fig 4.4.d**) and -26.4 mV (**Fig 4.4.e**) at pH 9 and pH 11, respectively. **Fig 4.3** presents a detailed proposal for the speciation of DOXY at different pH levels along with the corresponding net surface charge. A similar speciation diagram proposed by Álvarez-Esmorís *et al.* [276], shown in **Fig 4.5**, supports the validity of the current study's proposal. Nevertheless, this is merely a proposed mechanism of DOXY speciation derived from the literature and zeta potential results, and it may not fully represent the actual processes occurring during the removal of DOXY.

pKa3 = 9.15

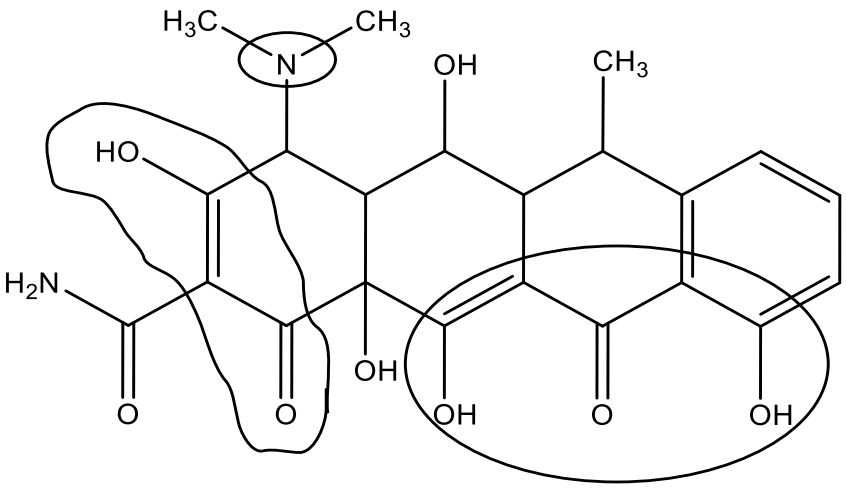

pKa1 = 3.02 **pKa2 = 7.97**

Chemical formula of doxycycline: $C_{22}H_{24}N_2O_8$

Fig 4.2. The structure of DOXY species showing its three dissociation constants (pKa) at pKa1 = 3.02, pKa2 = 7.97, and pKa3 = 9.15.

pKa3 = 9.15

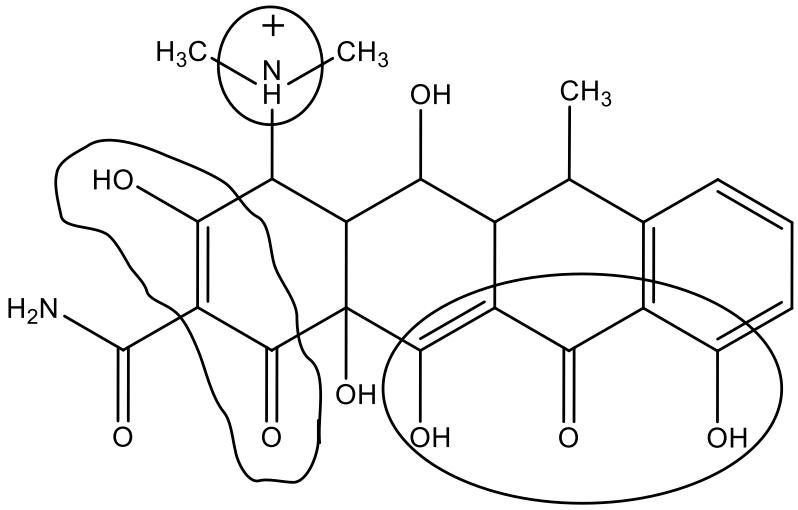

pKa1 = 3.02 **pKa2 = 7.97**

Doxycycline at pH ≤ 3.02 and the overall charge is positive (Cationic form)

pKa3 = 9.15

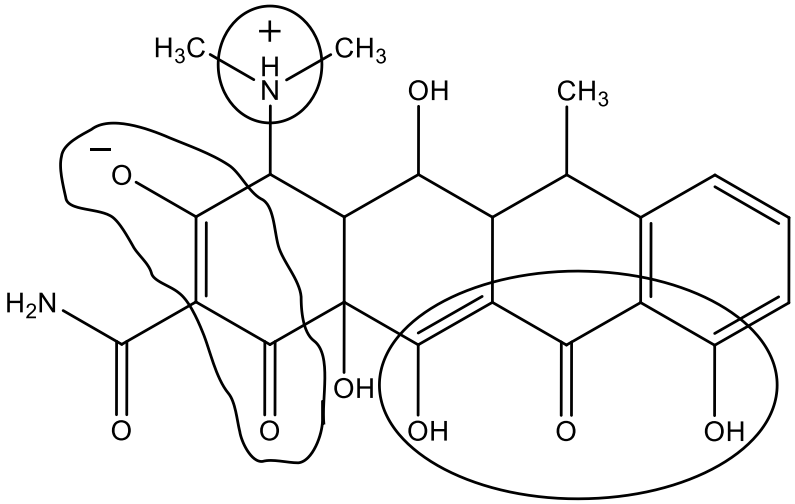

pKa1 = 3.02 **pKa2 = 7.97**

Doxycycline at 3.02 < pH < 7 and the overall charge is 0 (Zwitterionic form)

pKa3 = 9.15

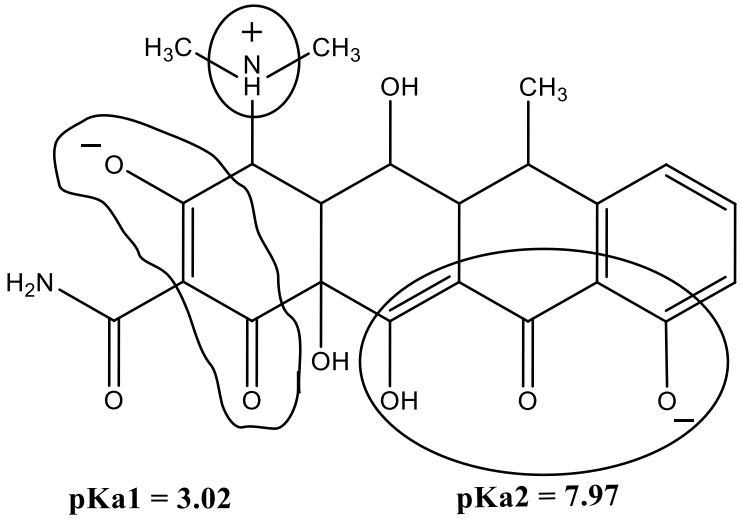

pKa1 = 3.02 **pKa2 = 7.97**

Doxycycline at 7 ≤ pH ≤ 9.15 and the overall charge is negative (Anionic form)

pKa3 = 9.15

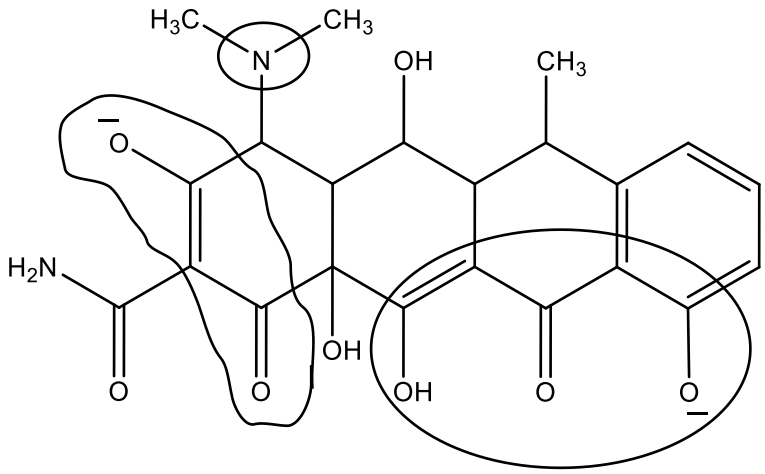

pKa1 = 3.02 **pKa2 = 7.97**

Doxycycline at pH ≥ 9.15 and the overall charge is more negative (Anionic form)

Fig 4.3. Proposed speciation of DOXY structures at different pH levels to show the net positive charge (cationic form) at pH ≤ 3, the Zwitterionic structure at 3.02 < pH < 7, the net negative charge (anionic form) at 7 ≤ pH ≤ 9.15, and the more negative charge (anionic form) at pH ≥ 9.15.

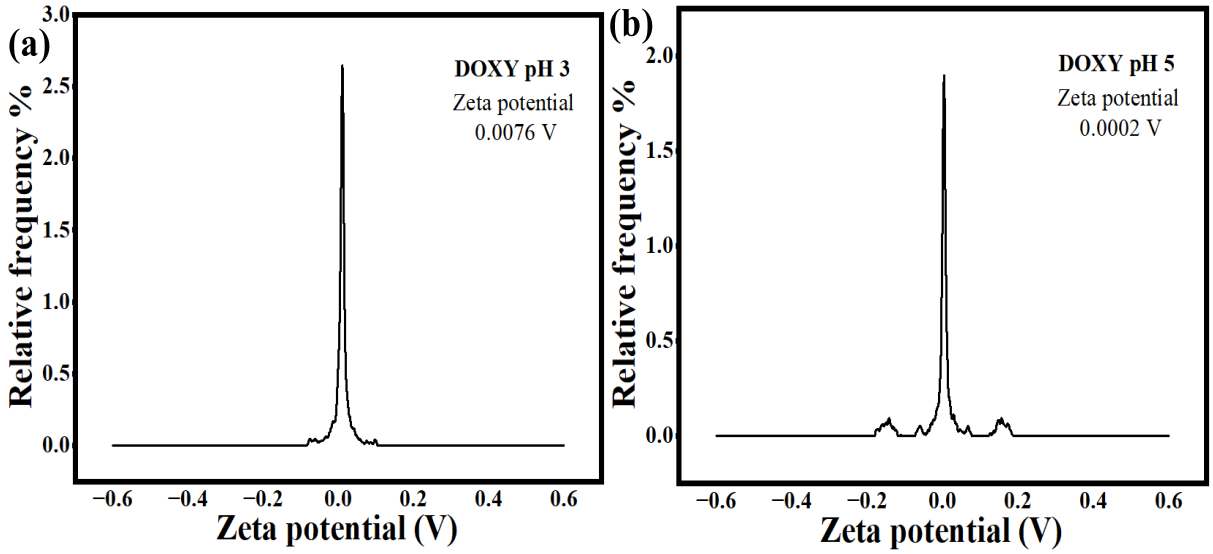

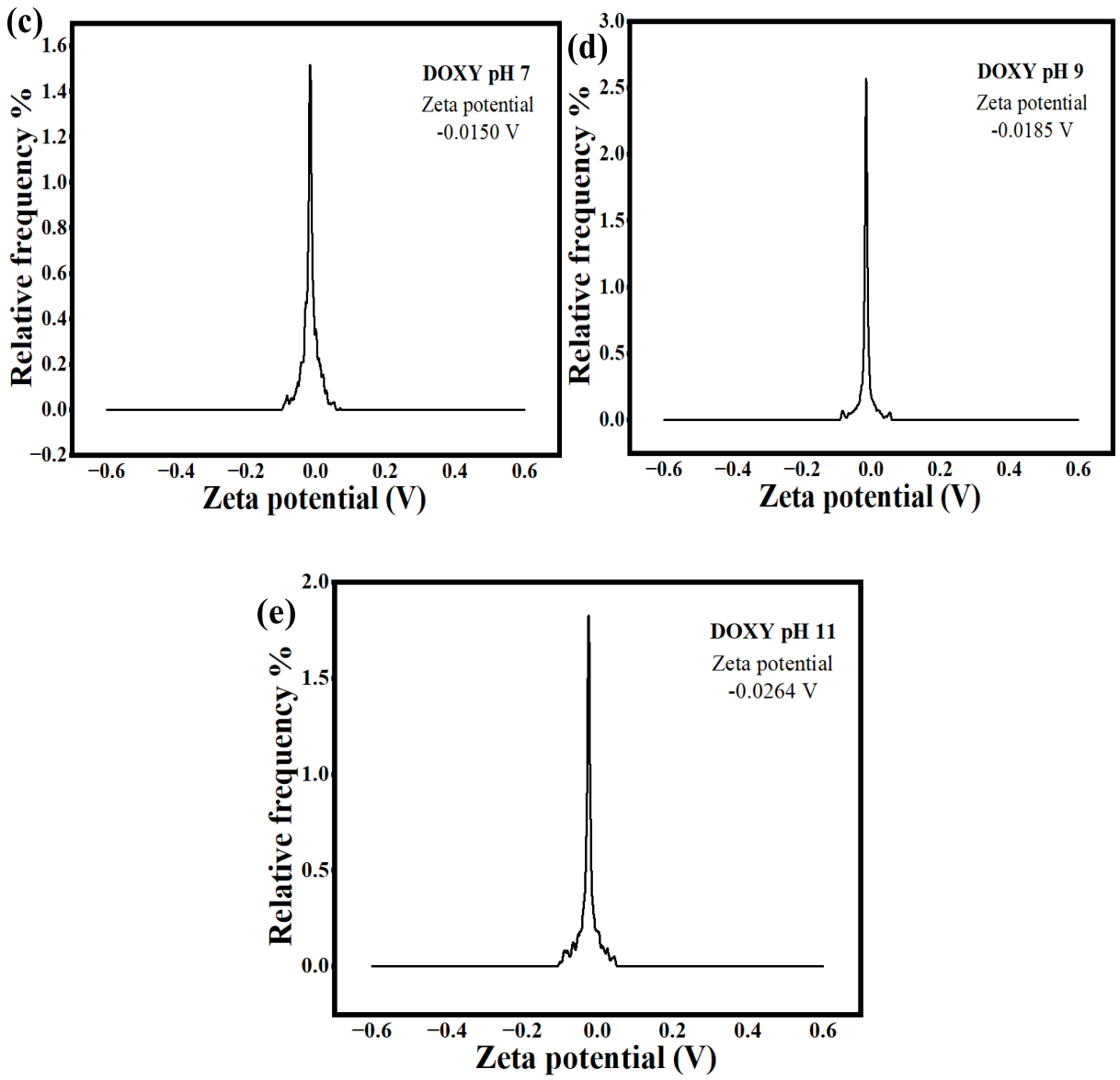

Fig 4.4. Zeta potential measurements of aqueous solutions of DOXY with a net positive charge (7.6 mV) at pH 3 due to the protonation of the nitrogen atom of the dimethyl amine group (**a**), an almost zero charge (Zwitterionic from -0.2 mV) at pH 5 because of the deprotonation of the hydroxyl group (**b**), a net negative charge of -15.0 mV at pH 7 due to the deprotonation of the phenolic OH group (**c**), a more negative charge (-18.5 mV) at pH 9 resulting from the deprotonation of the nitrogen atom (**d**), and -26.4 mV pH 11 (**e**).

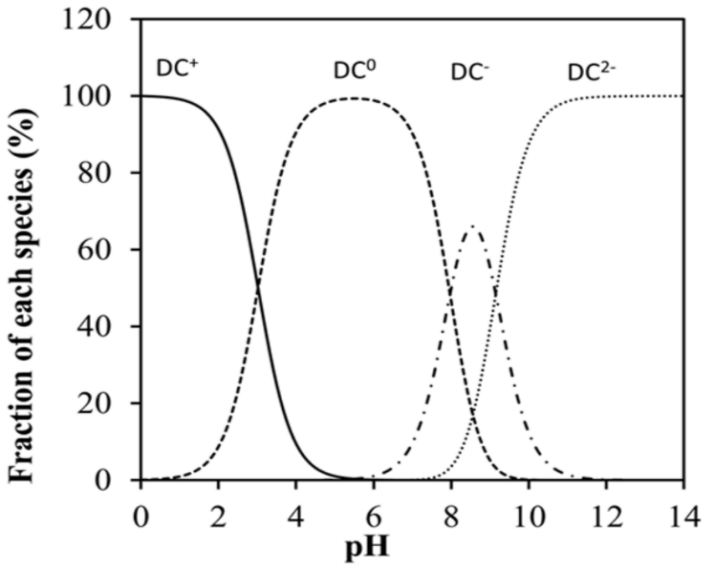

Fig 4.5. The speciation of DOXY as a function of pH [276] showing the change of the overall surface charge of DOXY species from the cationic to the Zwitterionic and then to the anionic form by increasing the pH of the solution.

The removal efficiency of raw red mud, P25, and commercial α-Fe_2O_3 was evaluated as a control to assess the performance of red mud-extracted materials relative to their commercial counterparts. The highest removal efficiency of red mud was observed at pH 5 (**Fig 4.7.a**), where DOXY predominantly exists in its Zwitterionic form. This result indicated that the electrostatic interaction between Zwitterionic DOXY and positively charged red mud, which has a PZC of 7.4 (**Table 4.1**), is the main mechanism of DOXY removal.

Regarding the commercial and the red mud-extracted TiO_2, their PZCs were relatively low (4.9 and 4, respectively). However, both exhibited their highest removal efficiency at pH 7 (**Fig 4.7.b** and **d**). This could be attributed to the potential formation of hydrogen bonds between the surface hydroxyl groups of the two adsorbents and the functional groups of DOXY (e.g., amine or amide groups). The absence of error bars in **Fig 4.7.b** is due to the irreproducibility of the adsorption results of P25; the displayed efficiencies represent the highest values recorded for this material. However, the lowest values were 0%, 18%, 20%, 15%, and 5% at pH 3, 5, 7, 9, and 11, respectively.

The commercial α-Fe_2O_3, which has a PZC of 6.5, showed its highest efficacy at pH 7 (**Fig 4.7.c**), likely due to its ability to form hydrogen bonds with DOXY. In contrast, red mud-derived α-Fe_2O_3, with a PZC of 6.7, demonstrated good performance across a wide pH range

(**Fig 4.7.e**), indicating its ability to remove DOXY via the multiple mechanisms described above. Despite the electrostatic repulsion at high pH levels between the above-mentioned adsorbents and DOXY, they were still able to remove DOXY. Such a result could be attributed to the self-degradation of DOXY under alkaline conditions, which accounted for 15% and 21% degradation at pH 9 and pH 11, respectively, after 90 minutes (**Fig. 4.6.a-b**). With extended reaction time, self-degradation continued, reaching 62% at pH 9 after 8 days and 52% at pH 11 after 7 days of stirring. A slight increase in absorbance was observed at both pH values after 9 days; however, by leaving the solutions without stirring for 14.5 months, the degradation progressed further, reaching 81% and 86% at pH 9 and pH 11, respectively. This could be considered a slight progression in such a very long time (14.5 months).

The wavelength of the second main UV peak of DOXY is around 350 nm in acidic and neutral conditions, but it increases to about 375 nm in alkaline conditions. As shown in **Fig. 4.8.a**, the UV peak of DOXY shifted from 350 to 375 nm as the pH drifted from 7 to about 8 due to the alkalinity of red mud. During the self-degradation, pH 11 and pH 9 drifted to lower values and fluctuated between 8.6-9 and 7.5-8, respectively. This explains the shift of the UV peak to a shorter wavelength after 90 minutes, and the subsequent fluctuation over the following days in wavelength in both cases. This is because DOXY is acidic, and no buffer solution was used to keep the pH constant. The adsorption experiments were run for 90 minutes beyond which no further removal was observed (**Fig. 4.8.a-d**). Both red mud and P25 exhibited lower removal efficiencies than the self-degradation of DOXY at pH 9 and pH 11, which may be attributed to interference between the materials and DOXY.

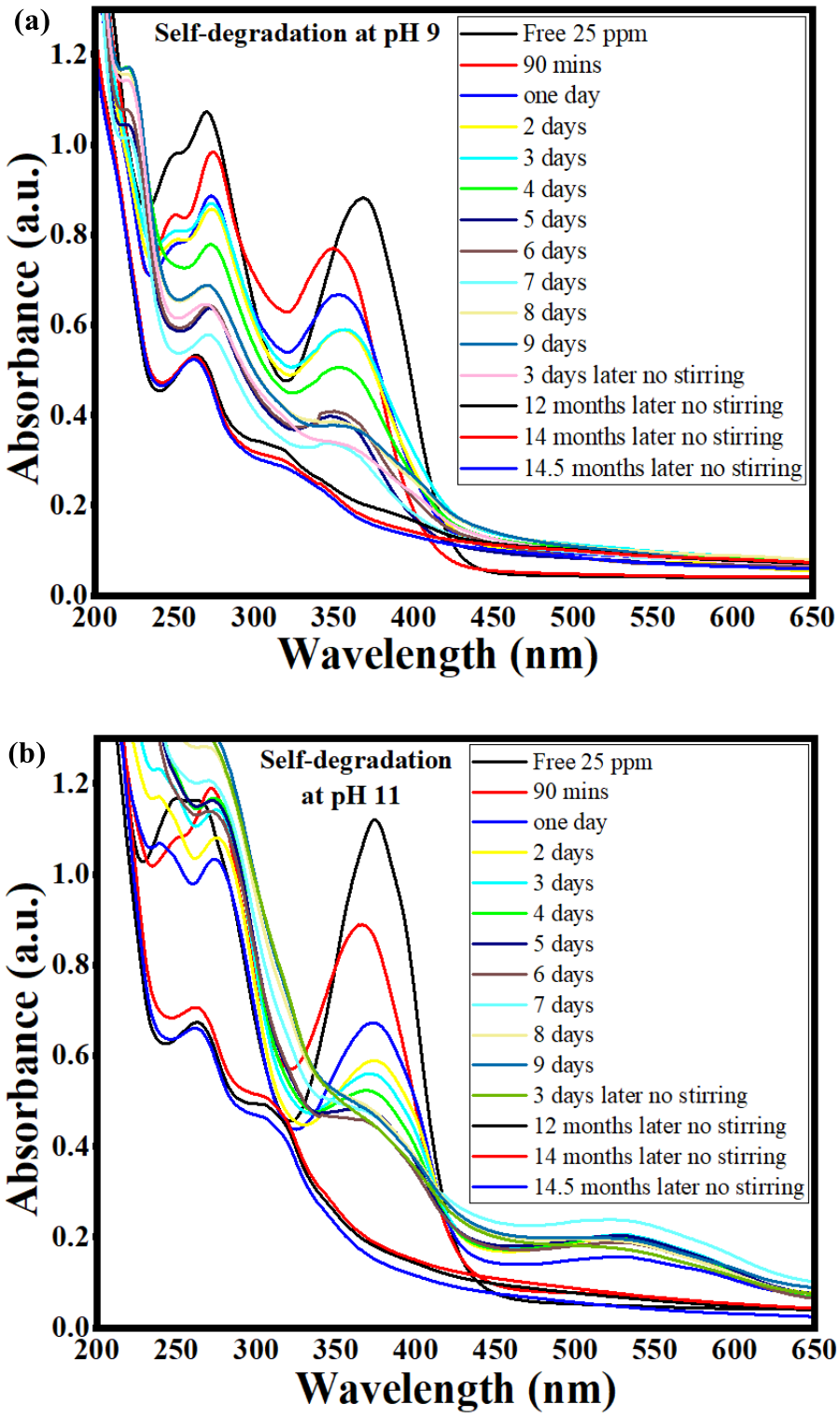

Fig 4.6. Control experiments of the pH effect on the self-degradation of DOXY at pH 9 **(a)** and pH 11 **(b)** for 14.5 months. [C_o = 25 ppm, volume = 20 mL, stirring rate = 750 rpm, T = 20 ± 2 °C].

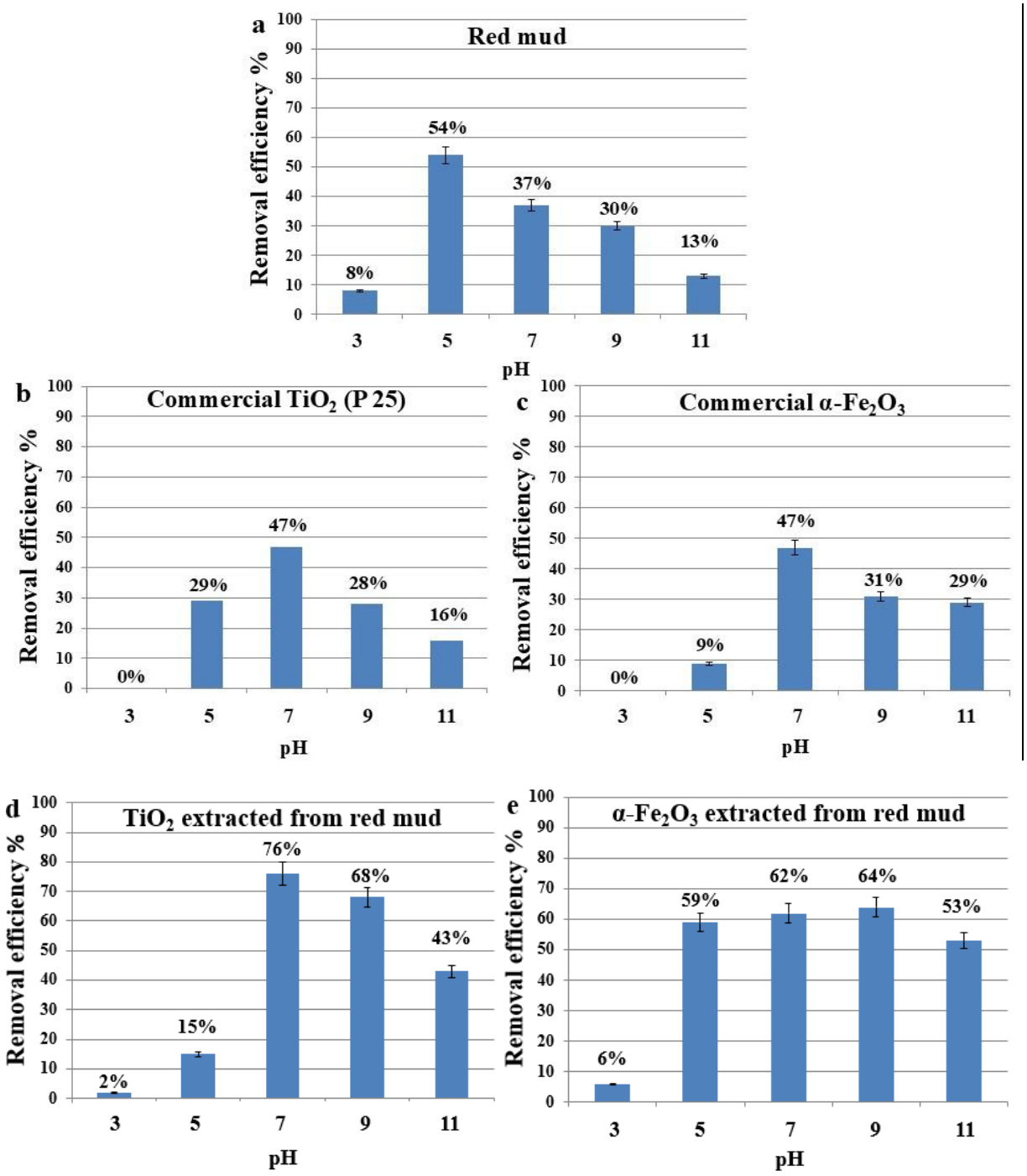

Fig 4.7. A comparison between the efficiency of pristine red mud **(a)**, P25 **(b)**, commercial α-Fe_2O_3 **(c)**, red mud-derived TiO_2 **(d)**, and red mud-derived α-Fe_2O_3 **(e)** in removing DOXY after 90 minutes. [C_o = 25 ppm, stirring rate = 750 rpm, T = 20 ± 2 °C, volume = 20 mL, and dose = 0.01 g].

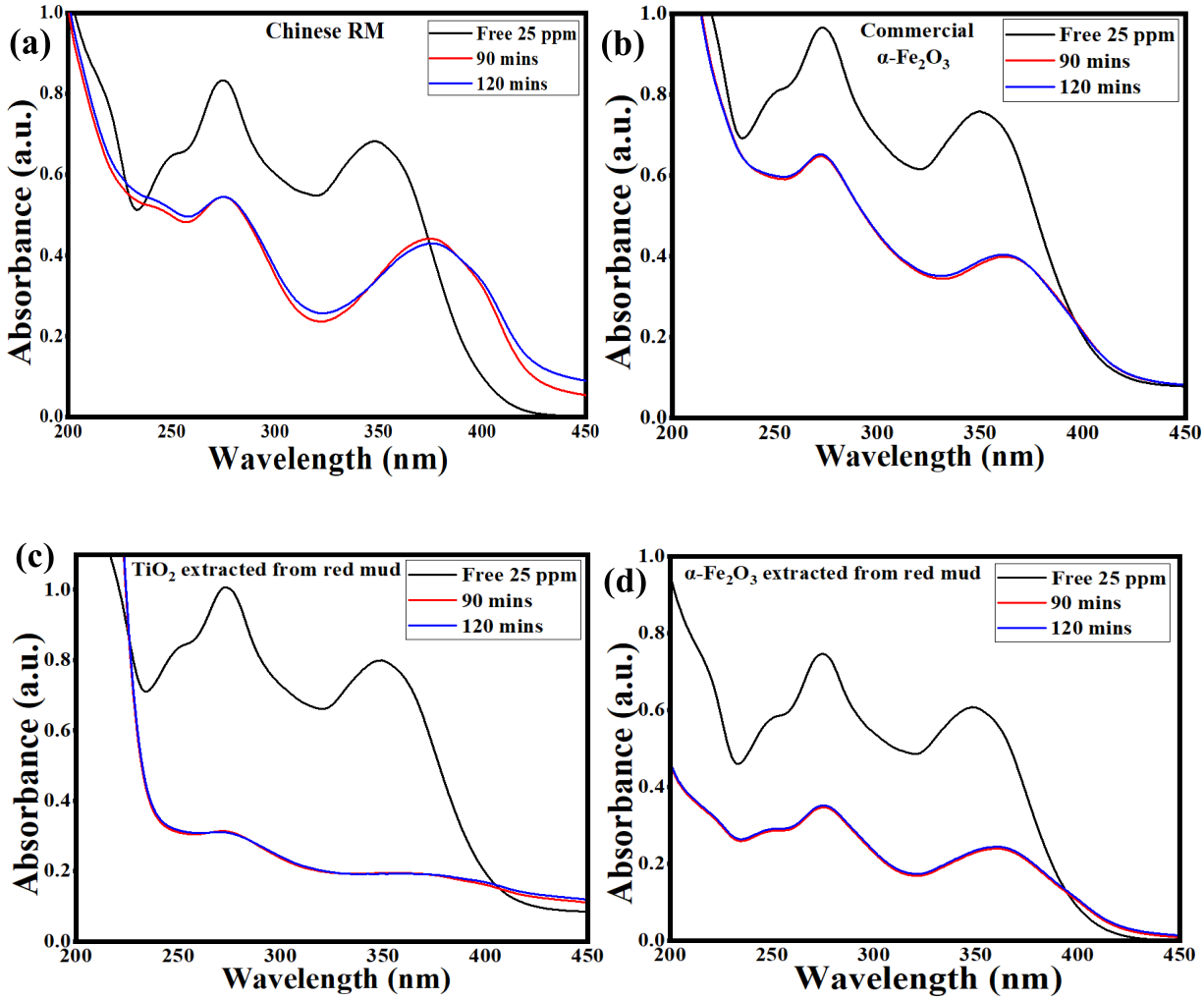

Fig 4.8. The UV-Vis spectra of pristine red mud **(a)**, commercial α-Fe_2O_3 **(b)**, red mud-derived TiO_2 **(c)**, and red mud-derived α-Fe_2O_3 **(d)** in adsorbing DOXY. [C_o = 25 ppm, pH = 7, stirring rate = 750 rpm, T = 20 ± 2 °C, volume = 20 mL, and dose = 0.01 g].

α-Fe_2O_3 extracted from red mud under visible light (PZC = 7) showed its highest adsorption efficiency (70%) at pH 5 due to the above-mentioned electrostatic attraction (**Fig. 4.9.a**). However, the removal efficacy fluctuated by increasing the pH. The powder XRD pattern of this material exhibited some reflections that may correspond to other iron oxides, such as Fe_3O_4 (**Fig. 4.9.b**). When commercial Fe_3O_4 was tested as a control experiment, its highest adsorption efficiency was 45% at pH 5, and the efficiency fluctuated with increasing pH (**Fig. 4.9.c**), showing a trend similar to that of the red mud-derived α-Fe_2O_3 under visible light. Therefore, the presence of Fe_3O_4 within the structure of red mud-derived α-Fe_2O_3 under visible light, although the exact formation mechanism is unclear, is the reason behind its fluctuating adsorption efficacy. This observation could be linked to the findings of Gu *et al.*

[205] who detected Fe_3O_4 without α-Fe_2O_3 reflections in the powder XRD pattern of a ferrous oxalate sample, which was reduced from ferric oxalate under natural laboratory light, after calcination at 500 °C for 2 hours. The relatively short calcination time could be the reason for their result. Using UV light could be considered more efficient than the laboratory visible light in reducing the partially-soluble ferric oxalates to insoluble ferrous oxalates, which resulted in a better separation/removal of the co-precipitated impurities from ferric oxalates and produced purer ferrous oxalates, which were calcined to produce purer α-Fe_2O_3.

Based on the above-mentioned results, red mud-derived TiO_2 and α-Fe_2O_3, which was extracted under UV light, demonstrated better performance, likely due to their higher surface areas. Their surface areas were 139 m^2/g and 85 m^2/g, respectively, compared to 56 m^2/g and 20 m^2/g for commercial TiO_2 and α-Fe_2O_3, respectively. Among them, red mud-derived α-Fe_2O_3 showed the best overall performance and was therefore selected for further investigation in Chapter 5 alongside other iron-based adsorbents.

Table 4.1. The PZC of the adsorbents reported in Chapter 4.

Adsorbent	**PZC**
Red mud-derived TiO_2	4.0
P25	4.9
Commercial α-Fe_2O_3	6.5
Red mud-derived α-Fe_2O_3	6.7
Red mud-derived α-Fe_2O_3 under visible light	7.0
Red mud	7.4

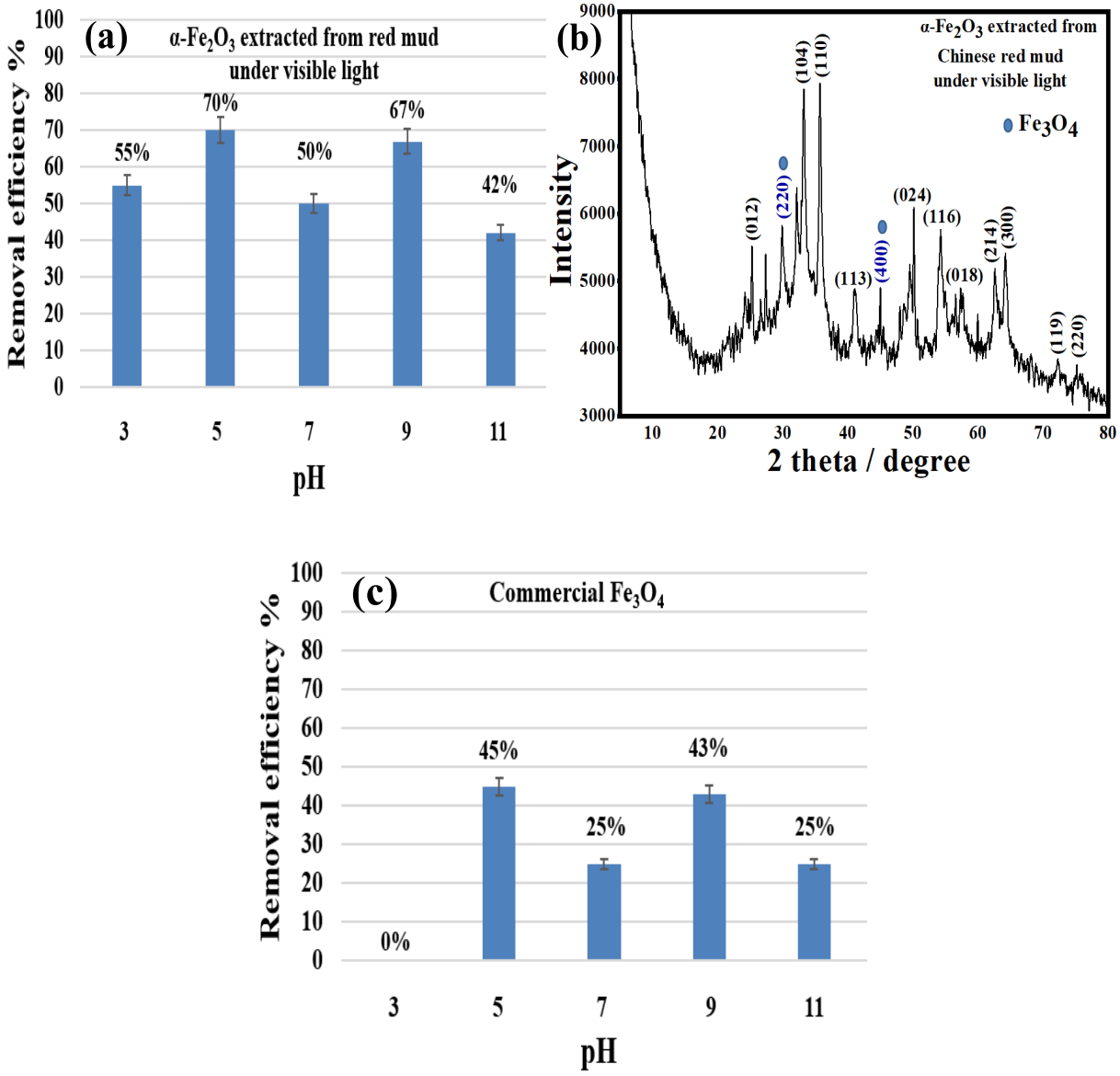

Fig 4.9. The efficiency of red mud-derived α-Fe_2O_3 under visible light that contained both α-Fe_2O_3 and Fe_3O_4 in removing DOXY (**a**) its powder XRD pattern (**b**), and the removal efficiency of commercial Fe_3O_4 after 90 minutes (**c**), which was used as a control test. [C_o = 25 ppm, stirring rate = 750 rpm, T = 20 ± 2 °C, volume = 20 mL, and dose = 0.01 g].

4.4. EDX and SEM analysis of red mud-derived α-Fe_2O_3

SEM images of red mud-extracted α-Fe_2O_3 revealed aggregates with rod-shaped morphology of varying sizes, some of which were partially covered by irregularly shaped particles (**Fig. 4.10.a, c, e, g,** and **h**). EDX spectra of the sample indicated the presence of iron in concentrations ranging from 8% to 13%, which were significantly higher than those of titanium (0.2% - 0.3%) (**Fig 4.10.b, d,** and **f**).

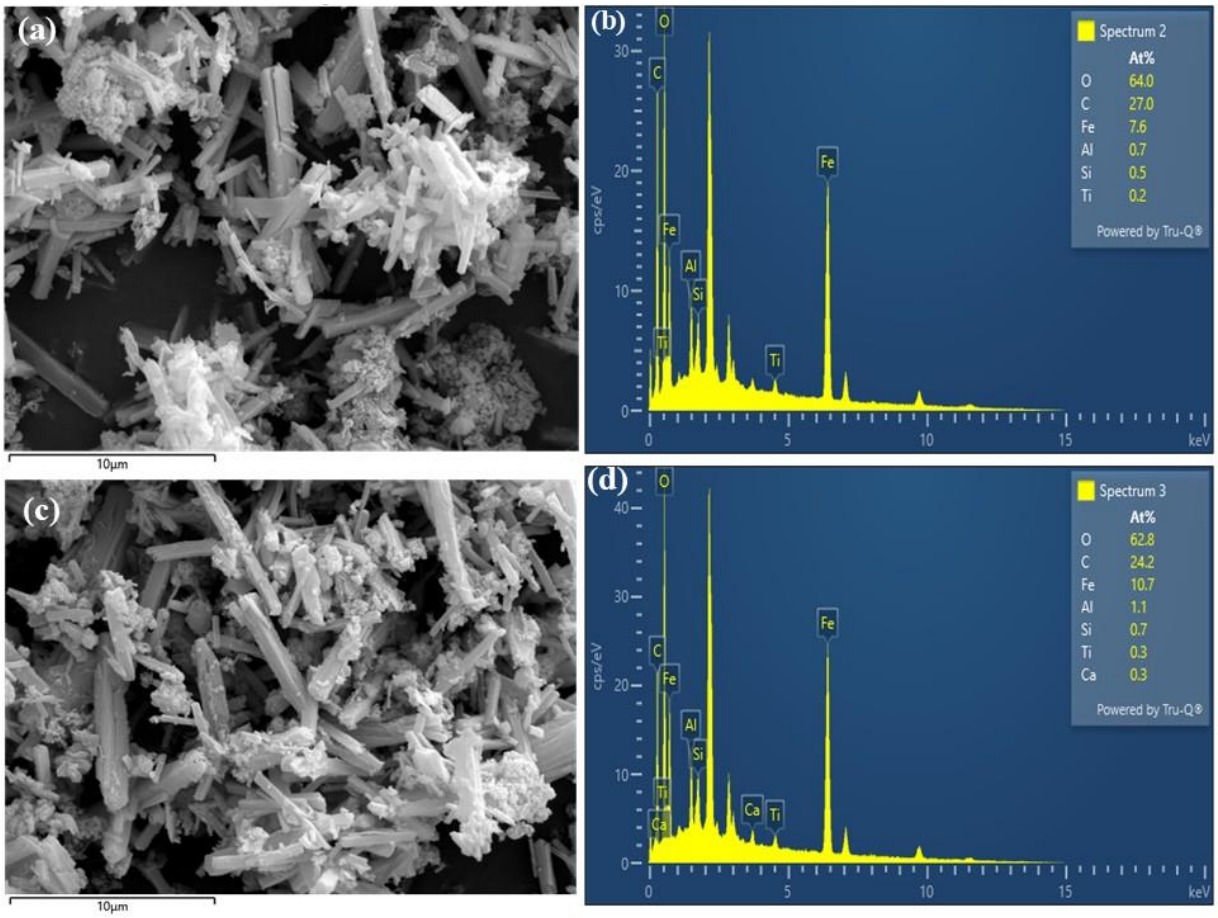
(a)
10μm
(b)
O
C
Fe
Al
Si
Ti
Fe
Ti
cps/eV
keV
Spectrum 2
At%
O 64.0
C 27.0
Fe 7.6
Al 0.7
Si 0.5
Ti 0.2
Powered by Tru-Q®
(c)
10μm
(d)
O
C
Fe
Al
Si
Ti
Ca
Fe
Ca
Ti
cps/eV
keV
Spectrum 3
At%
O 62.8
C 24.2
Fe 10.7
Al 1.1
Si 0.7
Ti 0.3
Ca 0.3
Powered by Tru-Q®

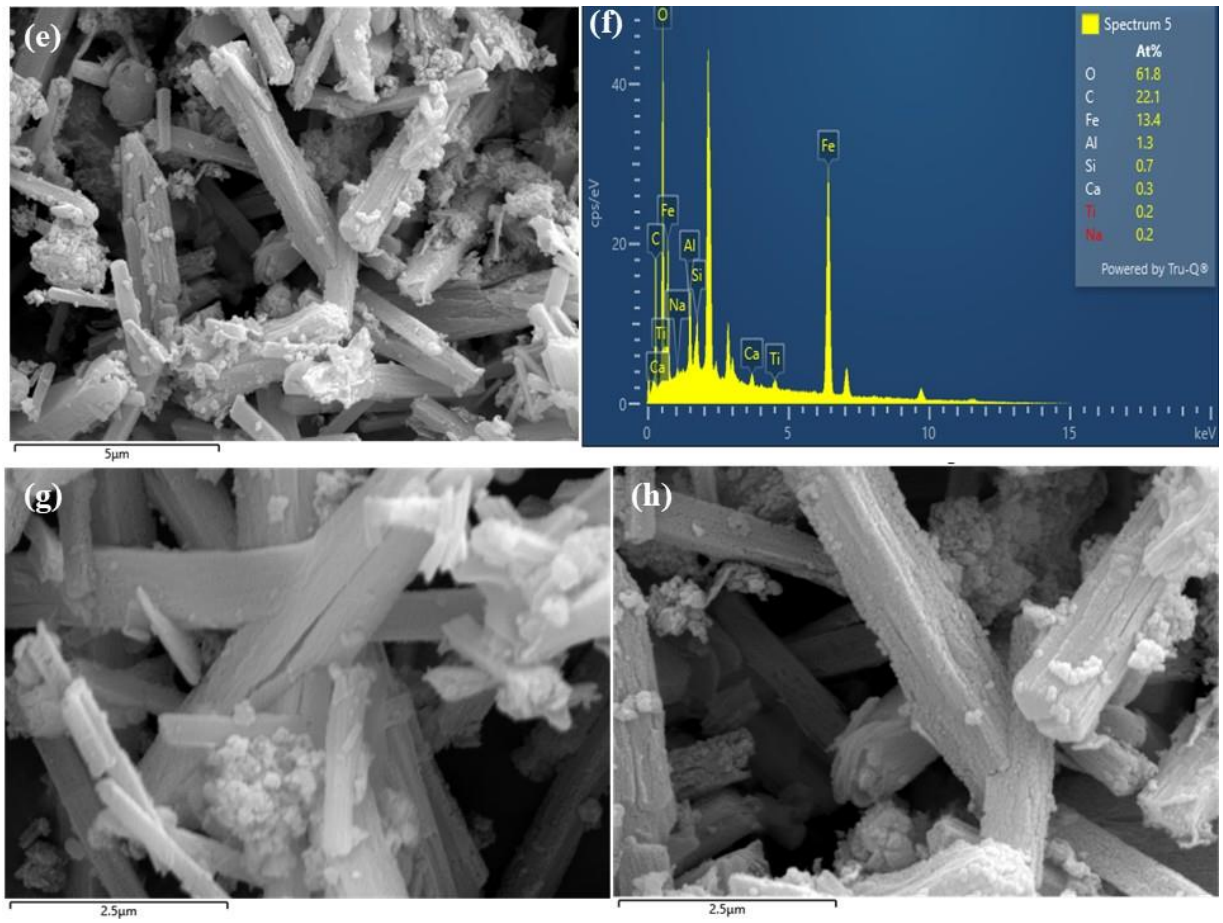

Fig 4.10. SEM images **(a, c, e, g,** and **h)** and EDX spectra of α-Fe_2O_3 **(b, d,** and **f)** show high iron content compared to the other components. The images revealed clusters of rod-shaped materials that varied in size. Irregularly shaped particles were observed to partially cover some of these clusters.

4.5. Investigation of DOXY self-degradation and photolysis, and identification of potential degradation products

Many studies are addressing the adsorption and degradation of DOXY in the context of water treatment. In this regard, Vasanthakumar *et al.* [277] reported a 5% degradation efficiency after 120 minutes under visible light irradiation using a solution of 30 ppm at pH 7. Similarly, a degradation efficacy of 10% at pH 8 after 180 minutes of stirring of 5 ppm DOXY solution under visible light was mentioned by Li *et al.* [278]. Another study was carried out recently by Omar *et al.* [279] to investigate the photocatalytic degradation of 50 ppm tetracycline, which is very similar to DOXY, and the degradation after 120 minutes at pH 7 was about 15% and

18% under sunlight and xenon lamp irradiation, respectively, due to the higher irradiation power of xenon lamp.

However, only one study confirmed the self-degradation of DOXY in dark conditions. This study was undertaken by Zhong *et al.* [212] who indicated the hydrolytic transformation/degradation of DOXY under alkaline conditions into 4-epi-doxycycline, 6-epi-doxycycline, and other unknown products. They proposed different transformation pathways such as epimerization, isomerization, decarbonylation, deamidation, and hydroxylation as shown in **Fig 4.11**. However, none of these transformation products were found in the LC-MS spectra in the current study except for the product with a m/z of 463. This finding suggested the formation of different degradation products of DOXY under the conditions used in the current study. Continuing with the same study [212], the authors investigated the toxicity of three additional tetracyclines: tetracycline, chlortetracycline, and oxytetracycline. The toxicity of 32 degradation products derived from the four tetracyclines was assessed, and computational toxicology analysis indicated their toxic effects on green algae, fish, and daphnia, some of which exhibited higher toxicity than their parent compounds. However, as the authors mentioned, that these preliminary tests are not sufficient, and further research into the toxicity of these products is necessary.

All of this highlighted the critical role of pH in maintaining the stability of DOXY. Therefore, investigating the effect of pH on the stability of other antibiotics under dark conditions is strongly recommended for future research.

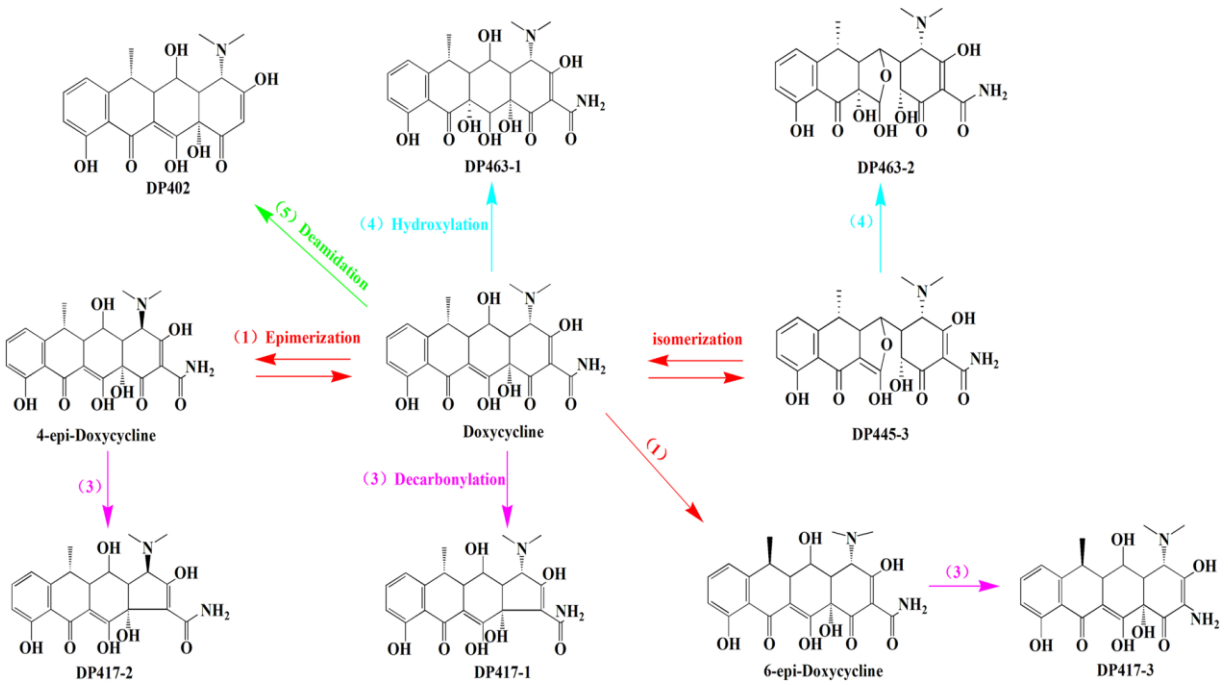

Fig 4.11. The proposed transformation pathways of DOXY hydrolysis showing different mechanisms such as decarbonylation and deamidation [212].

4.5.1. The photolysis of DOXY under UV light, the photocatalytic activity of α-Fe_2O_3 and TiO_2, and the effect of temperature on DOXY stability

The photolysis of DOXY under visible and UVA light (λ = 365 nm) at 5 cm between the solution and the LED or the mercury lamp, respectively, was undertaken at pH 11 and the unadjusted pH (4.5) to test the stability of DOXY. The visible light did not have any effect. However, the UVA light degraded 74% of DOXY after 300 minutes at pH 4.5 and no further degradation was observed beyond this time. Although the degradation efficacy was the same, the degradation at pH 11 was much faster as it was 69% after 30 minutes, slightly increased to 74% after 60 minutes, and remained constant after that time (**Fig 4.12.a**). The faster degradation at pH 11 could be attributed to self-degradation. The degradation products of DOXY were mainly nitrites as previously investigated and quantified in **Section 3.8** Using the Griess reagent assay.

The UV-Vis spectra at the two pH values are shown in **Fig 4.12.b-c**. Some measurements at pH 11 were omitted to prevent overlapping lines and to improve clarity of the graph. To further confirm the degradation, LC-MS analysis was performed, and it showed the decreased

intensity of the molecular ion peak of DOXY at 1.9 minutes retention time at pH 4.5 (**Fig 4.12.d** and **f**) and pH 11 (**Fig 4.12.e** and **g**).

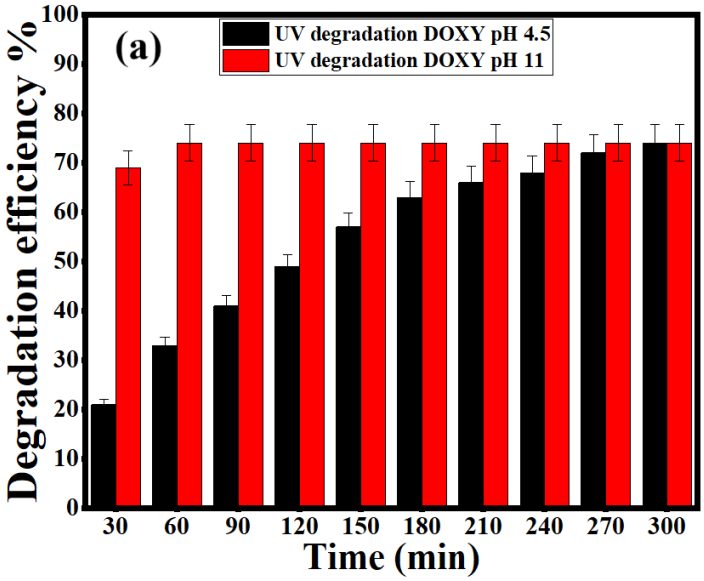

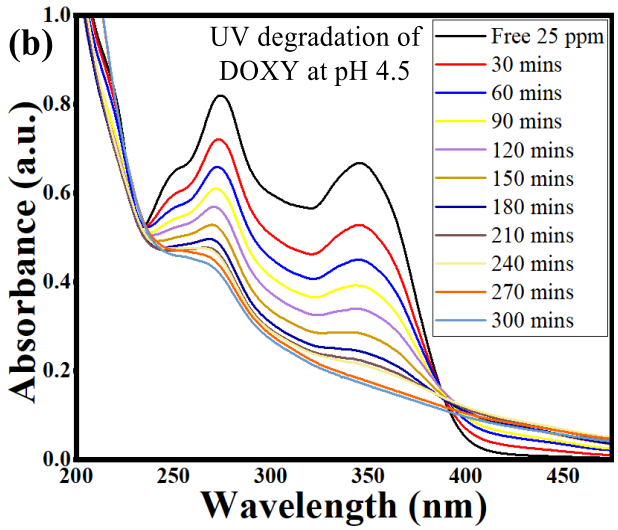

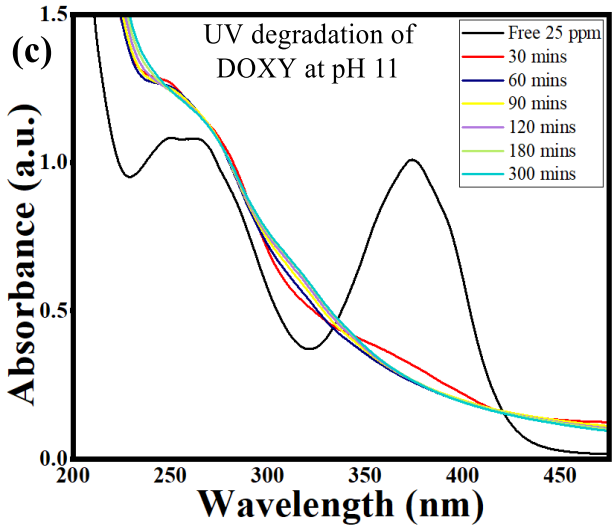

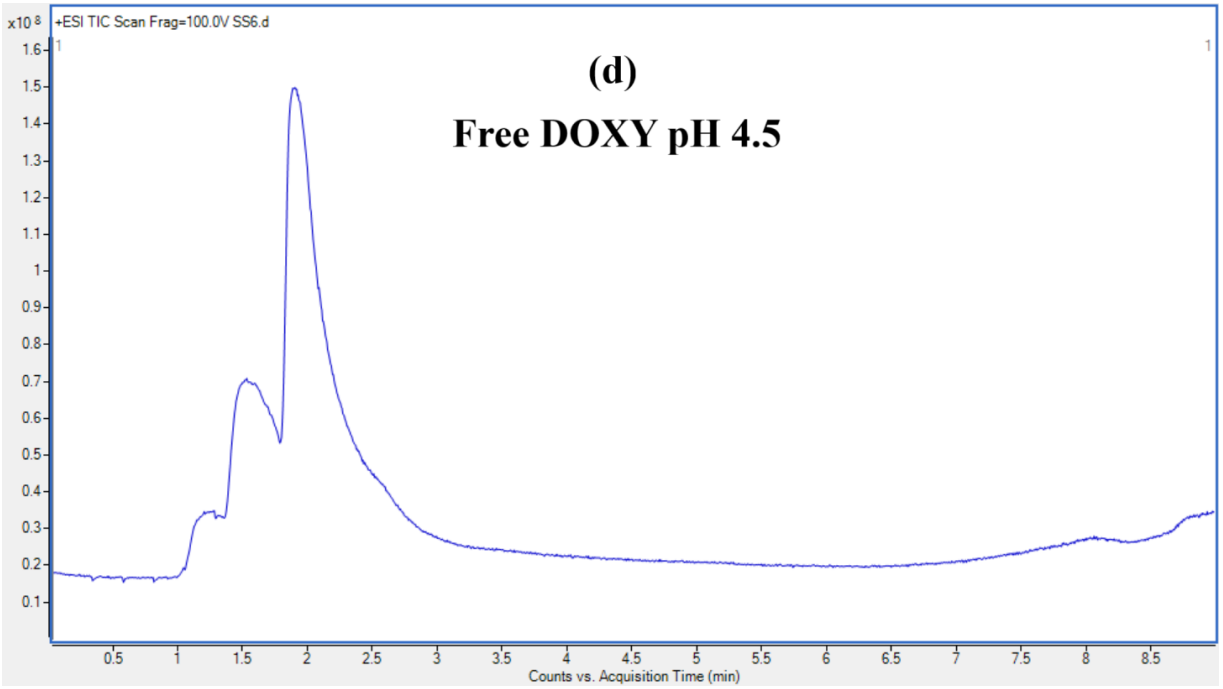
x10 8
+ESI TIC Scan Frag=100.0V SS6.d
(d)
Free DOXY pH 4.5
Counts vs. Acquisition Time (min)

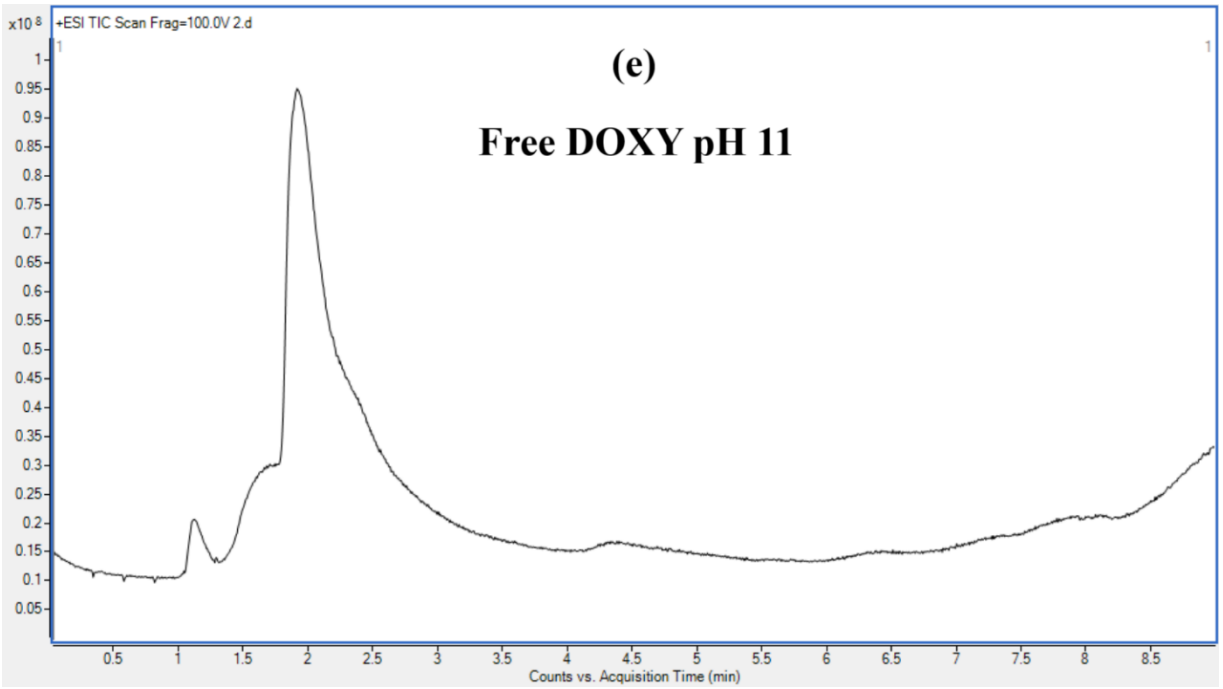
x10 8
+ESI TIC Scan Frag=100.0V 2.d
(e)
Free DOXY pH 11
Counts vs. Acquisition Time (min)

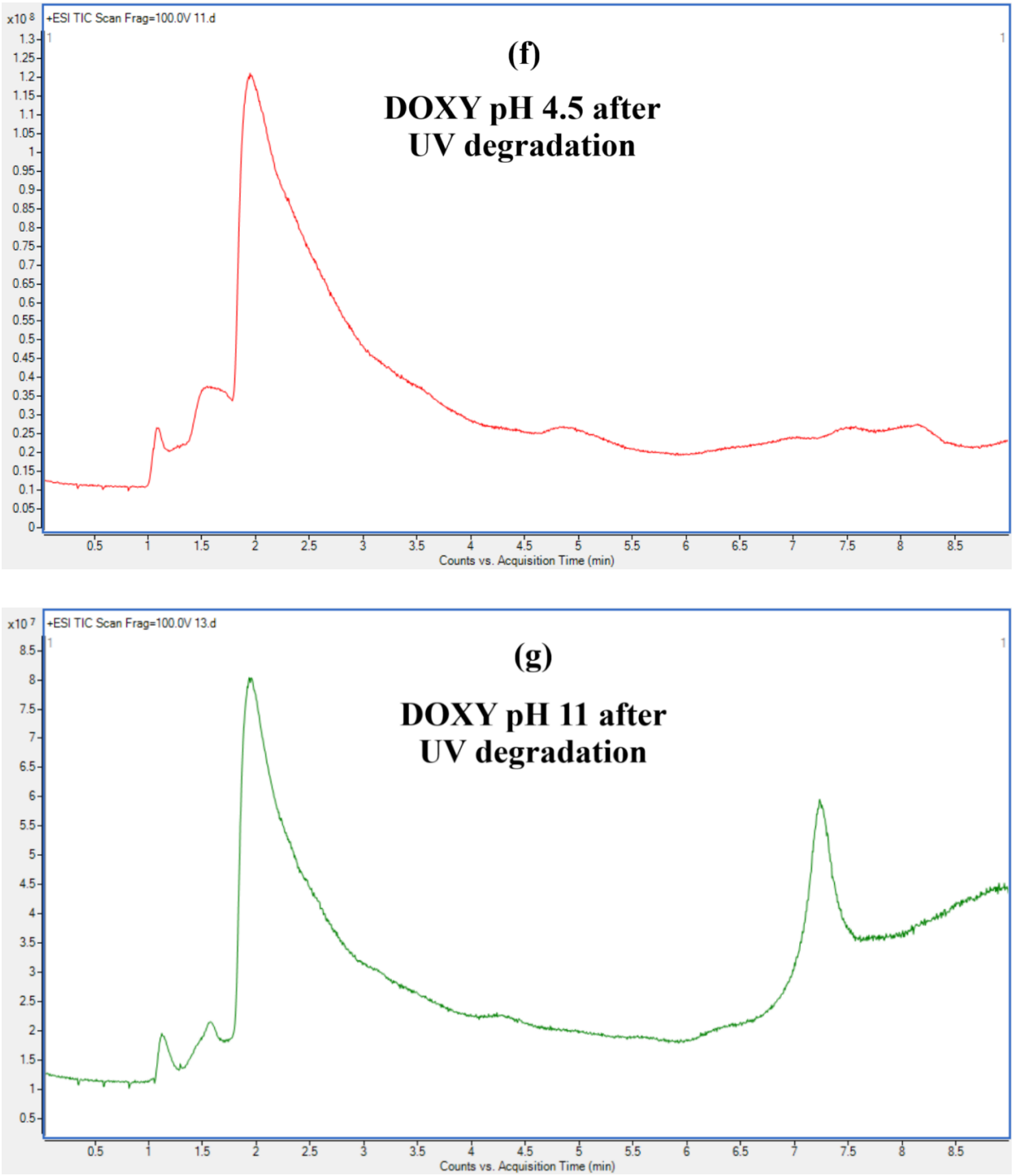

Fig 4.12. The degradation of DOXY under UVA light (photolysis) at pH 4.5 and pH 11 at 5 cm (**a**) and their UV-Vis (**b-c**) and the chromatographic part of LC-MS spectra prior to (**d-e**) and after (**f-g**) the degradation. [$C_o = 25$ ppm, stirring rate = 750 rpm, $T = 20 \pm 2$ °C, and volume = 20 mL].

Red mud-derived α-Fe_2O_3 and TiO_2 did not exhibit any photocatalytic activity under visible and UV light, respectively, in contrast to the commercial materials, which showed

photocatalytic activity. However, the results for P25 were inconsistent, with some experiments showing increased absorbance after the dark adsorption stage, similar to previous observations with CEF in the previous chapter. As shown in **Fig. 4.13.a**, P25 achieved 47% adsorption efficiency, followed by 20% degradation via photolysis after 60 minutes. The absorbance increased upon extending the photolysis time to 120 minutes due to solution evaporation. Considering the slightly increased absorbance after the 120 minutes of UV photolysis, subsequent photocatalytic degradation by P25 reached 18% after 60 minutes and almost remained constant up to 180 minutes, particularly at the 350 nm wavelength.

In **Fig. 4.13.b**, the results varied: the adsorption efficiency was 35%, followed by 15% degradation via photolysis and 33% degradation via photocatalysis. Due to these inconsistencies, the experiment was repeated two more times. In **Fig. 4.13.c** and **d**, the absorbance increased after the adsorption step. Thus, the photolysis time was extended to 90 minutes. The degradation rate did not increase beyond that point by extending the time either to 180 (**Fig 4.13.c**) or 120 minutes (**Fig 4.13.d**). The photocatalytic efficiencies of P25 in these two experiments were 16% and 22% after 60 minutes, respectively, with no further improvement observed beyond that point.

The commercial α-Fe_2O_3 exhibited 47% adsorption efficiency (**Fig. 4.13.e**). Its photocatalytic degradation performance was 7% after 60 minutes, increasing to 16% after 120 minutes, beyond which no further removal of DOXY was observed.

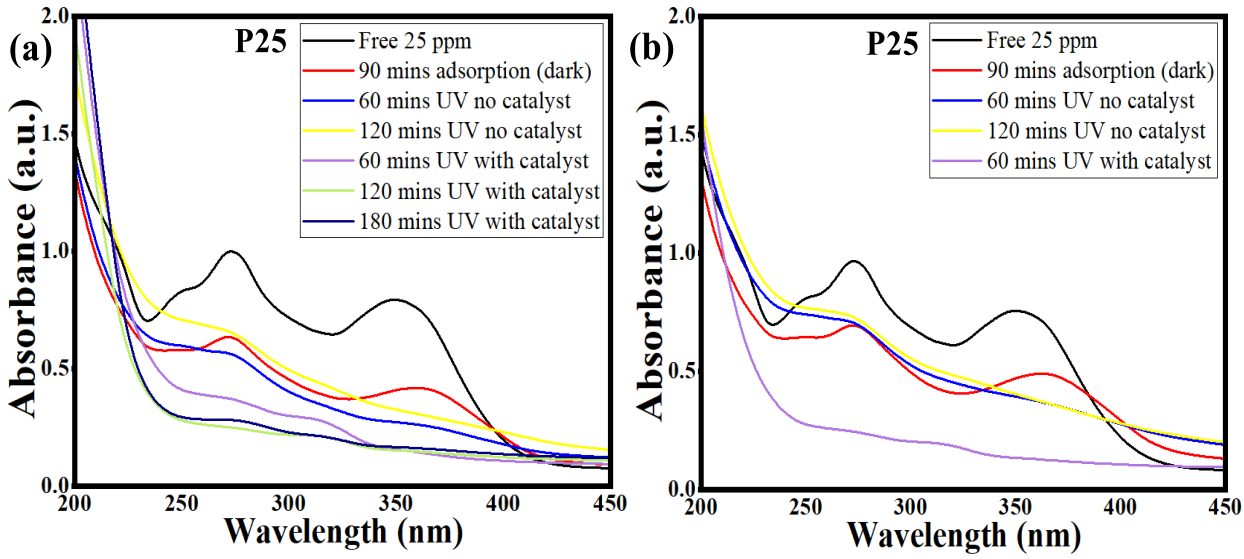

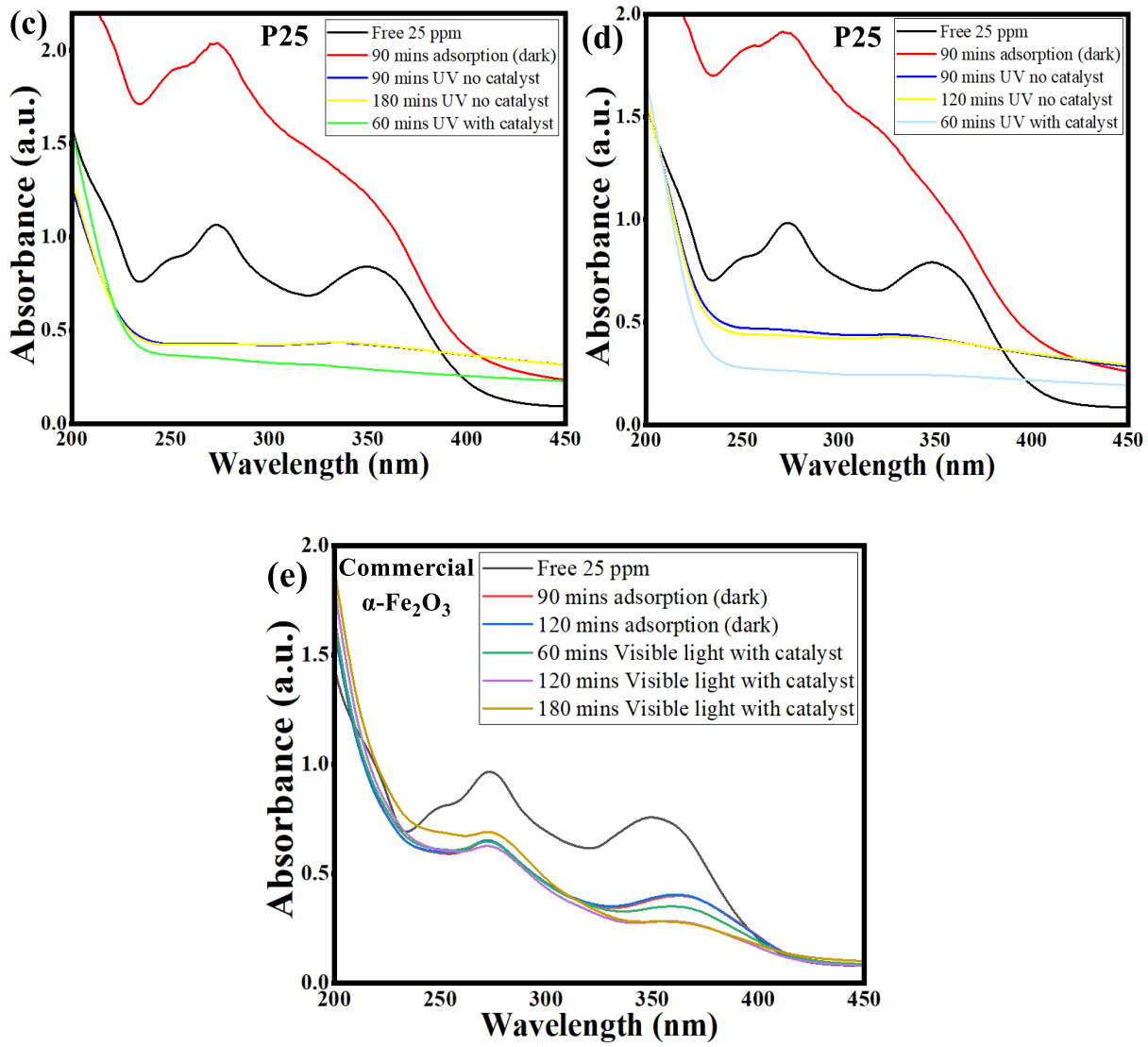

Fig 4.13. The photocatalytic degradation of DOXY under UV light using P25 (**a-d**) and visible light using commercial α-Fe_2O_3 (**e**). [C_o = 25 ppm, pH = 7, dose = 0.01 g, stirring rate = 750 rpm, T = 20 ± 2 °C, and volume = 20 mL].

No thermal degradation of DOXY was observed at 20 °C and pH 7 (**Fig. 4.14.a**). However, at 25 °C and higher temperatures, the behavior became inconsistent, with the absorbance sometimes remaining unchanged and at other times increasing or decreasing for no obvious reasons as observed at 35 °C (**Fig. 4.14.b-d**). Therefore, it was not feasible to systematically evaluate the effect of temperature on the performance of the materials used for DOXY removal.

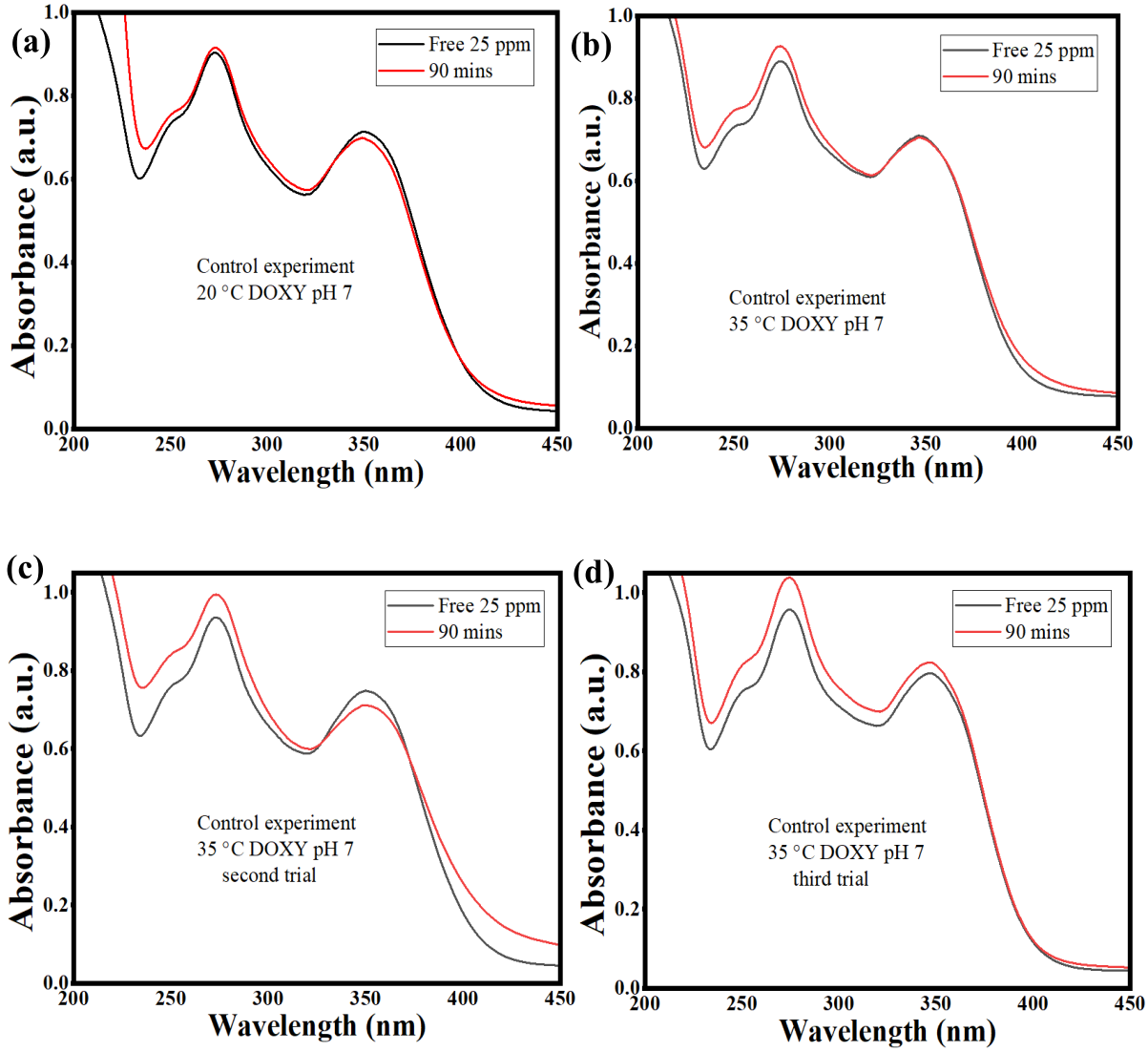

Fig 4.14. The UV-Vis spectra of DOXY after 90 minutes of stirring at 20 °C (**a**) and three times at 35 °C (**b-d**). [C_o = 25 ppm, pH 7, stirring rate = 750 rpm, and volume = 20 mL].

4.5.2. Identification of potential degradation products of DOXY powder

TGA(DSC)-MS analysis was used in this chapter to investigate the gaseous degradation products of DOXY powder. As shown in **Fig 4.15.a**, three main stages of mass loss were detected at 145 °C, 221 °C, and 719 °C that corresponded to a weight loss of 3.5%, 13%, and 50%, respectively. The total weight loss was 83%. Several gases were released including H_2 with a main peak at approximately 440 °C (**Fig 4.15.b**). A sharp peak of water vapour (18 m/z) was observed at around 180 °C (**Fig 4.15.d**). The broad peak of 16 m/z centered at about 400 °C might be attributed to the release of CH_4 (**Fig 4.15.c**). This result is in partial agreement with Cervini *et al.* [280], who reported the evolution of methane during the thermal

degradation of DOXY at approximately 510 °C. The possible release of NO (30 m/z) was indicated by two main peaks at about 130 °C and 700 °C (**Fig 4.15.e**), which were obviously different from those of the oxygen (32 m/z) in **Fig 4.15.f**. The mass spectra ion curve of 44 m/z (**Fig 4.15.h**) confirmed the release of CO_2 primarily at around 175 °C and 640 °C. The mass spectra ion curves of 43 m/z (**Fig 4.15.g**) and 45 m/z (**Fig 4.15.i**) exhibited a similar pattern to that of CO_2 making it difficult to distinguish the possible release of HNCO (43 m/z) and $(CH_3)_2NH$ (45 m/z) during the thermal degradation of DOXY. These results are consistent with those of Freitas *et al.* in 2022 [281] and 2024 [270] who detected various gases including H_2O, CH_4, CO_2, NH_3, HNCO, and $(CH_3)_2NH$ from the thermal degradation of DOXY using TG-FTIR. However, the possibility of detecting some of these gases in the current study was not available due to the interference between their m/z ratios such as NH_3 and CH_4 with H_2O, and HNCO and $(CH_3)_2NH$ with CO_2. Most of these gases are harmful. Therefore, the degradation of DOXY, either thermal or any other sort of degradation, is not recommended. The degradation products of DOXY in aqueous solutions, which are mainly nitrites, were already investigated and quantified in **Section 3.8**.

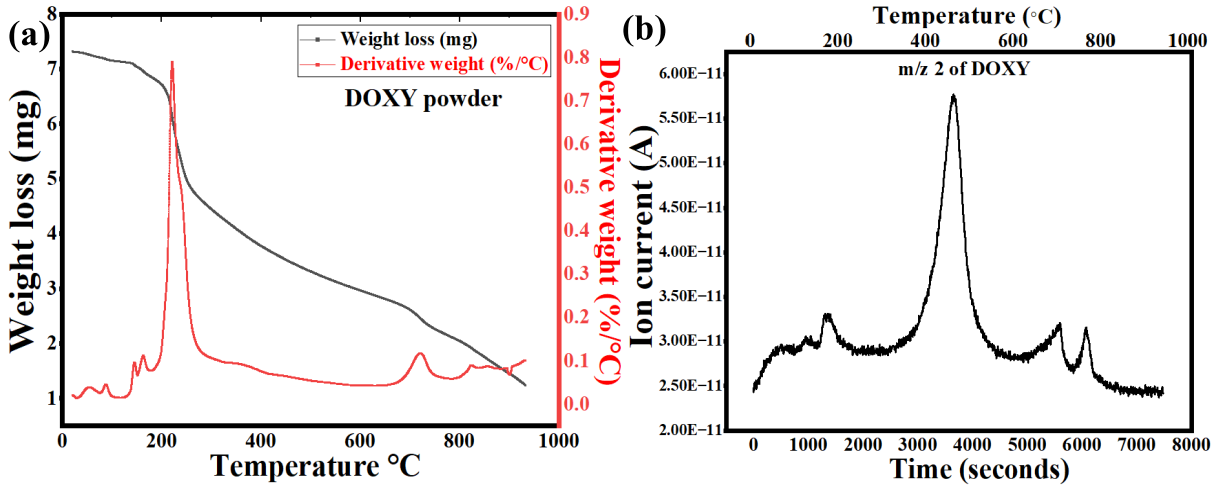

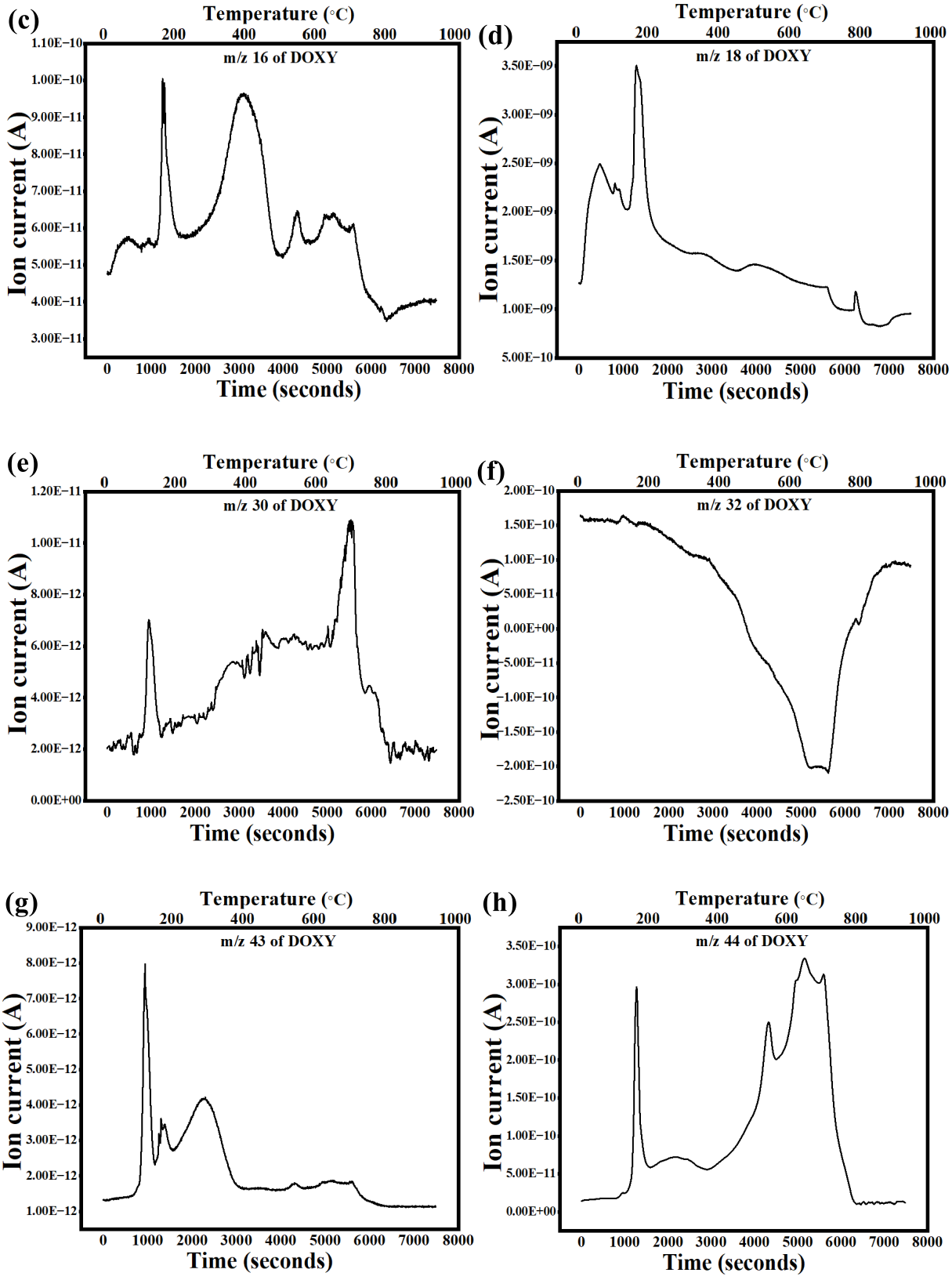
(c)
Temperature (°C)
0 200 400 600 800 1000
m/z 16 of DOXY
Ion current (A)
1.10E−10
1.00E−10
9.00E−11
8.00E−11
7.00E−11
6.00E−11
5.00E−11
4.00E−11
3.00E−11
0 1000 2000 3000 4000 5000 6000 7000 8000
Time (seconds)
(d)
Temperature (°C)
0 200 400 600 800 1000
m/z 18 of DOXY
Ion current (A)
3.50E−09
3.00E−09
2.50E−09
2.00E−09
1.50E−09
1.00E−09
5.00E−10
0 1000 2000 3000 4000 5000 6000 7000 8000
Time (seconds)
(e)
Temperature (°C)
0 200 400 600 800 1000
m/z 30 of DOXY
Ion current (A)
1.20E−11
1.00E−11
8.00E−12
6.00E−12
4.00E−12
2.00E−12
0.00E+00
0 1000 2000 3000 4000 5000 6000 7000 8000
Time (seconds)
(f)
Temperature (°C)
0 200 400 600 800 1000
m/z 32 of DOXY
Ion current (A)
2.00E−10
1.50E−10
1.00E−10
5.00E−11
0.00E+00
−5.00E−11
−1.00E−10
−1.50E−10
−2.00E−10
−2.50E−10
0 1000 2000 3000 4000 5000 6000 7000 8000
Time (seconds)
(g)
Temperature (°C)
0 200 400 600 800 1000
m/z 43 of DOXY
Ion current (A)
9.00E−12
8.00E−12
7.00E−12
6.00E−12
5.00E−12
4.00E−12
3.00E−12
2.00E−12
1.00E−12
0 1000 2000 3000 4000 5000 6000 7000 8000
Time (seconds)
(h)
Temperature (°C)
0 200 400 600 800 1000
m/z 44 of DOXY
Ion current (A)
3.50E−10
3.00E−10
2.50E−10
2.00E−10
1.50E−10
1.00E−10
5.00E−11
0.00E+00
0 1000 2000 3000 4000 5000 6000 7000 8000
Time (seconds)

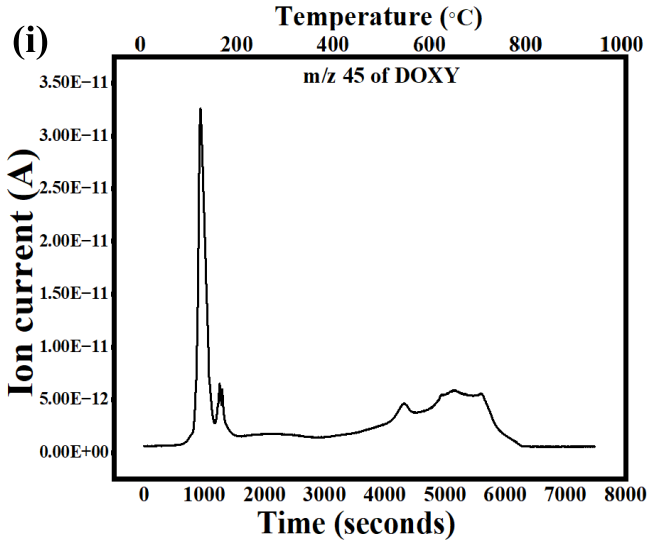

Fig 4.15. TGA and derivative weight profile of DOXY powder (**a**) and the mass spectrum ion curve for 2 m/z (**b**), 16 (**c**), 18 (**d**), 30 (**e**), 32 (**f**), 43 (**g**), 44 (**h**), and 45 (**i**).

4.6. Economic cost analysis of α-Fe_2O_3 production

Regarding the chemical cost required to produce of α-Fe_2O_3 from red mud in October 2024; 36 g of anhydrous oxalic acid powder was used to prepare 200 mL oxalic acid solution with a concentration of 2 $mol.L^{-1}$. 1 Kg of anhydrous oxalic acid currently costs £ 75.69 [282], so the cost of 36 g is £ 2.72. On average 200 mL of ethanol were used for washing the ferric oxalate crystals, which cost about £ 0.89 because 2.5 L of ethanol by an internal order from the stores of the School of Chemistry costs £ 11.14. In addition, an average of 100 L of water was estimated to be used for preparing the oxalic acid solution and cooling the UV lamp would cost £ 0.6. The water cost is based on the charges provided [265] including both water and wastewater charges in the fiscal year of 2023/2024. It has to be mentioned that the amount of cooling water could be eliminated by using a small fan for cooling.

Furthermore, the current standard charge of electricity per day is £ 0.62 [266], which is assumed to be the average cost of the total number of hours of using stirrers, the electric furnaces, and ovens in this work. The amount of α-Fe_2O_3 produced using the abovementioned chemicals was 3.3 g from 10 g of red mud. The total cost of these 3.3 g was £ 4.83 using water for cooling the UV lamp and £ 4.29 using the small fan. Therefore, the cost ranges between £ 1.3 and £ 1.46 for one gram of α-Fe_2O_3 depending on which cooling method is used. One gram of commercial α-Fe_2O_3 costs about £ 0.10 as 250 g are sold for £ 25.07 [283].

Comparing the cost of the red mud-extracted α-Fe_2O_3 with the commercial one, it is clear that the cost of the commercial α-Fe_2O_3 is much lower. However, the performance of red mud-extracted α-Fe_2O_3 is obviously better at all pH levels. Although the amount of red mud-extracted TiO_2 (1 g of TiO_2 from 10 g of red mud) is less than that of α-Fe_2O_3, it is cheaper to extract and more economically viable to use compared to its commercial competitor (P25).

4.7. The environmental considerations of extracting α-Fe_2O_3 and TiO_2 from red mud

The purpose of this analysis is to provide an environmental consideration of the possible effects of the chemicals used in the extraction of α-Fe_2O_3 and TiO_2 from red mud. When released into the environment, oxalic acid can contribute to water and soil acidification. In addition, it can form complexes with heavy metals, increasing their bioavailability. However, it is biodegradable and can be broken down by bacteria in soil and water, reducing its long-term environmental impact [284]. Ethanol is biodegradable and breaks down relatively quickly once introduced into the environment. However, its production and use in large quantities can contribute to air pollution due to the release of volatile organic compounds (VOCs) [285].

H_2SO_4 is a highly corrosive and toxic chemical with significant environmental and health risks. When released into the environment, it can contribute to acidification of water bodies and soil, harming aquatic life, plants, and microorganisms [286]. However, a very small volume of H_2SO_4 is used in the current study (10 mL) to produce one gram of TiO_2. Additionally, it is not discarded until it gets neutralized by water. Sodium carbonate is not considered to be environmentally hazardous or toxic, but it can increase the pH of water and soil [287]. However, the mixture of red mud, calcium oxide, and sodium carbonate gets closer to neutrality after grinding and washing with water. Also, using calcium oxide is associated with the same issue [288], yet it gets neutralized with water as well. Therefore, the above-mentioned chemicals are used in small quantities to extract α-Fe_2O_3 and TiO_2 from red mud. Therefore, these chemicals and their discharge at the end of the extraction processes are not supposed to be causing environmental issues.

4.8. Conclusions

α-Fe_2O_3 and TiO_2 were successfully extracted from red mud with yields of 118 wt% and 265 wt%, respectively. These high yields can be attributed to the presence of impurities in both extracted metal oxide samples, as they were derived from a multi-component waste material. Both materials demonstrated superior performance compared to their commercial counterparts and raw red mud in removing DOXY likely due to their higher surface areas. However, they did not exhibit any photocatalytic activity under UV and visible light, respectively. The proposed removal mechanism was primarily based on electrostatic interactions, hydrogen bonding, and the self-degradation of DOXY species in alkaline media, as confirmed by UV-Vis spectra. Photolysis of DOXY under UV light resulted in 74% degradation after 60 minutes at pH 11 and after 300 minutes at pH 4.5 because of the self-degradation of DOXY in alkaline conditions. The possible degradation products of DOXY powder, suggested to be in gaseous form based on LC-MS results, were identified as H_2O, CO_2, NO, and possibly CH_4, according to TGA-MS analysis. In aqueous solutions, the degradation products are mainly nitrites that were confirmed by the Griess reagent method in Chapter 3. This is related to the presence of nitrogen-based functional groups such as amines and amides in DOXY structure. These findings highlight a sustainable strategy for transforming corrosive waste material such as red mud into an effective adsorbent for antibiotic removal.

Chapter 5

5. Transforming biogenic iron oxide into zero-valent iron for sustainable removal of antibiotics from water

5.1. Introduction

This chapter focuses on the study of biogenic iron oxide (BIOX) produced by *Leptothrix* bacteria. This naturally occurring material offers a sustainable alternative to synthetic iron oxides, with promising applications in water treatment, pollution control, and resource recovery. The efficiency of pristine BIOX in DOXY removal is compared with that of calcined BIOX and reduced BIOX, the latter prepared under either pure H_2 or an H_2/N_2 gas mixture. The effects of extended reduction time and/or increased temperature on both the intensity of zero-valent iron (Fe^0) reflections and the removal efficacy are investigated. The influence of seasonal variation on the characteristics and performance of BIOX is also discussed. 2-line ferrihydrite is used as a benchmark material. Additionally, the efficiency of some of the materials reported in this chapter was further evaluated for CEF removal. The performance of other waste materials, such as Chinese red mud (RM) and its derived α-Fe_2O_3, in removing both antibiotics was investigated after reduction under a H_2/N_2 atmosphere. As in the previous chapters, this work also includes an economic and environmental evaluation. The selectivity and scalability of reduced BIOX 1, identified as the most efficient adsorbent in this chapter, were further examined.

5.2. Powder XRD analysis of BIOX and 2-line ferrihydrite samples

Powder XRD analysis of all BIOX samples showed their amorphous structure with only two broad reflections at 2θ of 35° and 61° (**Fig 5.1.a-c**), which could be attributed to the (110) and (115) planes of 2-line ferrihydrite [289], respectively. Upon calcining the first sample, some reflections of α-Fe_2O_3 were detected at 2θ ranges of 26.64°, 33.11°, 35.70°, 40.77°, 49.53°, 54.03°, 57.63°, 62.57°, and 63.98° that correspond to (012), (104), (110), (113), (024), (116), (018), (214), and (300) reflections, respectively, [JCPDS Card No. 33-0664]. Other reflections of Fe_3O_4, some of which overlap with α-Fe_2O_3, were detected at 35.70°, 37.67°, 43.67°, 57.63°, and 62.57° as shown in **Fig 5.1.a**. These reflections correspond to (311), (222), (400), (511), and (440), respectively, [JCPDS:19-0629].

The second sample (crag) collected during the summertime showed a sharp Fe_3O_4 reflection at 29.43° and another one at 35.66° after calcination (**Fig 5.1.b**), which overlaps with the α-Fe_2O_3 reflection. Additionally, other α-Fe_2O_3 reflections appeared at 33.15° and 50.22°. The same Fe_3O_4 reflection at 29.43° appeared in the calcined wintertime sample. Some α-Fe_2O_3 reflections were observed after calcination at 27.72°, 32.93°, 35.60°, 49.73°, 53.93°, and 62.91°, and the reflection at 35.60° could potentially be assigned to Fe_3O_4 (**Fig 5.1.c**) in the pattern of the third BIOX sample (Pond). The appearance of Fe_3O_4 reflections, which could be attributed to the presence of residual organics that can act as reducing agents, has been confirmed by the developed magnetic property of the calcined samples by which these samples were attracted to an external magnet as presented in **Fig 5.2.a-c**.

The detected silica (SiO_2) reflections in the patterns of these samples, which was expected as SiO_2 is ubiquitous in these environments, were similar to those reported by Rico and Hargreaves [190], who used a BIOX sample collected from the Milngavie area. Such reflections are further confirmed by detecting Si in the EDX spectra (**Fig 5.7**, **Fig 5.8**, and **Fig 5.9**). The amorphous structure of the pristine BIOX samples is quite similar to the structure of the 2-line ferrihydrite as shown in **Fig 5.1.b**.

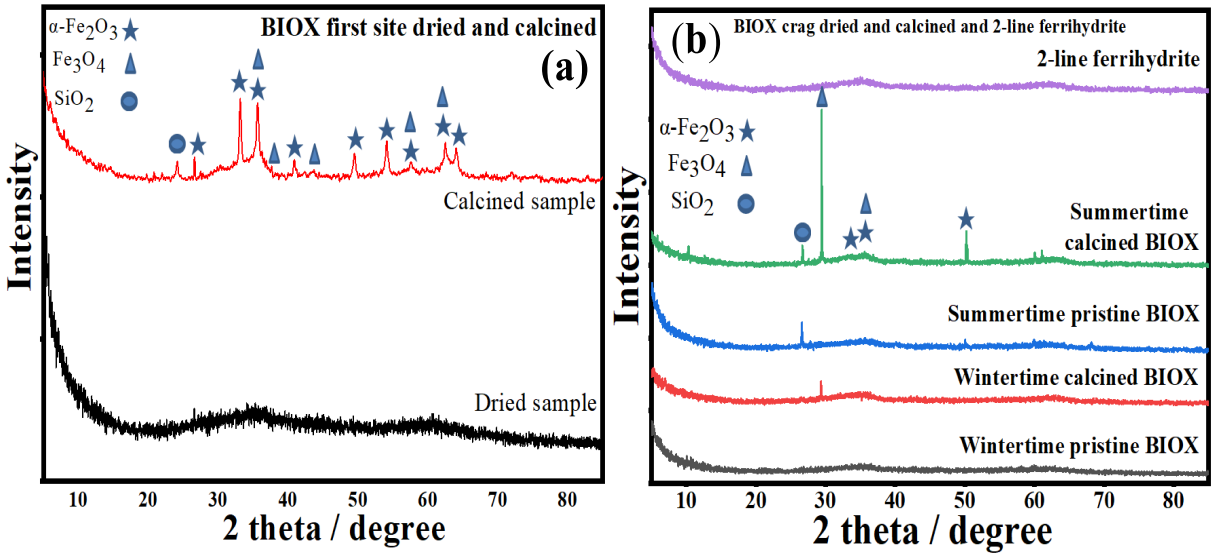

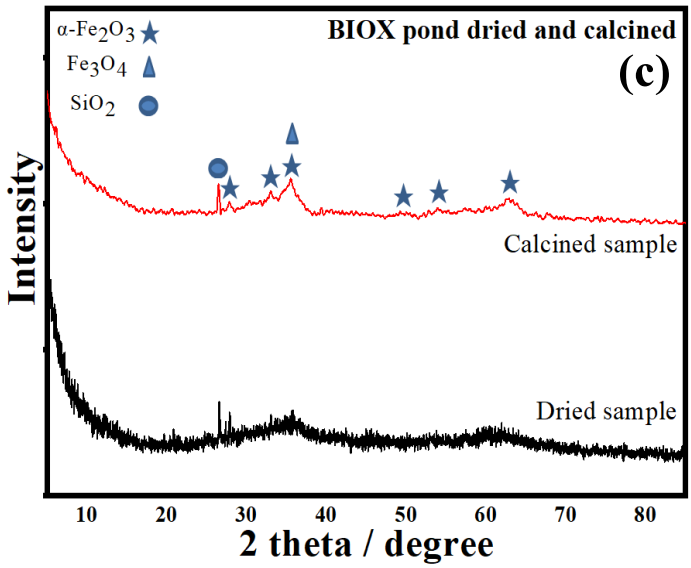

Fig 5.1. Powder XRD patterns of pristine and calcined BIOX (first site) **(a)** second site (crag) and 2-line ferrihydrite **(b)**, and third site (pond) **(c)**.

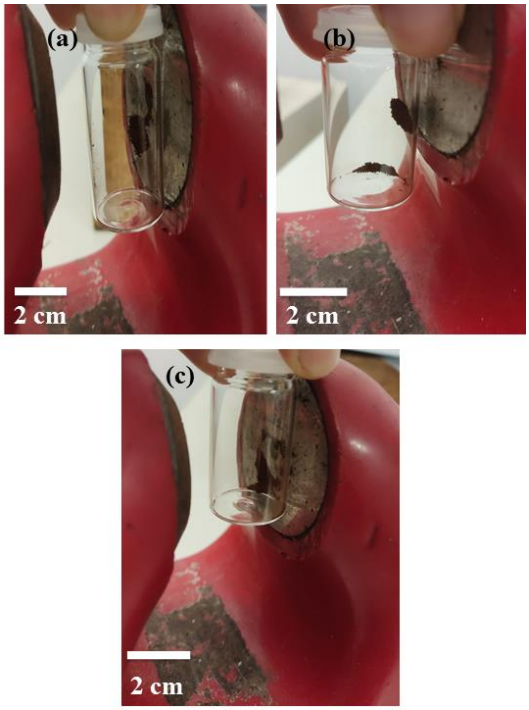

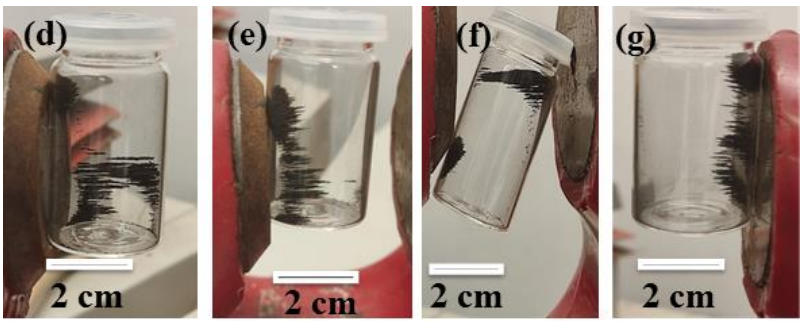

Fig 5.2. The magnetic property of calcined BIOX samples: BIOX first site **(a)**, BIOX crag **(b)**, Pond **(c)**, and reduced BIOX 1 **(d-g)**.

After reducing the crag (wintertime) sample at different temperatures ranging from 300 °C to 700 °C for one hour under pure H_2, it was clear that crag is still mostly amorphous at 300 °C. Only one Fe_3O_4 plane (400) was observed using either pure H_2 or H_2/N_2 (**Fig 5.3.a-b**). However, the reflections of the zero-valent Fe started to appear at 44.45°, 65.22°, and 82.47° [JCPDS:06-0696] upon increasing the temperature to 400 °C and the intensity of these reflections grew as a function of increasing the temperature up to 700 °C (**Fig 5.4.b**). The zero-valent Fe reflections are stable as they are detected immediately and even months after exposing the samples to air, water, and after adsorbing DOXY in aqueous solutions as discussed in detail below in **Section 5.5.4 and Fig 5.20**. Commercial TiO_2 (P25) (**Fig 5.4.a**) was used as an internal standard to determine the ratio of the intensity of the main reflection of Fe^0 at 44.45° under all reduction times and temperatures to that of TiO_2 at 25.26°.

Similarly, Rico and Hargreaves [190] proposed the reduction of BIOX to Fe_3O_4 and then to Fe^0 under H_2/N_2 (75%:25%) flow by increasing the temperature to 700 °C. According to the same reference, the possibility of forming wüstite as an intermediate during the reduction under H_2 at temperatures 570 °C cannot be ruled out. This claim was verified by Jozwiak *et al.* [290] by running an *in-situ* powder XRD during the reduction of iron oxides. The powder XRD patterns of all reduced samples without the internal standard are in **Fig 5.5.a-g** where some of them showed very low-intensity reflections of α-Fe_2O_3 and Fe_3O_4 at different reduction temperatures, which could be formed upon the discharge of the samples from the reaction tube and the exposure to the air. Also, SiO_2 was detected in many reduced samples.

The same BIOX sample was reduced under a flow of H_2/N_2 mixture (75%:25%) to investigate the possibility of decreasing the amount of pure H_2 in reducing the sample and the effect of that on the adsorption efficacy. Thus, other H_2/N_2 ratios should be investigated in future work.

H_2/N_2 is a reactive gas mixture used in Haber-Bosch Process that relies on iron-based catalysts such as BIOX materials to synthesize ammonia. Similar to the reduction under pure H_2, the intensities of the Fe^0 reflections increased with increasing temperature (**Fig 5.4.c**), and they were higher than those using pure H_2 at most temperatures.

The coherent diffraction domain sizes of the zero-valent iron produced under pure H_2 were 19 nm, 26 nm, 33 nm, and 48 nm at 400 °C, 500 °C, 600 °C, and 700 °C, respectively. Under the H_2/N_2 atmosphere, the corresponding domain sizes were 29 nm, 33 nm, 40 nm, and 52 nm. The increase in domain size with temperature, evidenced by sharper diffraction reflections, may partly explain the improved performance of the adsorbents as they become more crystalline. Although there are no significant differences in the adsorption efficacy of the two sets of the BIOX materials as will be discussed in **Fig 5.13.a** and **b**, the higher intensity of the Fe^0 reflections of the BIOX samples treated under H_2/N_2 along with their slightly larger domain sizes (more crystalline) could be the reason for their marginally better performance.

It was generally found that increasing the reduction temperature and/or time leads to an increased intensity of Fe^0 reflections, which can possibly mean an increased content of Fe^0. Also, this is related to the growth of iron crystallites. Subsequently, more interaction (e.g.: complexation) can occur between Fe^0 and DOXY and results in better DOXY removal. However, it does not always improve the adsorption efficacy across all pH levels. The BIOX sample was reduced under H_2/N_2 at 700 °C for two hours and then at 400 °C for four hours followed by another four hours at 500 °C, which is a common procedure employed for ammonia synthesis testing [207]. This procedure was mainly undertaken to investigate the potential of BIOX in synthesizing NH_3, and it showed a low activity in this process, but instead of disposing of the resultant material, it was tested as an adsorbent for DOXY and the results were promising.

The results of NH_3 synthesis are presented at the end of this chapter. This material was given the name reduced BIOX 1 in this study and it showed the most intense and sharpest Fe^0 reflections along with the biggest domain size of 89 nm in the current study (**Fig 5.4.d**). To understand the reason for the powder XRD and adsorption results of reduced BIOX 1, different reduction programmes under H_2/N_2 were used to identify the main factors behind this promising performance of reduced BIOX 1.

Reducing BIOX at 700 °C for four hours showed a higher intensity of the Fe^0 reflections than that of the same temperature for two hours (**Fig 5.4.e**). Although the intensity fluctuated by increasing the reduction time at 700 °C, it was generally growing by increasing the time. Similarly, the reduction at a lower temperature (500 °C) for ten hours resulted in a higher intensity than that of the four hours, which indicates that the reduction time also has a major effect on the intensity of Fe^0 reflections.

Reducing BIOX at 700 °C for eight hours led to a higher intensity accompanied by better adsorption performance compared to the reduction for six hours comprised of 700 °C for two hours followed by four hours of 400 °C (**Fig 5.4.d**). This six-hour reduction programme was used to investigate the effect of the different steps used in the reduction programme of reduced BIOX 1. Within the same context, BIOX was reduced at 400 °C for four hours followed by another four hours at 500 °C. The reflections' intensity of this programme was less than that of ten hours at 700 °C and even less than that of 500 °C (**Fig 5.4.f**). Consequently, the adsorption efficacy of 500 °C (ten hours) was better. Such a result confirms the essential role of the reduction time along with the temperature. Hence, the reduction of reduced BIOX 1 at different temperatures including the highest one (700 °C) and for ten hours exhibited highly intense Fe^0 reflections along with very good adsorption efficiency.

As a reference material, synthesized 2-line ferrihydrite was reduced under H_2/N_2 for one hour at 700 °C and also using the long reduction programme of reduced BIOX 1 (**Fig 5.4.g**) and their reflections were significantly less intense compared to the reduced BIOX 1. Consequently, the adsorption efficiency of these samples was clearly lower than that of reduced BIOX 1 as shown in **Fig 5.13.e**.

All reduced BIOX samples either under pure H_2 or H_2/N_2 were black-coloured and magnetic. Their magnetic property was stronger than that of the calcined BIOX sample as shown in **Fig 5.2.d-g**, which is for the reduced BIOX 1. Similarly, the reduced 2-line ferrihydrite samples were magnetic, but their colour was grey. The same reduction profile of reduced BIOX 1 was used to reduce other waste materials such as RM and its derived α-Fe_2O_3 to assess the applicability of using this programme in producing highly efficient adsorbents. The intensity of Fe^0 reflections of the reduced RM and α-Fe_2O_3 were less than that of reduced BIOX 1 (**Fig 5.4.g**), but their adsorption results were still promising.

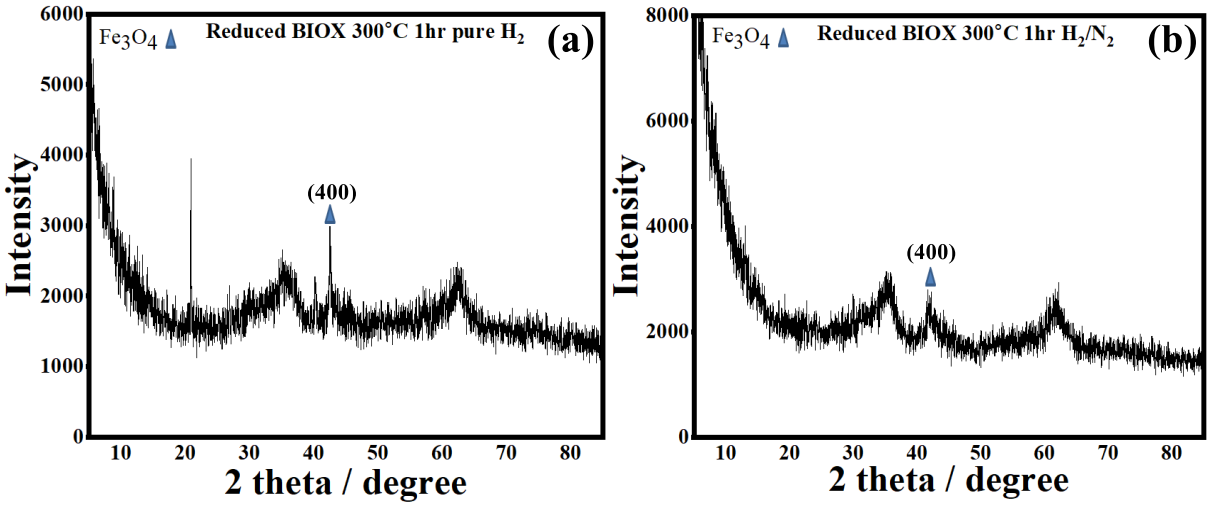

Fig 5.3. Powder XRD patterns of reduced BIOX at 300 °C for 1 hour under pure H_2 **(a)** and H_2/N_2 **(b)**.

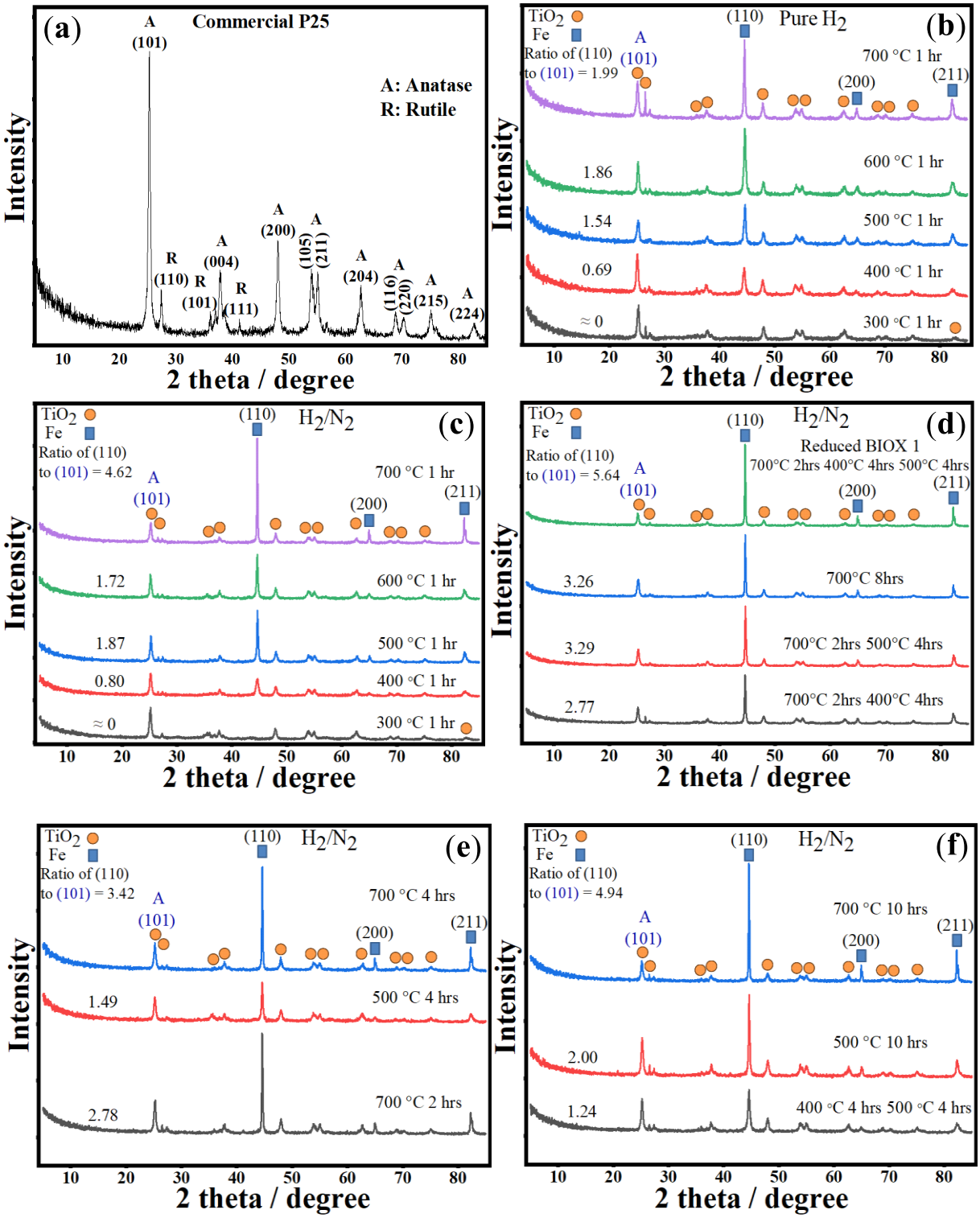
(a)
Commercial P25
A: Anatase
R: Rutile
A (101)
R (110)
R (101)
A (004)
R (111)
A (200)
A (105)
A (211)
A (204)
A (116)
A (220)
A (215)
A (224)
Intensity
2 theta / degree
(b)
TiO2
Fe
Ratio of (110) to (101) = 1.99
Pure H2
700 °C 1 hr
1.86
600 °C 1 hr
1.54
500 °C 1 hr
0.69
400 °C 1 hr
≈ 0
300 °C 1 hr
(c)
H2/N2
Ratio of (110) to (101) = 4.62
700 °C 1 hr
1.72
600 °C 1 hr
1.87
500 °C 1 hr
0.80
400 °C 1 hr
≈ 0
300 °C 1 hr
(d)
H2/N2
Ratio of (110) to (101) = 5.64
Reduced BIOX 1
700°C 2hrs 400°C 4hrs 500°C 4hrs
3.26
700°C 8hrs
3.29
700°C 2hrs 500°C 4hrs
2.77
700°C 2hrs 400°C 4hrs
(e)
H2/N2
Ratio of (110) to (101) = 3.42
700 °C 4 hrs
1.49
500 °C 4 hrs
2.78
700 °C 2 hrs
(f)
H2/N2
Ratio of (110) to (101) = 4.94
700 °C 10 hrs
2.00
500 °C 10 hrs
1.24
400 °C 4 hrs 500 °C 4 hrs

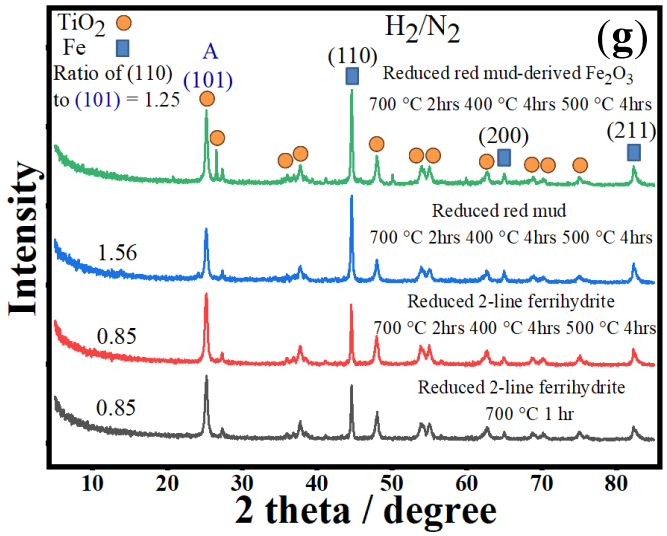

Fig 5.4. Powder XRD patterns of P25 **(a)**, reduced BIOX material under pure H_2 **(b)**, H_2/N_2 for 1 hour at different temperatures **(c)**, at different temperatures for 6, 8, and 10 hours (H_2/N_2) **(d)**, at 500 °C and 700 °C for different times (H_2/N_2) **(e)**, at different temperatures for 8 and 10 hours (H_2/N_2) **(f)**, reduced 2-line ferrihydrite at various temperatures for different times (H_2/N_2) and reduced Chinese RM and reduced Chinese RM-derived α-Fe_2O_3 (H_2/N_2) **(g)**. P25 was used as an internal standard in panels **b-g**.

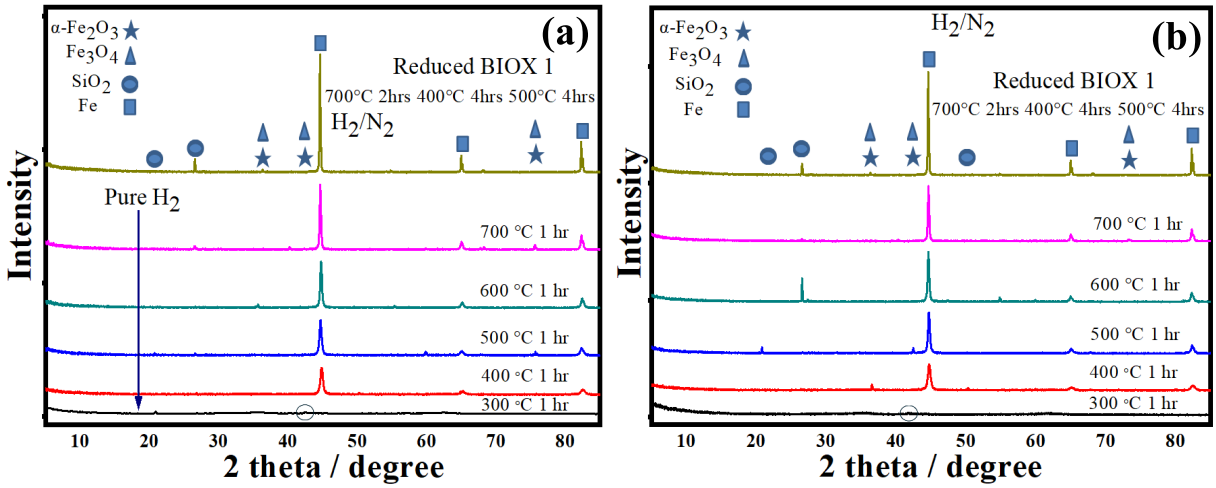

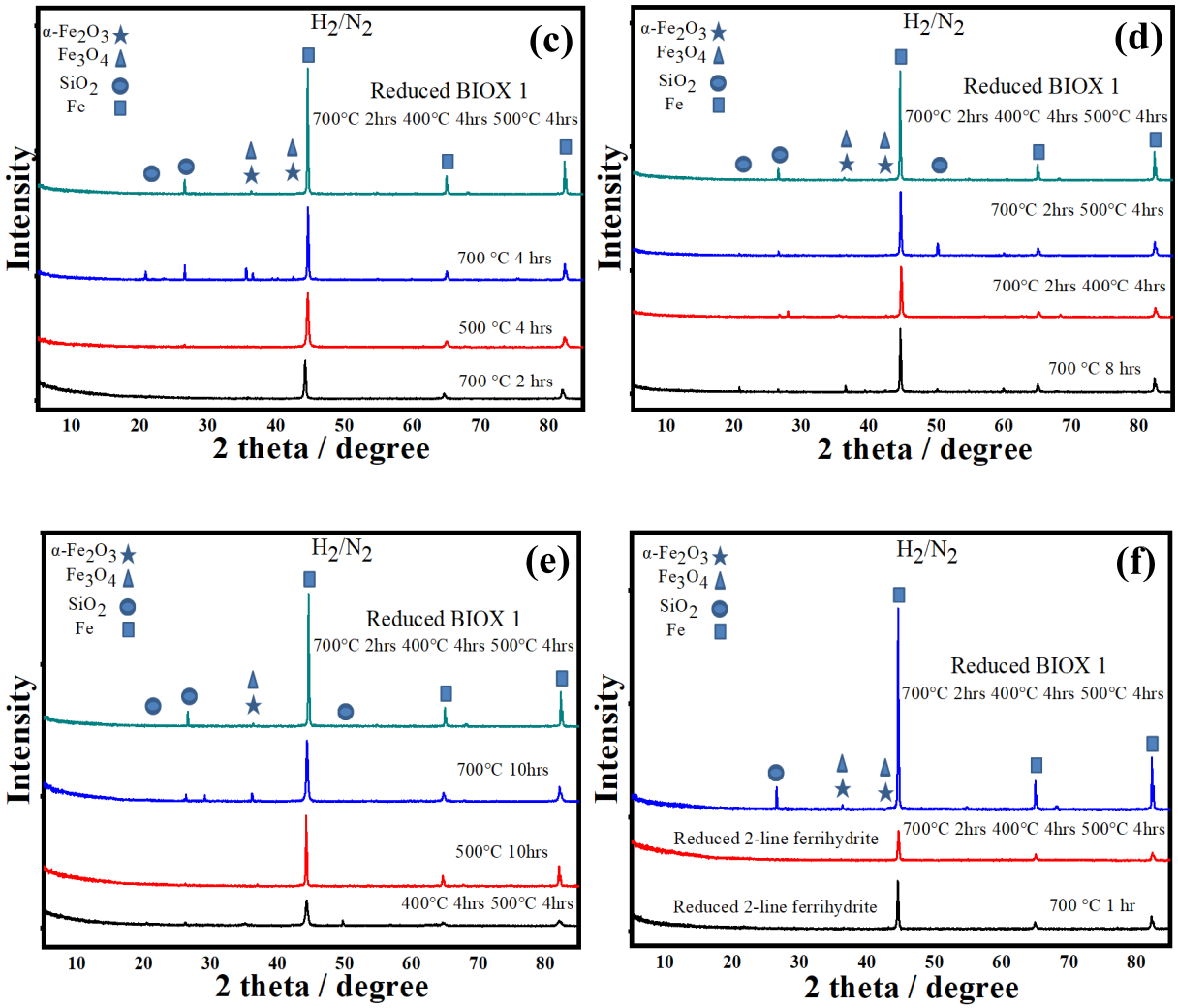
(c)
H2/N2
α-Fe2O3
Fe3O4
SiO2
Fe
Reduced BIOX 1
700°C 2hrs 400°C 4hrs 500°C 4hrs
700 °C 4 hrs
500 °C 4 hrs
700 °C 2 hrs
Intensity
2 theta / degree
(d)
H2/N2
α-Fe2O3
Fe3O4
SiO2
Fe
Reduced BIOX 1
700°C 2hrs 400°C 4hrs 500°C 4hrs
700°C 2hrs 500°C 4hrs
700°C 2hrs 400°C 4hrs
700 °C 8 hrs
Intensity
2 theta / degree
(e)
H2/N2
α-Fe2O3
Fe3O4
SiO2
Fe
Reduced BIOX 1
700°C 2hrs 400°C 4hrs 500°C 4hrs
700°C 10hrs
500°C 10hrs
400°C 4hrs 500°C 4hrs
Intensity
2 theta / degree
(f)
H2/N2
α-Fe2O3
Fe3O4
SiO2
Fe
Reduced BIOX 1
700°C 2hrs 400°C 4hrs 500°C 4hrs
Reduced 2-line ferrihydrite
700°C 2hrs 400°C 4hrs 500°C 4hrs
Reduced 2-line ferrihydrite
700 °C 1 hr
Intensity
2 theta / degree

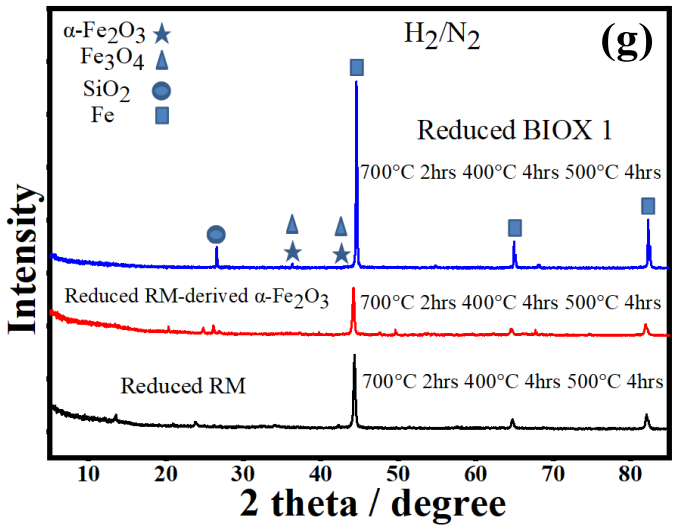

Fig 5.5. Powder XRD patterns of reduced BIOX material under pure H_2 **(a)**, H_2/N_2 for 1 hour at different temperatures **(b)**, at 500 °C and 700 °C for different times (H_2/N_2) **(c)**, at different temperatures for 6 and 8 hours (H_2/N_2) **(d)**, at different temperatures for 8 and 10 hours (H_2/N_2) **(e)**, reduced 2-line ferrihydrite at various temperatures for different times (H_2/N_2) **(f)**, and reduced Chinese RM and reduced Chinese RM-derived α-Fe_2O_3 (H_2/N_2) **(g)**. Reduced BIOX 1 at 700 °C for 2 hours followed by 400 °C for 4 hours and then 500 °C for 4 hours was used as a standard in all panels.

5.3. BET analysis of BIOX and 2-line ferrihydrite

Unlike the high surface area of BIOX samples which is usually higher than 250 m^2/g [184, 291] as reported in previous studies, the surface area of the BIOX collected from the first site is only 71 m^2/g (**Fig 5.6.a**) and that of the crag sample (wintertime) is 197 m^2/g (**Fig 5.6.b**). All materials shown in **Fig 5.6** were microporous as their pore size was less than 2 nm, but their BET isotherms seemed to be type IV. The hysteresis type of both samples is probably H3 with wedge-shaped pores. After undergiong reduction for 10 hours at different temperatures, the surface area of reduced BIOX 1 was 29 m^2/g (**Fig 5.6.c**) probably with the same hysteresis type as that of the crag sample (H3). Additionally, the reduced BIOX materials at 500 °C for 10 hours and at 700 °C for 8 hours were analyzed to further clarify the surface area of the reduced materials, revealing surface areas of 50 and 34 m^2/g, respectively (**Fig 5.6.d** and **e**). This is because the surface area loss might be similar, but the particles are slightly larger in the case of the 700 °C. The type of hysteresis of the reduced sample at 500 °C was H3, while that of the sample reduced at 700 °C was H1 with possible cylindrical pores. Some nitrogen

physisorption isotherms show a low-quality hystersis loop because of issues encountered with the instrument and these are the best results obtained after multiple trials.

The low surface areas of the reduced materials could be attributed to sintering at the high reduction temperatures as reported by Rico and Hargreaves [190]. Despite their lower surface areas, the reduced BIOX materials demonstrated improved performance, which can be linked to the formation of Fe^0 and the grown intensity of its reflections as a function of the reduction temperature and time. The surface area of the 2-line ferrihydrite is 223 m^2/g (**Fig 5.6.f**) with a hysteresis type of H4 and possible slit-shaped pores. Previously published results of 2-line ferrihydrite prepared by a precipitation method similar to the one used in the current study such as Zhu *et al.* [292] and Yoo [293], reported surface areas of 331 m^2/g and 276 m^2/g, respectively. Other preparation methods of 2-line ferrihydrite resulted in different surface areas including those reported by Rout *et al.* [294] and Smith *et al.* [295] that were 176 m^2/g and 248 m^2/g, respectively.

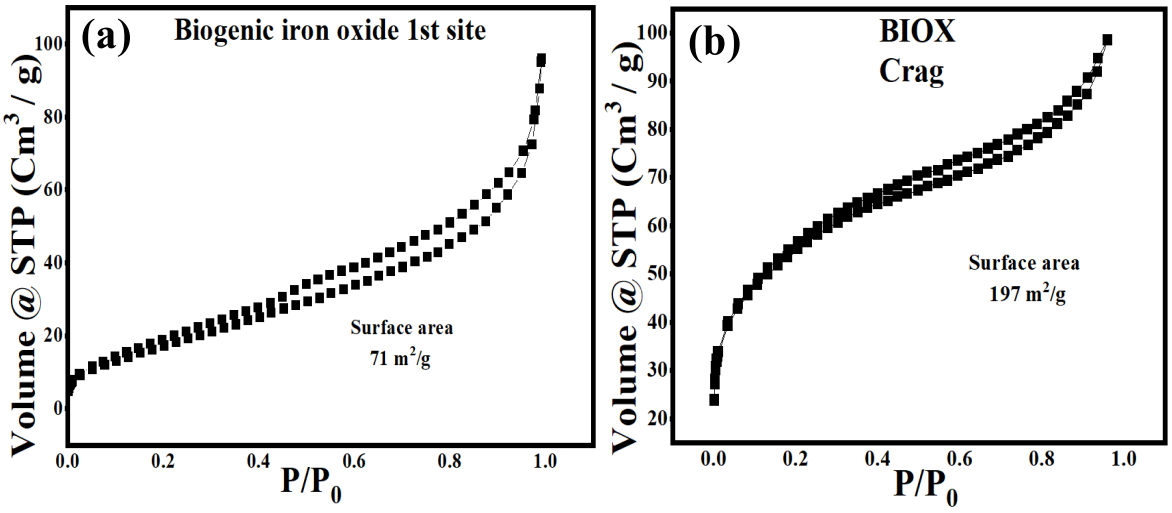

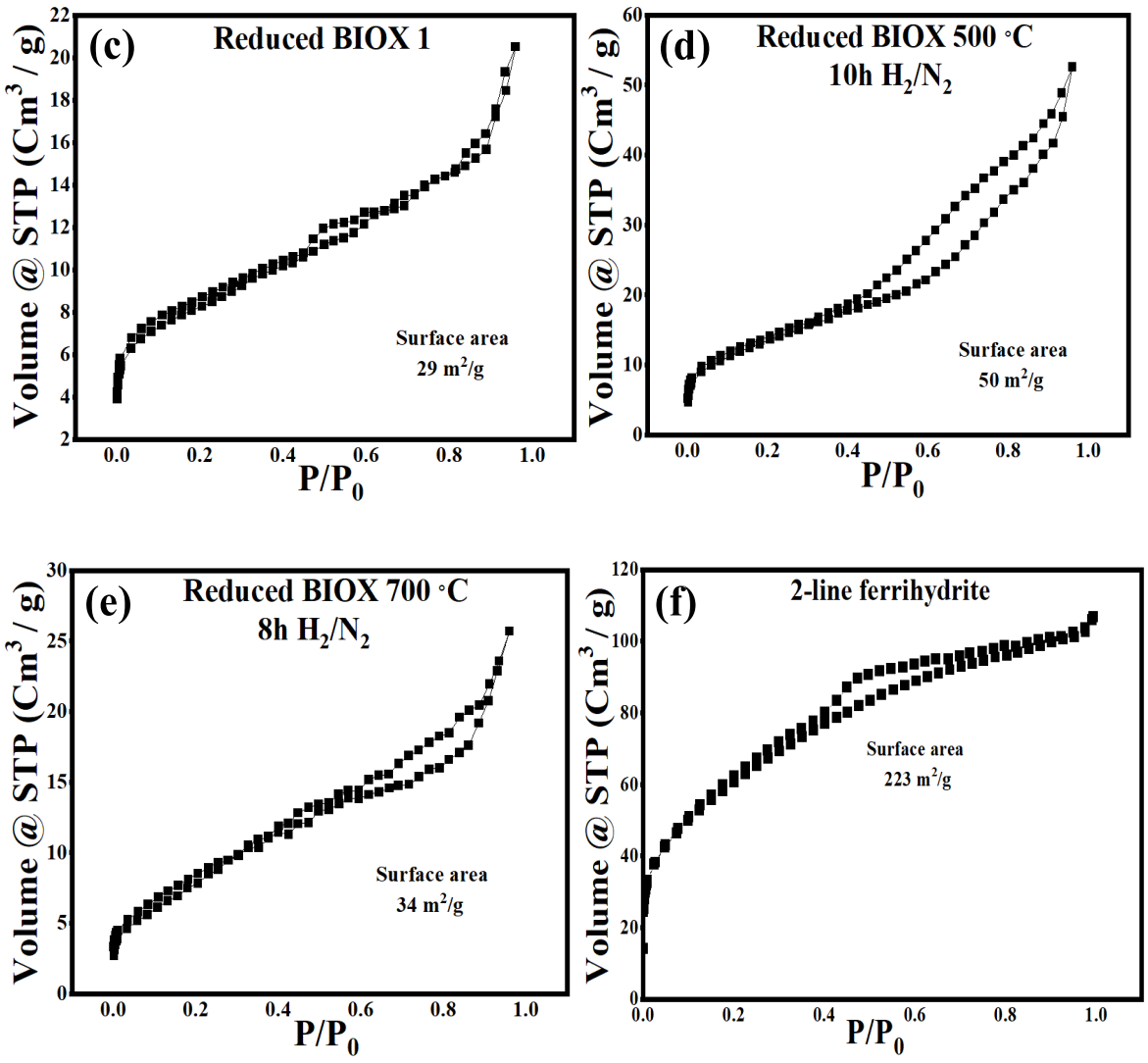

Fig 5.6. Nitrogen physisorption isotherms of the pristine BIOX first site **(a)**, second site (crag) **(b)**, reduced BIOX 1 **(c)**, reduced BIOX 500 °C 10h H_2/N_2 **(d)**, reduced BIOX 700 °C 8h H_2/N_2 **(e)**, and 2-line ferrihydrite **(f)**.

5.4. SEM and EDX analysis of BIOX and 2-line ferrihydrite

SEM images of BIOX samples that were collected in July 2024 from three different sites in River Allander show a mixture of irregularly shaped aggregates and hollow, open-end microtubes, which are synthesized by *Leptothrix* as an extracellular coating [182] (**Fig 5.7.a**, **b**, **d**, **e**, **f**, **h**, and **i**). The tubes exhibited different diameters and lengths, which could be attributed to variations in growth stage, nutritional and environmental conditions, and physiological (phenotypic) heterogeneity [296]. The tubes were similar to those observed by

Alharthi *et al.* [184] and Hargreaves and Alharthi [291] who obtained the samples from the same river in 2014.

The EDX spectra of the three samples showed the presence of the main elements (iron and oxygen) along with other minor constituents such as calcium, silicon, and aluminium (**Fig 5.7.c**, **g**, and **j**). Although the lab-synthesized 2-line ferrihydrite has a very similar amorphous structure to that of BIOX samples, SEM images of this material showed only irregular morphology (**Fig 5.7.k** and **l**) with fewer elements compared to the BIOX samples evident from EDX (**Fig 5.7.m**).

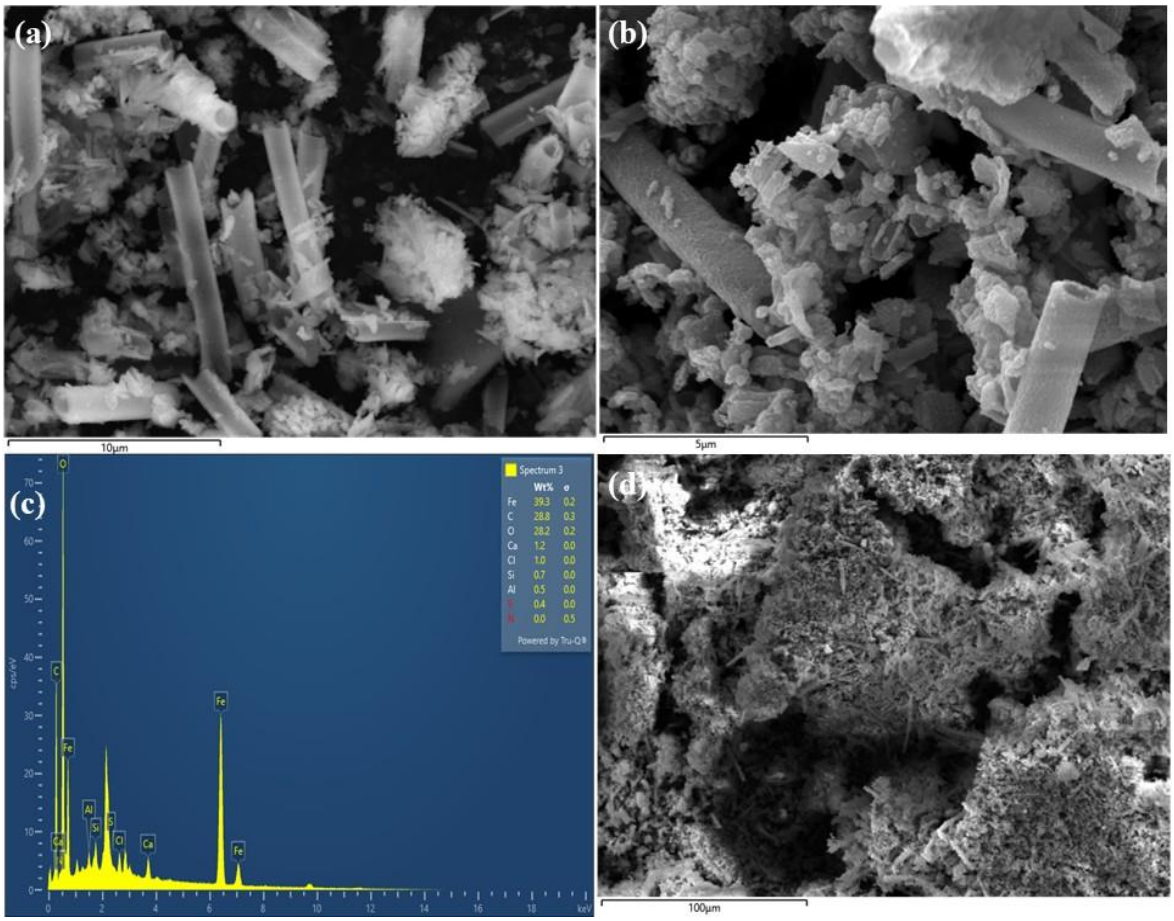

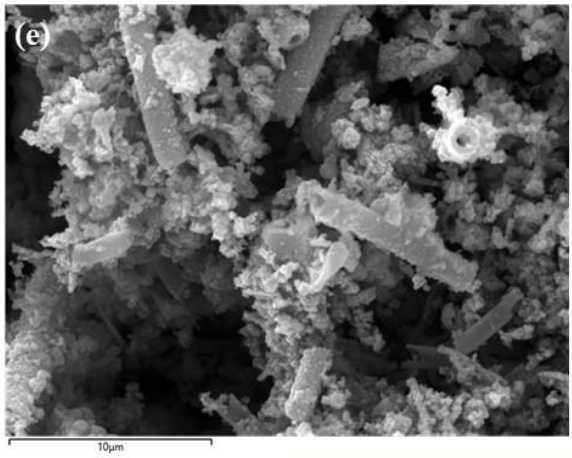
(e)
10µm

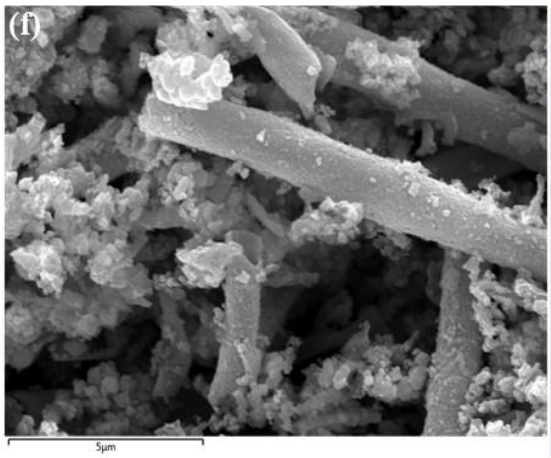
(f)
5µm

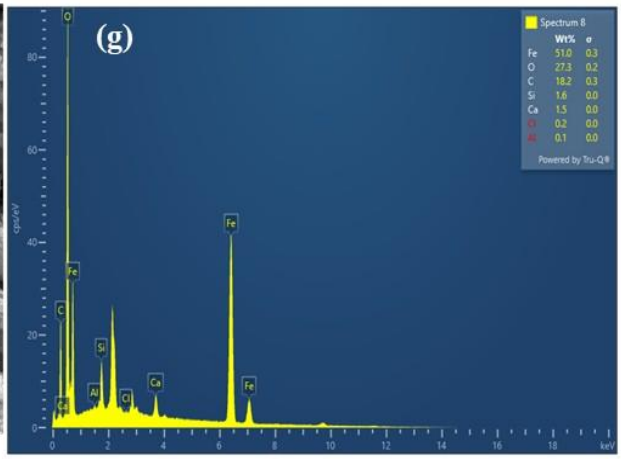
(g)
Spectrum 8
Wt% σ
Fe 51.0 0.3
O 27.3 0.2
C 18.2 0.3
Si 1.6 0.0
Ca 1.5 0.0
Cl 0.2 0.0
Al 0.1 0.0
Powered by Tru-Q®
cps/eV
keV

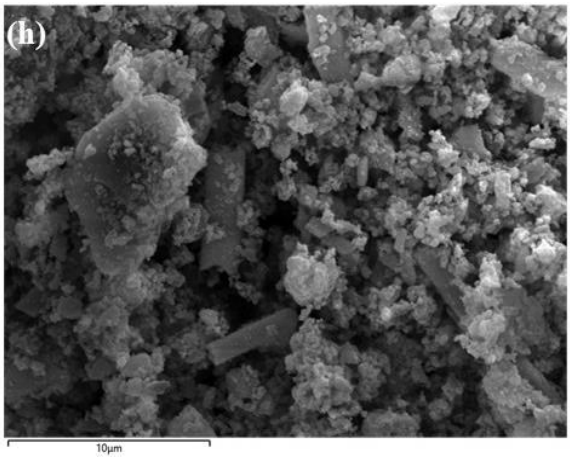
(h)
10µm

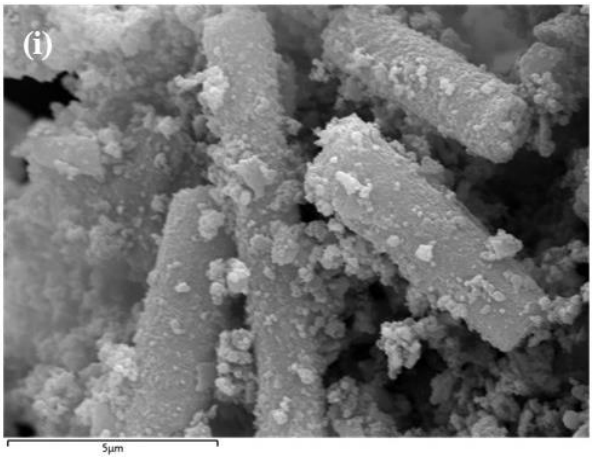
(i)
5µm

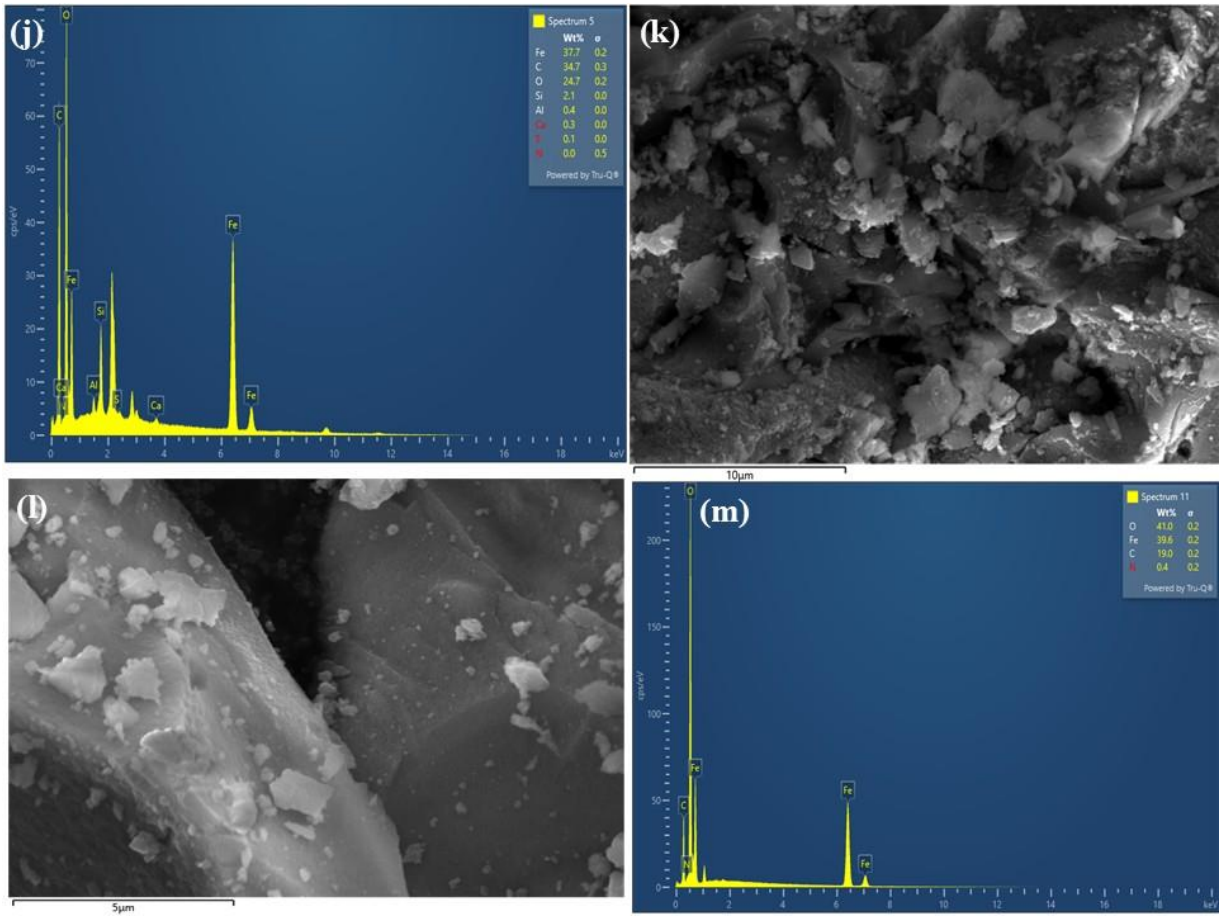

Fig 5.7. SEM images **(a** and **b)** and EDX spectrum of BIOX first site **(c)**, SEM images **(d-f)** and EDX spectrum of BIOX second site (crag) **(g)**, SEM images **(h** and **i)** and EDX spectrum of BIOX third site (Pond) **(j)**, SEM images **(k** and **l)** and EDX spectrum of 2-line ferrihydrite **(m)**.

Upon calcining the BIOX samples, the microtubular structure of the three samples was almost the same as it was before the calcination as shown in **Fig 5.8.a-m**. Similarly, the EDX spectra of the calcined samples showed very similar elemental composition to the uncalcined ones (**Fig 5.8. d, i,** and **m**). This could be very important for future applications of these BIOX materials.

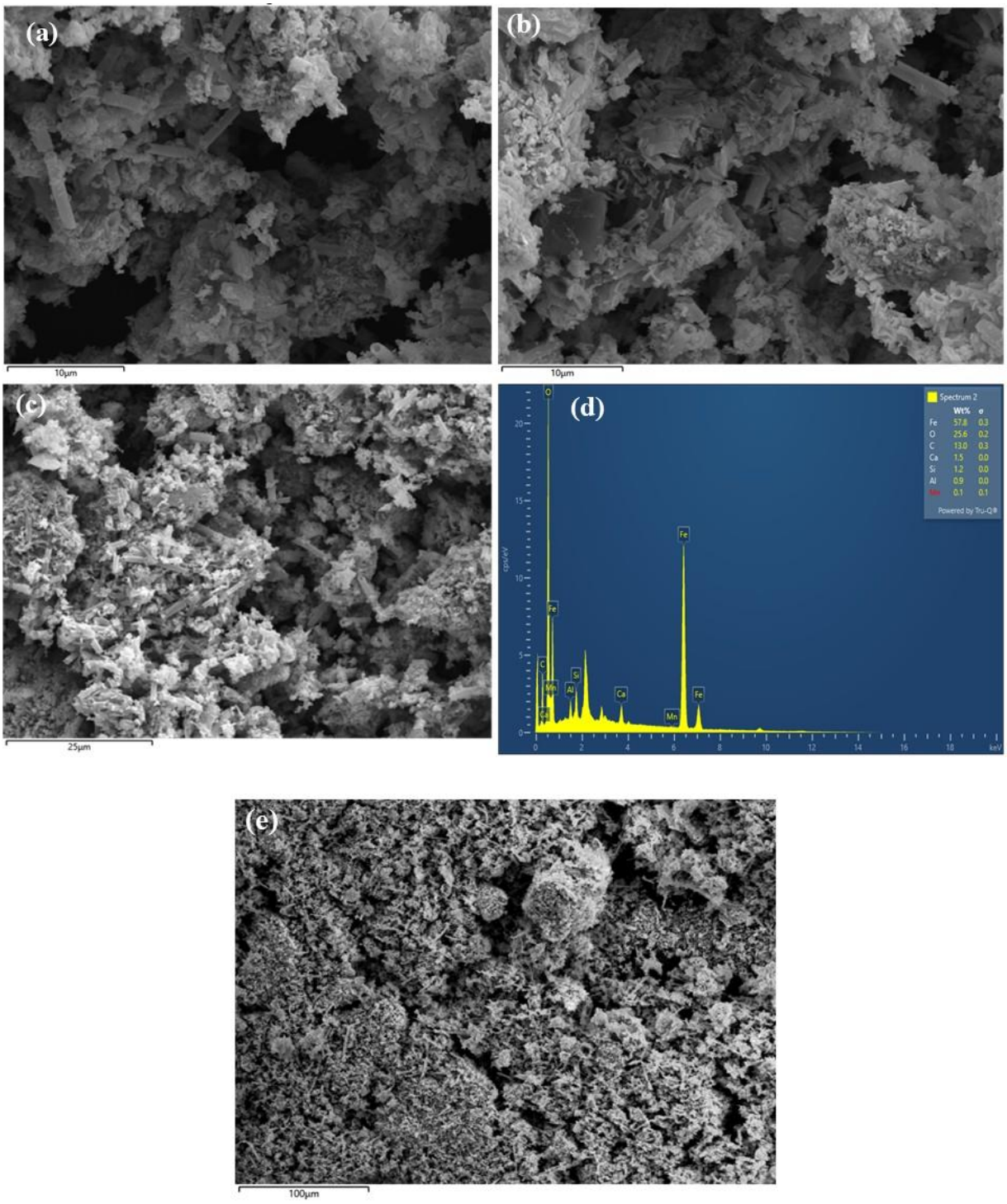
(a)
10μm
(b)
10μm
(c)
25μm
(d)
Spectrum 2
Wt% σ
Fe 57.8 0.3
O 25.6 0.2
C 13.0 0.3
Ca 1.5 0.0
Si 1.2 0.0
Al 0.9 0.0
Mn 0.1 0.1
Powered by Tru-Q®
O
Fe
C
Mn
Al
Si
Ca
Mn
Fe
cps/eV
keV
(e)
100μm

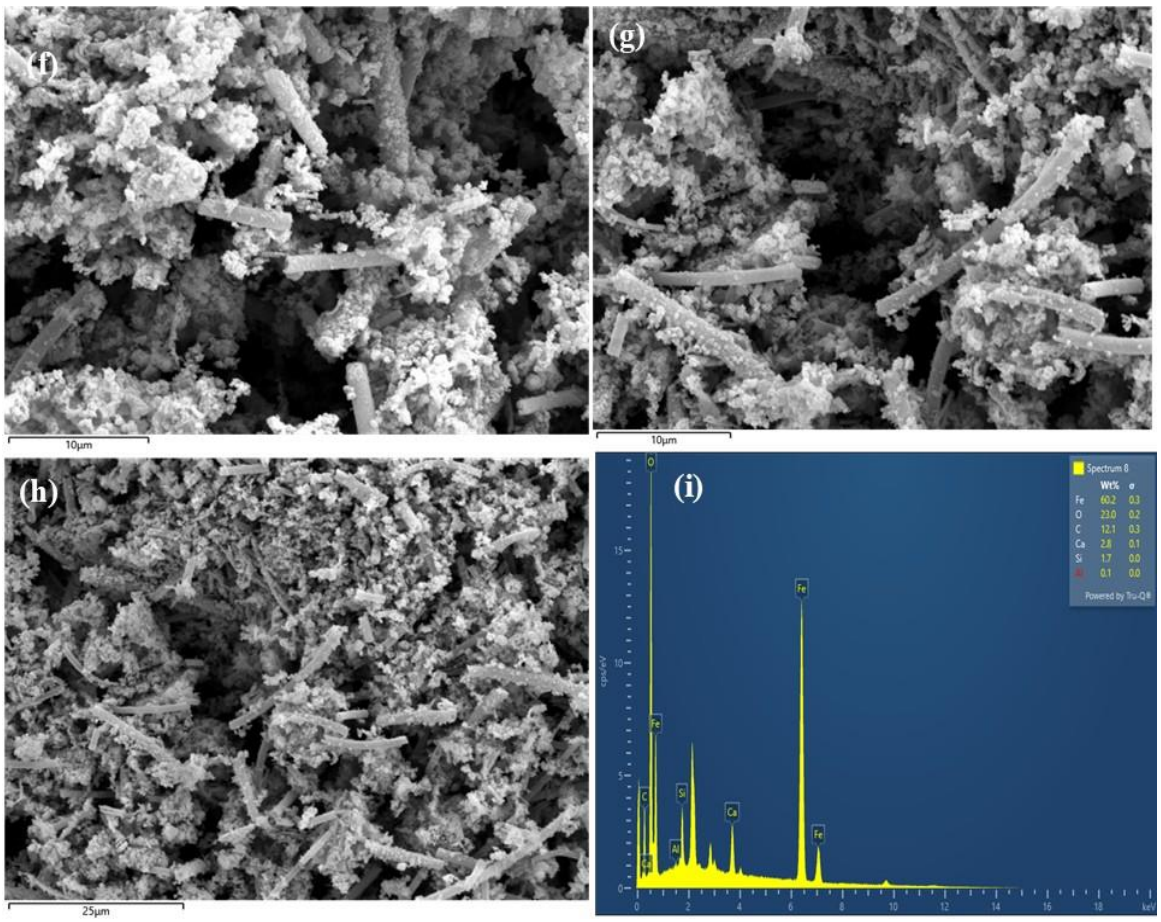
(f)
10µm
(g)
10µm
(h)
25µm
(i)
Spectrum 8
Wt%
Fe 60.2 0.3
O 23.0 0.2
C 12.1 0.3
Ca 2.8 0.1
Si 1.7 0.0
Al 0.1 0.0
Powered by Tru-Q®
O
Fe
C
Si
Ca
Al
Fe
cps/eV
keV

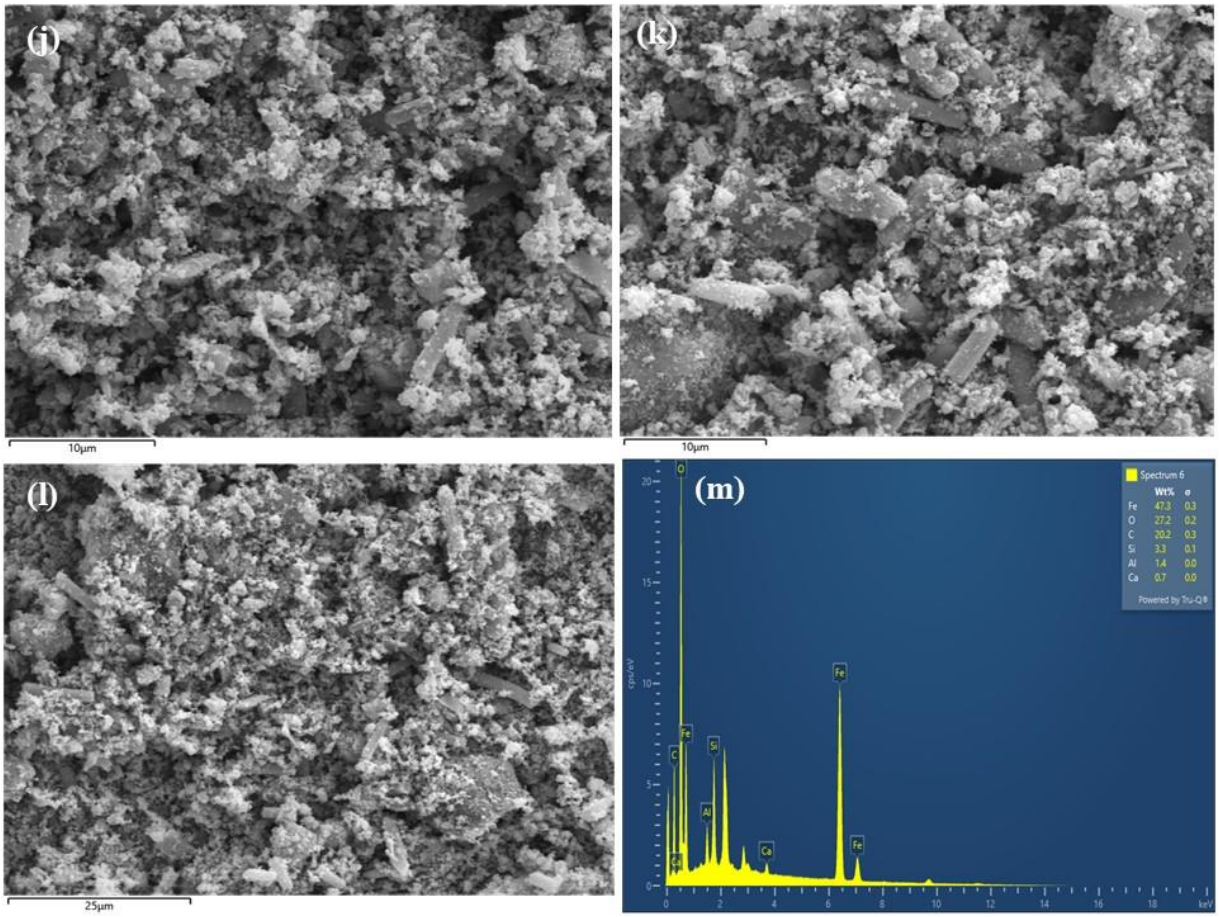

Fig 5.8. SEM images **(a-c)** and EDX spectrum of calcined BIOX first site **(d)**, SEM images **(e-h)** and EDX spectrum of calcined BIOX second site (crag) **(i)**, SEM images **(j-l)** and EDX spectrum of calcined BIOX third site (Pond) **(m)**.

The wintertime crag sample, which was collected in January 2025, showed the same tubular morphology. However, other closed-end tubes that are long, solid, and made of silica, were observed, indicating the possible contamination of this sample with silica from the environment (**Fig 5.9.a-b**). This result could be related to the low consumption of silicon by planktonic microorganisms during the wintertime. In contrast, these microorganisms consume large amounts of silicon during the summertime to build their cell walls as reported by Neal *et al.* [211] who conducted a study across a wide range of water bodies in the UK in 2005.

The focus was then on the morphology of the reduced wintertime crag under H_2/N_2 which has been called reduced BIOX 1. The tubular morphology and the elemental composition did not change after the reduction (**Fig 5.9.c-e**). Some tubes are curved, and others are straight. Also, they have various sizes and/or diameters. Light blue and black arrows are used to refer to

some long and short tubes in the images. These long tubes were still observed along with the short ones in the images of reduced BIOX 1 with a similar elemental composition after being used in DOXY adsorption in DW (**Fig 5.9.f-h**) and the River Clyde water (**Fig 5.9.i-l**).

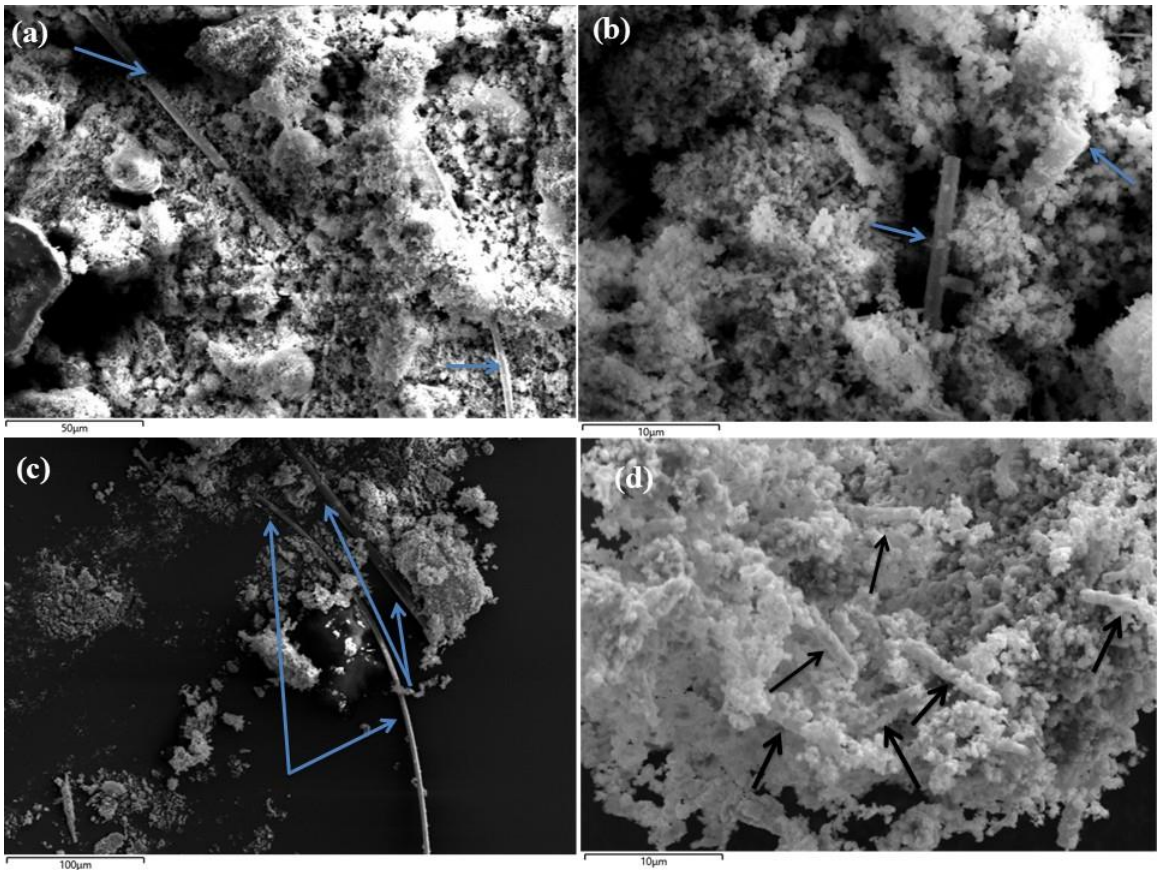

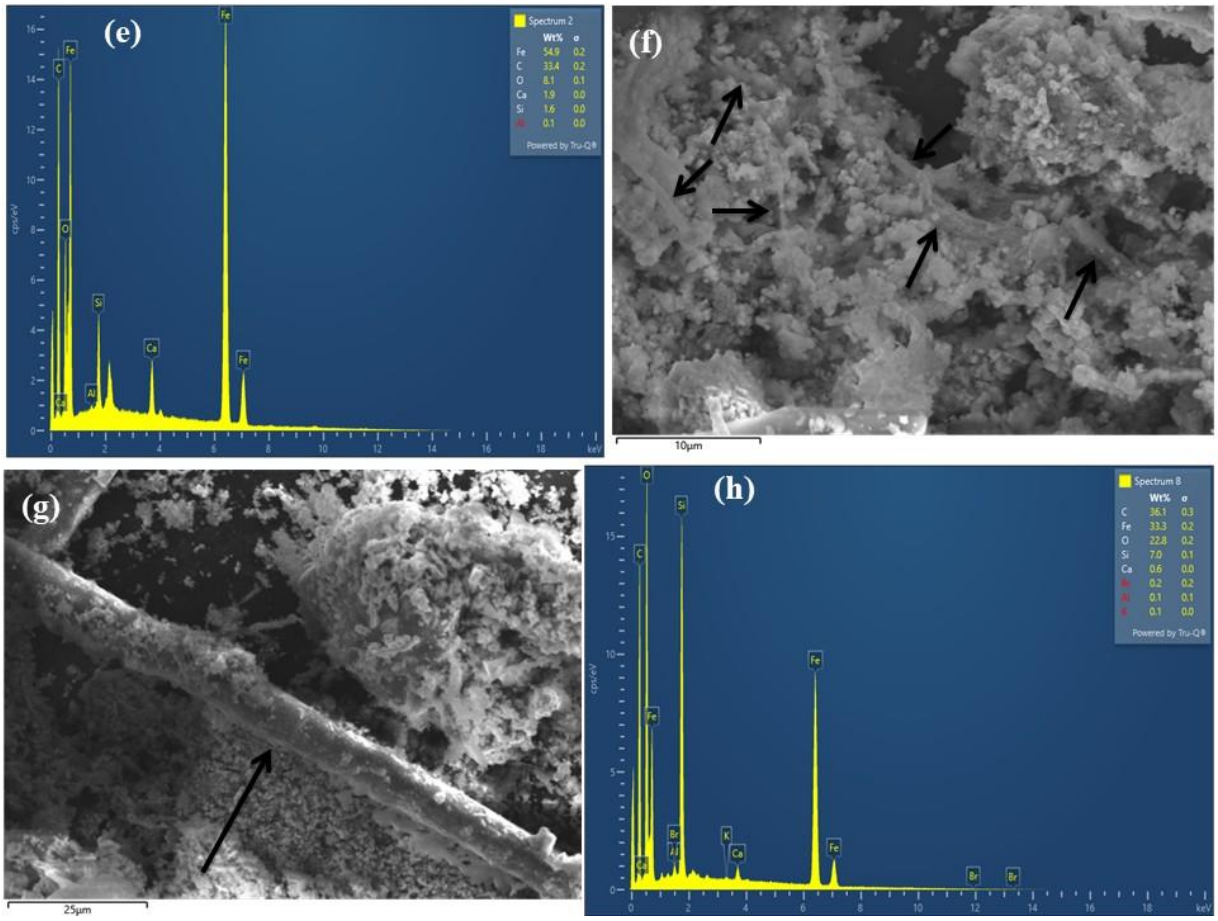
(e)
Spectrum 2
Wt%
Fe 54.9 0.2
C 33.4 0.2
O 8.1 0.1
Ca 1.9 0.0
Si 1.6 0.0
Powered by Tru-Q®
(f)
10µm
(g)
25µm
(h)
Spectrum 8
Wt%
C 36.1 0.3
Fe 33.3 0.2
O 22.8 0.2
Si 7.0 0.1
Ca 0.6 0.0
Powered by Tru-Q®

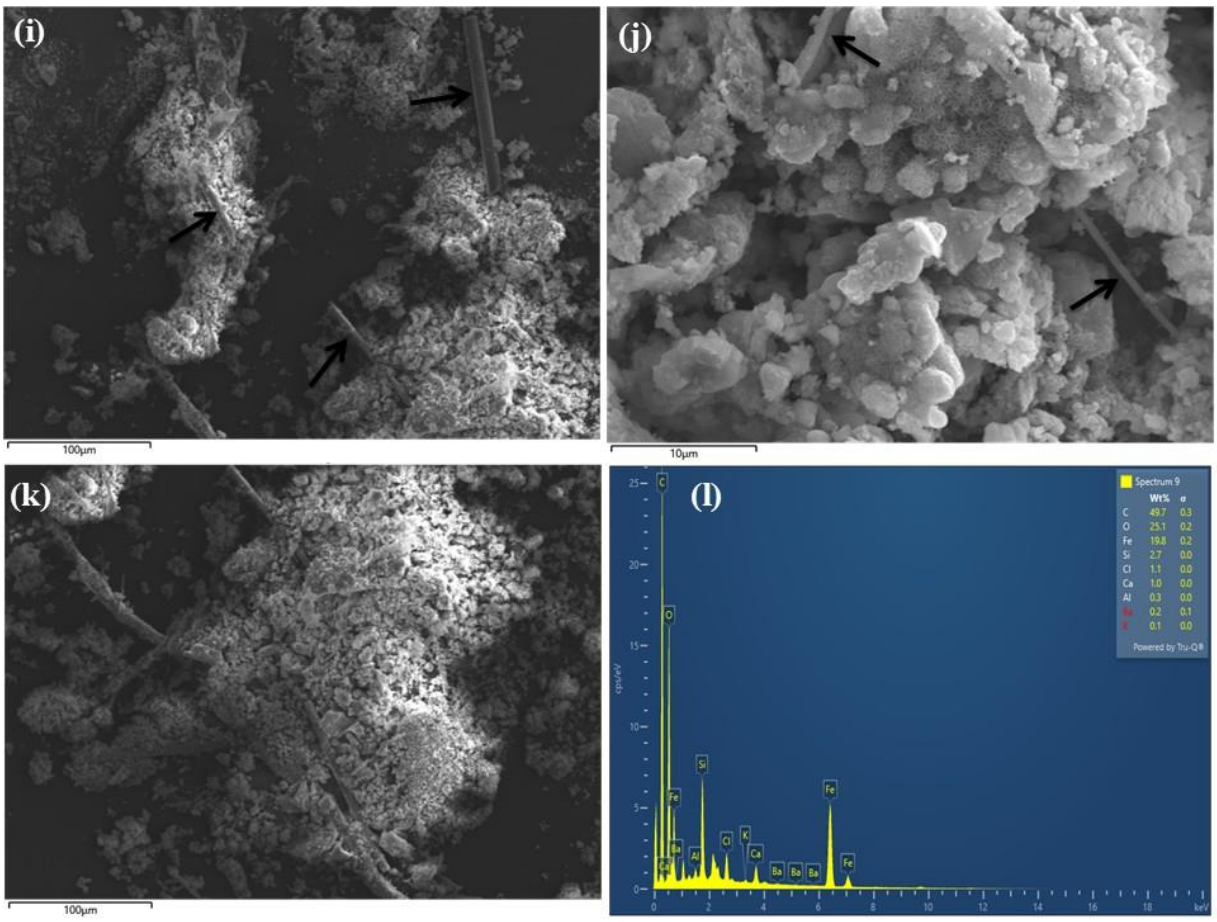

Fig 5.9. SEM images of pristine BIOX (crag) collected in January 2025 **(a-b)**, SEM **(c-d)** and EDX spectrum of reduced BIOX 1 **(e)**, SEM **(f-g)** and EDX after DOXY adsorption in DW **(h)**, and in the River Clyde water sample **(i-l)**.

The mapping results of the reduced BIOX 1 show that the short tubes are mainly made of iron (**Fig 5.10.a-g**). Also, other elements such as silicon, calcium, and aluminium were detected in the aggregates of these tubes as indicated by the EDX analysis. These results are in agreement with those reported by Johannessen *et al.* [297] who investigated biogenic siliceous Fe-oxyhydroxides deposits in an extinct part of the Jan Mayen Vent Fields on the Arctic Mid-Ocean Ridge and found tubular morphology, which is similar to the current results. Other SEM images and maps of different areas of the reduced BIOX 1 and other reduced BIOX materials using the wintertime crag sample are provided in **Appendix 5** (**Fig S15-23**) and the one collected during summertime in **Fig S24** to indicate the statistical relevance of the obtained results.

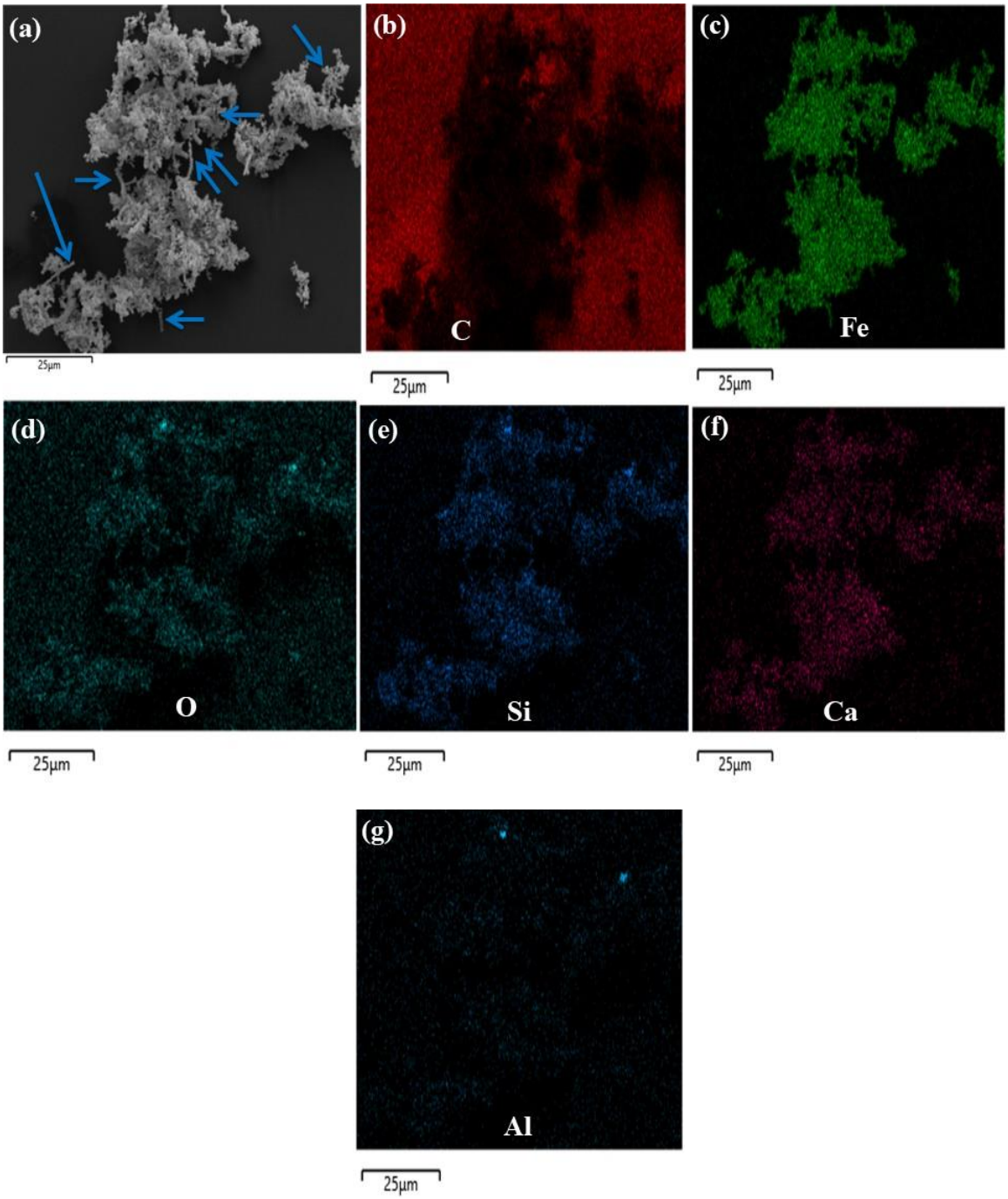

Fig 5.10. SEM image of reduced BIOX 1 **(a)** and its elemental mapping; C (**b**), Fe **(c)**, O **(d)**, Si **(e)**, Ca **(f)**, and Al **(g)**.

5.5. The investigation of BIOX and 2-line ferrihydrite materials in the removal of DOXY

The performance of the three BIOX samples collected during the summertime was similar as they all exhibited the highest adsorption efficacy of DOXY at pH 5 (**Fig 5.11.a**). Among the

three BIOX samples, the sample sourced from the first site showed a better performance compared to the other two samples, particularly at pH 3, 5, and 9. The performance of the crag sample collected during the wintertime was better than that of the summertime, which could be attributed to the synergistic effect of silica microtubes that were detected by the SEM. To confirm that, commercial amorphous silica was tested, and it exhibited a similar adsorption trend (**Fig 5.11.b**). Additionally, the iron content of the two crag samples was leached using 37% HCl, leaving behind silica, similar to the approach of Hashimoto *et al.* [298], who extracted amorphous silica from BIOX for use as an acid catalyst in epoxide ring-opening reactions and Friedel-Crafts-type alkylation.

As shown in **Fig 5.12.a** and **b**, the adsorption efficiency of both samples declined after leaching. Notably, the summertime sample caused an increase in DOXY absorbance rather than a decrease, further confirming the slightly better performance of the wintertime sample. Similar to the BIOX materials, the highest adsorption efficacy of 2-line ferrihydrite was observed at pH 5 and it was 71%. The calcination effect on the performance of both crag samples was similar as it showed a slight improvement across some of the pH levels (5, 7, and 9) as shown in **Fig 5.11.a** and **b**. The wintertime and summertime labels in **Fig 5.11.a** and **b** are only used to differentiate between the two crag samples.

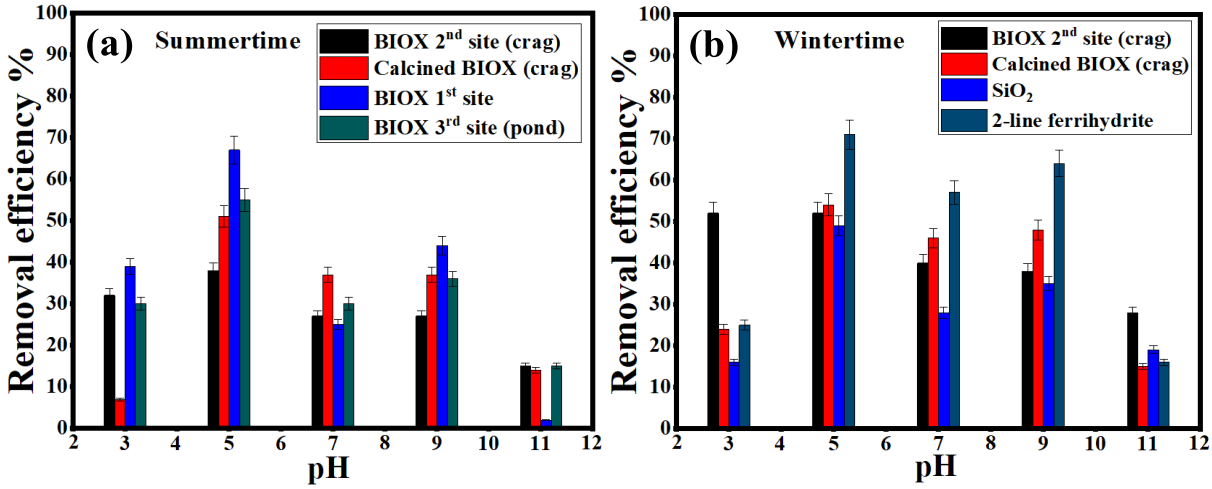

Fig 5.11. The efficiency of three BIOX samples collected during the summertime and the calcined crag **(a)**, and pristine and calcined crag (wintertime), SiO_2, and 2-line ferrihydrite (**b**) in removing DOXY after 90 minutes. [C_o = 25 ppm, stirring rate = 750 rpm, T = 20 ± 2 °C, volume = 10 mL, and dose = 0.005 g].

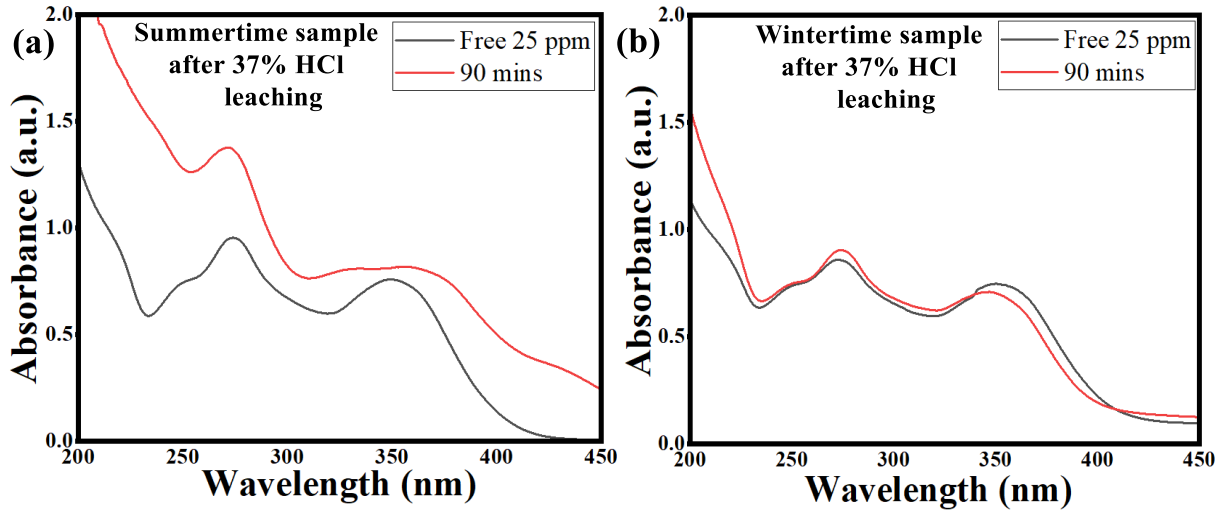

Fig 5.12. The efficiency of 37% HCl-leached summertime **(a)** and wintertime **(b)** crag samples in adsorbing DOXY after 90 minutes. [C_o = 25 ppm, pH = 7, stirring rate = 750 rpm, T = 20 ± 2 °C, volume = 10 mL, and dose = 0.005 g].

The focus was placed on the wintertime crag sample, as the summertime collection did not provide enough material. At least 5-10 g of the pristine crag is required to obtain sufficient reduced BIOX material for testing different synthesis conditions and performing adsorption experiments. The removal efficiency of the reduced material from the winter sample, treated under pure H_2 for one hour, was clearly higher than that of the pristine and calcined materials across most pH levels. The efficacy of the reduced materials was generally going down by increasing the pH from 3 to 11 (**Fig 5.13.a**). Such a result could be attributed to the electrostatic repulsion between these adsorbents and DOXY, which becomes more predominant by increasing the pH. As mentioned in Chapter 4, the Zwitterionic range of DOXY is 3.02 < pH < 7, so the high adsorption efficacies are expected to be within this pH range, particularly at pH 5, and also because the PZC of all the reduced BIOX materials are about 7-8 (**Table 5.4**). However, the result of some of these reduced materials is slightly better at pH 3, which is attributed to the low electrostatic repulsion at that pH compared to the high pH levels. Also, the self-degradation of DOXY in alkaline conditions, which was discussed in the previous chapter, constituted another contributing factor to the removal of DOXY.

Similar to the above-mentioned results, the removal efficacy of the reduced BIOX samples under H_2/N_2 for one hour decreased with increasing the pH (**Fig 5.13.b**). The results of both groups are comparable, but the performance of the H_2/N_2 group is slightly better at pH 3, 7,

and 9 for most of the reduction temperatures, which could possibly be related to the higher intensity of their powder XRD reflections (**Fig 5.4.c**). Based on these promising preliminary results, a further investigation using other reduction durations and temperatures under H_2/N_2 was undertaken. Another reason for conducting this investigation is to understand the performance of reduced BIOX 1 by studying each step in its reduction programme along with other programmes. In agreement with the previous results, the removal efficiency in **Fig 5.13.c** was decreasing by increasing the pH using the reduced BIOX materials at different temperatures and times. The performance of this set exhibits no big difference between the five materials and in general the material reduced at 700 °C for 8 hours has the highest efficacy. Such a result is in line with the powder XRD results as the intensity of this material is higher than the other three materials and close to that reduced at 700 °C for 4 hours (**Fig 5.4.d, e,** and **f**).

Another set of samples was reduced at 700 °C for 2 hours followed by 4 hours either at 400 °C or 500 °C and their results indicate that using the lower temperature (400 °C) leads to better performance across most of the pH levels (**Fig 5.13.d**). This result is in favour of the high efficiency of reduced BIOX 1 as its reduction programme starts at 700 °C for 2 hours followed by 4 hours at 400 °C. Two 10-hour reduction programmes were carried out at 500 °C and 700 °C to clarify the effect of the long reduction time (10 hours) of reduced BIOX 1 on its performance. As shown in **Fig 5.13.d**, the efficacy of the 500 °C was better, which is also in favour of the reduced BIOX 1 as the reduction at 500 °C is longer than that at 700 °C.

Although there are some discrepancies between the performance of the above-mentioned materials and the intensity of their reflections in the powder XRD patterns, the general removal trend shows improved performance as a result of the increased intensity. This is possibly the main reason for the best performance exhibited by reduced BIOX 1 across many pH levels as shown in **Fig 5.13.e** since it has the most intense Fe^0 reflections. This high intensity might indicate more Fe^0 active sites, which could be resulting in more basic surface sites and higher electrostatic attraction with DOXY as will be explained in the removal mechanism. Also, the performance of the reduced BIOX at 300 °C, which did not exhibit any Fe^0 but only one Fe_3O_4 reflection, was better than that of the pristine material because of its higher concentration of basic sites.

Within the same context, the reduced 2-line ferrihydrite samples for 1 hour at 700 °C and for 10 hours at similar temperatures to those of reduced BIOX 1, which were used as a benchmark, showed lower removal efficacies compared to reduced BIOX 1 (**Fig 5.13.e**). Such a result is also related to the low intensity of their powder XRD reflections (**Fig 5.4.g**) compared to that of reduced BIOX 1. Unlike the reduced BIOX samples, the reduction under H_2/N_2 had a negative influence on the performance of 2-line ferrihydrite across most of the pH levels.

To further assess the applicability of this reduction technique, which is used to synthesize NH_3, in improving the adsorption efficiency of other materials, it was used to reduce the Chinese RM sample and the haematite extracted from this sample. The results showed enhanced performance of the reduced RM across all pH levels and the reduced haematite over acidic and neutral conditions (**Fig 5.13.e**) compared to the results shown in Chapter 4. Additionally, the performance of reduced BIOX 1 is generally better than that of the two materials, which is also related to the intensity of Fe^0 reflections. Also, reduced BIOX 1 using the summertime crag sample showed a very similar trend to that using the wintertime sample, but with a slightly better performance across the whole pH scale (**Fig 5.13.f**). Therefore, the reduction of different materials under H_2/N_2 generally had a positive impact on the removal efficiency.

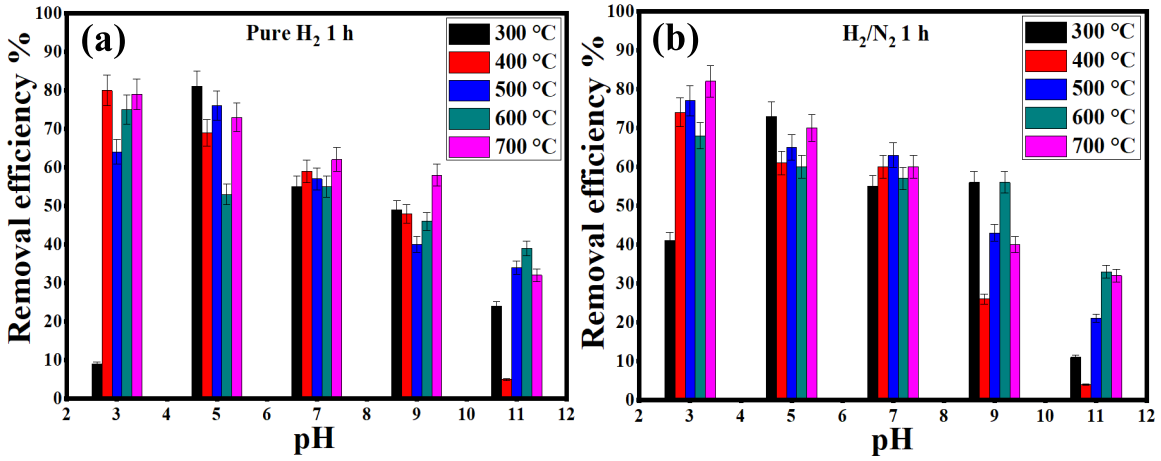

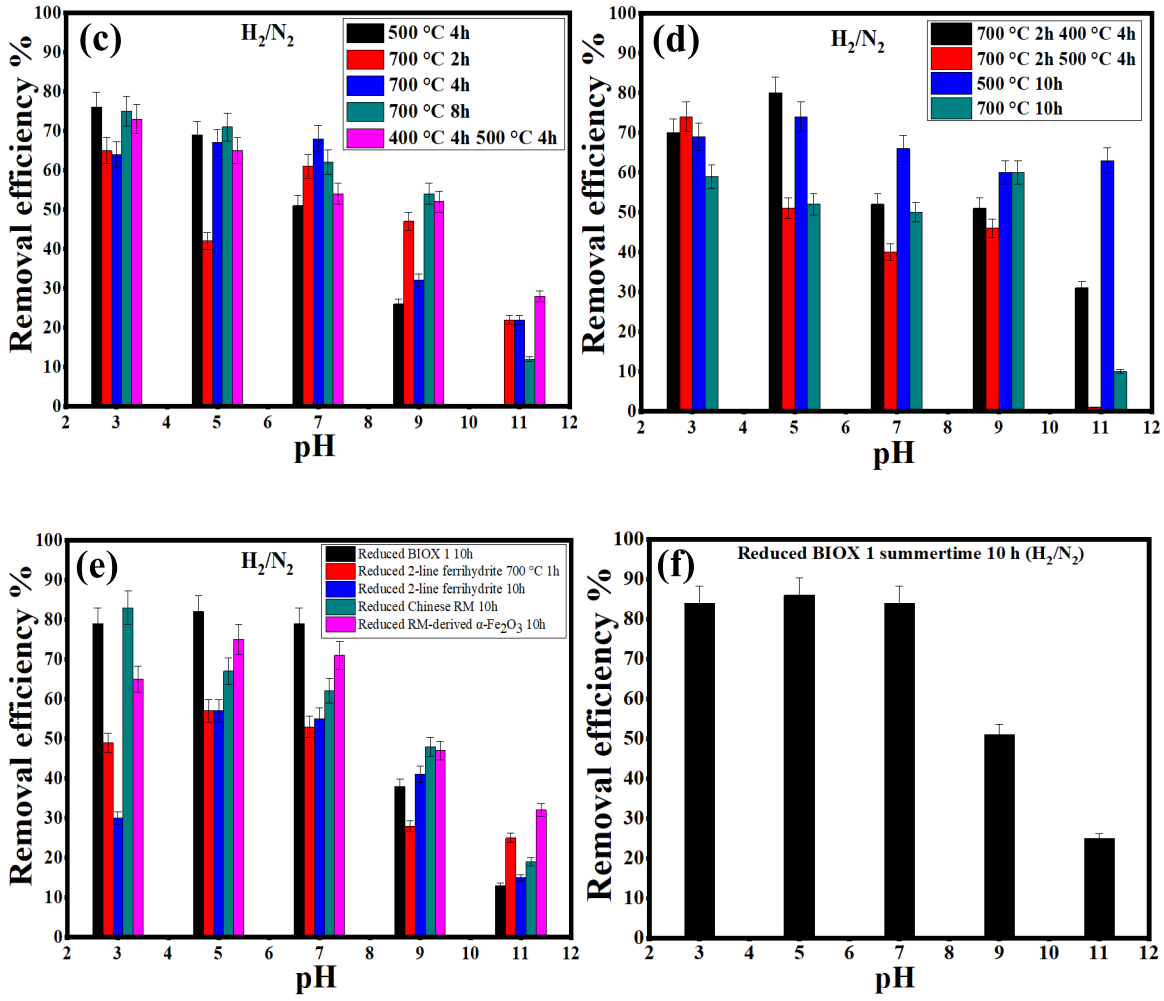

Fig 5.13. The efficiency of reduced BIOX materials under pure H_2 for 1 hour at different temperatures (**a**), under H_2/N_2 for 1 hour at different temperatures (**b**), under H_2/N_2 for different times at different temperatures (**c** and **d**), reduced BIOX 1, reduced 2-line ferrihydrite materials, reduced Chinese RM, and reduced Chinese RM-derived α-Fe_2O_3 (**e**), and reduced BIOX 1 (summertime) (**f**) under H_2/N_2 in removing DOXY from DW after 90 minutes. [$C_o = 25$ ppm, stirring rate = 750 rpm, T = 20 ± 2 °C, volume = 10 mL, and dose = 0.005 g]. The solid-to-liquid ratio in all these experiments is equivalent to 0.5 g/L.

5.5.1. Investigating the effect of initial concentration of DOXY, adsorbent dose, stirring rate, adsorption time on the removal of DOXY, and recycling of reduced BIOX 1

Unlike most of the published studies, increasing the initial concentration of DOXY from 25 ppm to 100 ppm at pH 7 resulted in improving the adsorption efficacy from 55% to 85% accompanied by an enhancement of the adsorption capacity from 55 to 340 mg/g (**Fig 5.14.a**).

However, the efficiency dropped to 52% and 22% by increasing the concentration to 200 and 500 ppm, respectively, which could be attributed to the adsorbent's surface blockage because of these high concentrations. This may also be explained by Le Chatelier's principle as the equilibrium was reached at 100 ppm of DOXY, and further increases in concentration to 200 and 500 ppm caused the equilibrium to shift.

A similar trend was observed upon increasing the dose to 0.005 and 0.01 g (**Fig 5.14.b** and **c**). However, in these cases the efficacy continued increasing at 200 ppm and even at the highest concentration of 500 ppm using 0.005 and 0.01 g, respectively. These results could be attributed to the enhanced mass transfer due to the increased initial concentration along with the increased adsorbent's dose, which improved the efficacy at the high concentrations (200 and 500 ppm).

The highest adsorption capacity (455 mg/g) in this study with an adsorbent dose of 0.01 g and a DOXY initial concentration of 500 ppm is higher than most of the reported capacities in the literature such as Kaur *et al.* [299] who reported a maximum adsorption capacity of 23.6 mg/g using pumpkin seed shell-activated carbon after 300 minutes. On the other hand, Li *et al.* [300] obtained a capacity of 1278.5 mg/g after 540 minutes using 0.12 g/L of nitrogen-doped activated carbon and 200 ppm of DOXY at pH ≈ 7. The significant variation in the adsorption capacity of these materials arises from differences in the experimental conditions under which they were studied as mentioned in Chapter 3. A comparison between the adsorption capacity of reduced BIOX 1 and other materials is provided in **Table 5.1**. The surface area of some adsorbents were not mentioned in the studies reported in **Table 5.1**, and one of them [301] is unreliable because the adsorption-desorption isotherms fail to close at a relative pressure of 0.42, as would normally be expected due to the tensile strength effect. This comparison does not aim to prove or disprove the superiority of reduced BIOX 1; rather, it highlights the wide variation in the results reported in the literature. Adsorption experiments in a continuous flow mode using a column reactor for example are suggested to be further investigated in future studies.

Table 5.1. A comparison of the adsorption capacity of reduced BIOX 1 with other materials reported in the literature for the removal of DOXY

The adsorbent	Adsorption capacity (mg/g)	Initial DOXY concentration (ppm)	Adsorption time (min)	pH	Surface area (m^2/g)	Reference
Pumpkin seed shell-activated carbon	23.6	25	300	8	968	[299]
Nitrogen-doped activated carbon	1278.5	200	540	≈ 7	3141	[300]
Cu-modified biochar	93.4	20	1440	8	N/A	[302]
Fe-loaded sludge biochar	128.9	60	2880	6	83	[303]
Ferrihydrite with 10% silica rice husk	178	100	600	8	255	[252]
Sea buckthorn biocarbon-haematite composite	12.8	10	60	11	N/A	[304]
Fe_3O_4 modified with metal organic framework of Zn^{2+}	21.5	20	10	7	N/A	[305]
Graphene oxide-nano zero valent iron composite	33.43	50	60	7	153	[306]
Iron modified *syzygium cumini* l. Wood	4.32	20	60	7	17	[301]

biochar						
Goethite modified phosphogypsum	722.91	30	90	4-11	74	[307]
Reduced BIOX 1	455	500	90	7	29	This study

The stirring rate effect, which is essential to provide an insight into mass transfer limitation, was checked over the range of 0 up to 1000 rpm and the efficacy went up from 40% to 79% by increasing the rate to 750 rpm, which could be related to the improved diffusion of DOXY into the microtubes of reduced BIOX 1 (**Fig 5.14.d**). However, it went down to 69% by further increasing the rate to 1000 rpm which can be attributed to the increased turbulence and disrupted equilibrium.

The time effect experiment (kinetic profile) showed that the efficiency was 25% after just one minute and then it increased to 68% after 30 minutes followed by a slow increase to 75% and 79% after 60 and 90, respectively (**Fig 5.14.e**). Then it did not change even after 180 minutes. Such a result indicated that the removal of DOXY was mainly achieved by its chemical adsorption on reduced BIOX 1, which is further discussed in the adsorption mechanism. This result can be explained by the initial abundance of active sites on the adsorbent surface at the beginning of the adsorption process, which are quickly filled with DOXY as the adsorption goes on leading to slower adsorption with time. Another factor that should be investigated to determine the potential of the reduced BIOX 1 is regeneration. The regeneration was conducted *via* centrifugation, followed by mixing with 0.1 mol/L NaOH to desorb DOXY from the reduced BIOX 1 surface through the electrostatic repulsion along with the self-degradation of DOXY in alkaline conditions. Subsequently, reduced BIOX 1 was washed many times by DW until the rinsings became neutral (around pH 7), followed by oven-drying at 110-120 °C. The efficiency was 79% in the first cycle, and it started to steadily go down as it was recycled till it reached 17% and an adsorption capacity of just 8.5 mg/g after six cycles (**Fig 5.14.f**) because of iron leaching.

In response to this issue, sodium alginate was used to synthesize a calcium alginate reduced BIOX 1-bead composite through the ionic exchange of Na^+ with Ca^{2+} ions. Calcium alginate beads, which are prepared using sodium alginate that is obtained from polysaccharides found in brown algae, have gained attention as sustainable and environmentally friendly materials

for water purification due to their biocompatibility, safety, and strong binding ability with a variety of pollutants [308]. These beads are rich in carboxyl and hydroxyl functional groups [309]. So, they are negatively charged across weakly acidic, neutral, and alkaline conditions because of the deprotonated carboxyl groups. This characteristic allows them to effectively attract and bind cationic and Zwitterionic compounds, through electrostatic interactions, ion exchange, and hydrogen bonding. Therefore, the reduced BIOX 1-bead composite should, in theory, be efficient, easier to recycle, and a good option to stop the iron leaching.

The removal trend of the composite was generally similar to that of reduced BIOX 1, but the differences in neutral and alkaline conditions are related to the performance of the pristine beads (**Fig 5.15.a**). However, the composite beads, which retained the magnetic property of reduced BIOX 1 (**Fig 5.15.b**), were unstable and broke apart due to stirring during the experiment as shown in **Fig 5.15.c** because of their low mechanical stability.

Due to the unavailability of reduced BIOX 1 powder, the same preparation procedures of alginate bead-composites with the same concentration (1 wt/v%) were used with reduced BIOX at 500 °C for 10 hours. Additional bead formulations were also prepared using higher concentrations of sodium alginate and calcium chloride solutions (2 wt/v% and 4 wt/v%).

In contrast to reduced BIOX 1, the beads composite of reduced BIOX at 500 °C for 10 hours (1 wt/v%) showed lower removal efficiency across the whole pH scale (**Fig 5.16.a**) compared to the corresponding reduced BIOX (500 °C for 10 hours) powder (**Fig 5.13.d**). This decrease may be attributed to limited mass transfer and slower reaction kinetics caused by immobilising the adsorbent within the beads. Moreover, this bead composite exhibited the same low mechanical stability issues observed with the reduced BIOX 1 beads.

To address this, higher alginate/$CaCl_2$ concentrations (2 wt/v% and 4 wt/v%) were tested. These formulations successfully resolved the mechanical stability problem, as the beads produced were robust and remained intact in solution (**Fig 5.16.b-c**). However, the removal efficiency decreased with increasing concentration from 1 wt/v% to 2 wt/v% (**Fig 5.16.b**) and further to 4 wt/v% (**Fig 5.16.c**). A similar decline was also observed for the pristine beads prepared at these high concentrations. Thus, increasing the alginate/$CaCl_2$ concentration to 2 wt/v% and 4 wt/v% effectively improved bead stability. However, further optimisation is required to enhance the adsorption performance during recycling.

Continuing with reduced BIOX 1 powder, the material was tested in removing DOXY from a water sample collected from the River Clyde in Glasgow, particularly at Kelvingrove Park in the West End on 10th February 2025, which was spiked with 25 ppm of DOXY, to see how it works under partially uncontrolled conditions. The removal trend was similar to that in DW as the highest efficacy (83%) was detected at pH 5, and more interestingly the performance was better over the alkaline conditions using the River Clyde sample (**Fig 5.14.g**). This could be attributed to the enhanced self-degradation of DOXY from 15% and 21% to 36% and 38%, at pH 9 and 11, respectively, possibly due to the presence of organic contaminants similar to the coexistence effect of CEF in Chapter 3. This result indicates the potential of using reduced BIOX 1 in removing DOXY from different water samples. pH 7, which is the pH of the River Clyde water, was selected to study the effects of the different factors to simulate natural water conditions.

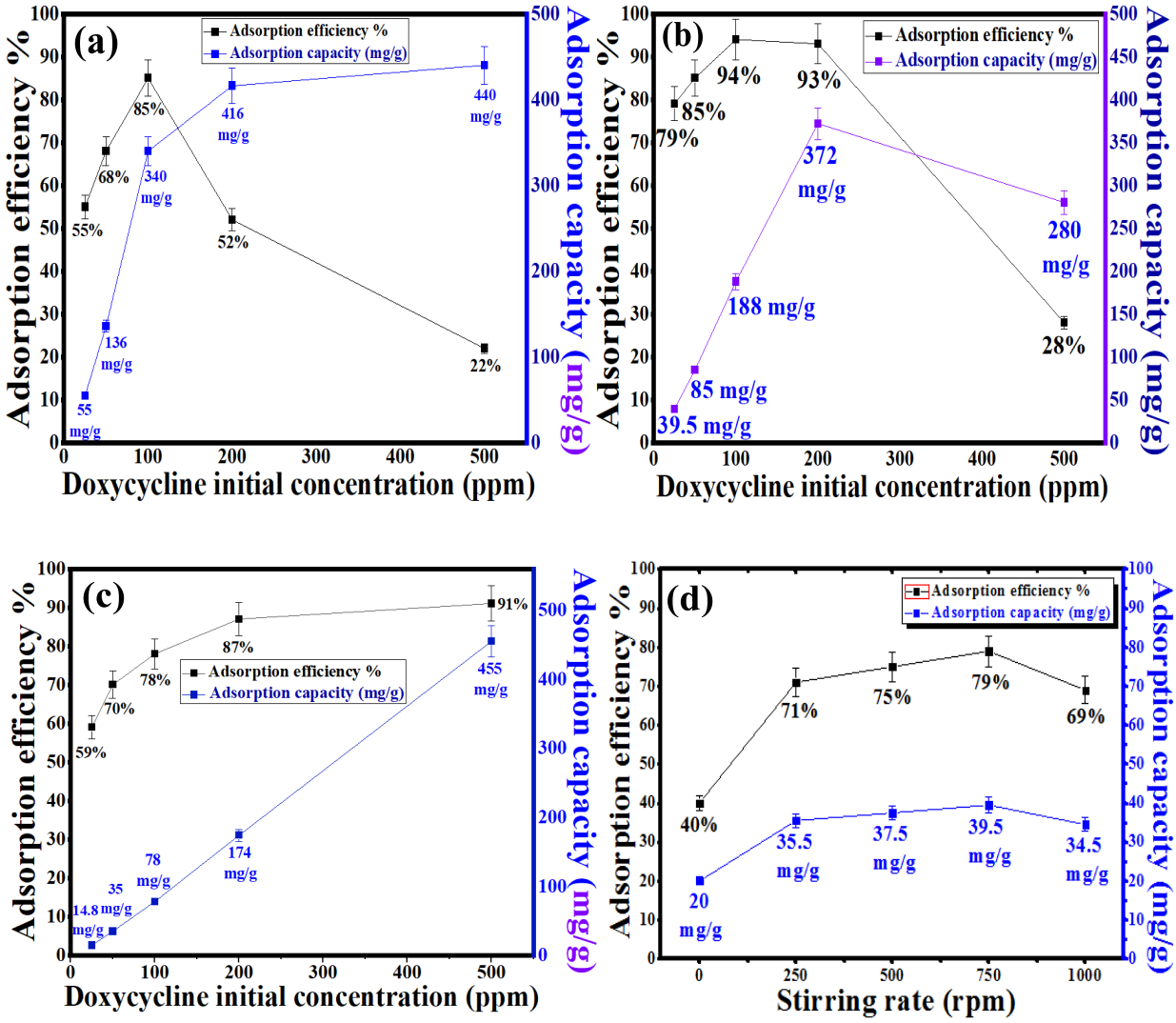

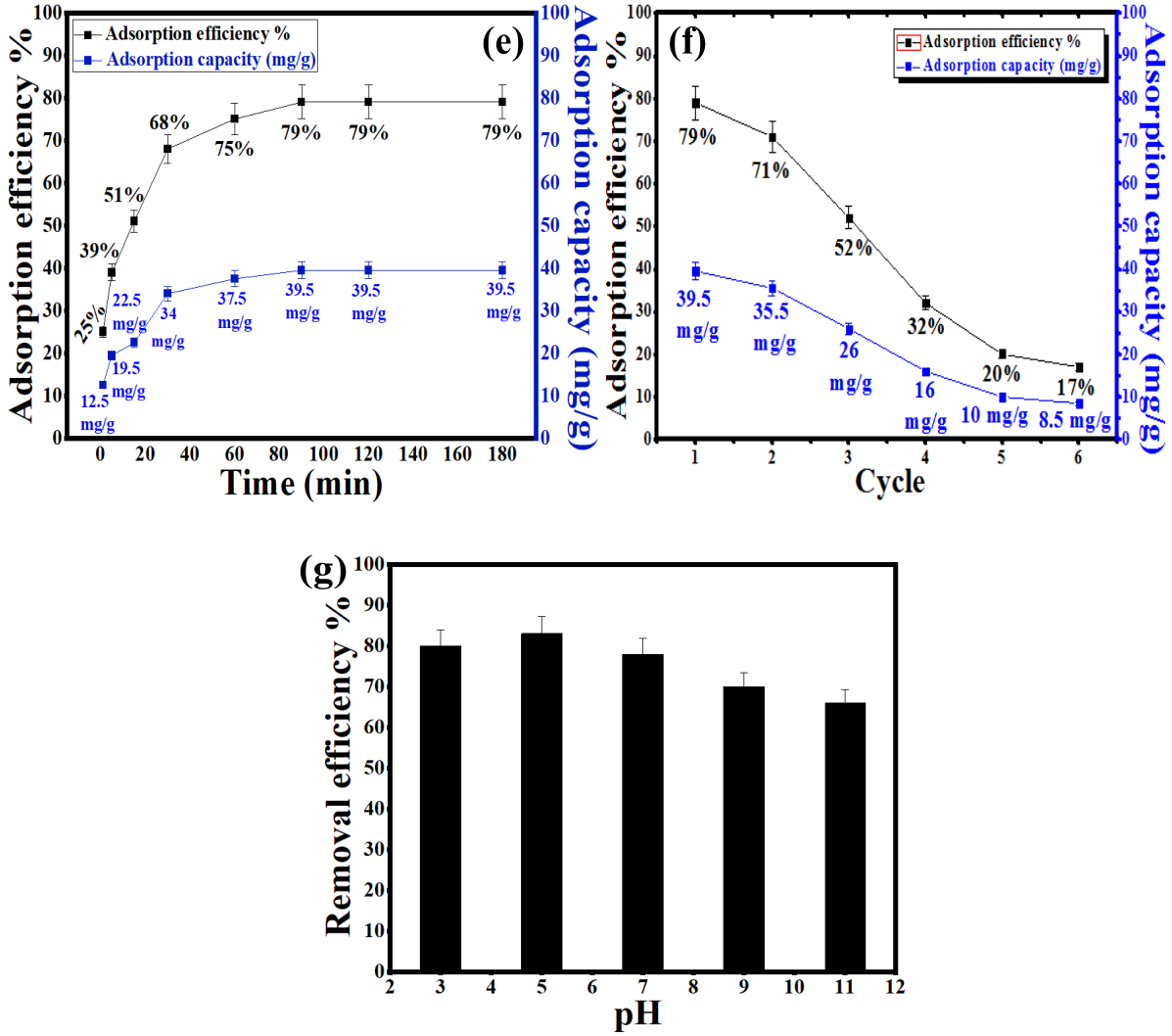

Fig 5.14. The effect of variation in initial concentration of DOXY using 0.0025 g **(a)**, 0.005 g **(b)**, and 0.01 g **(c)** [pH = 7 and stirring rate = 750 rpm], stirring rate **(d)** [C_o = 25 ppm, pH = 7, and dose = 0.005 g], time effect **(e)** [C_o = 25 ppm, pH = 7, stirring rate = 750 rpm, and dose = 0.005 g], recycling **(f)** [C_o = 25 ppm, pH = 7, stirring rate = 750 rpm, and dose = 0.005 g] on the adsorption efficiency and capacity of 10 mL of DOXY by reduced BIOX 1 after 90 minutes. The pH variation of the River Clyde water sample **(g)** [C_o = 25 ppm, stirring rate = 750 rpm, and dose = 0.005 g].

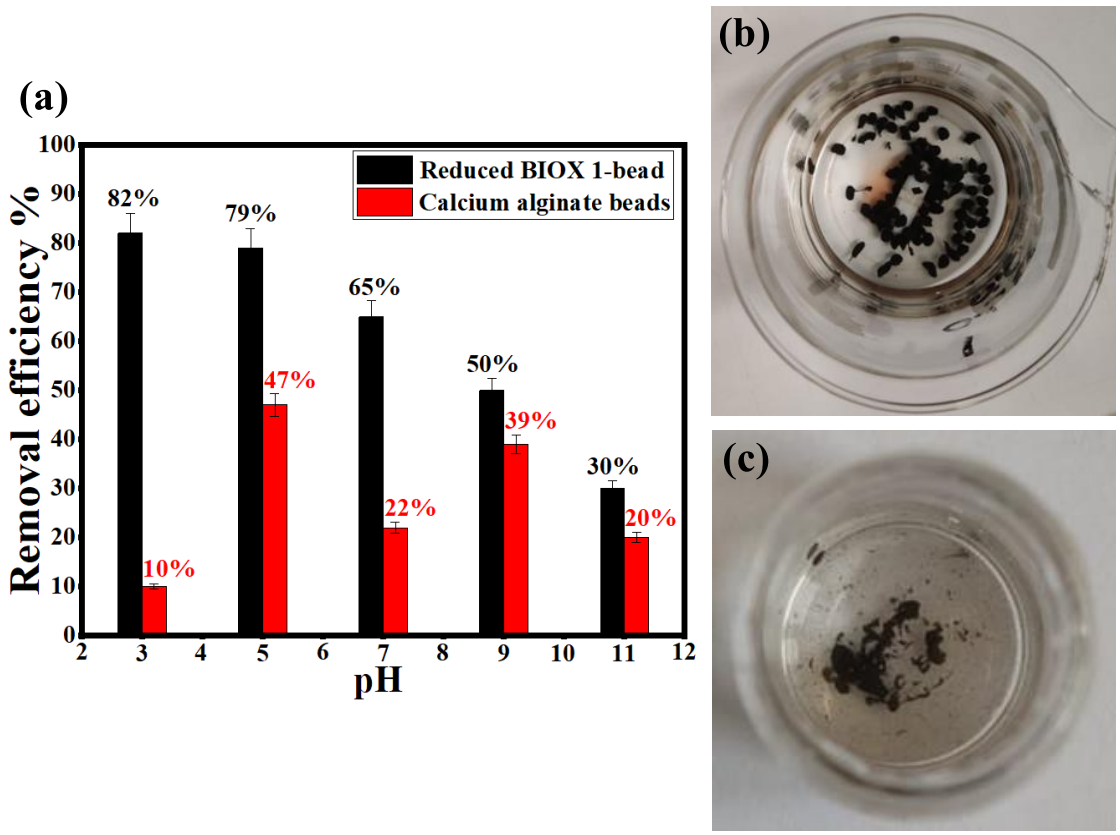

Fig 5.15. The removal of DOXY by reduced BIOX 1-bead composite and pristine calcium alginate beads after 90 minutes (**a**), and the composite beads prior to (**b**), and after DOXY removal (**c**). [C_o = 25 ppm, stirring rate = 750 rpm, and dose = 0.1 g].

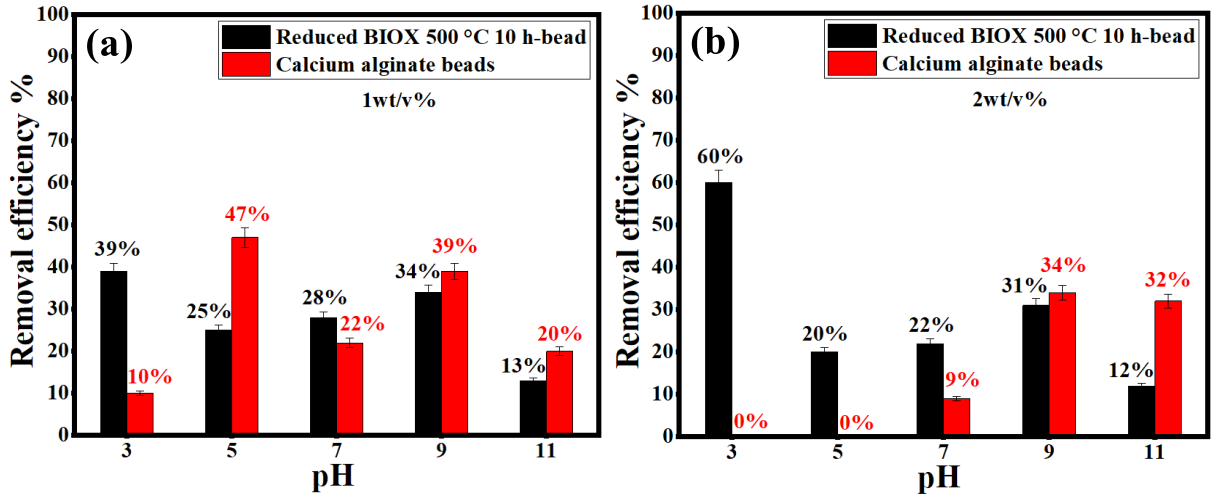

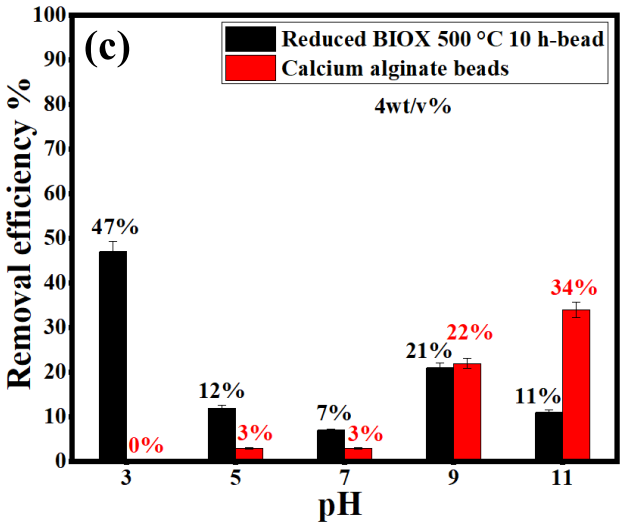

Fig 5.16. The removal of DOXY by reduced BIOX (500 °C for 10 hours) bead composite and pristine calcium alginate beads after 90 minutes using 1wt/v% (**a**), 2wt/v% (**b**), and 4wt/v% (**c**) concentration of calcium chloride and sodium alginate solutions. [C_o = 25 ppm, stirring rate = 750 rpm, and dose = 0.1 g].

5.5.2. The adsorption isotherms of DOXY adsorption using reduced BIOX 1

The adsorption of DOXY in the concentration range of 25 to 500 ppm using reduced BIOX 1 was better described by the Freundlich model than the Langmuir model, based on its higher R^2 value (**Fig. 5.17.a-b**). This result indicated heterogeneous adsorption of DOXY on the surface of reduced BIOX 1; in other words, DOXY molecules are unevenly distributed across the adsorbent surface [261]. The concentration of basic sites of reduced BIOX 1 was 3.5 times higher than that of pristine crag, as detailed below in **Table 5.2**. However, the efficiency did not increase proportionally. This discrepancy could be attributed to the heterogeneous nature of DOXY adsorption on the reduced BIOX 1 surface, which is better described by the Freundlich model.

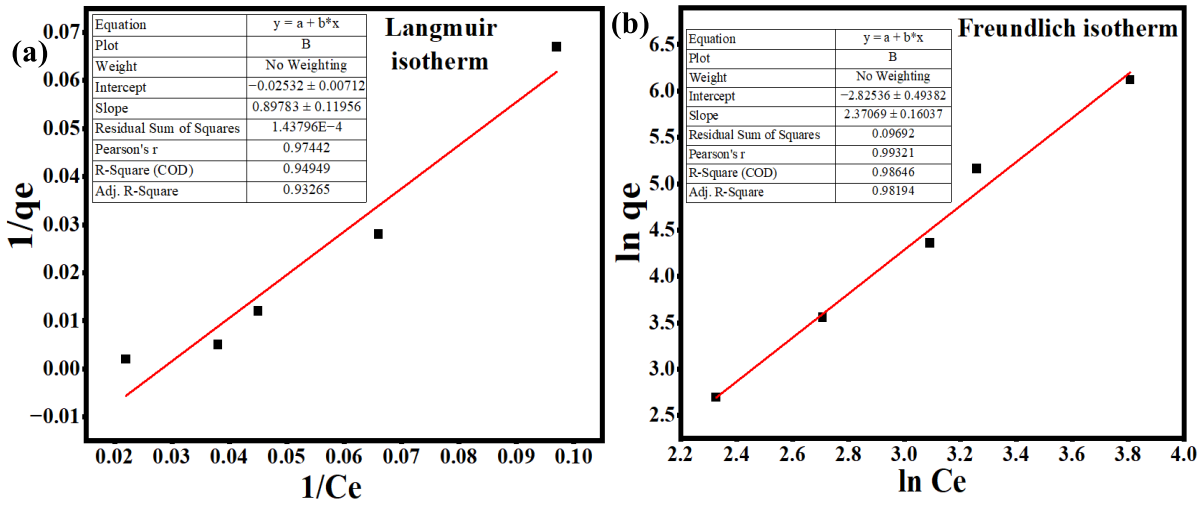

Fig 5.17. Linear adsorption isotherm plots of Langmuir (**a**) and Freundlich (**b**) models. [pH = 7, stirring rate = 750 rpm, and dose = 0.005 g].

5.5.3. The effect of ionic strength and interfering ions on the adsorption efficiency of reduced BIOX 1

As discussed in Chapter 3, the salting out effect can be induced by adding salts such as NaCl to precipitate and separate DOXY from solutions, which can then result in improving the adsorption efficacy. Upon testing the effect of 0.01 M of NaCl, the efficiency was 75% and it increased to 87% by increasing the concentration to 0.4 M (**Fig 5.18.a**).

This result is attributed to the increased ionic strength of the solution upon increasing the salt concentration from 0.01 M to 0.4 M, which leads to disrupting the hydration shell around DOXY species by competing with them for water molecules. Subsequently, NaCl ions attract water molecules as they are more strongly hydrated than DOXY causing their precipitation out of the solution and promoting their enhanced adsorption on reduced BIOX 1 surface. This result is similar to that of Zaidi *et al.* [310] who observed a direct correlation between the concentration of NaCl and the adsorption of DOXY using electro-generated adsorbents due to the salting out effect [257, 311]. No removal was observed upon running a control experiment using the same NaCl concentrations without adding reduced BIOX 1.

The ionic strength effect of divalent ions such as Ca^{2+} was also covered in this chapter. As shown in **Fig 5.18.b**, the adsorption efficacy of reduced BIOX 1 fluctuated and very slightly decreased by increasing the concentration of added Ca^{2+} to 500 mg/L. Another experiment was carried out with the same concentrations of Ca^{2+} but using CaO (**Fig 5.18.d**) to further confirm

the effect of Ca^{2+}, and the decline in adsorption efficiency was clearer. The stronger inhibitory effect of CaO is similar to that reported and discussed in Chapter 3, but this time interaction between Ca^{2+} and the deprotonated (negatively charged) hydroxyl group of DOXY at pH 7. This result is in line with Zeng *et al.* [312] who observed a similar interfering effect using negatively-charged biochar.

According to these results, the presence of a relatively high concentration of calcium (18 ppm) in the River Clyde water sample, as clarified in Chapter 3, is not supposed to be affecting the efficiency of reduced BIOX 1 in this water sample unless it is in the form of $Ca(OH)_2$. The addition of 50 and 200 mg/L Mg^{2+} in the form of MgO showed minimal interference. However, the interference was more obvious by increasing the Mg^{2+} concentration to 500 mg/L (**Fig 5.18.f**). The stronger inhibitory effect of Mg^{2+} compared to Ca^{2+} at the high concentration of 500 mg/L could be attributed to its higher charge density resulting from its smaller ionic radius.

In agreement with the above-mentioned experiments, SO_4^{2-} ions within the range of 50 - 1000 mg/L were used as an example of anions to investigate their effect on the performance of reduced BIOX 1. A slight decrease in the adsorption efficiency was observed at the lowest SO_4^{2-} concentration, and then it became more evident by increasing the SO_4^{2-} concentration (**Fig 5.18.h**). This result, which is in agreement with Zaidi *et al.* [313] about the inhibiting effect of SO_4^{2-} ions on DOXY adsorption, could be attributed to the electrostatic attraction of SO_4^{2-} ions toward the nearly neutral surface of reduced BIOX 1 at pH 7. Consequently, the ions compete with DOXY over the active sites of reduced BIOX 1, negatively affecting its ability to adsorb DOXY. Additionally, the possible interaction of Na^+ ions from the salt precursor with the deprotonated (negatively charged) hydroxyl group of DOXY at pH 7 might increase the solubility of DOXY and make it harder to remove.

The control experiments of Ca^{2+}, Mg^{2+}, and SO_4^{2-} showed a very low removal efficiency in the range of 10-12%, 4-8%, 10-4% and 2-7% using $CaCl_2.6H_2O$, CaO, MgO, and Na_2SO_4, respectively (**Fig 5.18.c**, **e**, **g**, and **i**). These results could be attributed to the complexation of these ions with DOXY species. Also, the weak negative charge of DOXY at pH 7 could explain the slightly better performance of the positively charged ions. The coexistence of Si(IV) up to a 100 ppm had a negligible effect on the adsorption process (**Fig 5.18.j**) and the

control experiment did not show any removal of DOXY. Ca^{2+}, Mg^{2+}, and Si(IV) were mainly investigated due to their presence in the River Clyde water and DW.

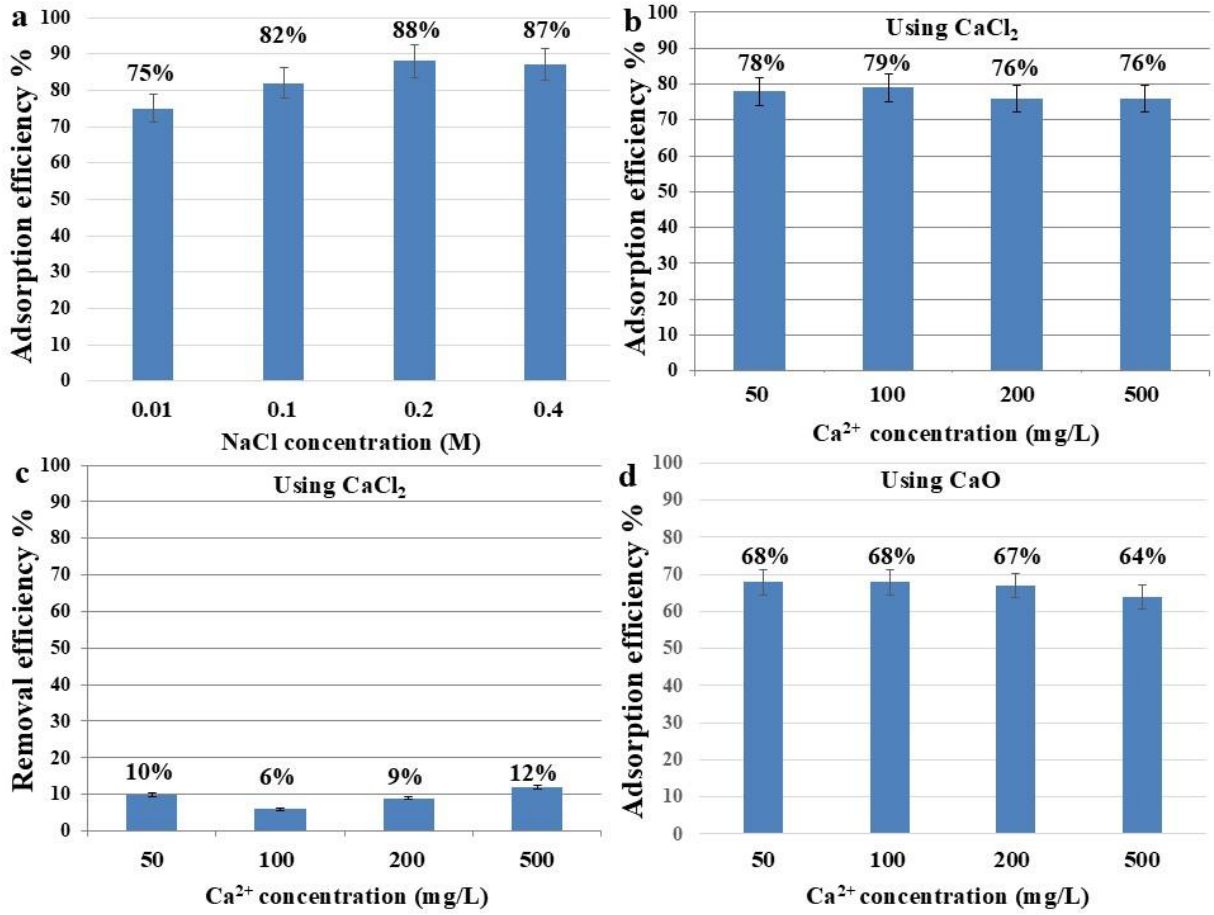

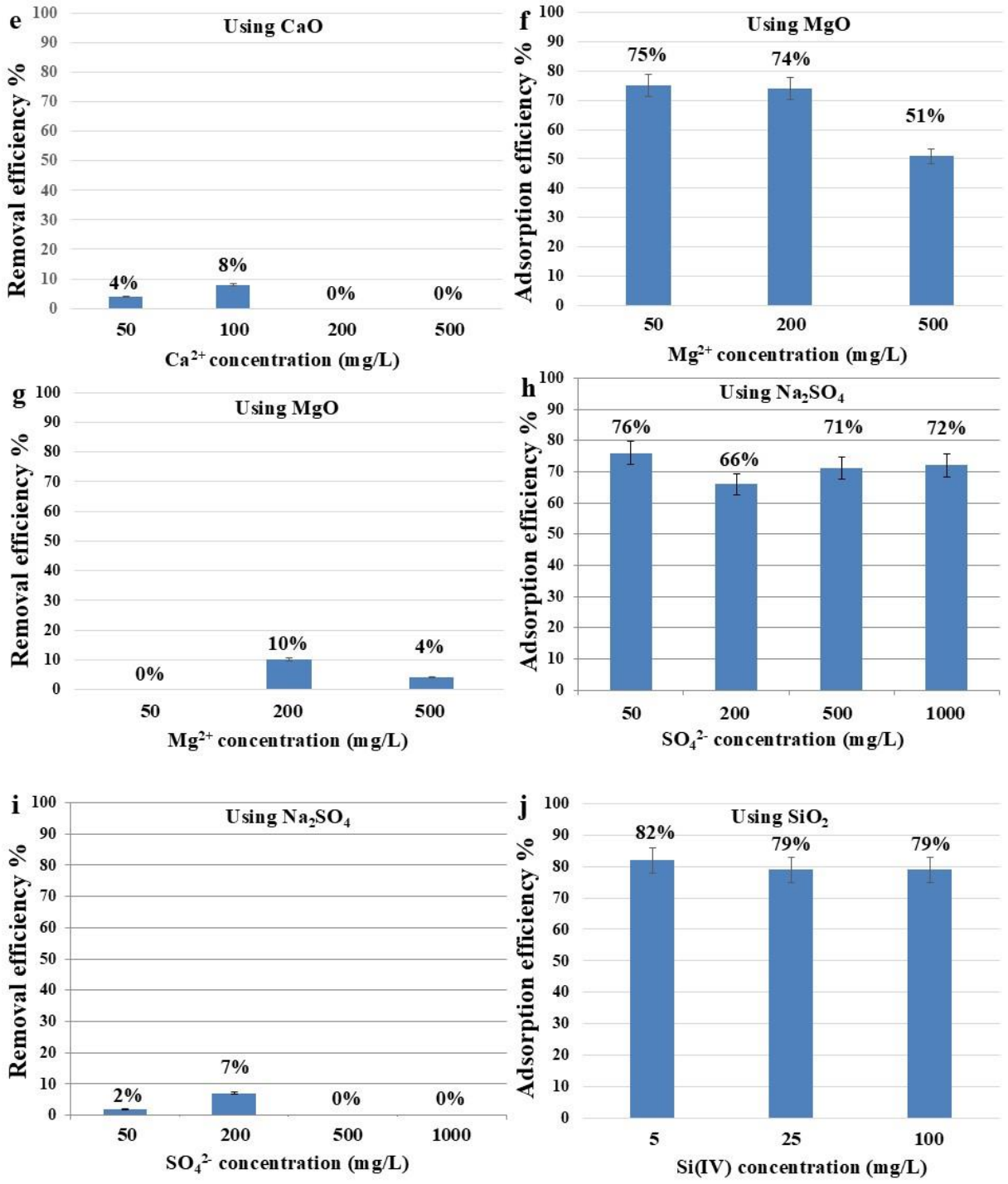

Fig 5.18. The efficiency of reduced BIOX 1 in adsorbing DOXY in the presence of different concentrations of NaCl (**a**), Ca^{2+} ($CaCl_2$) **(b)**, control experiment of Ca^{2+} ($CaCl_2$) **(c)**, Ca^{2+} (CaO) **(d)**, control experiment of Ca^{2+} (CaO) **(e)**, Mg^{2+} (MgO) **(f)**, control experiment of Mg^{2+} (MgO) **(g)**, SO_4^{2-} **(h)**, control experiment of SO_4^{2-} **(i)**, and Si(IV) (SiO_2) **(j)** after 90 minutes. [C_o = 25 ppm, pH = 7, volume = 10 mL, dose = 0.005 g, stirring rate = 750 rpm, and T = 20 ± 2 °C].

5.5.4. Investigation of DOXY removal mechanism

The increased electrostatic repulsion as we move away from the Zwitterionic range between DOXY and reduced BIOX 1 was further confirmed by the decreased removal efficacy to only 20% at pH 2 and 11% at pH 12. Therefore, the electrostatic forces were considered an important factor controlling the adsorption process. Additionally, hydrogen bonding between the hydroxyl groups on reduced BIOX 1 surface and DOXY can contribute to the removal process. In this context, the concentration of basic and acidic surface sites of some of the materials employed in this chapter was measured via simple titration against HCl and NaOH, respectively. The basic sites' concentration of reduced BIOX 1 was 14 mmol/g and that of the acidic sites was 12 mmol/g (**Table 5.2**). The basic sites' concentration of the BIOX materials reduced for one hour at temperatures from 300 up to 700 °C was 10, 18, 10, 14, and 26 mmol/g, respectively. The acidic sites' concentration of the same materials was 16, 22, 24, 21, and 28 mmol/g, respectively. The pristine crag had 4 mmol/g and 10 mmol/g of basic and acidic sites, respectively.

Regarding the reduced 2-line ferrihydrite, the basic sites' concentration was only 3 mmol/g and that of the acidic sites was 2 mmol/g compared to 4 and 12 mmol/g, respectively, of 2-line ferrihydrite. This result could explain the decreased efficiency of 2-line ferrihydrite after reduction.

Despite the absence of a specific trend in the concentration of these surface sites, it is clear that the reduced BIOX materials have more basic sites and most of them have more acidic sites, which could be related to their better performance compared to the pristine crag and reduced 2-line ferrihydrite. To further support this conclusion, the basic and acidic sites' concentration of Chinese RM and its derived-α-Fe_2O_3 increased after the reduction process accompanied by an improved performance in DOXY adsorption.

Table 5.2. Concentration of basic and acidic sites of some of the adsorbents used in this chapter.

Material	Concentration of basic sites (mmol/g)	Concentration of acidic sites (mmol/g)
Pristine crag	4	10
Reduced BIOX 1 (wintertime sample)	14	12
Reduced BIOX 300 °C 1h H_2/N_2	10	16
Reduced BIOX 400 °C 1h H_2/N_2	18	22
Reduced BIOX 500 °C 1h H_2/N_2	10	24
Reduced BIOX 600 °C 1h H_2/N_2	14	21
Reduced BIOX 700 °C 1 h H_2/N_2	26	28
2-line ferrihydrite	4	12
Reduced 2-line ferrihydrite	3	2
Reduced BIOX 500 °C 4h H_2/N_2	14	10
Reduced BIOX 500 °C 10h H_2/N_2	16	10
Reduced BIOX 700 °C 2h H_2/N_2	12	6
Reduced BIOX 700 °C 8h H_2/N_2	10	6
Reduced BIOX 700 °C 10h H_2/N_2	10	4
Chinese RM	10	10
Reduced Chinese RM	16	12
Chinese RM-derived α-Fe_2O_3	6	16
Reduced Chinese RM-derived α-Fe_2O_3	14	18

In addition to the above-mentioned factors, the complexation can play a role, and it was investigated by the XPS analysis. The wide scan of reduced BIOX 1 before the adsorption confirmed its elemental composition including Fe, O, C, Ca, S, and Si (**Fig 5.19.a**) that was identified by the EDX. Some elements disappeared such as calcium and others were detected such as nitrogen after DOXY adsorption (**Fig 5.19.b**), which is an indication of the interaction between reduced BIOX 1 and DOXY. As shown in **Fig 5.19.c**, iron exhibited three oxidation states at 707.1 eV, 710.9 eV, and 712.9 eV, which are assigned to the Fe^0, Fe^{2+}, and Fe^{3+}, respectively. The Fe $2p_{1/2}$ peaks of Fe^{2+} and Fe^{3+} were detected at 724.5 eV and 726.9 eV,

respectively. The presence of three Fe oxidation states is a result of the reduced BIOX 1 exposure to the air.

After stirring the adsorbent in DW and before DOXY adsorption, the Fe^{2+} and Fe^{3+} peaks slightly shifted to higher binding energies along with the disappearance of the Fe^{0} peak (**Fig 5.19.d**). This result refers to the oxidation of Fe^{0} to Fe^{2+} and Fe^{3+} on the reduced BIOX 1 surface by water itself not DOXY. Such a simple control experiment is not mentioned in some of the previous publications that used Fe^{0} in the removal of different pollutants from wastewater such as Meng *et al.* [314] who used an S-doped zero-valent iron supported on biochar in the removal of tetracycline, which is a very similar antibiotic to DOXY. Other studies included using zero-valent iron-based adsorbents such as spent bleaching earth carbon modified with Fe^{0} [315] and red mud-zero-valent iron composites [316] to remove diclofenac and mercury (II), respectively, from water samples. Therefore, it is not clear if Fe^{0} was oxidized because of its reaction with the pollutant or just water itself in these publications. After DOXY adsorption, the Fe^{2+} and Fe^{3+} peaks slightly shifted to lower binding energies with higher intensities and no changes in the oxidation state (**Fig 5.19.e**).

The O 1s spectrum showed two peaks at 530.3 eV and 532.4 eV, which could be attributed to the iron oxide and iron hydroxide, respectively (**Fig 5.19.f**). Upon DOXY adsorption, the two peaks shifted to lower binding energies, and a new peak was detected at 532.3 eV that might be assigned to the C-O bond (**Fig 5.19.g**), which could result from the interaction of the oxygen in reduced BIOX 1 with carbon from DOXY. This result could be supported by the increased intensity of the oxygen peaks after the adsorption. Three peaks were observed in the C 1s spectrum at 284.7 eV, 285.7 eV, and 288.3 eV (**Fig 5.19.h**) and very slightly shifted to higher binding energies after the adsorption (**Fig 5.19.i**) as further confirmation of the above-mentioned interaction.

Lastly, the N 1s spectrum, which was not detected before the adsorption, showed the appearance of two peaks at 400.0 eV and 402.5 eV after the adsorption, which could be assigned to Fe-N and C-N-C, respectively (**Fig 5.19.j**). Such a result confirmed the complexation of the iron in reduced BIOX 1 with the nitrogen in DOXY and it is in agreement with the result of Huang *et al.* [317] who used an alginate composite to remove DOXY.

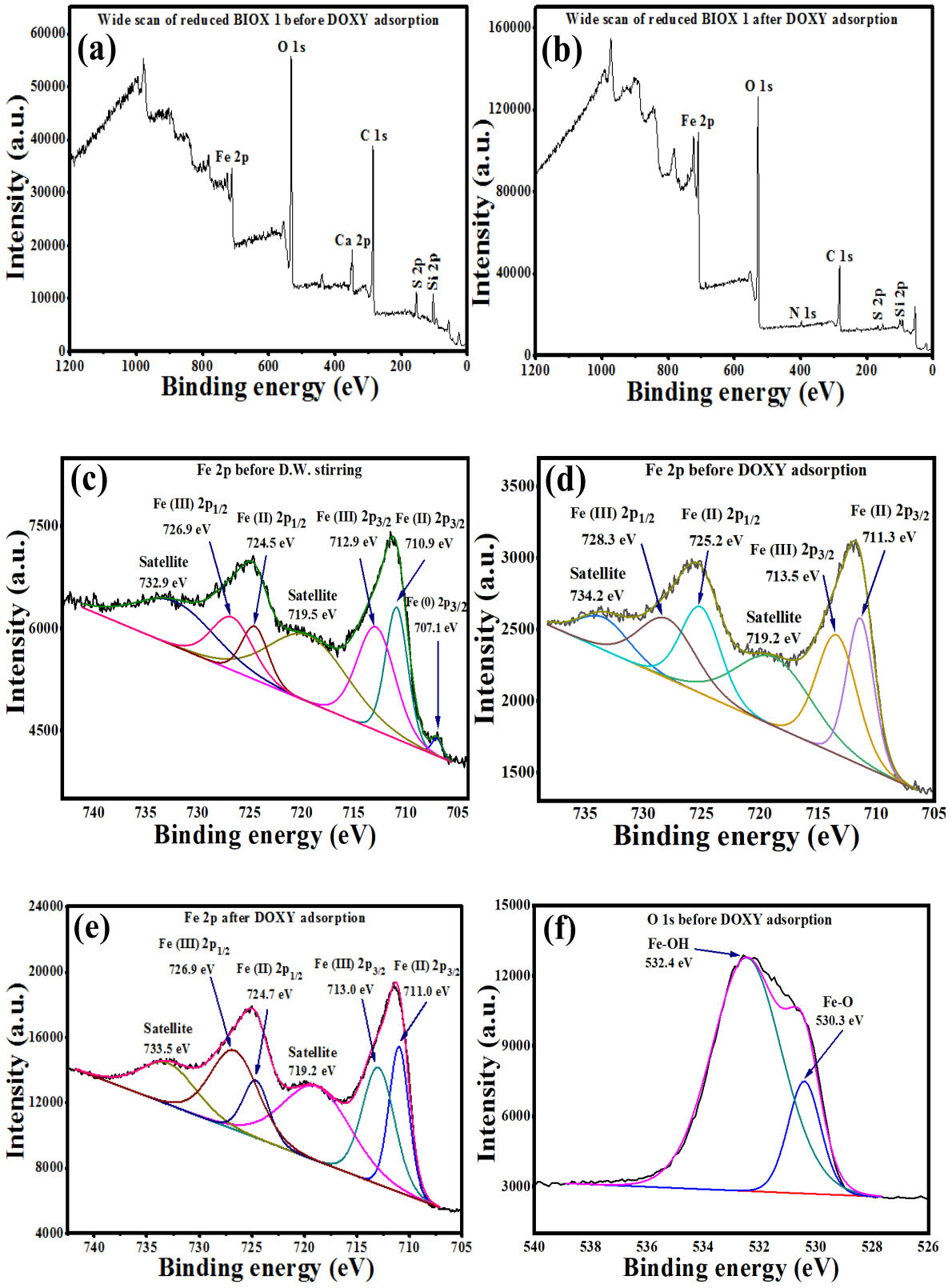
(a)
Wide scan of reduced BIOX 1 before DOXY adsorption
O 1s
Fe 2p
C 1s
Ca 2p
S 2p
Si 2p
Intensity (a.u.)
Binding energy (eV)
(b)
Wide scan of reduced BIOX 1 after DOXY adsorption
O 1s
Fe 2p
C 1s
N 1s
S 2p
Si 2p
Intensity (a.u.)
Binding energy (eV)
(c)
Fe 2p before D.W. stirring
Fe (III) 2p1/2
726.9 eV
Fe (II) 2p1/2
724.5 eV
Fe (III) 2p3/2
712.9 eV
Fe (II) 2p3/2
710.9 eV
Satellite
732.9 eV
Satellite
719.5 eV
Fe (0) 2p3/2
707.1 eV
Intensity (a.u.)
Binding energy (eV)
(d)
Fe 2p before DOXY adsorption
Fe (III) 2p1/2
728.3 eV
Fe (II) 2p1/2
725.2 eV
Fe (III) 2p3/2
713.5 eV
Fe (II) 2p3/2
711.3 eV
Satellite
734.2 eV
Satellite
719.2 eV
Intensity (a.u.)
Binding energy (eV)
(e)
Fe 2p after DOXY adsorption
Fe (III) 2p1/2
726.9 eV
Fe (II) 2p1/2
724.7 eV
Fe (III) 2p3/2
713.0 eV
Fe (II) 2p3/2
711.0 eV
Satellite
733.5 eV
Satellite
719.2 eV
Intensity (a.u.)
Binding energy (eV)
(f)
O 1s before DOXY adsorption
Fe-OH
532.4 eV
Fe-O
530.3 eV
Intensity (a.u.)
Binding energy (eV)

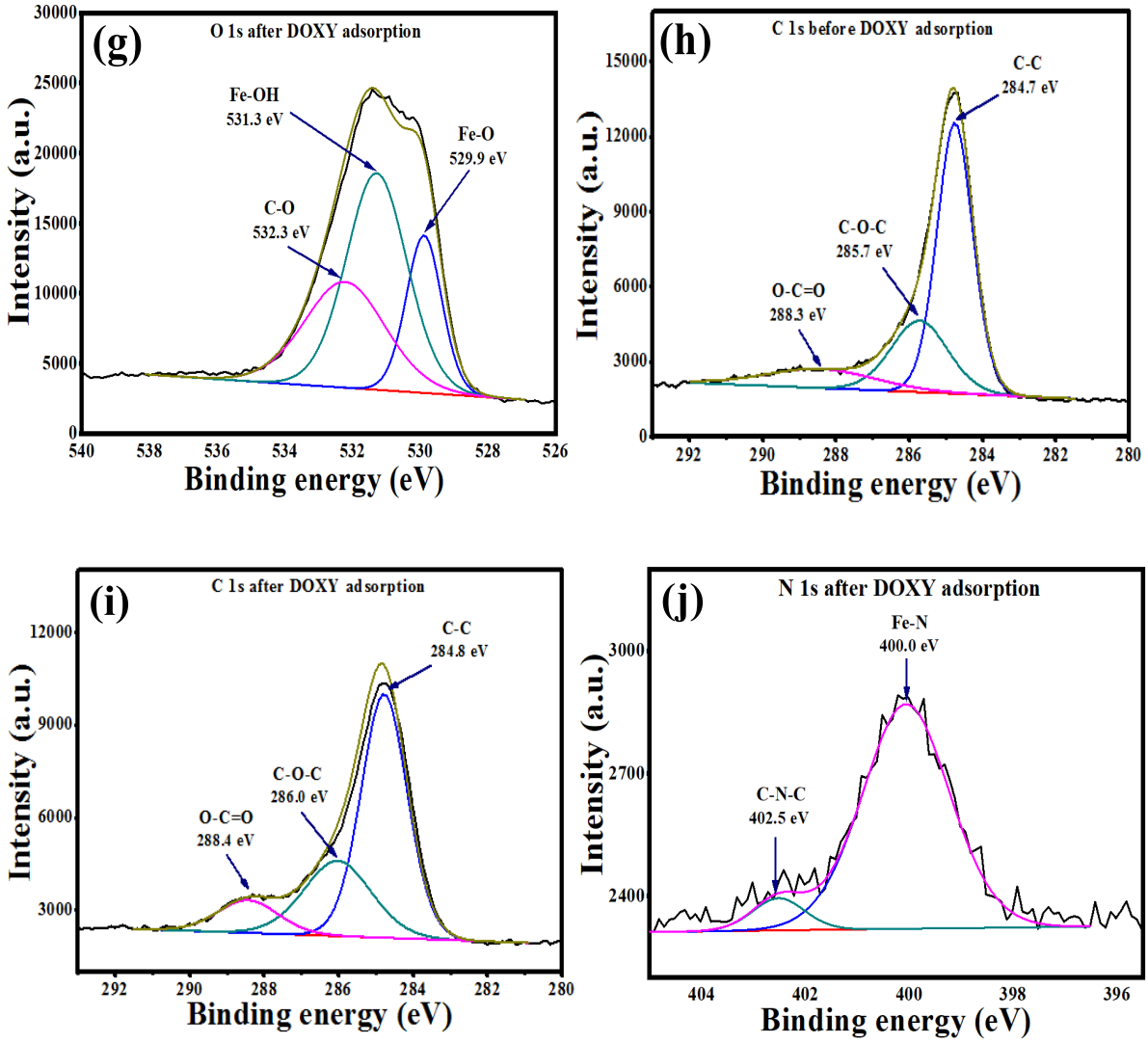

Fig 5.19. XPS spectra of reduced BIOX 1 including a wide scan before **(a)**, and after **(b)**, Fe 2p before DW stirring **(c)**, Fe 2p before **(d)**, and after **(e)**, O 1s before **(f)**, and after **(g)**, C 1s before **(h)**, and after **(i)**, and N 1s after DOXY adsorption (**j**).

In agreement with the XPS results, no nitrogen was detected by CHN analysis in reduced BIOX 1 and 0.2%, 0.7%, 1.0% were detected after 25 ppm, 200 ppm, and 500 ppm DOXY adsorption, respectively (**Table 5.3**). At pH 7 (**Fig 5.14.b**), the theoretical carbon content following 79% adsorption of 25 ppm DOXY was estimated at 4.2%, and the experimental result was 4.5%, which is within the experimental error percentage. The theoretical %C after adsorption of 87% of 200 ppm DOXY (**Fig 5.14.c**) was calculated to be 12.3%, which is the same as the experimental value of 12.3%. By increasing the initial concentration to 500 ppm, the efficiency increased to 91% (**Fig 5.14.c**), and the theoritical %C increased to 29.2%. The measured %C by CHN was 29.7%, which was slightly off the error range but still acceptable.

These results indicated that DOXY removal by Fe^0 occurred solely through adsorption, with no evidence of degradation.

Table 5.3. CHN analysis of reduced BIOX 1 before and after DOXY adsorption at pH 7.

Element	The atomic % before DOXY adsorption	The atomic % after 25 ppm DOXY adsorption	The atomic % after 200 ppm DOXY adsorption	The atomic % after 500 ppm DOXY adsorption
C	1.9%	4.5%	12.3%	29.7%
H	0.5%	1.2%	1.5%	1.7%
N	0.0%	0.2%	0.7%	1.0%

TGA-MS analysis was employed in this chapter to further support the CHN results. As shown in **Fig. 5.20.a**, the weight loss of pristine reduced BIOX 1 was only 1.2% at 200 °C. However, upon increasing the temperature to 934 °C, the sample exhibited an unexpected weight gain, from 8.2 g to 9.2 g. As mentioned in Chapter 3, the analysis was conducted under argon; however, the presence of residual oxygen in the chamber may have led to oxidation of the sample. To rule out instrumental error, the analysis was repeated and yielded the same result, suggesting that the anomaly was not due to equipment malfunction. The oxygen ion mass spectrum of reduced BIOX 1 (**Fig. 5.20.d**) was similar to that observed after adsorption of 200 ppm DOXY (**Fig. 5.20.e**), and no unusual features were detected. This oxygen could be related to the oxidation of the pristine reduced BIOX 1 during the TGA analysis. After using reduced BIOX 1 in adsorbing 200 ppm of DOXY, the weight loss was 29% (**Fig 5.20.b**) and by increasing the initial concentration of DOXY to 500 ppm, the mass loss increased to 53% (**Fig 5.20.c**).

Powder XRD patterns of reduced BIOX 1, which had been soaked in water and dried to simulate adsorption conditions, as well as after adsorption of different concentrations of DOXY (**Fig. 5.21**) were similar and indicated that the Fe^0 phase in the bulk of these samples remained unchanged. Therefore, the oxidation of Fe^0 might have happened during the TGA analysis of all samples, to varying extents, depending on the possible differences in the amount of oxygen present. However, in the DOXY-loaded samples (**Fig. 5.20.b-c**), thermal

degradation of the adsorbed DOXY could have been the primary cause of the observed weight loss, which outweighed the weight gain seen in the unloaded sample (**Fig. 5.20.a**).

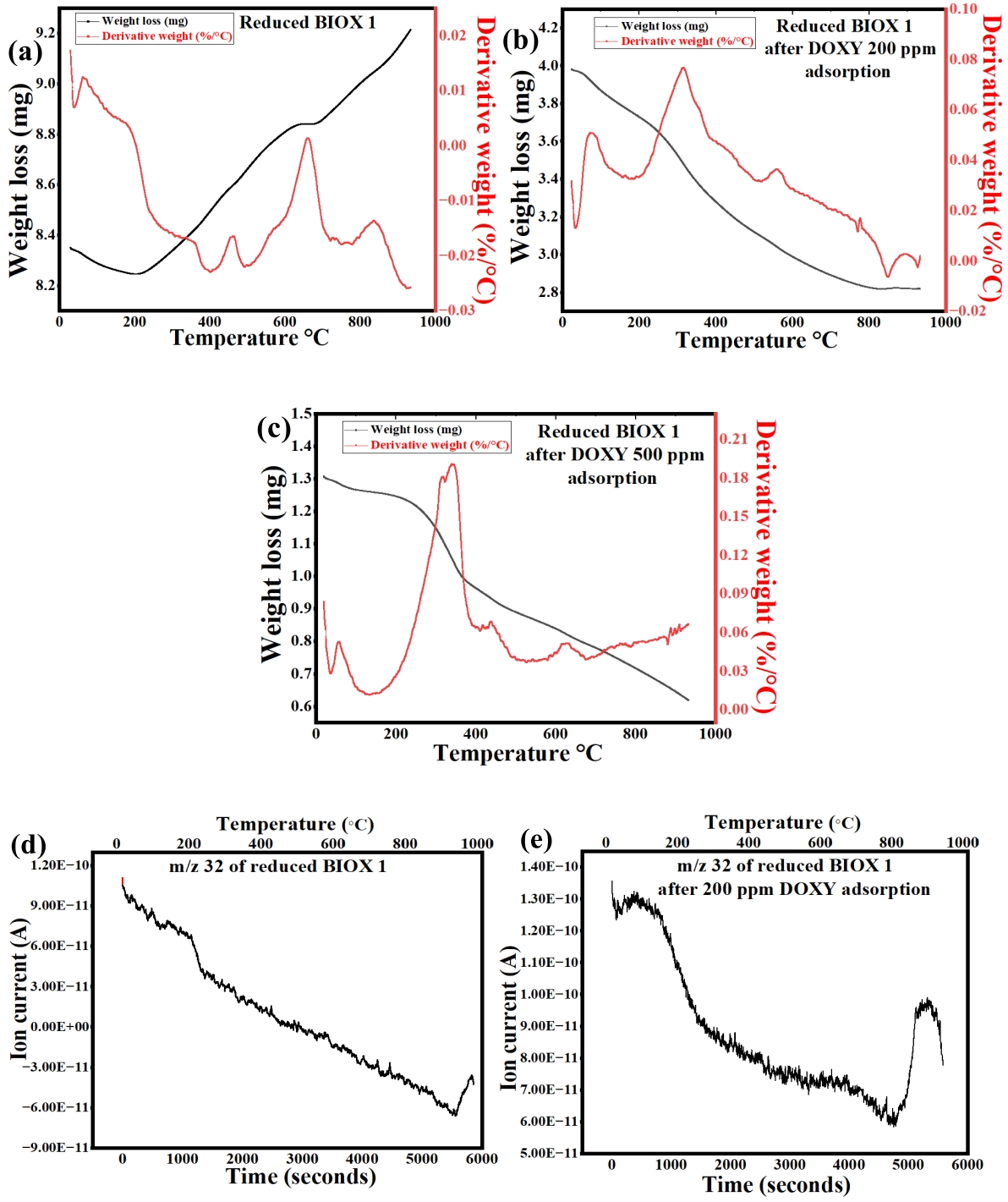

Fig 5.20. TGA and derivative weight profile of reduced BIOX 1 before (**a**) and after adsorption of 200 ppm (**b**), and 500 ppm (**c**) of DOXY, and the mass spectrum ion curve for 32 m/z before (**d**), and after 200 ppm DOXY adsorption (**e**).

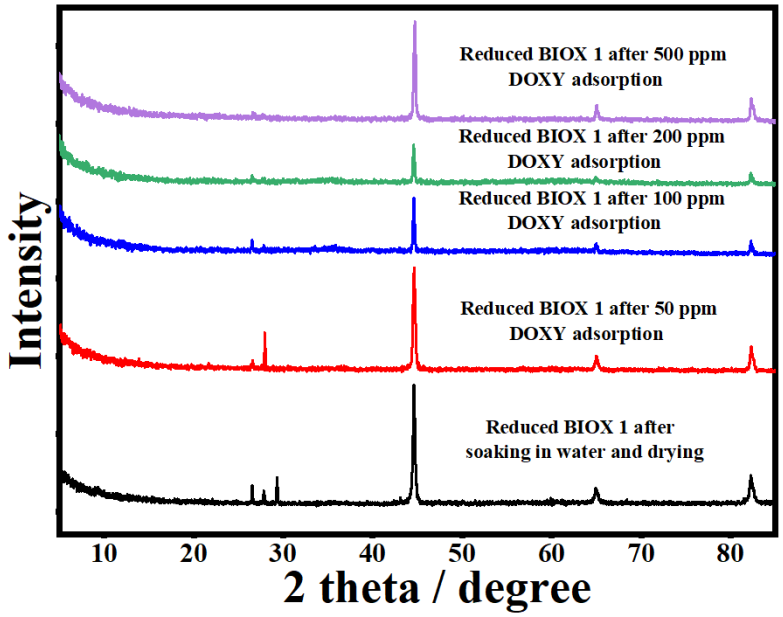

Fig 5.21. Powder XRD patterns of reduced BIOX 1 after being soaked in water and dried, and after adsorption of different concentrations (50, 100, 200, and 500 ppm) of DOXY to show the stability of zero-valent iron after being used in water and aqueous DOXY solutions.

5.5.5. The economic and the environmental analyses of using reduced BIOX materials in the removal of DOXY

On average, only 1 L of DW is used to wash about 20 grams of the BIOX material after collecting from the sampling site. This volume of water costs less than one pence (£ 0.006). Subsequently, this amount of the BIOX material goes down to about 10 grams after drying in the oven followed by the reduction in the electric furnace. The average cost of electricity per day is £ 0.62. Regarding reducing gas, it cost about £ 346 from BOC company in the UK and the shipping cost was £ 87 in 2024 for a 75% H_2/ 25% N_2 gas cylinder that is 200 bar [318]. The gas volume is 9.3 m^3 and the average flow rate used in the current study is 60 mL/min, which means that the gas required to produce reduced BIOX 1 in 10 hours plus the time required to heat and cool the sample is about 41.4 L costing about £ 1.92. This cost is to produce 0.5 g of reduced BIOX 1.

In addition, the rental cost of the cylinder itself is £ 8.5 per month. So, the cost for the reduction programme of reduced BIOX 1 is £ 0.13. Therefore, the average total cost of producing 1 gram of reduced BIOX 1 is 3.84 + 0.62 + 0.006 = £ 4.46. This cost can be significantly cut down to just £ 0.38 if many gas cylinders (e.g., 20) are ordered at the same

time so the shipping cost is reduced, and if the reduction time is only one hour, which was also confirmed to produce reduced BIOX adsorbents at different temperatures with good performance across all pH levels. This price (£ 0.38) is higher than that of the commercial reduced iron powder produced by Sigma Aldrich, which is about £ 0.06 per gram (£ 60 per kg) [319]. However, the cost of £ 0.38 is not only paid to produce one g of Fe^0 as it helps solve the environmental issues caused by the BIOX material in rivers and waterways.

From an environmental perspective, the production of reduced BIOX materials does not involve any solid or liquid chemicals, but it needs H_2 as a reducing gas either with or without N_2. Although H_2 is expensive, it is preferred over carbon-based reductants because it supports the decarbonization of water treatment processes by reducing CO_2 emissions, an essential step in addressing climate change. The production and transport of these gases as well as the production of electricity that is used in labs result in different levels of carbon dioxide emissions. However, this issue can be solved, and the process can be carbon neutral if we shift to renewable energy sources, but this shift is not as straightforward as it may sound. Regarding the possible synthesis and release of ammonia gas from the reactors, the results showed that these BIOX materials are not effective in producing ammonia at all.

ICP-OES analysis was undertaken as a further step towards investigating the environmental effect of using reduced BIOX 1 in removing DOXY with a concentration of 25 ppm from DW and the River Clyde water samples by measuring the concentration of leached iron after the removal. As shown in **Fig 5.22.a** and **b**, the concentration of leached iron was very high in acidic conditions (pH 3) in both water samples, mainly because of the high solubility of iron compounds in acidic media, and the leached iron was obviously off the WHO limit. The iron leaching dropped to 0.08 ppm at pH 7. However, it went up at pH 9 and pH 11 (**Fig 5.22.a**), which was unexpected.

Although the iron leaching from reduced BIOX 1 increased over the neutral and alkaline conditions in the River Clyde water sample (**Fig 5.22.b**), it was still within the WHO limit. Such a result could be related to the better performance of reduced BIOX 1 in this water sample. Additionally, this result indicates the possibility of using reduced BIOX 1 in real wastewater treatment over a wide pH range without releasing significant amounts of iron into the water.

The iron leached in DW samples at pH 7 using higher concentrations of DOXY up to 200 ppm was also within the WHO limit (**Fig 5.22.c**). However, there was a high iron leaching upon using 500 ppm of DOXY, which could be related to the drop in the adsorption efficiency observed in **Fig 5.14.b**. These results indicate the safe and the efficient use of reduced BIOX 1 in adsorbing DOXY in neutral conditions up to 200 ppm of DOXY in the first cycle. However, upon recycling the adsorbent up to five times in DW at pH 7, the iron leaching increased, and the highest concentration was 1.70 ppm (**Fig 5.22.d**), which might cause aesthetic water problems. This result is related to the drop in the adsorption efficiency of reduced BIOX 1, which was observed in **Fig 5.14.f**.

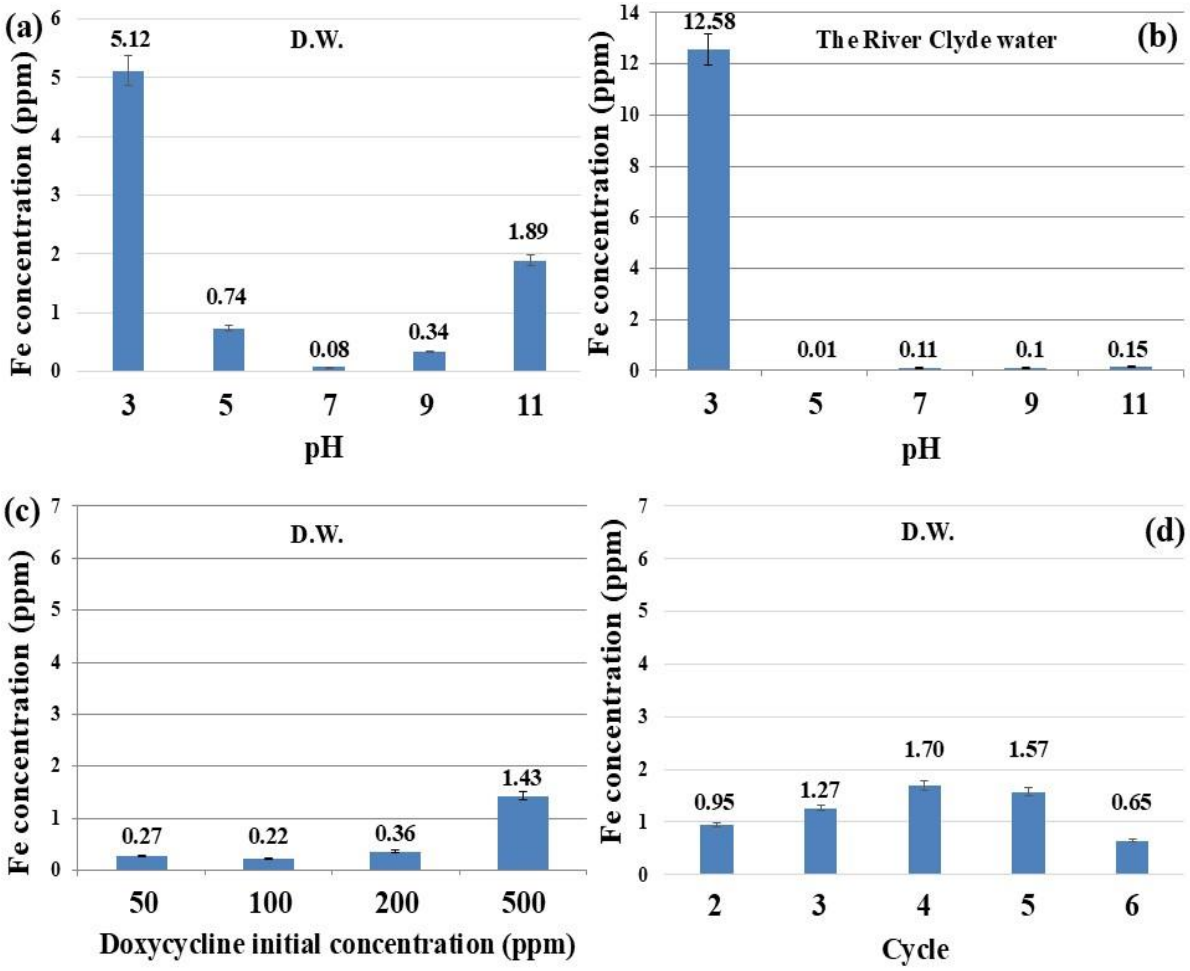

Fig 5.22. The concentration of leached iron from reduced BIOX 1 after 90 minutes of 25 ppm DOXY removal in DW **(a)**, the River Clyde water samples **(b)**, different concentrations of DOXY in DW at pH 7 **(c)**, and upon recycling for 5 times in DW at pH 7 (**d**) as measured by ICP-OES analysis. [Stirring rate = 750 rpm, T = 20 ± 2 °C, volume = 10 mL, and dose = 0.005 g].

5.5.6. The scalability and selectivity of reduced BIOX 1

To investigate the scalability of reduced BIOX 1 in 100 mL of DOXY, the mass was increased to 0.05 g at pH 7, but the adsorption efficacy dropped to 48% and 42% in 90 minutes using 25 and 50 ppm, respectively (**Fig 5.23.a** and **b**), compared to 79% and 85% in 10 mL of DOXY (**Fig 5.14.b**). This drop could be attributed to the increased mass transfer limitation and the weakened interaction between the adsorbent and DOXY. To overcome this limitation, the adsorption time was extended. For the 25 ppm case, the efficiency increased gradually to 53% after 270 minutes and 55% after 360 minutes, beyond which it remained constant (**Fig. 5.23.a**). A similar trend was observed at 50 ppm, where the efficiency reached 56% after 360 minutes and then stabilized (**Fig. 5.23.b**). These results, though showing only a slight improvement over time, further indicate that reduced BIOX 1 maintained good performance at higher DOXY concentrations.

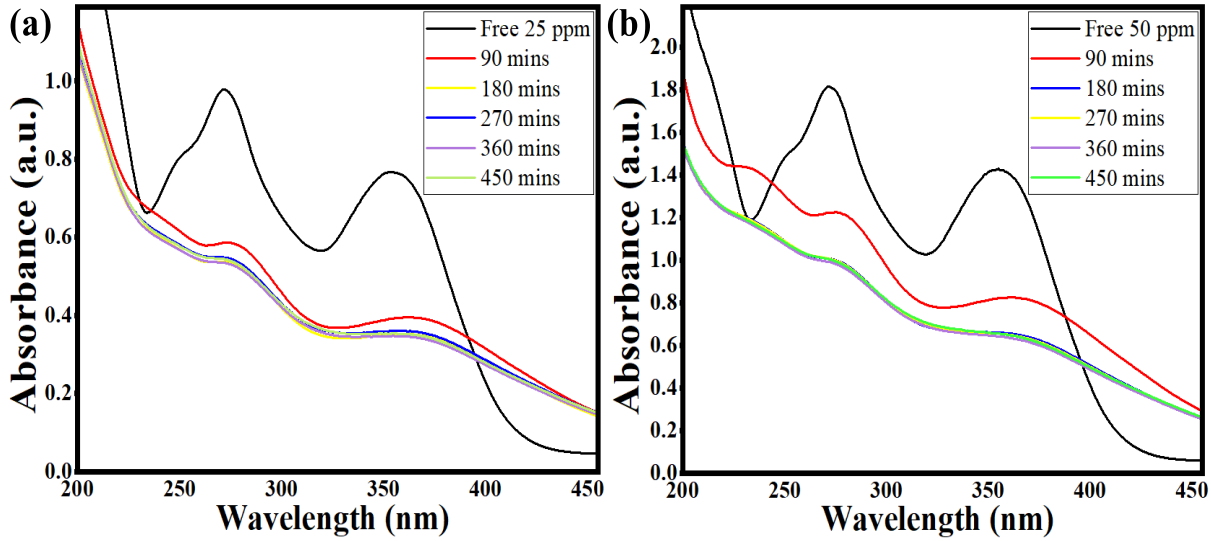

Fig 5.23. The upscaling of reduced BIOX 1 in adsorbing 25 ppm (**a**) and 50 ppm (**b**) of DOXY in 100 mL. [Dose = 0.05 g, pH 7, stirring rate = 750 rpm, and T = 20 ± 2 °C].

Another important aspect is the selectivity of reduced BIOX 1 towards DOXY removal in the presence of other pollutants such as CEF. As shown in **Fig 5.24.a**, the efficiency at pH 3 was almost the same in the presence of CEF, but it dropped to 62% and 53% at pH 5 and 7, respectively. The reason behind this drop could be the blockage of the active surface sites of the adsorbent caused by CEF. Unexpectedly, the presence of CEF exhibited a positive effect

on the removal efficiency in alkaline conditions, which is attributed to the higher self-degradation of DOXY upon adding CEF (**Fig 5.24.b**) that was discussed in Chapter 3.

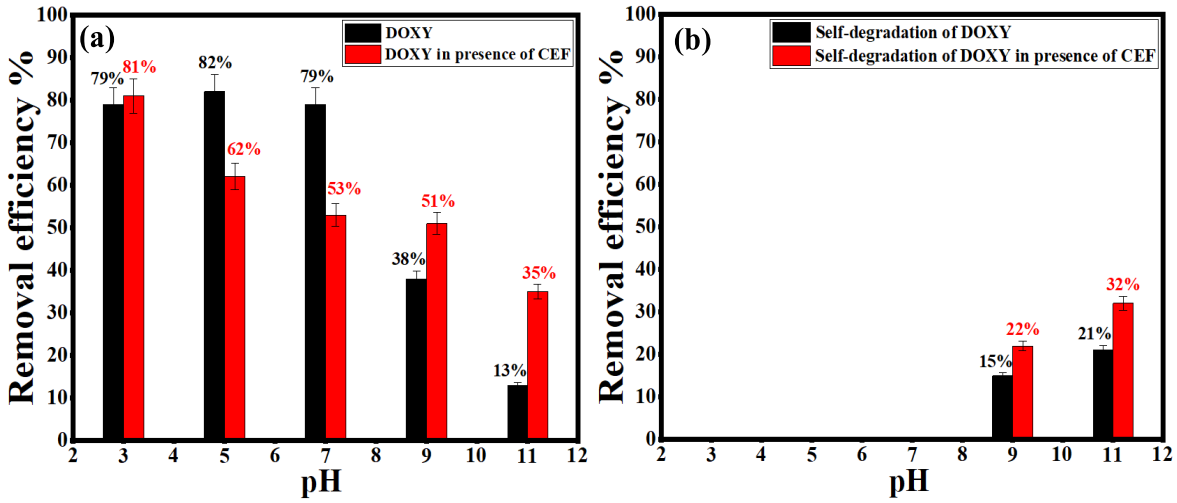

Fig 5.24. The efficiency of reduced BIOX 1 in removing DOXY and DOXY in presence of CEF (**a**) and the self-degradation of DOXY and in presence of CEF (**b**) after 90 minutes. [C_o = 25 ppm, volume = 10 mL, dose = 0.005 g, stirring rate = 750 rpm, and T = 20 ± 2 °C].

5.6. The investigation of BIOX and 2-line ferrihydrite materials in CEF removal

The BIOX materials, which were collected during the summertime, were also tested in the removal of CEF as a sort of screening without going into a detailed study to investigate the applicability of using BIOX materials with different antibiotics. BIOX from the first site was only effective at pH 3 by removing 52% (**Fig 5.25.a**). The same removal trend was shown by the BIOX samples from the other sites with a slightly better performance for the sample sourced from the third site (pond) as it removed 68% and 11% of CEF at pH 3 and 5, respectively. The high efficacy at pH 3 could be attributed to self-degradation of CEF.

Despite exhibiting low efficacy, the performance of 2-line ferrihydrite was better than all BIOX samples by removing CEF across most of the pH scale as shown in **Fig 5.25.b**. Although the reduction of BIOX materials at different temperatures and reduction times substantially improved the performance in the removal of DOXY, particularly reduced BIOX 1, there was no enhancement at all upon removing CEF using reduced BIOX 1 (**Fig 5.25.b**). Similarly, the reduced 2-line ferrihydrite, which was produced using the NH_3 synthesis conditions, did not show any improvements in CEF adsorption and the performance was even worse than that of the unreduced 2-line ferrihydrite. Therefore, the pristine and reduced BIOX

materials are suggested to be investigated with other antibiotics in future studies to gain further knowledge about their potential in wastewater treatment.

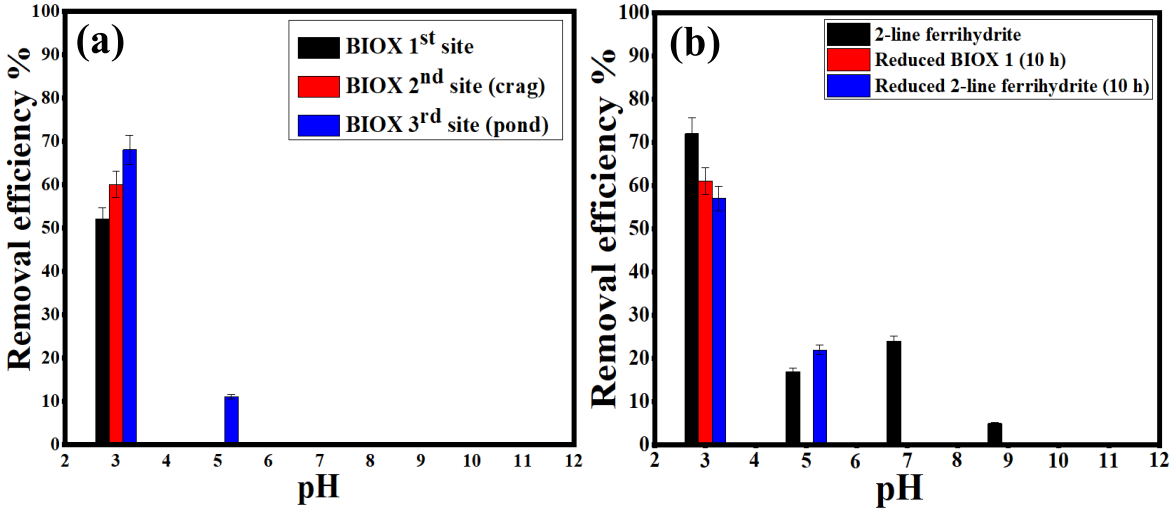

Fig 5.25. CEF removal efficiency by BIOX materials from different sites **(a)**, 2-line ferrihydrite, reduced BIOX 1, and reduced 2-line ferrihydrite (NH_3 synthesis conditions) **(b)**. [C_o = 25 ppm, stirring rate = 750 rpm, T = 20 ± 2 °C, volume = 10 mL, dose = 0.005 g, time = 90 minutes].

Table 5.4. The PZC of the BIOX and 2-line ferrihydrite materials used in this study.

Adsorbent	PZC
Pristine BIOX first site	4.4
2-line ferrihydrite	6.7
Pristine BIOX crag	7.3
Reduced BIOX 300 °C 1 h H_2	6.8
Reduced BIOX 400 °C 1 h H_2	7.2
Reduced BIOX 500 °C 1 h H_2	7.4
Reduced BIOX 600 °C 1 h H_2	7.5
Reduced BIOX 700 °C 1 h H_2	7.8
Reduced BIOX 300 °C 1h H_2/N_2	6.9
Reduced BIOX 400 °C 1h H_2/N_2	7.3
Reduced BIOX 500 °C 1h H_2/N_2	7.1
Reduced BIOX 600 °C 1h H_2/N_2	7.1
Reduced BIOX 700 °C 1 h H_2/N_2	7.5
Reduced BIOX 1 (crag) (NH_3 synthesis conditions) 10 h H_2/N_2	7.3
Reduced BIOX 400 °C 4h 500 °C 4h H_2/N_2	7.2
Reduced BIOX 700 °C 2h 500 °C 4h H_2/N_2	7.4
Reduced BIOX 700 °C 2h 400 °C 4h H_2/N_2	7.1
Reduced 2-line ferrihydrite (NH_3 synthesis conditions) 10 h H_2/N_2	7.5
Reduced BIOX 500 °C 4 h H_2/N_2	7.5
Reduced BIOX 500 °C 10h H_2/N_2	7.5
Reduced BIOX 700 °C 2 h H_2/N_2	7.1
Reduced BIOX 700 °C 4 h H_2/N_2	7.3
Reduced BIOX 700 °C 8 h H_2/N_2	7.4
Reduced BIOX 700 °C 10 h H_2/N_2	7.3

5.7. Conclusions

The investigation of BIOX produced by *Leptothrix* bacteria holds significant importance in environmental management. This naturally occurring material presents a sustainable and environmentally friendly alternative to synthetic iron oxides, with potential uses in water treatment, pollution mitigation, and resource recovery. Additionally, leveraging and enhancing the iron-oxidizing abilities of *Leptothrix* bacteria could pave the way for innovative strategies in managing iron-laden wastewater and remediating polluted areas. Reducing BIOX materials either under pure H_2 or H_2/N_2 mixture resulted in a considerable improvement in their removal efficacy of DOXY in model and real water samples from the River Clyde. Obtaining more crystalline materials, as indicated by the increased intensity of Fe^0 reflections and the larger coherent domain sizes achieved by increasing the reduction time and/or temperature, was generally associated with improved performance across many of the investigated pH levels, although not all.

Reduced BIOX 1, which was the most efficient material in removing DOXY at a concentration of 25 ppm, continued to exhibit an excellent performance at high concentrations up to 500 ppm by removing 91% corresponding to an adsorption capacity of 455 mg/g. The scalability of this material was acceptable as it achieved 56% adsorption in 100 mL of 50 ppm DOXY after 360 minutes. The removal of DOXY was mainly governed by electrostatic forces, complexation and the self-degradation of DOXY (specifically in alkaline conditions). The performance of the three pristine BIOX samples, including the crag sample collected from three different sites in Milngavie, differed from one another, which may be attributed to slight compositional variations. The long reduction programme for 10 hours at different temperatures (700 °C, 400 °C, and 500 °C) was effective in improving the performance of other waste materials such as Chinese RM and its derived α-Fe_2O_3. However, it did not lead to similar results when it was used to reduce lab-synthesized 2-line ferrihydrite due to the very low concentration of acidic and basic sites after the reduction. Furthermore, the same reduced materials did not show any promising results with CEF removal. Therefore, testing these reduced materials with other pollutants is highly recommended to gain a deeper insight into the full potential of such materials.

Chapter 6

6. Testing BIOX and red mud-based iron oxides in ammonia synthesis using the Haber-Bosch Process

6.1. Introduction

In this chapter, the catalytic activity of different iron oxides including BIOX, red mud-derived α-Fe_2O_3 along with their commercial counterparts is investigated synthesizing ammonia *via* the Haber-Bosch process. The main goal of this chapter was to find efficient catalytic materials sourced from waste materials, which can help reduce the cost of catalyst production. Different dopants such as potassium and cobalt were employed as promoters because they can improve the electron transfer from the catalyst to the nitrogen molecule to help break the triple bond between the two nitrogen atoms. Potassium has been previously confirmed by Strongin and Somorjai [320] to lower the adsorption energy of ammonia on the iron surface. Thus, it resulted in decreasing the ammonia concentration on the iron surface, and therefore, reducing the number of active sites blocked by the produced ammonia. Additionally, potassium can play a role in improving the hydrogen spillover and preventing the hydrogen poisoning of catalysts [321]. Therefore, it was tested with three different percentages (2, 5, and 10%) with red mud-derived α-Fe_2O_3.

6.2. Testing the catalytic activity of iron oxide-based waste materials and their composites in the ammonia synthesis process

One of the objectives of this study was to identify an iron oxide-based catalyst that can be sourced and used sustainably for ammonia synthesis, particularly one derived from a waste material, thereby addressing two issues simultaneously: catalyst development and waste valorization. The first waste material tested in NH_3 synthesis at atmospheric pressure was BIOX crag sample, which was collected during the summertime. As shown in **Fig. 6.1.a**, the rate of conductivity decrease, a measure of NH_3 production, was very low at 400 °C over a period of four hours. Unexpectedly, upon increasing the temperature to 500 °C, the conductivity increased from 832 to 840 µS/cm. A similar trend was observed with other materials, as shown below, which is likely due to impurities present in these waste-derived samples.

The increase in conductivity profile may be affected by the change in ambient temperature in the laboratory, specifically in the glass flask containing H_2SO_4 and the conductivity probe, since no steps were taken to keep this constant. Therefore, any apparent features should be treated with caution.

The phase transformation to zero-valent iron is unlikely to be the reason, as it occurred in all materials, as shown in the powder XRD patterns (**Fig. 5.4.a-g**). Therefore, the synthesis rate was only calculated at 400 °C for this material and it was 9 µmol h^{-1} g^{-1}. No induction period was observed for any of the tested materials.

In theory, the rate should go up by increasing the temperature from 400 °C to 500 °C as this is kinetically favored. However, NH_3 starts to decompose by increasing the temperature as the ammonia synthesis is an exothermic reaction, which needs a very fast desorption from the catalyst surface to minimize this decomposition. The catalytic activity of the synthetic 2-line ferrihydrite was quite similar by exhibiting 9 µmol h^{-1} g^{-1} at 400 °C, which then dropped to 2 µmol h^{-1} g^{-1} at 500 °C (**Fig 6.1.b**). Chinese red mud was tested as a control before extracting α-Fe_2O_3, and it showed 17 and 3 µmol h^{-1} g^{-1} at 400 °C and 500 °C, respectively (**Fig 6.1.c**). Upon extracting α-Fe_2O_3, the performance was even lower as it ranged between 13 (**Fig 6.1.e**) and 15 µmol h^{-1} g^{-1} at 400 °C (**Fig 6.1.d**) and was 4 µmol h^{-1} g^{-1} at 500 °C. Two identical reactors were used to test ammonia (NH_3) synthesis. However, slight differences were sometimes observed in the results for certain tested materials. To account for this variability, the results from both reactors, referred to as the "door side" and the "window side", are presented for those materials.

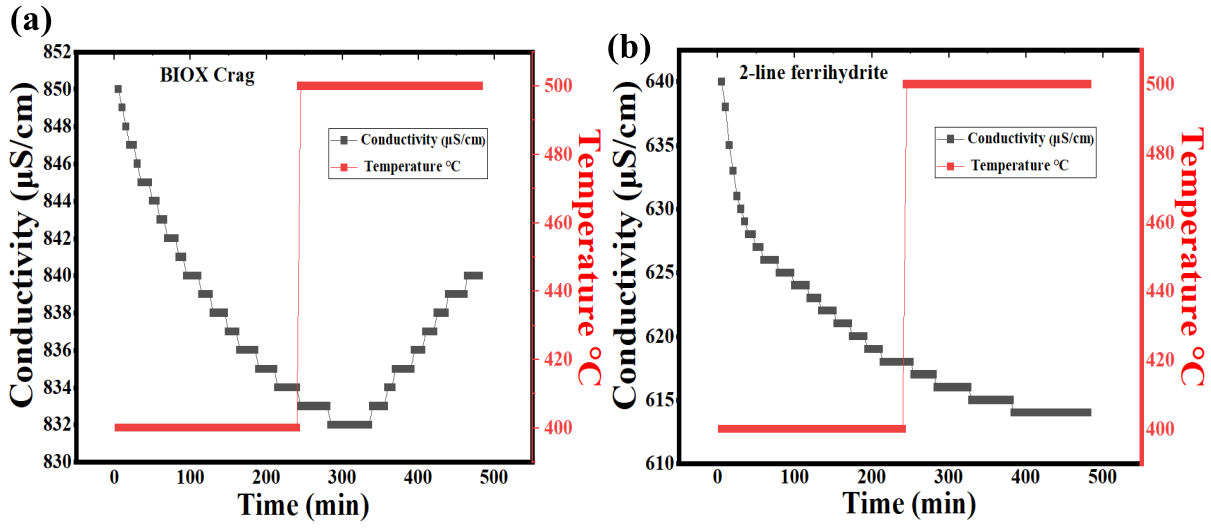

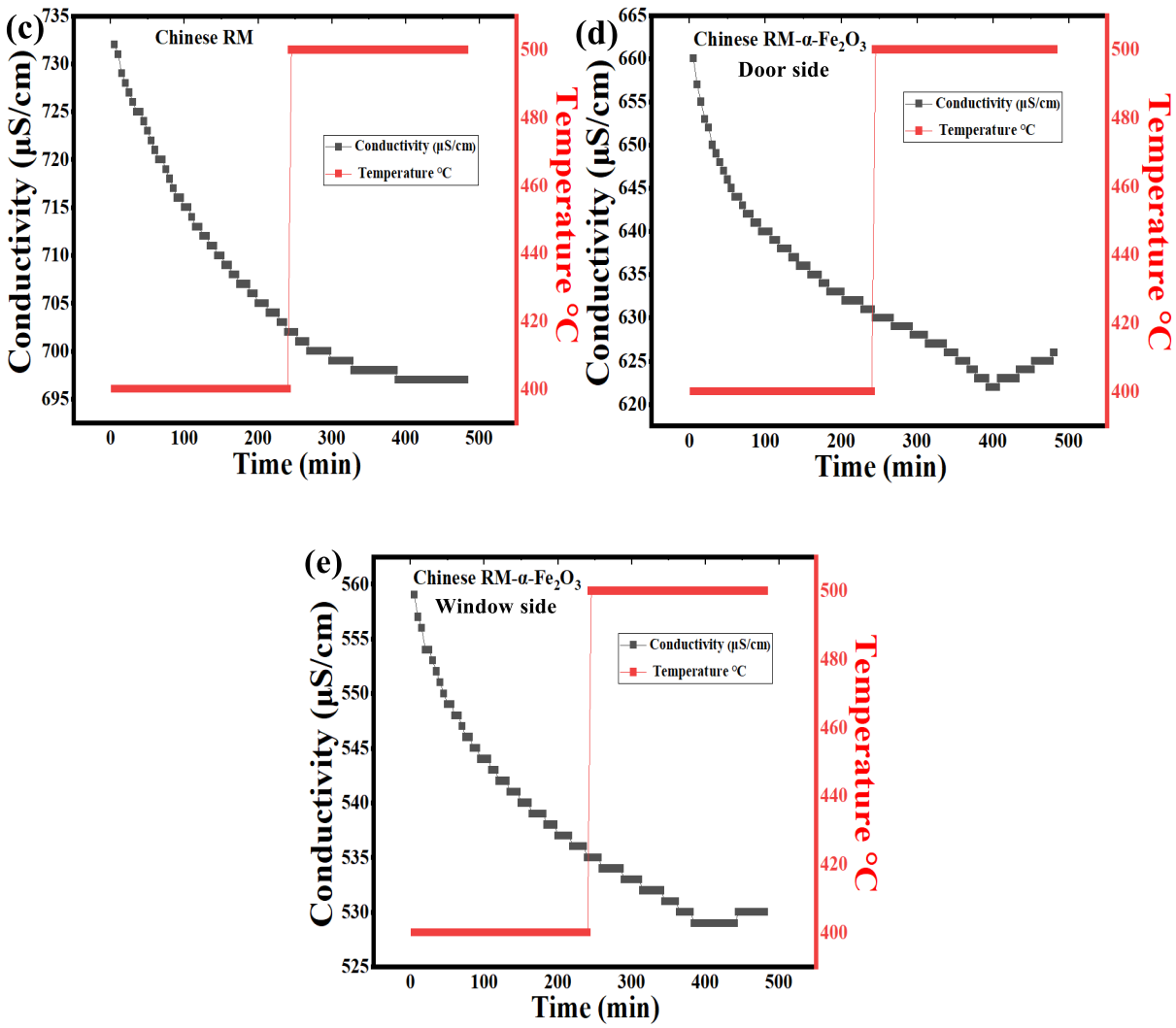

Fig 6.1. Conductivity profiles for BIOX crag **(a)**, synthetic 2-line ferrihydrite **(b)**, Chinese red mud **(c)**, and Chinese red mud-derived α-Fe_2O_3 door **(d)** and window side **(e)** after reaction with 3:1 H_2/N_2 at 400 °C and 500 °C for 4 hours each.

The very low synthesis rates observed for the above-mentioned materials were expected, as iron oxides are typically not catalytically active on their own [322]. The use of promoters such as potassium and cesium is a well-established strategy to enhance catalytic activity in NH_3 synthesis. These alkali metals act as electron donors, increasing the electron density on iron oxide surfaces and thereby improving their ability to adsorb and dissociate nitrogen molecules, a process considered the rate-limiting step in ammonia synthesis [323]. Accordingly, three different doping percentages of potassium were used to enhance the catalytic activity of the Chinese red mud-derived α-Fe_2O_3. 2% K-α-Fe_2O_3 was less catalytically active than the

derived α-Fe_2O_3, with synthesis rates of 11 and 2 µmol h^{-1} g^{-1} at 400 °C and 500 °C, respectively (**Fig 6.2.a**). 5% K-α-Fe_2O_3 was more active on the window-side reactor, achieving 17 µmol h^{-1} g^{-1} at 400 °C and increased to 24 µmol h^{-1} g^{-1} at 500 °C (**Fig 6.2.c**). However, the same material showed only 10 and 5 µmol h^{-1} g^{-1} at 400 °C and 500 °C, respectively, on the door-side reactor (**Fig 6.2.b**). Similarly, 10% K-α-Fe_2O_3 was more active on the window side by attaining 21 and 8 µmol h^{-1} g^{-1} at 400 °C and 500 °C, respectively (**Fig 6.2.d**), compared to 10 and 5 µmol h^{-1} g^{-1} on the door side at the same temperatures (**Fig 6.2.e**). However, all rates were very low compared to active ammonia synthesis catalysts under these conditions.

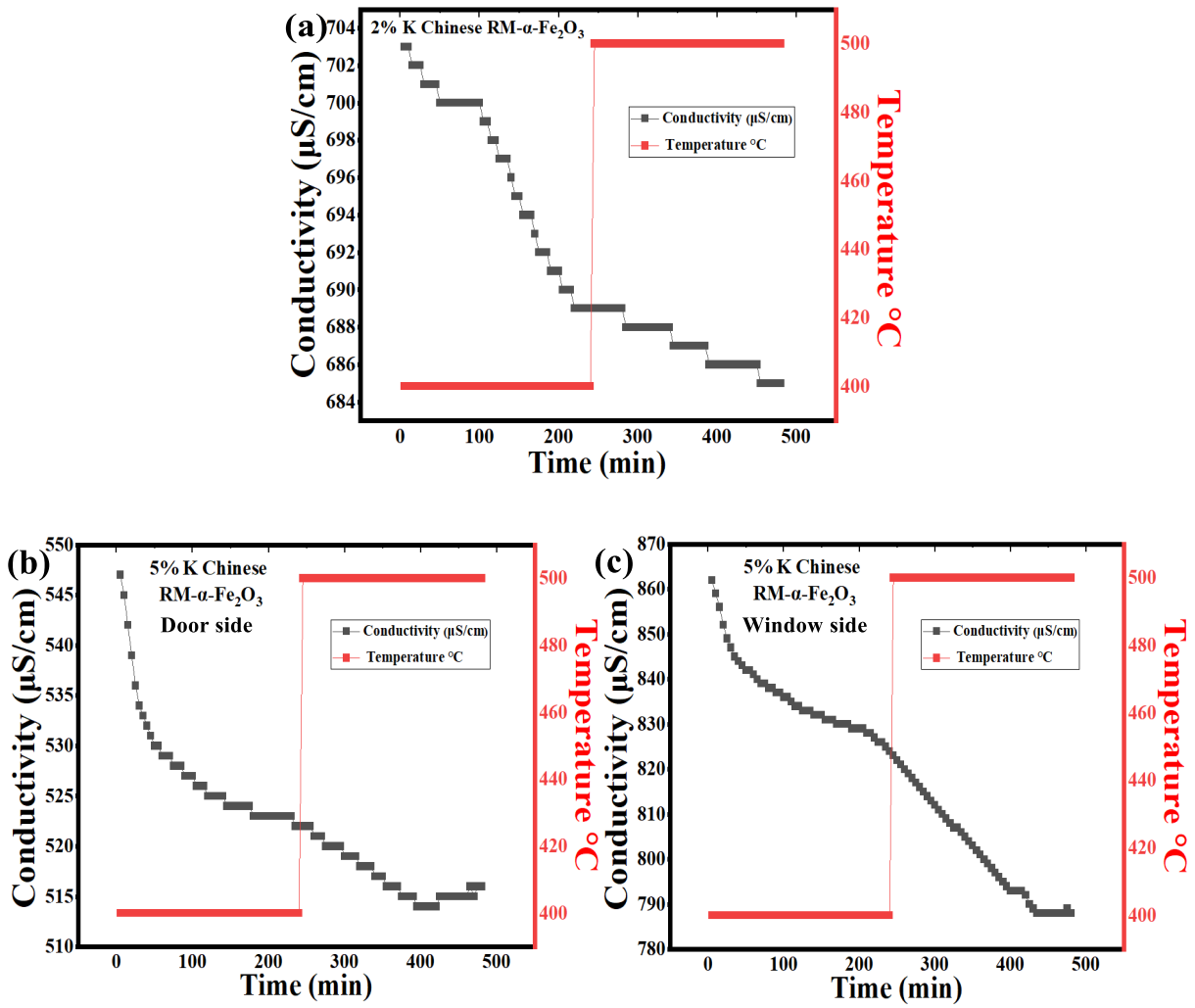

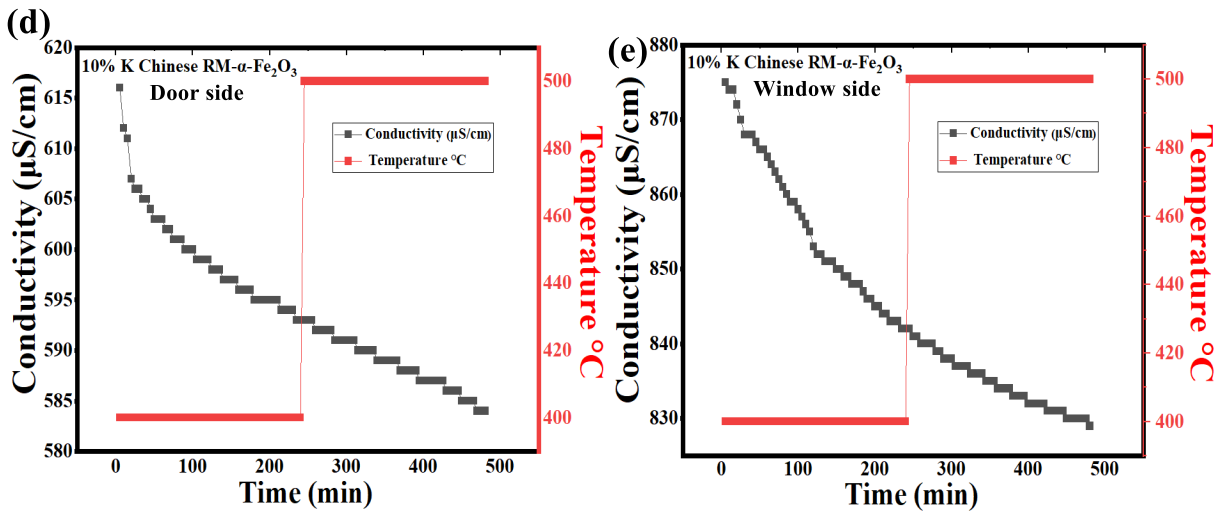

Fig 6.2. Conductivity profiles for 2% K-α-Fe_2O_3 **(f)**, 5% K-α-Fe_2O_3 door **(b)** and window side **(c)**, 10% K-α-Fe_2O_3 door **(d)** and window side **(e)** after reaction with 3:1 H_2/N_2 at 400 °C and 500 °C for 4 hours each.

The cause of this variation in catalytic performance between the two reactors is unclear, as it appears inconsistently across different samples. The gas flow rates and temperatures of both reactors were verified, and no differences were detected. Another promoter that can be used to improve the activity of iron catalysts in NH_3 synthesis is cobalt [324], which was previously tested by Kaleńczuk [325] who reported that 5.5 wt% of cobalt was the optimum loading for promoting NH_3 synthesis over iron catalysts. Consequently, 5% Co-α-Fe_2O_3 was tested in this study, but the material was even less active than the undoped α-Fe_2O_3, showing synthesis rates of 11 and 8 µmol h^{-1} g^{-1} at 400 °C on the window- (**Fig 6.3.b**) and the door-side reactors (**Fig 6.3.a**), respectively. No activity was observed for this material at 500 °C on either side.

The commercial α-Fe_2O_3 was used as a control, and it showed 4 µmol h^{-1} g^{-1} at 400 °C on both sides. However, at 500 °C, it exhibited 4 µmol h^{-1} g^{-1} on the window side but showed no catalytic activity on the door side (**Fig 6.3.c-d**). Therefore, none of these materials showed potential for ammonia synthesis, as their synthesis rates were considerably lower than those reported by many research groups worldwide, including the Hargreaves group using the same reactor setup, where rates can reach hundreds or even thousands of µmol h^{-1} g^{-1} of catalyst.

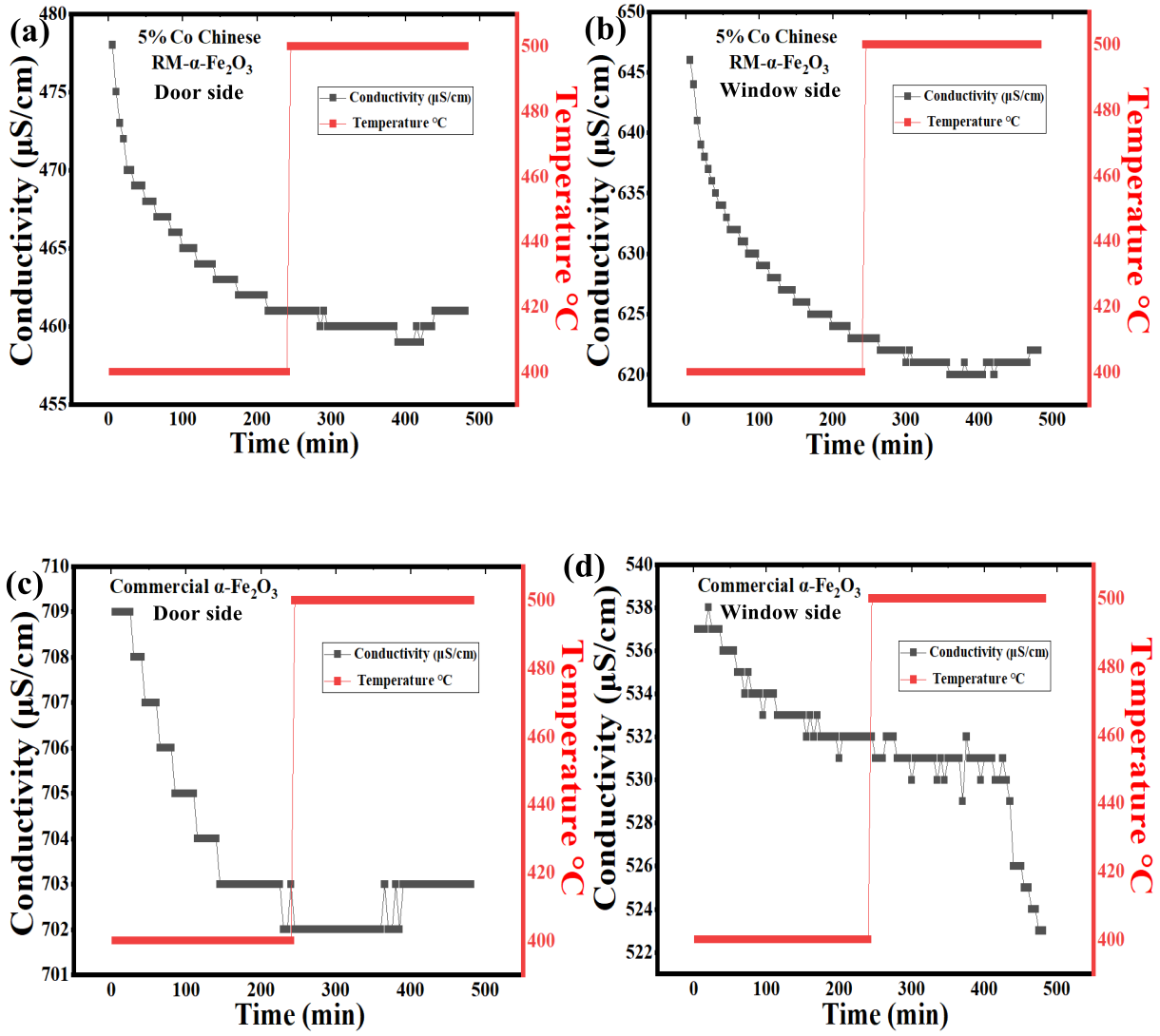

Fig 6.3. Conductivity profiles for 5% Co-α-Fe_2O_3 door side **(a)**, window side **(b)**, and commercial α-Fe_2O_3 door side **(c)**, and window side **(d)**, after reaction with 3:1 H_2/N_2 at 400 °C and 500 °C for 4 hours each.

6.3. Conclusions

Different iron oxides including BIOX, Chinese red mud, and red mud-derived α-Fe_2O_3 were tested as catalysts for ammonia synthesis. However, none of these materials demonstrated any promising results even after using promoters such as potassium, as their production rates were far below those reported by numerous research groups worldwide, where rates typically reach hundreds to thousands of μmol h^{-1} g^{-1} of catalyst. This poor performance may be attributed to two main factors: (i) the produced ammonia may not readily desorb from the catalyst surface, and (ii) trace amounts of oxygen likely poisoned the catalyst, since no precautions were taken to ensure an oxygen-free environment within the reactor tube (where the catalyst is placed). Additionally, these results could be related to the presence of impurities as all these catalysts were produced from waste materials.

Chapter 7

7. Conclusions and future recommendations

As concerns grow over water pollution and the persistent presence of pharmaceuticals, including antibiotics, in aquatic ecosystems worldwide, the need for sustainable wastewater treatment methods has become increasingly urgent. Equally important is preventing the formation and release of secondary pollutants, which, in some cases, may be even more harmful than the original contaminants. In this regard, adsorption provides a highly effective and environmentally friendly approach for removing antibiotics such as CEF, in contrast to UV-light degradation, which may generate potentially toxic byproducts. On another matter, challenges like resource depletion, water scarcity, soil pollution, climate change, and rising energy demands are becoming increasingly critical all over the world. Consequently, repurposing waste materials with potential benefits for these applications has become essential. In this regard, natural (e.g., *T. latifolia* and biogenic iron oxide) and industrial (red mud) waste materials, some of which were previously used in catalytic applications, were investigated in this work as potential adsorbents for water treatment.

Both the lab-synthesized and Chinese RM-derived TiO_2 (acid baking method) were more efficient than the commercial TiO_2 (P25) in CEF adsorption. Similarly, the RM-derived TiO_2 was more effective in DOXY adsorption. Within the same context, RM-derived α-Fe_2O_3 was more efficient in the removal of both antibiotics compared to its commercial counterpart.

An optimization study was provided in each chapter to investigate the effects of different factors including the solutions' pH, the adsorbent dose, the stirring rate, and the initial concentration of the antibiotic. Also, the effect of the interfering ions and the ionic strength was covered. Within the same optimization context, different transition and post-transition metals with different impregnation ratios were tested to achieve high removal efficacy across most of the pH scale.

According to the obtained results, the proposed removal mechanism of both antibiotics primarily involved electrostatic interactions, which are based on the Zwitterionic nature of both antibiotics along with the different PZC of the adsorbents by changing the pH. In addition, the synergistic effects of metal salt precursors, hydrogen bonding, and the possible complexation between the metals and both antibiotics are contributing to the removal process.

Moreover, the self-degradation of CEF and DOXY in acidic and alkaline conditions, respectively, is another factor that plays a role in their removal.

Impregnating lab-synthesized TiO_2 with different metals using metal nitrate precursors was confirmed as an effective strategy for enhancing its adsorption efficiency. Therefore, it was used to enhance the efficiency of RM-derived TiO_2. However, it is not always a good option as it sometimes leads to metals leaching in water mostly in highly acidic conditions (pH 3), which was confirmed by the ICP-OES results. The alkali roasting and the acid baking are the methods used to extract TiO_2 from the Chinese RM. The latter was more effective in producing a potentially purer crystalline phase composition as indicated by the EDX analysis. Such a result was linked to its better CEF adsorption efficacy. TiO_2 extracted by the two methods exhibited the anatase phase. Moreover, the production cost of TiO_2 using both methods is less than that of P25.

Among different Chinese RM-derived TiO_2 composites, 5% Fe 5% Cu-TiO_2 exhibited a good performance across the investigated pH range and demonstrated promising scalability, removing about 60% of CEF from a 1000 mL solution after 250 minutes. The salicylic acid nitration method further confirmed that all leached nitrate concentrations were well below the WHO guideline limit. In contrast to P25 and lab-prepared TiO_2, 5% Fe 5% Cu-TiO_2 showed very weak photocatalytic activity for CEF removal under UV irradiation. None of the α-Fe_2O_3 samples demonstrated photocatalytic activity to remove CEF under visible light.

Regarding the removal of DOXY, both RM-derived α-Fe_2O_3 and TiO_2 demonstrated higher adsorption efficacies than their commercial counterparts. However, unlike the commercial materials, they showed no photocatalytic activity under visible and UV light, respectively. TGA-MS analysis revealed that NO and SO_2 are potential toxic products from CEF degradation, whereas NO and CH_4 could be released from DOXY degradation. These gases resulted in the formation of nitrites from DOXY degradation, and nitrites and sulfates from CEF degradation in the water samples as confirmed by the Griess reagent and the turbidimetric methods, respectively.

Reducing the BIOX materials using either pure H_2 or a H_2/N_2 mixture significantly enhanced their ability to adsorb DOXY in both model and real water samples from the River Clyde. An increase in Fe^0 reflection intensity, achieved by extending the reduction duration and/or raising the temperature, generally correlated with enhanced adsorption across various pH

levels, though not all. The improved performance can also be attributed to the increased concentration of basic and acidic sites on the surface of the reduced materials. Among these materials, reduced BIOX 1 demonstrated the highest efficiency in removing DOXY over most pH levels at different concentrations ranging from 25 to 500 ppm. This leaves scope for further modifications and investigations into other pollutants in future work. Lastly, none of the investigated materials in the current study showed a catalytic activity in synthesizing ammonia.

According to the obtained results of this study, there are some recommendations that are suggested to be undertaken in future work.

1. Looking into the applicability of converting *T. latifolia* into different products such as graphene, which could be used in water treatment, concrete production, and other applications, using different techniques such as flash joule heating and microwave synthesis.
2. Exploring the possibility of using *T. latifolia* as a reducing agent of red mud and BIOX materials instead of H_2 or H_2/N_2 to make use of different waste materials at the same time.
3. Expanding the research of various waste materials, particularly those rejected by recycling companies such as low-quality plastic and paper wastes by transforming them into useful carbon-based materials for water treatment, supports for catalytic materials, and other uses.
4. Investigating different H_2/N_2 mixture ratios in reducing BIOX materials.
5. Testing the applicability of the reduced materials in the removal of different pollutants such as synthetic organic dyes (e.g., Congo red), not just antibiotics along with extended research in applications other than water treatment would provide a deeper insight into the potential of these materials.

References

1. Moosavi, S., C.W. Lai, O. Akbarzadeh, and M.R. Johan, *Recycled Activated Carbon-Based Materials for the Removal of Organic Pollutants from Wastewater*, in *Waste Recycling Technologies for Nanomaterials Manufacturing*. 2021, Springer. p. 513-539.
2. Palaniappan, M., P.H. Gleick, L. Allen, M.J. Cohen, J. Christian-Smith, C. Smith, and N. Ross, *Clearing the waters: a focus on water quality solutions*. 2010.
3. Sharma, A., A.S. Grewal, D. Sharma, and A.L. Srivastav, *Chapter 3 - Heavy metal contamination in water: consequences on human health and environment*, in *Metals in Water*, S.K. Shukla, et al., Editors. 2023, Elsevier. p. 39-52.
4. Saxena, R., M. Saxena, and A. Lochab, *Recent progress in nanomaterials for adsorptive removal of organic contaminants from wastewater.* ChemistrySelect, 2020. **5**(1): p. 335-353.
5. de Oliveira, M., B.E.F. Frihling, J. Velasques, F.J.C.M. Filho, P.S. Cavalheri, and L. Migliolo, *Pharmaceuticals residues and xenobiotics contaminants: Occurrence, analytical techniques and sustainable alternatives for wastewater treatment.* Science of The Total Environment, 2020. **705**: p. 135568.
6. Khan, S., M. Naushad, M. Govarthanan, J. Iqbal, and S.M. Alfadul, *Emerging contaminants of high concern for the environment: Current trends and future research.* Environmental Research, 2022. **207**: p. 112609.
7. Yang, G.C., C.-H. Yen, and C.-L. Wang, *Monitoring and removal of residual phthalate esters and pharmaceuticals in the drinking water of Kaohsiung City, Taiwan.* Journal of Hazardous Materials, 2014. **277**: p. 53-61.
8. Zaied, B.K., M. Rashid, M. Nasrullah, A.W. Zularisam, D. Pant, and L. Singh, *A comprehensive review on contaminants removal from pharmaceutical wastewater by electrocoagulation process.* Science of The Total Environment, 2020. **726**: p. 138095.
9. Luo, Y., W. Guo, H.H. Ngo, L.D. Nghiem, F.I. Hai, J. Zhang, S. Liang, and X.C. Wang, *A review on the occurrence of micropollutants in the aquatic environment and their fate and removal during wastewater treatment.* Science of the total environment, 2014. **473**: p. 619-641.
10. Bielen, A., A. Šimatović, J. Kosić-Vukšić, I. Senta, M. Ahel, S. Babić, T. Jurina, J.J. González Plaza, M. Milaković, and N. Udiković-Kolić, *Negative environmental impacts of antibiotic-contaminated effluents from pharmaceutical industries.* Water Research, 2017. **126**: p. 79-87.
11. Bolong, N., A. Ismail, M.R. Salim, and T. Matsuura, *A review of the effects of emerging contaminants in wastewater and options for their removal.* Desalination, 2009. **239**(1-3): p. 229-246.
12. Rozman, D., Z. Hrkal, M. Váňa, J. Vymazal, and Z. Boukalová, *Occurrence of pharmaceuticals in wastewater and their interaction with shallow aquifers: a case study of Horní Beřkovice, Czech Republic.* Water, 2017. **9**(3): p. 218.
13. Quesada, H.B., A.T.A. Baptista, L.F. Cusioli, D. Seibert, C. de Oliveira Bezerra, and R. Bergamasco, *Surface water pollution by pharmaceuticals and an alternative of removal by low-cost adsorbents: A review.* Chemosphere, 2019. **222**: p. 766-780.
14. Tijani, J.O., O.O. Fatoba, and L. Petrik, *A review of pharmaceuticals and endocrine-disrupting compounds: sources, effects, removal, and detections.* Water, Air, & Soil Pollution, 2013. **224**(11): p. 1-29.
15. Heindel, J.J., S. Howard, K. Agay-Shay, J.P. Arrebola, K. Audouze, P.J. Babin, R. Barouki, A. Bansal, E. Blanc, and M.C. Cave, *Obesity II: Establishing causal links between chemical exposures and obesity.* Biochemical Pharmacology, 2022. **199**: p. 115015.
16. Seralini, G.-E. and G. Jungers, *Endocrine disruptors also function as nervous disruptors and can be renamed endocrine and nervous disruptors (ENDs).* Toxicology Reports, 2021. **8**: p. 1538-1557.

17. Corona, G., L. Croce, C. Sparano, L. Petrone, A. Sforza, M. Maggi, L. Chiovato, and M. Rotondi, *Thyroid and heart, a clinically relevant relationship.* Journal of Endocrinological Investigation, 2021. **44**(12): p. 2535-2544.
18. Masood, Z., A. Ikhlaq, O.S. Rizvi, H.A. Aziz, M. Kazmi, and F. Qi, *A novel hybrid treatment for pharmaceutical wastewater implying electroflocculation, catalytic ozonation with Ni-Co Zeolite 5A° catalyst followed by ceramic membrane filtration.* Journal of Water Process Engineering, 2023. **51**: p. 103423.
19. Chen, C., *Antibiotics in the environment: impact of metal oxides and effect on denitrification*. 2023, Université de Rennes.
20. Walters, E., K. McClellan, and R.U. Halden, *Occurrence and loss over three years of 72 pharmaceuticals and personal care products from biosolids–soil mixtures in outdoor mesocosms.* Water Research, 2010. **44**(20): p. 6011-6020.
21. Zhang, X., H. Han, X. Zheng, T. Yu, and Y. Chen, *Tetracycline-induced effects on the nitrogen transformations in sediments: Roles of adsorption behavior and bacterial activity.* Science of The Total Environment, 2019. **695**: p. 133811.
22. Yin, G., L. Hou, M. Liu, Y. Zheng, X. Li, X. Lin, J. Gao, and X. Jiang, *Effects of thiamphenicol on nitrate reduction and N2O release in estuarine and coastal sediments.* Environmental Pollution, 2016. **214**: p. 265-272.
23. Kristensen, P., C. Whalley, F.N.N. Zal, and T. Christiansen, *European waters assessment of status and pressures 2018.* EEA Report, 2018(7/2018).
24. Zhou, S., C. Di Paolo, X. Wu, Y. Shao, T.-B. Seiler, and H. Hollert, *Optimization of screening-level risk assessment and priority selection of emerging pollutants–The case of pharmaceuticals in European surface waters.* Environment international, 2019. **128**: p. 1-10.
25. O'Flynn, D., J. Lawler, A. Yusuf, A. Parle-McDermott, D. Harold, T. Mc Cloughlin, L. Holland, F. Regan, and B. White, *A review of pharmaceutical occurrence and pathways in the aquatic environment in the context of a changing climate and the COVID-19 pandemic.* Analytical Methods, 2021. **13**(5): p. 575-594.
26. Nannou, C.I., C.I. Kosma, and T.A. Albanis, *Occurrence of pharmaceuticals in surface waters: analytical method development and environmental risk assessment.* International Journal of Environmental Analytical Chemistry, 2015. **95**(13): p. 1242-1262.
27. Cassini, A., L.D. Högberg, D. Plachouras, A. Quattrocchi, A. Hoxha, G.S. Simonsen, M. Colomb-Cotinat, M.E. Kretzschmar, B. Devleesschauwer, and M. Cecchini, *Attributable deaths and disability-adjusted life-years caused by infections with antibiotic-resistant bacteria in the EU and the European Economic Area in 2015: a population-level modelling analysis.* The Lancet infectious diseases, 2019. **19**(1): p. 56-66.
28. Mortazhejri, S., P.J. Hong, A.M. Yu, B.Y. Hong, D. Stacey, R.S. Bhatia, and J.M. Grimshaw, *Systematic review of patient-oriented interventions to reduce unnecessary use of antibiotics for upper respiratory tract infections.* Systematic Reviews, 2020. **9**(1): p. 106.
29. Demain, A.L., *Importance of microbial natural products and the need to revitalize their discovery.* Journal of industrial microbiology and biotechnology, 2014. **41**(2): p. 185-201.
30. Qin, K., L. Wei, J. Li, B. Lai, F. Zhu, H. Yu, Q. Zhao, and K. Wang, *A review of ARGs in WWTPs: Sources, stressors and elimination.* Chinese Chemical Letters, 2020. **31**(10): p. 2603-2613.
31. Klein, E.Y., T.P. Van Boeckel, E.M. Martinez, S. Pant, S. Gandra, S.A. Levin, H. Goossens, and R. Laxminarayan, *Global increase and geographic convergence in antibiotic consumption between 2000 and 2015.* Proceedings of the National Academy of Sciences, 2018. **115**(15): p. E3463-E3470.
32. Deblonde, T., C. Cossu-Leguille, and P. Hartemann, *Emerging pollutants in wastewater: A review of the literature.* International Journal of Hygiene and Environmental Health, 2011. **214**(6): p. 442-448.

33. Zhang, Q.-Q., G.-G. Ying, C.-G. Pan, Y.-S. Liu, and J.-L. Zhao, *Comprehensive evaluation of antibiotics emission and fate in the river basins of China: source analysis, multimedia modeling, and linkage to bacterial resistance.* Environmental science & technology, 2015. **49**(11): p. 6772-6782.
34. *Removal of antibiotics from wastewater*. 2025 [cited 2025 24/02/2025]; Available from: https://www.scopus.com/term/analyzer.uri?sort=plf-f&src=s&sid=4326fef87fc9efdc738289bc7851cf50&sot=a&sdt=a&sl=53&s=TITLE-ABS-KEY%28Removal+of+antibiotics+from+wastewater%29&origin=resultslist&count=10&analyzeResults=Analyze+results.
35. Abdelfatah, A.M., M. Fawzy, M.E. El-Khouly, and A.S. Eltaweil, *Efficient adsorptive removal of tetracycline from aqueous solution using phytosynthesized nano-zero valent iron.* Journal of Saudi Chemical Society, 2021. **25**(12): p. 101365.
36. Al-Musawi, T.J., A.H. Mahvi, A.D. Khatibi, and D. Balarak, *Effective adsorption of ciprofloxacin antibiotic using powdered activated carbon magnetized by iron(III) oxide magnetic nanoparticles.* Journal of Porous Materials, 2021. **28**(3): p. 835-852.
37. Zhou, Q., X. Li, S. Wu, Y. Zhong, and C. Yang, *Enhanced strategies for antibiotic removal from swine wastewater in anaerobic digestion.* Trends in Biotechnology, 2021. **39**(1): p. 8-11.
38. Ji, C., J. Hou, K. Wang, Y. Zhang, and V. Chen, *Biocatalytic degradation of carbamazepine with immobilized laccase-mediator membrane hybrid reactor.* Journal of Membrane Science, 2016. **502**: p. 11-20.
39. Wei, X., X. Xu, C. Li, J. Wu, J. Chen, B. Lv, and J. Wang, *Removal of Pharmaceuticals and Personal Care Products in Aquatic Environment by Membrane Technology*, in *Membranes for Environmental Applications*, Z. Zhang, W. Zhang, and E. Lichtfouse, Editors. 2020, Springer International Publishing: Cham. p. 177-242.
40. Chen, M., J. Zheng, R. Dai, Z. Wu, and Z. Wang, *Preferential removal of 2, 4-dichlorophenoxyacetic acid from contaminated waters using an electrocatalytic ceramic membrane filtration system: Mechanisms and implications.* Chemical Engineering Journal, 2020. **387**: p. 124132.
41. Wang, X., F. Li, X. Hu, and T. Hua, *Electrochemical advanced oxidation processes coupled with membrane filtration for degrading antibiotic residues: A review on its potential applications, advances, and challenges.* Science of The Total Environment, 2021. **784**: p. 146912.
42. Chen, M., L. Ren, K. Qi, Q. Li, M. Lai, Y. Li, X. Li, and Z. Wang, *Enhanced removal of pharmaceuticals and personal care products from real municipal wastewater using an electrochemical membrane bioreactor.* Bioresource Technology, 2020. **311**: p. 123579.
43. Lin, H., J. Niu, J. Xu, H. Huang, D. Li, Z. Yue, and C. Feng, *Highly Efficient and Mild Electrochemical Mineralization of Long-Chain Perfluorocarboxylic Acids (C9–C10) by Ti/SnO2–Sb–Ce, Ti/SnO2–Sb/Ce–PbO2, and Ti/BDD Electrodes.* Environmental Science & Technology, 2013. **47**(22): p. 13039-13046.
44. Zhang, Q., H. Zhang, Q. Zhang, and Q. Huang, *Degradation of norfloxacin in aqueous solution by atmospheric-pressure non-thermal plasma: Mechanism and degradation pathways.* Chemosphere, 2018. **210**: p. 433-439.
45. Saeid, S., P. Tolvanen, N. Kumar, K. Eränen, J. Peltonen, M. Peurla, J.-P. Mikkola, A. Franz, and T. Salmi, *Advanced oxidation process for the removal of ibuprofen from aqueous solution: A non-catalytic and catalytic ozonation study in a semi-batch reactor.* Applied Catalysis B: Environmental, 2018. **230**: p. 77-90.
46. Khatami, M. and S. Iravani, *Green and Eco-Friendly Synthesis of Nanophotocatalysts: An Overview.* Comments on Inorganic Chemistry, 2021. **41**(3): p. 133-187.
47. Li, D. and W. Shi, *Recent developments in visible-light photocatalytic degradation of antibiotics.* Chinese Journal of Catalysis, 2016. **37**(6): p. 792-799.

48. Jassby, D., T.Y. Cath, and H. Buisson, *The role of nanotechnology in industrial water treatment.* Nature nanotechnology, 2018. **13**(8): p. 670-672.
49. Salem, S.S. and A. Fouda, *Green synthesis of metallic nanoparticles and their prospective biotechnological applications: an overview.* Biological trace element research, 2021. **199**(1): p. 344-370.
50. Peng, Z., X. Liu, W. Zhang, Z. Zeng, Z. Liu, C. Zhang, Y. Liu, B. Shao, Q. Liang, and W. Tang, *Advances in the application, toxicity and degradation of carbon nanomaterials in environment: A review.* Environment international, 2020. **134**: p. 105298.
51. Lee, K.M., C.W. Lai, K.S. Ngai, and J.C. Juan, *Recent developments of zinc oxide based photocatalyst in water treatment technology: A review.* Water Research, 2016. **88**: p. 428-448.
52. Ansari Moghaddam, A., L. Mohammadi, E. Bazrafshan, M. Batool, M. Behnampour, M. Baniasadi, L. Mohammadi, and M. Nadeem Zafar, *Antibiotics sequestration using metal nanoparticles: An updated systematic review and meta-analysis.* Inorganica Chimica Acta, 2023. **550**: p. 121448.
53. Stan, M., I. Lung, M.-L. Soran, C. Leostean, A. Popa, M. Stefan, M.D. Lazar, O. Opris, T.-D. Silipas, and A.S. Porav, *Removal of antibiotics from aqueous solutions by green synthesized magnetite nanoparticles with selected agro-waste extracts.* Process Safety and Environmental Protection, 2017. **107**: p. 357-372.
54. Ezeuko, A.S., M.O. Ojemaye, O.O. Okoh, and A.I. Okoh, *Potentials of metallic nanoparticles for the removal of antibiotic resistant bacteria and antibiotic resistance genes from wastewater: A critical review.* Journal of Water Process Engineering, 2021. **41**: p. 102041.
55. Al-Thani, A.N., A.G. Jan, M. Abbas, M. Geetha, and K.K. Sadasivuni, *Nanoparticles in cancer theragnostic and drug delivery: A comprehensive review.* Life Sciences, 2024. **352**: p. 122899.
56. Du, C., Z. Zhang, G. Yu, H. Wu, H. Chen, L. Zhou, Y. Zhang, Y. Su, S. Tan, L. Yang, J. Song, and S. Wang, *A review of metal organic framework (MOFs)-based materials for antibiotics removal via adsorption and photocatalysis.* Chemosphere, 2021. **272**: p. 129501.
57. Yaghi, O.M., G. Li, and H. Li, *Selective binding and removal of guests in a microporous metal–organic framework.* Nature, 1995. **378**(6558): p. 703-706.
58. Pham, H.T.B., J.Y. Choi, S. Huang, X. Wang, A. Claman, M. Stodolka, S. Yazdi, S. Sharma, W. Zhang, and J. Park, *Imparting Functionality and Enhanced Surface Area to a 2D Electrically Conductive MOF via Macrocyclic Linker.* Journal of the American Chemical Society, 2022. **144**(23): p. 10615-10621.
59. Wu, C.-s., Z.-h. Xiong, C. Li, and J.-m. Zhang, *Zeolitic imidazolate metal organic framework ZIF-8 with ultra-high adsorption capacity bound tetracycline in aqueous solution.* Rsc Advances, 2015. **5**(100): p. 82127-82137.
60. Novoselov, K.S., A.K. Geim, S.V. Morozov, D. Jiang, Y. Zhang, S.V. Dubonos, I.V. Grigorieva, and A.A. Firsov, *Electric Field Effect in Atomically Thin Carbon Films.* Science, 2004. **306**(5696): p. 666-669.
61. Boehm, H.-P., A. Clauss, G. Fischer, and U. Hofmann, *Fifth conference on Carbon*. 1962, Pergamon Press, Oxford.
62. Ibrahim, A., A. Klopocinska, K. Horvat, and Z. Abdel Hamid, *Graphene-based nanocomposites: Synthesis, mechanical properties, and characterizations.* Polymers, 2021. **13**(17): p. 2869.
63. Balandin, A.A., S. Ghosh, W. Bao, I. Calizo, D. Teweldebrhan, F. Miao, and C.N. Lau, *Superior Thermal Conductivity of Single-Layer Graphene.* Nano Letters, 2008. **8**(3): p. 902-907.
64. Wassei, J.K. and R.B. Kaner, *Graphene, a promising transparent conductor.* Materials Today, 2010. **13**(3): p. 52-59.
65. Razaq, A., F. Bibi, X. Zheng, R. Papadakis, S.H.M. Jafri, and H. Li, *Review on graphene-, graphene oxide-, reduced graphene oxide-based flexible composites: From fabrication to applications.* Materials, 2022. **15**(3): p. 1012.

66. Wang, H., X. Mi, Y. Li, and S. Zhan, *3D Graphene-Based Macrostructures for Water Treatment.* Advanced Materials, 2020. **32**(3): p. 1806843.
67. Wang, Z., L. Colombi Ciacchi, and G. Wei, *Recent advances in the synthesis of graphene-based nanomaterials for controlled drug delivery.* Applied Sciences, 2017. **7**(11): p. 1175.
68. Liu, F., *Mechanical exfoliation of large area 2D materials from vdW crystals.* Progress in Surface Science, 2021. **96**(2): p. 100626.
69. Li, X., L. Colombo, and R.S. Ruoff, *Synthesis of Graphene Films on Copper Foils by Chemical Vapor Deposition.* Advanced Materials, 2016. **28**(29): p. 6247-6252.
70. Advincula, P.A., V. Granja, K.M. Wyss, W.A. Algozeeb, W. Chen, J.L. Beckham, D.X. Luong, C.F. Higgs, and J.M. Tour, *Waste plastic- and coke-derived flash graphene as lubricant additives.* Carbon, 2023. **203**: p. 876-885.
71. Deng, B., W. Meng, P.A. Advincula, L. Eddy, M.G. Ucak-Astarlioglu, K.M. Wyss, W. Chen, R.A. Carter, G. Li, Y. Cheng, S. Nagarajaiah, and J.M. Tour, *Heavy metal removal from coal fly ash for low carbon footprint cement.* Communications Engineering, 2023. **2**(1): p. 13.
72. Mishra, S. and B. Sundaram, *Efficacy and challenges of carbon nanotube in wastewater and water treatment.* Environmental Nanotechnology, Monitoring & Management, 2023. **19**: p. 100764.
73. Abdullah, T.A., T. Juzsakova, S.A. Hafad, R.T. Rasheed, N. Al-Jammal, M.A. Mallah, A.D. Salman, P. Le, E. Domokos, and M. Aldulaimi, *Functionalized multi-walled carbon nanotubes for oil spill cleanup from water.* Clean Technologies and Environmental Policy, 2022. **24**(2): p. 519-541.
74. Shoukat, R. and M.I. Khan, *Carbon nanotubes/nanofibers (CNTs/CNFs): a review on state of the art synthesis methods.* Microsystem Technologies, 2022. **28**(4): p. 885-901.
75. Díez-Pascual, A.M., *Chemical functionalization of carbon nanotubes with polymers: a brief overview.* Macromol, 2021. **1**(2): p. 64-83.
76. Yu, F., Y. Li, S. Han, and J. Ma, *Adsorptive removal of antibiotics from aqueous solution using carbon materials.* Chemosphere, 2016. **153**: p. 365-385.
77. Roegiers, J. and S. Denys, *Development of a novel type activated carbon fiber filter for indoor air purification.* Chemical Engineering Journal, 2021. **417**: p. 128109.
78. Lotfy, H.R. and H. Roubík, *Water purification using activated carbon prepared from agriculture waste — overview of a recent development.* Biomass Conversion and Biorefinery, 2023. **13**(17): p. 15577-15590.
79. Mohammad-Khah, A. and R. Ansari, *Activated charcoal: preparation, characterization and applications: a review article.* Int J Chem Tech Res, 2009. **1**(4): p. 859-864.
80. Montalvo, S., I. Cahn, R. Borja, C. Huiliñir, and L. Guerrero, *Use of solid residue from thermal power plant (fly ash) for enhancing sewage sludge anaerobic digestion: Influence of fly ash particle size.* Bioresource technology, 2017. **244**: p. 416-422.
81. Zhang, M., Y. Wangjin, H. Zhou, Z. Zhao, Z. Cao, and Z. Ying, *Fly ash and zero-valent iron-based in situ advanced anaerobic digestion with emphasis on the removal of antibiotics and antibiotic resistance genes from sewage sludge.* Waste Disposal & Sustainable Energy, 2022. **4**(1): p. 17-28.
82. Delihowski, J., P. Izak, Ł. Wójcik, M. Gajek, D. Kozień, and M. Jarosz, *Size fraction characterisation of highly-calcareous and siliceous fly ashes.* Journal of Thermal Analysis and Calorimetry, 2024. **149**(19): p. 10587-10603.
83. Zacco, A., L. Borgese, A. Gianoncelli, R.P.W.J. Struis, L.E. Depero, and E. Bontempi, *Review of fly ash inertisation treatments and recycling.* Environmental Chemistry Letters, 2014. **12**(1): p. 153-175.
84. Novais, R.M., T. Gameiro, J. Carvalheiras, M.P. Seabra, L.A. Tarelho, J.A. Labrincha, and I. Capela, *High pH buffer capacity biomass fly ash-based geopolymer spheres to boost methane yield in anaerobic digestion.* Journal of Cleaner Production, 2018. **178**: p. 258-267.

85. Woszuk, A., L. Bandura, and W. Franus, *Fly ash as low cost and environmentally friendly filler and its effect on the properties of mix asphalt.* Journal of Cleaner Production, 2019. **235**: p. 493-502.
86. Khanday, W.A. and B.H. Hameed, *Zeolite-hydroxyapatite-activated oil palm ash composite for antibiotic tetracycline adsorption.* Fuel, 2018. **215**: p. 499-505.
87. Ding, Y., Y. Liu, S. Liu, Z. Li, X. Tan, X. Huang, G. Zeng, L. Zhou, and B. Zheng, *Biochar to improve soil fertility. A review.* Agronomy for Sustainable Development, 2016. **36**(2): p. 36.
88. Thines, K.R., E.C. Abdullah, N.M. Mubarak, and M. Ruthiraan, *Synthesis of magnetic biochar from agricultural waste biomass to enhancing route for waste water and polymer application: A review.* Renewable and Sustainable Energy Reviews, 2017. **67**: p. 257-276.
89. Lee, J.E. and Y.-K. Park, *Applications of modified biochar-based materials for the removal of environment pollutants: A mini review.* Sustainability, 2020. **12**(15): p. 6112.
90. Ndoun, M.C., H.A. Elliott, H.E. Preisendanz, C.F. Williams, A. Knopf, and J.E. Watson, *Adsorption of pharmaceuticals from aqueous solutions using biochar derived from cotton gin waste and guayule bagasse.* Biochar, 2021. **3**(1): p. 89-104.
91. Boyd, C.E., *Further Studies on Productivity, Nutrient and Pigment Relationships in Typha latifolia Populations.* Bulletin of the Torrey Botanical Club, 1971. **98**(3): p. 144-150.
92. Klink, A., A. Macioł, M. Wisłocka, and J. Krawczyk, *Metal accumulation and distribution in the organs of Typha latifolia L.(cattail) and their potential use in bioindication.* Limnologica, 2013. **43**(3): p. 164-168.
93. Wang, M. and X. Liu, *Applications of red mud as an environmental remediation material: A review.* Journal of Hazardous Materials, 2021. **408**: p. 124420.
94. *Statista, 2023. Production of alumina worldwide in 2023, by country (in 1,000 metric tons). https://www.statista.com/statistics/264963/global-alumina-production-by-country/ (Accessed 24/02/2025).* 2023.
95. Khairul, M.A., J. Zanganeh, and B. Moghtaderi, *The composition, recycling and utilisation of Bayer red mud.* Resources, Conservation and Recycling, 2019. **141**: p. 483-498.
96. Liu, Y., C. Lin, and Y. Wu, *Characterization of red mud derived from a combined Bayer Process and bauxite calcination method.* Journal of Hazardous materials, 2007. **146**(1-2): p. 255-261.
97. Gelencsér, A., N. Kováts, B. Turóczi, Á. Rostási, A. Hoffer, K. Imre, I. Nyirő-Kósa, D. Csákberényi-Malasics, A.d.m. Tóth, and A.r. Czitrovszky, *The red mud accident in Ajka (Hungary): characterization and potential health effects of fugitive dust.* Environmental science & technology, 2011. **45**(4): p. 1608-1615.
98. Ma, Y., C. Si, and C. Lin, *Capping hazardous red mud using acidic soil with an embedded layer of zeolite for plant growth.* Environmental technology, 2014. **35**(18): p. 2314-2321.
99. Wang, S., H. Jin, Y. Deng, and Y. Xiao, *Comprehensive utilization status of red mud in China: A critical review.* Journal of Cleaner Production, 2021. **289**: p. 125136.
100. Evans, K., E. Nordheim, and K. Tsesmelis, *Bauxite Residue Management*, in *Light Metals 2012*, C.E. Suarez, Editor. 2016, Springer International Publishing: Cham. p. 63-66.
101. Holden, E., K. Linnerud, and D. Banister, *Sustainable development: Our common future revisited.* Global environmental change, 2014. **26**: p. 130-139.
102. Davris, P., E. Balomenos, D. Panias, and I. Paspaliaris, *Selective leaching of rare earth elements from bauxite residue (red mud), using a functionalized hydrophobic ionic liquid.* Hydrometallurgy, 2016. **164**: p. 125-135.
103. Liu, X. and N. Zhang, *Utilization of red mud in cement production: a review.* Waste management & research, 2011. **29**(10): p. 1053-1063.
104. Liu, S., X. Guan, S. Zhang, Z. Dou, C. Feng, H. Zhang, and S. Luo, *Sintered bayer red mud based ceramic bricks: microstructure evolution and alkalis immobilization mechanism.* Ceramics International, 2017. **43**(15): p. 13004-13008.

105. Rukhlyadeva, M., M. Belousov, E. Nikonenko, G. Ismagilova, and M. Kolesnikova, *Production of black iron oxide from red mud.* Russian Journal of Applied Chemistry, 2015. **88**(3): p. 377-381.
106. Reddy, N.G., K. Chandra, and B.H. Rao. *Assessment of industrial wastes as a road construction material: a review*. in *Proceedings of 1st International Conference on Recent Innovations in Engineering and Technology (ICREIAT-2016)*. 2016.
107. Panda, I., S. Jain, S.K. Das, and R. Jayabalan, *Characterization of red mud as a structural fill and embankment material using bioremediation.* International biodeterioration & biodegradation, 2017. **119**: p. 368-376.
108. Youssef, N., M. Shater, M. Abadir, and O. Ibrahim, *Utilization of red mud in the manufacture of ceramic tiles.* Key Engineering Materials, 2002. **206**.
109. Atan, E., M. Sutcu, and A.S. Cam, *Combined effects of bayer process bauxite waste (red mud) and agricultural waste on technological properties of fired clay bricks.* Journal of Building Engineering, 2021. **43**: p. 103194.
110. Paramguru, R., P. Rath, and V. Misra, *Trends in red mud utilization–a review.* Mineral Processing & Extractive Metall. Rev., 2004. **26**(1): p. 1-29.
111. Chao, X., T.-a. Zhang, G. Lyu, Z. Liang, and Y. Chen, *Sustainable application of sodium removal from red mud: Cleaner production of silicon-potassium compound fertilizer.* Journal of Cleaner Production, 2022. **352**: p. 131601.
112. Chen, J., Y. Wang, and Z. Liu, *Red mud-based catalysts for the catalytic removal of typical air pollutants: A review.* Journal of Environmental Sciences, 2023. **127**: p. 628-640.
113. Yang, W., A. Hussain, J. Zhang, and Y. Liu, *Removal of elemental mercury from flue gas using red mud impregnated by KBr and KI reagent.* Chemical Engineering Journal, 2018. **341**: p. 483-494.
114. Nadaroglu, H., E. Kalkan, and N. Demir, *Removal of copper from aqueous solution using red mud.* Desalination, 2010. **251**(1): p. 90-95.
115. Balarak, D., F.K. Mostafapour, and A. Joghataei, *Kinetics and mechanism of red mud in adsorption of ciprofloxacin in aqueous solution.* Bioscience biotechnology research communications, 2017. **10**(1): p. 243-250.
116. Poulin, É., J.-F. Blais, and G. Mercier, *Transformation of red mud from aluminium industry into a coagulant for wastewater treatment.* Hydrometallurgy, 2008. **92**(1): p. 16-25.
117. Oliveira, A., I. Teixeira, T. Christofani, J. Tristão, I. Guimarães, and F. Moura, *Biphasic oxidation reactions promoted by amphiphilic catalysts based on red mud residue.* Applied Catalysis B: Environmental, 2014. **144**: p. 144-151.
118. Matthaiou, V., Z. Frontistis, A. Petala, M. Solakidou, Y. Deligiannakis, G.N. Angelopoulos, and D. Mantzavinos, *Utilization of raw red mud as a source of iron activating the persulfate oxidation of paraben.* Process Safety and Environmental Protection, 2018. **119**: p. 311-319.
119. Shi, W., H. Ren, M. Li, K. Shu, Y. Xu, C. Yan, and Y. Tang, *Tetracycline removal from aqueous solution by visible-light-driven photocatalytic degradation with low cost red mud wastes.* Chemical Engineering Journal, 2020. **382**: p. 122876.
120. Mishra, S., R. Bal, and R.K. Dey, *Heterogeneous recyclable copper oxide supported on activated red mud as an efficient and stable catalyst for the one pot hydroxylation of benzene to phenol.* Molecular Catalysis, 2021. **499**: p. 111310.
121. Camilleri, M.A., *A Circular Economy Strategy for Sustainable Value Chains: A European Perspective*, in *Global Challenges to CSR and Sustainable Development: Root Causes and Evidence from Case Studies*, S. Vertigans and S.O. Idowu, Editors. 2021, Springer International Publishing: Cham. p. 141-161.
122. Allen, N.S., N. Mahdjoub, V. Vishnyakov, P.J. Kelly, and R.J. Kriek, *The effect of crystalline phase (anatase, brookite and rutile) and size on the photocatalytic activity of calcined polymorphic titanium dioxide (TiO2).* Polymer Degradation and Stability, 2018. **150**: p. 31-36.

123. Wang, Y., Y. He, Q. Lai, and M. Fan, *Review of the progress in preparing nano TiO2: An important environmental engineering material.* Journal of Environmental Sciences, 2014. **26**(11): p. 2139-2177.
124. Kim, D.S., S.J. Han, and S.-Y. Kwak, *Synthesis and photocatalytic activity of mesoporous TiO2 with the surface area, crystallite size, and pore size.* Journal of Colloid and Interface Science, 2007. **316**(1): p. 85-91.
125. Fujishima, A. and K. Honda, *Electrochemical Photolysis of Water at a Semiconductor Electrode.* Nature, 1972. **238**(5358): p. 37-38.
126. Sujatha, G., S. Shanthakumar, and F. Chiampo, *UV Light-Irradiated Photocatalytic Degradation of Coffee Processing Wastewater Using TiO2 as a Catalyst.* Environments, 2020. **7**(6): p. 47.
127. Pelaez, M., N.T. Nolan, S.C. Pillai, M.K. Seery, P. Falaras, A.G. Kontos, P.S.M. Dunlop, J.W.J. Hamilton, J.A. Byrne, K. O'Shea, M.H. Entezari, and D.D. Dionysiou, *A review on the visible light active titanium dioxide photocatalysts for environmental applications.* Applied Catalysis B: Environmental, 2012. **125**: p. 331-349.
128. Gan, Y., M. Zhang, J. Xiong, J. Zhu, W. Li, C. Zhang, and G. Cheng, *Impact of Cu particles on adsorption and photocatalytic capability of mesoporous Cu@TiO2 hybrid towards ciprofloxacin antibiotic removal.* Journal of the Taiwan Institute of Chemical Engineers, 2019. **96**: p. 229-242.
129. Sanguanpak, S., W. Shongkittikul, C. Saengam, W. Chiemchaisri, and C. Chiemchaisri, *TiO2-immobilized porous geopolymer composite membrane for removal of antibiotics in hospital wastewater.* Chemosphere, 2022. **307**: p. 135760.
130. Lin, H., L. Li, M. Zhao, X. Huang, X. Chen, G. Li, and R. Yu, *Synthesis of High-Quality Brookite TiO2 Single-Crystalline Nanosheets with Specific Facets Exposed: Tuning Catalysts from Inert to Highly Reactive.* Journal of the American Chemical Society, 2012. **134**(20): p. 8328-8331.
131. Etacheri, V., C. Di Valentin, J. Schneider, D. Bahnemann, and S.C. Pillai, *Visible-light activation of TiO2 photocatalysts: Advances in theory and experiments.* Journal of Photochemistry and Photobiology C: Photochemistry Reviews, 2015. **25**: p. 1-29.
132. Macwan, D.P., P.N. Dave, and S. Chaturvedi, *A review on nano-TiO2 sol–gel type syntheses and its applications.* Journal of Materials Science, 2011. **46**(11): p. 3669-3686.
133. Chen, C., W. Cai, M. Long, J. Zhang, B. Zhou, Y. Wu, and D. Wu, *Template-free sol–gel preparation and characterization of free-standing visible light responsive C,N-modified porous monolithic TiO2.* Journal of Hazardous Materials, 2010. **178**(1): p. 560-565.
134. Lee, S., I.-S. Cho, J.H. Lee, D.H. Kim, D.W. Kim, J.Y. Kim, H. Shin, J.-K. Lee, H.S. Jung, N.-G. Park, K. Kim, M.J. Ko, and K.S. Hong, *Two-Step Sol–Gel Method-Based TiO2 Nanoparticles with Uniform Morphology and Size for Efficient Photo-Energy Conversion Devices.* Chemistry of Materials, 2010. **22**(6): p. 1958-1965.
135. Chen, Z., G. Zhao, H. Li, G. Han, and B. Song, *Effects of Water Amount and pH on the Crystal Behavior of a TiO2 Nanocrystalline Derived from a Sol–Gel Process at a Low Temperature.* Journal of the American Ceramic Society, 2009. **92**(5): p. 1024-1029.
136. Byrappa, K. and T. Adschiri, *Hydrothermal technology for nanotechnology.* Progress in Crystal Growth and Characterization of Materials, 2007. **53**(2): p. 117-166.
137. Du, J., W. Chen, C. Zhang, Y. Liu, C. Zhao, and Y. Dai, *Hydrothermal synthesis of porous TiO2 microspheres and their photocatalytic degradation of gaseous benzene.* Chemical Engineering Journal, 2011. **170**(1): p. 53-58.
138. Wender, H., A.F. Feil, L.B. Diaz, C.S. Ribeiro, G.J. Machado, P. Migowski, D.E. Weibel, J. Dupont, and S.R. Teixeira, *Self-Organized TiO2 Nanotube Arrays: Synthesis by Anodization in an Ionic Liquid and Assessment of Photocatalytic Properties.* ACS Applied Materials & Interfaces, 2011. **3**(4): p. 1359-1365.

139. Wilson, G.J., G.D. Will, R.L. Frost, and S.A.J.J.o.M.C. Montgomery, *Efficient microwave hydrothermal preparation of nanocrystalline anatase TiO 2 colloids.* 2002. **12**(6): p. 1787-1791.
140. Wu, J.-M., T.-W. Zhang, Y.-W. Zeng, S. Hayakawa, K. Tsuru, and A. Osaka, *Large-Scale Preparation of Ordered Titania Nanorods with Enhanced Photocatalytic Activity.* Langmuir, 2005. **21**(15): p. 6995-7002.
141. Agatzini-Leonardou, S., P. Oustadakis, P.E. Tsakiridis, and C. Markopoulos, *Titanium leaching from red mud by diluted sulfuric acid at atmospheric pressure.* Journal of Hazardous Materials, 2008. **157**(2): p. 579-586.
142. Ujaczki, É., V. Feigl, M. Molnár, P. Cusack, T. Curtin, R. Courtney, L. O'Donoghue, P. Davris, C. Hugi, M.W.H. Evangelou, E. Balomenos, and M. Lenz, *Re-using bauxite residues: benefits beyond (critical raw) material recovery.* Journal of Chemical Technology & Biotechnology, 2018. **93**(9): p. 2498-2510.
143. Pasechnik, L.A., V.M. Skachkov, E.A. Bogdanova, A.Y. Chufarov, D.G. Kellerman, I.S. Medyankina, and S.P. Yatsenko, *A promising process for transformation of hematite to magnetite with simultaneous dissolution of alumina from red mud in alkaline medium.* Hydrometallurgy, 2020. **196**: p. 105438.
144. Schwertmann, U. and R.M. Cornell, *Iron oxides in the laboratory: preparation and characterization*. 2008: John Wiley & Sons.
145. Banerjee, S.K. and B.M. Moskowitz, *Ferrimagnetic Properties of Magnetite*, in *Magnetite Biomineralization and Magnetoreception in Organisms: A New Biomagnetism*, J.L. Kirschvink, D.S. Jones, and B.J. MacFadden, Editors. 1985, Springer US: Boston, MA. p. 17-41.
146. Wu, W., Z. Wu, T. Yu, C. Jiang, W.-S.J.S. Kim, and t.o.a. materials, *Recent progress on magnetic iron oxide nanoparticles: synthesis, surface functional strategies and biomedical applications.* 2015. **16**(2): p. 023501.
147. Bassal, F., J. Roques, and C. Gautheron, *Neon diffusion in goethite, α-FeO(OH): a theoretical multi-scale study.* Physics and Chemistry of Minerals, 2020. **47**(3): p. 14.
148. Taran, M.N., *Is the mean value of the 3d-electron radius in the equation of the crystal-field theory constant?* Physics and Chemistry of Minerals, 2021. **48**(3): p. 13.
149. Cook, W.G. and R.P. Olive, *Pourbaix diagrams for the iron–water system extended to high-subcritical and low-supercritical conditions.* Corrosion Science, 2012. **55**: p. 326-331.
150. Beverskog, B. and I. Puigdomenech, *Revised pourbaix diagrams for iron at 25–300 °C.* Corrosion Science, 1996. **38**(12): p. 2121-2135.
151. McCafferty, E., *Thermodynamics of Corrosion: Pourbaix Diagrams*, in *Introduction to Corrosion Science*, E. McCafferty, Editor. 2010, Springer New York: New York, NY. p. 95-117.
152. Drummond, A., *A study of iron-oxidising bacteria, their habitats and their associated biogenic iron ochre, sampled from the Greater Glasgow area*. 2023, University of Glasgow.
153. Kong, H., T. Zhou, X. Yang, Y. Gong, M. Zhang, and H. Yang, *Iron Recovery Technology of Red Mud—A review.* Energies, 2022. **15**(10): p. 3830.
154. Li, Y., J. Wang, X. Wang, B. Wang, and Z. Luan, *Feasibility study of iron mineral separation from red mud by high gradient superconducting magnetic separation.* Physica C: Superconductivity, 2011. **471**(3): p. 91-96.
155. Huang, Y., G. Han, J. Liu, and W. Wang, *A facile disposal of Bayer red mud based on selective flocculation desliming with organic humics.* Journal of Hazardous Materials, 2016. **301**: p. 46-55.
156. Drzymala, J. and D.W. Fuerstenau, *Selective flocculation of hematite in quartz–hematite–ferric ion–polyacrylic acid system. Part 2. Effect of grinding and a hydrofluoric treatment on selectivity of flocculation.* International Journal of Mineral Processing, 2014. **129**: p. 1-5.

157. Panda, L., P.K. Banerjee, S.K. Biswal, R. Venugopal, and N.R. Mandre, *Performance evaluation for selectivity of the flocculant on hematite in selective flocculation.* International Journal of Minerals, Metallurgy, and Materials, 2013. **20**(12): p. 1123-1129.
158. Tanvar, H. and B. Mishra, *Hydrometallurgical recycling of red mud to produce materials for industrial applications: Alkali separation, iron leaching and extraction.* Metallurgical and Materials Transactions B, 2021. **52**(5): p. 3543-3557.
159. Liu, Z. and H. Li, *Metallurgical process for valuable elements recovery from red mud—A review.* Hydrometallurgy, 2015. **155**: p. 29-43.
160. Nath, H., P. Sahoo, and A. Sahoo, *Characterization of Red Mud treated under high temperature fluidization.* Powder Technology, 2015. **269**: p. 233-239.
161. Jayasankar, K., P. Ray, A. Chaubey, A. Padhi, B. Satapathy, and P. Mukherjee, *Production of pig iron from red mud waste fines using thermal plasma technology.* International Journal of Minerals, Metallurgy, and Materials, 2012. **19**(8): p. 679-684.
162. Agrawal, S., V. Rayapudi, and N. Dhawan, *Comparison of microwave and conventional carbothermal reduction of red mud for recovery of iron values.* Minerals Engineering, 2019. **132**: p. 202-210.
163. Maihatchi Ahamed, A., M.-N. Pons, Q. Ricoux, F. Goettmann, and F. Lapicque, *Production of electrolytic iron from red mud in alkaline media.* Journal of Environmental Management, 2020. **266**: p. 110547.
164. Vakilchap, F., S.M. Mousavi, and S.A. Shojaosadati, *Role of Aspergillus niger in recovery enhancement of valuable metals from produced red mud in Bayer process.* Bioresource Technology, 2016. **218**: p. 991-998.
165. Wan, H., L. Hu, X. Liu, Y. Zhang, G. Chen, N. Zhang, and R. Ma, *Advanced hematite nanomaterials for newly emerging applications.* Chemical Science, 2023. **14**(11): p. 2776-2798.
166. Cornell, R.M. and U. Schwertmann, *The iron oxides: structure, properties, reactions, occurrences, and uses*. Vol. 664. 2003: Wiley-vch Weinheim.
167. Zhang, Z., C. Boxall, and G. Kelsall, *Photoelectrophoresis of colloidal iron oxides 1. Hematite (α-Fe2O3)*, in *Colloids in the Aquatic Environment*. 1993, Elsevier. p. 145-163.
168. Al-Hakkani, M.F., G.A. Gouda, and S.H.A. Hassan, *A review of green methods for phyto-fabrication of hematite (α-Fe2O3) nanoparticles and their characterization, properties, and applications.* Heliyon, 2021. **7**(1): p. e05806.
169. Sivula, K., F. Le Formal, and M. Grätzel, *Solar Water Splitting: Progress Using Hematite (α-Fe2O3) Photoelectrodes.* ChemSusChem, 2011. **4**(4): p. 432-449.
170. Sable, H., V. Kumar, V. Singh, S. Rustagi, S. Chahal, and V. Chaudhary, *Strategically engineering advanced nanomaterials for heavy-metal remediation from wastewater.* Coordination Chemistry Reviews, 2024. **518**: p. 216079.
171. Lu, H., J. Wang, M. Stoller, T. Wang, Y. Bao, and H. Hao, *An Overview of Nanomaterials for Water and Wastewater Treatment.* Advances in Materials Science and Engineering, 2016. **2016**(1): p. 4964828.
172. Aquino, C.L.E., M.J.C. Bongar, A.B. Silvestre, and M.D.L. Balela, *Synthesis of Hematite (α-Fe2O3) Nanostructures by Thermal Oxidation of Iron Sheet for Cr (VI) Adsorption.* Key Engineering Materials, 2018. **775**: p. 395-401.
173. Gunawardhana, B., C. Gunathilake, K. Dayananda, D. Dissanayake, M. Mantilaka, C. Kalpage, R. Rathnayake, R. Rajapakse, A. Manchanda, and T.N. Etampawala, *Synthesis of Hematite Nanodiscs from Natural Laterites and Investigating Their Adsorption Capability of Removing Ni2+ and Cd2+ Ions from Aqueous Solutions.* Journal of Composites Science, 2020. **4**(2): p. 57.
174. Yang, X., X. Zhang, Z. Wang, S. Li, J. Zhao, G. Liang, and X. Xie, *Mechanistic insights into removal of norfloxacin from water using different natural iron ore – biochar composites: more*

rich free radicals derived from natural pyrite-biochar composites than hematite-biochar composites. Applied Catalysis B: Environmental, 2019. **255**: p. 117752.
175. Chen, L., S. Yang, Y. Huang, B. Zhang, F. Kang, D. Ding, and T. Cai, *Degradation of antibiotics in multi-component systems with novel ternary AgBr/Ag3PO4@natural hematite heterojunction photocatalyst under simulated solar light.* Journal of Hazardous Materials, 2019. **371**: p. 566-575.
176. Kaur, A., W.A. Anderson, S. Tanvir, and S.K. Kansal, *Solar light active silver/iron oxide/zinc oxide heterostructure for photodegradation of ciprofloxacin, transformation products and antibacterial activity.* Journal of colloid and interface science, 2019. **557**: p. 236-253.
177. Du, Y., Z. Tao, J. Guan, Z. Sun, W. Zeng, P. Wen, K. Ni, J. Ye, S. Yang, and P. Du, *Microwave-assisted synthesis of hematite/activated graphene composites with superior performance for photocatalytic reduction of Cr (VI).* RSC advances, 2015. **5**(99): p. 81438-81444.
178. Zhu, Y., S. Murali, W. Cai, X. Li, J.W. Suk, J.R. Potts, and R.S. Ruoff, *Graphene and Graphene Oxide: Synthesis, Properties, and Applications.* Advanced Materials, 2010. **22**(35): p. 3906-3924.
179. Nanda, B., B.B. Mishra, R. Nayak, and N. Devi, *Hydrometallurgical recovery of α-Fe2O3 from red mud and photo-Fenton degradation of organic dye using CuO promoted α-Fe2O3.* Indian Chemical Engineer, 2022. **64**(1): p. 68-79.
180. Hashimoto, H., S. Yokoyama, H. Asaoka, Y. Kusano, Y. Ikeda, M. Seno, J. Takada, T. Fujii, M. Nakanishi, and R. Murakami, *Characteristics of hollow microtubes consisting of amorphous iron oxide nanoparticles produced by iron oxidizing bacteria, Leptothrix ochracea.* Journal of Magnetism and Magnetic Materials, 2007. **310**(2, Part 3): p. 2405-2407.
181. Johannessen, K.C., N. McLoughlin, P.E. Vullum, and I.H. Thorseth, *On the biogenicity of Fe-oxyhydroxide filaments in silicified low-temperature hydrothermal deposits: Implications for the identification of Fe-oxidizing bacteria in the rock record.* Geobiology, 2020. **18**(1): p. 31-53.
182. Ema, T., Y. Miyazaki, I. Kozuki, T. Sakai, H. Hashimoto, and J. Takada, *Highly active lipase immobilized on biogenous iron oxide via an organic bridging group: the dramatic effect of the immobilization support on enzymatic function.* Green chemistry, 2011. **13**(11): p. 3187-3195.
183. Eggerichs, T., T. Otte, O. Opel, and W.K.L. Ruck, *Direct and Mn-Controlled Indirect Iron Oxidation by Leptothrix discophora SS-1 and Leptothrix cholodnii.* Geomicrobiology Journal, 2015. **32**(10): p. 934-943.
184. Alharthi, A., R.A. Blackley, T.H. Flowers, J.S.J. Hargreaves, I.D. Pulford, J. Wigzell, and W. Zhou, *Iron ochre – a pre-catalyst for the cracking of methane.* Journal of Chemical Technology & Biotechnology, 2014. **89**(9): p. 1317-1323.
185. Shopska, M., D. Paneva, G. Kadinov, S. Todorova, M. Fabián, I. Yordanova, Z. Cherkezova-Zheleva, and I. Mitov, *Composition and catalytic behavior in CO oxidation of biogenic iron-containing materials.* Reaction Kinetics, Mechanisms and Catalysis, 2016. **118**(1): p. 179-198.
186. Mandai, K., T. Korenaga, T. Ema, T. Sakai, M. Furutani, H. Hashimoto, and J. Takada, *Biogenous iron oxide-immobilized palladium catalyst for the solvent-free Suzuki–Miyaura coupling reaction.* Tetrahedron Letters, 2012. **53**(3): p. 329-332.
187. Rentz, J.A., *Phosphorus Removal Potential Using Biogenic Iron Oxides*. 2011, IWA Publishing.
188. Ferris, F.G., R.O. Hallberg, B. Lyvén, and K. Pedersen, *Retention of strontium, cesium, lead and uranium by bacterial iron oxides from a subterranean environment.* Applied Geochemistry, 2000. **15**(7): p. 1035-1042.
189. Sowers, T.D., K.L. Holden, E.K. Coward, and D.L. Sparks, *Dissolved Organic Matter Sorption and Molecular Fractionation by Naturally Occurring Bacteriogenic Iron (Oxyhydr)oxides.* Environmental Science & Technology, 2019. **53**(8): p. 4295-4304.
190. Rico, J.L. and J.S.J. Hargreaves, *Synthesis and characterization of iron and iron nitride microtubes obtained from biogenic iron oxide.* Journal of Materials Science, 2017. **52**(9): p. 5188-5193.

191. Michalsky, R. and P.H. Pfromm, *An Ionicity Rationale to Design Solid phase Metal Nitride Reactants for Solar Ammonia Production.* The Journal of Physical Chemistry C, 2012. **116**(44): p. 23243-23251.
192. Friedrich, B., D. Hoffmann, and J. James, *One Hundred Years of the Fritz Haber Institute.* Angewandte Chemie International Edition, 2011. **50**(43): p. 10022-10049.
193. Pool, J.A., E. Lobkovsky, and P.J. Chirik, *Hydrogenation and cleavage of dinitrogen to ammonia with a zirconium complex.* Nature, 2004. **427**(6974): p. 527-530.
194. Moghadam, M.R., A. Bazmandegan-Shamili, and H. Bagheri, *Chapter one - The current methods of ammonia synthesis by Haber-Bosch process*, in *Progresses in Ammonia: Science, Technology and Membranes*, A. Basile and M.R. Rahimpour, Editors. 2024, Elsevier. p. 1-32.
195. Yang, J. and X. Luo, *Ag-doped TiO2 immobilized cellulose-derived carbon beads: One-Pot preparation, photocatalytic degradation performance and mechanism of ceftriaxone sodium.* Applied Surface Science, 2021. **542**: p. 148724.
196. Grauso, L., M. Zotti, W. Sun, B. de Falco, V. Lanzotti, and G. Bonanomi, *Spectroscopic and multivariate data-based method to assess the metabolomic fingerprint of Mediterranean plants.* Phytochemical Analysis, 2019. **30**(5): p. 572-581.
197. Williams, C.A., J.B. Harborne, and H.T. Clifford, *Flavonoid patterns in the monocotyledons. Flavonols and flavones in some families associated with the Poaceae.* Phytochemistry, 1971. **10**(5): p. 1059-1063.
198. Naz, S., M. Islam, S. Tabassum, N.F. Fernandes, E.J. Carcache de Blanco, and M. Zia, *Green synthesis of hematite (α-Fe2O3) nanoparticles using Rhus punjabensis extract and their biomedical prospect in pathogenic diseases and cancer.* Journal of Molecular Structure, 2019. **1185**: p. 1-7.
199. Raghavan, P.K.N., N.K. Kshatriya, and K. Wawrynink, *Recovery of Metal Values from Red Mud*, in *Light Metals 2011*, S.J. Lindsay, Editor. 2016, Springer International Publishing: Cham. p. 103-106.
200. Li, G., M. Liu, M. Rao, T. Jiang, J. Zhuang, and Y. Zhang, *Stepwise extraction of valuable components from red mud based on reductive roasting with sodium salts.* Journal of Hazardous Materials, 2014. **280**: p. 774-780.
201. Agrawal, S. and N. Dhawan, *Microwave acid baking of red mud for extraction of titanium and scandium values.* Hydrometallurgy, 2021. **204**: p. 105704.
202. Hosny, M. and J.S.J. Hargreaves, *Towards sustainable environmental remediation: Ceftriaxone adsorption by titania derived from red mud.* Catalysis Today, 2024. **430**: p. 114539.
203. Agrawal, S. and N. Dhawan, *Evaluation of red mud as a polymetallic source – A review.* Minerals Engineering, 2021. **171**: p. 107084.
204. Gu, H., J.S.J. Hargreaves, A.R. McFarlane, and G. MacKinnon, *The carbon deposits formed by reaction of a series of red mud samples with methanol.* RSC advances, 2016. **6**(52): p. 46421-46426.
205. Gu, H., J.S.J. Hargreaves, J.Q. Jiang, and J.L. Rico, *Potential Routes to Obtain Value-Added Iron-Containing Compounds from Red Mud.* Journal of Sustainable Metallurgy, 2017. **3**(3): p. 561-569.
206. Lee, W.C., S.-O. Kim, J. Ranville, S.-T. Yun, and S.H. Choi, *Sequestration of arsenate from aqueous solution using 2-line ferrihydrite: equilibria, kinetics, and X-ray absorption spectroscopic analysis.* Environmental Earth Sciences, 2014. **71**(8): p. 3307-3318.
207. Daisley, A., *The role of composition on the ammonia synthesis activity of nitrides, carbonitrides, carbides and osmium based compounds*. 2020, University of Glasgow.
208. Mckay, D., *Catalysis over molybdenum containing nitride materials*. 2008, University of Glasgow.

209. Nayfeh, M.H. and A. Nayfeh, *Chapter 13 - Hydrogen fuel generation: Interaction of silicon-based grains with metal ions*, in *Integrated Silicon-Metal Systems At the Nanoscale*, M.H. Nayfeh and A. Nayfeh, Editors. 2023, Elsevier. p. 345-367.
210. Organization, W.H., *Guidelines for drinking-water quality: incorporating the first and second addenda*. Fourth edition incorporating the first and second addenda ed. 2022: World Health Organization.
211. Neal, C., M. Neal, B. Reynolds, S.C. Maberly, L. May, R.C. Ferrier, J. Smith, and J.E. Parker, *Silicon concentrations in UK surface waters.* Journal of Hydrology, 2005. **304**(1): p. 75-93.
212. Zhong, S.-F., B. Yang, Q. Xiong, W.-W. Cai, Z.-G. Lan, and G.-G. Ying, *Hydrolytic transformation mechanism of tetracycline antibiotics: Reaction kinetics, products identification and determination in WWTPs.* Ecotoxicology and Environmental Safety, 2022. **229**: p. 113063.
213. Mahmood, T., M.T. Saddique, A. Naeem, P. Westerhoff, S. Mustafa, and A. Alum, *Comparison of different methods for the point of zero charge determination of NiO.* Industrial & Engineering Chemistry Research, 2011. **50**(17): p. 10017-10023.
214. Ayoup, M.S., A.S. Eltaweil, A.M. Omer, and E.M. Abd El-Monaem, *Zwitterionic MOF-embedded alginate beads with polydopamine surface functionalization for efficient doxycycline removal: Optimization and mechanistic study.* International Journal of Biological Macromolecules, 2024. **281**: p. 136288.
215. Yu, K., N. Kumar, A. Aho, J. Roine, I. Heinmaa, D.Y. Murzin, and A. Ivaska, *Determination of acid sites in porous aluminosilicate solid catalysts for aqueous phase reactions using potentiometric titration method.* Journal of Catalysis, 2016. **335**: p. 117-124.
216. Cataldo, D.A., M. Maroon, L.E. Schrader, and V.L. Youngs, *Rapid colorimetric determination of nitrate in plant tissue by nitration of salicylic acid.* Communications in Soil Science and Plant Analysis, 1975. **6**(1): p. 71-80.
217. Kolmert, Å., P. Wikström, and K.B. Hallberg, *A fast and simple turbidimetric method for the determination of sulfate in sulfate-reducing bacterial cultures.* Journal of Microbiological Methods, 2000. **41**(3): p. 179-184.
218. Filgueiras, M.F., P.C. de Jesus, and E.M. Borges, *Quantification of Nitrite in Food and Water Samples Using the Griess Assay and Digital Images Acquired Using a Desktop Scanner.* Journal of Chemical Education, 2021. **98**(10): p. 3303-3311.
219. Owens, H.M. and A.K. Dash, *Ceftriaxone Sodium: Comprehensive Profile*, in *Profiles of Drug Substances, Excipients and Related Methodology*, H.G. Brittain, Editor. 2003, Academic Press. p. 21-57.
220. Duncan, C.J.A., D.A. Barr, and R.A. Seaton, *Outpatient parenteral antimicrobial therapy with ceftriaxone, a review.* International Journal of Clinical Pharmacy, 2012. **34**(3): p. 410-417.
221. Newton, G.G.F. and E.P. Abraham, *Cephalosporin C, a New Antibiotic containing Sulphur and D-α-Aminoadipic Acid.* Nature, 1955. **175**(4456): p. 548-548.
222. Neu, H.C., N.J. Meropol, and K.P. Fu, *Antibacterial activity of ceftriaxone (Ro 13-9904), a beta-lactamase-stable cephalosporin.* Antimicrobial Agents and Chemotherapy, 1981. **19**(3): p. 414-423.
223. Abbasi, S., *Photocatalytic activity study of coated anatase-rutile titania nanoparticles with nanocrystalline tin dioxide based on the statistical analysis.* Environmental monitoring and assessment, 2019. **191**(4): p. 206.
224. Weng, W., M. Ma, P. Du, G. Zhao, G. Shen, J. Wang, and G. Han, *Superhydrophilic Fe doped titanium dioxide thin films prepared by a spray pyrolysis deposition.* Surface and Coatings Technology, 2005. **198**(1-3): p. 340-344.
225. Hargreaves, J.S.J., *Some considerations related to the use of the Scherrer equation in powder X-ray diffraction as applied to heterogeneous catalysts.* Catalysis, Structure & Reactivity, 2016. **2**(1-4): p. 33-37.

226. Gu, H., N. Wang, and J.S.J. Hargreaves, *Sequential Extraction of Valuable Trace Elements from Bayer Process-Derived Waste Red Mud Samples.* Journal of Sustainable Metallurgy, 2018. **4**(1): p. 147-154.
227. Hanaor, D.A.H. and C.C. Sorrell, *Review of the anatase to rutile phase transformation.* Journal of Materials Science, 2011. **46**(4): p. 855-874.
228. Güner, E.K. and A.K. Özer, *Synthesis and characterization of copper hydroxynitrate by hydrothermal method.* Journal of the Turkish Chemical Society Section B: Chemical Engineering, 2017. **1**(1): p. 183-192.
229. Hamzah, H.T., V. Sridevi, D.V. Surya, S. Palla, A. Yadav, and P.V. Rao, *Conventional and microwave-assisted acid pretreatment of tea waste powder: analysis of functional groups using FTIR.* Environmental Science and Pollution Research, 2024. **31**(46): p. 57523-57532.
230. Hu, K. and H. Mischo, *High-Pressure Methane Adsorption and Desorption in Shales from the Sichuan Basin, Southwestern China.* Energy & Fuels, 2020. **34**(3): p. 2945-2957.
231. Mogal, S.I., V.G. Gandhi, M. Mishra, S. Tripathi, T. Shripathi, P.A. Joshi, and D.O. Shah, *Single-Step Synthesis of Silver-Doped Titanium Dioxide: Influence of Silver on Structural, Textural, and Photocatalytic Properties.* Industrial & Engineering Chemistry Research, 2014. **53**(14): p. 5749-5758.
232. Tiwari, V., J. Jiang, V. Sethi, and P. Biswas, *One-step synthesis of noble metal–titanium dioxide nanocomposites in a flame aerosol reactor.* Applied Catalysis A: General, 2008. **345**(2): p. 241-246.
233. Di Paola, A., G. Marci, L. Palmisano, M. Schiavello, K. Uosaki, S. Ikeda, and B. Ohtani, *Preparation of polycrystalline TiO2 photocatalysts impregnated with various transition metal ions: characterization and photocatalytic activity for the degradation of 4-nitrophenol.* The Journal of Physical Chemistry B, 2002. **106**(3): p. 637-645.
234. Abdelouahab Reddam, H., R. Elmail, S.C. Lloria, G. Monrós Tomás, Z.A. Reddam, and F. Coloma-Pascual, *Synthesis of Fe, Mn and Cu modified TiO2 photocatalysts for photodegradation of Orange II.* Boletín de la Sociedad Española de Cerámica y Vidrio, 2020. **59**(4): p. 138-148.
235. Grover, I.S., S. Singh, and B. Pal, *The preparation, surface structure, zeta potential, surface charge density and photocatalytic activity of TiO2 nanostructures of different shapes.* Applied Surface Science, 2013. **280**: p. 366-372.
236. Abramović, B.F., M.M. Uzelac, and N.L. Finčur, *Photocatalytic degradation of thiotriazinone, stable hydrolysis product of antibiotic ceftriaxone.* Acta Periodica Technologica, 2019(50): p. 1-11.
237. Abramović, B.F., M.M. Uzelac, S.J. Armaković, U. Gašić, D.D. Četojević-Simin, and S. Armaković, *Experimental and computational study of hydrolysis and photolysis of antibiotic ceftriaxone: Degradation kinetics, pathways, and toxicity.* Science of The Total Environment, 2021. **768**: p. 144991.
238. Qi, S., X. Chong, S. Yao, B. Ning, and C. Hu, *Research on storage stability differences between ceftriaxone sodium products.* Scientific Reports, 2023. **13**(1): p. 20996.
239. Barrett, A.G.M., M.J. Betts, and A. Fenwick, *Acyl and sulfonyl isocyanates in .beta.-lactam synthesis.* The Journal of Organic Chemistry, 1985. **50**(2): p. 169-175.
240. Masoud, M.S., A.E. Ali, and G.S. Elasala, *Synthesis, spectral, computational and thermal analysis studies of metalloceftriaxone antibiotic.* Journal of Molecular Structure, 2015. **1084**: p. 259-273.
241. Zhao, Y., X. Liang, Y. Wang, H. Shi, E. Liu, J. Fan, and X. Hu, *Degradation and removal of Ceftriaxone sodium in aquatic environment with Bi2WO6/g-C3N4 photocatalyst.* Journal of Colloid and Interface Science, 2018. **523**: p. 7-17.

242. Chen, J., J. Wan, C. Li, Y. Wei, and H. Shi, *Synthesis of novel Fe0-Fe3O4/CeO2/C composite cathode for efficient heterogeneous electro-Fenton degradation of ceftriaxone sodium.* Journal of Hazardous Materials, 2022. **437**: p. 129393.
243. Zhao, Y., Y. Wang, E. Liu, J. Fan, and X. Hu, *Bi2WO6 nanoflowers: An efficient visible light photocatalytic activity for ceftriaxone sodium degradation.* Applied Surface Science, 2018. **436**: p. 854-864.
244. Heizer, W.D., R.S. Sandler, E. Seal, S.C. Murray, M.G. Busby, B.G. Schliebe, and S.N. Pusek, *Intestinal Effects of Sulfate in Drinking Water on Normal Human Subjects.* Digestive Diseases and Sciences, 1997. **42**(5): p. 1055-1061.
245. Chen, J., P. Sun, X. Zhou, Y. Zhang, and C.-H. Huang, *Cu(II)–Catalyzed Transformation of Benzylpenicillin Revisited: The Overlooked Oxidation.* Environmental Science & Technology, 2015. **49**(7): p. 4218-4225.
246. Shrestha, B., N.R. Bhuyan, and B.N. Sinha, *Development and validation of a stability indicating HPLC method for estimation of ceftriaxone in sterile powder for injection without using ion pairing reagent.* International Journal of Pharmacy and Pharmaceutical Sciences, 2013. **5**(3): p. 948-52.
247. Aleksić, M., V. Savić, G. Popović, N. Burić, and V. Kapetanović, *Acidity constants of cefetamet, cefotaxime and ceftriaxone; the effect of the substituent at C3 position.* Journal of Pharmaceutical and Biomedical Analysis, 2005. **39**(3): p. 752-756.
248. Zaki, N.M. and M.M. Hafez, *Enhanced antibacterial effect of ceftriaxone sodium-loaded chitosan nanoparticles against intracellular Salmonella typhimurium.* Aaps Pharmscitech, 2012. **13**: p. 411-421.
249. Fan, H.-J., S.-T. Huang, W.-H. Chung, J.-L. Jan, W.-Y. Lin, and C.-C. Chen, *Degradation pathways of crystal violet by Fenton and Fenton-like systems: Condition optimization and intermediate separation and identification.* Journal of Hazardous Materials, 2009. **171**(1): p. 1032-1044.
250. Abdullah, M., J. Iqbal, M.S. Ur Rehman, U. Khalid, F. Mateen, S.N. Arshad, A.G. Al-Sehemi, H. Algarni, O.A. Al-Hartomy, and T. Fazal, *Removal of ceftriaxone sodium antibiotic from pharmaceutical wastewater using an activated carbon based TiO2 composite: Adsorption and photocatalytic degradation evaluation.* Chemosphere, 2023. **317**: p. 137834.
251. Dávila-Estrada, M., J.J. Ramírez-García, M.J. Solache-Ríos, and J.L. Gallegos-Pérez, *Kinetic and equilibrium sorption studies of ceftriaxone and paracetamol by surfactant-modified zeolite.* Water, Air, & Soil Pollution, 2018. **229**: p. 1-9.
252. Olusegun, S.J., N.D. Mohallem, and V.S. Ciminelli, *Reducing the negative impact of ceftriaxone and doxycycline in aqueous solutions using ferrihydrite/plant-based composites: mechanism pathway.* Environmental Science and Pollution Research, 2022. **29**(44): p. 66547-66561.
253. Mahmoud, M.E., A.M. El-Ghanam, R.H.A. Mohamed, and S.R. Saad, *Enhanced adsorption of Levofloxacin and Ceftriaxone antibiotics from water by assembled composite of nanotitanium oxide/chitosan/nano-bentonite.* Materials Science and Engineering: C, 2020. **108**: p. 110199.
254. Lykhin, A.O., G.V. Novikova, A.A. Kuzubov, N.A. Staloverova, N.I. Sarmatova, S.A. Varganov, and P.O. Krasnov, *A complex of ceftriaxone with Pb(II): synthesis, characterization, and antibacterial activity study.* Journal of Coordination Chemistry, 2014. **67**(16): p. 2783-2794.
255. AbouElleef, E.M., M.M. Mahrouka, and S.E. Salem, *A Physical-Chemical Study of the Interference of Ceftriaxone Antibiotic with Copper Chloride Salt.* Bioinorganic Chemistry and Applications, 2021. **2021**(1): p. 4018843.
256. Refat, M.S., T. Altalhi, H. Fetooh, A.M. Alsuhaibani, and R.F. Hassan, *In neutralized medium five new Ca(II), Zn(II), Fe(III), Au(III) and Pd(II) complexity of ceftriaxone antibiotic drug: Synthesis, spectroscopic, morphological and anticancer studies.* Journal of Molecular Liquids, 2021. **322**: p. 114816.
257. Zhou, J.L., *Sorption and Remobilization Behavior of 4-tert-Octylphenol in Aquatic Systems.* Environmental Science & Technology, 2006. **40**(7): p. 2225-2234.

258. Chao, Y., W. Zhu, X. Wu, F. Hou, S. Xun, P. Wu, H. Ji, H. Xu, and H. Li, *Application of graphene-like layered molybdenum disulfide and its excellent adsorption behavior for doxycycline antibiotic.* Chemical Engineering Journal, 2014. **243**: p. 60-67.
259. MacQueen, J.T., *Some observations concerning the van't Hoff equation.* Journal of Chemical Education, 1967. **44**(12): p. 755.
260. Chung, H.-K., W.-H. Kim, J. Park, J. Cho, T.-Y. Jeong, and P.-K. Park, *Application of Langmuir and Freundlich isotherms to predict adsorbate removal efficiency or required amount of adsorbent.* Journal of Industrial and Engineering Chemistry, 2015. **28**: p. 241-246.
261. Ali, R.M., H.A. Hamad, M.M. Hussein, and G.F. Malash, *Potential of using green adsorbent of heavy metal removal from aqueous solutions: Adsorption kinetics, isotherm, thermodynamic, mechanism and economic analysis.* Ecological Engineering, 2016. **91**: p. 317-332.
262. *Sulfuric Acid, 96% Solution in Water, Extra Pure, Thermo Scientific Chemicals*. 2024 [cited 2024 05 January 2024]; Available from: https://www.fishersci.co.uk/shop/products/sulfuric-acid-96-solution-water-extra-pure-thermo-scientific/10715801#?keyword=.
263. *Calcium oxide, Reagent Grade, Thermo Scientific Chemicals*. 2024 [cited 2024 05 January 2024]; Available from: https://www.fishersci.co.uk/shop/products/calcium-oxide-reagent-grade-thermo-scientific/11317618#?keyword=calcium%20oxide.
264. *Sodium carbonate, 98%, Thermo Scientific Chemicals*. 2024 [cited 2024 05 January 2024]; Available from: https://www.fishersci.co.uk/shop/products/sodium-carbonate-98-thermo-scientific/11317886#?keyword=sodium%20carbonate.
265. *Metered Household Charges 2023/24*. 2023 [cited 2024 05 January 2024]; Available from: https://www.scottishwater.co.uk/Help-and-Resources/Document-Hub/Your-Home/Charges.
266. *Tarrif information labels*. 2023 [cited 2024 05 January 2024]; Available from: https://www.scottishpower.co.uk/tariff-information-labels/tariff-information-label/5788.
267. *Iron(III) nitrate nonahydrate, ACS, 98.0-101.0%, Thermo Scientific Chemicals*. 2024 [cited 2024 05 January 2024]; Available from: https://www.thermofisher.com/order/catalog/product/033315.36?SID=srch-srp-033315.36.
268. *Copper(II) nitrate trihydrate, Honeywell*. 2024 [cited 2024 05 January 2024]; Available from: https://lab.honeywell.com/shop/copper-ii-nitrate-trihydrate-61194.
269. *Titanium(IV) oxide, Aeroxide(R) P25, Thermo Scientific Chemicals*. 2024 [cited 2024 05 January 2024]; Available from: https://www.thermofisher.com/order/catalog/product/384290500?SID=srch-srp-384290500.
270. de Freitas, J., A.P.G. Ferreira, and É.T.G. Cavalheiro, *Thermal analysis of tetracyclines: a review.* Journal of Thermal Analysis and Calorimetry, 2024. **149**(20): p. 11375-11387.
271. Chopra, I. and M. Roberts, *Tetracycline Antibiotics: Mode of Action, Applications, Molecular Biology, and Epidemiology of Bacterial Resistance.* Microbiology and Molecular Biology Reviews, 2001. **65**(2): p. 232-260.
272. Gonzalez Ronquillo, M. and J.C. Angeles Hernandez, *Antibiotic and synthetic growth promoters in animal diets: Review of impact and analytical methods.* Food Control, 2017. **72**: p. 255-267.
273. Granados-Chinchilla, F. and C. Rodríguez, *Tetracyclines in Food and Feedingstuffs: From Regulation to Analytical Methods, Bacterial Resistance, and Environmental and Health Implications.* Journal of Analytical Methods in Chemistry, 2017. **2017**(1): p. 1315497.
274. Karimi, Z. and A. Rahbar-Kelishami, *Efficient utilization of red mud waste via stepwise leaching to obtain α-hematite and mesoporous γ-alumina.* Scientific Reports, 2023. **13**(1): p. 8527.
275. Ali, T.A., G.G. Mohamed, A.Z. El-Sonbati, M.A. Diab, and A.M. Elkfass, *A Potentiometric Sensor for Determination of Doxycycline Hydrochloride in Pharmaceutical Preparation and Biological Fluids.* Russian Journal of Electrochemistry, 2018. **54**(12): p. 1081-1095.
276. Álvarez-Esmorís, C., L. Rodríguez-López, D. Fernández-Calviño, A. Núñez-Delgado, E. Álvarez-Rodríguez, and M. Arias-Estévez, *Degradation of Doxycycline, Enrofloxacin, and*

Sulfamethoxypyridazine under Simulated Sunlight at Different pH Values and Chemical Environments. Agronomy, 2022. **12**(2): p. 260.
277. Vasanthakumar, V., M. Alsawalha, J. K, M.-L. Fu, and B. Yuan, *Z-scheme direct dual semiconductor photocatalytic system with porous g-C3N4/Fe2(MoO4)3 composite: A promising approach for enhanced photocatalytic degradation of doxycycline.* Journal of Environmental Chemical Engineering, 2024. **12**(1): p. 111710.
278. Li, D., T. Hua, X. Li, J. Cheng, K. Du, Y. Hu, and Y. Chen, *In-situ fabrication of ionic liquids/MIL-68(In)–NH2 photocatalyst for improving visible-light photocatalytic degradation of doxycycline hydrochloride.* Chemosphere, 2022. **292**: p. 133461.
279. Omar, M., S. Omar, A. Eltaweil, G.M. El-Subruiti, and N.F. Attia, *Engineering of ternary photocatalysts nanocomposites based NiS/ZrO2/CdS for boosting of photocatalytic degradation of organic pollutants.* Surfaces and Interfaces, 2023. **43**: p. 103606.
280. Cervini, P., B. Ambrozini, L.C.M. Machado, A.P.G. Ferreira, and É.T.G. Cavalheiro, *Thermal behavior and decomposition of oxytetracycline hydrochloride.* Journal of Thermal Analysis and Calorimetry, 2015. **121**(1): p. 347-352.
281. de Freitas, J., A.P.G. Ferreira, and É.T.G. Cavalheiro, *Investigating the thermal behavior of doxycycline and meclocycline.* Journal of Thermal Analysis and Calorimetry, 2022. **147**(23): p. 13413-13423.
282. *Oxalic acid, 98%, anhydrous, Thermo Scientific Chemicals*. 2024 [cited 2024 05/09/2024]; Available from: https://www.fishersci.com/shop/products/oxalic-acid-98-anhydrous-thermo-scientific/AC186430010#?keyword=.
283. *Iron(III) oxide, red (Hematite) (99.8%-Fe), STREM*. 2024 [cited 2024 05/09/2024]; Available from: https://www.strem.com/product/ironiii-oxide-red-hematite-998fe/01tVN000003kDsCYAU.
284. Palmieri, F., A. Estoppey, G.L. House, A. Lohberger, S. Bindschedler, P.S.G. Chain, and P. Junier, *Chapter Two - Oxalic acid, a molecule at the crossroads of bacterial-fungal interactions*, in *Advances in Applied Microbiology*, G.M. Gadd and S. Sariaslani, Editors. 2019, Academic Press. p. 49-77.
285. Mellouki, A., T.J. Wallington, and J. Chen, *Atmospheric Chemistry of Oxygenated Volatile Organic Compounds: Impacts on Air Quality and Climate.* Chemical Reviews, 2015. **115**(10): p. 3984-4014.
286. Marwa, M., A. Soumaya, N. Hajjaji, and M.R. Jeday, *An environmental life cycle assessment of an industrial system: case of industrial sulfuric acid.* International Journal of Energy, Environment and Economics, 2017. **25**(4): p. 255-268.
287. Murtaza, G., M.Z. Rehman, M. Qadir, M.T. Shehzad, N. Zeeshan, H.R. Ahmad, Z.R. Farooqi, and R. Naidu, *High residual sodium carbonate water in the Indian subcontinent: concerns, challenges and remediation.* International Journal of Environmental Science and Technology, 2021. **18**(10): p. 3257-3272.
288. Wang, W.-H., Y. Wang, P. Fan, L.-F. Chen, B.-H. Chai, J.-C. Zhao, and L.-Q. Sun, *Effect of calcium peroxide on the water quality and bacterium community of sediment in black-odor water.* Environmental Pollution, 2019. **248**: p. 18-27.
289. Snyder, M.M. and W. Um, *Adsorption mechanisms and transport behavior between selenate and selenite on different sorbents.* International Journal of Waste Resources, 2014. **4**(144): p. 2.
290. Jozwiak, W., E. Kaczmarek, T. Maniecki, W. Ignaczak, and W. Maniukiewicz, *Reduction behavior of iron oxides in hydrogen and carbon monoxide atmospheres.* Applied Catalysis A: General, 2007. **326**(1): p. 17-27.
291. Hargreaves, J.S.J. and A. Alharthi, *Biogenic and bio-structured inorganic materials in heterogeneous catalysis: a brief overview.* Journal of Chemical Technology & Biotechnology, 2016. **91**(2): p. 296-303.

292. Zhu, B.-S., Y. Jia, Z. Jin, B. Sun, T. Luo, L.-T. Kong, and J.-H. Liu, *A facile precipitation synthesis of mesoporous 2-line ferrihydrite with good fluoride removal properties.* RSC advances, 2015. **5**(103): p. 84389-84397.
293. Yoo, S.-J., *Synthesis of mesoporous 2-line ferrihydrite/γ-Al2O3 hybrid adsorbent for the effective adsorption of phosphate for water remediation.* Korean Journal of Chemical Engineering, 2021. **38**(2): p. 326-336.
294. Rout, K., M. Mohapatra, and S. Anand, *2-Line ferrihydrite: synthesis, characterization and its adsorption behaviour for removal of Pb (II), Cd (II), Cu (II) and Zn (II) from aqueous solutions.* Dalton Transactions, 2012. **41**(11): p. 3302-3312.
295. Smith, S.J., K. Page, H. Kim, B.J. Campbell, J. Boerio-Goates, and B.F. Woodfield, *Novel Synthesis and Structural Analysis of Ferrihydrite.* Inorganic Chemistry, 2012. **51**(11): p. 6421-6424.
296. Fleming, E.J., T. Woyke, R.A. Donatello, M.M.M. Kuypers, A. Sczyrba, S. Littmann, and D. Emerson, *Insights into the Fundamental Physiology of the Uncultured Fe-Oxidizing Bacterium Leptothrix ochracea.* Applied and Environmental Microbiology, 2018. **84**(9): p. e02239-17.
297. Johannessen, K.C., N. McLoughlin, P.E. Vullum, and I.H. Thorseth, *On the biogenicity of Fe-oxyhydroxide filaments in silicified low-temperature hydrothermal deposits: Implications for the identification of Fe-oxidizing bacteria in the rock record.* Geobiology, 2020. **18**(1): p. 31-53.
298. Hashimoto, H., A. Itadani, T. Kudoh, Y. Kuroda, M. Seno, Y. Kusano, Y. Ikeda, M. Nakanishi, T. Fujii, and J. Takada, *Acidic Amorphous Silica Prepared from Iron Oxide of Bacterial Origin.* ACS Applied Materials & Interfaces, 2013. **5**(3): p. 518-523.
299. Kaur, G., N. Singh, and A. Rajor, *Adsorption of doxycycline hydrochloride onto powdered activated carbon synthesized from pumpkin seed shell by microwave-assisted pyrolysis.* Environmental Technology & Innovation, 2021. **23**: p. 101601.
300. Li, Q., N. Liang, W. Zou, X. Han, C. Chang, and J. Chen, *Nitrogen-doped activated carbon derived from biomass waste for effective removal of doxycycline from aqueous solution: characterization and adsorption mechanism.* Journal of Porous Materials, 2024. **31**(4): p. 1321-1334.
301. Srivastava, A., H. Dave, B. Prasad, D.M. Maurya, M. Kumari, M. Sillanpää, and K.S. Prasad, *Low cost iron modified syzygium cumini l. Wood biochar for adsorptive removal of ciprofloxacin and doxycycline antibiotics from aqueous solution.* Inorganic Chemistry Communications, 2022. **144**: p. 109895.
302. Liu, S., W.-h. Xu, Y.-g. Liu, X.-f. Tan, G.-m. Zeng, X. Li, J. Liang, Z. Zhou, Z.-l. Yan, and X.-x. Cai, *Facile synthesis of Cu(II) impregnated biochar with enhanced adsorption activity for the removal of doxycycline hydrochloride from water.* Science of The Total Environment, 2017. **592**: p. 546-553.
303. Wei, J., Y. Liu, J. Li, Y. Zhu, H. Yu, and Y. Peng, *Adsorption and co-adsorption of tetracycline and doxycycline by one-step synthesized iron loaded sludge biochar.* Chemosphere, 2019. **236**: p. 124254.
304. Zhang, X., B. Bai, H. Wang, and Y. Suo, *Facile fabrication of sea buckthorn biocarbon (SB)@α-Fe2O3 composite catalysts and their applications for adsorptive removal of doxycycline wastewater through a cohesive heterogeneous Fenton-like regeneration.* RSC advances, 2016. **6**(44): p. 38159-38168.
305. Ghassemi Nooreini, M. and H. Ahmad Panahi, *Fabrication of magnetite nano particles and modification with metal organic framework of Zn2+ for sorption of doxycyline.* International Journal of Pharmaceutics, 2016. **512**(1): p. 178-185.
306. Abdelfatah, A.M., N. El-Maghrabi, A.E.D. Mahmoud, and M. Fawzy, *Synergetic effect of green synthesized reduced graphene oxide and nano-zero valent iron composite for the removal of doxycycline antibiotic from water.* Scientific Reports, 2022. **12**(1): p. 19372.

307. Lu, M., Y. Wang, W. Jiao, J. Yu, P. Gao, Q. Zhao, D. Li, and R. Chi, *Eliminating waste with waste: Removal of doxycycline in water by goethite modified phosphogypsum.* Journal of Water Process Engineering, 2024. **63**: p. 105411.
308. Sorasitthiyanukarn, F.N., C. Muangnoi, P. Rojsitthisak, and P. Rojsitthisak, *Chitosan-alginate nanoparticles as effective oral carriers to improve the stability, bioavailability, and cytotoxicity of curcumin diethyl disuccinate.* Carbohydrate Polymers, 2021. **256**: p. 117426.
309. Yan, P., W. Lan, and J. Xie, *Modification on sodium alginate for food preservation: A review.* Trends in Food Science & Technology, 2024. **143**: p. 104217.
310. Zaidi, S., V. Sivasankar, T. Chaabane, V. Alonzo, K. Omine, R. Maachi, A. Darchen, and M. Prabhakaran, *Separate and simultaneous removal of doxycycline and oxytetracycline antibiotics by electro-generated adsorbents (EGAs).* Journal of Environmental Chemical Engineering, 2019. **7**(1): p. 102876.
311. Yang, W., Y. Lu, F. Zheng, X. Xue, N. Li, and D. Liu, *Adsorption behavior and mechanisms of norfloxacin onto porous resins and carbon nanotube.* Chemical Engineering Journal, 2012. **179**: p. 112-118.
312. Zeng, Z.-w., X.-f. Tan, Y.-g. Liu, S.-r. Tian, G.-m. Zeng, L.-h. Jiang, S.-b. Liu, J. Li, N. Liu, and Z.-h. Yin, *Comprehensive adsorption studies of doxycycline and ciprofloxacin antibiotics by biochars prepared at different temperatures.* Frontiers in chemistry, 2018. **6**: p. 80.
313. Zaidi, S., T. Chaabane, V. Sivasankar, A. Darchen, R. Maachi, T.A.M. Msagati, and M. Prabhakaran, *Performance efficiency of electro-coagulation coupled electro-flotation process (EC-EF) versus adsorption process in doxycycline removal from aqueous solutions.* Process Safety and Environmental Protection, 2016. **102**: p. 450-461.
314. Meng, Y., X. Chen, D. Ai, T. Wei, Z. Fan, and B. Wang, *Sulfur-doped zero-valent iron supported on biochar for tetracycline adsorption and removal.* Journal of Cleaner Production, 2022. **379**: p. 134769.
315. Zhang, J., Y. Chen, X. Song, Y. Liu, J. Zhao, and F. Wang, *Synergistic adsorption and degradation of diclofenac by zero-valent iron modified spent bleaching earth carbon: Mechanism and toxicity assessment.* Journal of Hazardous Materials, 2022. **432**: p. 128753.
316. Sahu, M.K., R.K. Patel, and S. Kurwadkar, *Mechanistic insight into the adsorption of mercury (II) on the surface of red mud supported nanoscale zero-valent iron composite.* Journal of Contaminant Hydrology, 2022. **246**: p. 103959.
317. Huang, X., C.-S. Lee, K. Zhang, A.G. Alhamzani, and B.S. Hsiao, *Sodium Alginate–Aldehyde Cellulose Nanocrystal Composite Hydrogel for Doxycycline and Other Tetracycline Removal.* Nanomaterials, 2023. **13**(7): p. 1161.
318. *BOC A Linde company*. 2025 [cited 2025 12/03/2025]; Available from: https://www.boconline.co.uk/shop/en/uk/home.
319. *Iron (Fe) ≥99%, reduced, powder (fine)*. 2025 [cited 2025 24/02/2025]; Available from: https://www.sigmaaldrich.com/EG/en/product/aldrich/12310.
320. Strongin, D.R. and G.A. Somorjai, *The effects of potassium on ammonia synthesis over iron single-crystal surfaces.* Journal of Catalysis, 1988. **109**(1): p. 51-60.
321. Peng, X., Y. Luo, T. Zhang, J. Deng, Y. Zhou, J. Li, J. Ni, B. Lin, J. Lin, D. Wu, L. Zheng, X. Wang, and L. Jiang, *Potassium promoter regulates electronic structure and hydrogen spillover of ultrasmall Ru nanoclusters catalyst for ammonia synthesis.* Chemical Engineering Science, 2024. **292**: p. 120021.
322. Humphreys, J., R. Lan, and S. Tao, *Development and Recent Progress on Ammonia Synthesis Catalysts for Haber–Bosch Process.* Advanced Energy and Sustainability Research, 2021. **2**(1): p. 2000043.
323. Al Maksoud, W., R.K. Rai, N. Morlanés, M. Harb, R. Ahmad, S. Ould-Chikh, D. Anjum, M.N. Hedhili, B.E. Al-Sabban, K. Albahily, L. Cavallo, and J.-M. Basset, *Active and stable Fe-based*

catalyst, mechanism, and key role of alkali promoters in ammonia synthesis. Journal of Catalysis, 2021. **394**: p. 353-365.
324. Wang, W.-X., H.-Q. Zhao, B.-S. Du, J.-M. Wen, F. Li, and D.-M. Wang, *Activity and reduction behavior of fused iron catalysts containing cobalt for ammonia synthesis: a structure study.* Applied Catalysis A: General, 1995. **122**(1): p. 5-20.
325. Kaleńczuk, R.J., *Cobalt promoted fused iron catalyst for ammonia synthesis.* International Journal of Inorganic Materials, 2000. **2**(2): p. 233-239.

Appendices

Appendix 1. Nitrogen physisorption isotherms of Fe and Cu-TiO_2 composites using TiO_2 extracted from Chinese red mud by the acid baking method reported in Chapter 3.

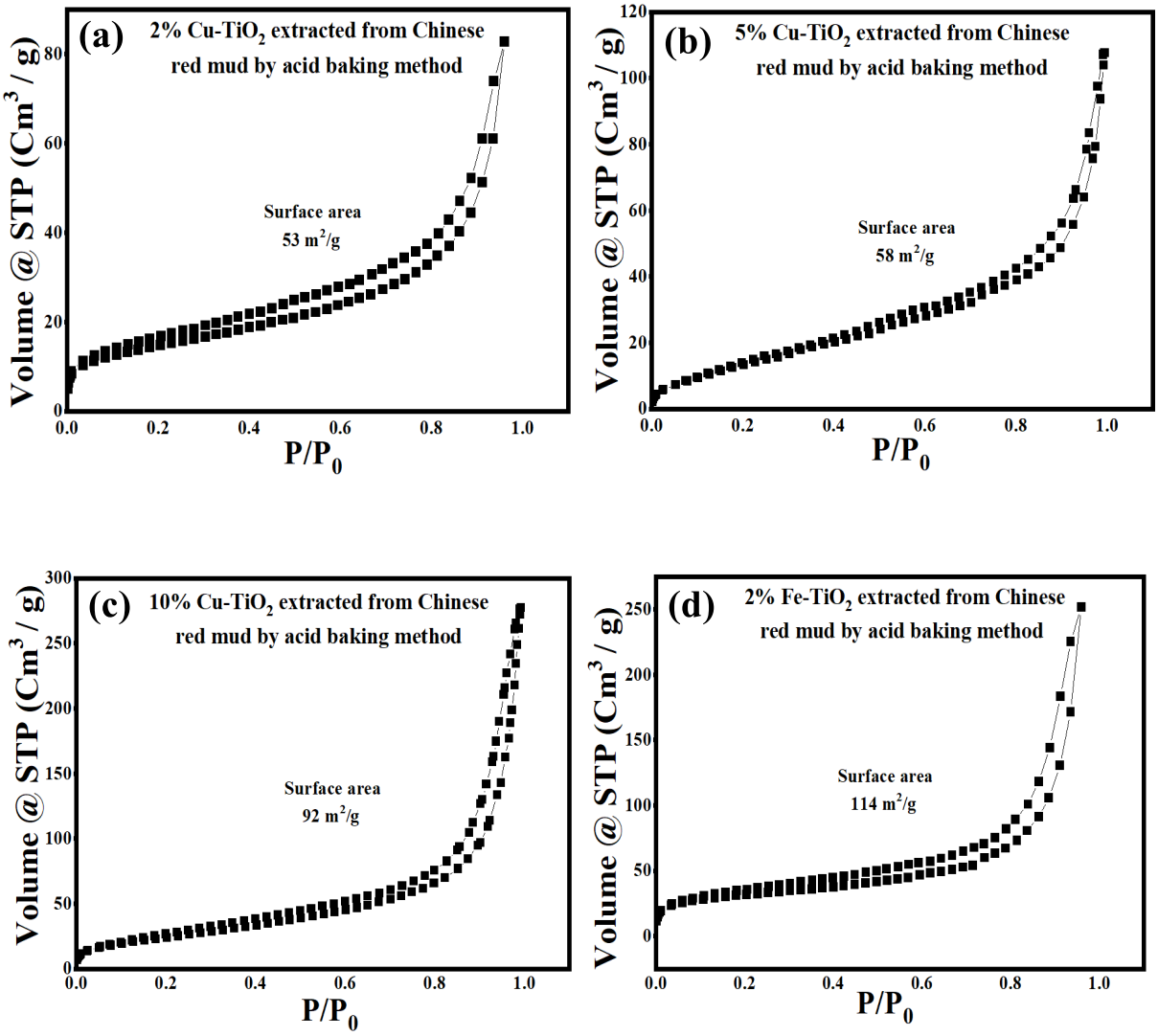

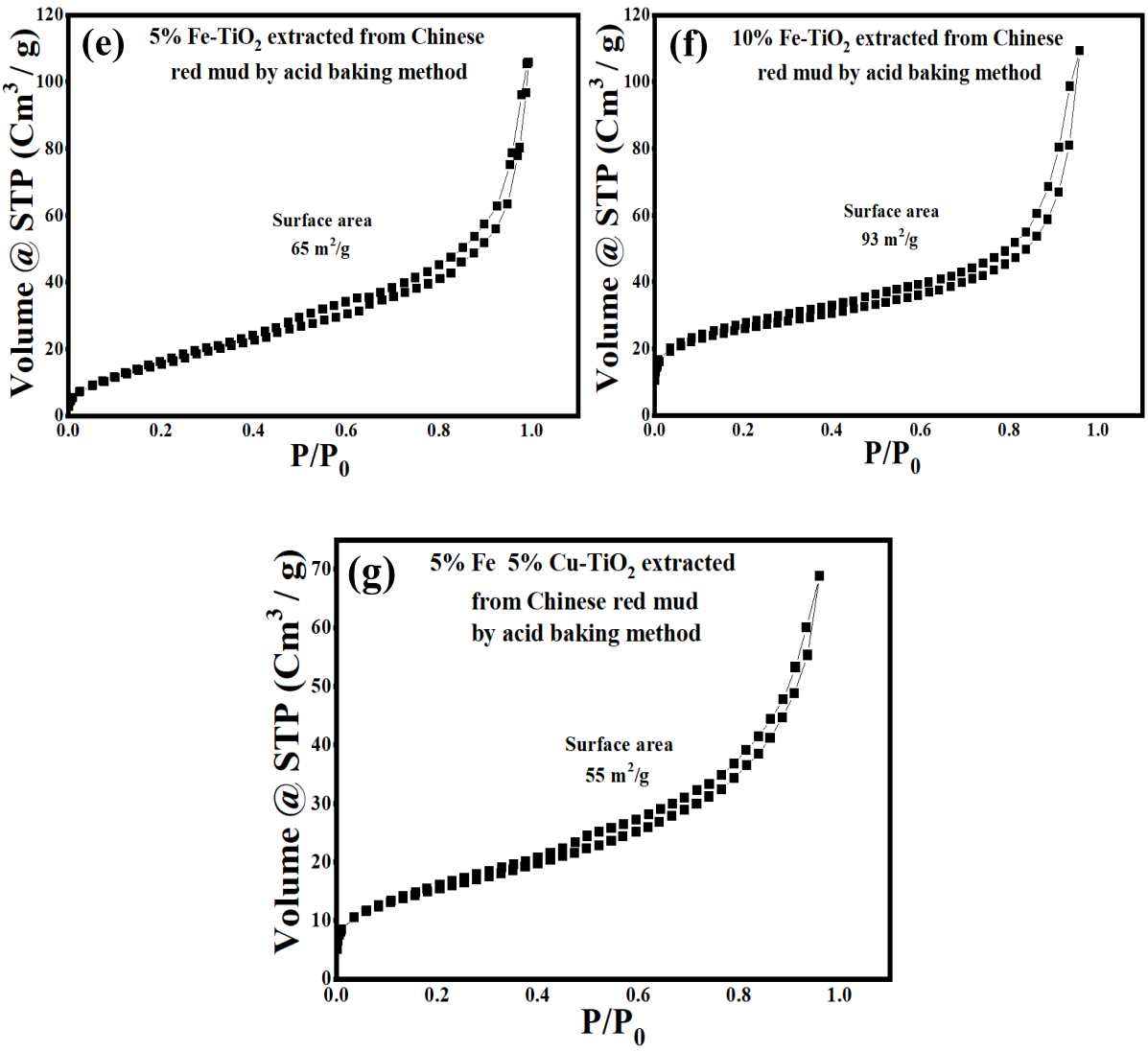

Fig S1. Nitrogen physisorption isotherms of 2% Cu-TiO_2 **(a)**, 5% Cu-TiO_2 **(b)**, 10% Cu-TiO_2 **(c)**, 2% Fe-TiO_2 **(d)**, 5% Fe-TiO_2 **(e)**, 10% Fe-TiO_2 **(f)**, and 5% Fe 5% Cu-TiO_2 **(g)**. These isotherms are all from [202]. All these Cu and Fe-TiO_2 composites are presented in wt%.

Appendix 2. LC-MS spectra of different samples reported in Chapter 3.

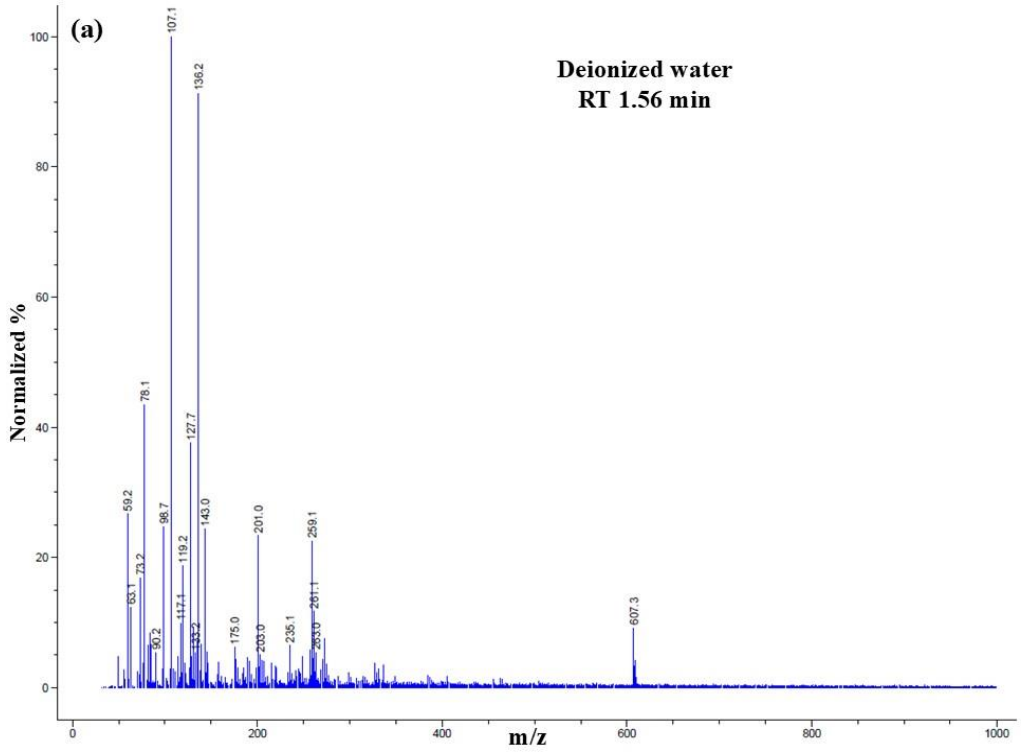

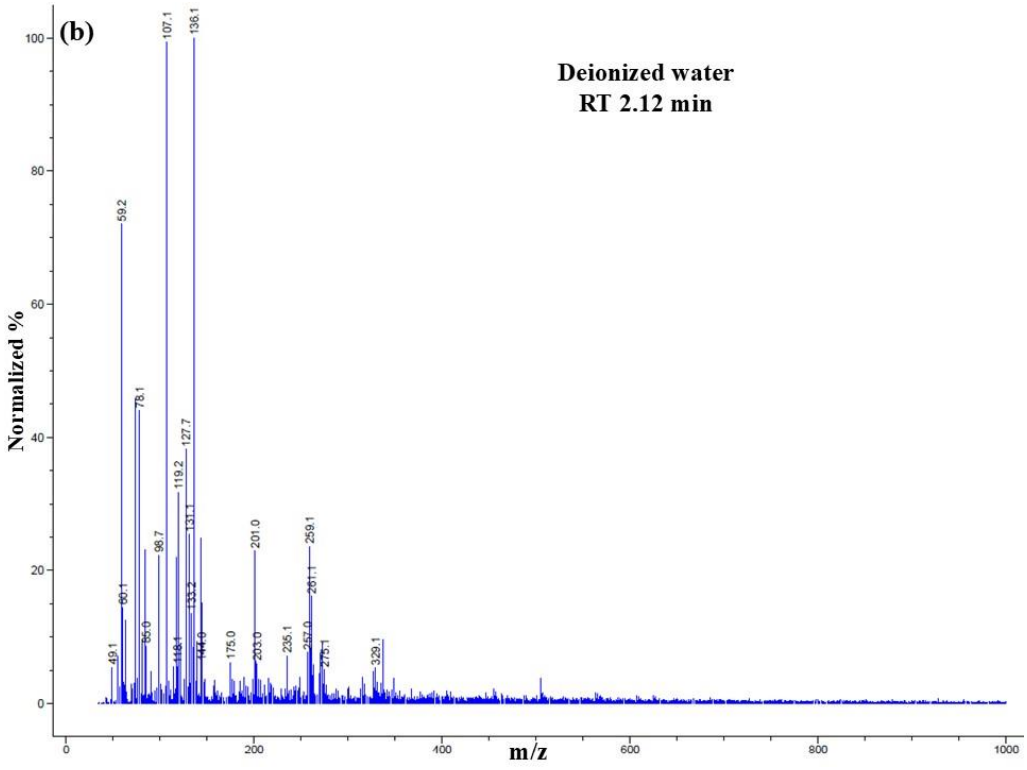

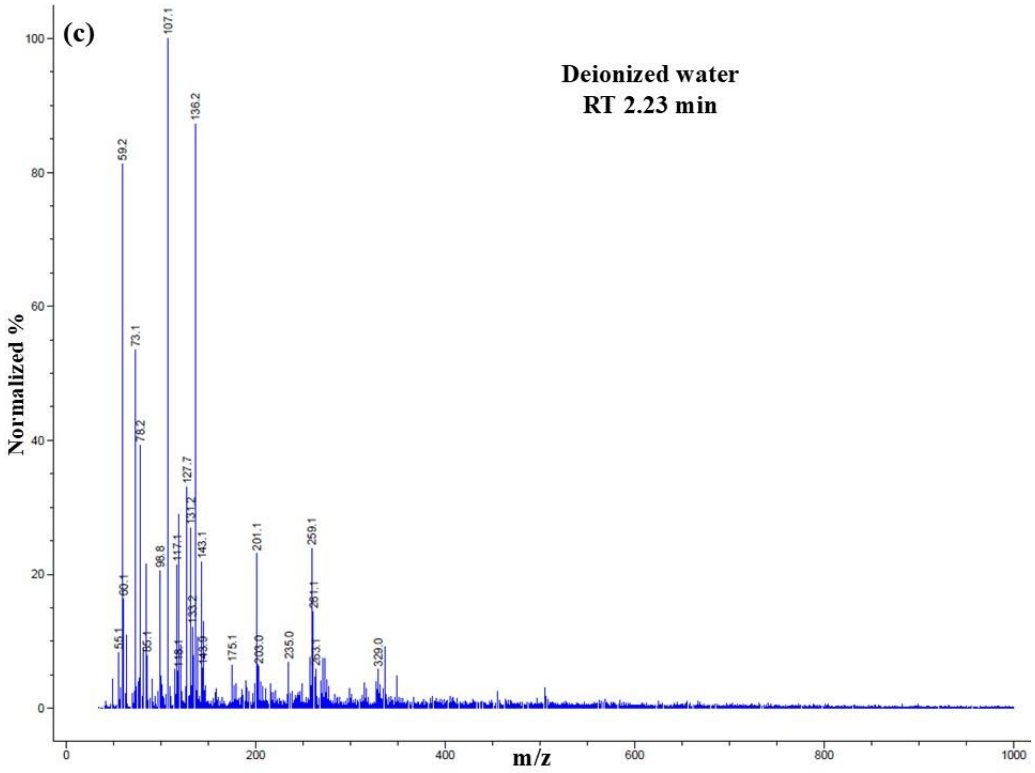
(c)
Deionized water
RT 2.23 min
Normalized %
m/z
107.1
136.2
59.2
73.1
78.2
127.7
131.2
143.1
201.1
259.1
60.1
96.8
117.1
133.2
261.1
55.1
86.1
175.1
203.0
235.0
329.0

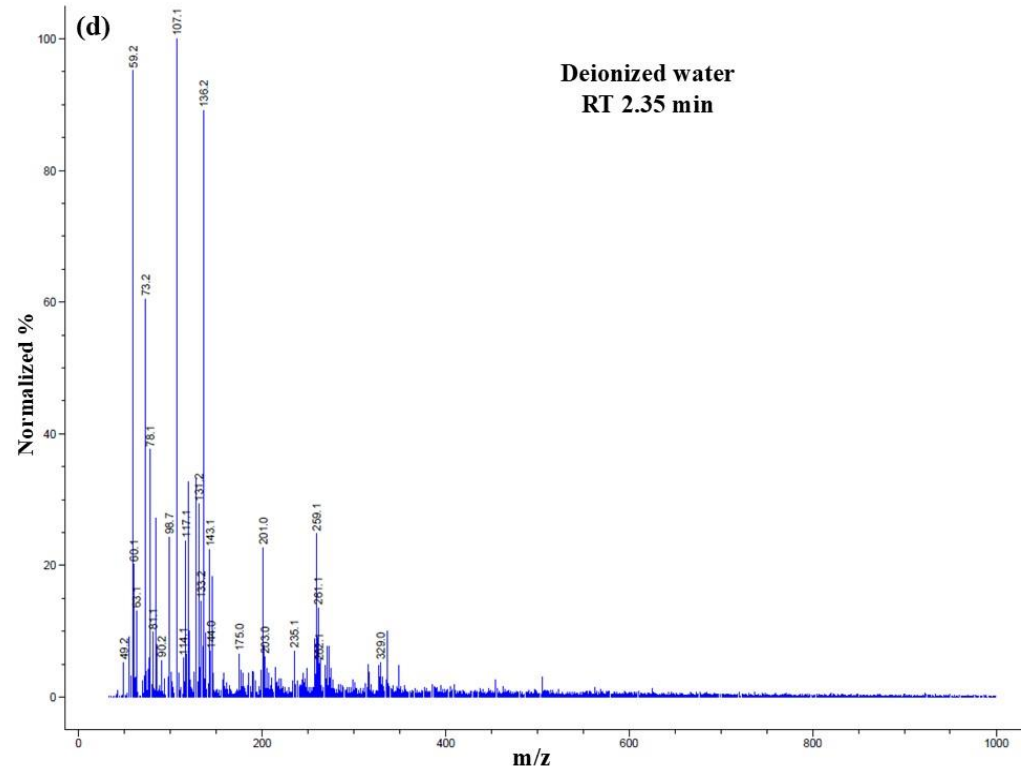
(d)
Deionized water
RT 2.35 min
Normalized %
m/z
107.1
59.2
136.2
73.2
78.1
131.2
143.1
201.0
259.1
60.1
98.7
117.1
133.2
261.1
49.2
63.1
81.1
90.2
114.1
144.0
175.0
203.0
235.1
329.0

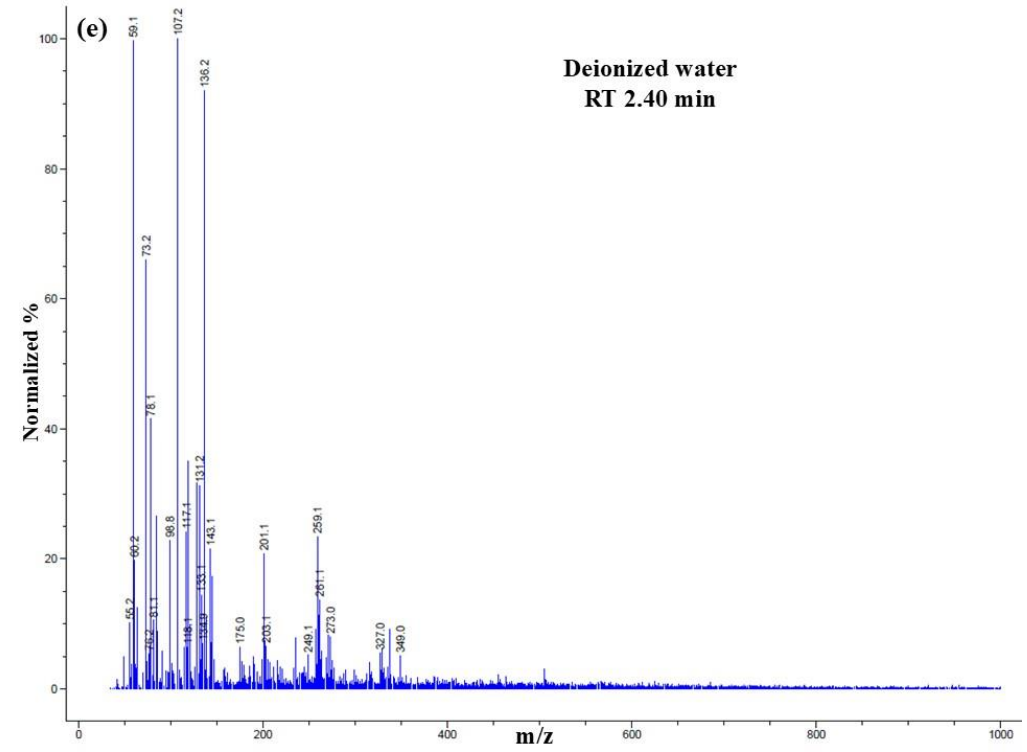
(e)
Deionized water
RT 2.40 min
Normalized %
m/z
59.1
107.2
136.2
73.2
78.1
131.2
98.8
117.1
143.1
201.1
259.1
60.2
55.2
81.1
261.1
273.0
175.0
203.1
249.1
327.0
349.0

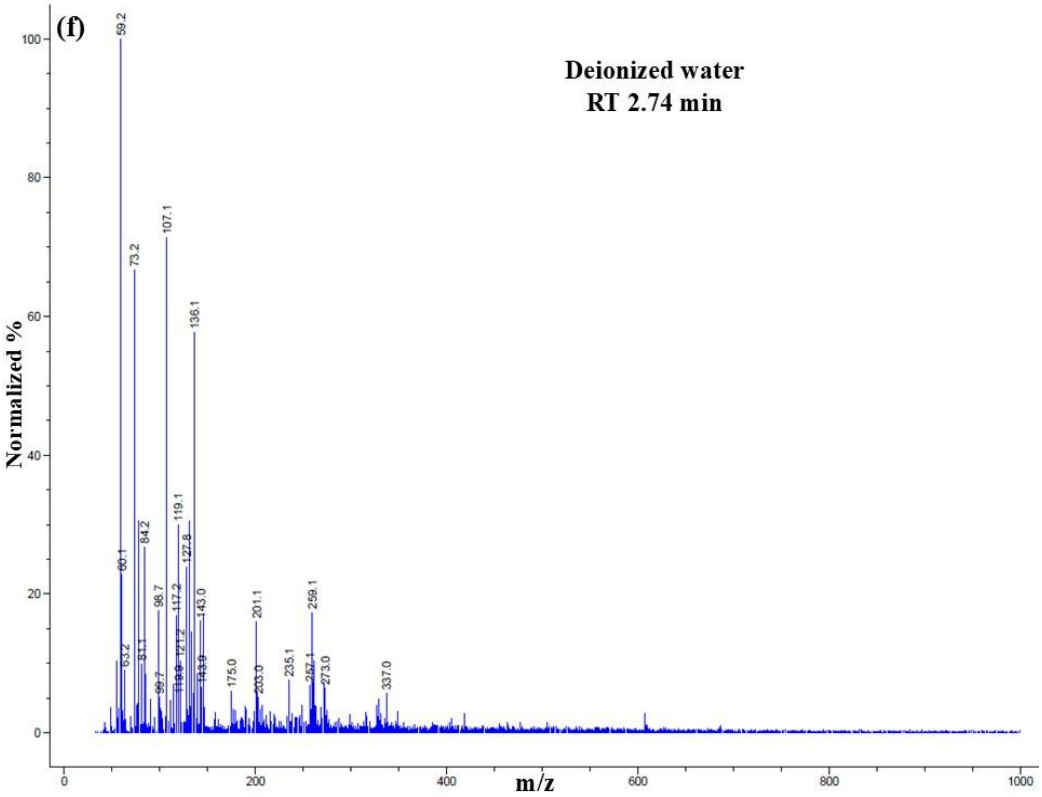
(f)
Deionized water
RT 2.74 min
Normalized %
m/z
59.2
107.1
73.2
136.1
119.1
84.2
60.1
127.8
98.7
117.2
143.0
201.1
259.1
81.1
175.0
203.0
235.1
257.1
273.0
337.0

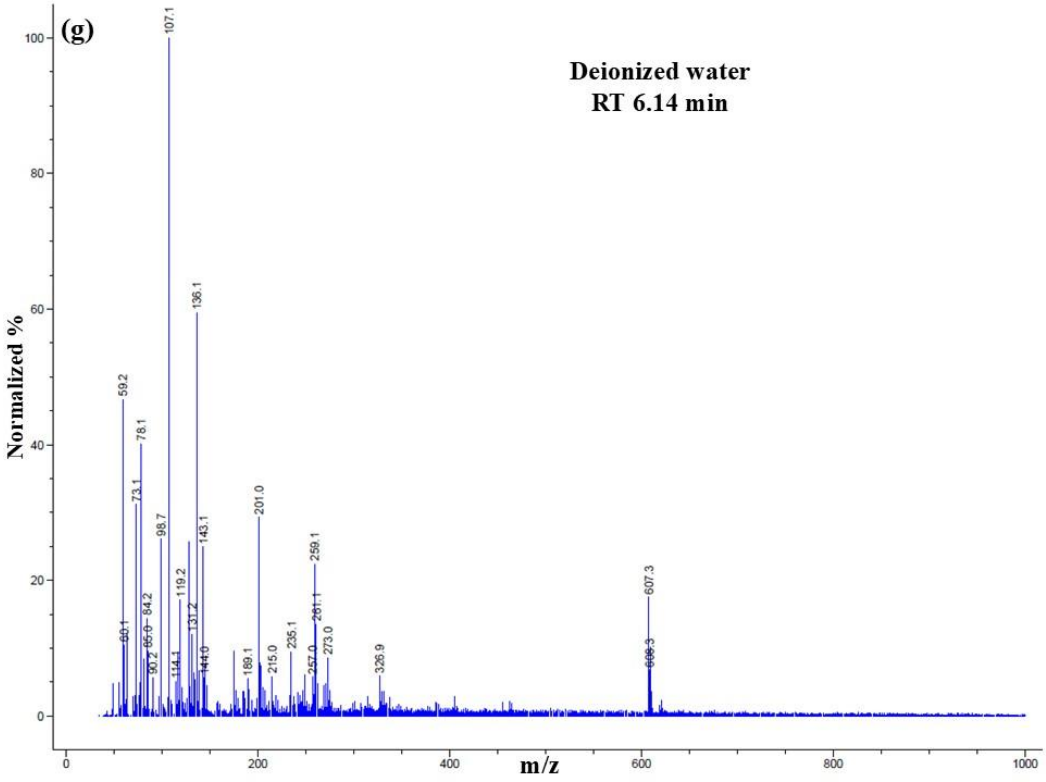

Fig S2. LC-MS spectra of deionized water at different retention times; 1.56 **(a)**, 2.12 **(b)**, 2.23 **(c)**, 2.35 **(d)**, 2.40 **(e)**, 2.74 **(f)**, and 6.14 minute **(g)** to show that all these peaks were just impurities in the LC-MS column not degradation production from CEF photodegradation.

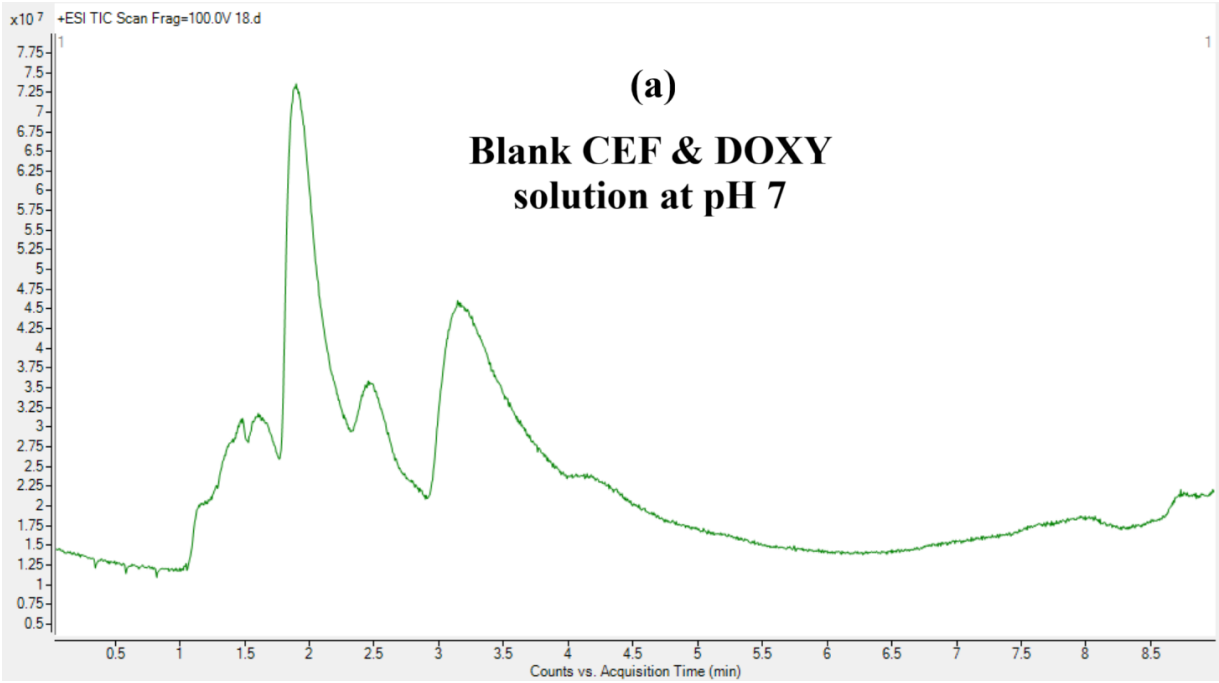

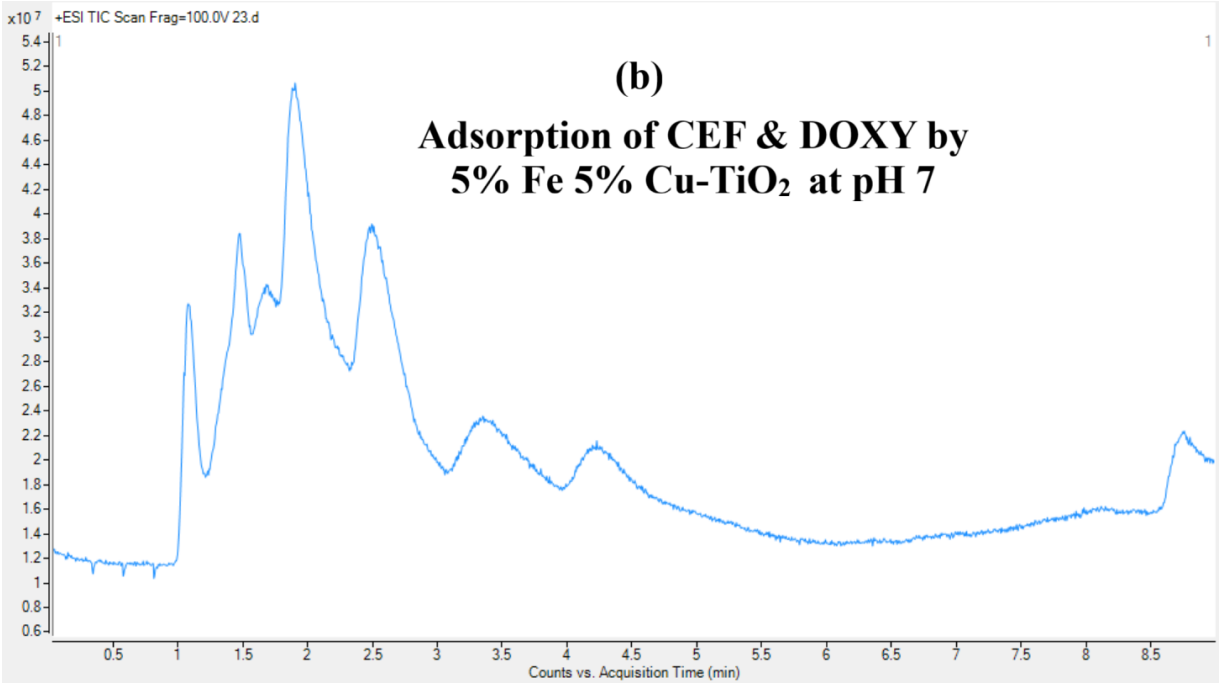
x10 7
+ESI TIC Scan Frag=100.0V 23.d
(b)
Adsorption of CEF & DOXY by
5% Fe 5% Cu-TiO2 at pH 7
Counts vs. Acquisition Time (min)

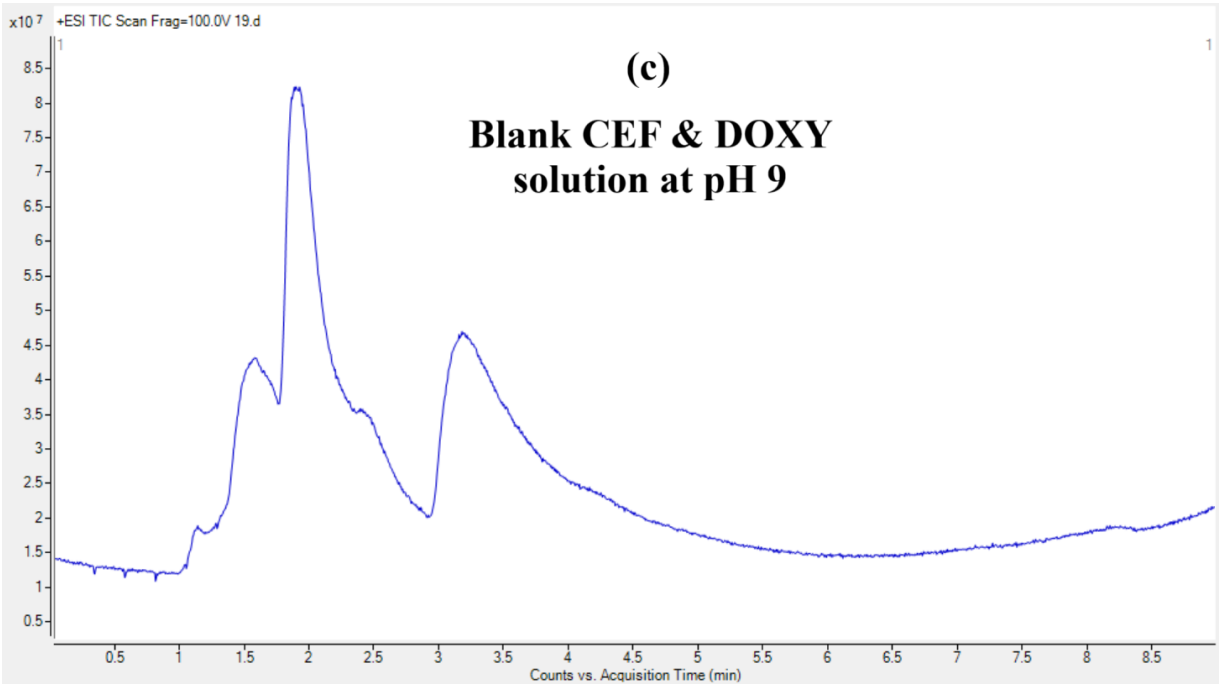
x10 7
+ESI TIC Scan Frag=100.0V 19.d
(c)
Blank CEF & DOXY
solution at pH 9
Counts vs. Acquisition Time (min)

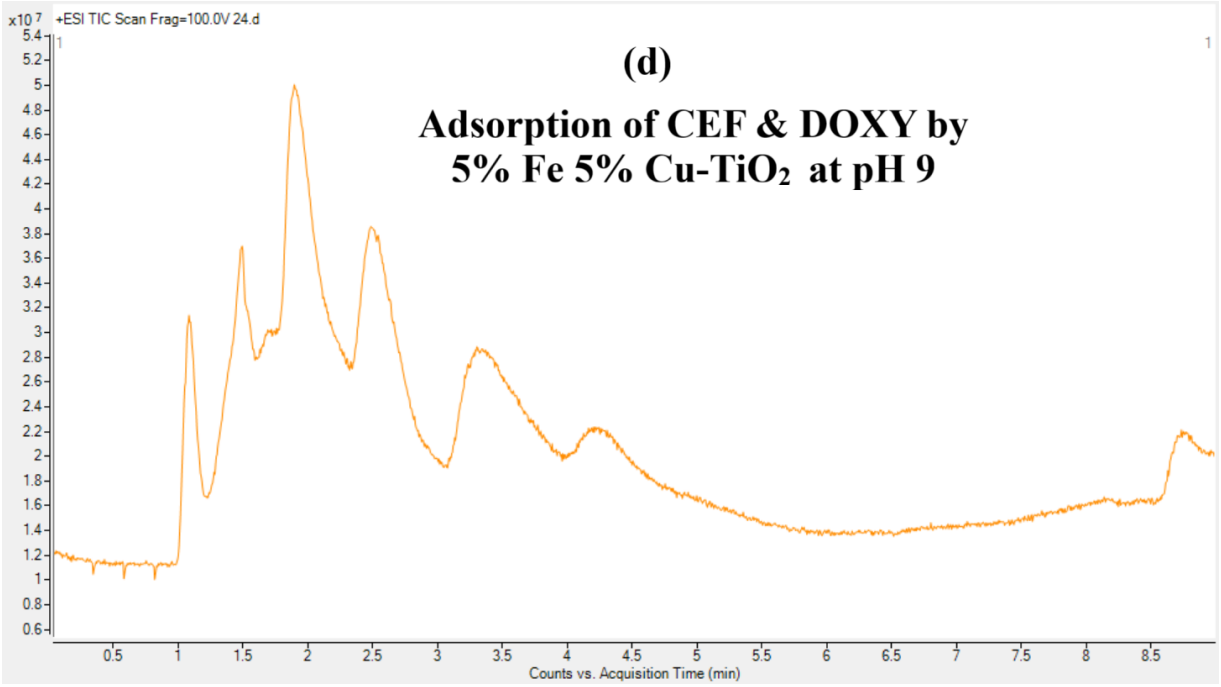
x10 7
+ESI TIC Scan Frag=100.0V 24.d
(d)
Adsorption of CEF & DOXY by
5% Fe 5% Cu-TiO2 at pH 9
Counts vs. Acquisition Time (min)

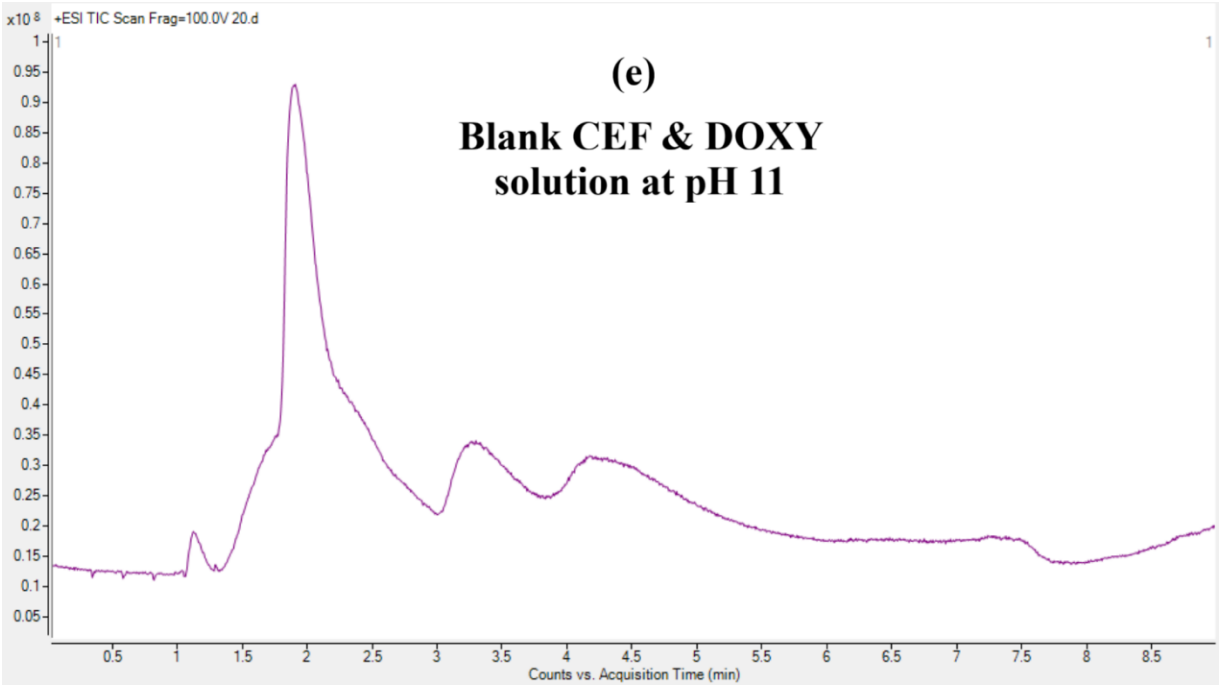
x10 8
+ESI TIC Scan Frag=100.0V 20.d
(e)
Blank CEF & DOXY
solution at pH 11
Counts vs. Acquisition Time (min)

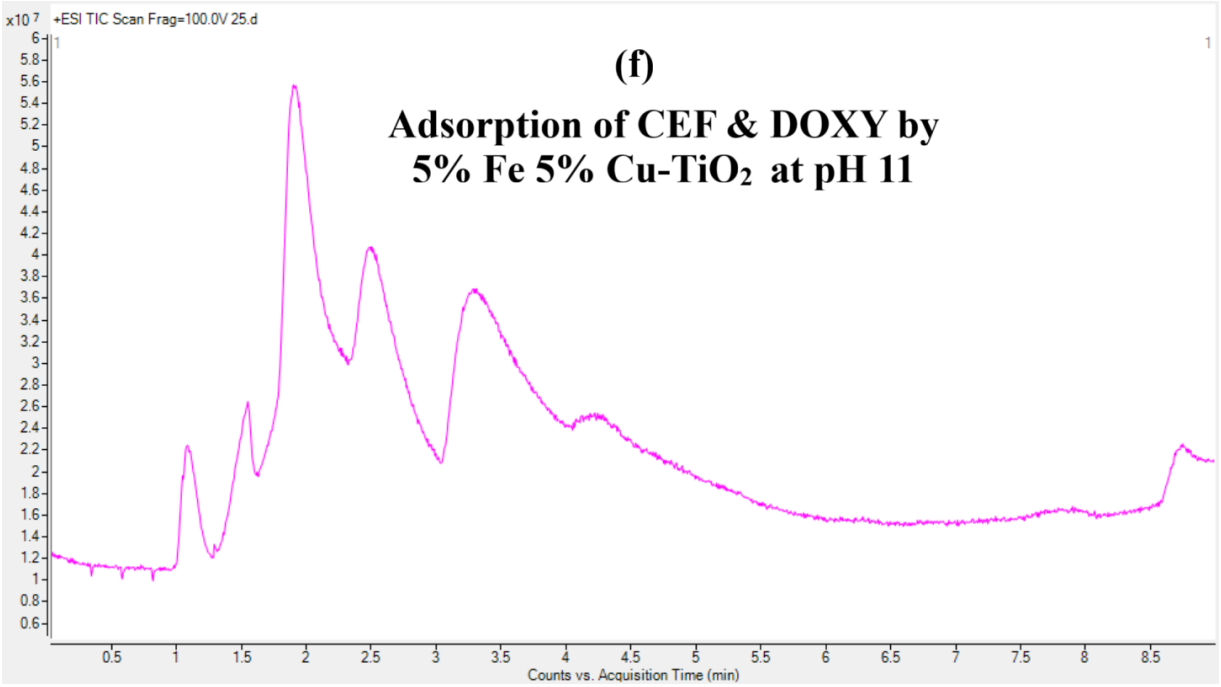

Fig S3. The chromatographic parts of the LC-MS spectra of blank CEF and DOXY solutions at pH 7 (**a**), pH 9 (**c**), pH 11 (**e**), and the same solutions but after the adsorption using 5% Fe 5% Cu-TiO_2 at the same pH levels with the same order (**b**, **d**, and **f**) after 90 minutes. [C_o = 25 ppm, volume = 20 mL, dose = 0.01 g, stirring rate = 800 rpm, and T = 20 ± 2 °C].

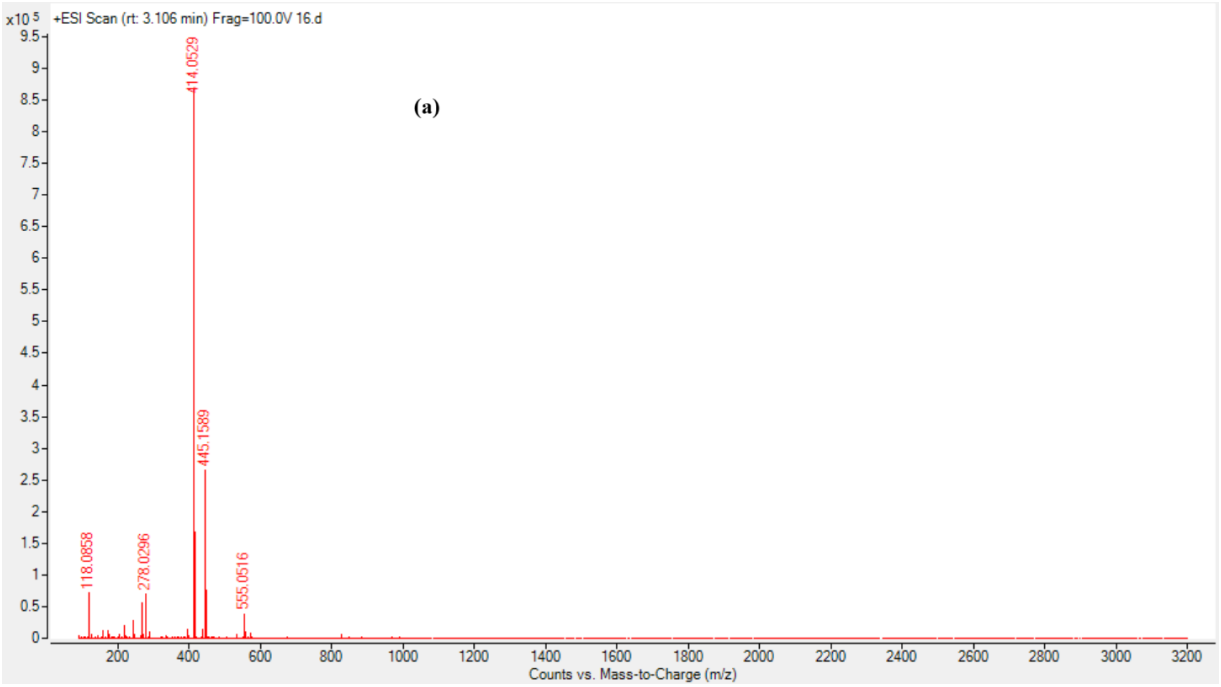

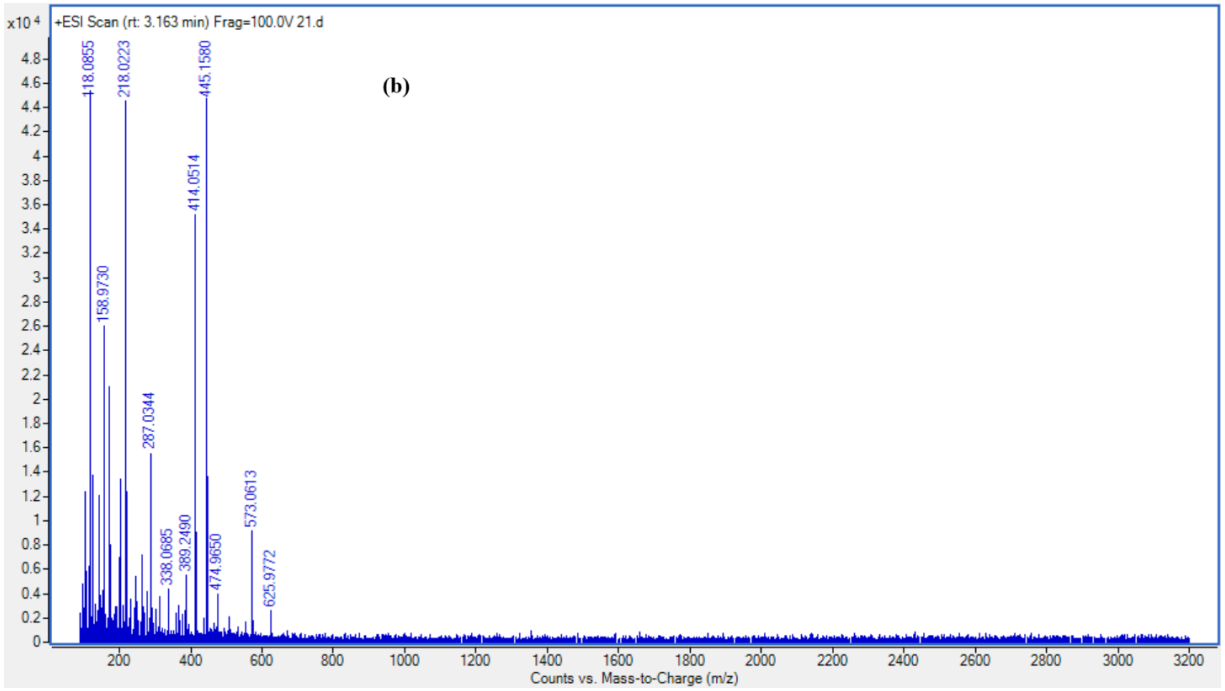
x10 4
+ESI Scan (rt: 3.163 min) Frag=100.0V 21.d
(b)
118.0855
218.0223
445.1580
414.0514
158.9730
287.0344
573.0613
338.0685
389.2490
474.9650
625.9772
Counts vs. Mass-to-Charge (m/z)

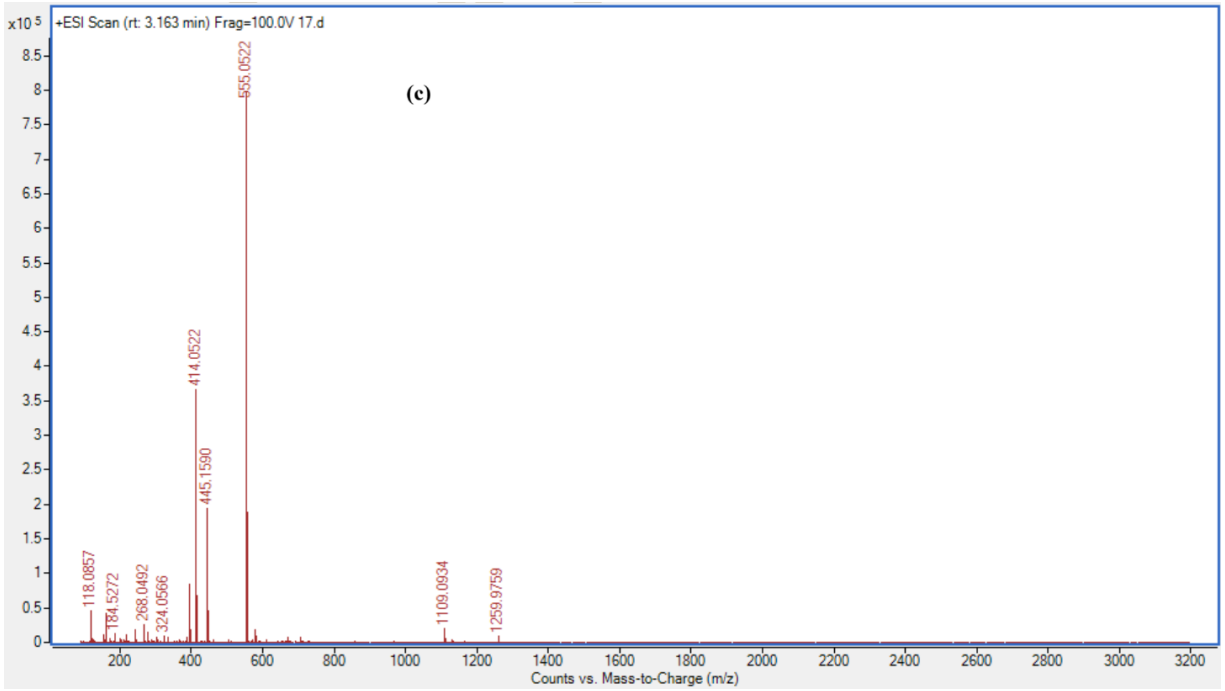
x10 5
+ESI Scan (rt: 3.163 min) Frag=100.0V 17.d
(c)
555.0522
414.0522
445.1590
118.0857
184.5272
268.0492
324.0566
1109.0934
1259.9759
Counts vs. Mass-to-Charge (m/z)

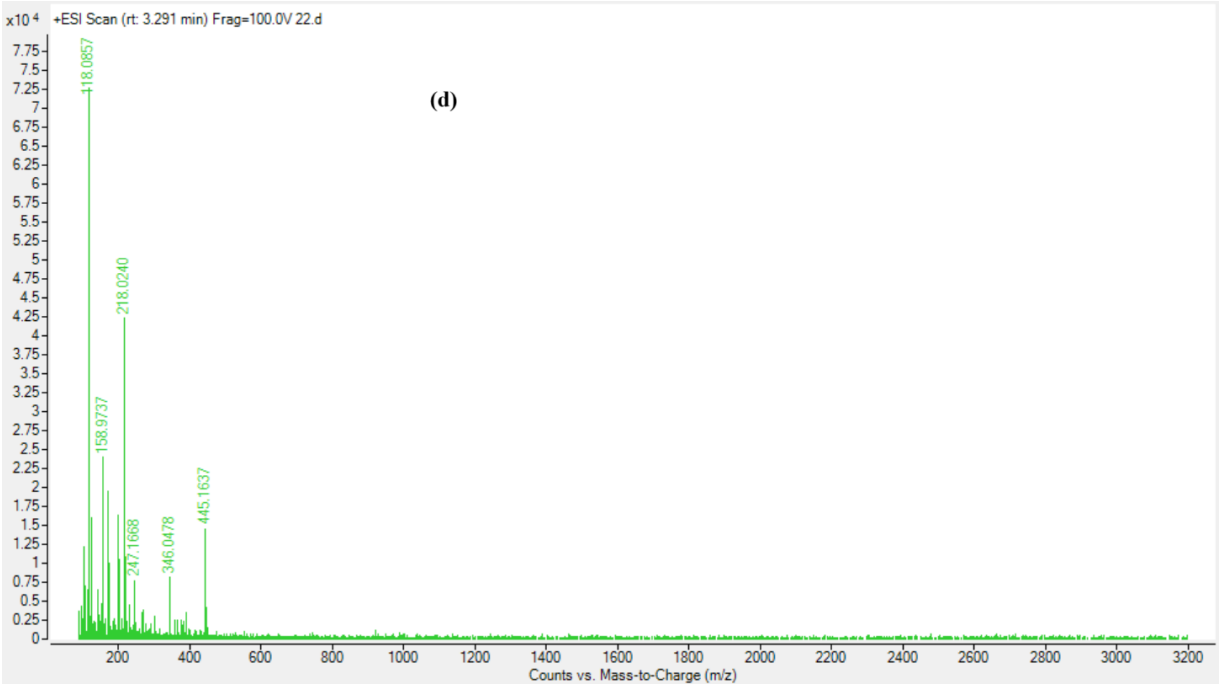
x10 4
+ESI Scan (rt: 3.291 min) Frag=100.0V 22.d
118.0857
218.0240
158.9737
247.1668
346.0478
445.1637
Counts vs. Mass-to-Charge (m/z)

(d)

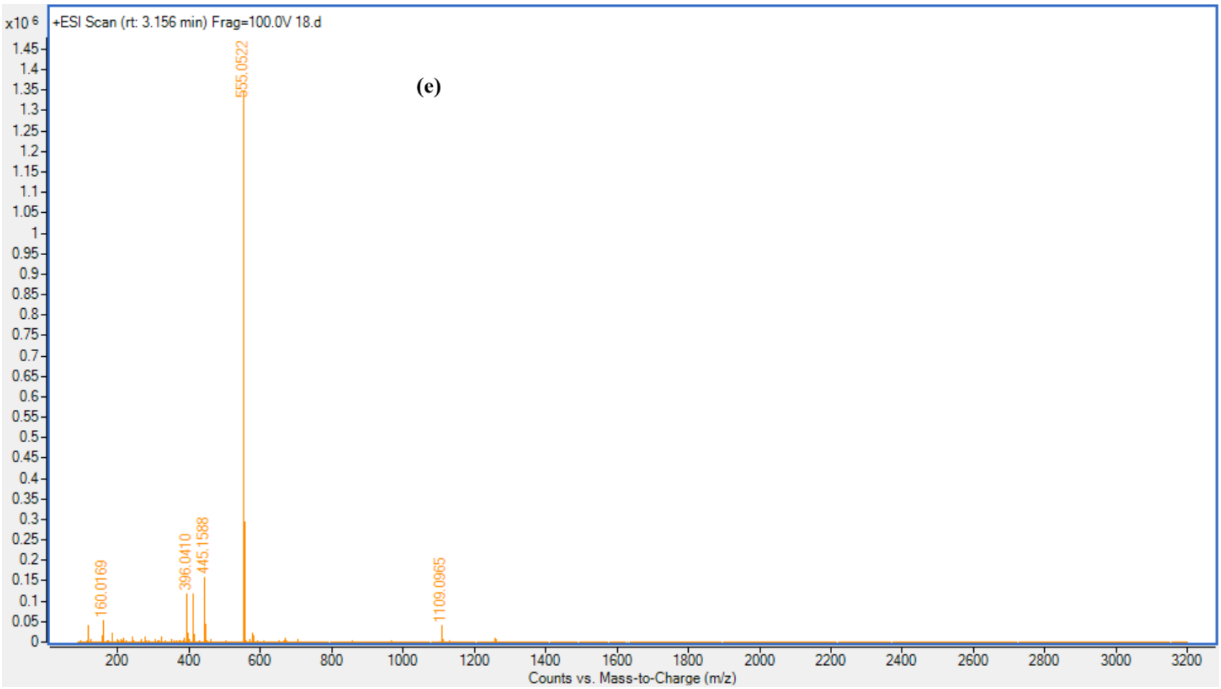
x10 6
+ESI Scan (rt: 3.156 min) Frag=100.0V 18.d
555.0522
160.0169
396.0410
445.1588
1109.0965
Counts vs. Mass-to-Charge (m/z)

(e)

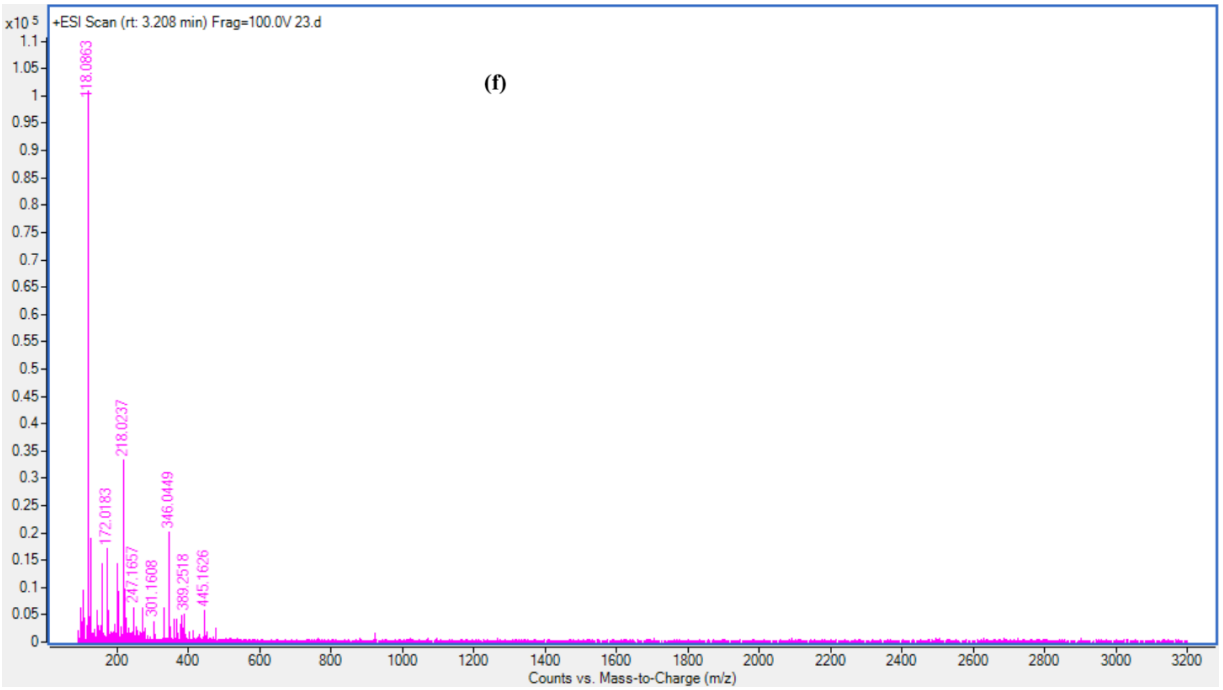
+ESI Scan (rt: 3.208 min) Frag=100.0V 23.d
x10 5
118.0863
172.0183
218.0237
247.1657
301.1608
346.0449
389.2518
445.1626
Counts vs. Mass-to-Charge (m/z)

(f)

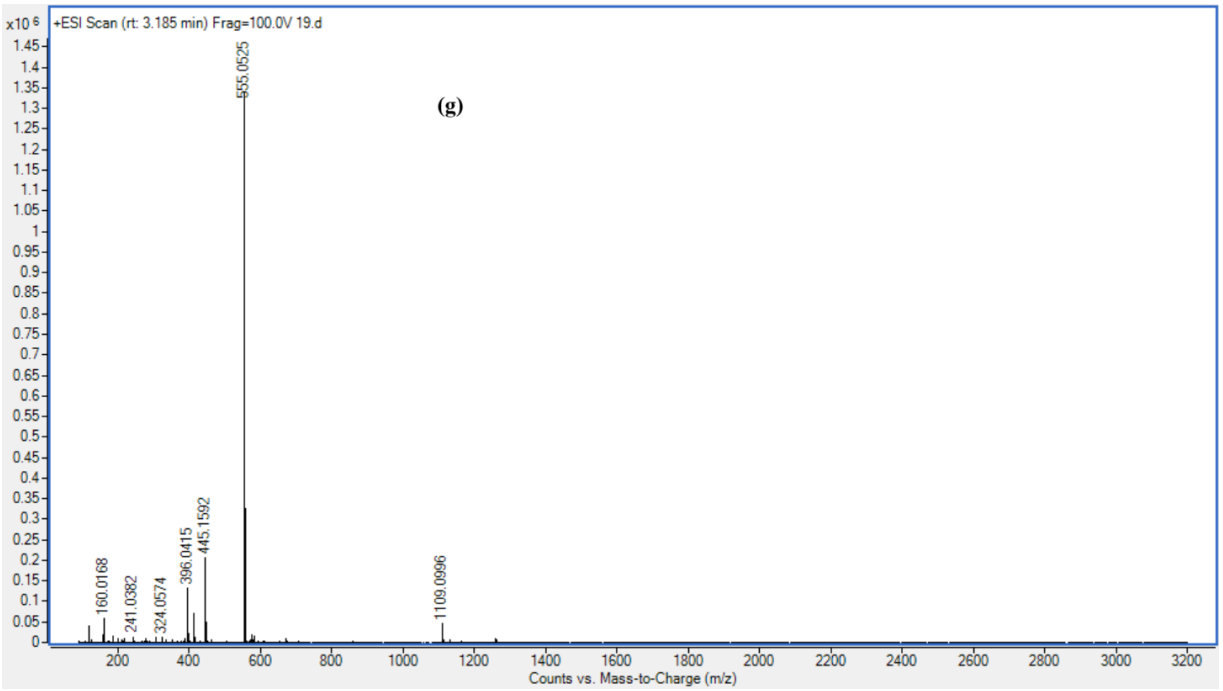
+ESI Scan (rt: 3.185 min) Frag=100.0V 19.d
x10 6
555.0525
160.0168
241.0382
324.0574
396.0415
445.1592
1109.0996
Counts vs. Mass-to-Charge (m/z)

(g)

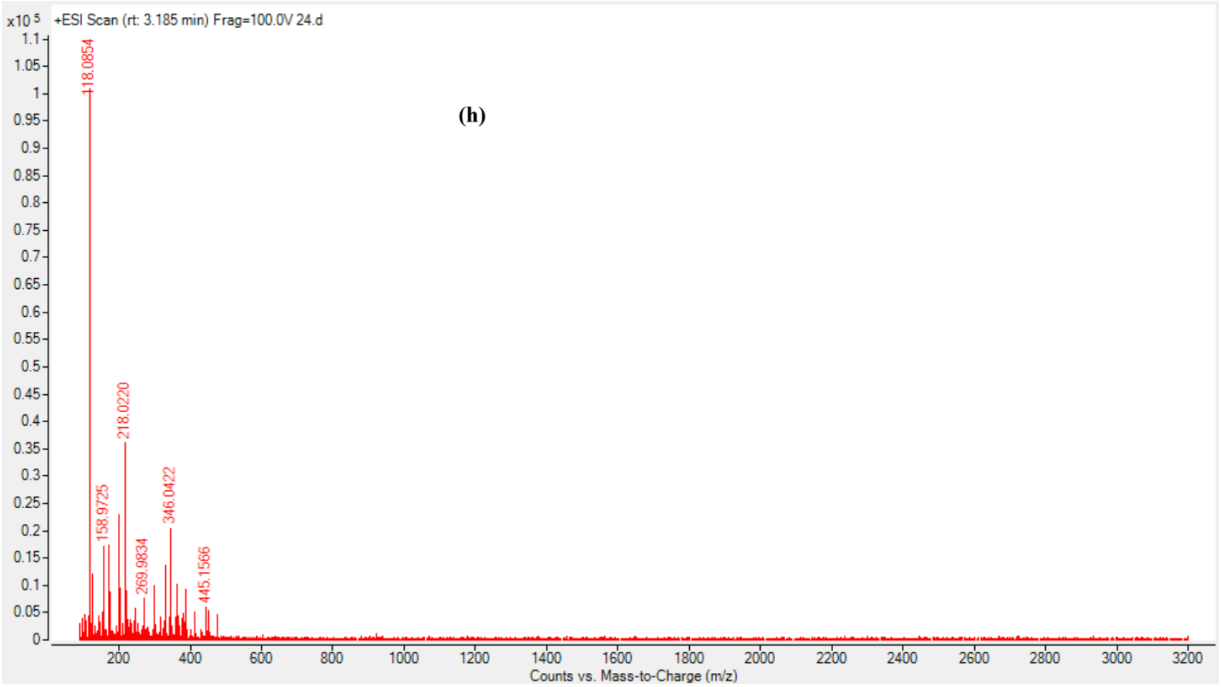
x10 5
+ESI Scan (rt: 3.185 min) Frag=100.0V 24.d
118.0854
218.0220
158.9725
346.0422
269.9834
445.1566
Counts vs. Mass-to-Charge (m/z)

(h)

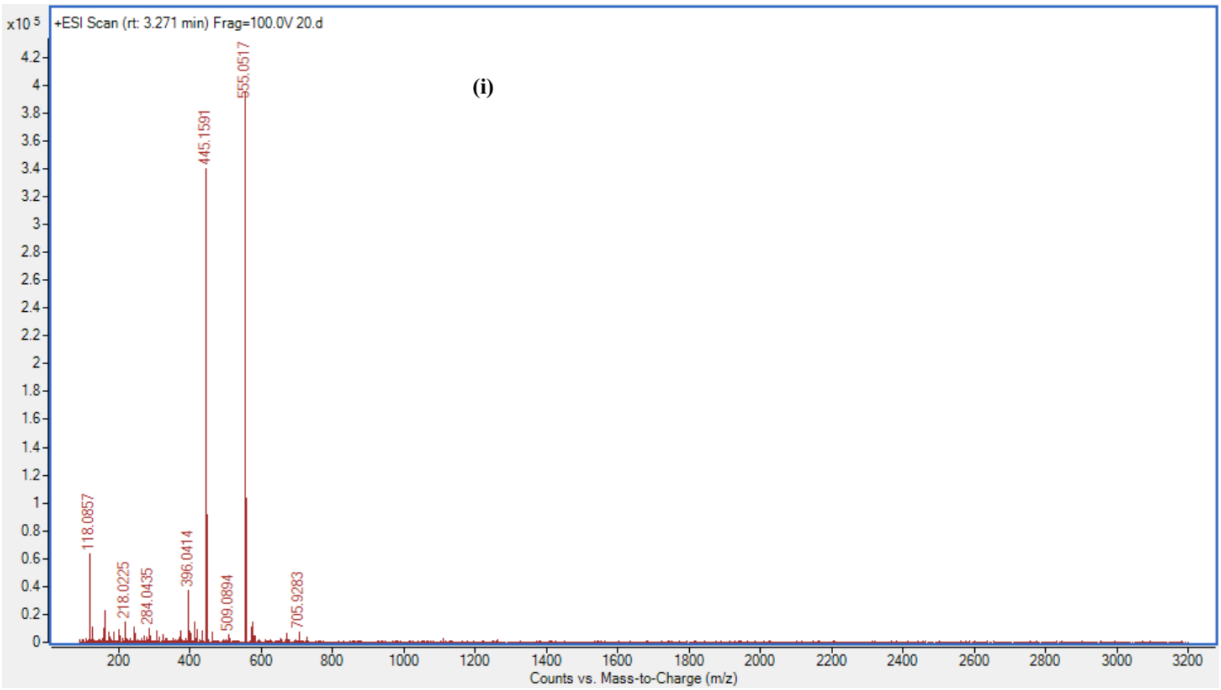
x10 5
+ESI Scan (rt: 3.271 min) Frag=100.0V 20.d
555.0517
445.1591
118.0857
396.0414
218.0225
284.0435
509.0894
705.9283
Counts vs. Mass-to-Charge (m/z)

(i)

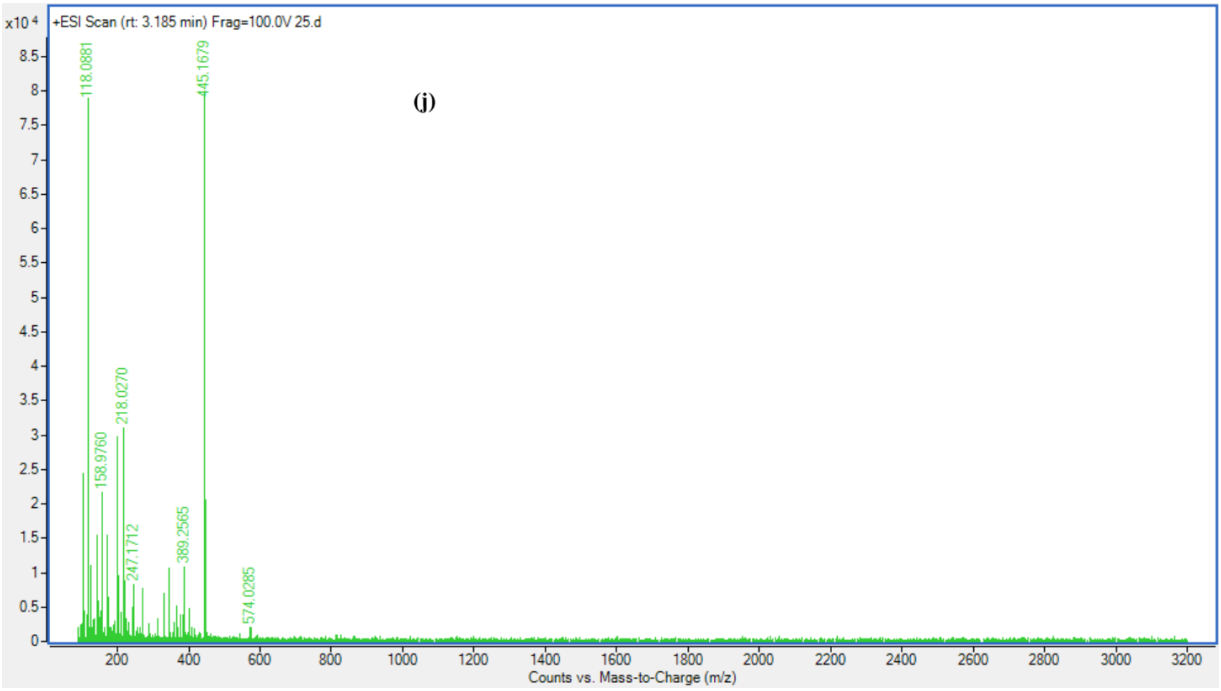

Fig S4. The LC-MS spectra of blank CEF and DOXY solutions at pH 3 (**a**), pH 5 (**c**), pH 7 (**e**), pH 9 (**g**), pH 11 (**i**), and the same solutions but after the adsorption using 5% Fe 5% Cu-TiO_2 at the same pH levels with the same order (**b**, **d**, **f**, **h**, and **j**) after 90 minutes. [C_o = 25 ppm, volume = 20 mL, dose = 0.01 g, stirring rate = 800 rpm, and T = 20 ± 2 °C].

Appendix 3.1. The UV-Visible spectra of the main CEF adsorption experiments in Chapter 3.

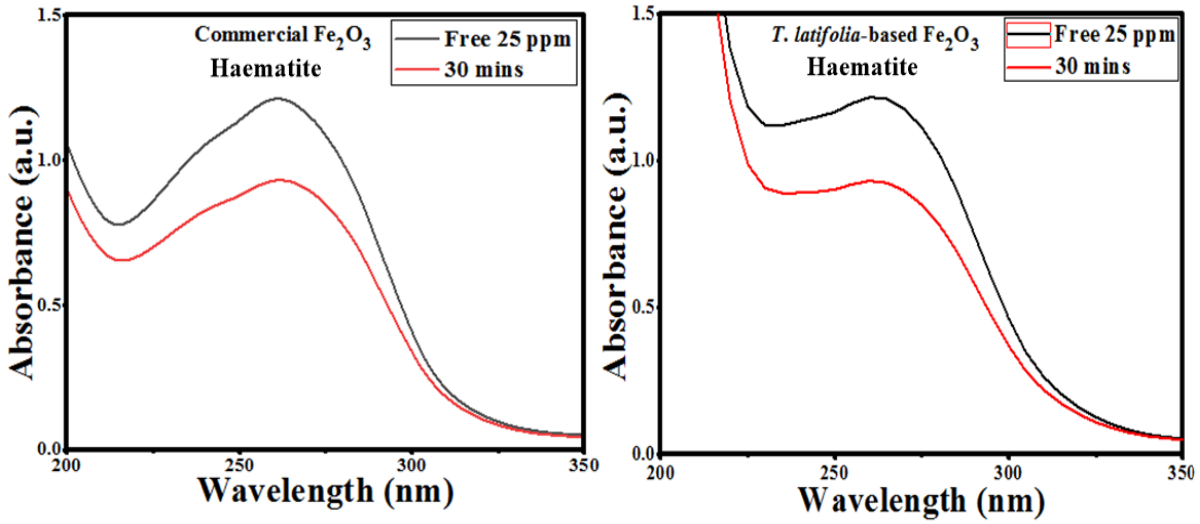

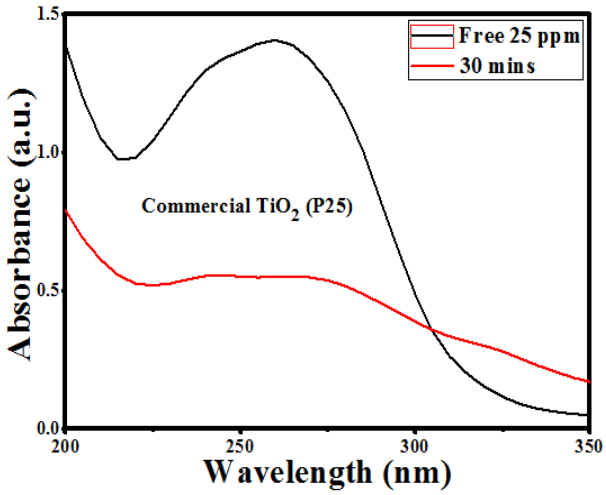
Free 25 ppm
30 mins
Commercial TiO2 (P25)
Absorbance (a.u.)
Wavelength (nm)
1.5
1.0
0.5
0.0
200
250
300
350

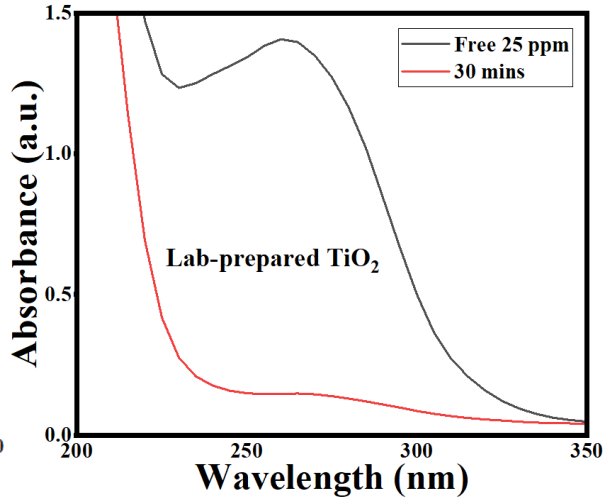
Free 25 ppm
30 mins
Lab-prepared TiO2
Absorbance (a.u.)
Wavelength (nm)
1.5
1.0
0.5
0.0
200
250
300
350

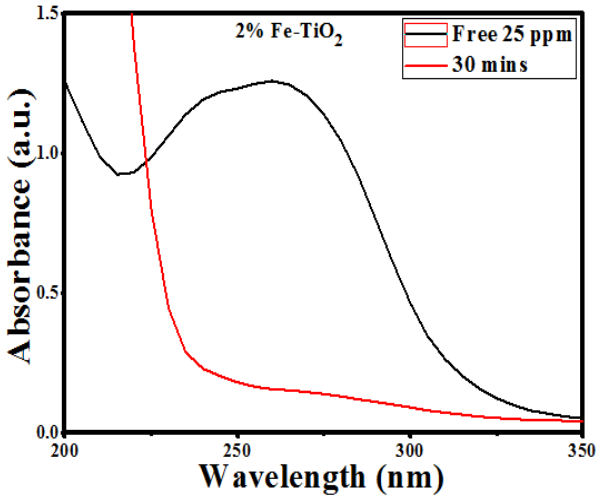
2% Fe-TiO2
Free 25 ppm
30 mins
Absorbance (a.u.)
Wavelength (nm)
1.5
1.0
0.5
0.0
200
250
300
350

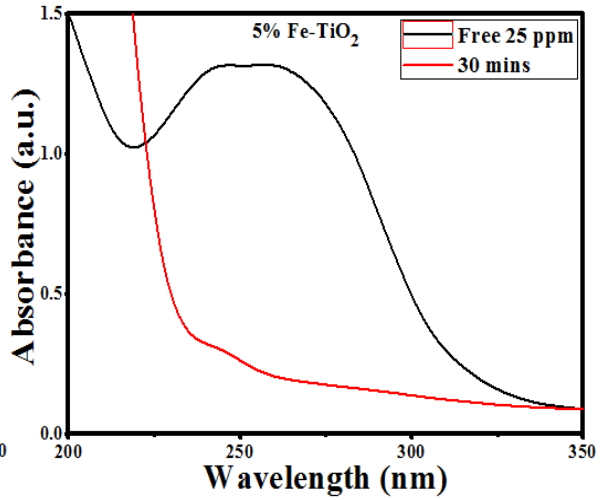
5% Fe-TiO2
Free 25 ppm
30 mins
Absorbance (a.u.)
Wavelength (nm)
1.5
1.0
0.5
0.0
200
250
300
350

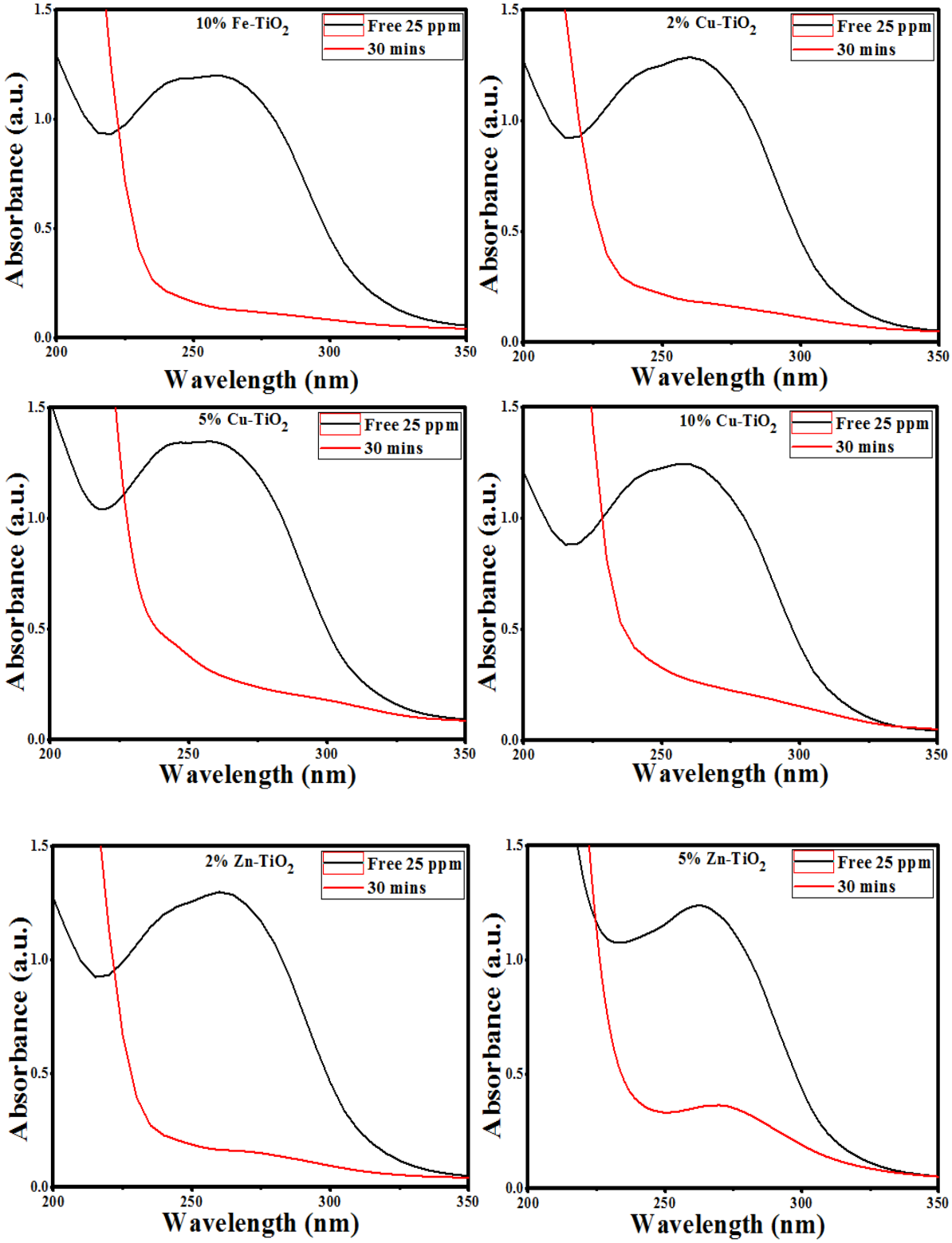
10% Fe-TiO2
Free 25 ppm
30 mins
Absorbance (a.u.)
Wavelength (nm)
2% Cu-TiO2
5% Cu-TiO2
10% Cu-TiO2
2% Zn-TiO2
5% Zn-TiO2

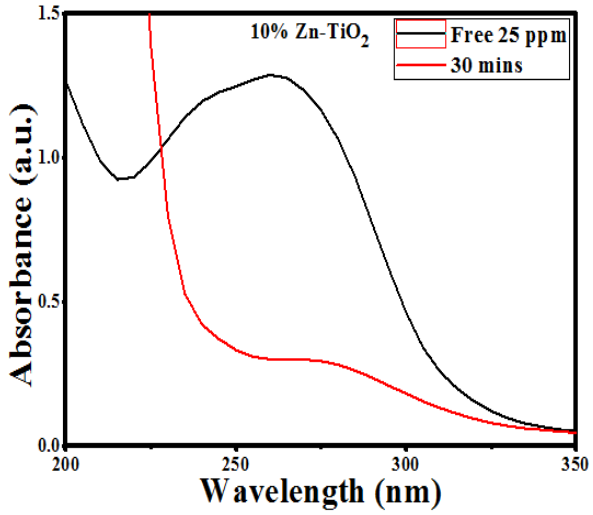
10% Zn-TiO2
Free 25 ppm
30 mins
Absorbance (a.u.)
Wavelength (nm)

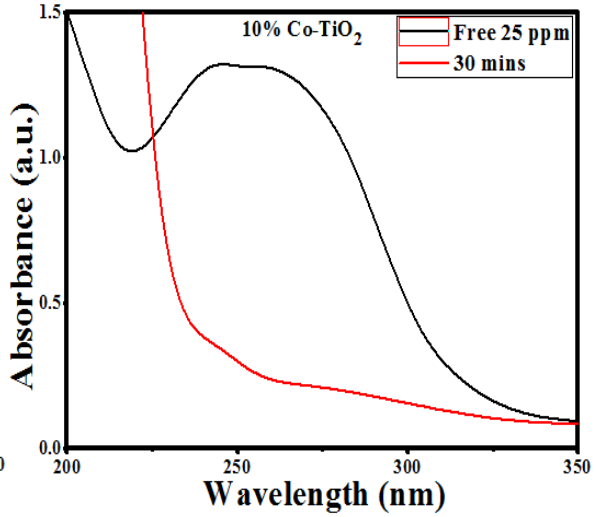
10% Co-TiO2
Free 25 ppm
30 mins
Absorbance (a.u.)
Wavelength (nm)

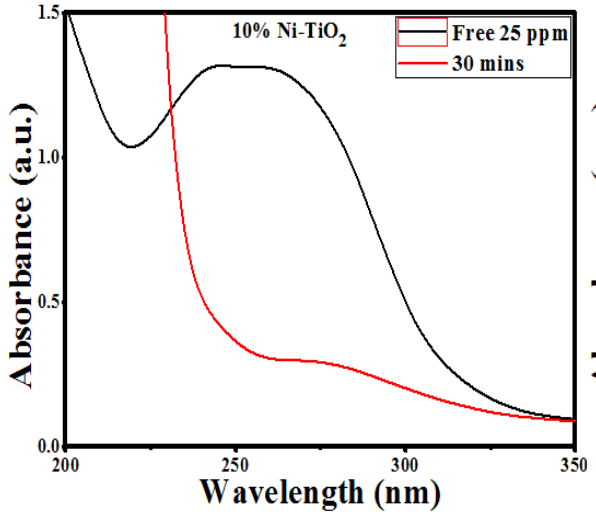
10% Ni-TiO2
Free 25 ppm
30 mins
Absorbance (a.u.)
Wavelength (nm)

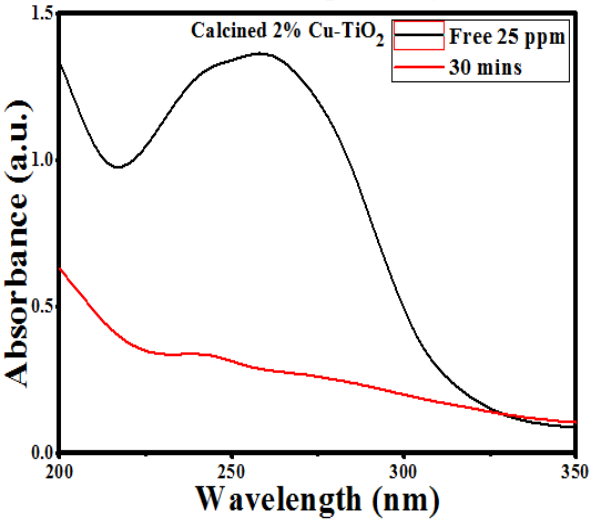
Calcined 2% Cu-TiO2
Free 25 ppm
30 mins
Absorbance (a.u.)
Wavelength (nm)

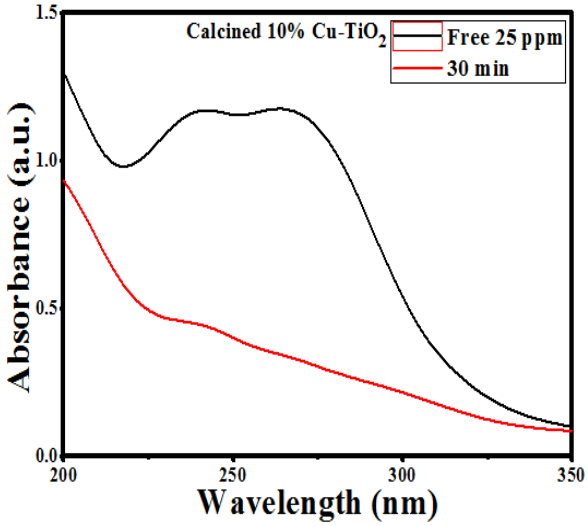
Calcined 10% Cu-TiO2
Free 25 ppm
30 min
Absorbance (a.u.)
Wavelength (nm)

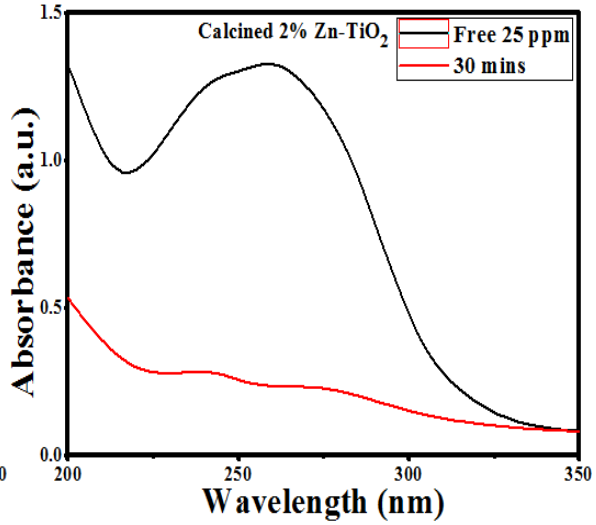
Calcined 2% Zn-TiO2
Free 25 ppm
30 mins
Absorbance (a.u.)
Wavelength (nm)

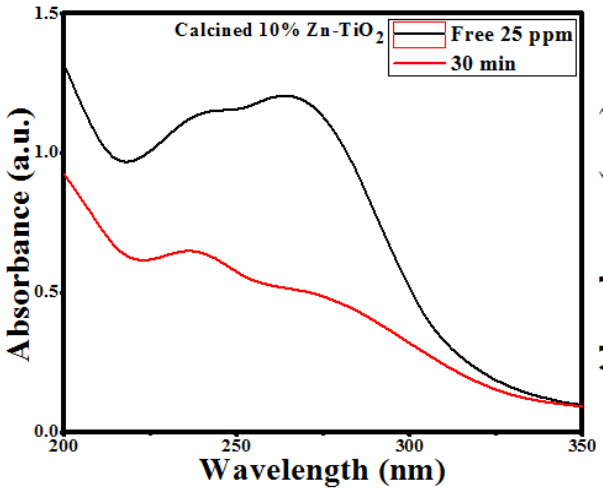
Calcined 10% Zn-TiO2
Free 25 ppm
30 min
Absorbance (a.u.)
Wavelength (nm)
0.0
0.5
1.0
1.5
200
250
300
350

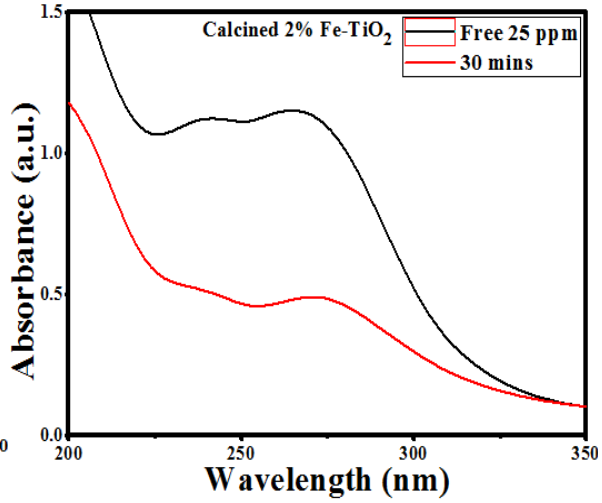
Calcined 2% Fe-TiO2
Free 25 ppm
30 mins
Absorbance (a.u.)
Wavelength (nm)
0.0
0.5
1.0
1.5
200
250
300
350

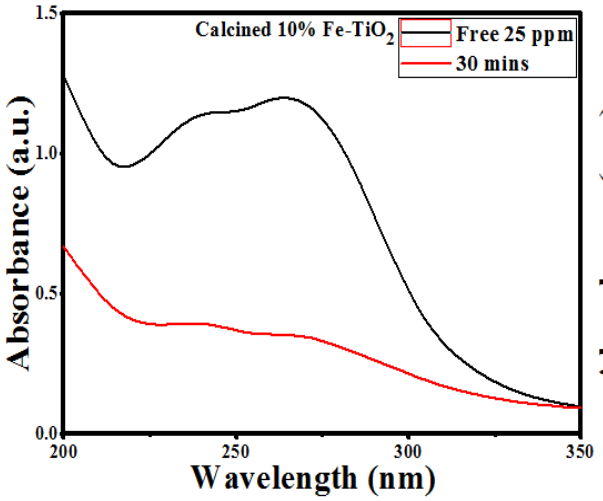
Calcined 10% Fe-TiO2
Free 25 ppm
30 mins
Absorbance (a.u.)
Wavelength (nm)
0.0
0.5
1.0
1.5
200
250
300
350

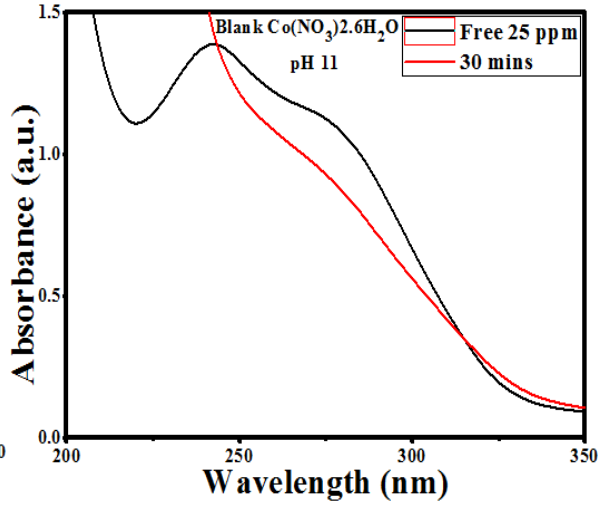
Blank Co(NO3)2.6H2O
pH 11
Free 25 ppm
30 mins
Absorbance (a.u.)
Wavelength (nm)
0.0
0.5
1.0
1.5
200
250
300
350

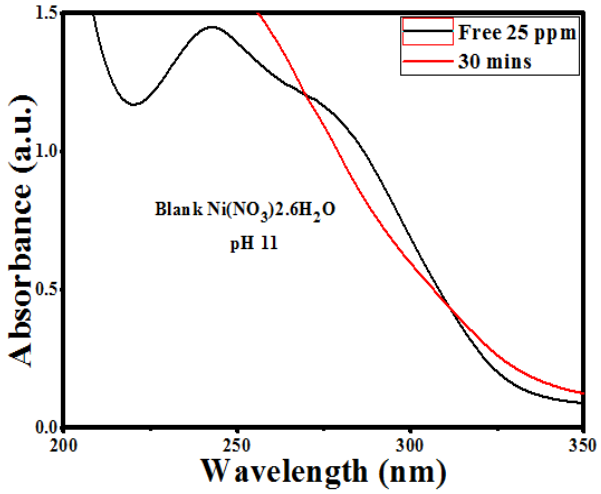
Free 25 ppm
30 mins
Blank Ni(NO3)2.6H2O
pH 11
Absorbance (a.u.)
Wavelength (nm)

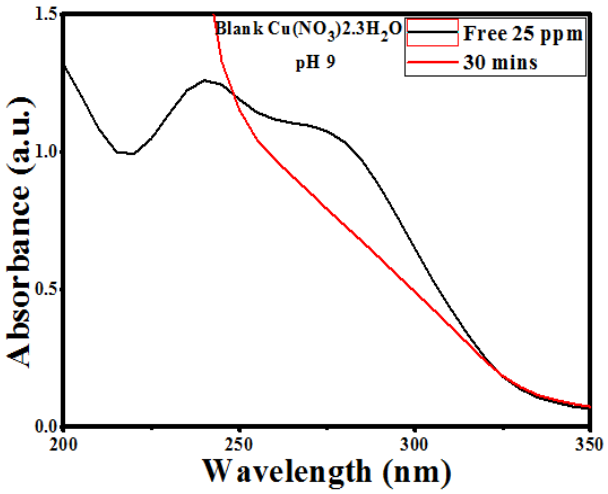
Blank Cu(NO3)2.3H2O
pH 9
Free 25 ppm
30 mins
Absorbance (a.u.)
Wavelength (nm)

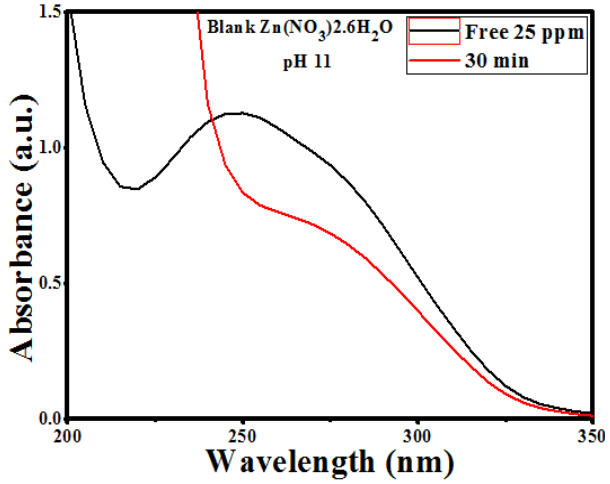
Blank Zn(NO3)2.6H2O
pH 11
Free 25 ppm
30 min
Absorbance (a.u.)
Wavelength (nm)

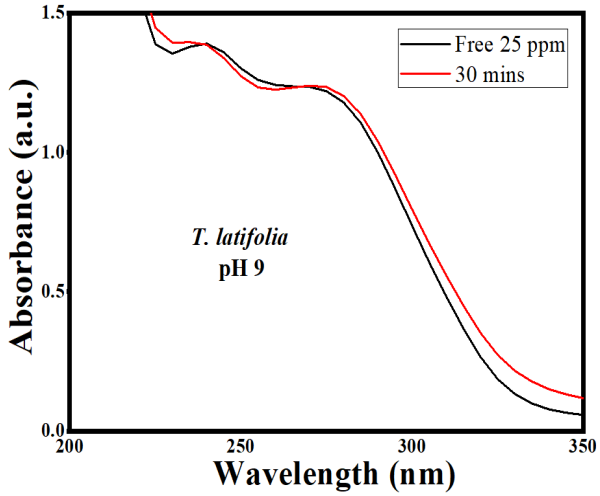
Free 25 ppm
30 mins
T. latifolia
pH 9
Absorbance (a.u.)
Wavelength (nm)

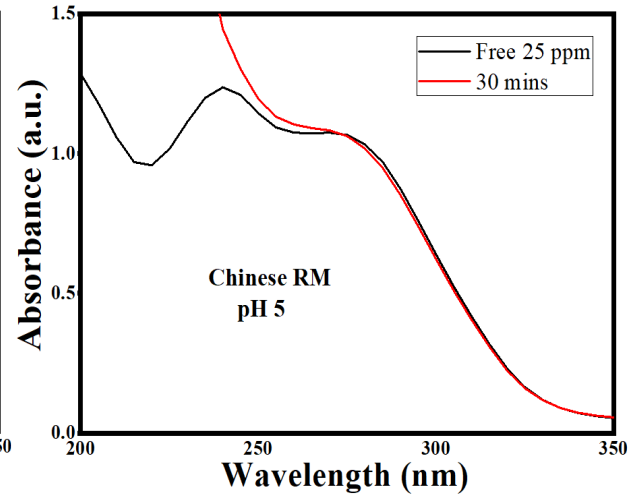
Free 25 ppm
30 mins
Chinese RM
pH 5
Absorbance (a.u.)
Wavelength (nm)

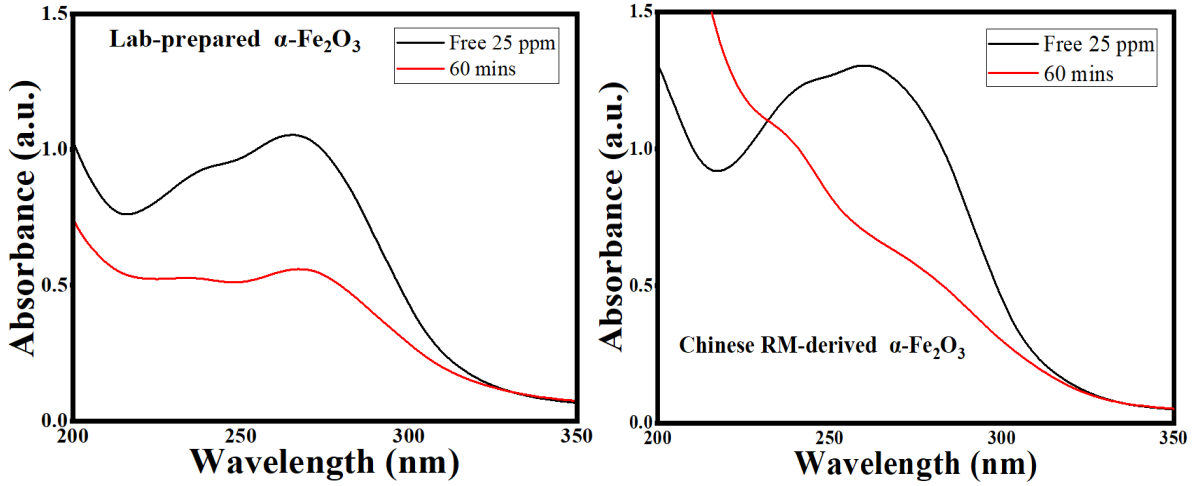

Fig S5. The UV-Visible spectra of the main adsorption experiments [C_o = 25 ppm, pH = 3, stirring rate = 800 rpm, T = 20 ± 2 °C, volume = 20 mL, and dose = 0.01 g]. Other pH levels are shown and indicated in the figures' labels where the highest removal efficacy was observed.

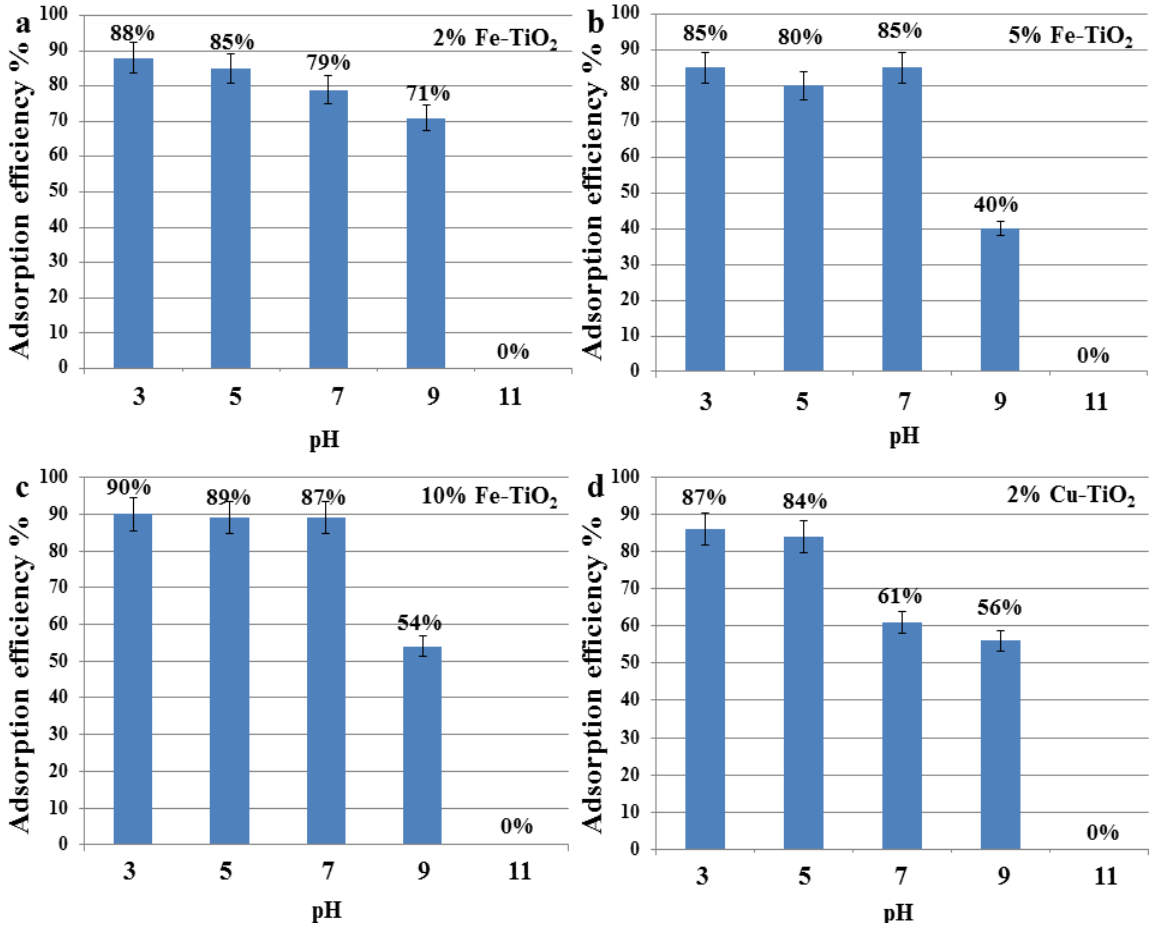

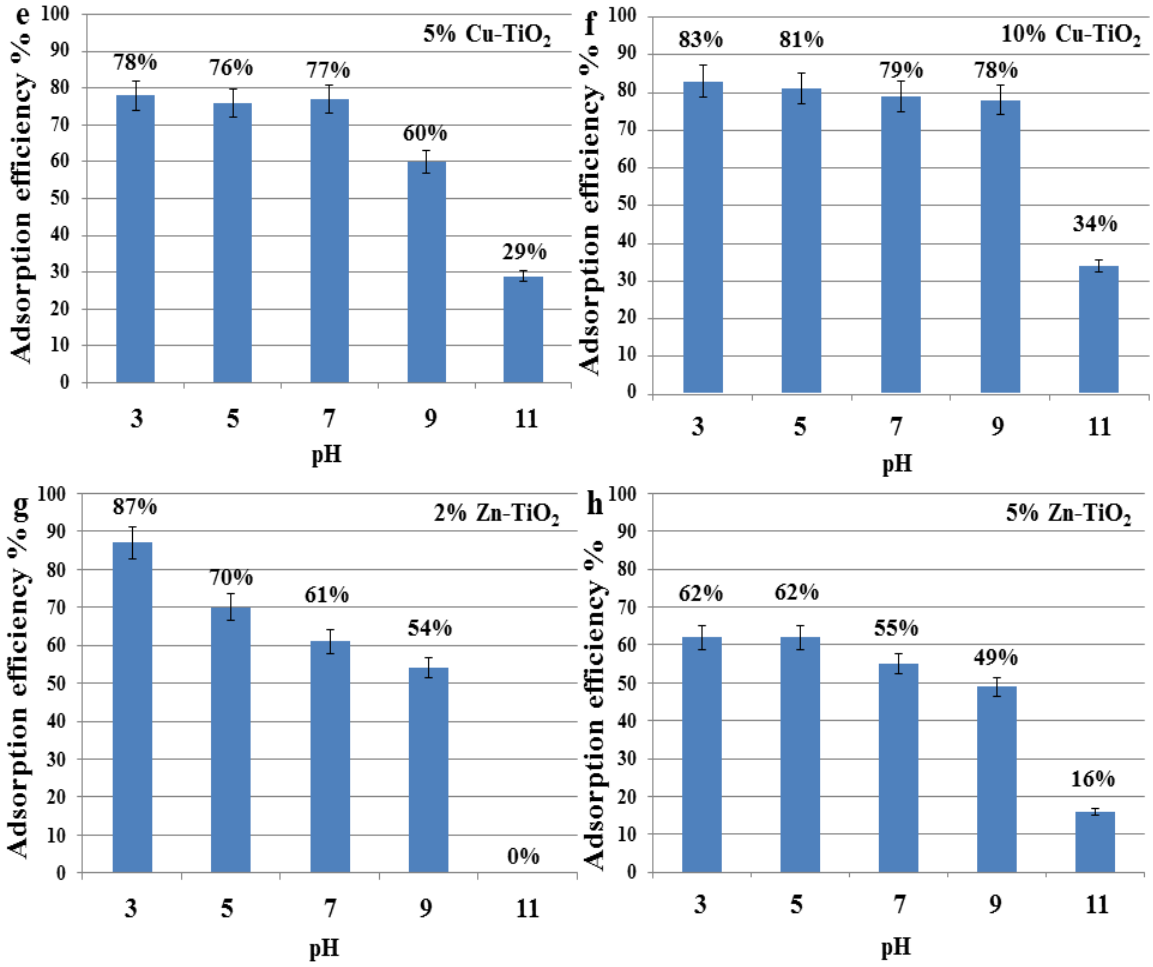
e
5% Cu-TiO2
Adsorption efficiency %
78%
76%
77%
60%
29%
pH
f
10% Cu-TiO2
Adsorption efficiency %
83%
81%
79%
78%
34%
pH
g
2% Zn-TiO2
Adsorption efficiency %
87%
70%
61%
54%
0%
pH
h
5% Zn-TiO2
Adsorption efficiency %
62%
62%
55%
49%
16%
pH

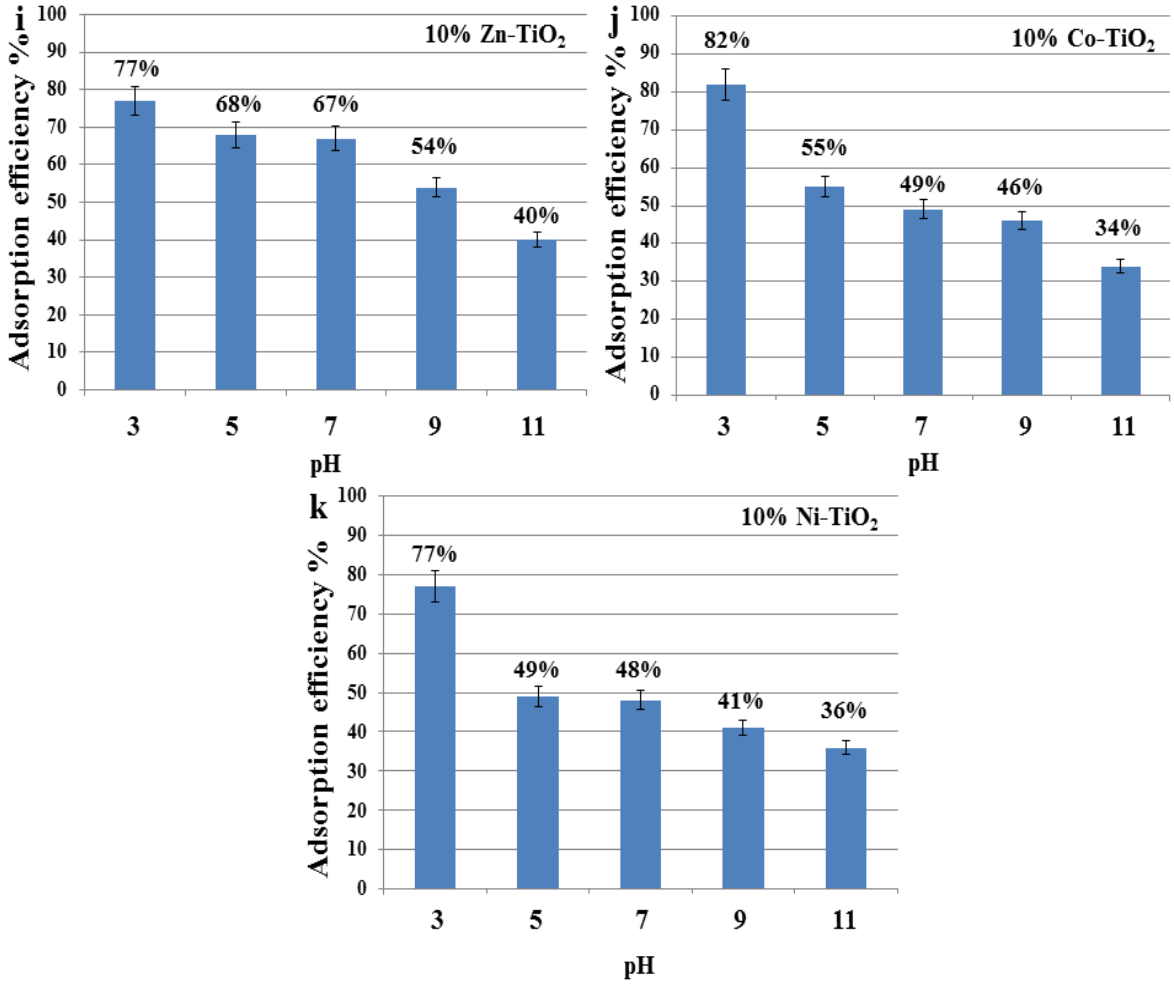

Fig S6. CEF adsorption efficiency by 2% Fe-TiO_2 **(a)**, 5% Fe-TiO_2 **(b)**, 10% Fe-TiO_2 **(c)**, 2% Cu-TiO_2 **(d)**, 5% Cu-TiO_2 **(e)**, 10% Cu-TiO_2 **(f)**, 2% Zn-TiO_2 **(g)**, 5% Zn-TiO_2 **(h)**, 10% Zn-TiO_2 **(i)**, 10% Co-TiO_2 **(j)**, and 10% Ni-TiO_2 **(k)** using Lab-prepared TiO_2. [C_o = 25 ppm, stirring rate = 800 rpm, T = 20 ± 2 °C, volume = 20 mL, and dose = 0.01 g].

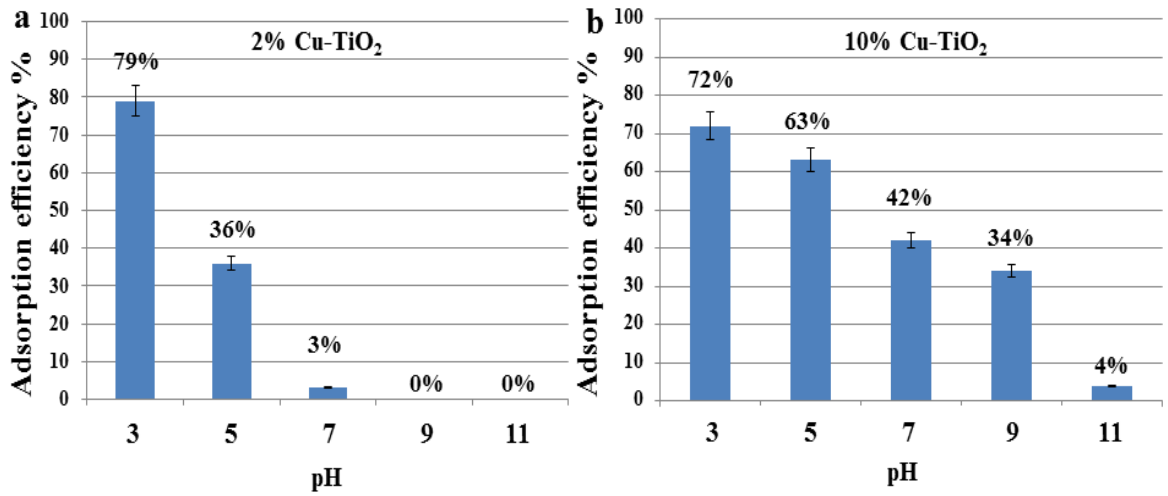

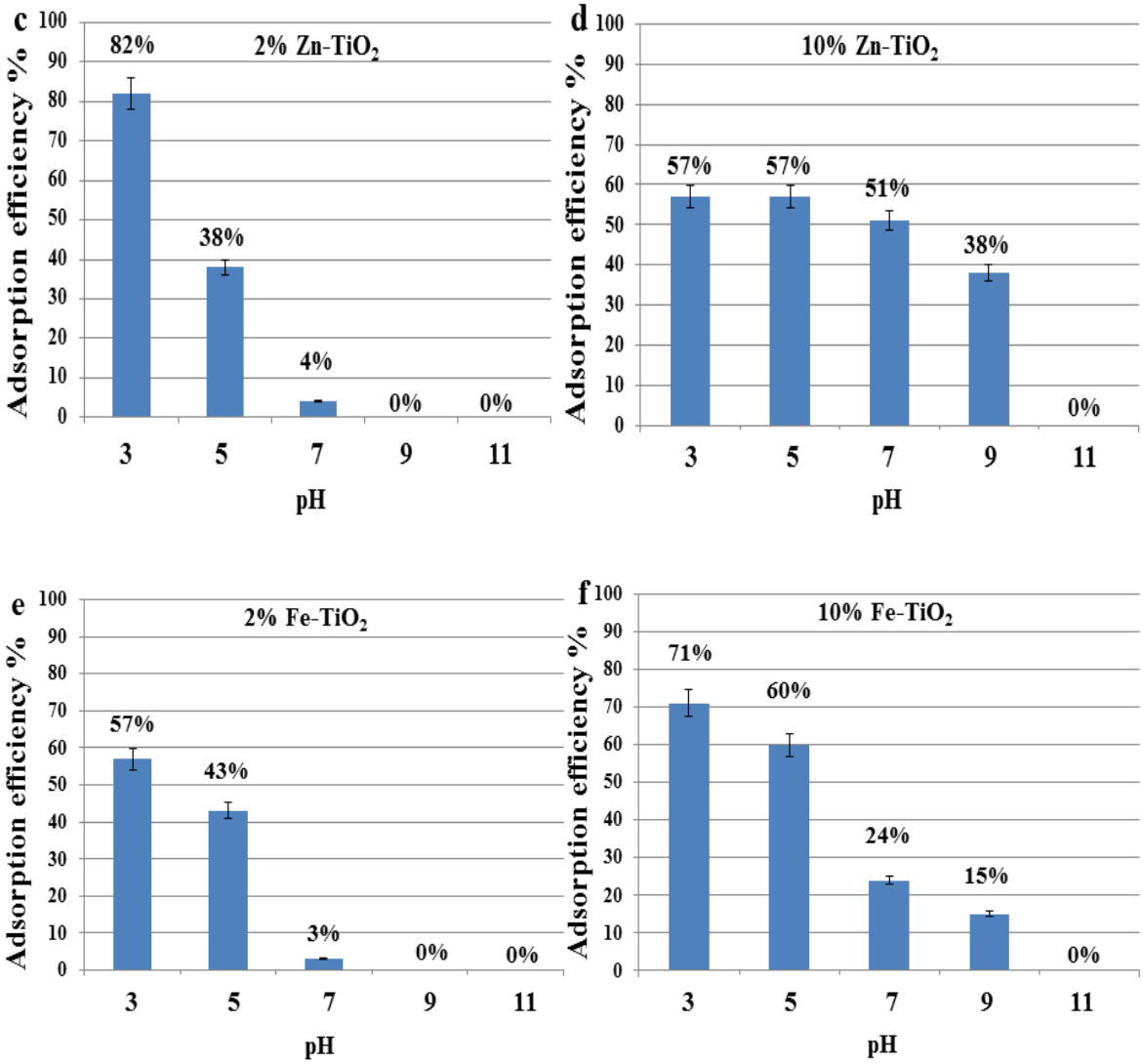

Fig S7. CEF adsorption efficiency by 2% Cu-TiO_2 **(a)**, 10% Cu-TiO_2 **(b)**, 2% Zn-TiO_2 **(c)**, 10% Zn-TiO_2 **(d)**, 2% Fe-TiO_2 **(e)**, and 10% Fe-TiO_2 **(f)** after calcination using Lab-prepared TiO_2. [C_o = 25 ppm, stirring rate = 800 rpm, T = 20 ± 2 °C, volume = 20 mL, and dose = 0.01 g].

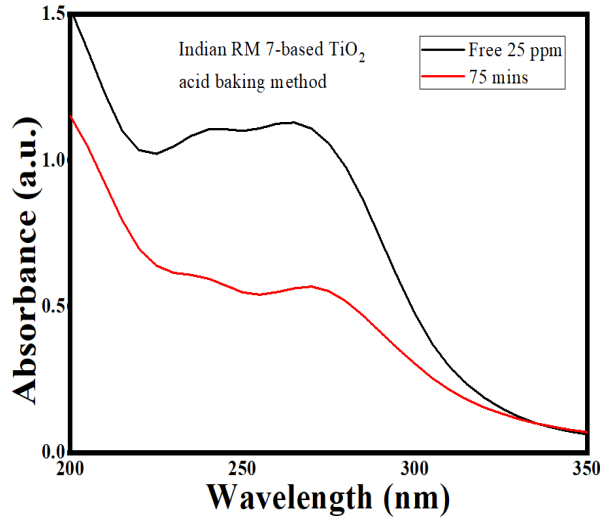
Indian RM 7-based TiO2
acid baking method
Free 25 ppm
75 mins
Absorbance (a.u.)
Wavelength (nm)

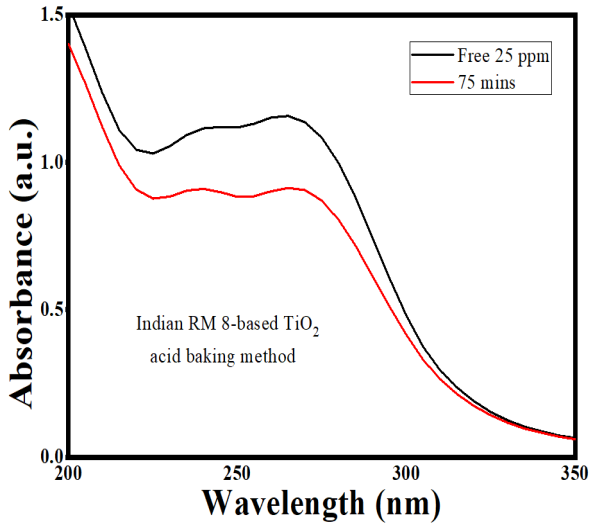
Free 25 ppm
75 mins
Indian RM 8-based TiO2
acid baking method
Absorbance (a.u.)
Wavelength (nm)

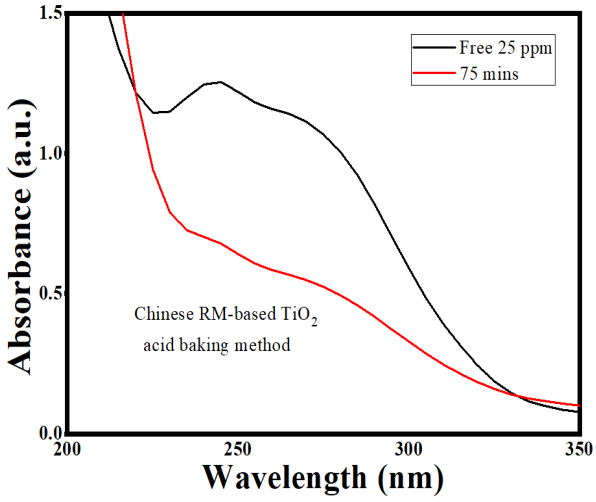
Free 25 ppm
75 mins
Chinese RM-based TiO2
acid baking method
Absorbance (a.u.)
Wavelength (nm)

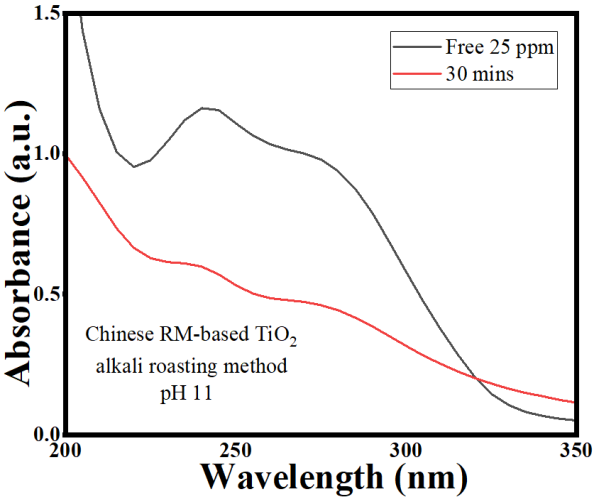
Free 25 ppm
30 mins
Chinese RM-based TiO2
alkali roasting method
pH 11
Absorbance (a.u.)
Wavelength (nm)

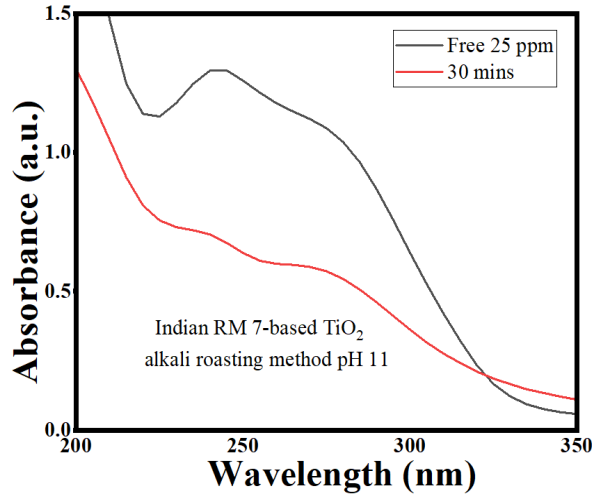
Free 25 ppm
30 mins
Indian RM 7-based TiO2
alkali roasting method pH 11
Absorbance (a.u.)
Wavelength (nm)

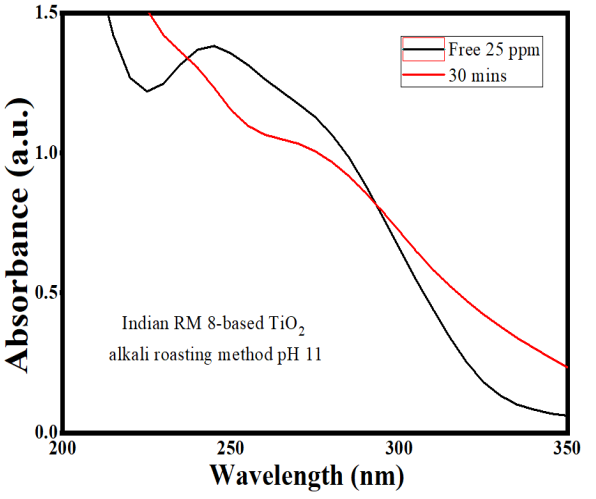
Free 25 ppm
30 mins
Indian RM 8-based TiO2
alkali roasting method pH 11
Absorbance (a.u.)
Wavelength (nm)

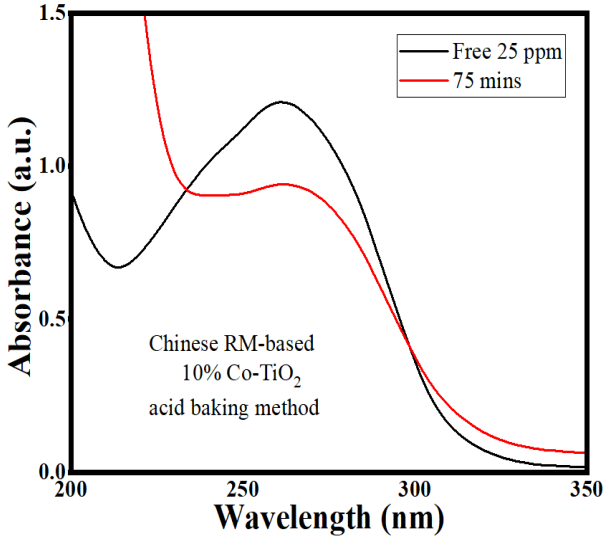
Free 25 ppm
75 mins
Absorbance (a.u.)
Wavelength (nm)
Chinese RM-based
10% Co-TiO2
acid baking method

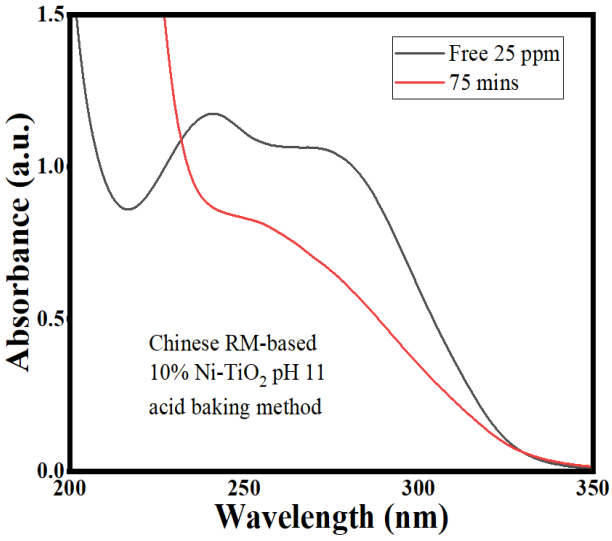
Free 25 ppm
75 mins
Absorbance (a.u.)
Wavelength (nm)
Chinese RM-based
10% Ni-TiO2 pH 11
acid baking method

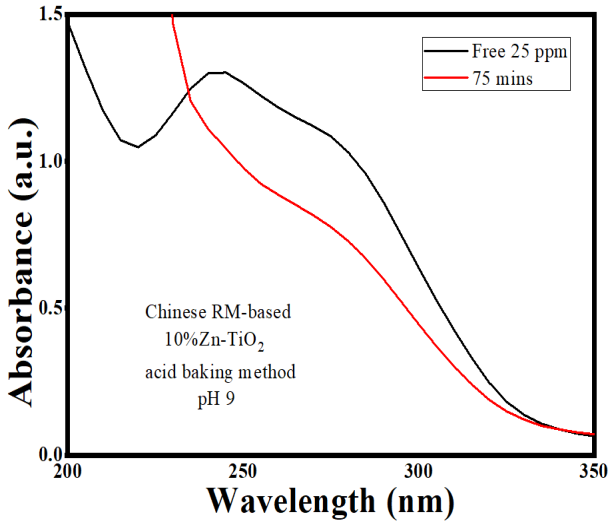
Free 25 ppm
75 mins
Absorbance (a.u.)
Wavelength (nm)
Chinese RM-based
10%Zn-TiO2
acid baking method
pH 9

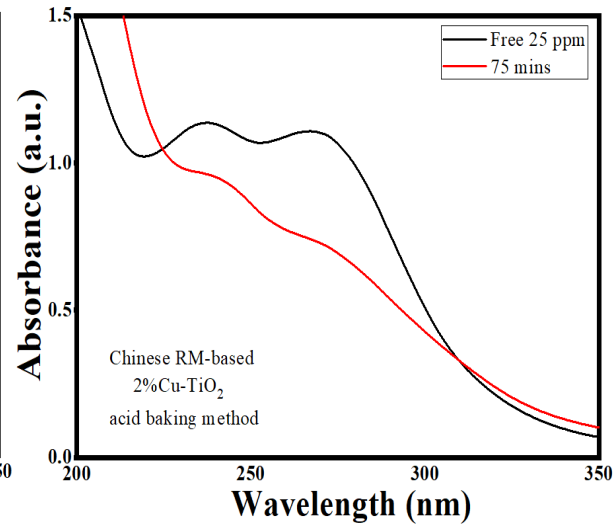
Free 25 ppm
75 mins
Absorbance (a.u.)
Wavelength (nm)
Chinese RM-based
2%Cu-TiO2
acid baking method

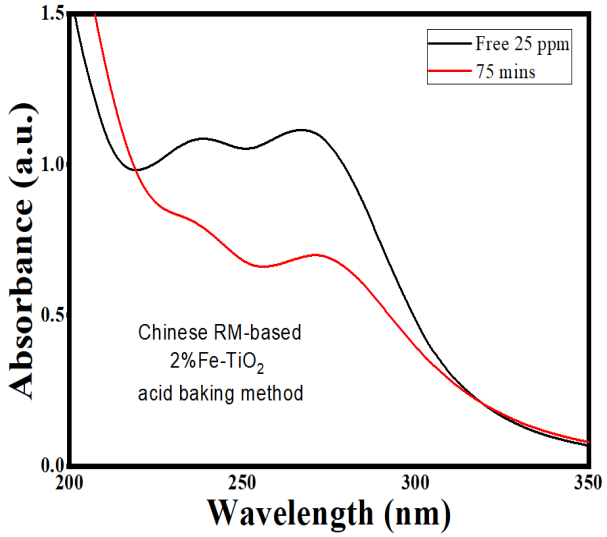
Free 25 ppm
75 mins
Absorbance (a.u.)
Wavelength (nm)
Chinese RM-based
2%Fe-TiO2
acid baking method

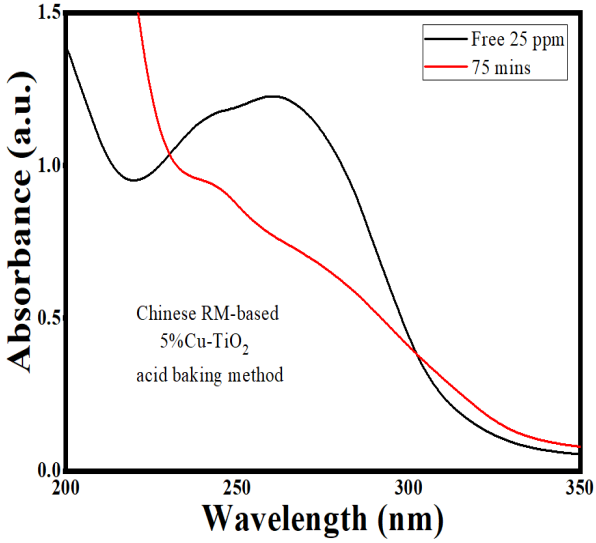
Free 25 ppm
75 mins
Absorbance (a.u.)
Wavelength (nm)
Chinese RM-based
5%Cu-TiO2
acid baking method

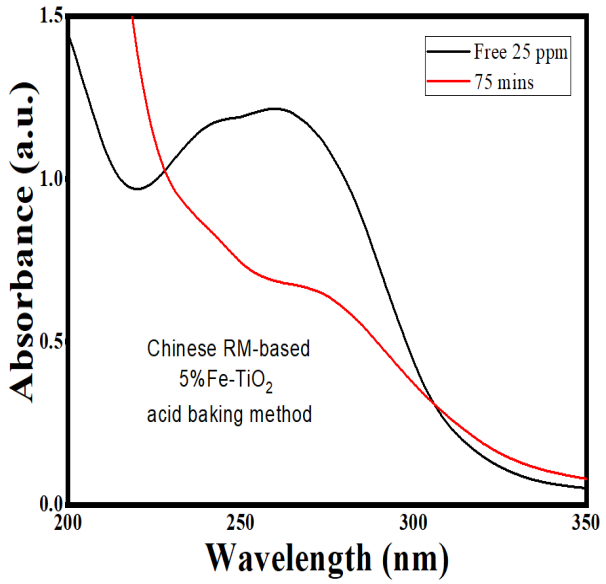
Free 25 ppm
75 mins
Chinese RM-based
5%Fe-TiO2
acid baking method
Absorbance (a.u.)
Wavelength (nm)
1.5
1.0
0.5
0.0
200
250
300
350

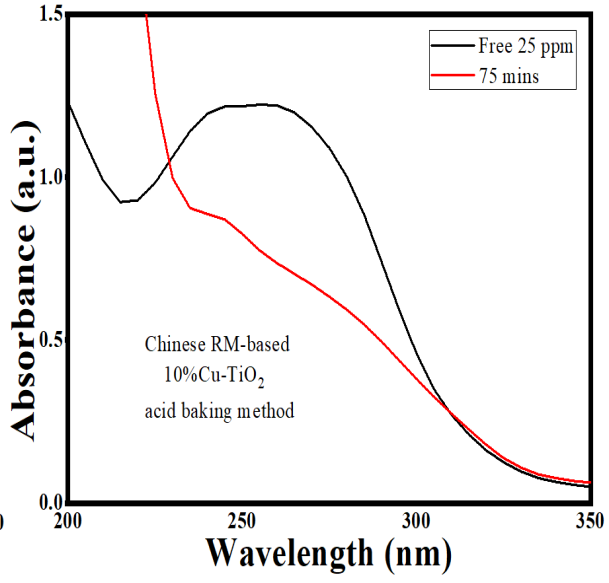
Free 25 ppm
75 mins
Chinese RM-based
10%Cu-TiO2
acid baking method
Absorbance (a.u.)
Wavelength (nm)
1.5
1.0
0.5
0.0
200
250
300
350

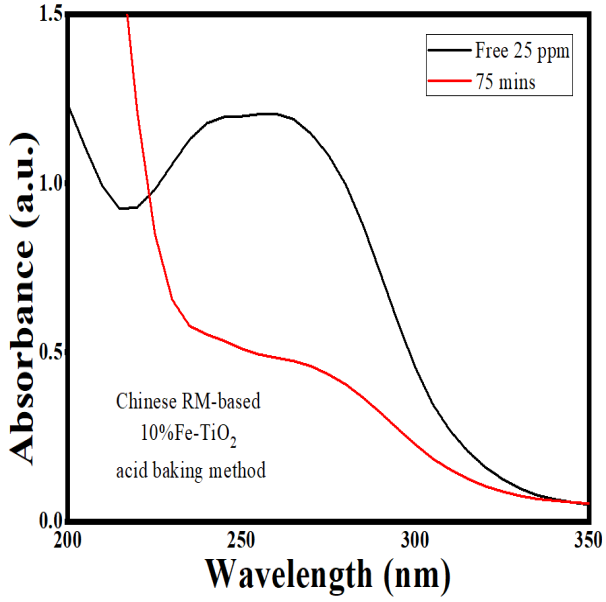
Free 25 ppm
75 mins
Chinese RM-based
10%Fe-TiO2
acid baking method
Absorbance (a.u.)
Wavelength (nm)
1.5
1.0
0.5
0.0
200
250
300
350

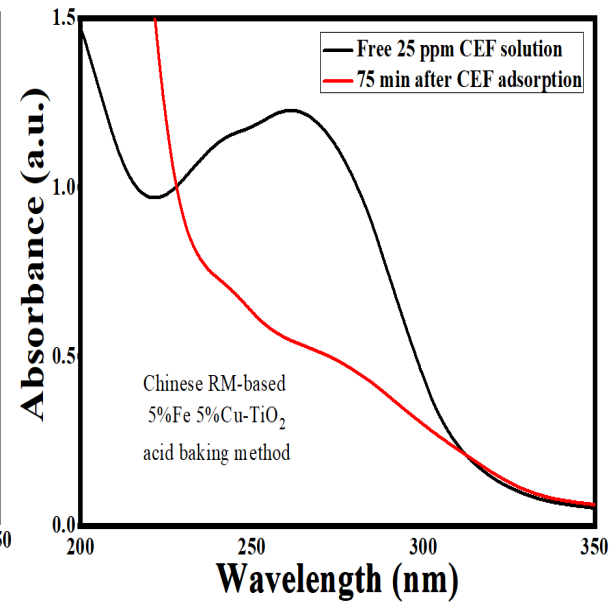
Free 25 ppm CEF solution
75 min after CEF adsorption
Chinese RM-based
5%Fe 5%Cu-TiO2
acid baking method
Absorbance (a.u.)
Wavelength (nm)
1.5
1.0
0.5
0.0
200
250
300
350

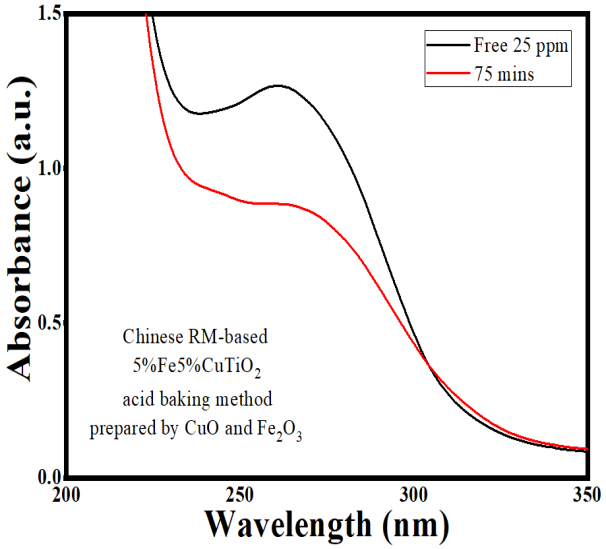
Free 25 ppm
75 mins
Chinese RM-based
5%Fe5%CuTiO2
acid baking method
prepared by CuO and Fe2O3
Absorbance (a.u.)
Wavelength (nm)

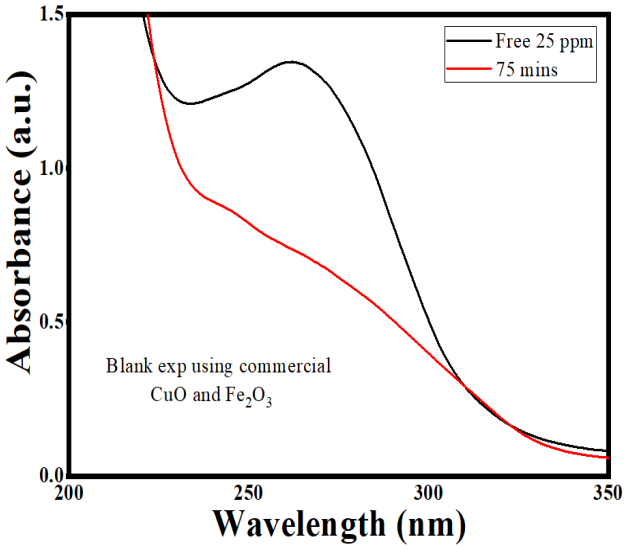
Free 25 ppm
75 mins
Blank exp using commercial
CuO and Fe2O3
Absorbance (a.u.)
Wavelength (nm)

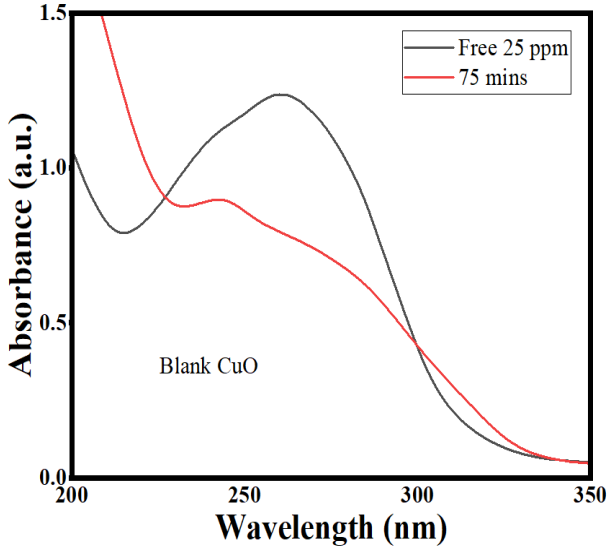
Free 25 ppm
75 mins
Blank CuO
Absorbance (a.u.)
Wavelength (nm)

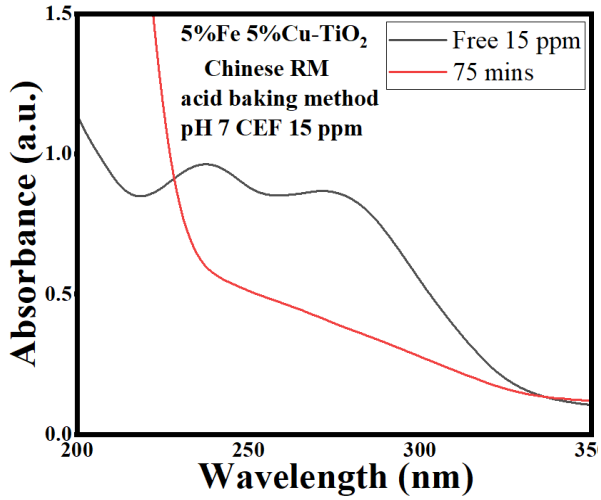
5%Fe 5%Cu-TiO2
Chinese RM
acid baking method
pH 7 CEF 15 ppm
Free 15 ppm
75 mins
Absorbance (a.u.)
Wavelength (nm)

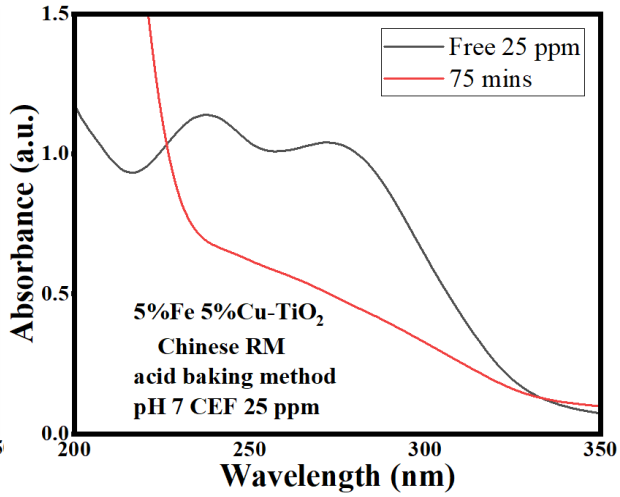
Free 25 ppm
75 mins
5%Fe 5%Cu-TiO2
Chinese RM
acid baking method
pH 7 CEF 25 ppm
Absorbance (a.u.)
Wavelength (nm)

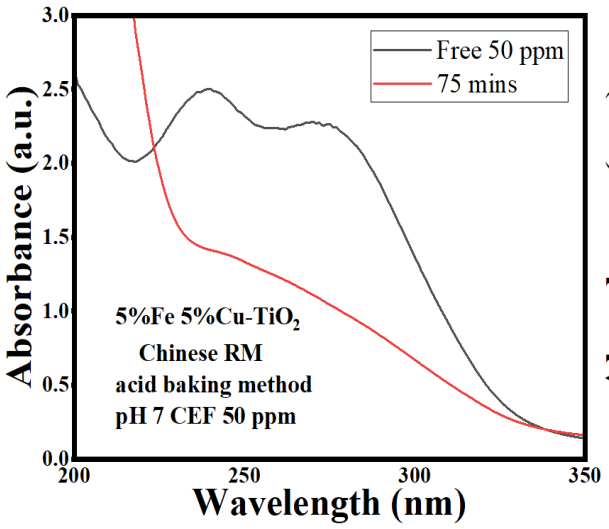
Free 50 ppm
75 mins
5%Fe 5%Cu-TiO2
Chinese RM
acid baking method
pH 7 CEF 50 ppm
Absorbance (a.u.)
Wavelength (nm)

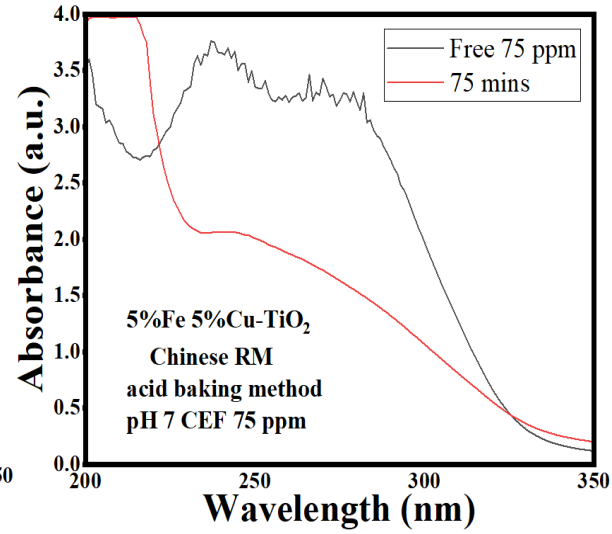
Free 75 ppm
75 mins
5%Fe 5%Cu-TiO2
Chinese RM
acid baking method
pH 7 CEF 75 ppm
Absorbance (a.u.)
Wavelength (nm)

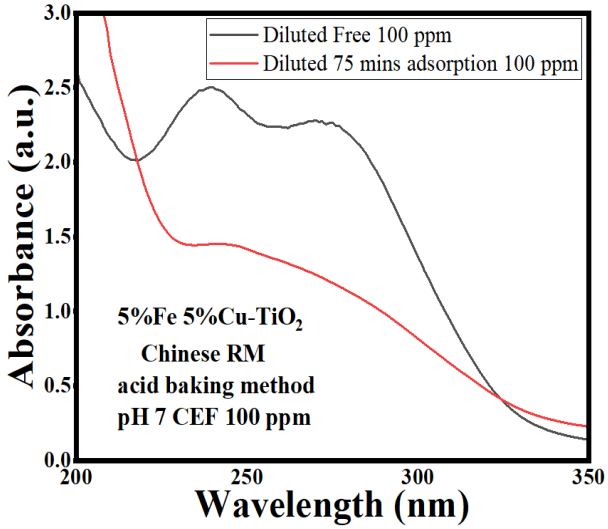
Diluted Free 100 ppm
Diluted 75 mins adsorption 100 ppm
5%Fe 5%Cu-TiO2
Chinese RM
acid baking method
pH 7 CEF 100 ppm
Absorbance (a.u.)
Wavelength (nm)

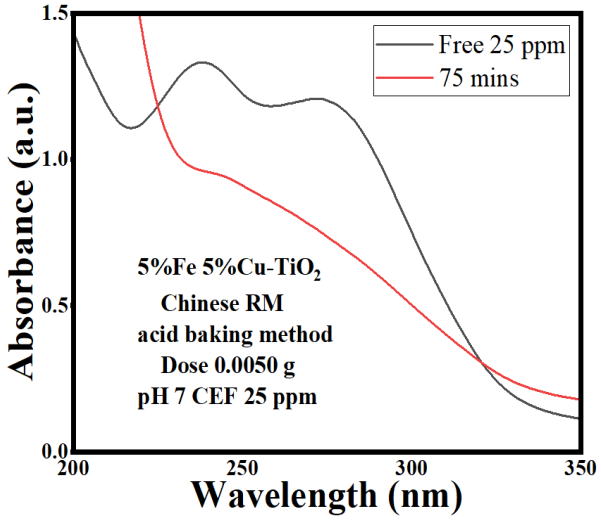
Free 25 ppm
75 mins
5%Fe 5%Cu-TiO2
Chinese RM
acid baking method
Dose 0.0050 g
pH 7 CEF 25 ppm
Absorbance (a.u.)
Wavelength (nm)

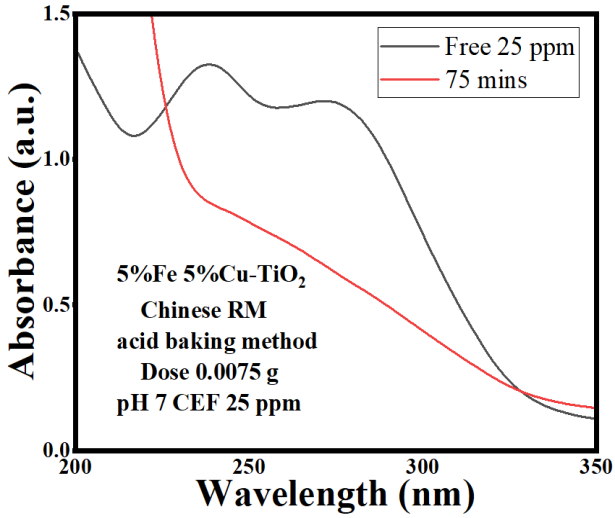
Free 25 ppm
75 mins
5%Fe 5%Cu-TiO2
Chinese RM
acid baking method
Dose 0.0075 g
pH 7 CEF 25 ppm
Absorbance (a.u.)
Wavelength (nm)

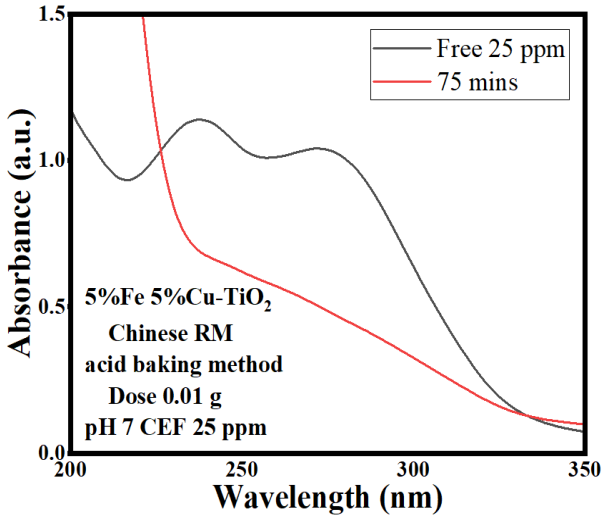
Free 25 ppm
75 mins
5%Fe 5%Cu-TiO2
Chinese RM
acid baking method
Dose 0.01 g
pH 7 CEF 25 ppm
Absorbance (a.u.)
Wavelength (nm)

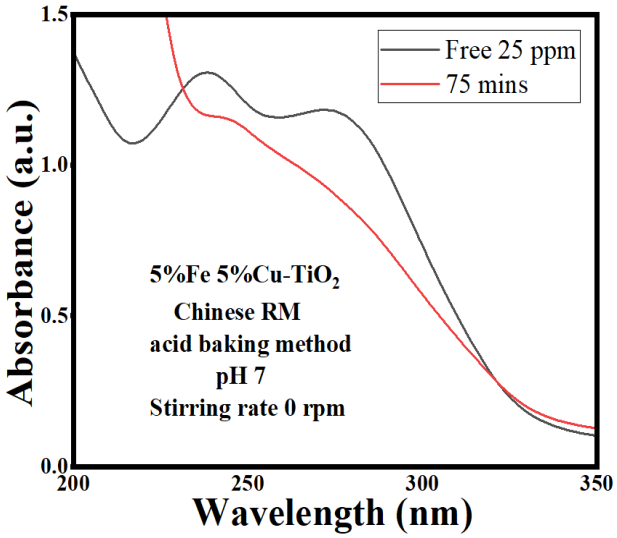
Free 25 ppm
75 mins
5%Fe 5%Cu-TiO2
Chinese RM
acid baking method
pH 7
Stirring rate 0 rpm
Absorbance (a.u.)
Wavelength (nm)

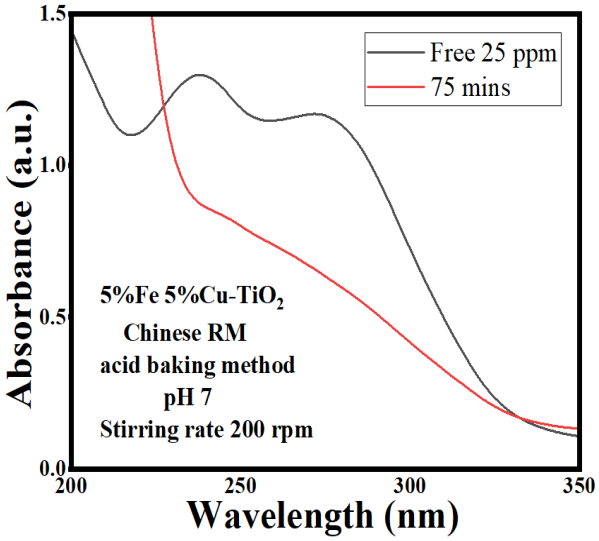
Free 25 ppm
75 mins
5%Fe 5%Cu-TiO2
Chinese RM
acid baking method
pH 7
Stirring rate 200 rpm
Absorbance (a.u.)
Wavelength (nm)

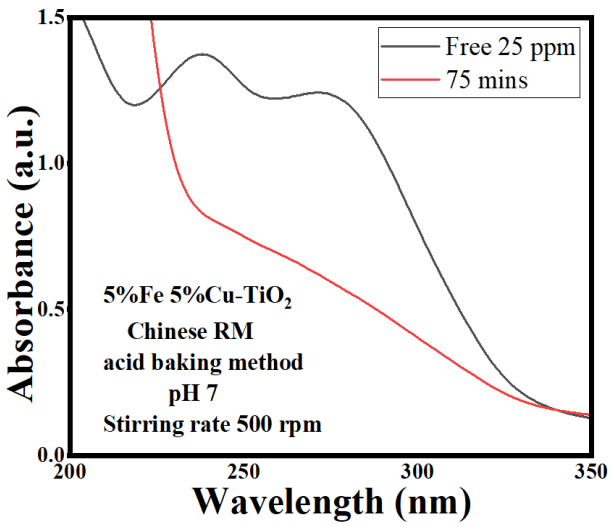
Free 25 ppm
75 mins
5%Fe 5%Cu-TiO2
Chinese RM
acid baking method
pH 7
Stirring rate 500 rpm
Absorbance (a.u.)
Wavelength (nm)

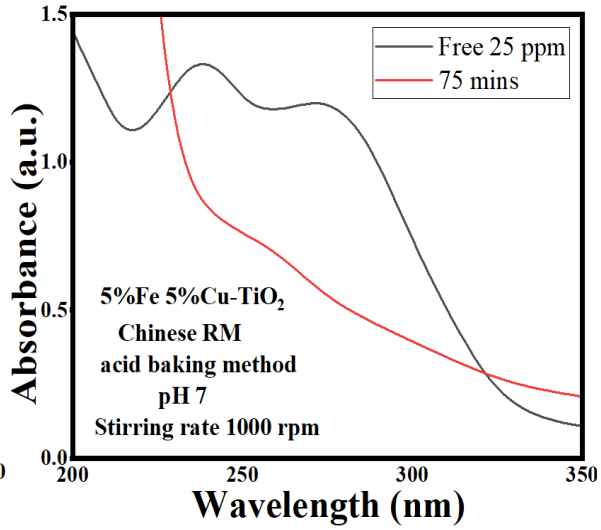
Free 25 ppm
75 mins
5%Fe 5%Cu-TiO2
Chinese RM
acid baking method
pH 7
Stirring rate 1000 rpm
Absorbance (a.u.)
Wavelength (nm)

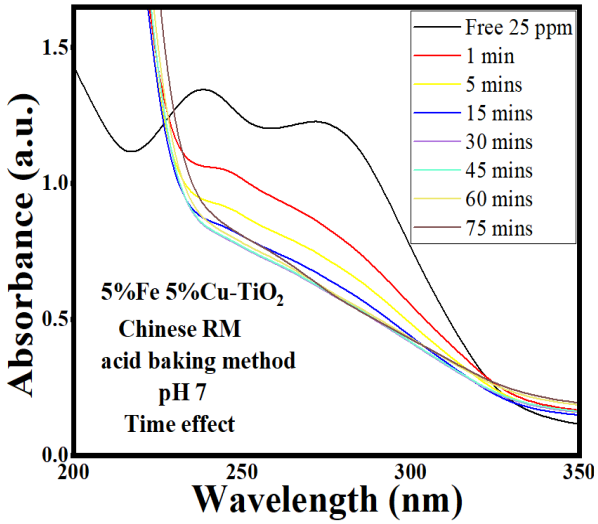
Free 25 ppm
1 min
5 mins
15 mins
30 mins
45 mins
60 mins
75 mins
5%Fe 5%Cu-TiO2
Chinese RM
acid baking method
pH 7
Time effect
Absorbance (a.u.)
Wavelength (nm)

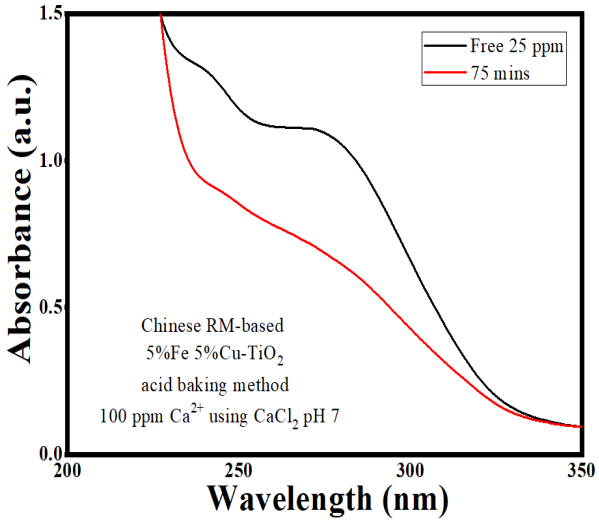
Free 25 ppm
75 mins
Chinese RM-based
5%Fe 5%Cu-TiO2
acid baking method
100 ppm Ca2+ using CaCl2 pH 7
Absorbance (a.u.)
Wavelength (nm)

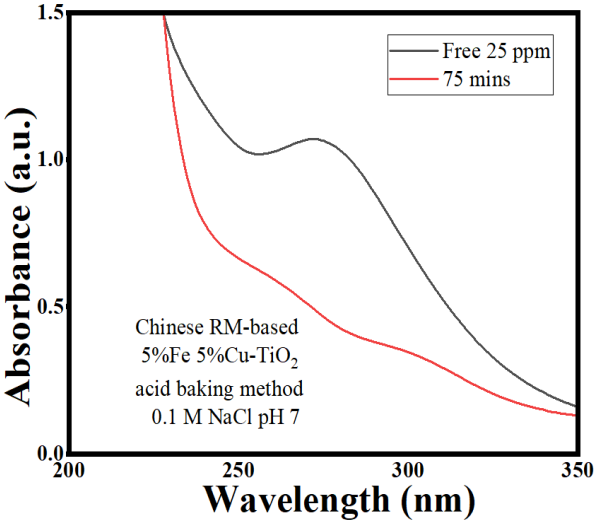
Free 25 ppm
75 mins
Chinese RM-based
5%Fe 5%Cu-TiO2
acid baking method
0.1 M NaCl pH 7
Absorbance (a.u.)
Wavelength (nm)

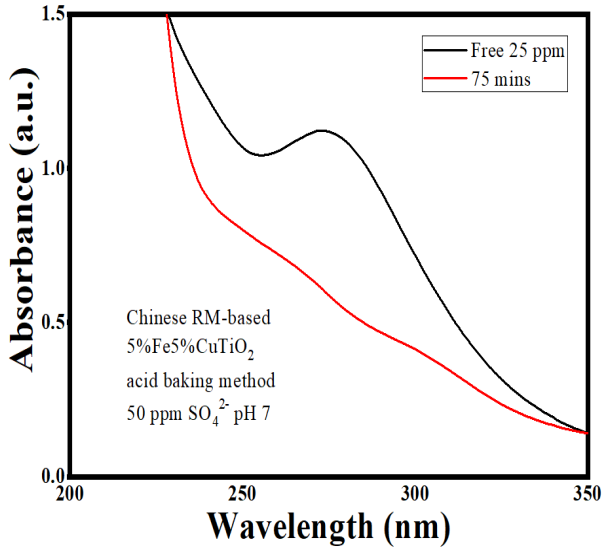
Free 25 ppm
75 mins
Chinese RM-based
5%Fe5%CuTiO2
acid baking method
50 ppm SO4 2- pH 7
Absorbance (a.u.)
Wavelength (nm)

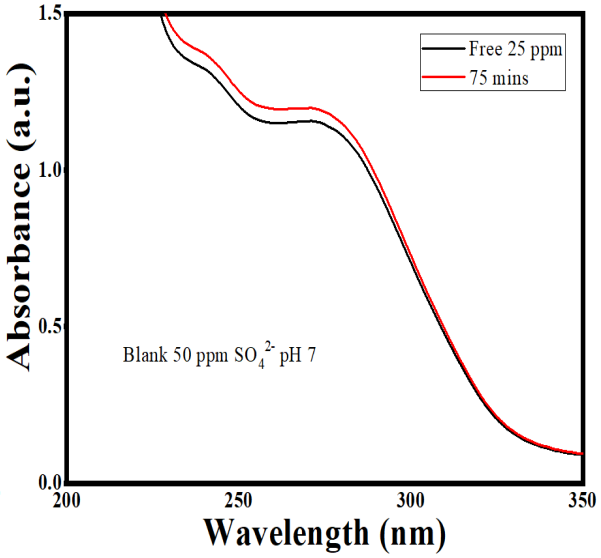
Free 25 ppm
75 mins
Blank 50 ppm SO4 2- pH 7
Absorbance (a.u.)
Wavelength (nm)

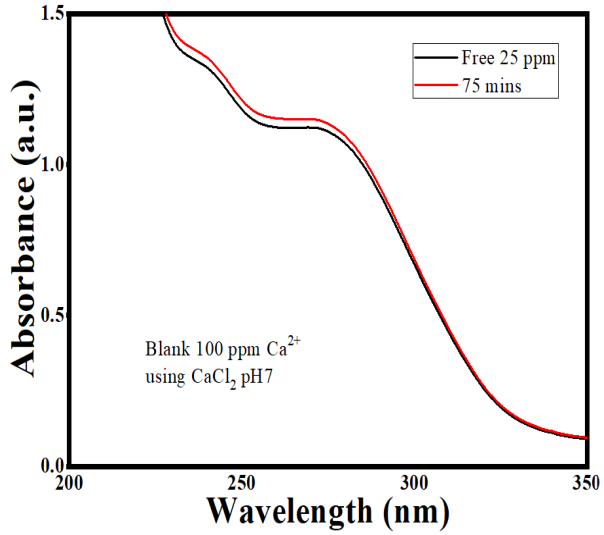
Free 25 ppm
75 mins
Blank 100 ppm Ca2+
using CaCl2 pH7
Absorbance (a.u.)
Wavelength (nm)

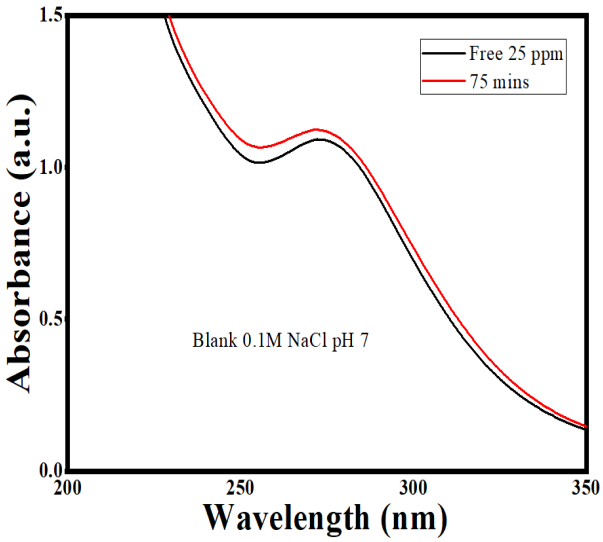
Free 25 ppm
75 mins
Blank 0.1M NaCl pH 7
Absorbance (a.u.)
Wavelength (nm)

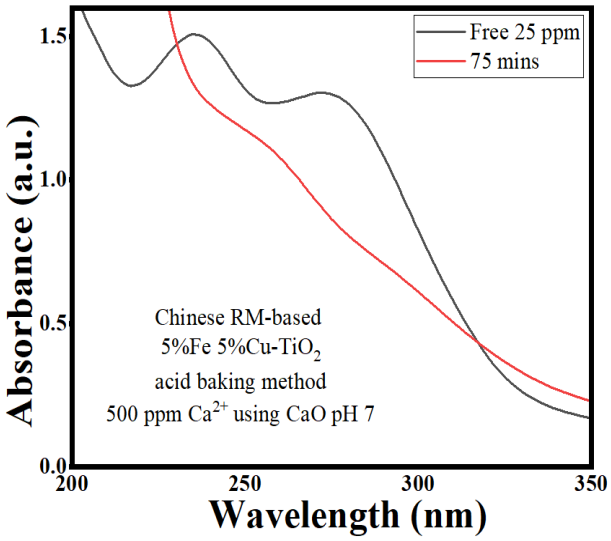
Free 25 ppm
75 mins
Chinese RM-based
5%Fe 5%Cu-TiO2
acid baking method
500 ppm Ca2+ using CaO pH 7
Absorbance (a.u.)
Wavelength (nm)

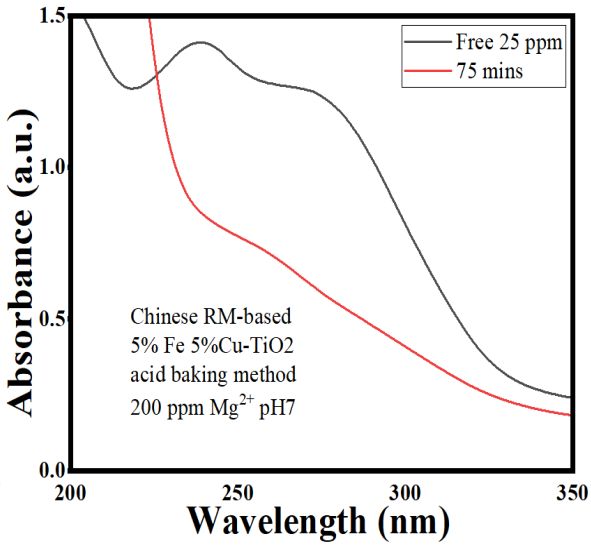
Free 25 ppm
75 mins
Chinese RM-based
5% Fe 5%Cu-TiO2
acid baking method
200 ppm Mg2+ pH7
Absorbance (a.u.)
Wavelength (nm)

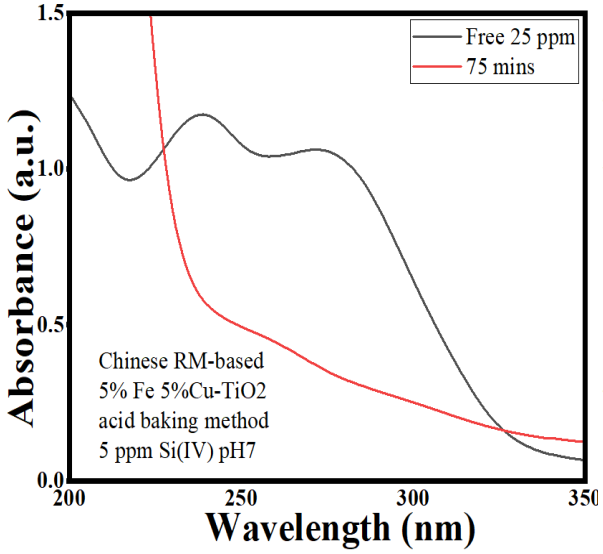
Free 25 ppm
75 mins
Chinese RM-based
5% Fe 5%Cu-TiO2
acid baking method
5 ppm Si(IV) pH7
Absorbance (a.u.)
Wavelength (nm)

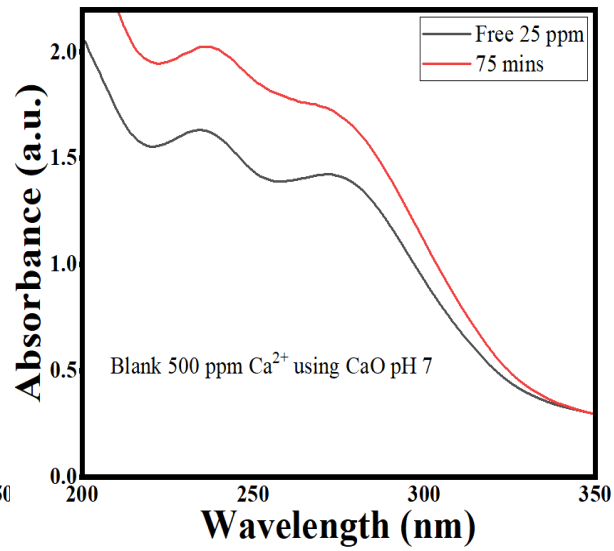
Free 25 ppm
75 mins
Blank 500 ppm Ca2+ using CaO pH 7
Absorbance (a.u.)
Wavelength (nm)

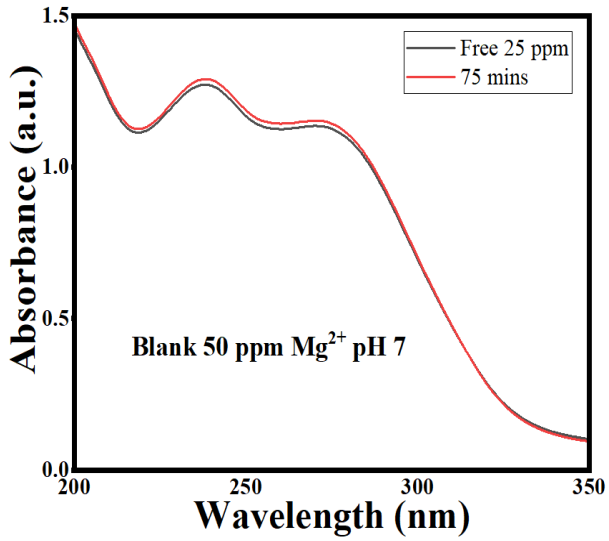
Free 25 ppm
75 mins
Blank 50 ppm Mg2+ pH 7
Absorbance (a.u.)
Wavelength (nm)

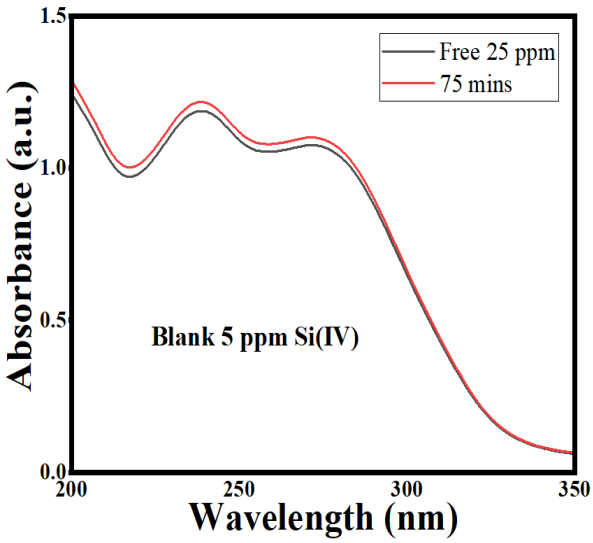
Free 25 ppm
75 mins
Blank 5 ppm Si(IV)
Absorbance (a.u.)
Wavelength (nm)

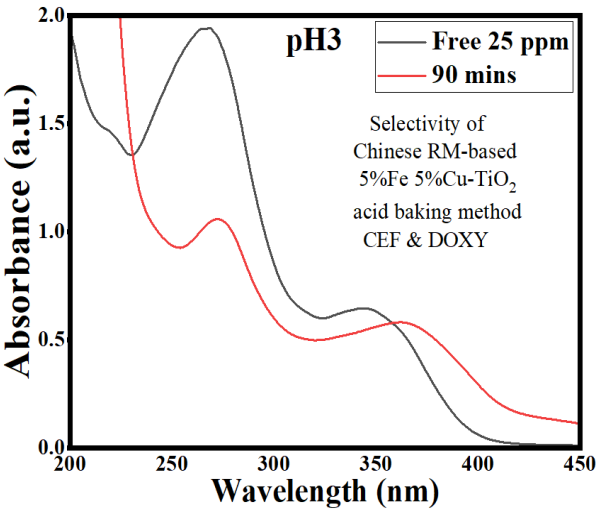
pH3
Free 25 ppm
90 mins
Selectivity of
Chinese RM-based
5%Fe 5%Cu-TiO2
acid baking method
CEF & DOXY
Absorbance (a.u.)
Wavelength (nm)

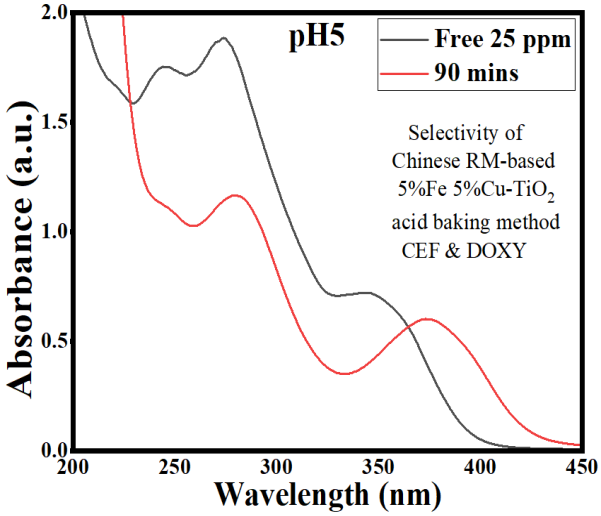
pH5
Free 25 ppm
90 mins
Selectivity of
Chinese RM-based
5%Fe 5%Cu-TiO2
acid baking method
CEF & DOXY
Absorbance (a.u.)
Wavelength (nm)

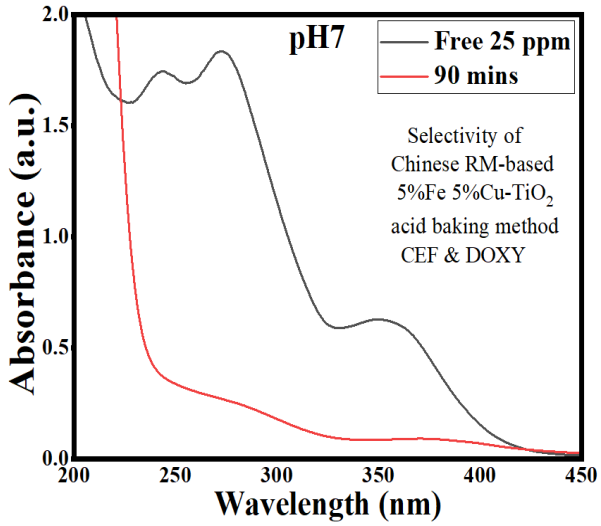
pH7
Free 25 ppm
90 mins
Selectivity of
Chinese RM-based
5%Fe 5%Cu-TiO2
acid baking method
CEF & DOXY
Absorbance (a.u.)
Wavelength (nm)

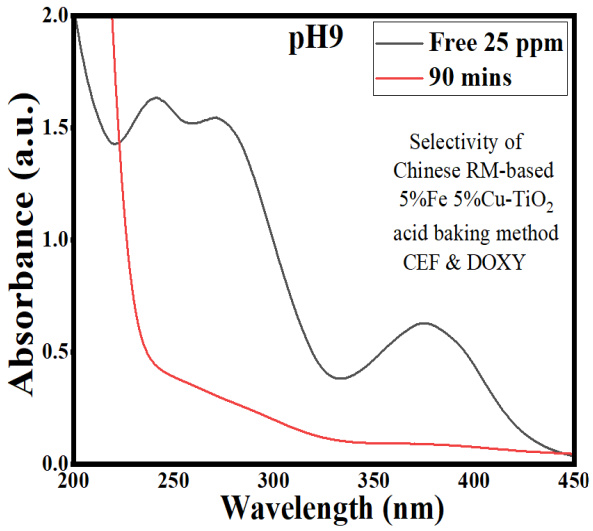
pH9
Free 25 ppm
90 mins
Selectivity of
Chinese RM-based
5%Fe 5%Cu-TiO2
acid baking method
CEF & DOXY
Absorbance (a.u.)
Wavelength (nm)

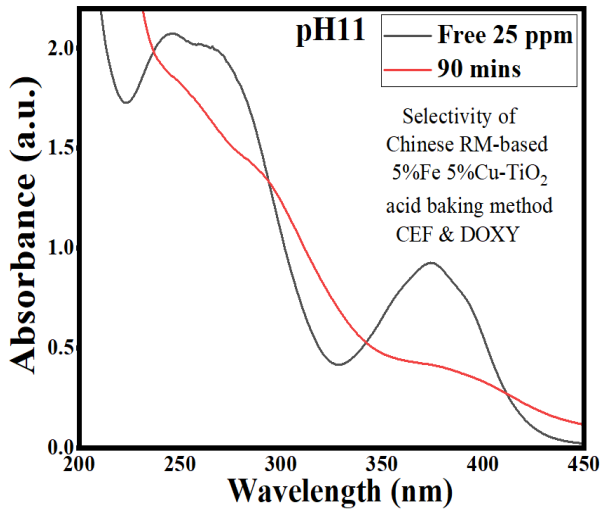
pH11
Free 25 ppm
90 mins
Selectivity of
Chinese RM-based
5%Fe 5%Cu-TiO2
acid baking method
CEF & DOXY
Absorbance (a.u.)
Wavelength (nm)

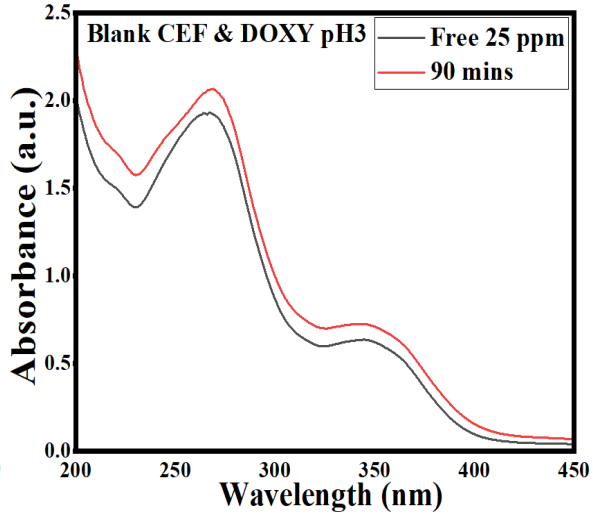
Blank CEF & DOXY pH3
Free 25 ppm
90 mins
Absorbance (a.u.)
Wavelength (nm)

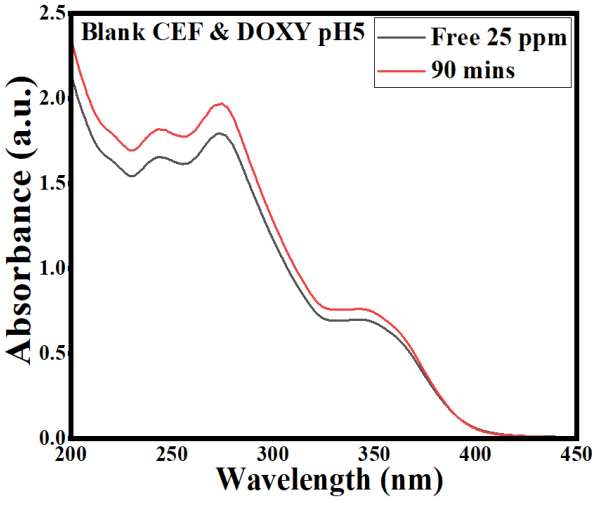
Blank CEF & DOXY pH5
Free 25 ppm
90 mins
Absorbance (a.u.)
Wavelength (nm)

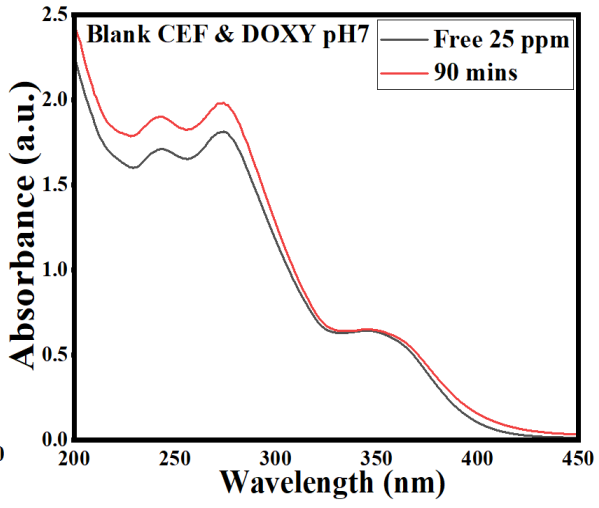
Blank CEF & DOXY pH7
Free 25 ppm
90 mins
Absorbance (a.u.)
Wavelength (nm)

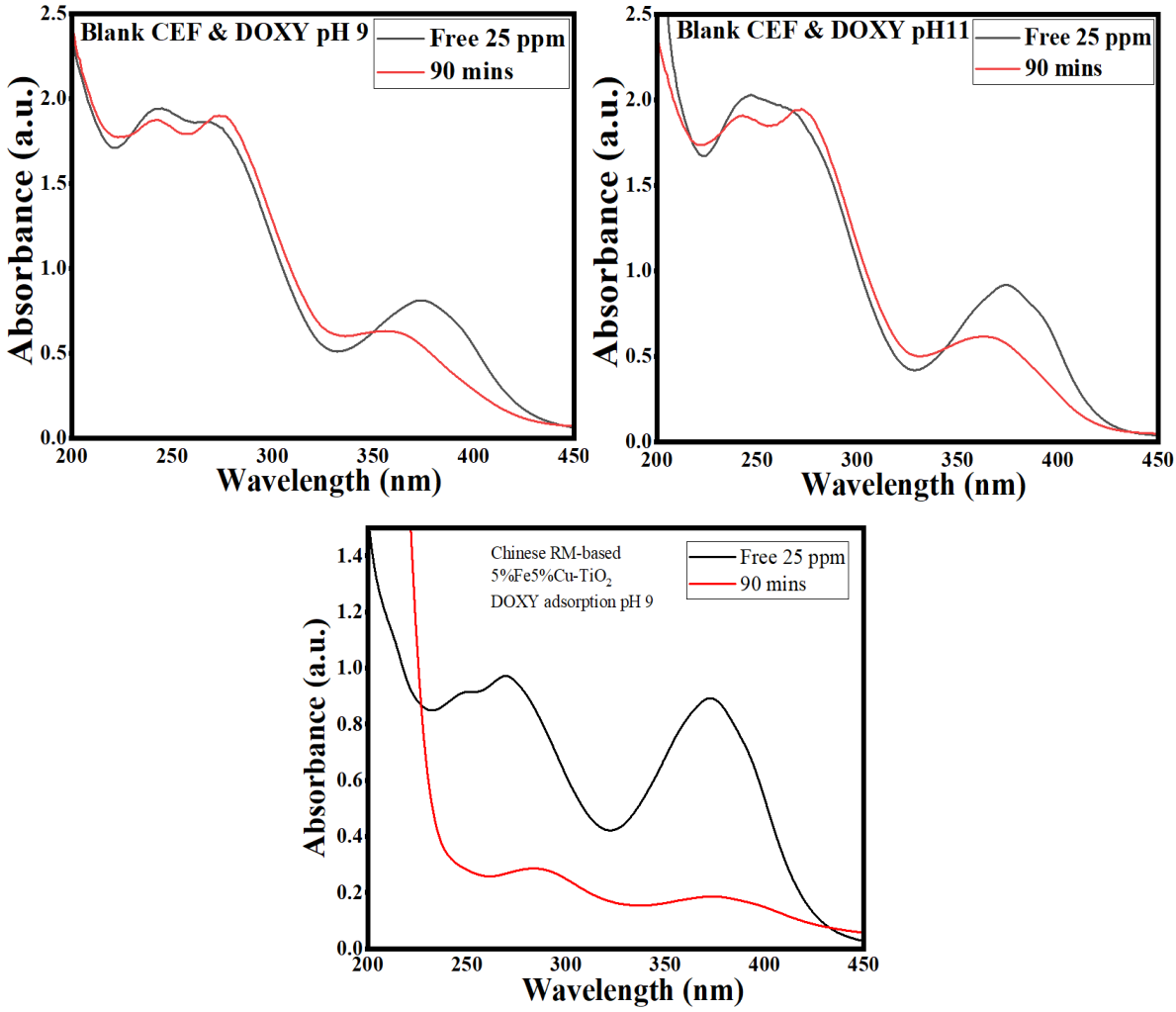

Fig S8. The UV-Visible spectra of the main adsorption experiments [C_o = 25 ppm, pH = 3, stirring rate = 800 rpm, T = 20 ± 2 °C, volume = 20 mL, and dose = 0.01 g]. Other pH levels are shown and indicated in the figures' labels where the highest removal efficacy was observed.

Appendix 3.2. The UV-Visible spectra of the main DOXY adsorption experiments in Chapter 4.

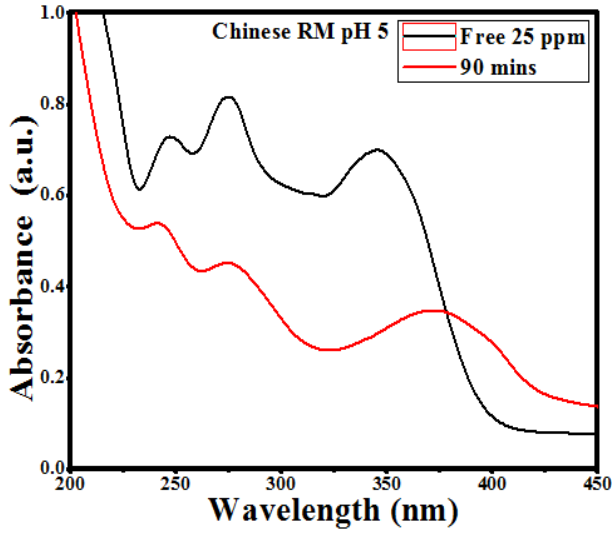
Chinese RM pH 5
Free 25 ppm
90 mins
Absorbance (a.u.)
Wavelength (nm)

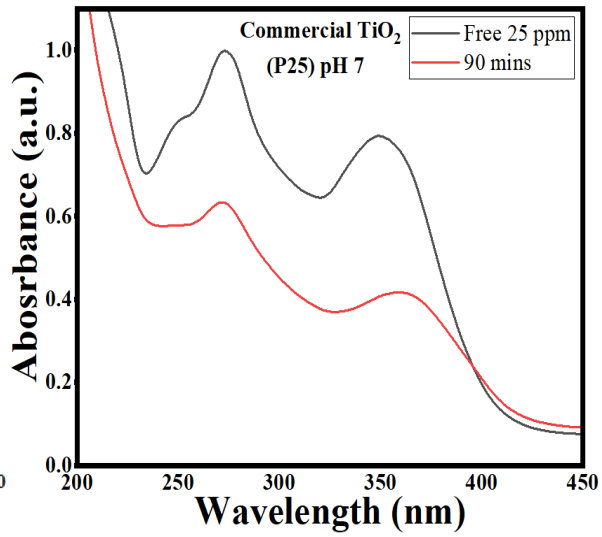
Commercial TiO2
(P25) pH 7
Free 25 ppm
90 mins
Absorbance (a.u.)
Wavelength (nm)

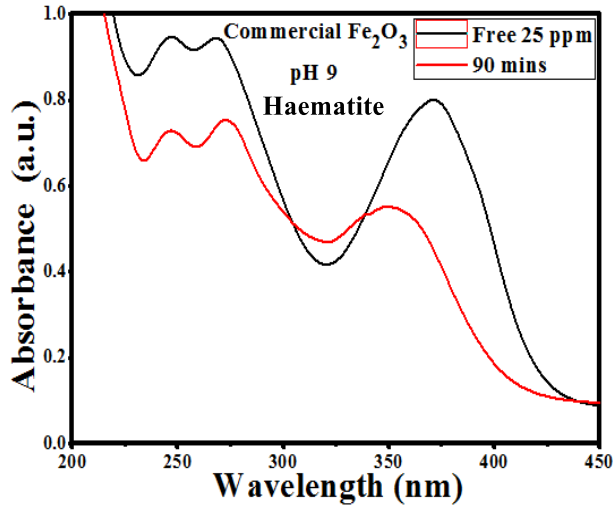
Commercial Fe2O3
pH 9
Haematite
Free 25 ppm
90 mins
Absorbance (a.u.)
Wavelength (nm)

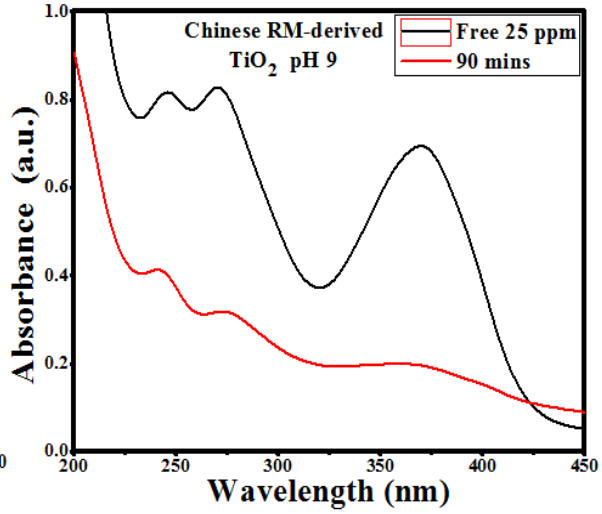
Chinese RM-derived
TiO2 pH 9
Free 25 ppm
90 mins
Absorbance (a.u.)
Wavelength (nm)

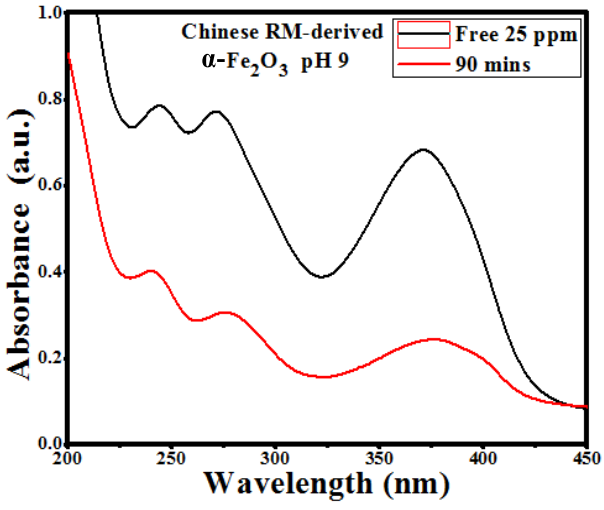
Chinese RM-derived
α-Fe2O3 pH 9
Free 25 ppm
90 mins
Absorbance (a.u.)
Wavelength (nm)

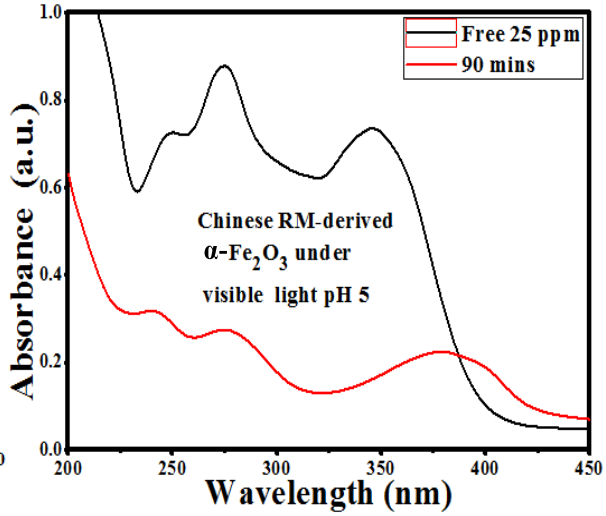
Free 25 ppm
90 mins
Chinese RM-derived
α-Fe2O3 under
visible light pH 5
Absorbance (a.u.)
Wavelength (nm)

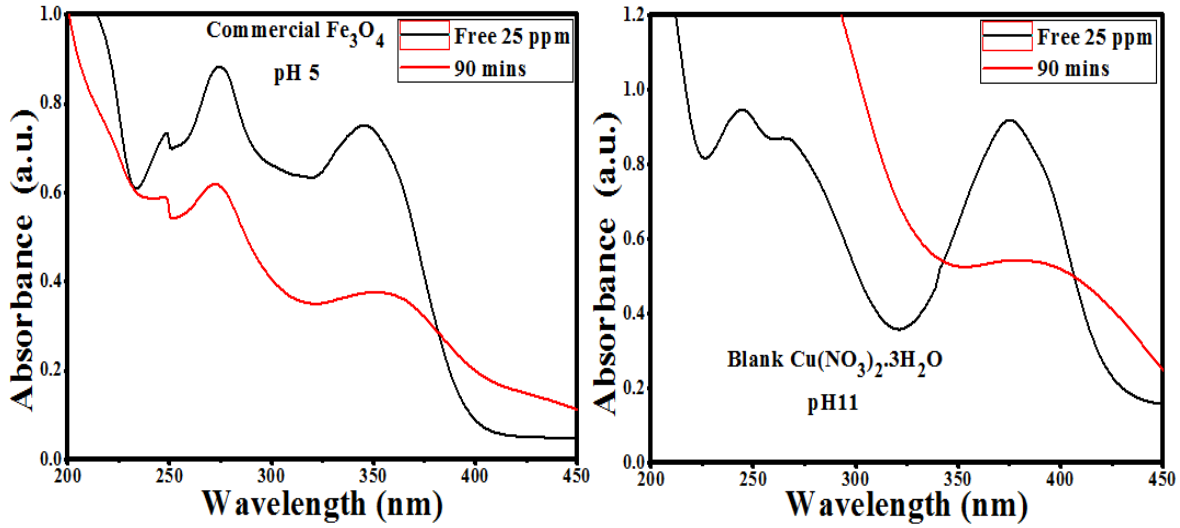

Fig S9. The UV-Visible spectra of the main DOXY adsorption experiments [C_o = 25 ppm, stirring rate = 800 rpm, T = 20 ± 2 °C, volume = 20 mL, and dose = 0.01 g].

Appendix 3.3. the UV-Visible spectra of the main DOXY adsorption experiments in Chapter 5

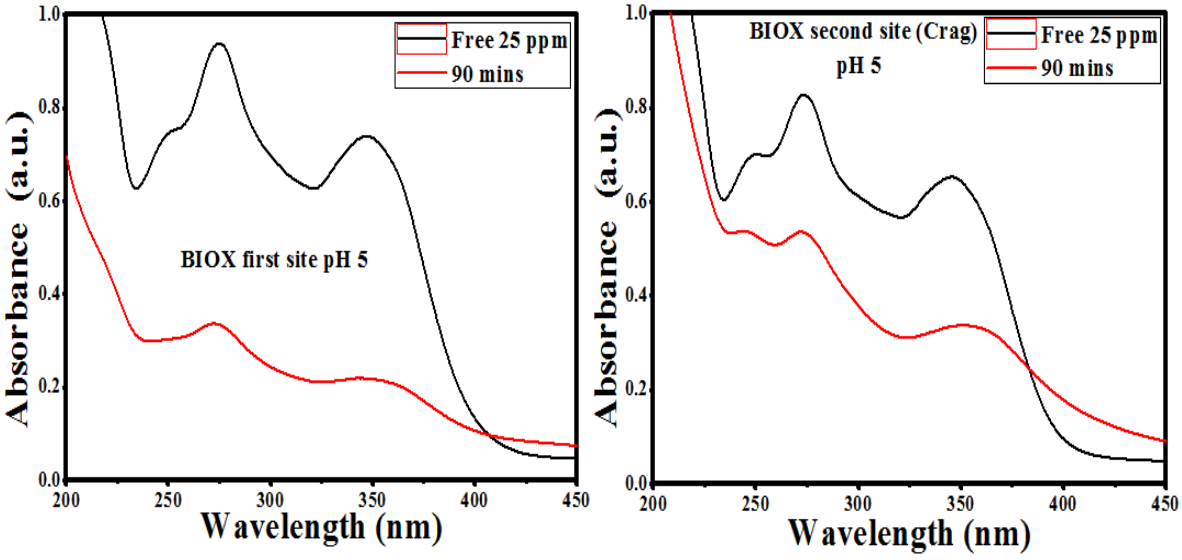

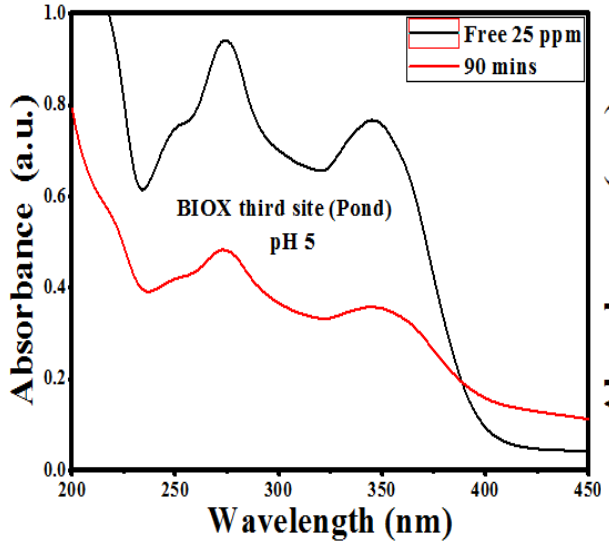
Free 25 ppm
90 mins
BIOX third site (Pond)
pH 5
Absorbance (a.u.)
Wavelength (nm)

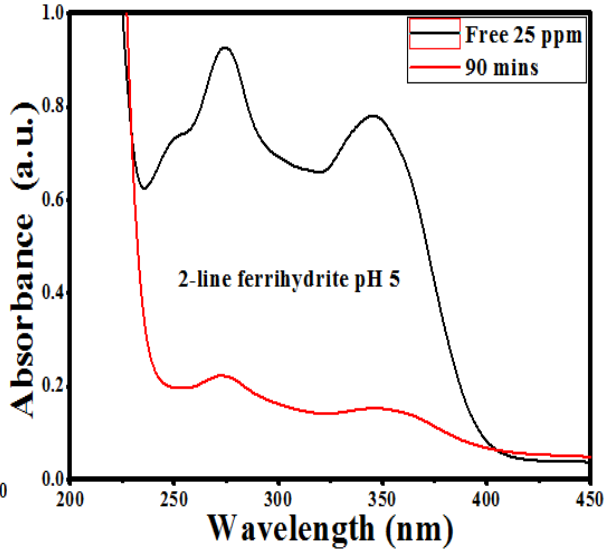
Free 25 ppm
90 mins
2-line ferrihydrite pH 5
Absorbance (a.u.)
Wavelength (nm)

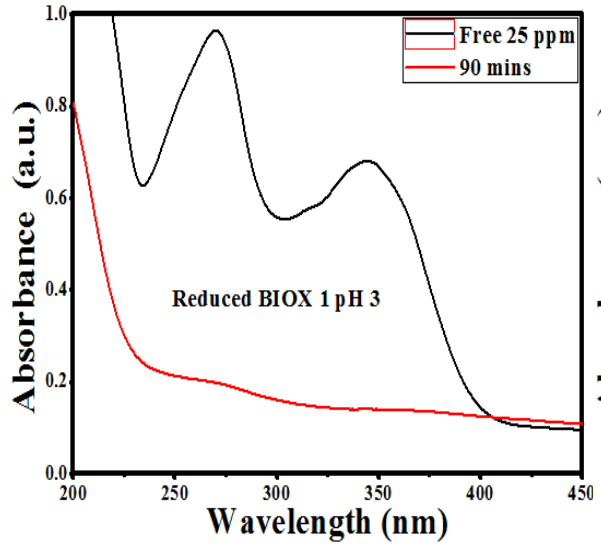
Free 25 ppm
90 mins
Reduced BIOX 1 pH 3
Absorbance (a.u.)
Wavelength (nm)

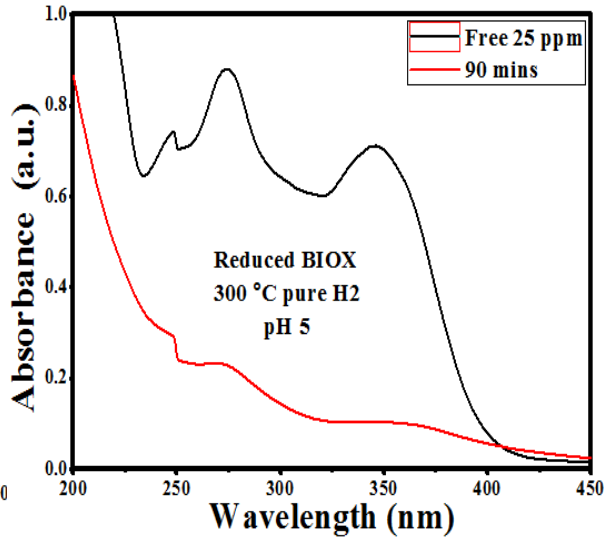
Free 25 ppm
90 mins
Reduced BIOX
300 °C pure H2
pH 5
Absorbance (a.u.)
Wavelength (nm)

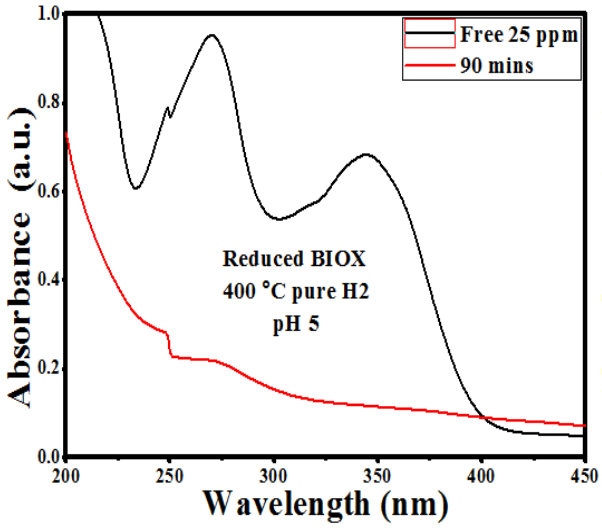
Free 25 ppm
90 mins
Reduced BIOX
400 °C pure H2
pH 5
Absorbance (a.u.)
Wavelength (nm)

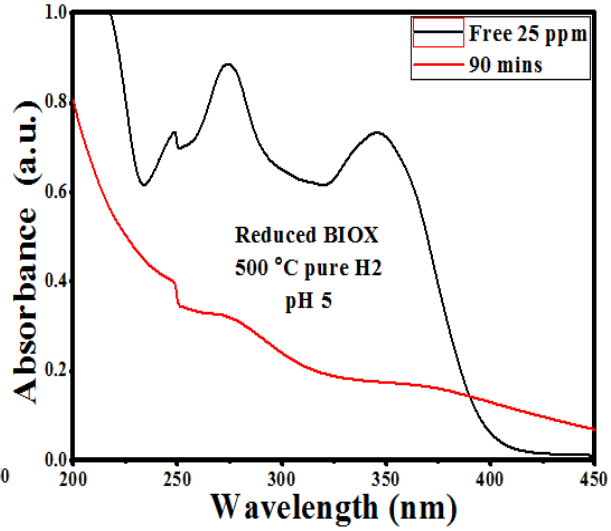
Free 25 ppm
90 mins
Reduced BIOX
500 °C pure H2
pH 5
Absorbance (a.u.)
Wavelength (nm)

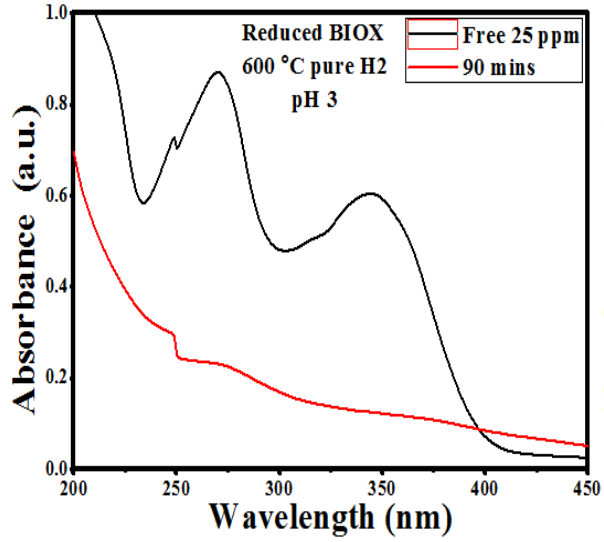
Reduced BIOX
600 °C pure H2
pH 3
Free 25 ppm
90 mins
Absorbance (a.u.)
Wavelength (nm)

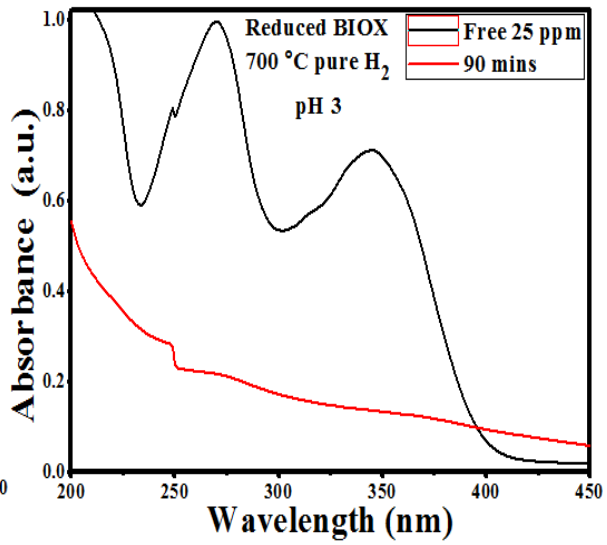
Reduced BIOX
700 °C pure H_2
pH 3
Free 25 ppm
90 mins
Absorbance (a.u.)
Wavelength (nm)

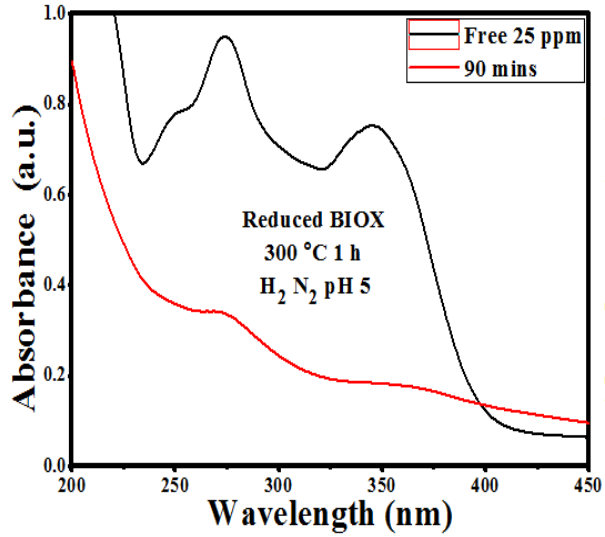
Reduced BIOX
300 °C 1 h
H_2 N_2 pH 5
Free 25 ppm
90 mins
Absorbance (a.u.)
Wavelength (nm)

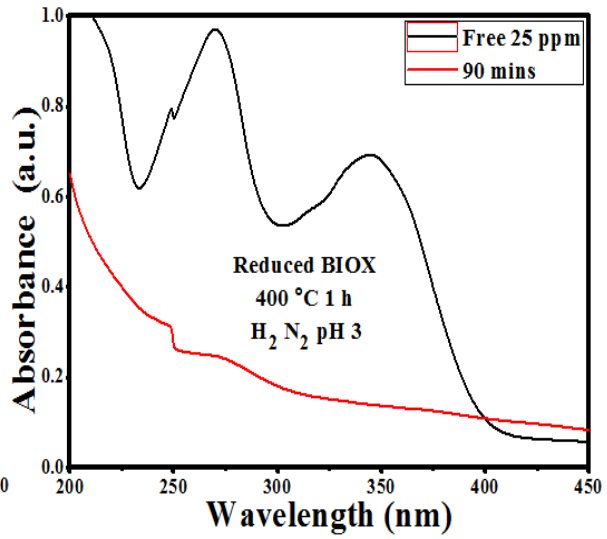
Reduced BIOX
400 °C 1 h
H_2 N_2 pH 3
Free 25 ppm
90 mins
Absorbance (a.u.)
Wavelength (nm)

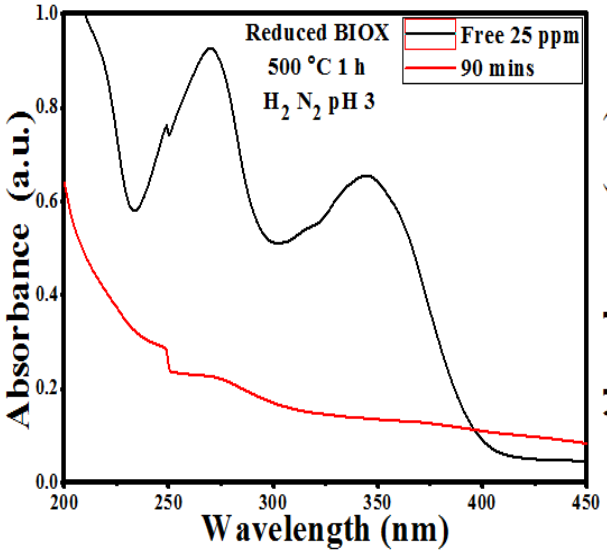
Reduced BIOX
500 °C 1 h
H_2 N_2 pH 3
Free 25 ppm
90 mins
Absorbance (a.u.)
Wavelength (nm)

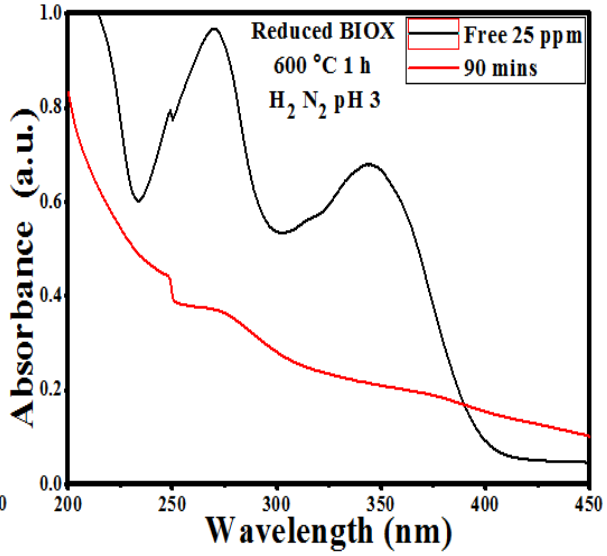
Reduced BIOX
600 °C 1 h
H_2 N_2 pH 3
Free 25 ppm
90 mins
Absorbance (a.u.)
Wavelength (nm)

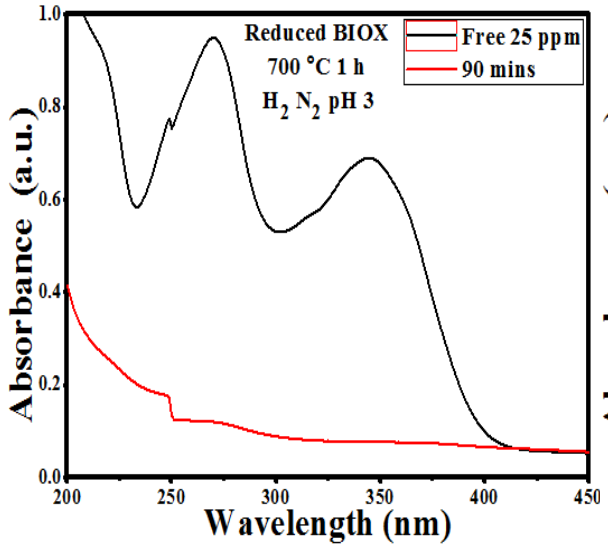
Reduced BIOX
700 °C 1 h
H2 N2 pH 3
Free 25 ppm
90 mins
Absorbance (a.u.)
Wavelength (nm)

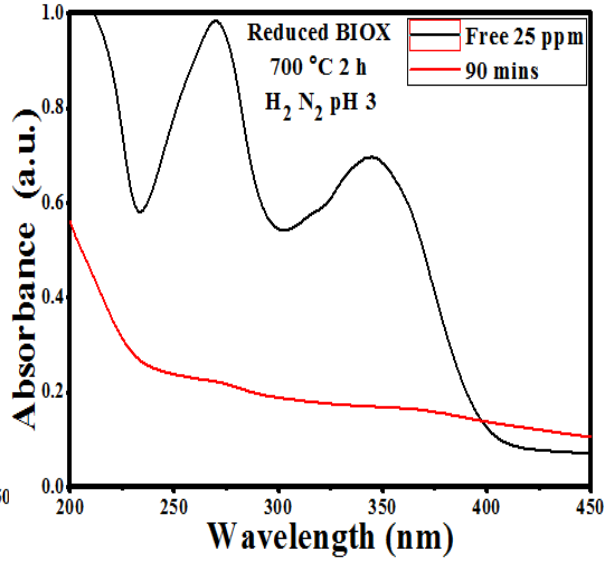
Reduced BIOX
700 °C 2 h
H2 N2 pH 3
Free 25 ppm
90 mins
Absorbance (a.u.)
Wavelength (nm)

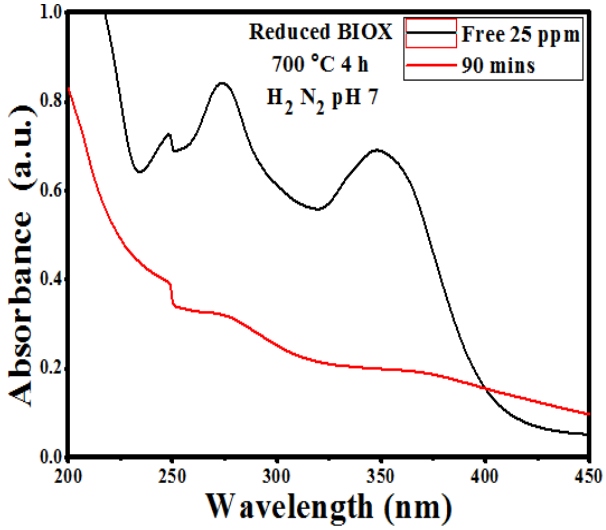
Reduced BIOX
700 °C 4 h
H2 N2 pH 7
Free 25 ppm
90 mins
Absorbance (a.u.)
Wavelength (nm)

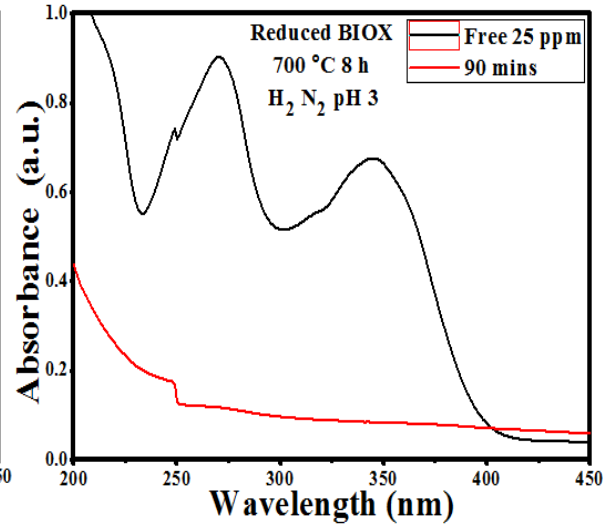
Reduced BIOX
700 °C 8 h
H2 N2 pH 3
Free 25 ppm
90 mins
Absorbance (a.u.)
Wavelength (nm)

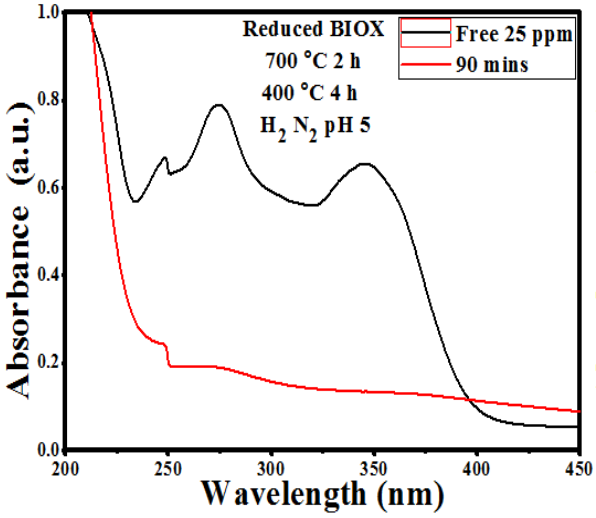
Reduced BIOX
700 °C 2 h
400 °C 4 h
H2 N2 pH 5
Free 25 ppm
90 mins
Absorbance (a.u.)
Wavelength (nm)

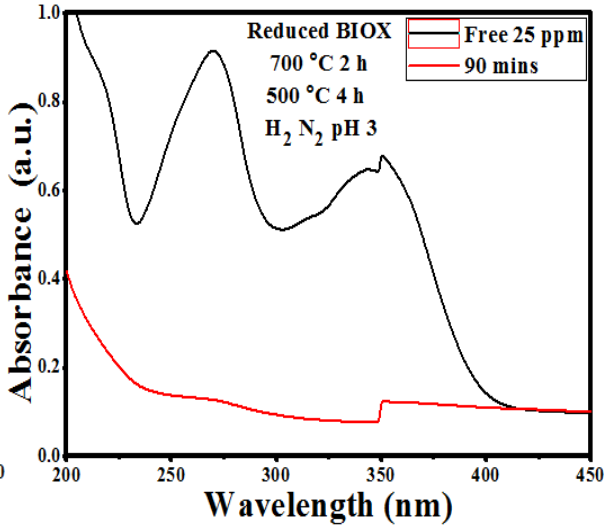
Reduced BIOX
700 °C 2 h
500 °C 4 h
H2 N2 pH 3
Free 25 ppm
90 mins
Absorbance (a.u.)
Wavelength (nm)

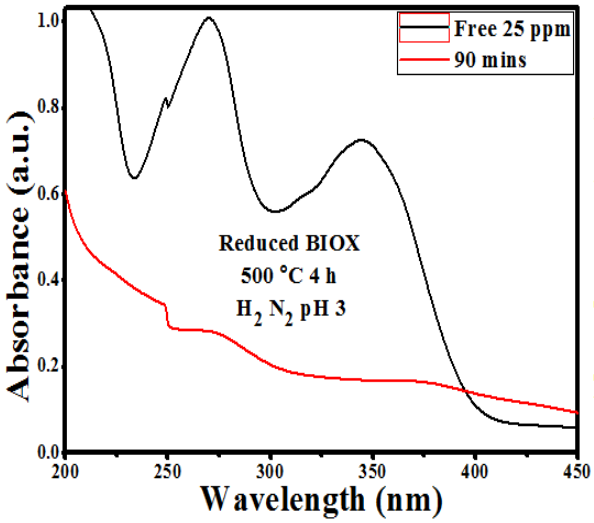
Reduced BIOX
500 °C 4 h
H2 N2 pH 3
Free 25 ppm
90 mins
Absorbance (a.u.)
Wavelength (nm)

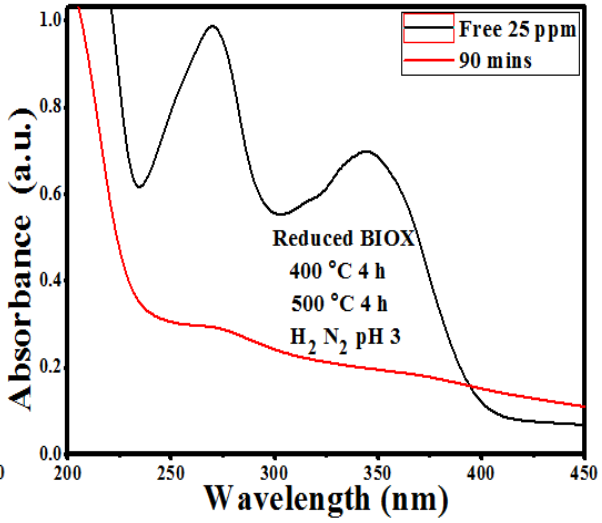
Reduced BIOX
400 °C 4 h
500 °C 4 h
H2 N2 pH 3
Free 25 ppm
90 mins
Absorbance (a.u.)
Wavelength (nm)

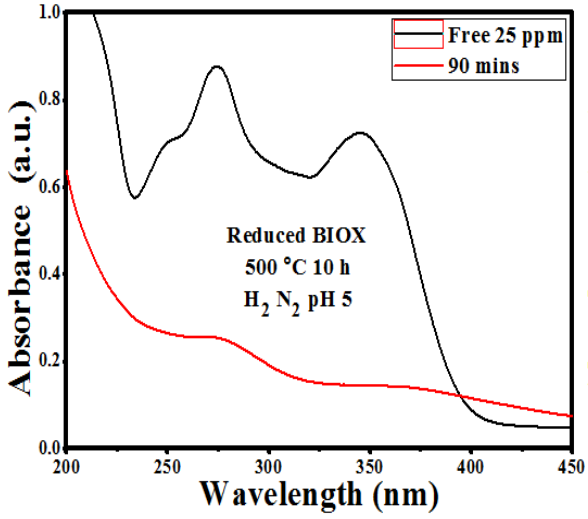
Reduced BIOX
500 °C 10 h
H2 N2 pH 5
Free 25 ppm
90 mins
Absorbance (a.u.)
Wavelength (nm)

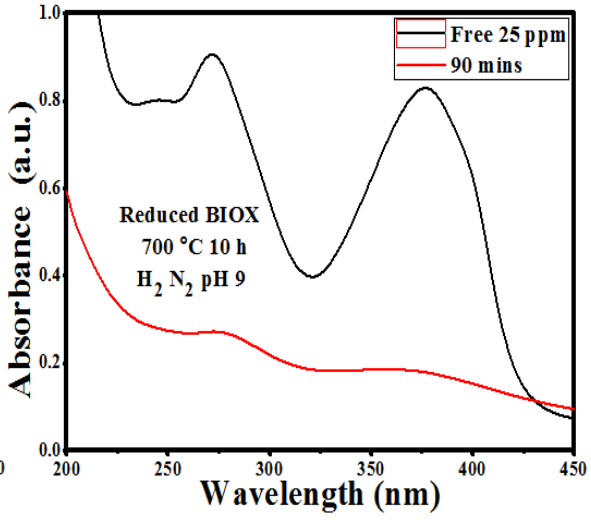
Reduced BIOX
700 °C 10 h
H2 N2 pH 9
Free 25 ppm
90 mins
Absorbance (a.u.)
Wavelength (nm)

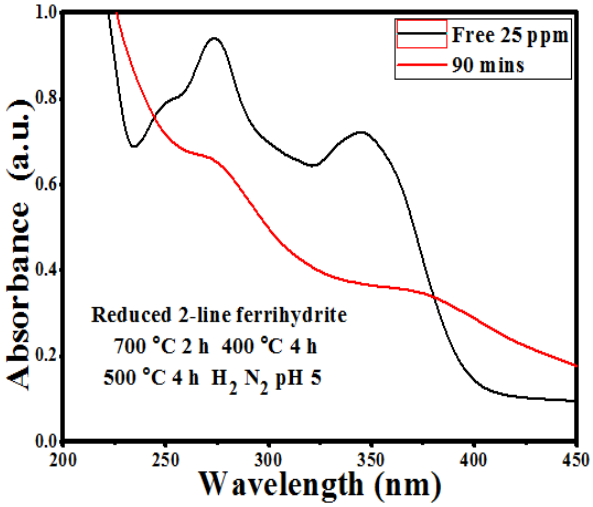
Free 25 ppm
90 mins
Reduced 2-line ferrihydrite
700 °C 2 h 400 °C 4 h
500 °C 4 h H2 N2 pH 5
Absorbance (a.u.)
Wavelength (nm)

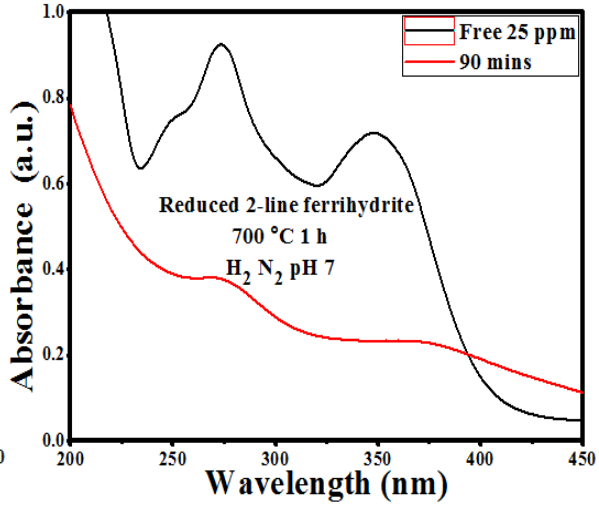
Free 25 ppm
90 mins
Reduced 2-line ferrihydrite
700 °C 1 h
H2 N2 pH 7
Absorbance (a.u.)
Wavelength (nm)

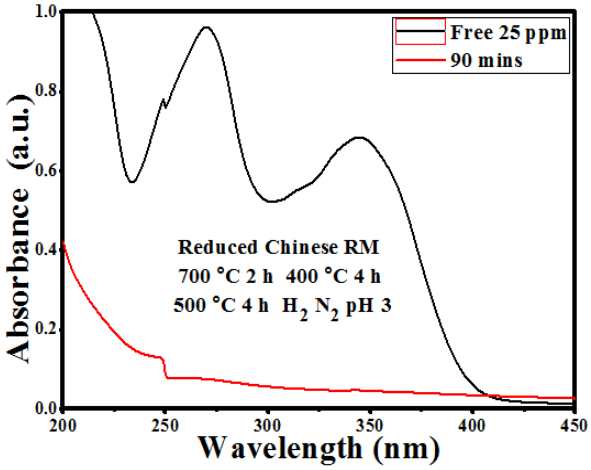
Free 25 ppm
90 mins
Reduced Chinese RM
700 °C 2 h 400 °C 4 h
500 °C 4 h H2 N2 pH 3
Absorbance (a.u.)
Wavelength (nm)

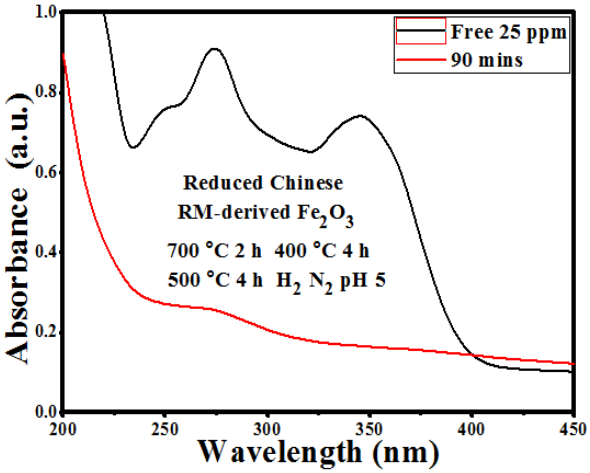
Free 25 ppm
90 mins
Reduced Chinese
RM-derived Fe2O3
700 °C 2 h 400 °C 4 h
500 °C 4 h H2 N2 pH 5
Absorbance (a.u.)
Wavelength (nm)

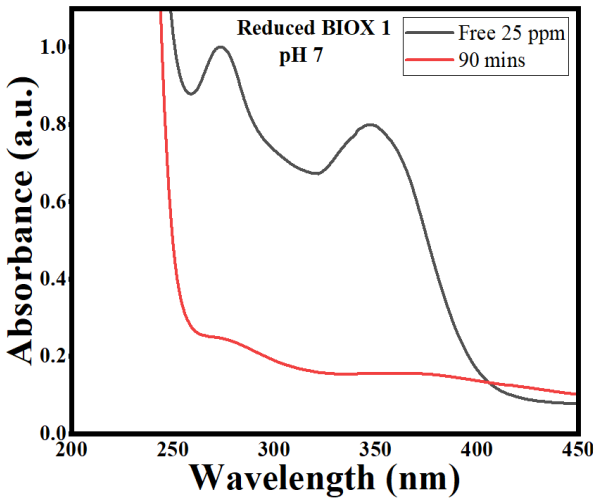
Reduced BIOX 1
pH 7
Free 25 ppm
90 mins
Absorbance (a.u.)
Wavelength (nm)

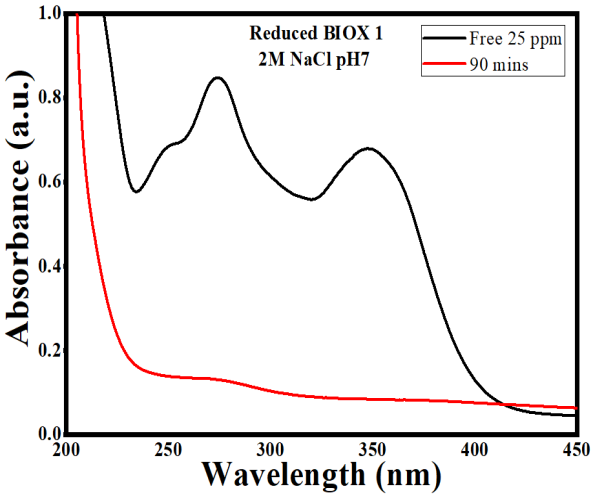
Reduced BIOX 1
2M NaCl pH7
Free 25 ppm
90 mins
Absorbance (a.u.)
Wavelength (nm)

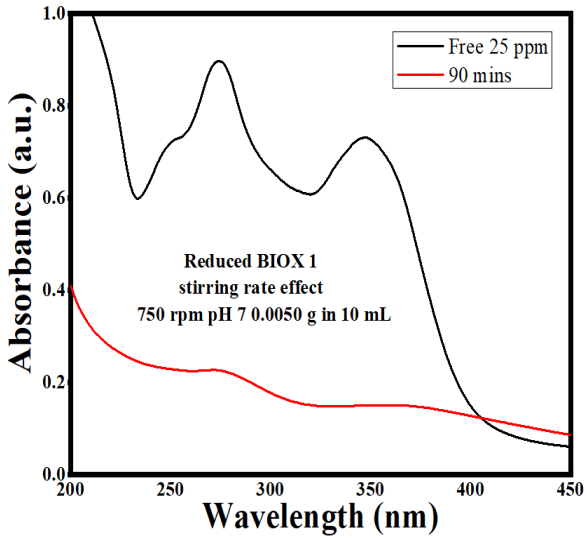
Free 25 ppm
90 mins
Reduced BIOX 1
stirring rate effect
750 rpm pH 7 0.0050 g in 10 mL
Absorbance (a.u.)
Wavelength (nm)

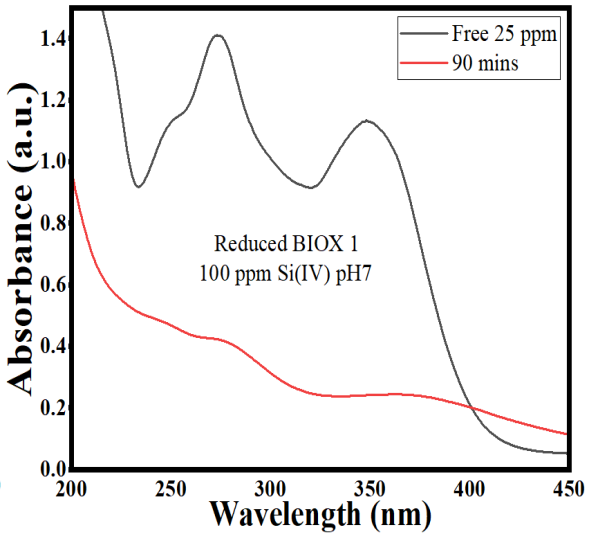
Free 25 ppm
90 mins
Reduced BIOX 1
100 ppm Si(IV) pH7
Absorbance (a.u.)
Wavelength (nm)

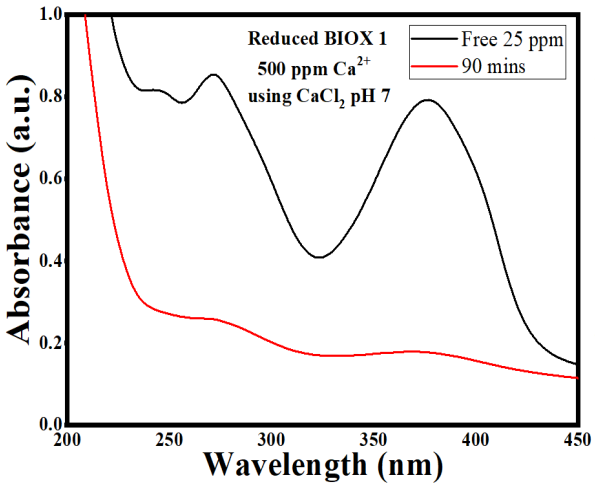
Free 25 ppm
90 mins
Reduced BIOX 1
500 ppm Ca2+
using CaCl2 pH 7
Absorbance (a.u.)
Wavelength (nm)

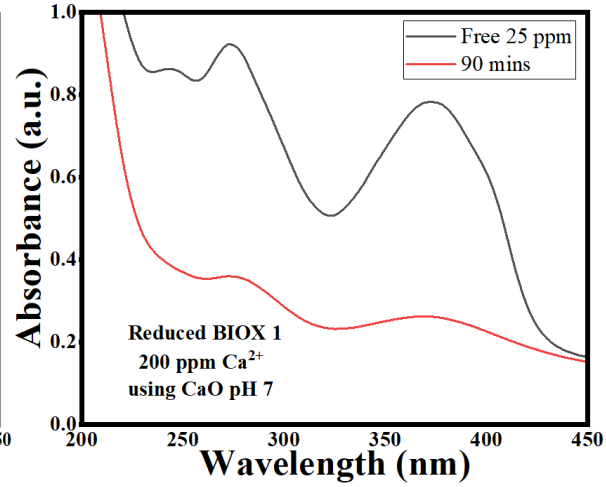
Free 25 ppm
90 mins
Reduced BIOX 1
200 ppm Ca2+
using CaO pH 7
Absorbance (a.u.)
Wavelength (nm)

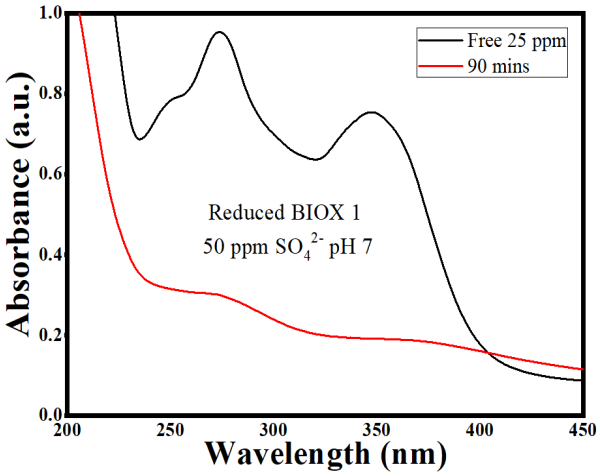
Free 25 ppm
90 mins
Reduced BIOX 1
50 ppm SO4 2- pH 7
Absorbance (a.u.)
Wavelength (nm)

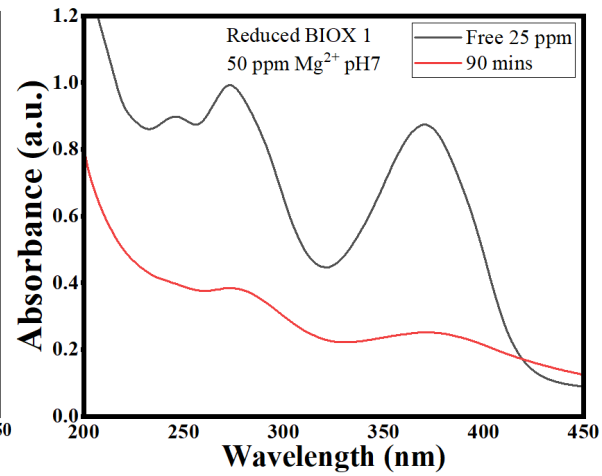
Free 25 ppm
90 mins
Reduced BIOX 1
50 ppm Mg2+ pH7
Absorbance (a.u.)
Wavelength (nm)

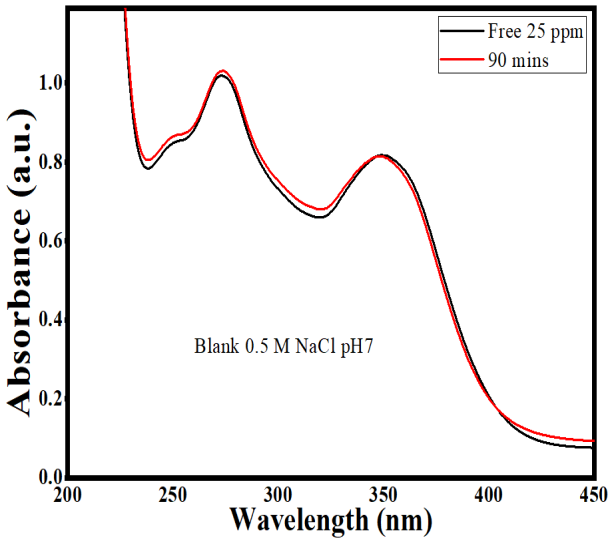
Free 25 ppm
90 mins
Blank 0.5 M NaCl pH7
Absorbance (a.u.)
Wavelength (nm)

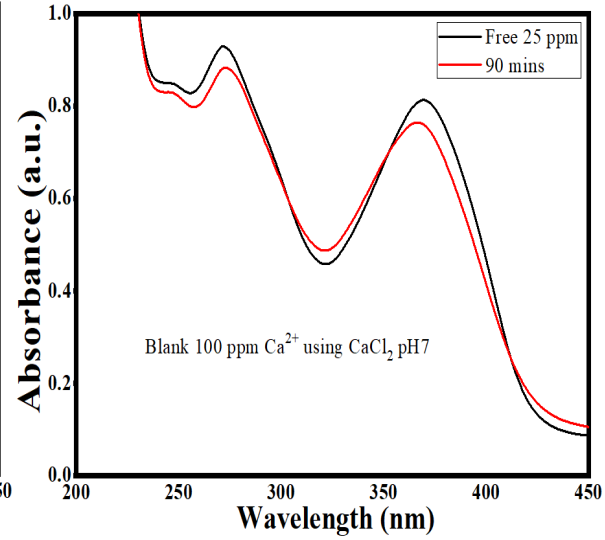
Free 25 ppm
90 mins
Blank 100 ppm Ca2+ using CaCl2 pH7
Absorbance (a.u.)
Wavelength (nm)

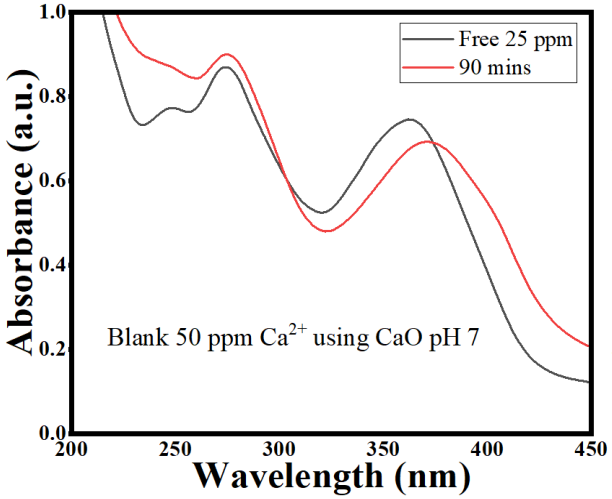
Free 25 ppm
90 mins
Blank 50 ppm Ca2+ using CaO pH 7
Absorbance (a.u.)
Wavelength (nm)

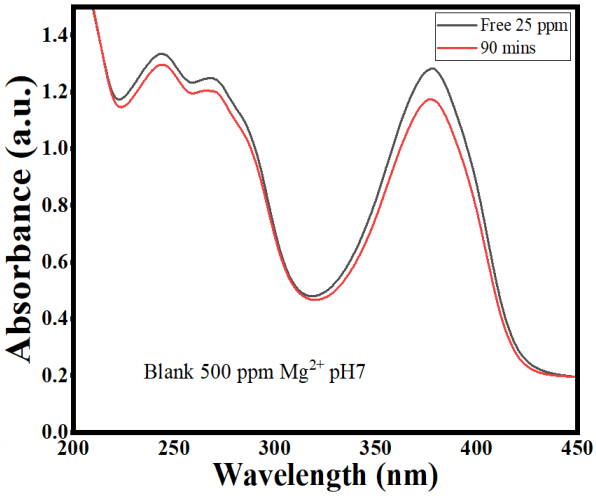
Free 25 ppm
90 mins
Blank 500 ppm Mg2+ pH7
Absorbance (a.u.)
Wavelength (nm)

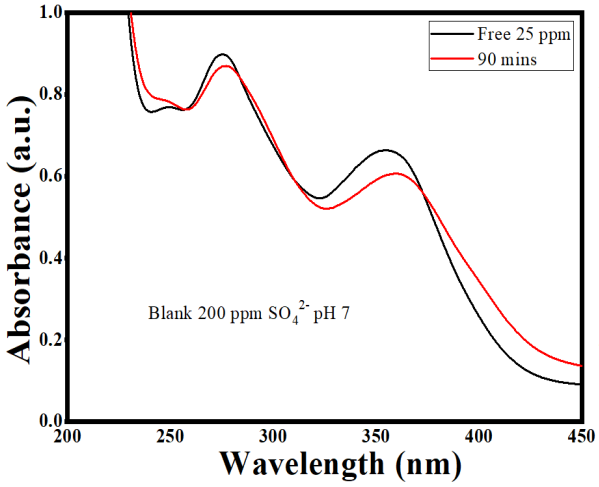
Free 25 ppm
90 mins
Blank 200 ppm SO4 2- pH 7
Absorbance (a.u.)
Wavelength (nm)

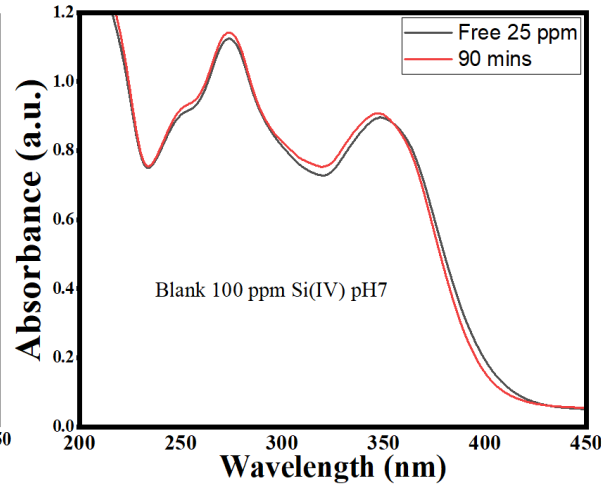
Free 25 ppm
90 mins
Blank 100 ppm Si(IV) pH7
Absorbance (a.u.)
Wavelength (nm)

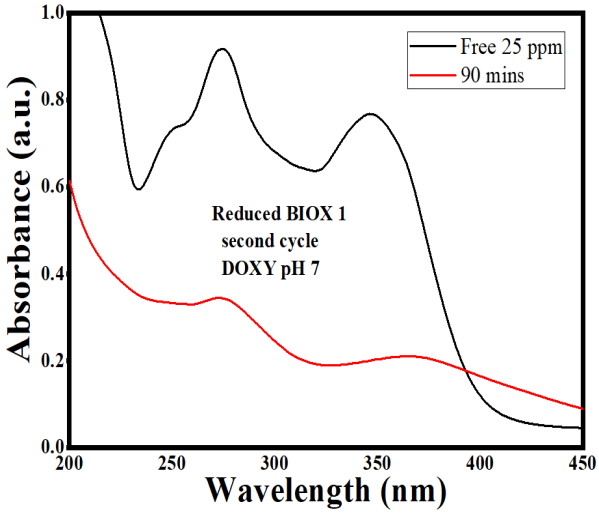
Free 25 ppm
90 mins
Reduced BIOX 1
second cycle
DOXY pH 7
Absorbance (a.u.)
Wavelength (nm)

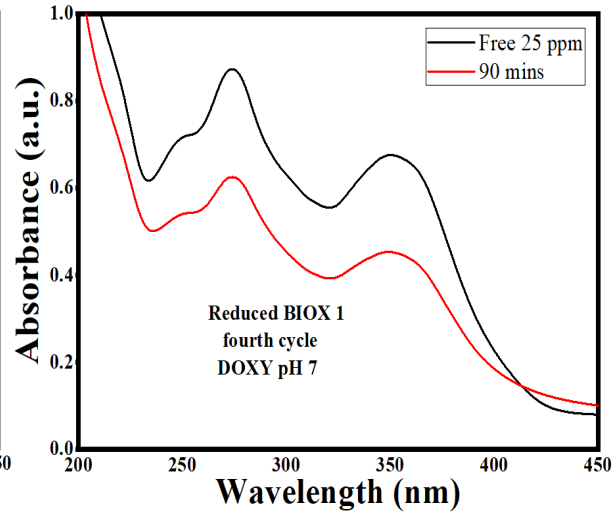
Free 25 ppm
90 mins
Reduced BIOX 1
fourth cycle
DOXY pH 7
Absorbance (a.u.)
Wavelength (nm)

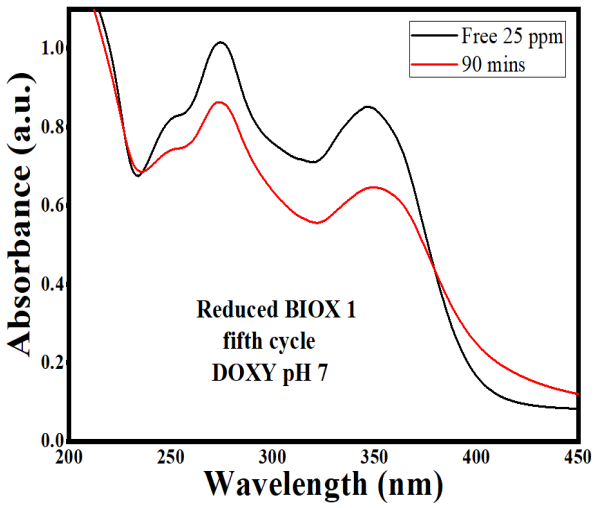
Free 25 ppm
90 mins
Reduced BIOX 1
fifth cycle
DOXY pH 7
Absorbance (a.u.)
Wavelength (nm)

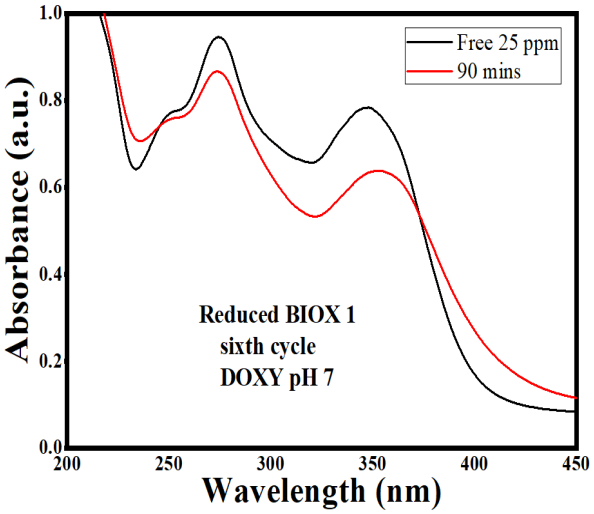
Free 25 ppm
90 mins
Reduced BIOX 1
sixth cycle
DOXY pH 7
Absorbance (a.u.)
Wavelength (nm)

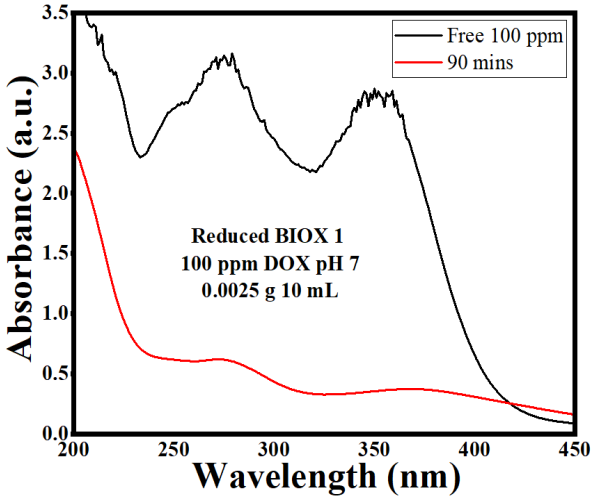
Free 100 ppm
90 mins
Reduced BIOX 1
100 ppm DOX pH 7
0.0025 g 10 mL
Absorbance (a.u.)
Wavelength (nm)

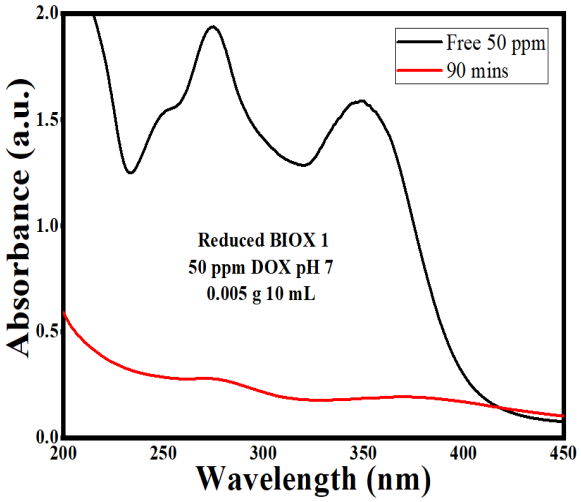
Free 50 ppm
90 mins
Reduced BIOX 1
50 ppm DOX pH 7
0.005 g 10 mL
Absorbance (a.u.)
Wavelength (nm)

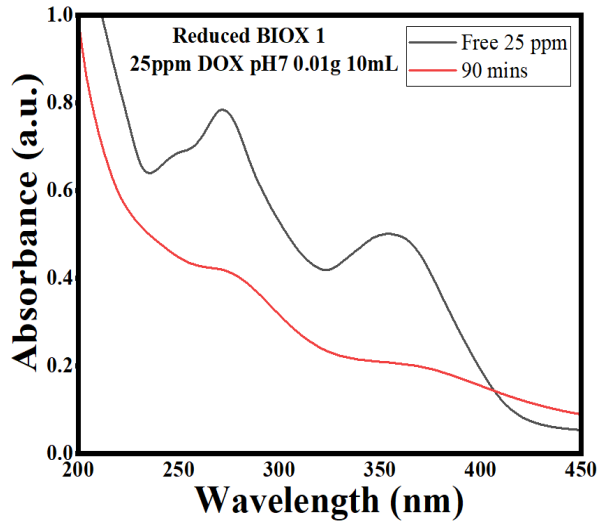
Reduced BIOX 1
25ppm DOX pH7 0.01g 10mL
Free 25 ppm
90 mins
Absorbance (a.u.)
Wavelength (nm)

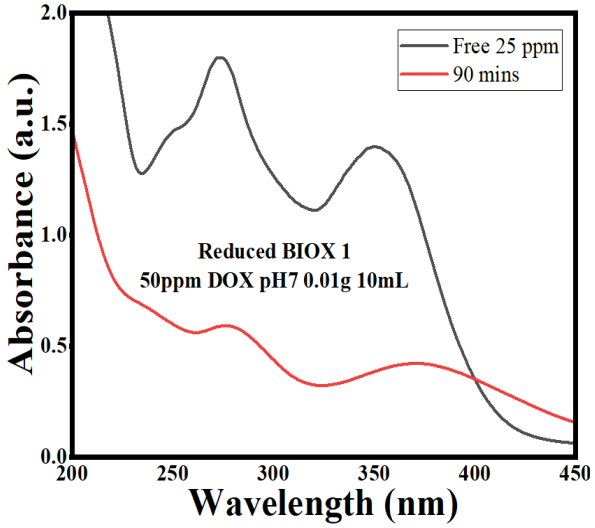
Free 25 ppm
90 mins
Reduced BIOX 1
50ppm DOX pH7 0.01g 10mL
Absorbance (a.u.)
Wavelength (nm)

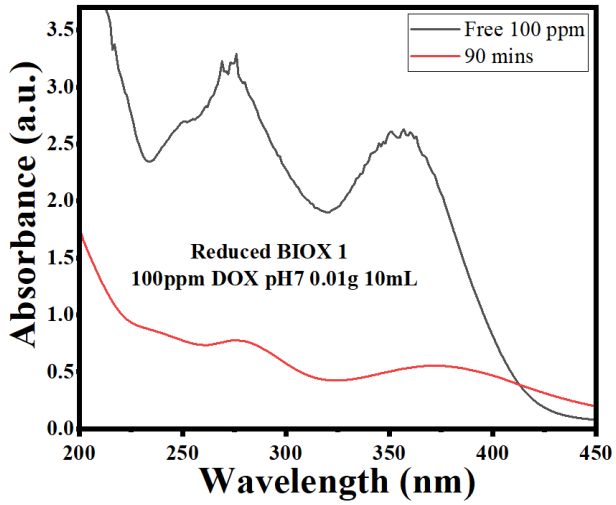
Free 100 ppm
90 mins
Reduced BIOX 1
100ppm DOX pH7 0.01g 10mL
Absorbance (a.u.)
Wavelength (nm)

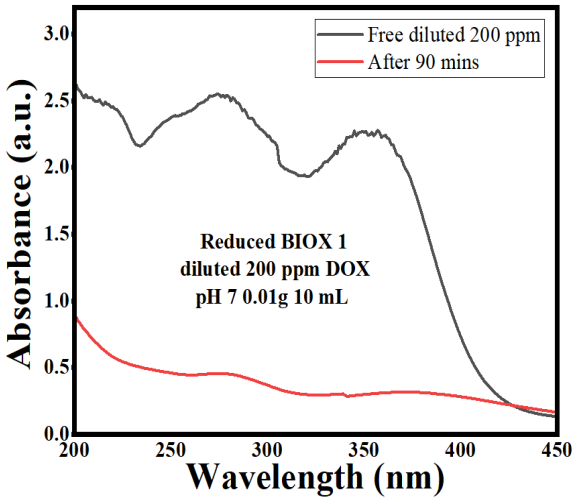
Free diluted 200 ppm
After 90 mins
Reduced BIOX 1
diluted 200 ppm DOX
pH 7 0.01g 10 mL
Absorbance (a.u.)
Wavelength (nm)

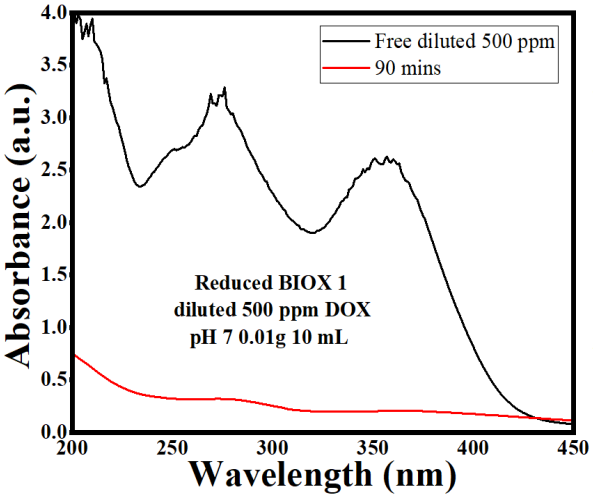
Free diluted 500 ppm
90 mins
Reduced BIOX 1
diluted 500 ppm DOX
pH 7 0.01g 10 mL
Absorbance (a.u.)
Wavelength (nm)

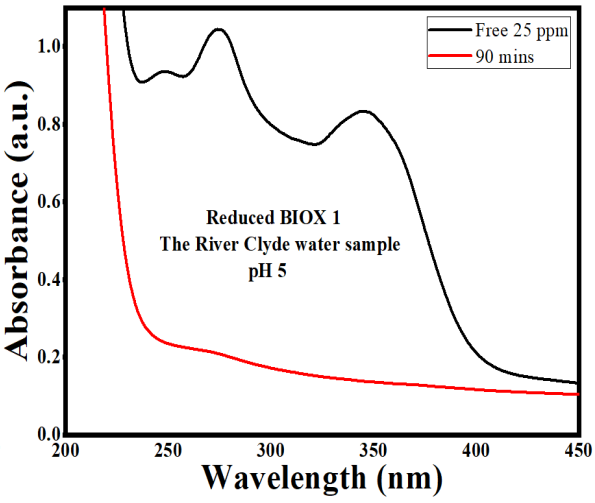
Free 25 ppm
90 mins
Reduced BIOX 1
The River Clyde water sample
pH 5
Absorbance (a.u.)
Wavelength (nm)

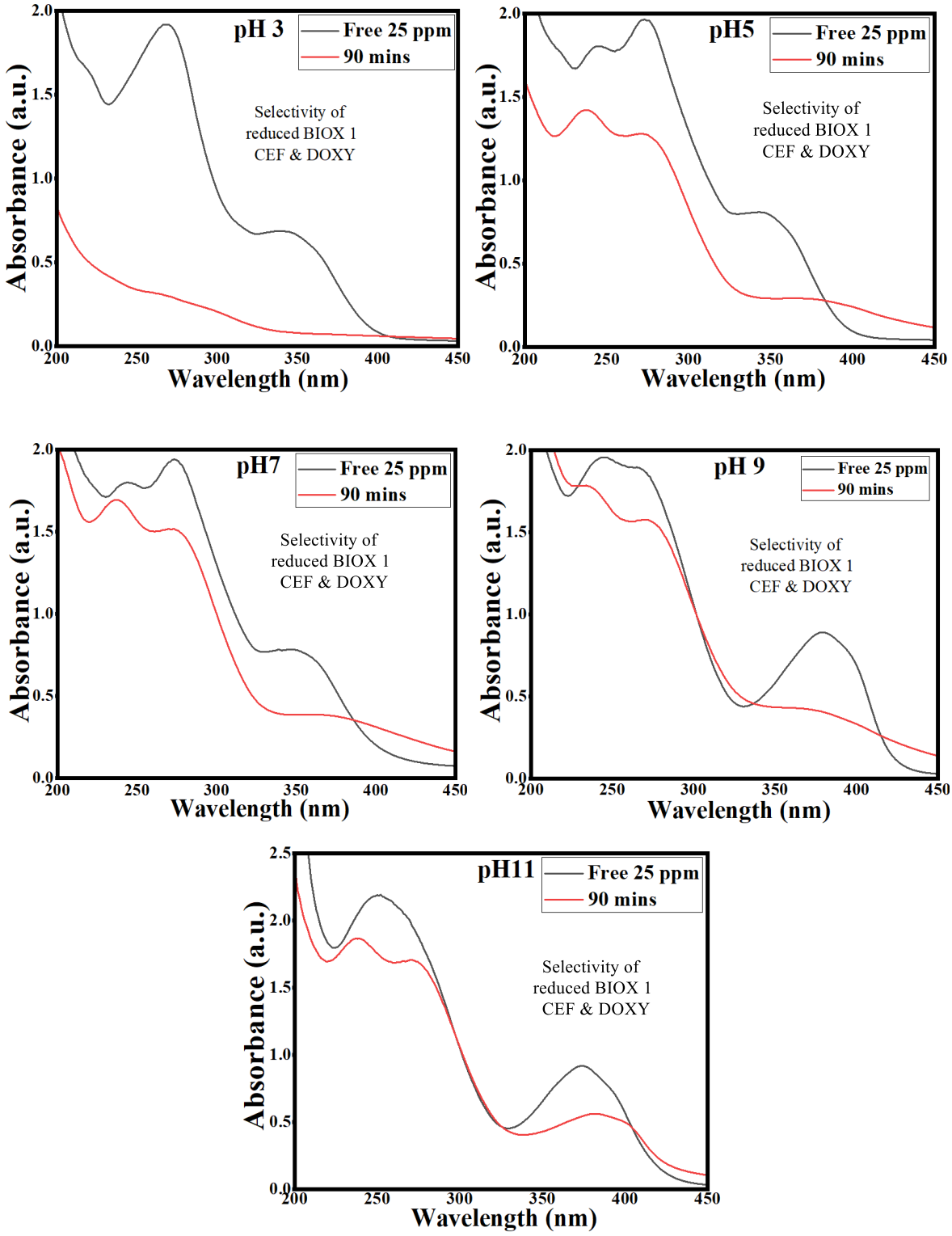
pH 3
Free 25 ppm
90 mins
Selectivity of
reduced BIOX 1
CEF & DOXY
Absorbance (a.u.)
Wavelength (nm)
pH5
pH7
pH 9
pH11

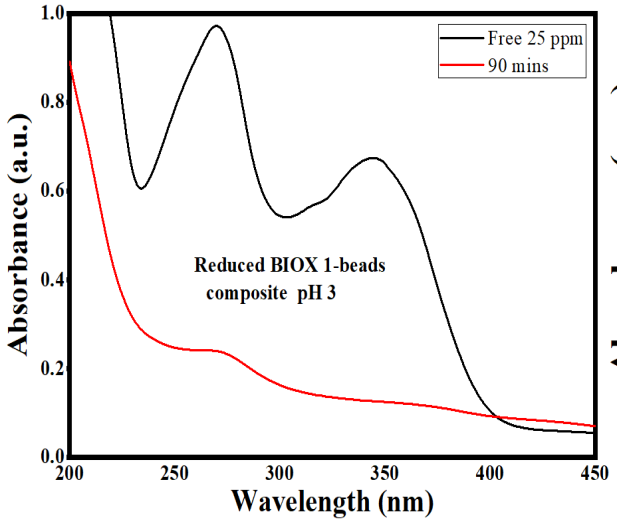
Free 25 ppm
90 mins
Reduced BIOX 1-beads
composite pH 3
Absorbance (a.u.)
Wavelength (nm)

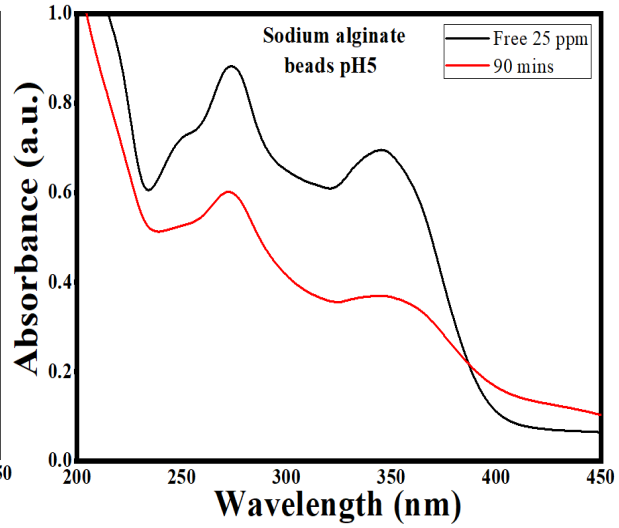
Sodium alginate
beads pH5
Free 25 ppm
90 mins
Absorbance (a.u.)
Wavelength (nm)

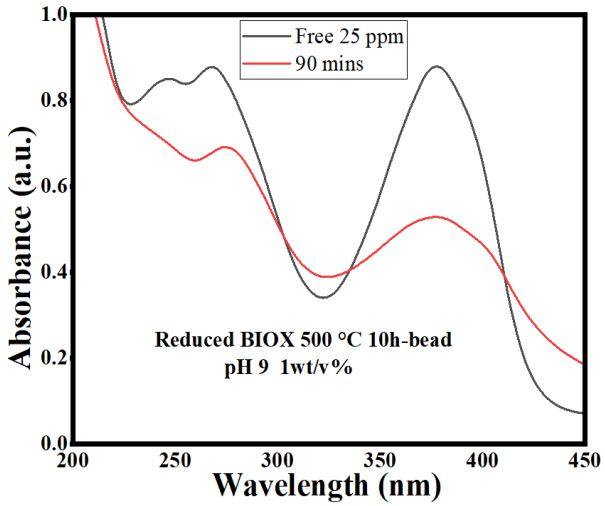
Free 25 ppm
90 mins
Reduced BIOX 500 °C 10h-bead
pH 9 1wt/v%
Absorbance (a.u.)
Wavelength (nm)

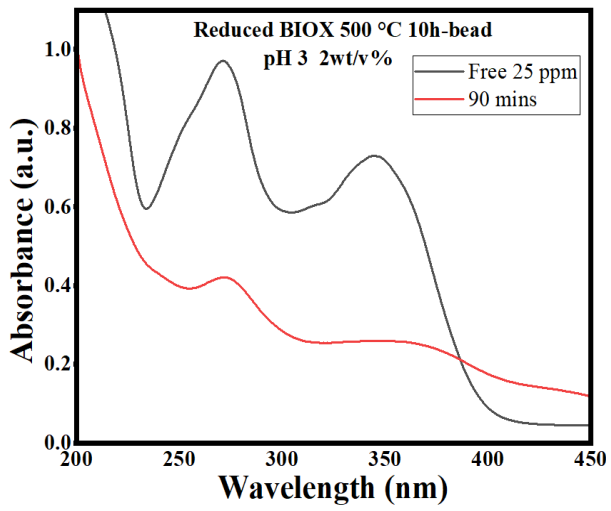
Reduced BIOX 500 °C 10h-bead
pH 3 2wt/v%
Free 25 ppm
90 mins
Absorbance (a.u.)
Wavelength (nm)

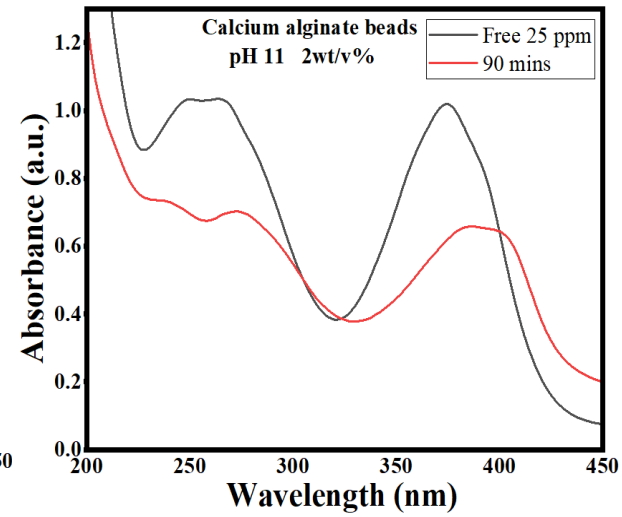
Calcium alginate beads
pH 11 2wt/v%
Free 25 ppm
90 mins
Absorbance (a.u.)
Wavelength (nm)

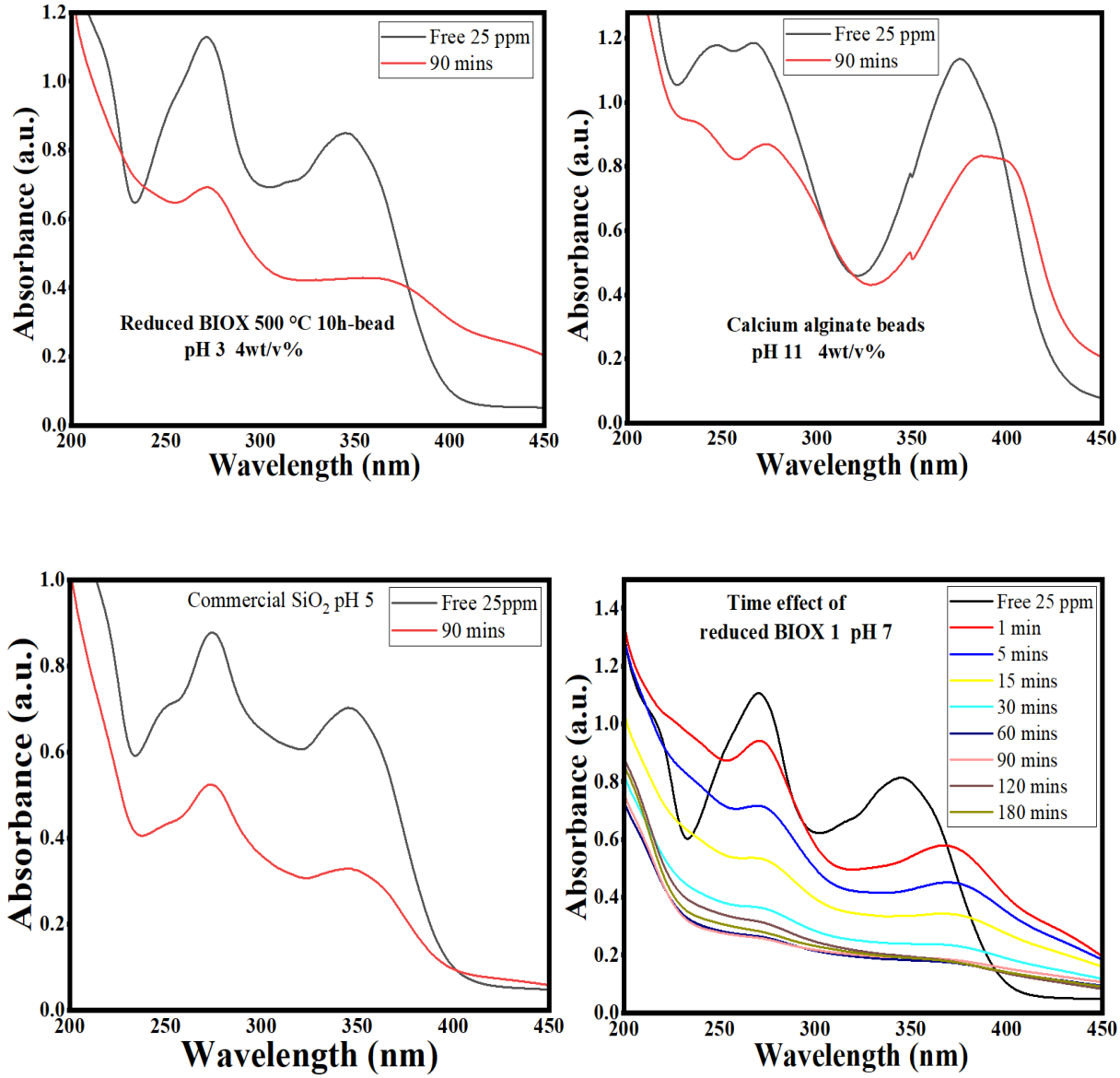

Fig S10. The UV-Visible spectra of the main DOXY adsorption experiments [C_o = 25 ppm, stirring rate = 750 rpm, T = 20 ± 2 °C, volume = 10 mL, and dose = 0.005 g].

Appendix 3.4. The UV-Visible spectra of the main CEF adsorption experiments in Chapter 5.

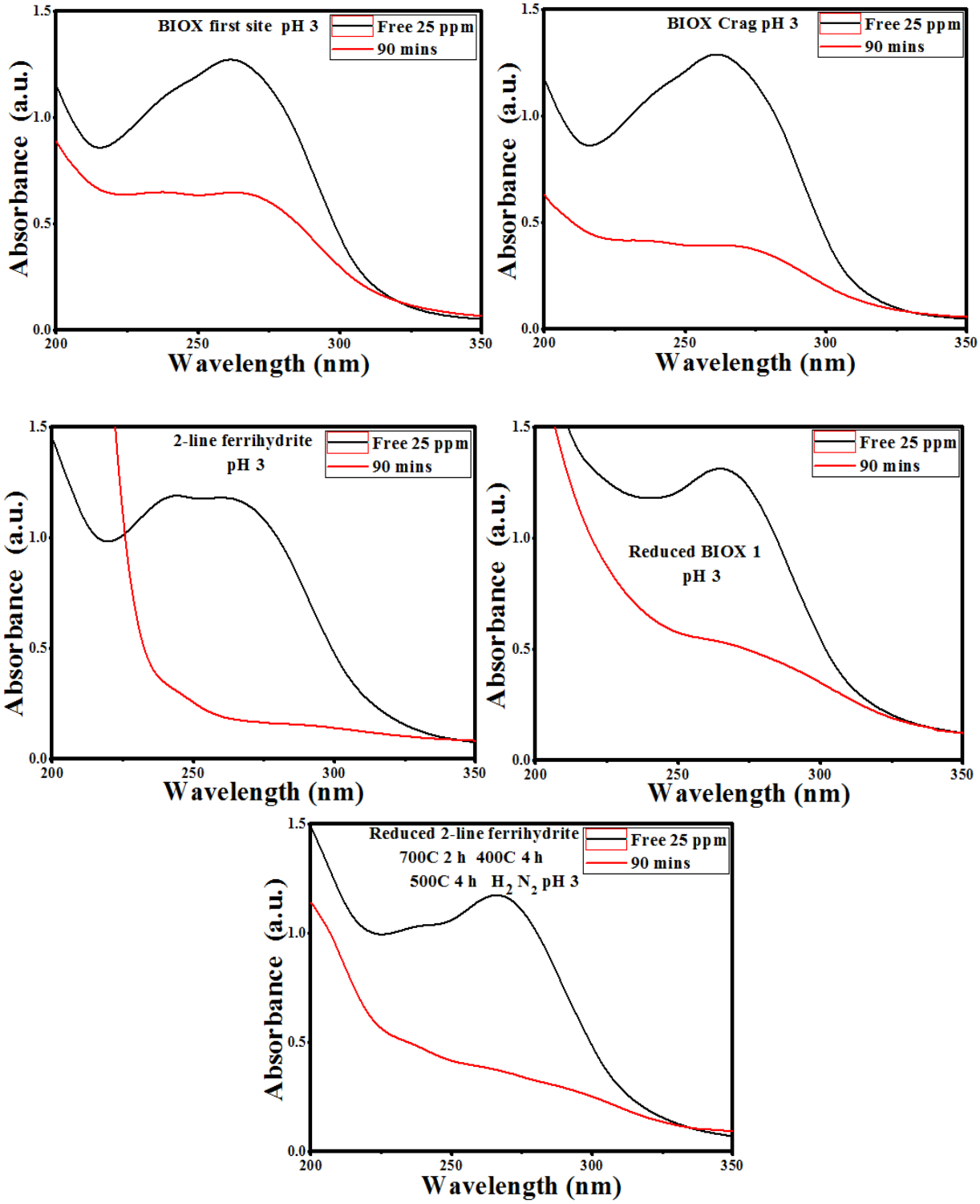

Fig S11. The UV-Visible spectra of the main CEF adsorption experiments [$C_o = 25$ ppm, stirring rate = 750 rpm, T = 20 ± 2 °C, volume = 10 mL, and dose = 0.005 g].

Appendix 4.1. The raw data of determining the point of zero charge (PZC) of the materials reported in Chapter 3.

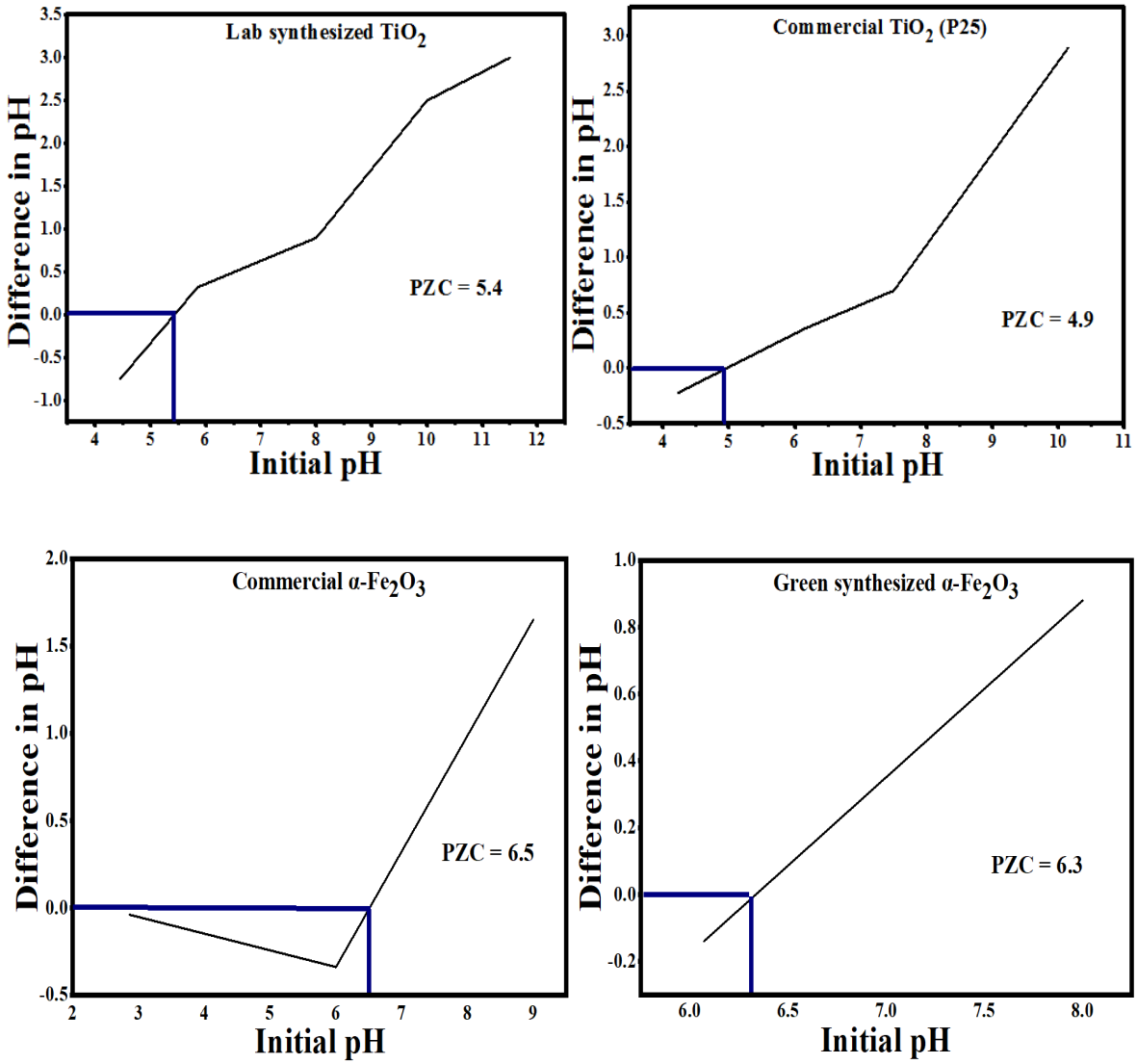

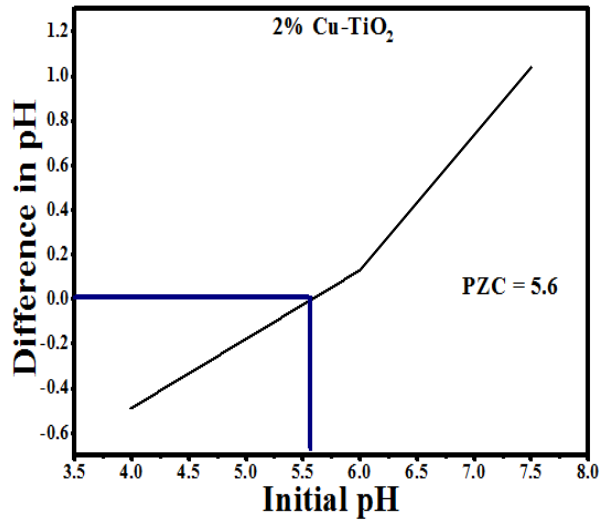
2% Cu-TiO2
Difference in pH
Initial pH
PZC = 5.6

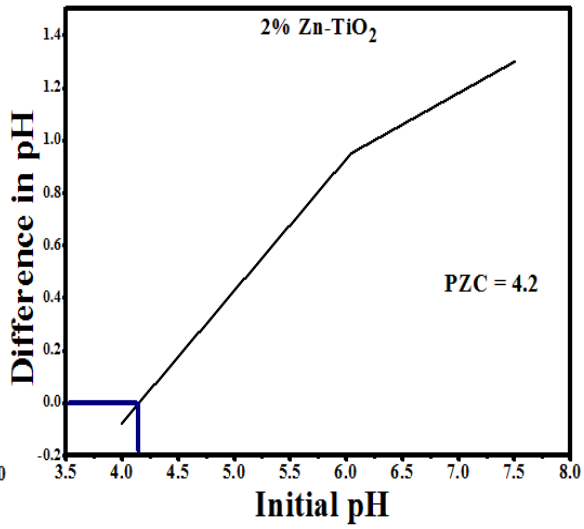
2% Zn-TiO2
Difference in pH
Initial pH
PZC = 4.2

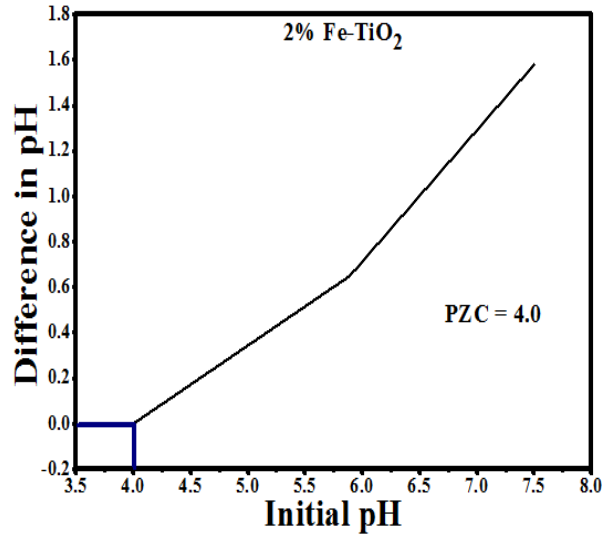
2% Fe-TiO2
Difference in pH
Initial pH
PZC = 4.0

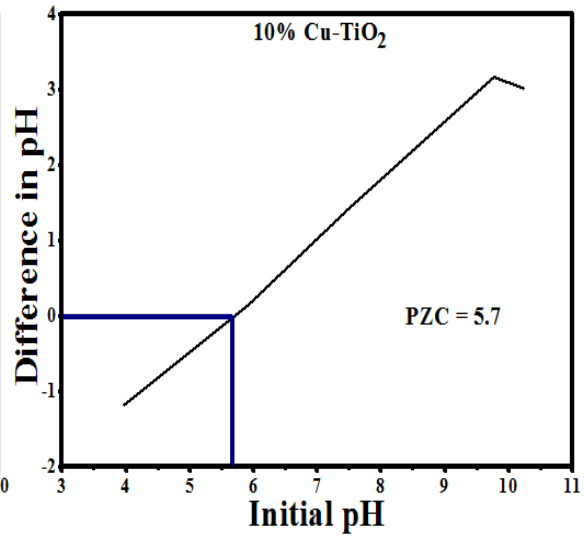
10% Cu-TiO2
Difference in pH
Initial pH
PZC = 5.7

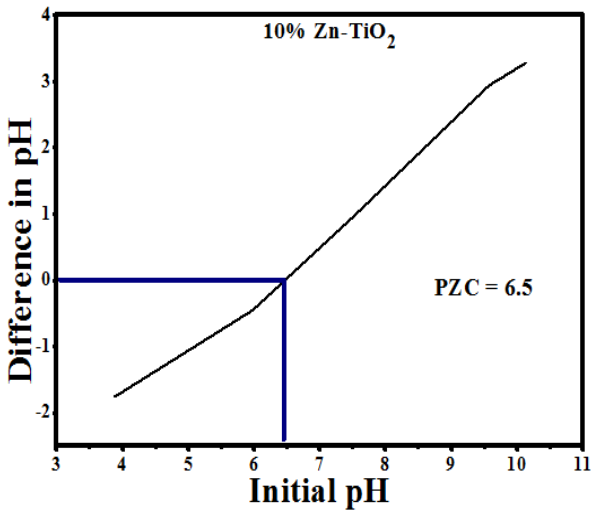
10% Zn-TiO2
Difference in pH
Initial pH
PZC = 6.5

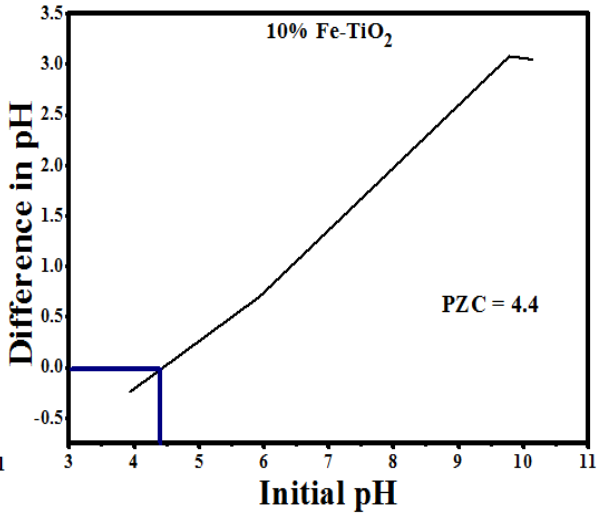
10% Fe-TiO2
Difference in pH
Initial pH
PZC = 4.4

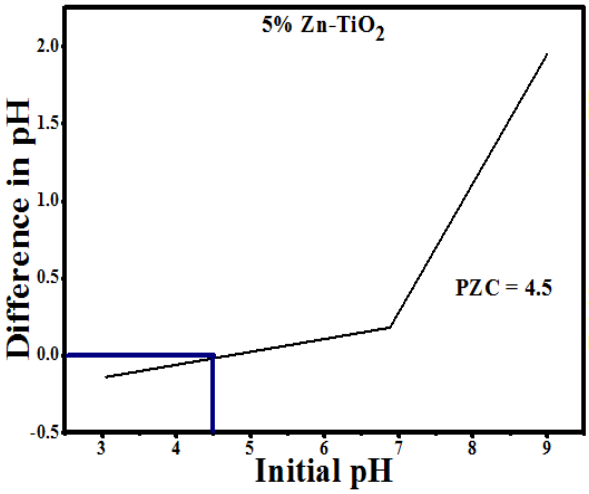
5% Zn-TiO2
Difference in pH
Initial pH
PZC = 4.5

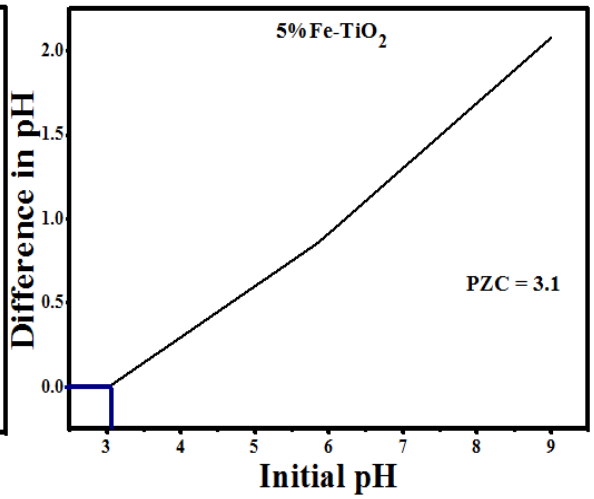
5% Fe-TiO2
Difference in pH
Initial pH
PZC = 3.1

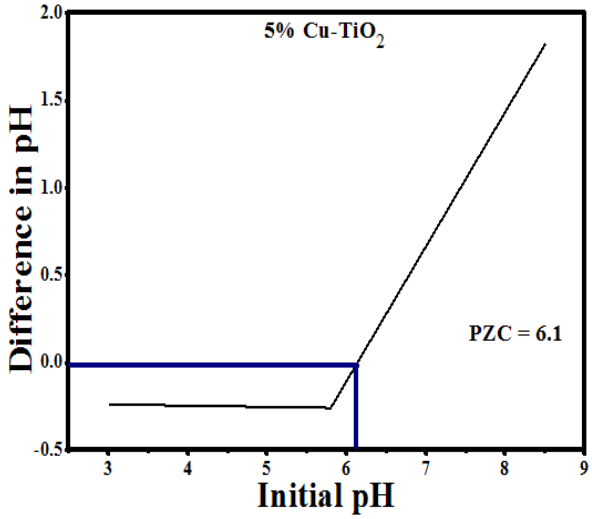
5% Cu-TiO2
Difference in pH
Initial pH
PZC = 6.1

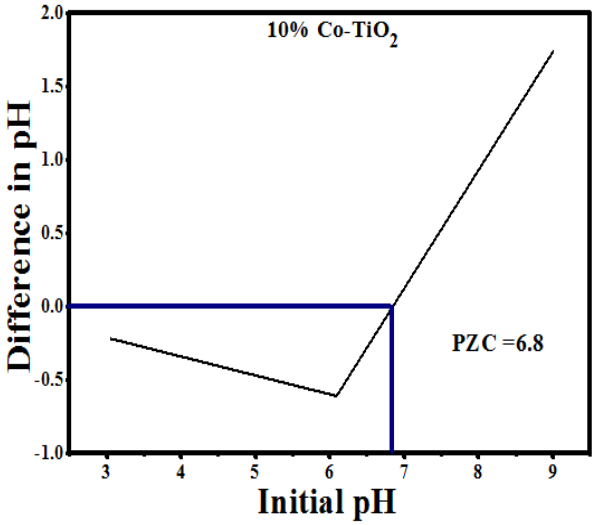
10% Co-TiO2
Difference in pH
Initial pH
PZC =6.8

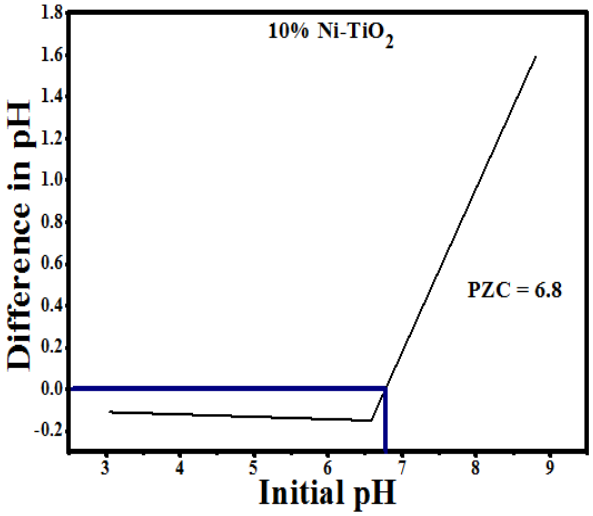
10% Ni-TiO2
Difference in pH
Initial pH
PZC = 6.8

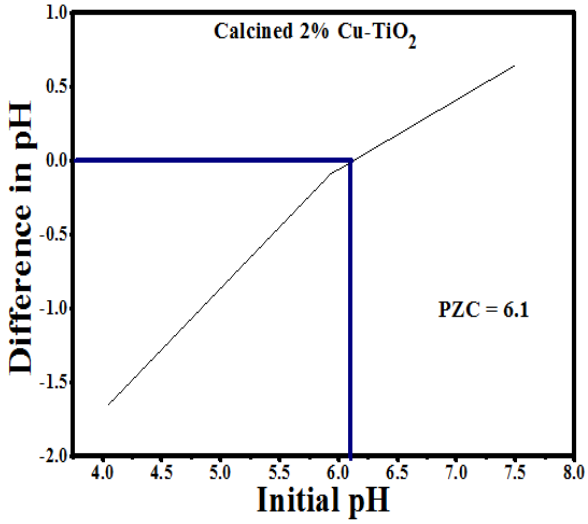
Calcined 2% Cu-TiO2
Difference in pH
Initial pH
PZC = 6.1

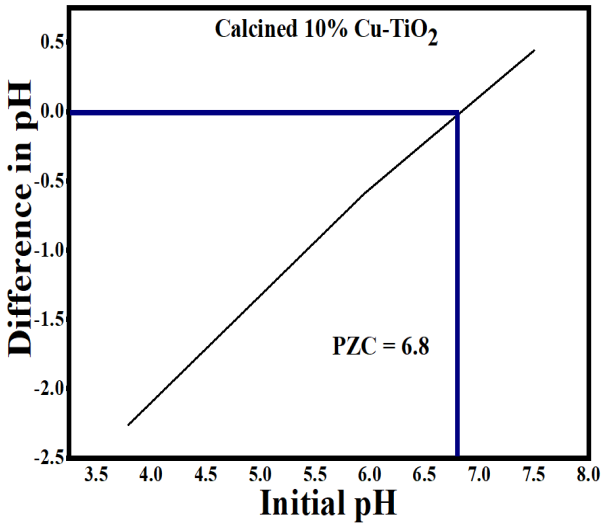
Calcined 10% Cu-TiO2
Difference in pH
Initial pH
PZC = 6.8

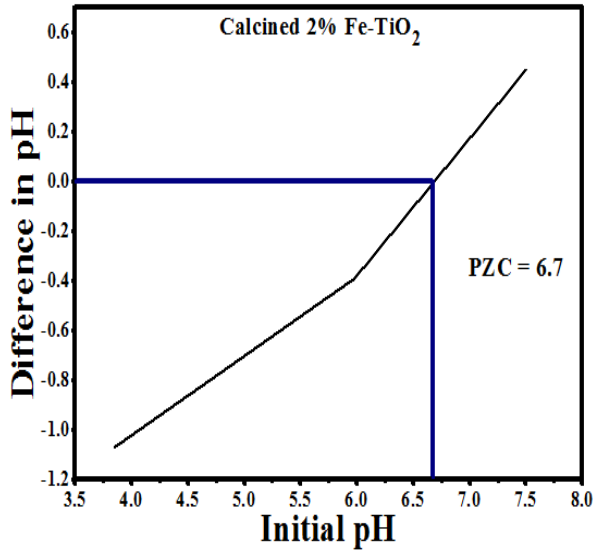
Calcined 2% Fe-TiO2
Difference in pH
Initial pH
PZC = 6.7

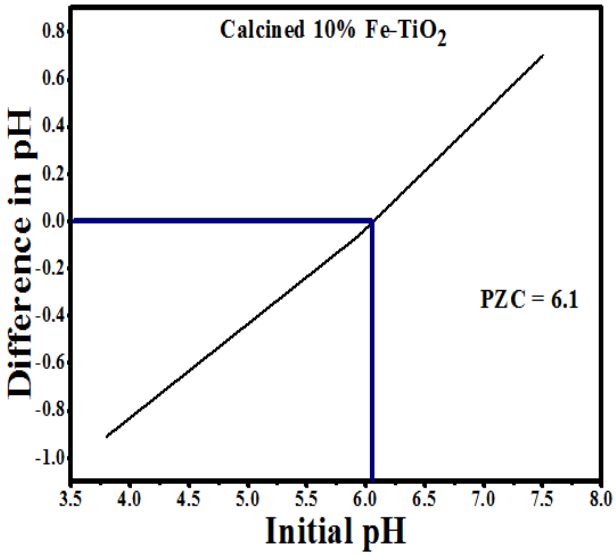
Calcined 10% Fe-TiO2
Difference in pH
Initial pH
PZC = 6.1

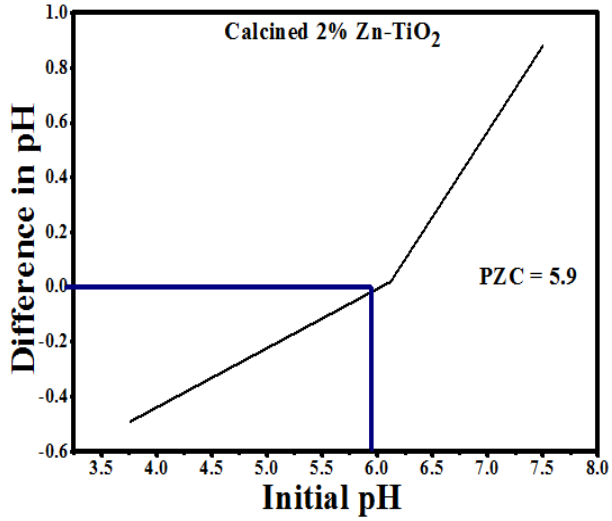
Calcined 2% Zn-TiO2
Difference in pH
Initial pH
PZC = 5.9

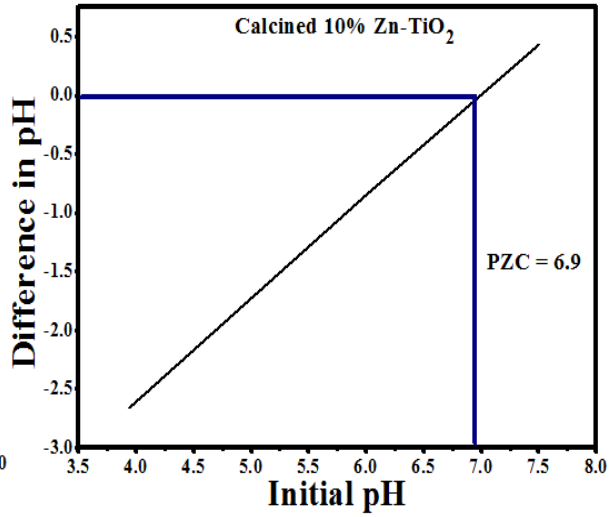
Calcined 10% Zn-TiO2
Difference in pH
Initial pH
PZC = 6.9

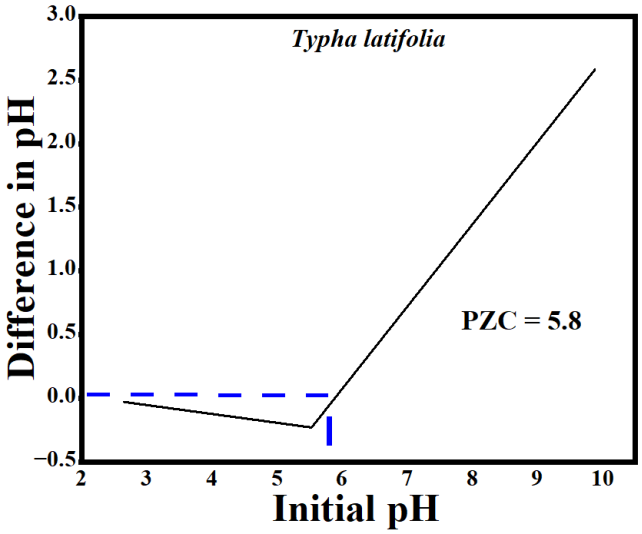
Typha latifolia
Difference in pH
Initial pH
PZC = 5.8

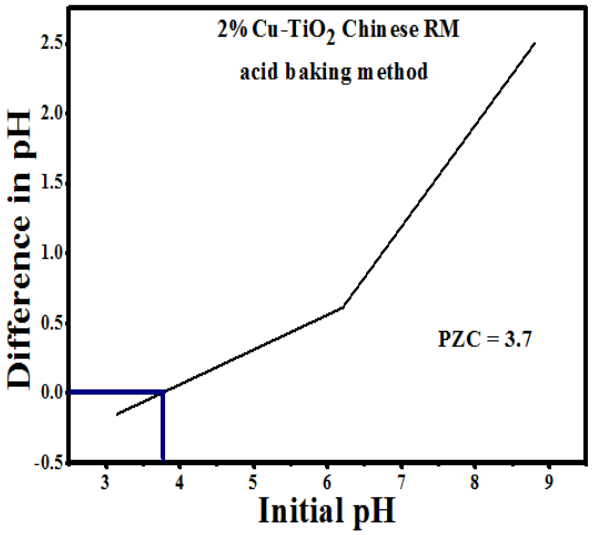
2% Cu-TiO2 Chinese RM
acid baking method
Difference in pH
Initial pH
PZC = 3.7

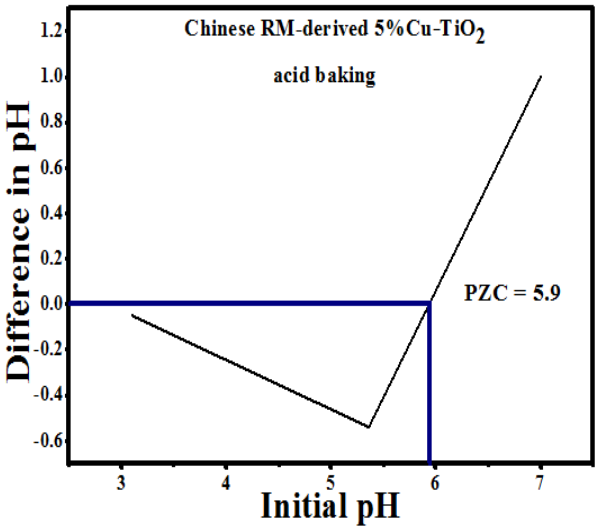
Chinese RM-derived 5% Cu-TiO2
acid baking
Difference in pH
Initial pH
PZC = 5.9

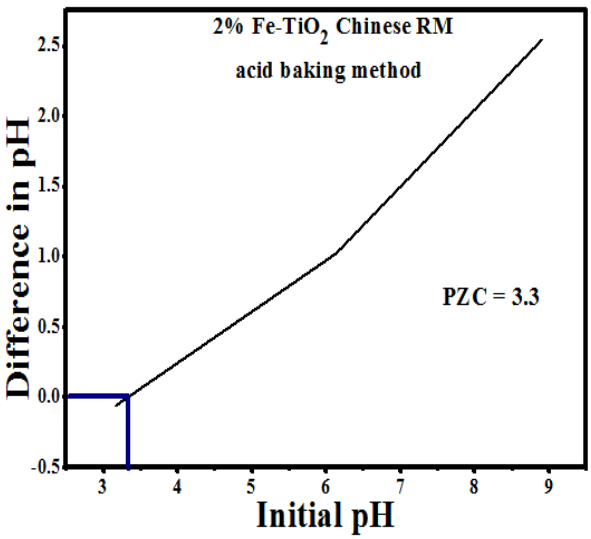
2% Fe-TiO2 Chinese RM
acid baking method
Difference in pH
Initial pH
PZC = 3.3

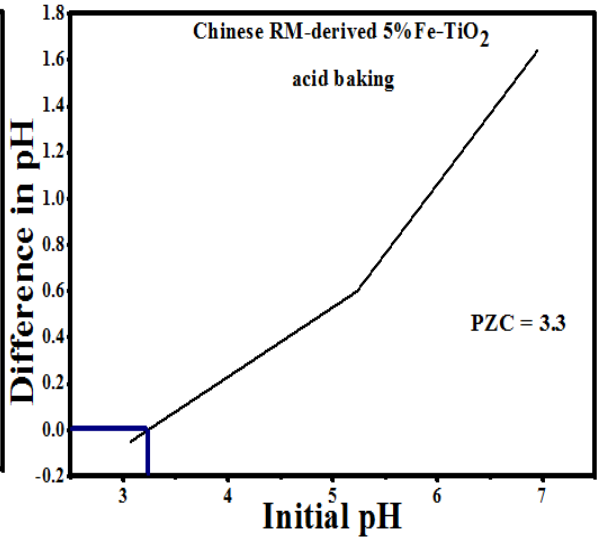
Chinese RM-derived 5% Fe-TiO2
acid baking
Difference in pH
Initial pH
PZC = 3.3

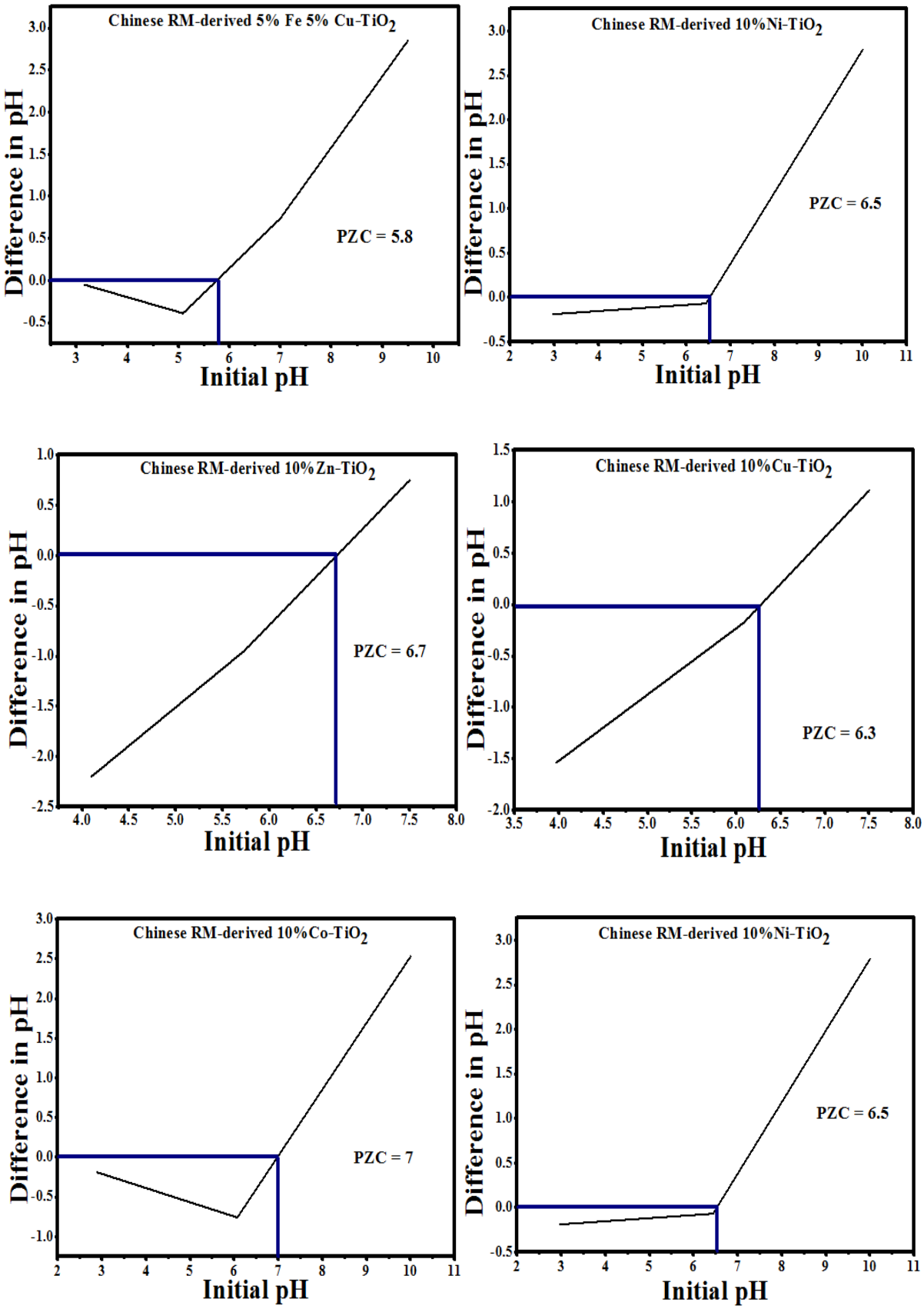

Fig S12. The PZC measurements of the adsorbents used in Chapter 3.

Appendix 4.2. The raw data of determining the point of zero charge (PZC) of the materials reported in Chapter 4.

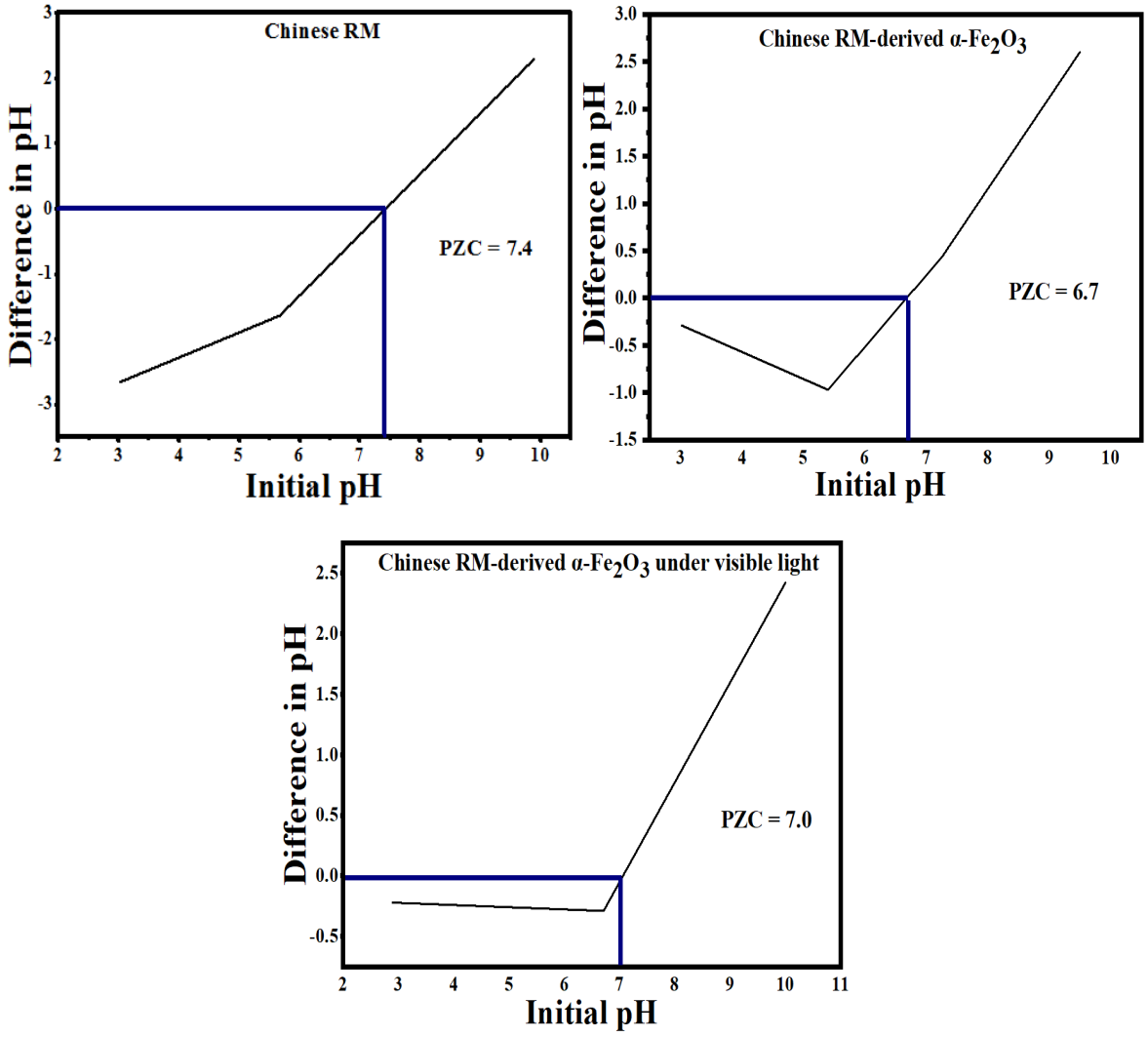

Fig S13. The PZC measurements of the adsorbents used in Chapter 4.

Appendix 4.3. The raw data of determining the point of zero charge (PZC) of the materials reported in Chapter 5.

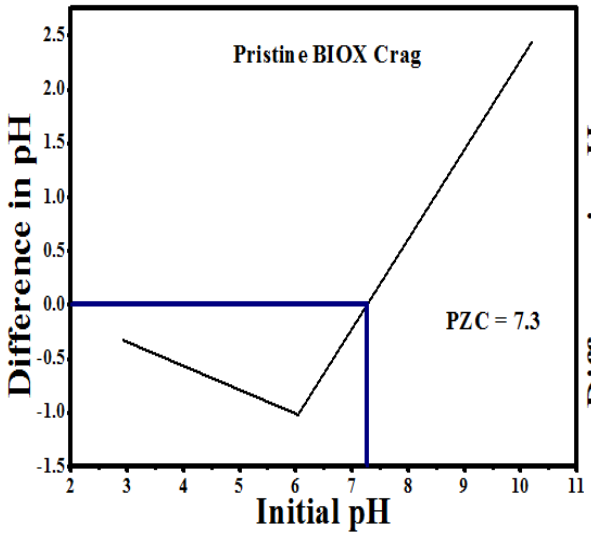

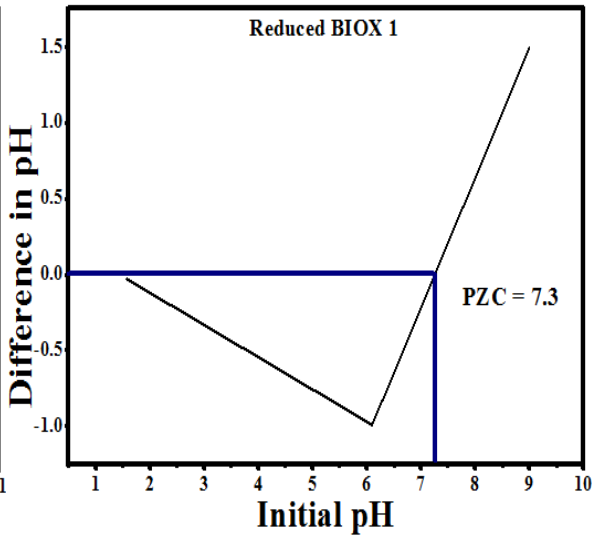

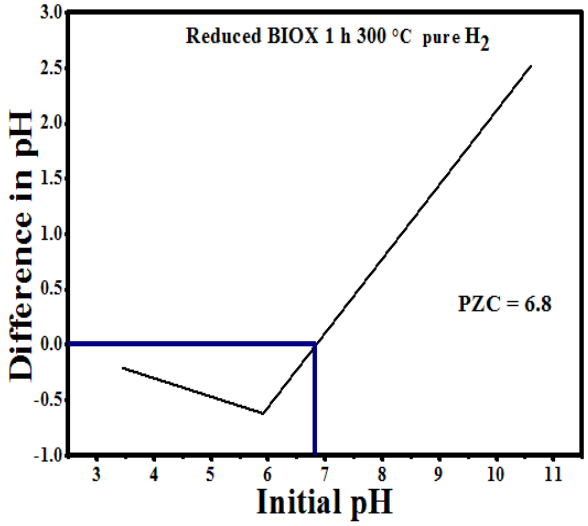

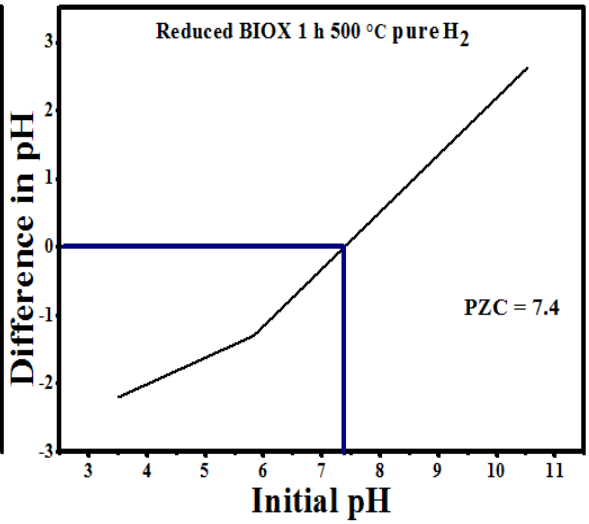

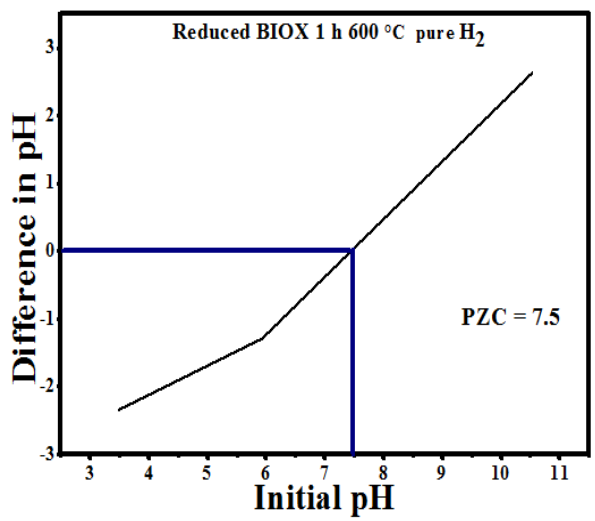
Reduced BIOX 1 h 600 °C pure H_2
Difference in pH
Initial pH
PZC = 7.5

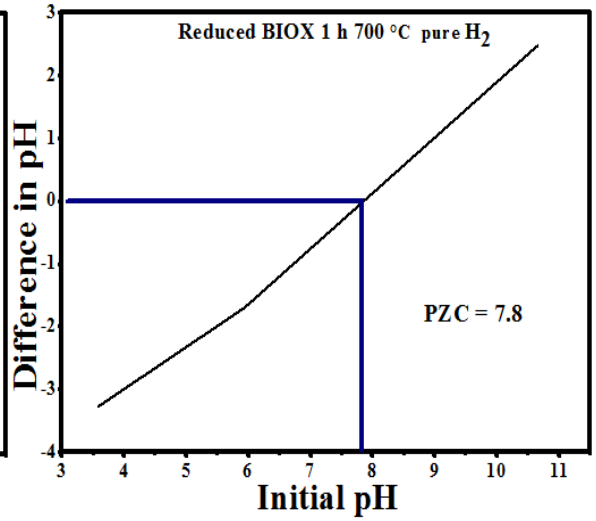
Reduced BIOX 1 h 700 °C pure H_2
Difference in pH
Initial pH
PZC = 7.8

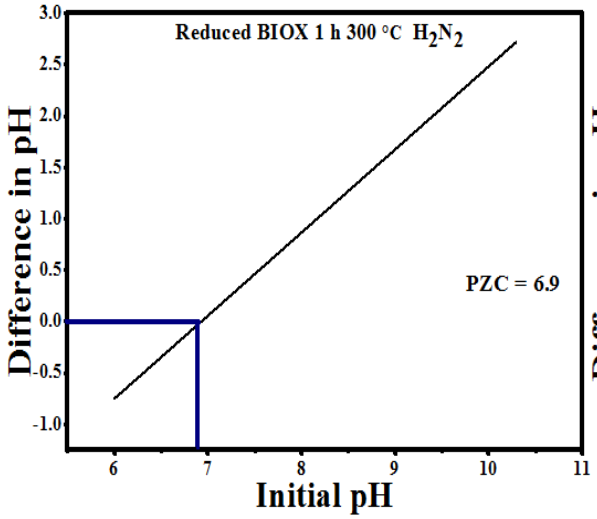
Reduced BIOX 1 h 300 °C H_2N_2
Difference in pH
Initial pH
PZC = 6.9

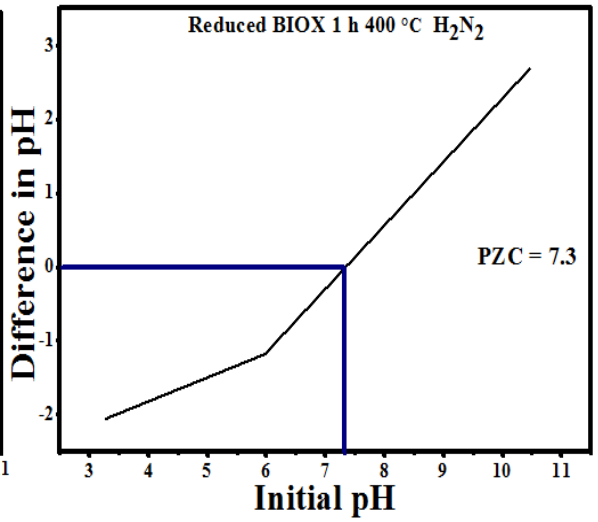
Reduced BIOX 1 h 400 °C H_2N_2
Difference in pH
Initial pH
PZC = 7.3

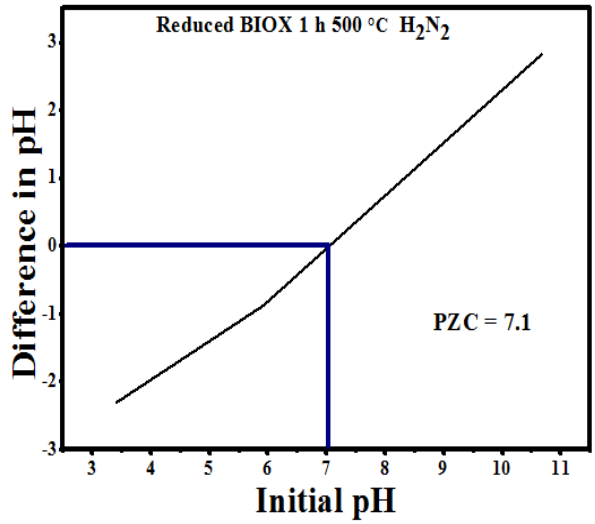
Reduced BIOX 1 h 500 °C H_2N_2
Difference in pH
Initial pH
PZC = 7.1

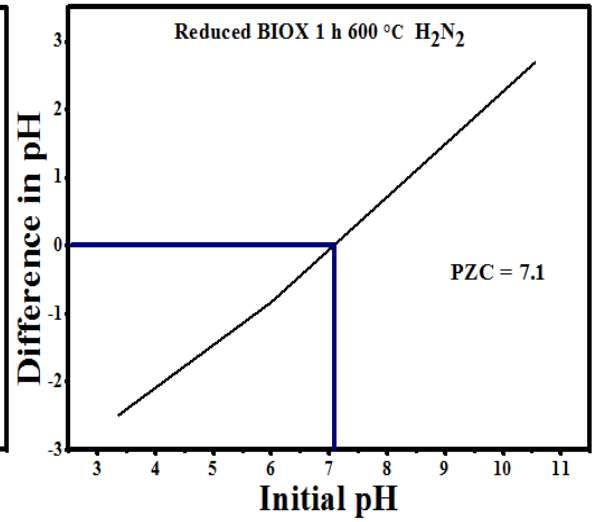
Reduced BIOX 1 h 600 °C H_2N_2
Difference in pH
Initial pH
PZC = 7.1

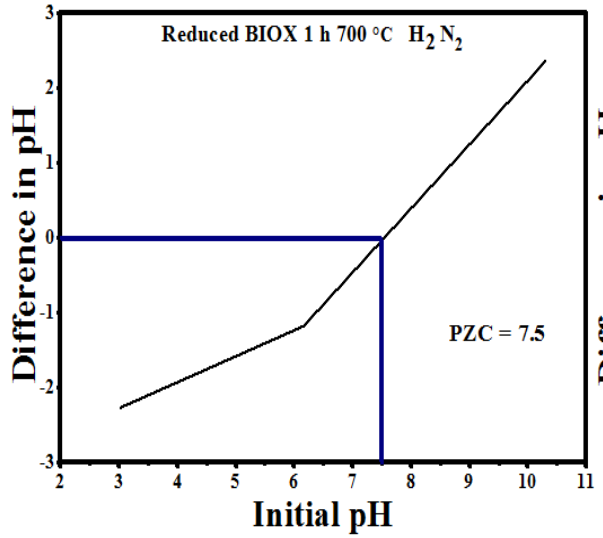
Reduced BIOX 1 h 700 °C H2 N2
Difference in pH
Initial pH
PZC = 7.5

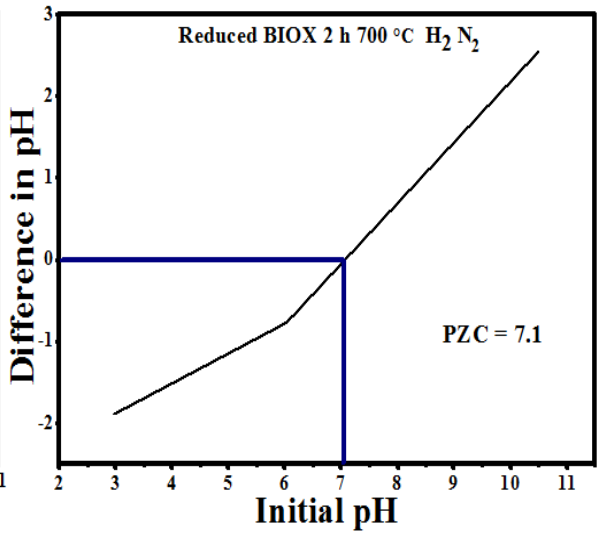
Reduced BIOX 2 h 700 °C H2 N2
Difference in pH
Initial pH
PZC = 7.1

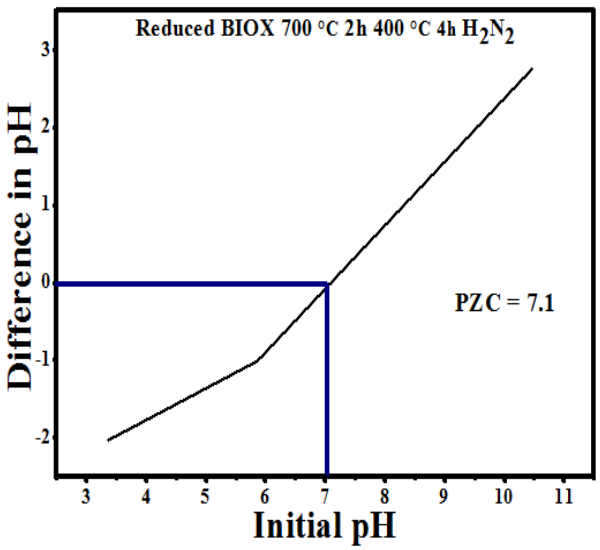
Reduced BIOX 700 °C 2h 400 °C 4h H2N2
Difference in pH
Initial pH
PZC = 7.1

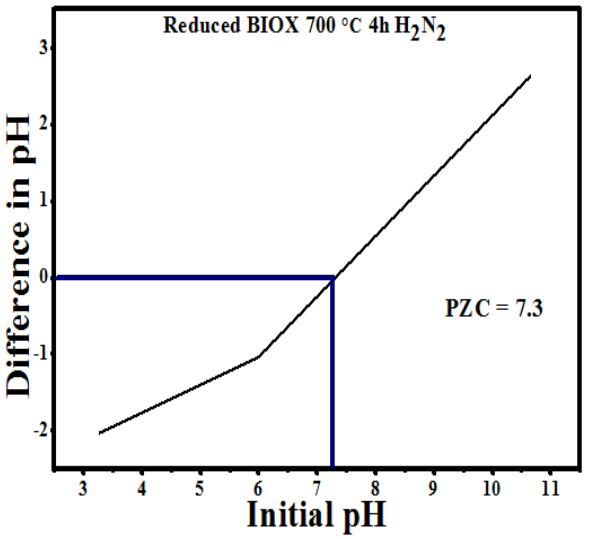
Reduced BIOX 700 °C 4h H2N2
Difference in pH
Initial pH
PZC = 7.3

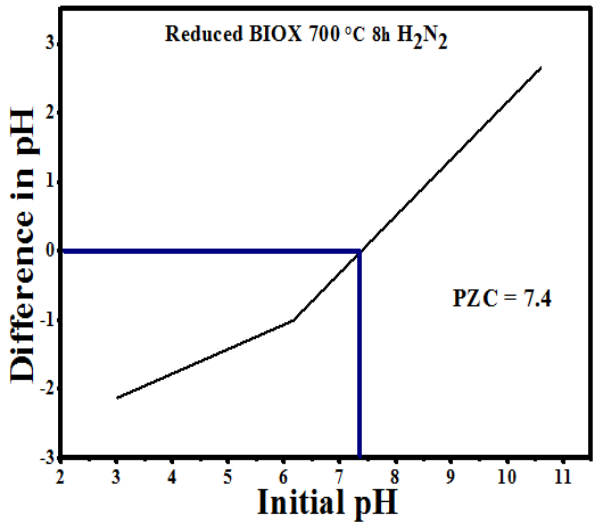
Reduced BIOX 700 °C 8h H2N2
Difference in pH
Initial pH
PZC = 7.4

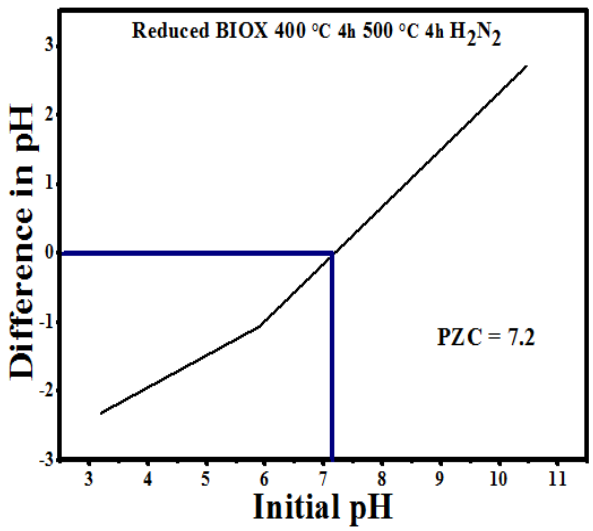
Reduced BIOX 400 °C 4h 500 °C 4h H2N2
Difference in pH
Initial pH
PZC = 7.2

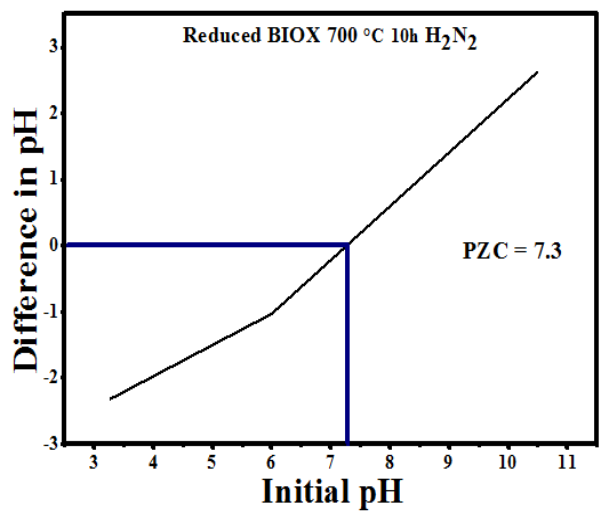
Reduced BIOX 700 °C 10h H_2N_2
Difference in pH
Initial pH
PZC = 7.3

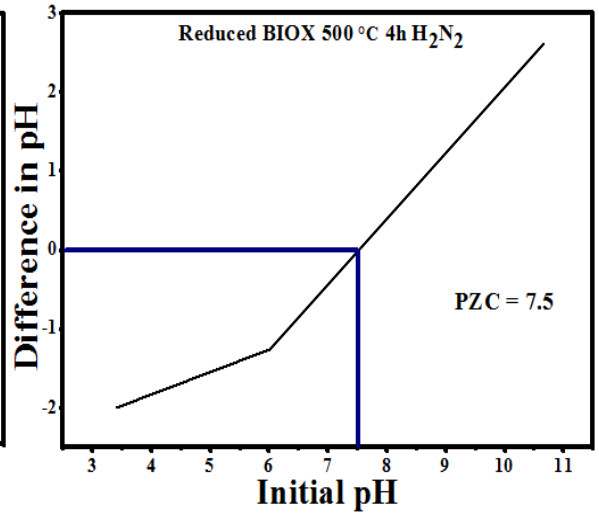
Reduced BIOX 500 °C 4h H_2N_2
Difference in pH
Initial pH
PZC = 7.5

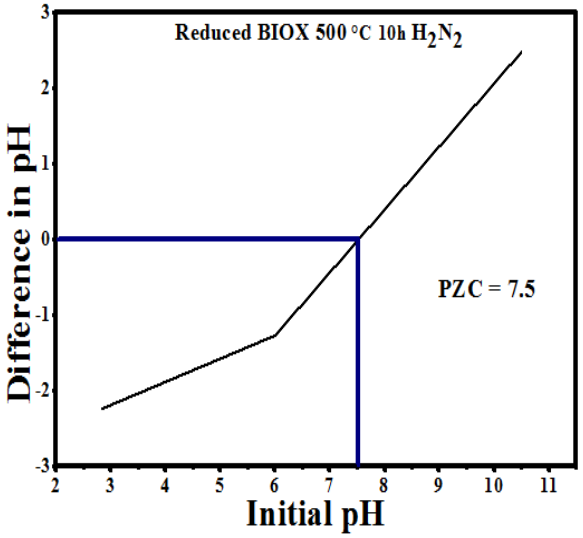
Reduced BIOX 500 °C 10h H_2N_2
Difference in pH
Initial pH
PZC = 7.5

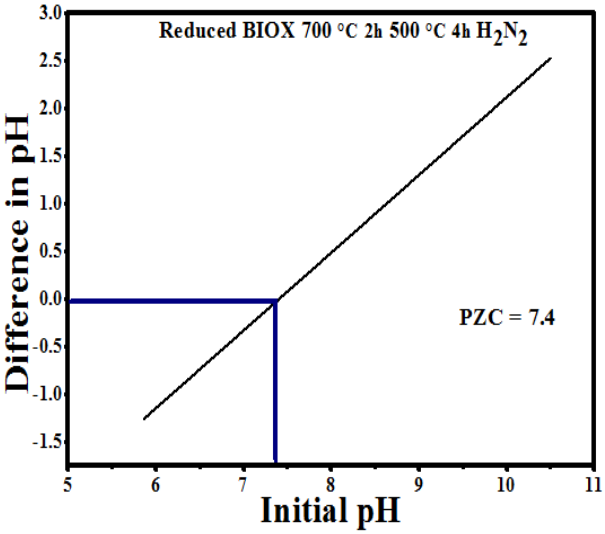
Reduced BIOX 700 °C 2h 500 °C 4h H_2N_2
Difference in pH
Initial pH
PZC = 7.4

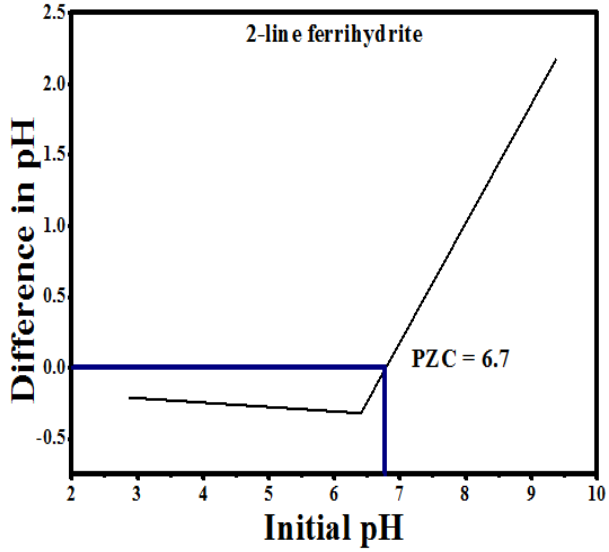
2-line ferrihydrite
Difference in pH
Initial pH
PZC = 6.7

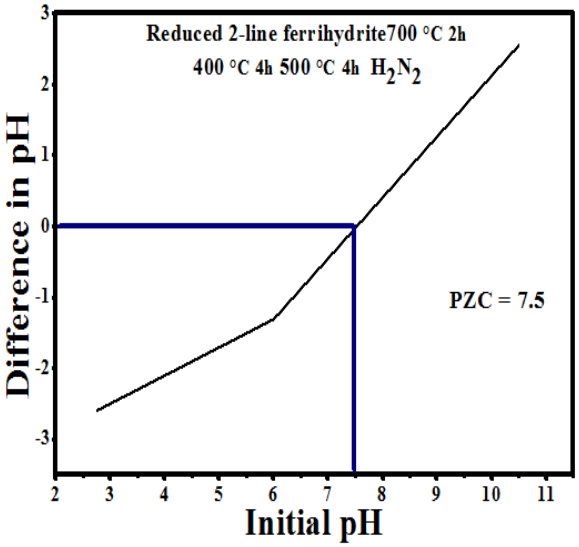
Reduced 2-line ferrihydrite700 °C 2h
400 °C 4h 500 °C 4h H_2N_2
Difference in pH
Initial pH
PZC = 7.5

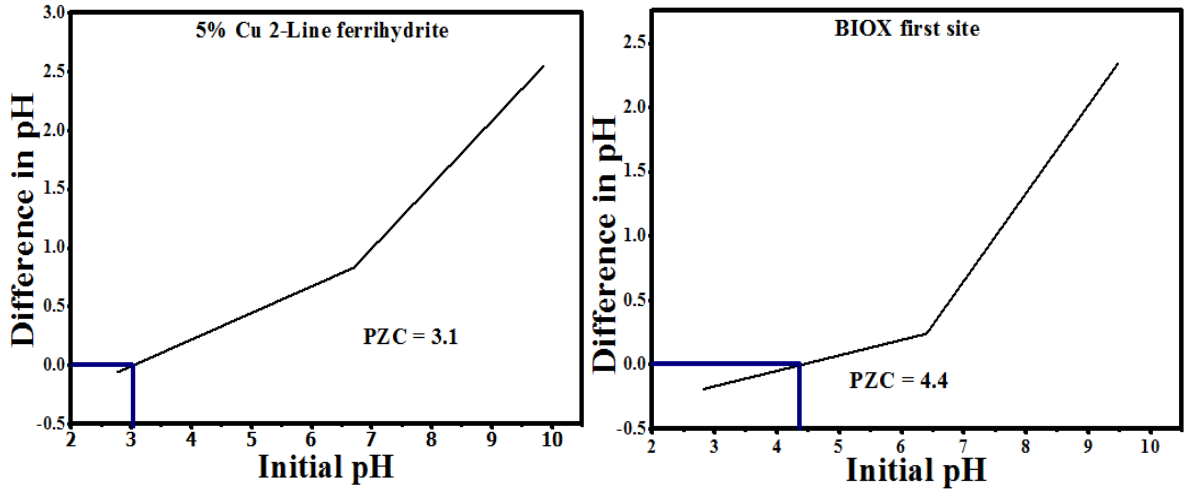

Fig S14. The PZC measurements of the adsorbents used in Chapter 5.

Appendix 5. EDX and SEM of reduced BIOX materials of Chapter 5.

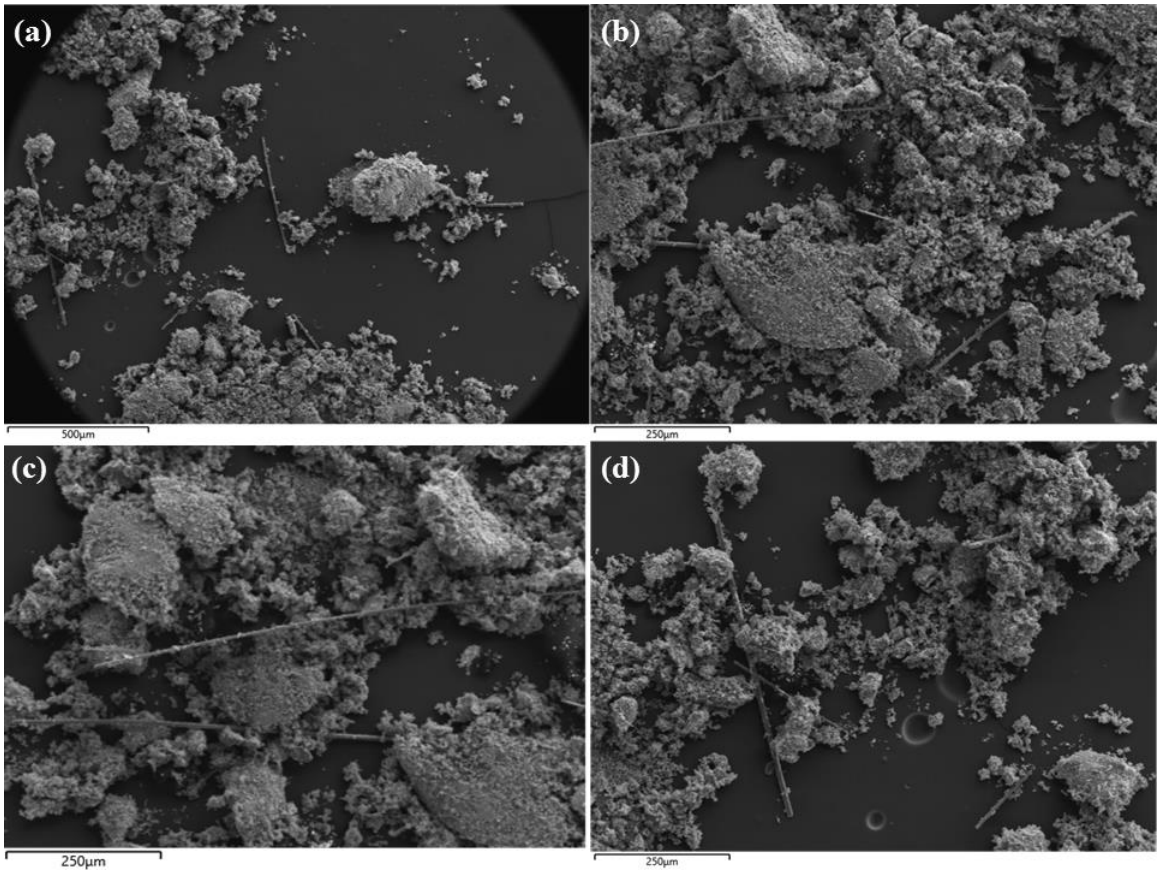

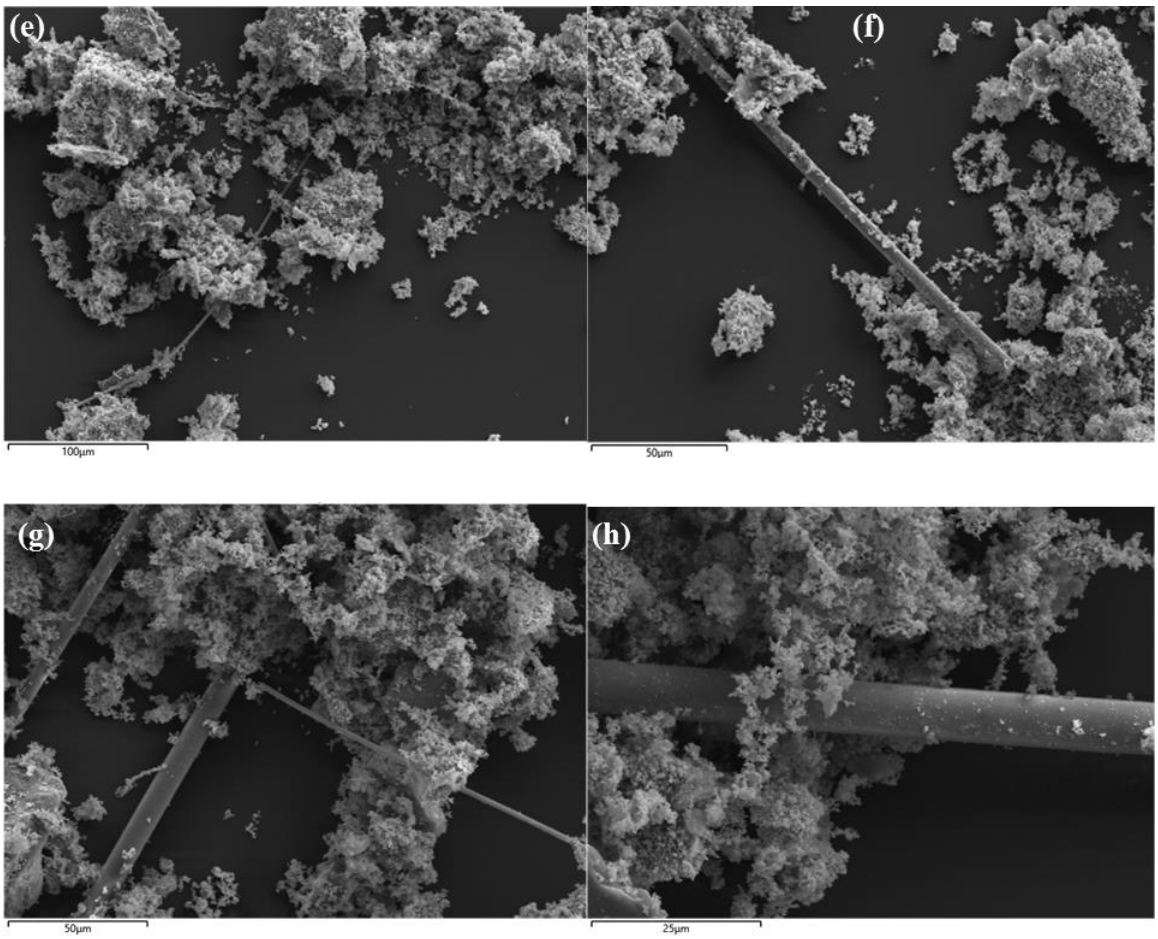

Fig S15. SEM images of reduced BIOX 1 (**a-h**).

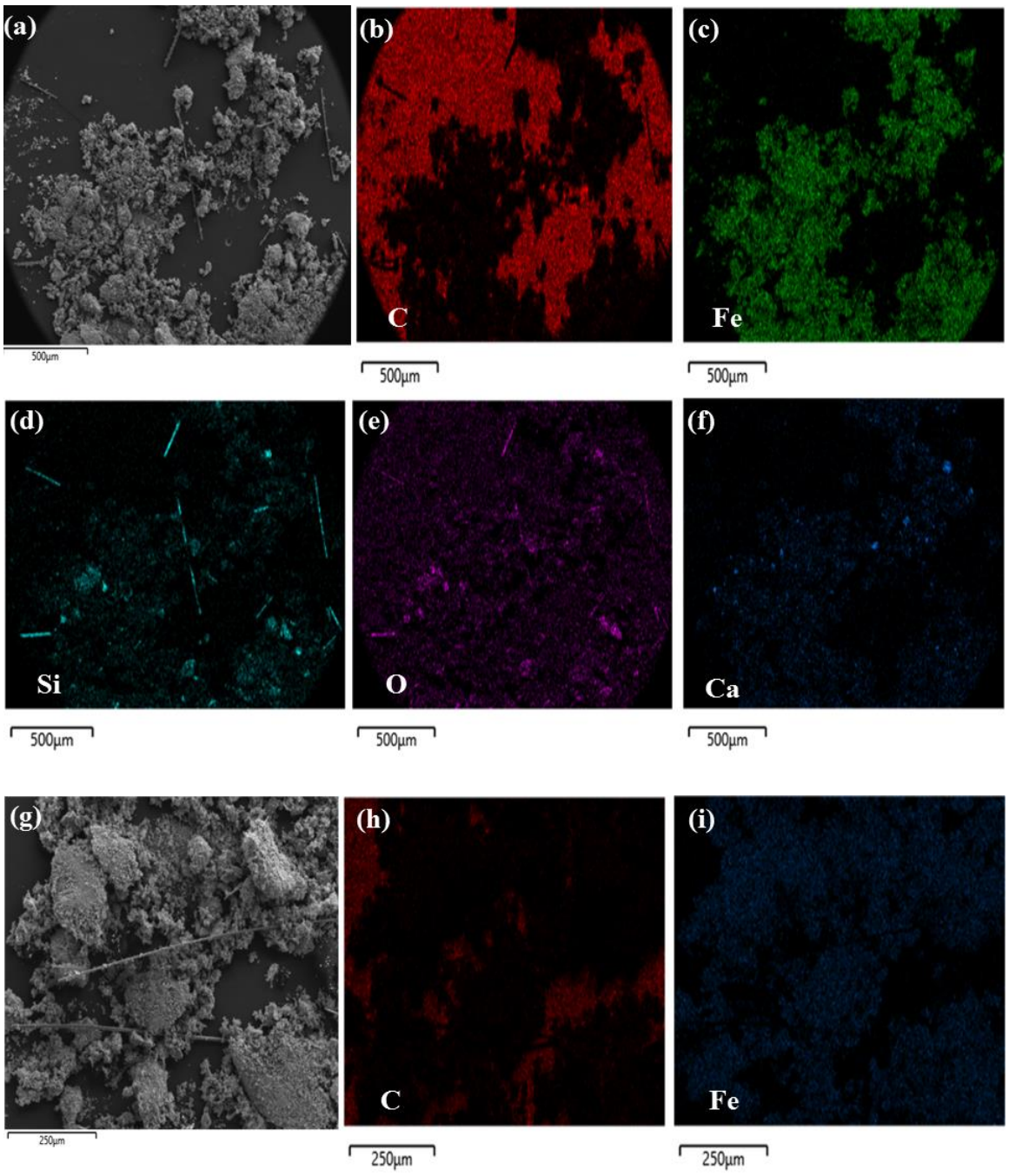
(a)
500µm
(b)
C
500µm
(c)
Fe
500µm
(d)
Si
500µm
(e)
O
500µm
(f)
Ca
500µm
(g)
250µm
(h)
C
250µm
(i)
Fe
250µm

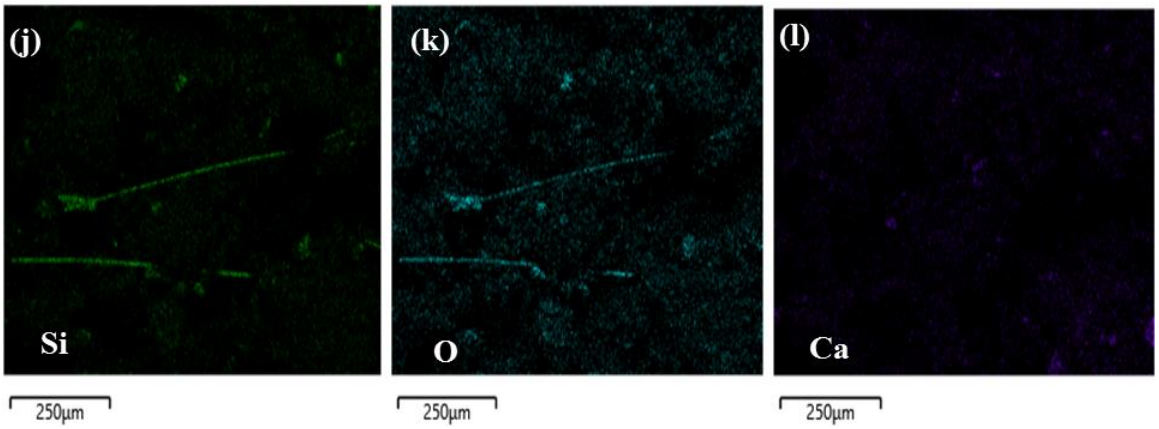

Fig S16. SEM images of reduced BIOX 1 (**a** and **g**) and their elemental mapping; (**b-f**) and (**h-l**).

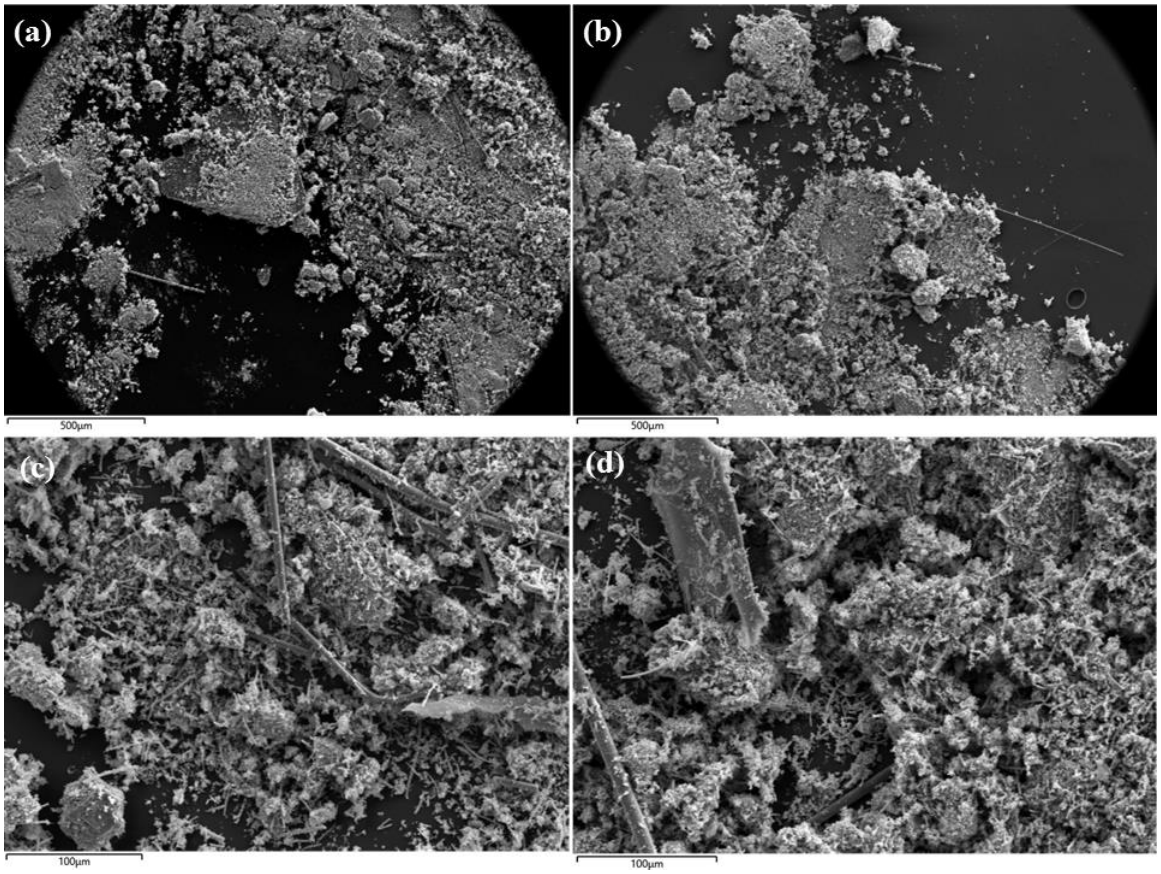

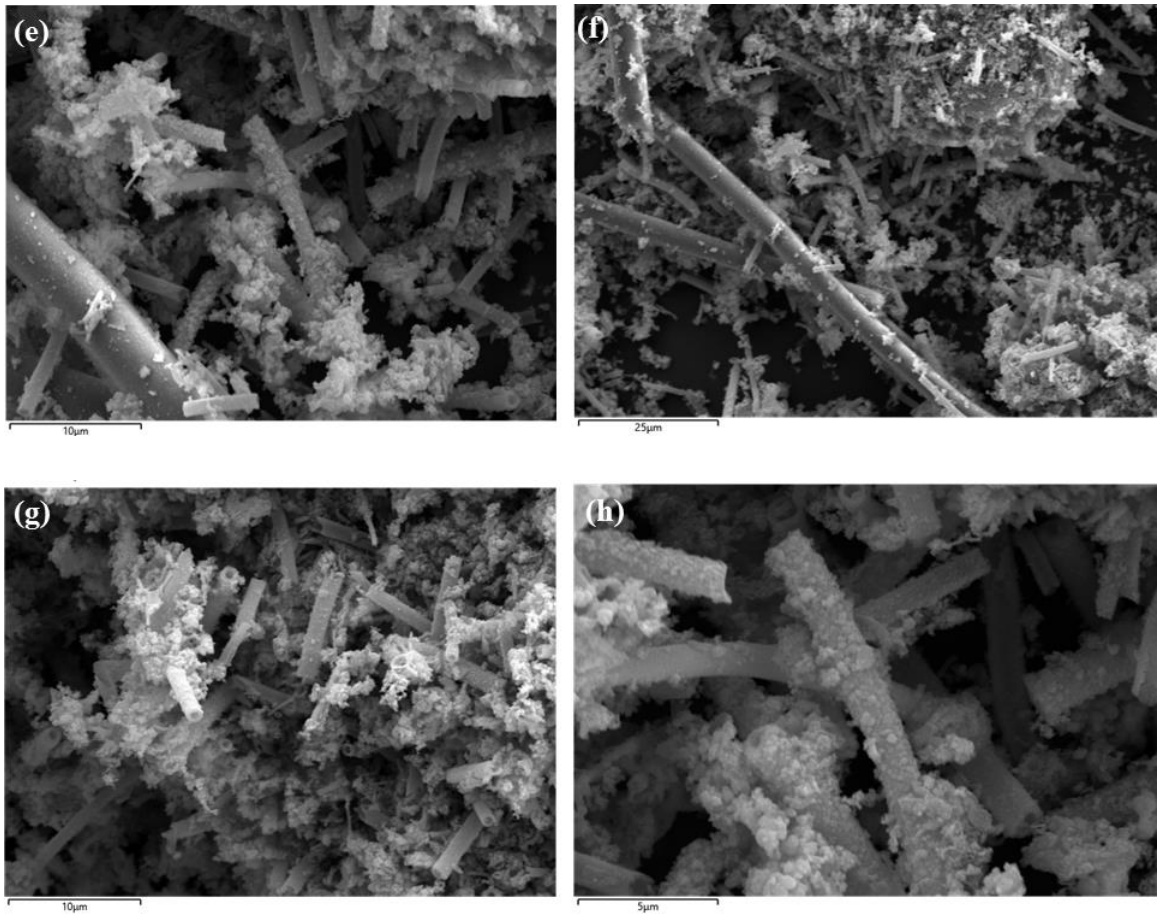

Fig S17. SEM images of reduced BIOX 300 °C 1 h H_2/N_2 (**a-h**).

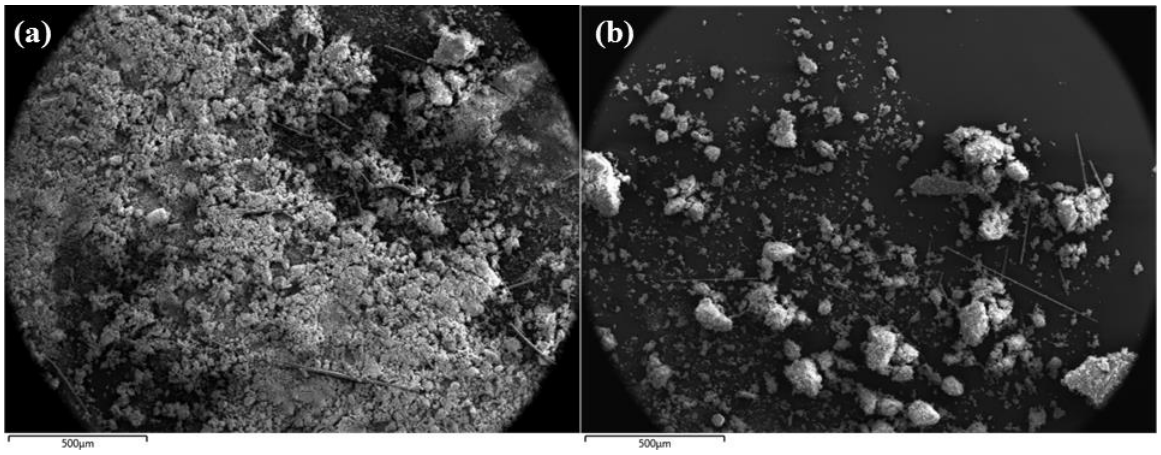

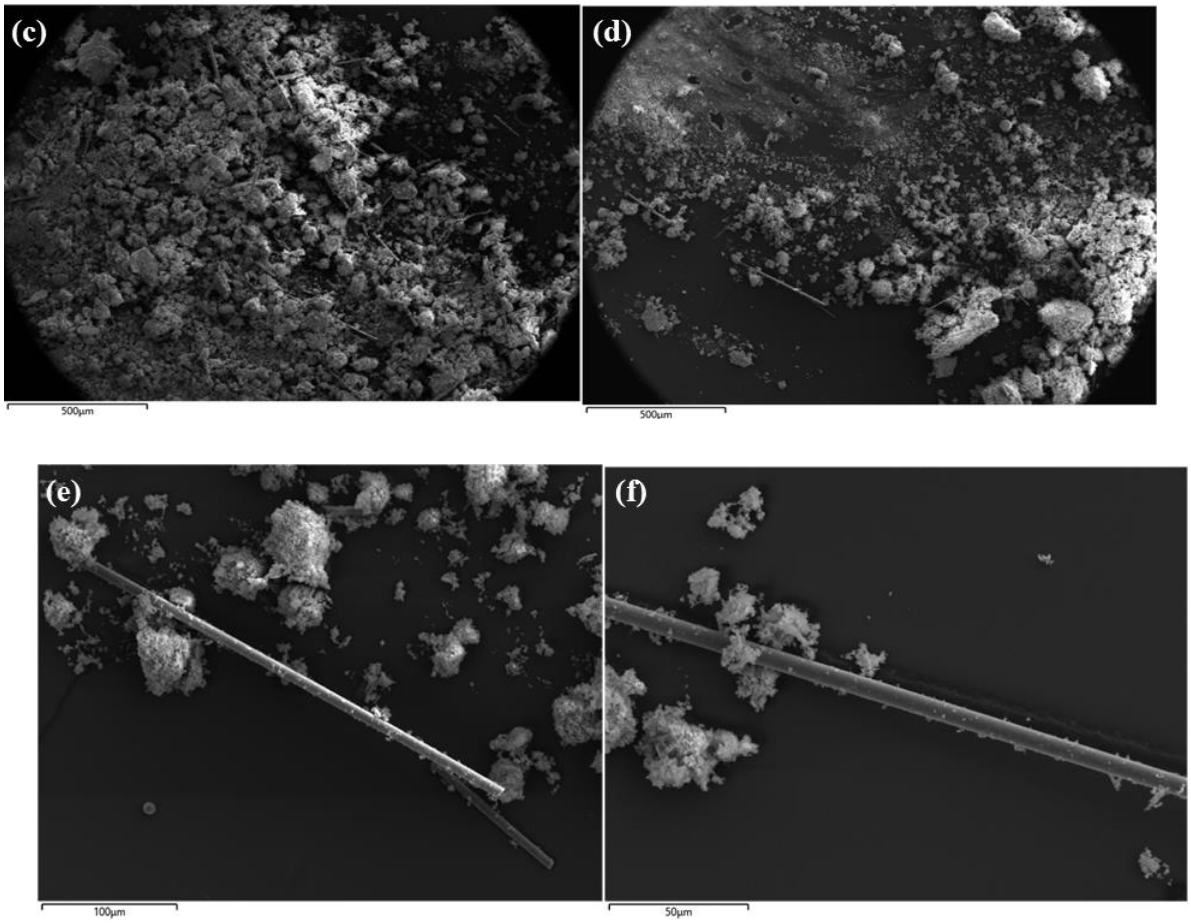

Fig S18. SEM images of reduced BIOX 500 °C 10 h H_2/N_2 (**a-f**).

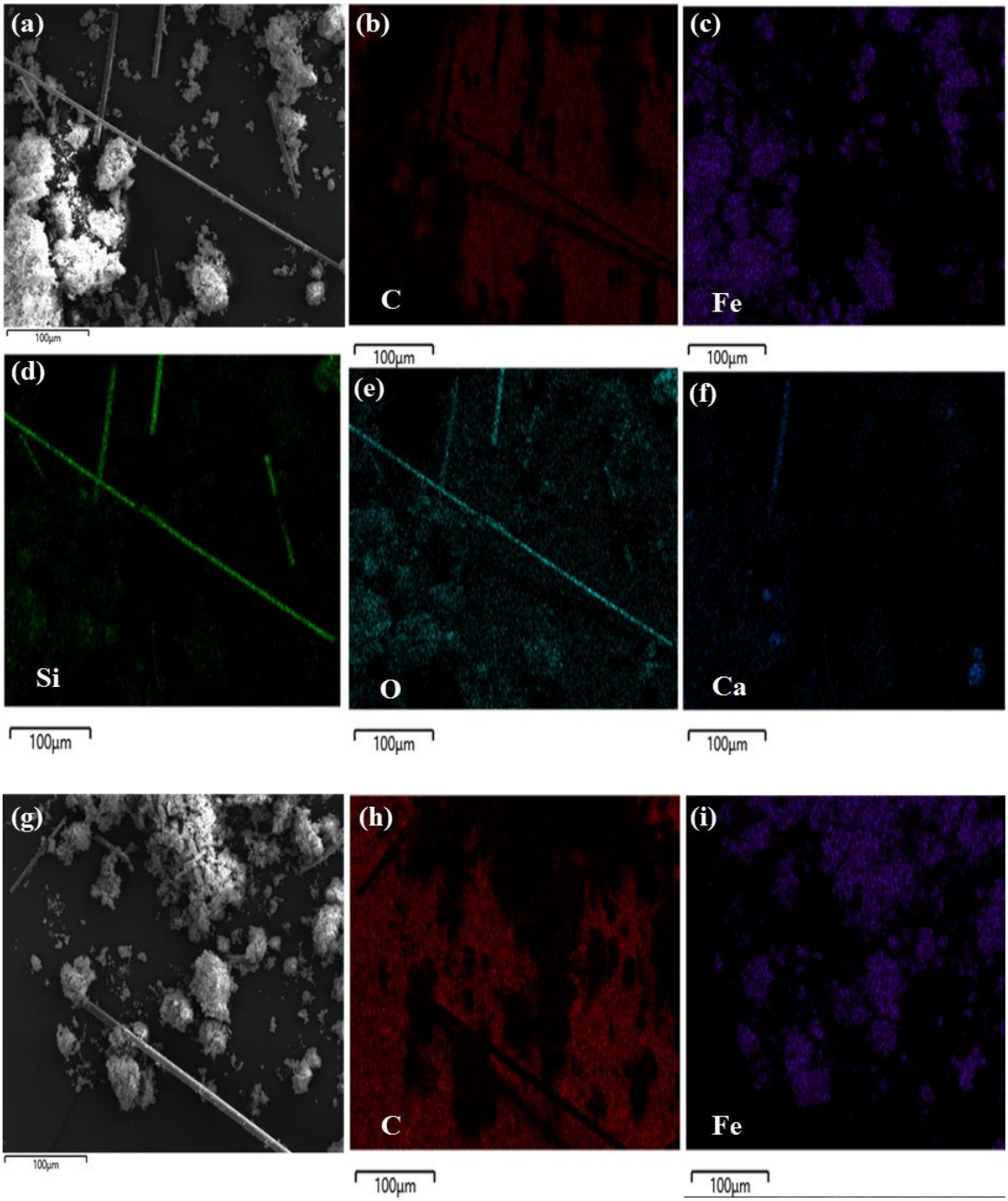
(a)
(b)
C
(c)
Fe
100µm
100µm
100µm
(d)
Si
(e)
O
(f)
Ca
100µm
100µm
100µm
(g)
(h)
C
(i)
Fe
100µm
100µm
100µm

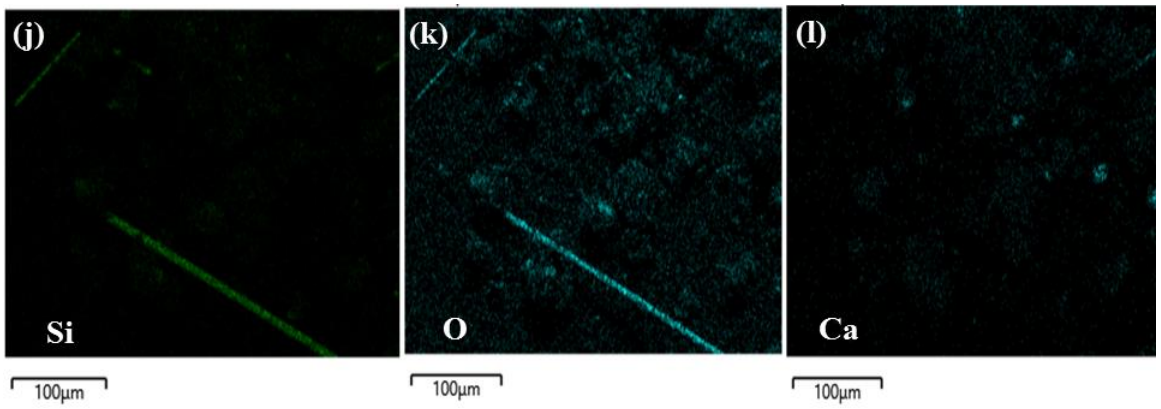

Fig S19. SEM images of reduced BIOX 500 °C 10 h H_2/N_2 (**a** and **g**) and their elemental mapping; (**b-f**) and (**h-l**).

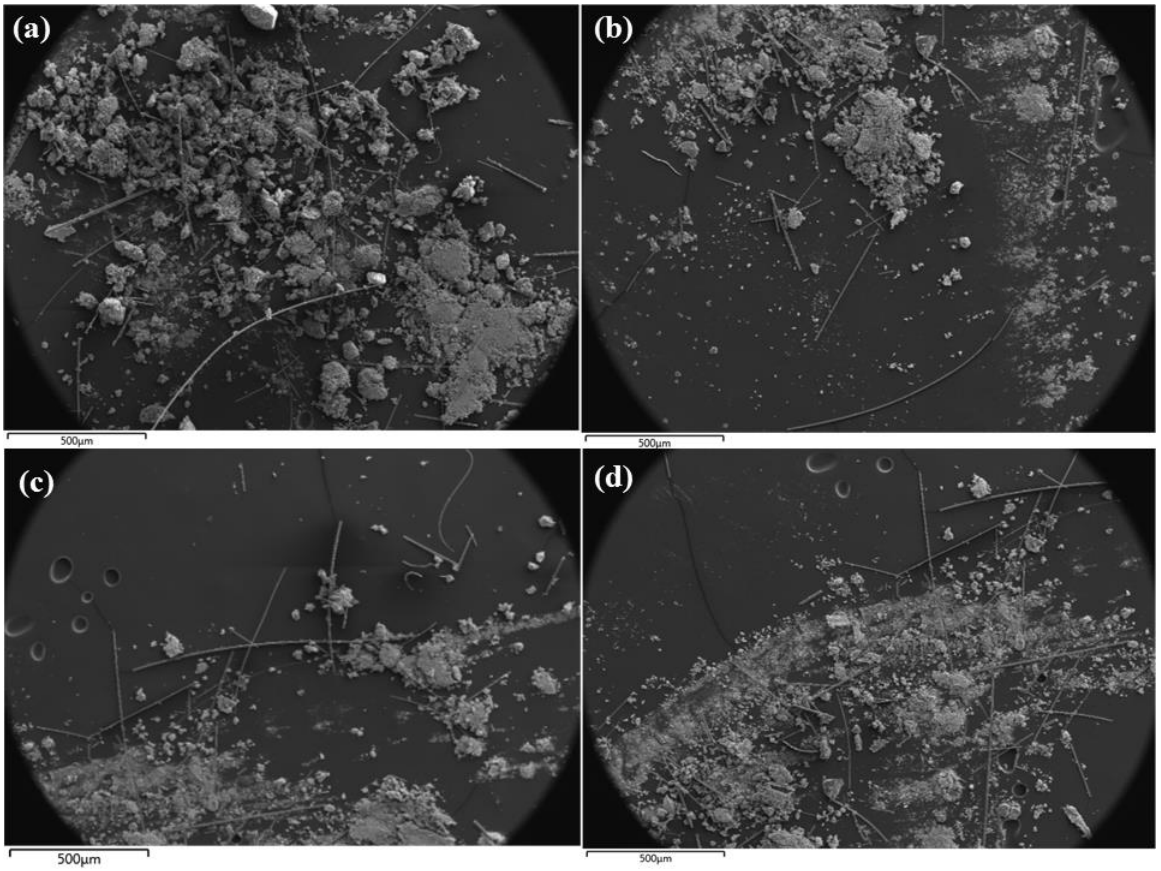

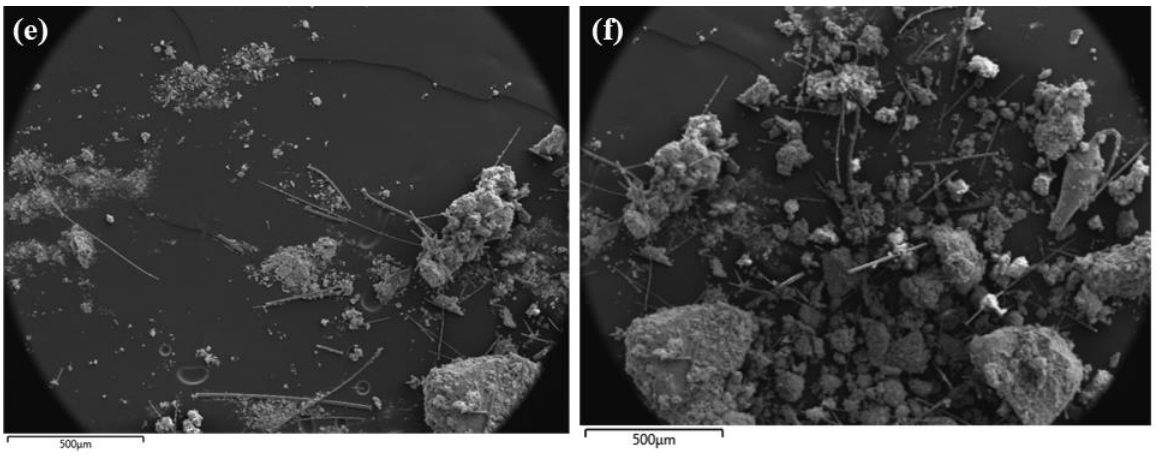
(e)
500µm
(f)
500µm

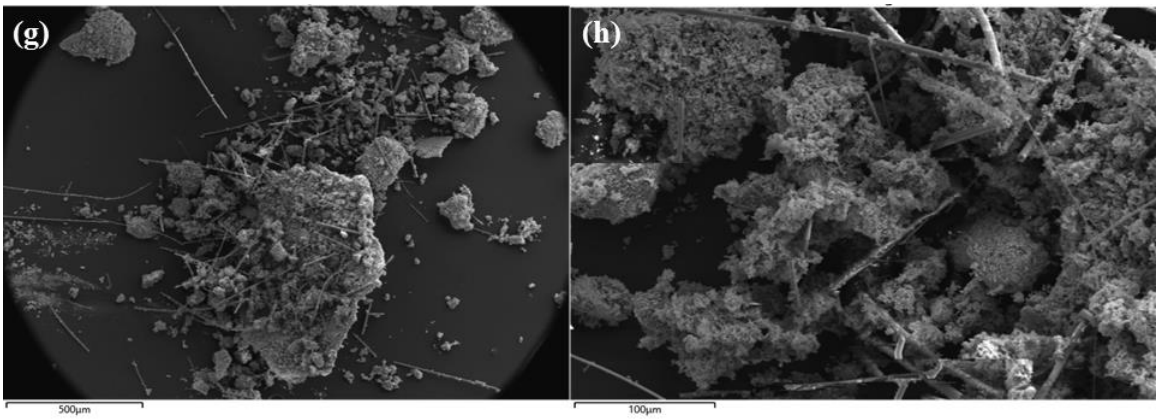
(g)
500µm
(h)
100µm

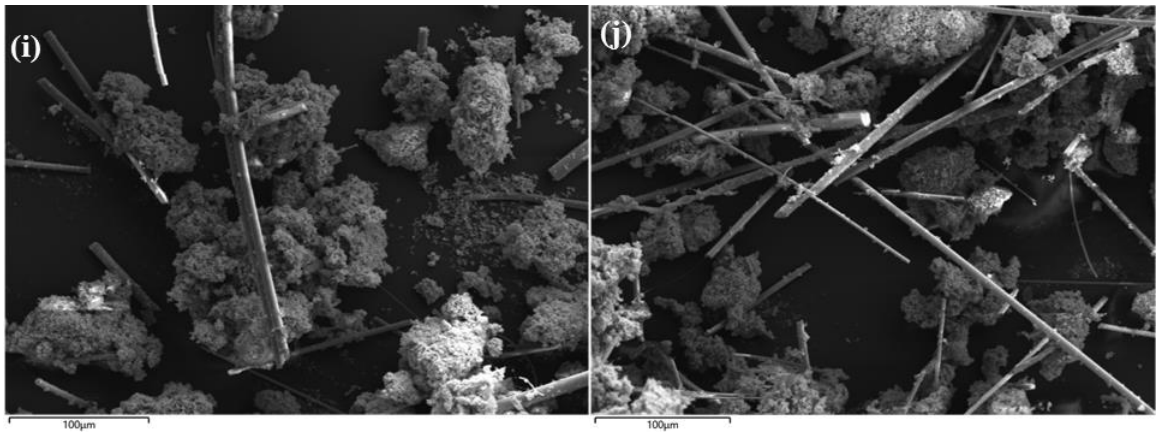
(i)
100µm
(j)
100µm

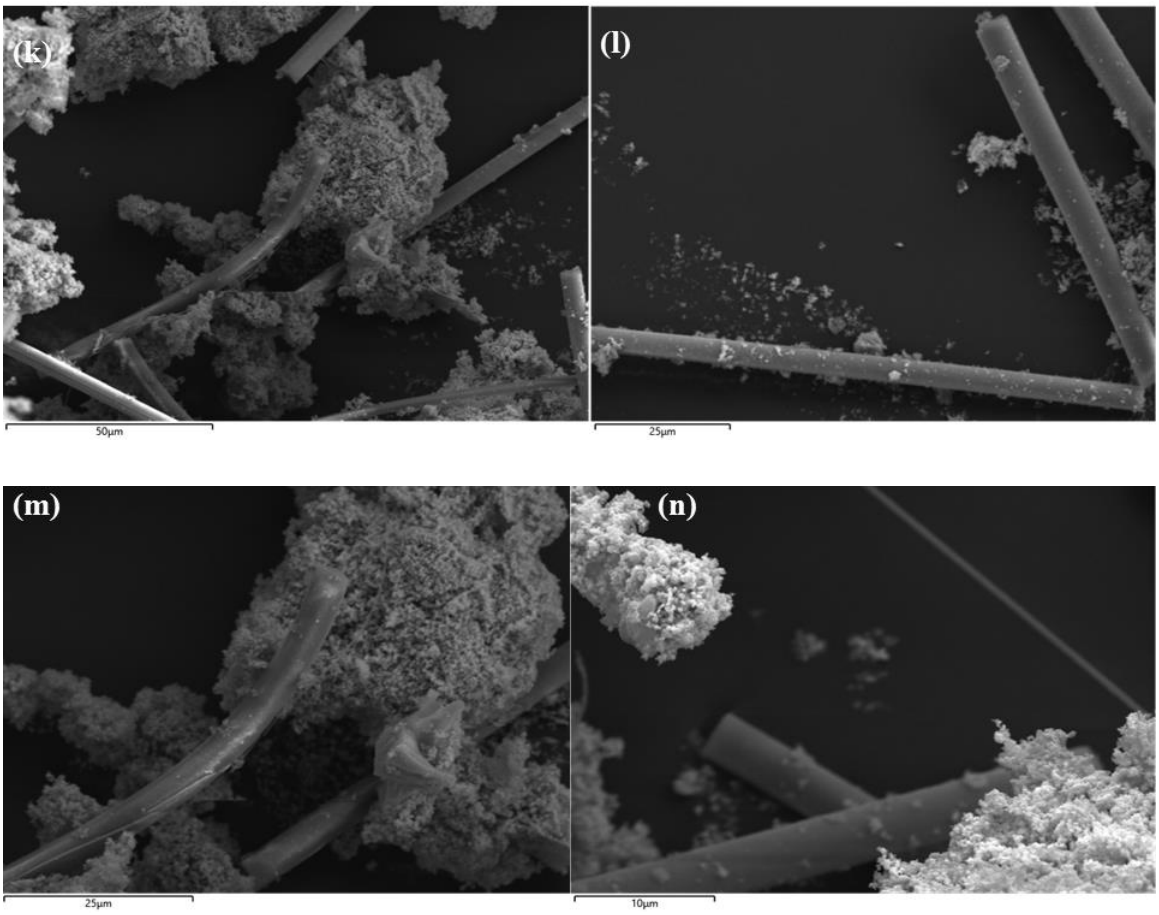

Fig S20. SEM images of reduced BIOX 700 °C 1 h H_2/N_2 (**a-n**).

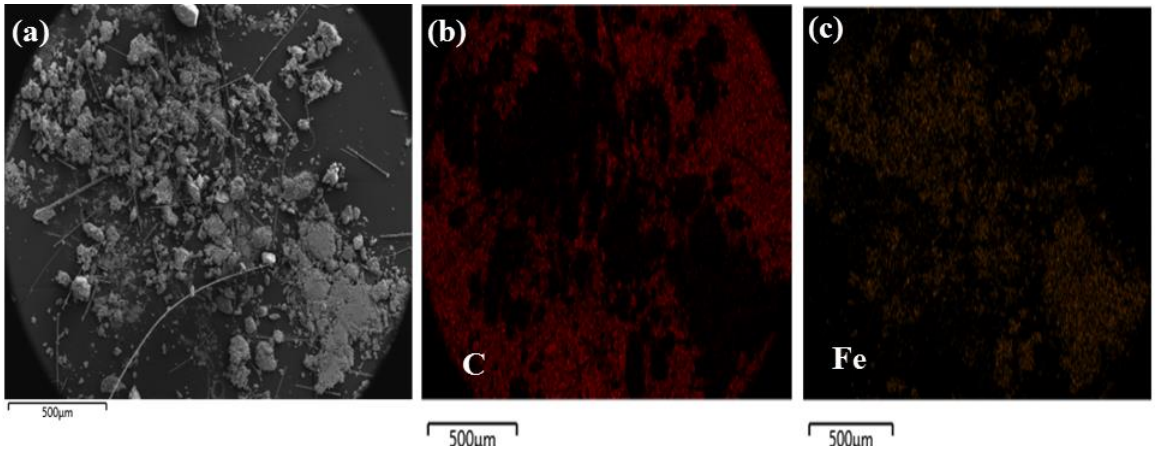

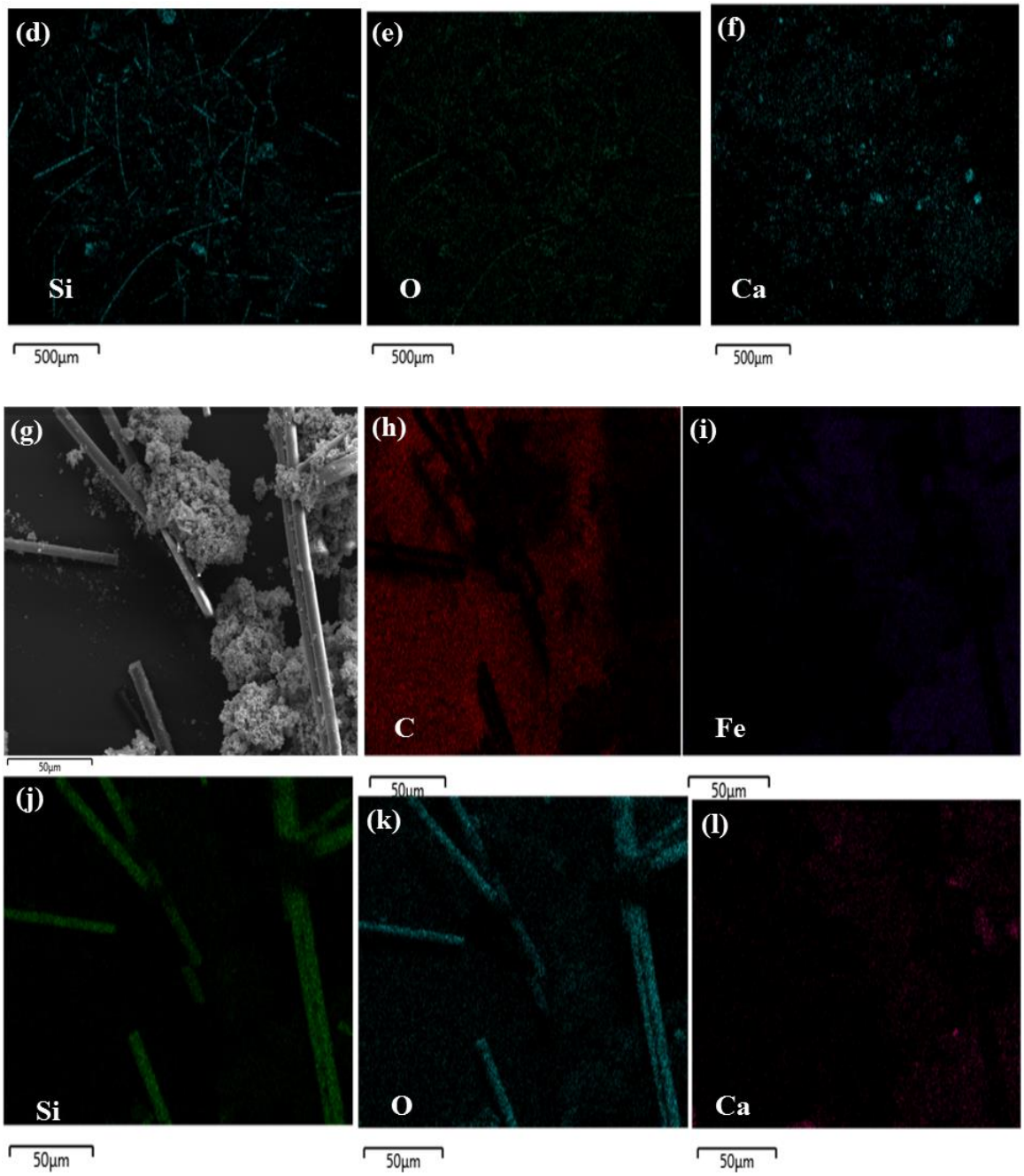

Fig S21. SEM images of reduced BIOX 700 °C 1 h H_2/N_2 (**a** and **g**) and their elemental mapping; (**b-f**) and (**h-l**).

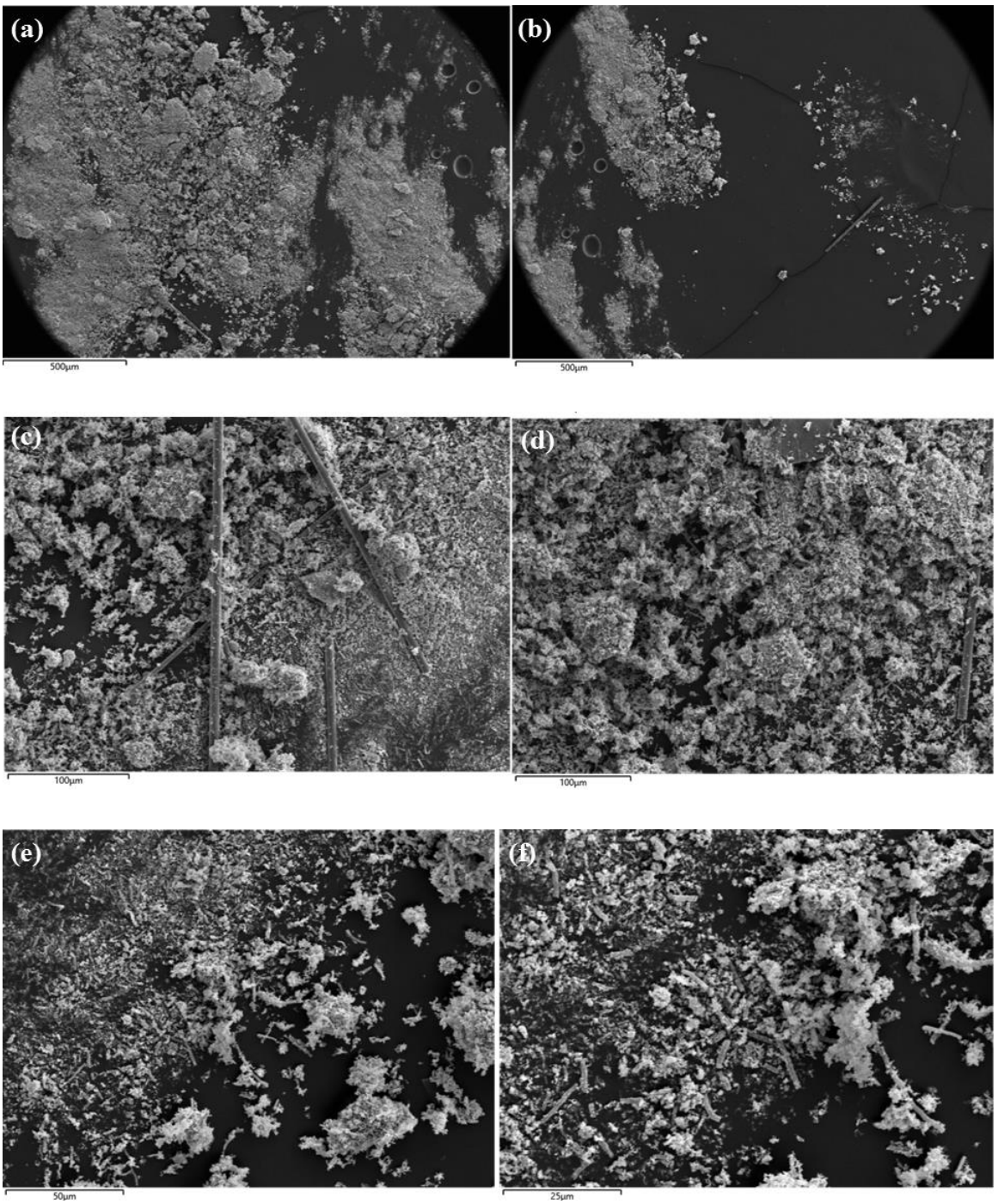
(a)
500µm
(b)
500µm
(c)
100µm
(d)
100µm
(e)
50µm
(f)
25µm

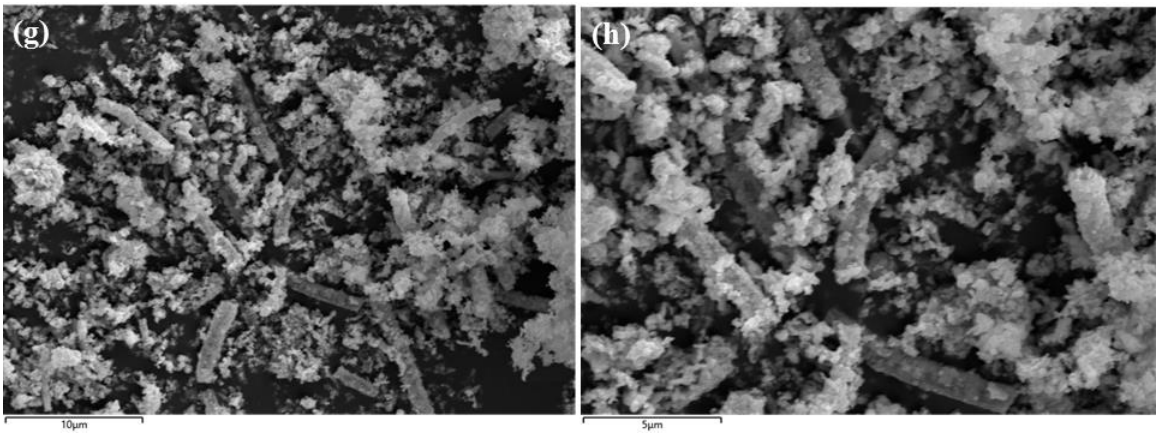

Fig S22. SEM images of reduced BIOX 700 °C 4 h H_2/N_2 (**a-h**).

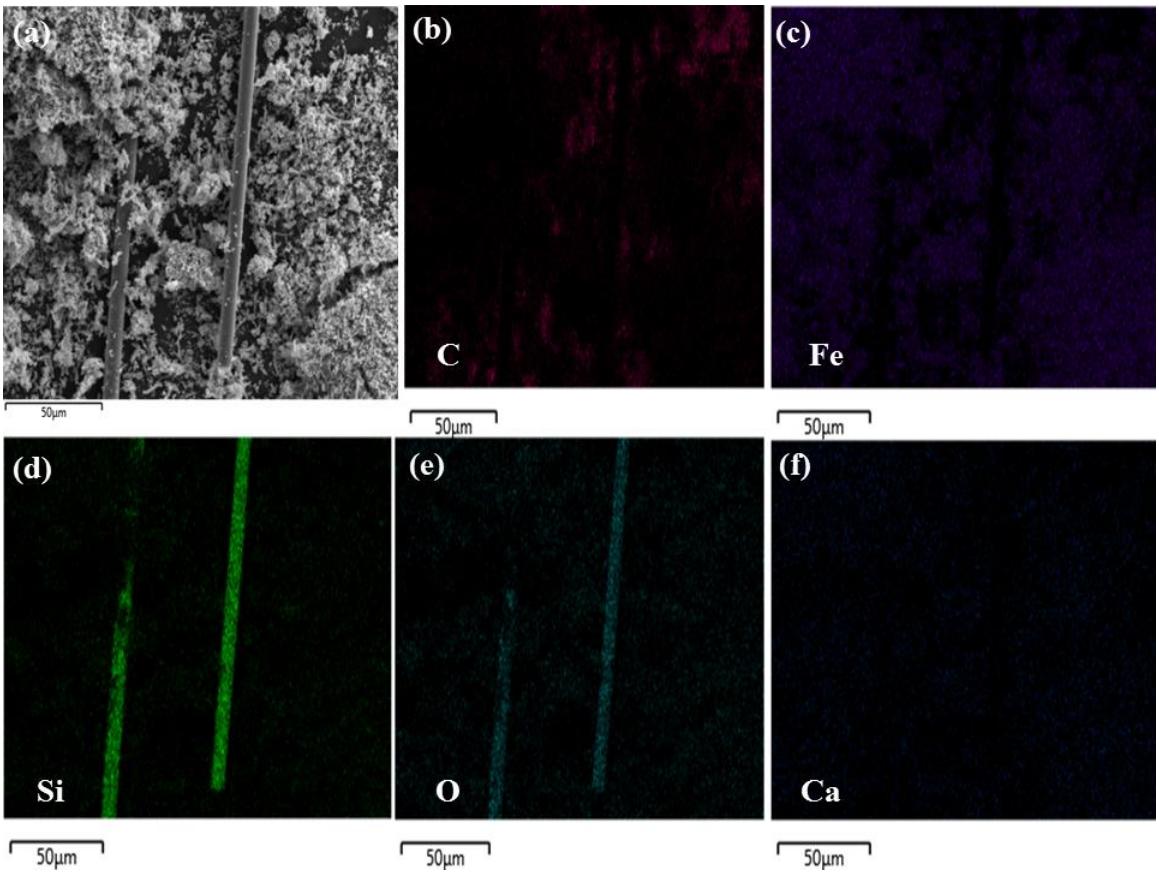

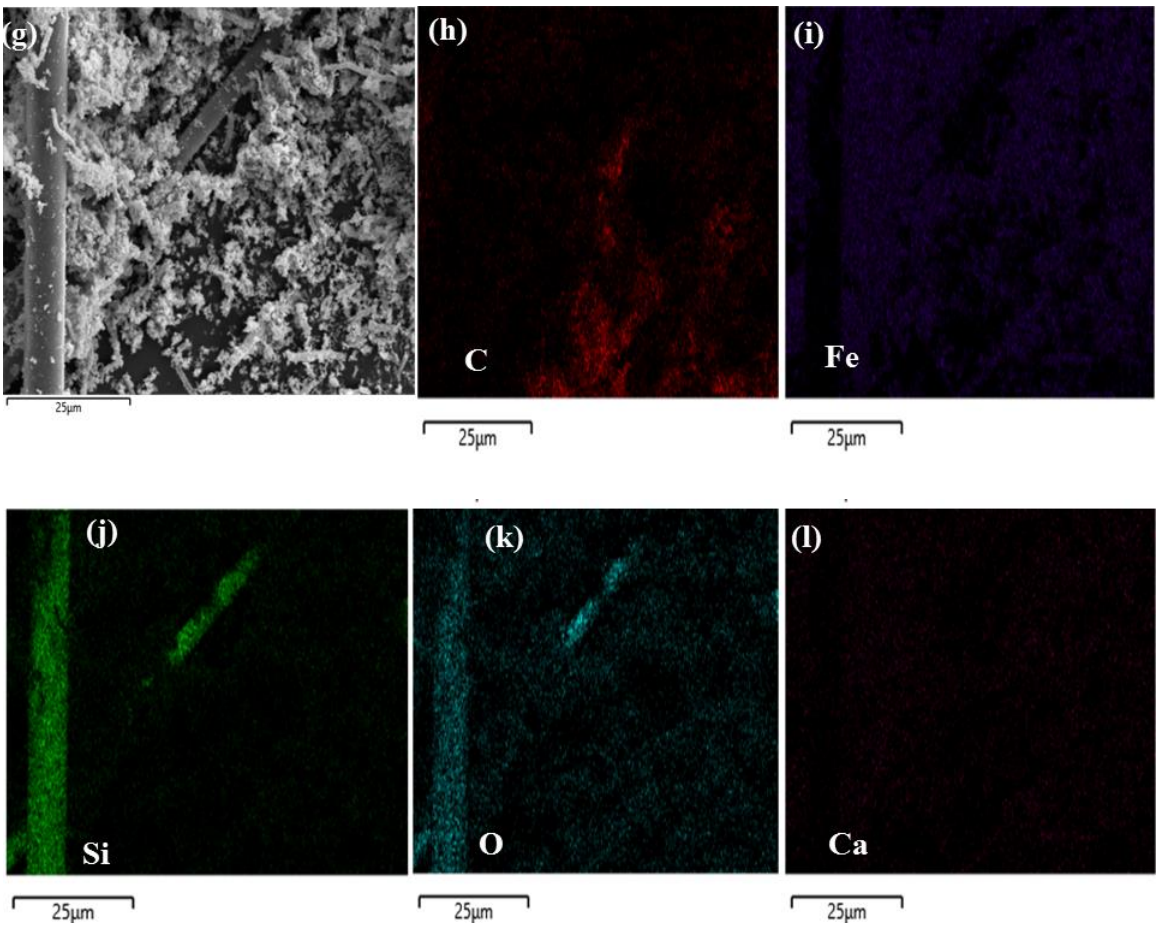

Fig S23. SEM images of reduced BIOX 700 °C 4 h H_2/N_2 (**a** and **g**) and their elemental mapping; (**b-f**) and (**h-l**).

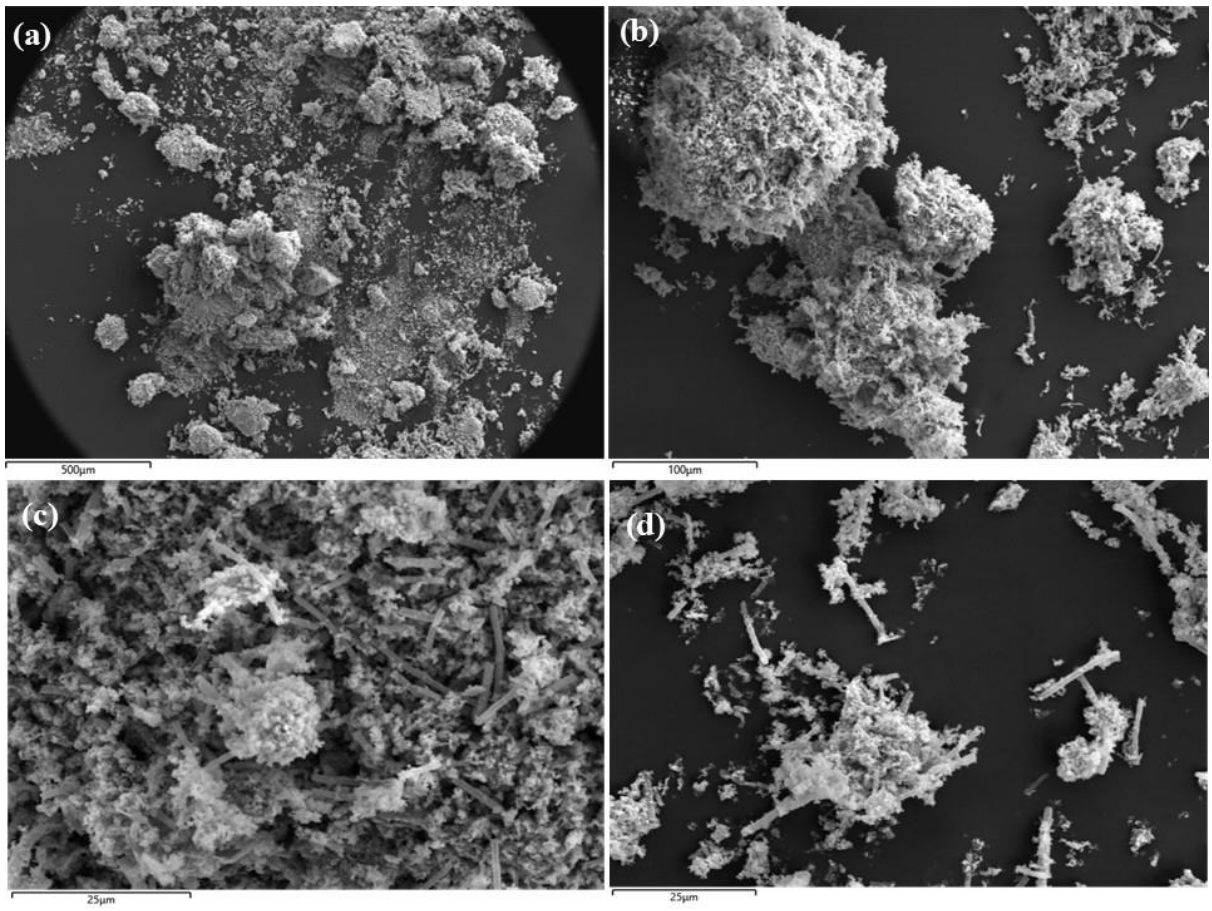
(a)
500µm
(b)
100µm
(c)
25µm
(d)
25µm

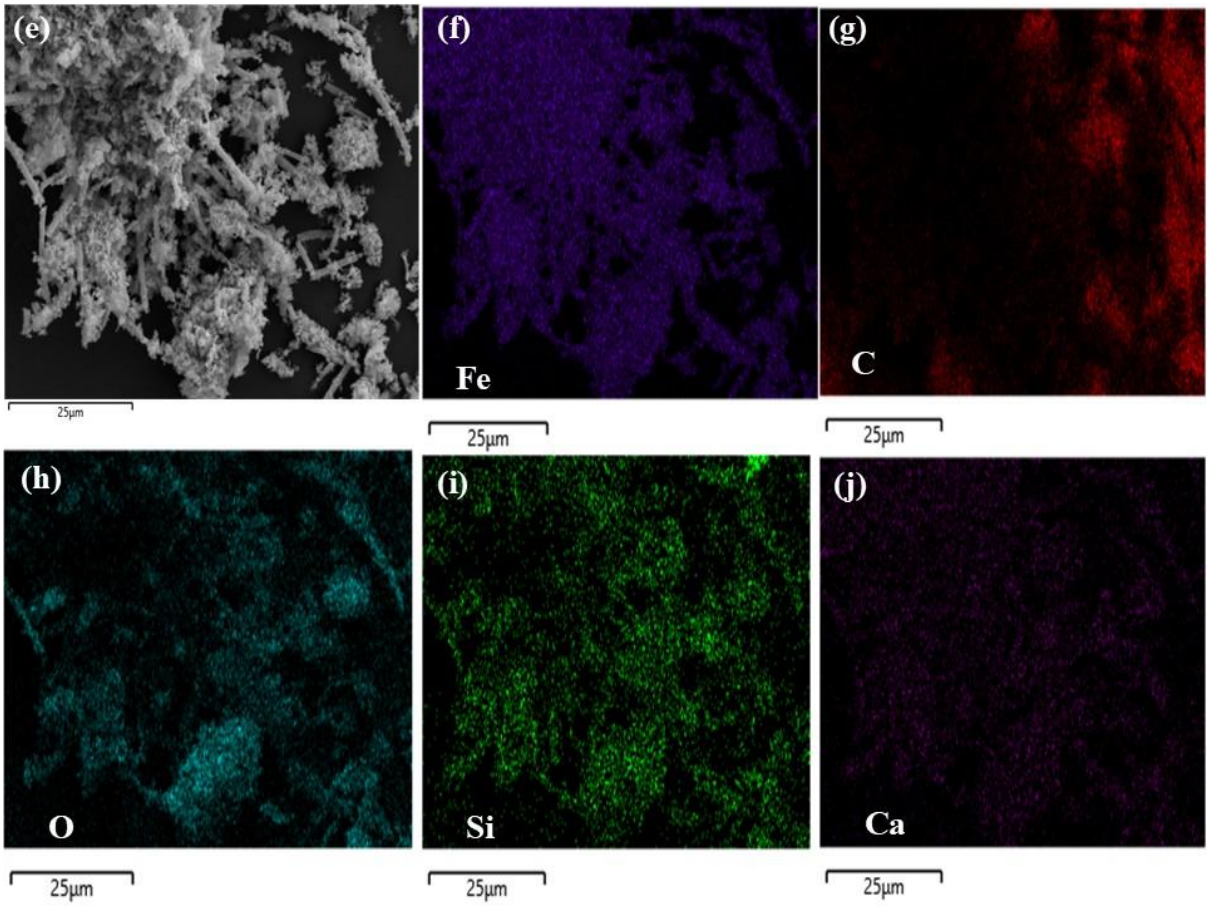
(e)
25μm
(f)
Fe
25μm
(g)
C
25μm
(h)
O
25μm
(i)
Si
25μm
(j)
Ca
25μm

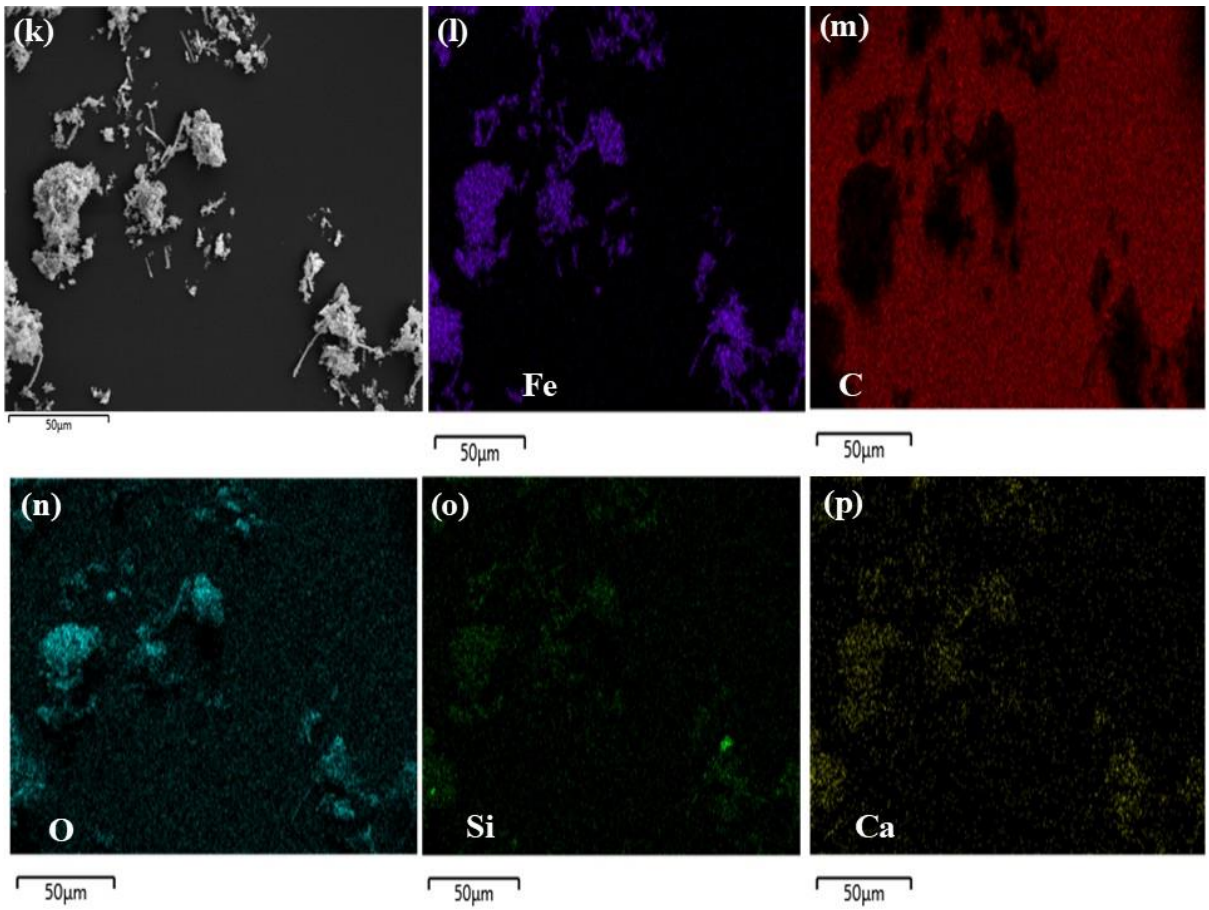

Fig S24. SEM images of reduced BIOX 500 °C 1 h H_2/N_2 (**a-d**) and other images (**e** and **k**) with their elemental mapping; (**f-j**) and (**l-p**) using the sample collected during the summertime.